

INVESTIGATION ON THE MITIGATION OF EARTHQUAKE HAZARDS WITH
INCLUSION OF TIRE WASTES INTO THE SAND

by

Özgür Yıldız

B.S., Civil Engineering, Yıldız Technical University, 2005

Submitted to the Institute for Graduate Studies in
Science and Engineering in partial fulfillment of
the requirements for the degree of

Master of Science

Graduate Program in Civil Engineering

Bogaziçi University

2011

INVESTIGATION ON THE MITIGATION OF EARTHQUAKE HAZARDS WITH
INCLUSION OF TIRE WASTES INTO THE SAND

APPROVED BY:

Assoc. Prof. Ayse Edinçliler

(Thesis Supervisor)

Prof. Gökhan Baykal

(Thesis Co-Supervisor)

Prof. Ayfer Erken

Prof. Erol Güler

Assoc. Prof. İsmail Hakkı Aksoy

DATE OF APPROVAL: 15.06.2011

ACKNOWLEDGEMENTS

First of all, I would like to thank my thesis supervisor, Assoc. Prof. Ayse Edinçliler for her assistance, advices and motivating approaches in all stages of my thesis studies. Working with her has been a very special experience. Her guidance, encouragement, excitement, dedication and trust have helped to create this thesis.

I would like to specifically thank Prof. Ayfer Erken, Civil Engineer Araz Torabi and Civil Engineer Aytaç Yaşargün for their help and great support.

I would like to thank my committee members; Prof. Gökhan Baykal, Prof. Erol Güler and Assoc. Prof. İsmail Hakkı Aksoy for their time and contributions.

Especially, I would like to thank my manager Mr. Ahmet Erhan Gökcal for his great support and understanding.

I am very grateful to Electric-Electronic Engineer Oktay Çırağ for his ineffable support, generous help and endless cooperation.

Finally, I would like to thank all my family and friends who stood behind me during my study, for I would not be able to accomplish this thesis without their support.

This thesis has been supported by Bogazici University Scientific Research Project with 09T102P project code.

ABSTRACT

INVESTIGATION ON THE MITIGATION OF EARTHQUAKE HAZARDS WITH INCLUSION OF TIRE WASTES INTO THE SAND

With the development of technology, tire wastes disposed in the environment, cause serious problems. In the 21st century, cost, environment and seismic performance are going to be most important factors in the design, construction and retrofitting of structures against to earthquake loadings. Tire wastes have many properties which result in their being of value from a civil and geotechnical engineering perspective: low density, high strength, thermal insulation, energy absorption capacity, permeability, durability, compressibility, resilience and high frictional strength. It is due to these properties, the use of tire wastes are yet to be exploited in common civil engineering applications such as lightweight material for backfill of retaining structures, drainage layer, thermal insulation layer or seismic isolation layer. Also, it is well known to utilize tire waste derived recycled scrap tires to minimize the earthquake related hazards of structures. The main objective of this study is to develop a new technique to mitigate earthquake induced liquefaction hazards by utilizing different tire waste with different ratios, shapes and aspect ratios. In this study, a series of laboratory tests are performed to evaluate the liquefaction susceptibility of soil and to determine engineering properties of specimens. A flexible shear stack is designed and constructed to be used in shaking table tests. A set of shaking table tests is performed at different temperatures to investigate the liquefaction mitigation effect of tire waste inclusion under different thermal conditions. These shaking table tests are conducted at Shaking Table Laboratory of Kandilli Observatory and Earthquake Research Institute. As a result of these laboratory studies, the liquefaction mitigation effect of different type of tire wastes are investigated. The test results also demonstrated that the proposed mitigation method not only minimizes liquefaction effect but also reduces the earthquake induced permanent displacement of structures.

ÖZET

ATIK LASTİK İLAVELERİNİN KUMUN SIVILAŞMASINI AZALTMADAKİ ETKİLERİNİN İNCELENMESİ

Teknolojinin gelişimi ile atık lastik birikimi doğada ciddi problemlere yol açmıştır. 21. yüzyılda maliyet, çevre ve sismik performans, yapıların depreme karşı dizaynı, inşaatı ve güçlendirmesinde en önemli faktörler olma yolundadır. Düşük yoğunluk, yüksek mukavemet, düşük ısı iletimi, permeabilite, uzun ömürlülük, sıkıştırılabilme, esneklik ve yüksek sürtünme mukavemeti atık lastikleri inşaat ve geoteknik mühendisliği açısından değerli kılan özelliklerdir. Bu özellikleri nedeniyle, inşaat mühendisliği uygulamalarında atık lastiklerin kullanımı, özellikle istinat yapılarının geridolguları için hafif dolgu malzemesi, drenaj tabakası, termal yalıtım, güçlendirme tabakası olarak kullanılmak amacıyla önerilir. Atık lastiklerin, deprem zararlarını azaltmada kullanımı da yaygın olarak bilinen bir değerlendirme biçimidir. Bu çalışmanın esas amacı, atık lastikleri farklı en/boy oranı, şekil ve birleşim oranlarında kullanarak deprem hasarlarını azaltmada yeni bir method geliştirmektir. Bu çalışma dahilinde, zeminin sivilaşma etkilerini ölçmek ve mühendislik özelliklerini belirlemek amacıyla bir dizi laboratuvar testi yapılmıştır. Esnek Numune Kutusu dizayn ve imal edilmiştir. Farklı sıcaklık değerleri altında bir dizi sarsma masası testi yapılmıştır. Sarsma masası testleri Kandilli Rasathanesi Deprem Araştırma Enstitüsü laboratuvarında gerçekleştirilmiştir. Bu laboratuvar çalışmaları sonucunda atık lastiklerin zemin sivilaşmasını azaltma etkileri incelenmiştir. Test sonuçları, uygulanan methodun yalnızca sivilaşma etkilerini azaltmakla kalmadığı, aynı zamanda yapılarda deprem sonucu oluşan yer değiştirmeleri de azalttığı görülmüştür.

TABLE OF CONTENTS

ACKNOWLEDGEMENTS	iii
ABSTRACT	iv
ÖZET	v
LIST OF FIGURES	vi
LIST OF TABLES	xxxii
LIST OF SYMBOLS	xxxiii
LIST OF ACRONYMS/ABBREVIATIONS	xxxiv
1. INTRODUCTION	1
1.1. General	1
1.2. Problem Statement	2
1.3. Objective of the Thesis.....	2
1.4. Organization of Thesis	2
2. LITERATURE REVIEW	3
2.1. General Information About Scrap Tires.....	3
2.2. Enviromental Problems with Scrap Tire	5
2.2.1. Tire Fires.....	5
2.2.2. Health Hazards.....	6
2.3. Material Properties of Scrap Tires	7
2.3.1. Physical Properties.....	7
2.3.2. Chemical Properties	9
2.3.3. Mechanical Properties.....	9
2.3.4. Engineering Properties.....	9
2.3.5. Thermal Properties.....	11
2.4. Tire Waste Utilization Fields	13
2.4.1. Tire Derived Fuel.....	14

2.4.2.	Ground Rubber Applications	15
2.4.3.	Civil Engineering Applications	16
2.4.4.	Case Histories of Geotechnical Uses of Scrap Tires	19
2.5.	Scrap Tire as a Geomaterial	26
2.6.	Improvement of Soil Properties with Scrap Tire	26
2.7.	Unresolved Issues.....	26
2.8.	Scrap Tire Management Options	27
3.	GENERAL INFORMATION ABOUT TIRE WASTE INCLUSIONS	28
3.1.	Previous Studies of Direct Shear Tests	28
3.2.	Previous Studies on Dynamic Laboratory Tests	36
4.	LIQUEFACTION.....	38
4.1.	General Information About Liquefaction.....	38
4.2.	Liquefaction Susceptibility of Soils	41
4.3.	Soil Liquefaction and Ground Failures	43
4.4.	Main Factors that Govern Liquefaction of The Field	43
4.4.1.	Earthquake Intensity and Duration	43
4.4.2.	Groundwater Table	43
4.4.3.	Soil Type.....	44
4.4.4.	Soil Relative Density	44
4.4.5.	Particle Size Gradation	44
4.4.6.	Placement Conditions or Depositional Environment.....	45
4.4.7.	Confining Pressure.....	45
4.4.8.	Particle Shape	46
4.4.9.	Aging and Cementation	46
4.4.10.	Historical Environment.....	46
4.4.11.	Building Load	46

4.5.	Methods to Evaluate The Liquefaction Potential of a Site	46
4.6.	Methods to Reduce Liquefaction Hazards	48
4.7.	Sample Preparation Methods applied in Liquefaction Tests.....	52
4.8.	Background on Liquefaction Tests	54
5.	MODELLING TECHNIQUES	60
5.1.	Numerical Modelling	62
5.2.	Physical Modelling.....	63
5.2.1.	Centrifuge Model Tests	65
5.2.2.	Shaking Table Model Tests	66
5.3.	Modelling in Geotechnical Engineering	68
5.3.1.	Physical Modelling of Flexible Shear Boxes.....	71
5.3.2.	Design of a Flexible Shear Box	72
5.3.3.	Performance Criteria of the Flexible Shear Stack	73
5.3.4.	Previous Studies of Shaking Table Model Tests	74
6.	EXPERIMENTAL PROGRAM.....	81
6.1.	General	81
6.1.1.	Geotechnical Laboratory Tests	81
6.2.	Materials Used in Experiments	82
6.2.1.	Sand	82
6.2.2.	Tire Waste Material	83
6.2.3.	Unit Weight Determination Tests	86
6.2.4.	California Bearing Ratio (CBR) Tests.....	89
6.2.5.	Direct Shear Tests	91
6.2.6.	Specific Gravity Test	94
6.3.	Dynamic Laboratory Tests	95
6.3.1.	Principles of Cyclic Triaxial Test	96

6.3.2.	Cyclic Triaxial Test Apparatus	97
6.3.3.	Sample Preparation	98
6.3.4.	Cyclic Triaxial Test Procedure	99
6.4.	Numerical Design of Shear Stack	100
6.5.	Shaking Table Tests	101
6.5.1.	Sample Preparation	102
6.5.2.	Preparation of Test Set Up.....	102
6.5.3.	Shaking Table Test Procedure	103
7.	EXPERIMENTAL RESULTS	108
7.1.	California Bearing Ratio (CBR) Test Results	108
7.1.1.	Analysis of California Bearing Ratio Test Results.....	108
7.1.2.	Direct Shear Test Results.....	111
7.1.3.	100% Sand	111
7.1.4.	100% Tire Crumbs.....	113
7.1.5.	5% Tire Crumbs.....	114
7.1.6.	10% Tire Crumbs.....	116
7.1.7.	15% Tire Crumbs.....	117
7.1.8.	20% Tire Crumbs.....	119
7.1.9.	30% Tire Crumbs.....	120
7.1.10.	40% Tire Crumbs.....	122
7.1.11.	100% Tire Buffings	123
7.1.12.	5% Tire Buffings	125
7.1.13.	10% Tire Buffings	127
7.1.14.	15% Tire Buffings	128
7.1.15.	20% Tire Buffings	130
7.1.16.	30% Tire Buffings	131

7.1.17. 40% Tire Buffings	133
7.1.18. Analysis of Direct Shear Test Results	134
7.2. Analysis of Geotechnical Laboratory Tests	139
7.3. Cyclic Triaxial Test Results	141
7.3.1. Sand Material	143
7.3.2. TB-Sand Mixtures.....	144
7.3.3. TC-Sand Mixtures.....	155
7.3.4. Analysis of Cyclic Triaxial Laboratory Tests.....	166
7.4. Shaking Table Test Results	171
7.4.1. Tests Performed Under 0°C Temperature	173
7.4.2. Tests Performed Under Room Temperature	193
7.4.3. Tests Performed at 50°C	213
7.4.4. Analysis of Shaking Table Test Results	232
7.5. Discussion of Results.....	241
8. CONCLUSION AND RECOMMENDATIONS	246
APPENDIX A: SHAKING TABLE TEST RESULTS OF SAKARYA (N-S)	
GROUND MOTIONS.....	249
APPENDIX B: SHAKING TABLE TEST RESULTS OF TABAS (N-S)	
GROUND MOTIONS	317
REFERENCES.....	385

LIST OF FIGURES

Figure 2.1.	An example of tire waste stockpile	3
Figure 2.2.	Millions of Scrap Tires Remaining in U.S. Stockpiles, 1990-2005 (RMA, 2006)	4
Figure 2.3.	Disposal, recycled and reused amount of tire waste (Washington Department of Ecology, 2010)	5
Figure 2.4.	Recycle, Reuse or Disposal Alternatives for Scrap Tires (UNCTAD secretariat and OECD, 1998)	6
Figure 2.5.	Example of different shapes and sizes of processed tires (Çağatay, 2008)	8
Figure 2.6.	The compressive strength variation before and after 50 cycles of freezing- thawing test (Turgut and Yesilata, 2007)	13
Figure 2.7.	Scrap Tire Market Trends, 1990-2005, (RMA, 2006)	14
Figure 2.8.	Co-processing tire derived fuel	15
Figure 2.9.	Schematic cross-section of an embankment constructed with tire shreds and sand (Yoon <i>et al.</i> , 2008)	17
Figure 2.10.	Tire chip-seal construction	18
Figure 4.1.	Earthquake hazards caused by liquefaction	41
Figure 4.2.	Liquefaction Susceptibility Chart of Soils (Tsuchida, 1970)	45
Figure 4.3.	Conditions assumed for the derivation of the CSR earthquake equation.....	47
Figure 4.4.	Sample Preparation Methods (Ishihara, 1994)	54
Figure 4.5.	Pluvator for specimen preparation (Ueng <i>et al.</i> , 2006)	55
Figure 4.6.	Measurement of the settlements after liquefaction test (Ueng <i>et al.</i> , 2009)	56
Figure 4.7.	Example of partially saturated specimen (Yegian <i>et al.</i> , 2006)	57

Figure 4.8.	Sand pluviation system and model sand column seated on shaking table (Özener <i>et al.</i> , 2009)	58
Figure 5.1.	Reflective practice loop (Blockley, 1992)	61
Figure 5.2.	Beam Centrifuge Test Machine	66
Figure 5.3.	Drum Centrifuge Test Machine	66
Figure 5.4.	Shaking Table Test Machine	67
Figure 5.5.	Mass Components (Hack <i>et al.</i> , 2006)	69
Figure 5.6.	Laminar Shear Box (Ueng <i>et al.</i> , 2006)	71
Figure 5.7.	Shear Stack concept (Crewe <i>et al.</i> , 1995)	73
Figure 5.8.	Semi-infinite soil deposit movement (Crewe <i>et al.</i> , 1995)	74
Figure 6.1.	Grain size distribution of the sand	82
Figure 6.2.	Sand used in experiments	83
Figure 6.3.	Grain size distribution of the Tire Crumbs Material	83
Figure 6.4.	Tire Crumbs material	84
Figure 6.5.	Grain size distribution of Tire Buffings	84
Figure 6.6.	Tire Buffings used in the experiments	85
Figure 6.7.	Tire Buffings and Tire Crumbs materials	85
Figure 6.8.	Sieves used in experiments	86
Figure 6.9.	Compaction Mold and Hammer	86
Figure 6.10.	CBR Machine	91
Figure 6.11.	Direct Shear Test Machine	92
Figure 6.12.	Volumetric flask with sand-water, tire crumbs-water and tire buffings-water mixtures	94
Figure 6.13.	Triaxial Test Machine	96
Figure 6.14.	Triaxial Test Apparatus	98

Figure 6.15. Schematic figure of Triaxial Test Machine (http://www.astm.org/Standards/D5311.htm)	98
Figure 6.16. View of Flexible Shear Stack used in tests	102
Figure 6.17. Instrumentation on shaking Table Model	107
Figure 7.1. CBR vs. Tirepercentage of materials	111
Figure 7.2. Shear Stress vs. Horizontal Displacement Graph of Sand	112
Figure 7.3. Shear Stress vs. Normal Stress graph of Sand	112
Figure 7.4. Shear Stress vs. Horizontal Displacement Graph of TC	113
Figure 7.5. Shear Stress vs. Normal Stress graph of TC	114
Figure 7.6. Shear Stress vs. Horizontal Displacement Graph of TC5	115
Figure 7.7. Shear Stress vs. Normal Stress graph of TC5	115
Figure 7.8. Shear Stress vs. Horizontal Displacement Graph of TC10	116
Figure 7.9. Shear Stress vs. Normal Stress graph of TC10	117
Figure 7.10. Shear Stress vs. Horizontal Displacement Graph of TC15	118
Figure 7.11. Shear Stress vs. Normal Stress graph of TC15	118
Figure 7.12. Shear Stress vs. Horizontal Displacement Graph of TC20	119
Figure 7.13. Shear Stress vs. Normal Stress graph of TC20	120
Figure 7.14. Shear Stress vs. Horizontal Displacement Graph of TC30	121
Figure 7.15. Shear Stress vs. Normal Stress graph of TC30.....	121
Figure 7.16. Shear Stress vs. Horizontal Displacement Graph of TC40	122
Figure 7.17. Shear Stress vs. Normal Stress graph of TC40	123
Figure 7.18. Shear Stress vs. Horizontal Displacement Graph of TB	124
Figure 7.19. Shear Stress vs. Normal Stress graph of TB	124
Figure 7.20. 20% tire buffings-sand specimen tested in direct shear test machine .	125
Figure 7.21. Shear Stress vs. Horizontal Displacement Graph of TB5	126
Figure 7.22. Shear Stress vs. Normal Stress graph of TB5	126

Figure 7.23.	Shear Stress vs. Horizontal Displacement Graph of TB10	127
Figure 7.24.	Shear Stress vs. Normal Stress graph of TB10	128
Figure 7.25.	Shear Stress vs. Horizontal Displacement Graph of TB15	129
Figure 7.26.	Shear Stress vs. Normal Stress graph of TB15	129
Figure 7.27.	Shear Stress vs. Horizontal Displacement Graph of TB20	130
Figure 7.28.	Shear Stress vs. Normal Stress graph of TB20	131
Figure 7.29.	Shear Stress vs. Horizontal Displacement Graph of TB30	132
Figure 7.30.	Shear Stress vs. Normal Stress graph of TB30	132
Figure 7.31.	Shear Stress vs. Horizontal Displacement Graph of TB40	133
Figure 7.32.	Shear Stress vs. Normal Stress graph of TB40	134
Figure 7.33.	Cohesion vs. Tire percentages for all samples	136
Figure 7.34.	Internal Friction Angle vs. Tire percentages for all samples	136
Figure 7.35.	Damping Ratio vs. Shear Strain curve for only sand	143
Figure 7.36.	Shear Modulus vs. Shear Strain curve for only sand	144
Figure 7.37.	Damping Ratio vs. Shear Strain curve for TB 10 specimen	145
Figure 7.38.	Shear Modulus vs. Shear Strain curve for TB 10 specimen	145
Figure 7.39.	Damping Ratio vs. Shear Strain curve for TB 20	146
Figure 7.40.	Shear Modulus vs. Shear Strain curve for TB 20	147
Figure 7.41.	Damping Ratio vs. Shear Strain curve for TB 30	148
Figure 7.42.	Shear Modulus vs. Shear Strain curve for TB 30	148
Figure 7.43.	Damping Ratio vs. Shear Strain curves for all tire buffings–sand mixtures	149
Figure 7.44.	Shear Modulus vs. Shear Strain curve for all tire buffings–sand mixtures	150
Figure 7.45.	Damping Ratio vs. Shear Strain curves for tire buffings –sand mixtures under 40 kPa. confining pressure	151

Figure 7.46. Shear Modulus vs. Shear Strain curves for tire buffings–sand mixtures under 40 kPa. confining pressure 151

Figure 7.47. Damping Ratio vs. Shear Strain curves for tire buffings –sand mixtures under 100 kPa. confining pressure 152

Figure 7.48. Shear Modulus vs. Shear Strain curves for tire buffings –sand mixtures under 100 kPa. confining pressure 153

Figure 7.49. Damping Ratio vs. Shear Strain curves for tire buffings –sand mixtures under 200 kPa. confining pressure 154

Figure 7.50. Shear Modulus vs. Shear Strain curves for tire buffings –sand mixtures under 200 kPa. confining pressure 154

Figure 7.51. Damping Ratio vs. Shear Strain curve for TC10 156

Figure 7.52. Shear Modulus vs. Shear Strain curve for TC10 156

Figure 7.53. Damping Ratio vs. Shear Strain curve for TC 20 157

Figure 7.54. Shear Modulus vs. Shear Strain curve for TC 20 158

Figure 7.55. Damping Ratio vs. Shear Strain curve for TC 30 159

Figure 7.56. Shear Modulus vs. Shear Strain curve for TC 30 159

Figure 7.57. Damping Ratio vs. Shear Strain curves for tire crumbs–sand mixtures 160

Figure 7.58. Shear Modulus vs. Shear Strain curves for tire crumbs–sand mixtures 161

Figure 7.59. Damping Ratio vs. Shear Strain curves for tire crumbs –sand mixtures under 40 kPa confining pressure 162

Figure 7.60. Shear Modulus vs. Shear Strain curves for tire crumbs–sand mixtures under 40 kPa confining pressure 162

Figure 7.61. Damping Ratio vs. Shear Strain curves for tire crumbs –sand mixtures under 100 kPa confining pressure 163

Figure 7.62. Shear Modulus vs. Shear Strain curves for tire crumbs –sand mixtures under 100 kPa confining pressure 164

Figure 7.63.	Damping Ratio vs. Shear Strain curves for Tire Crumbs–Sand mixtures under 200 kPa confining pressure	165
Figure 7.64.	Shear Modulus vs. Shear Strain curves for tire crumbs–sand mixtures under 200 kPa confining pressure	165
Figure 7.65.	Damping Ratio vs. Shear Strain curves for all tests	168
Figure 7.66.	Shear Modulus vs. Shear Strain curves for all tests	169
Figure 7.67.	Acceleration time history of İzmit (E-W) Earthquake Ground Motion.....	172
Figure 7.68.	Acceleration time history of Sakarya (N-S) Earthquake Ground Motion	172
Figure 7.69.	Acceleration time history of Tabas (E-W) Earthquake Ground Motion	173
Figure 7.70.	A1, acceleration time history of sand specimen tested under 0°C ..	174
Figure 7.71.	Sand specimen tested under 0°C ..	174
Figure 7.72.	Pore water pressure distribution of sand specimen tested under 0°C ..	175
Figure 7.73.	Time histories of accelerations of sand specimen tested under 0°C ..	175
Figure 7.74.	Displacement time history of sand specimen tested under 0°C	176
Figure 7.75.	A1, acceleration time history of TB10 specimen tested under 0°C ..	176
Figure 7.76.	Pore water pressure distribution of TB10 specimen tested under 0°C ..	177
Figure 7.77.	Time histories of accelerations of TB10 specimen tested under 0°C	177
Figure 7.78.	Displacement time history of TB10 specimen tested under 0°C	178
Figure 7.79.	TB15 specimen tested on shaking table below 0°C	178
Figure 7.80.	A1, acceleration time history of TB15 specimen tested under 0°C ..	179
Figure 7.81.	Pore water pressure distribution of TB15 specimen tested under 0°C ..	179

Figure 7.82.	Time histories of accelerations of TB15 specimen tested under 0°C...	180
Figure 7.83.	Displacement time history of TB15 specimen tested under 0°C	180
Figure 7.84.	A1, acceleration time history of TB20 specimen tested under 0°C...	181
Figure 7.85.	Pore water pressure distribution of TB20 specimen tested under 0°C	182
Figure 7.86.	Time histories of accelerations of TB20 specimen tested under 0°C..	182
Figure 7.87.	Displacement time history of TB20 specimen tested under 0°C	183
Figure 7.88.	A1, acceleration time history of TB30 specimen tested under 0°C .	183
Figure 7.89.	Pore water pressure distribution of TB30 specimen tested under 0°C	184
Figure 7.90.	Time histories of accelerations of TB30 specimen tested under 0°C	184
Figure 7.91.	Displacement time history of TB30 specimen tested under 0°C	185
Figure 7.92.	A1, acceleration time history of TC10 specimen tested under 0°C .	185
Figure 7.93.	Pore water pressure distribution of TC10 specimen tested under 0°C	186
Figure 7.94.	Time histories of accelerations of TC10 specimen tested under 0°C	186
Figure 7.95.	Displacement time history of TC10 specimen tested under 0°C	187
Figure 7.96.	A1, acceleration time history of TC15 specimen tested under 0°C...	187
Figure 7.97.	Pore water pressure distribution of TC15 specimen tested under 0°C.	188
Figure 7.98.	Time histories of accelerations of TC15 specimen tested under 0°C	188
Figure 7.99.	Displacement time history of TC15 specimen tested under 0°C	189
Figure 7.100.	A1, acceleration time history of TC20 specimen tested under 0°C .	189
Figure 7.101.	Pore water pressure distribution of TC20 specimen tested under 0°C.....	190
Figure 7.102.	Time histories of accelerations of TC20 specimen tested under 0°C.	190

Figure 7.103. Displacement time history of TC20 specimen tested under 0°C	191
Figure 7.104. A1, acceleration time history of TC30 specimen tested under 0°C .	191
Figure 7.105. Pore water pressure distribution of TC30 specimen tested under 0°C.	192
Figure 7.106. Time histories of accelerations of TC30 specimen tested under 0°C.	192
Figure 7.107. Displacement time history of TC30 specimen tested under 0°C	193
Figure 7.108. A1, acceleration time history of sand specimen tested at room temperature.....	193
Figure 7.109. Pore water pressure distribution of sand specimen tested at room temperature.....	194
Figure 7.110. Time histories of accelerations of sand specimen tested at room temperature	194
Figure 7.111. Displacement time history of sand specimen tested at room temperature	195
Figure 7.112. TB10 specimen tested on shaking table at room temperature	195
Figure 7.113. A1, acceleration time history of TB10 specimen tested at room temperature	196
Figure 7.114. Pore water pressure distribution of TB10 specimen tested at room temperature	196
Figure 7.115. Time histories of accelerations of TB10 specimen tested at room temperature	197
Figure 7.116. Displacement time history of TB10 specimen tested at room temperature	197
Figure 7.117. A1, acceleration time history of TB15 specimen tested at room temperature	198
Figure 7.118. Pore water pressure distribution of TB15 specimen tested at room temperature	199

Figure 7.119. Time histories of accelerations of TB15 specimen tested at room temperature	199
Figure 7.120. Displacement time history of TB15 specimen tested at room temperature	200
Figure 7.121. A1, acceleration time history of TB20 specimen tested at room temperature	200
Figure 7.122. Pore water pressure distribution of TB20 specimen tested at room temperature	201
Figure 7.123. Time histories of accelerations of TB20 specimen tested at room temperature	201
Figure 7.124. Displacement time history of TB20 specimen tested at room temperature	202
Figure 7.125. A1, acceleration time history of TB30 specimen tested at room temperature	202
Figure 7.126. Pore water pressure distribution of TB30 specimen tested at room temperature	203
Figure 7.127. Time histories of accelerations of TB30 specimen tested at room temperature	203
Figure 7.128. Displacement time history of TB30 specimen tested at room temperature	204
Figure 7.129. A1, acceleration time history of TC10 specimen tested at room temperature	204
Figure 7.130. Pore water pressure distribution of TC10 specimen tested at room temperature	205
Figure 7.131. Time histories of accelerations of TC10 specimen tested at room temperature	205
Figure 7.132. Displacement time history of TC10 specimen tested at room temperature	206

Figure 7.133. A1, acceleration time history of TC15 specimen tested at room temperature	206
Figure 7.134. Pore water pressure distribution of TC15 specimen tested at room temperature	207
Figure 7.135. Time histories of accelerations of TC15 specimen tested at room temperature	207
Figure 7.136. Displacement time history of TC15 specimen tested at room temperature	208
Figure 7.137. A1, acceleration time history of TC20 specimen tested at room temperature	208
Figure 7.138. Pore water pressure distribution of TC20 specimen tested at room temperature	209
Figure 7.139. Time histories of accelerations of TC20 specimen tested at room temperature	209
Figure 7.140. Displacement time history of TC20 specimen tested at room temperature	210
Figure 7.141. A1, acceleration time history of TC30 specimen tested at room temperature	210
Figure 7.142. Pore water pressure distribution of TC30 specimen tested at room temperature	211
Figure 7.143. Time histories of accelerations of TC30 specimen tested at room temperature	212
Figure 7.144. Displacement time history of TC30 specimen tested at room temperature	212
Figure 7.145. Only Sand Specimen tested at 50°C	213
Figure 7.146. A1, acceleration time history of sand specimen tested at 50°C	214
Figure 7.147. Pore water pressure distribution of TC30 specimen tested at room temperature	214
Figure 7.148. Time histories of accelerations of sand specimen tested at 50°C	215

Figure 7.149. Displacement time history of sand specimen tested at room temperature tested at 50°C	215
Figure 7.150. A1, acceleration time history of TB10 specimen tested at 50°C	216
Figure 7.151. Pore water pressure distribution of TB10 specimen tested at 50°C .	217
Figure 7.152. Time histories of accelerations of TB10 specimen tested at 50° C .	217
Figure 7.153. Displacement time history of TB10 specimen tested at 50°C	218
Figure 7.154. A1, acceleration time history of TB15 specimen tested at 50°C	218
Figure 7.155. Pore water pressure distribution of TB15 specimen tested at 50°C .	219
Figure 7.156. Time histories of accelerations of TB15 specimen tested at 50° C ..	219
Figure 7.157. Displacement time history of TB15 specimen tested at 50°C	220
Figure 7.158. A1, acceleration time history of TB 20 specimen tested at 50°C	220
Figure 7.159. Pore water pressure distribution of TB20 specimen tested at 50°C	221
Figure 7.160. Time histories of accelerations of TB20 specimen tested at 50° C ..	221
Figure 7.161. Displacement time history of TB20 specimen tested at 50°C	222
Figure 7.162. A1, acceleration time history of TB 30 specimen tested at 50°C	222
Figure 7.163. Pore water pressure distribution of TB30 specimen tested at 50°C .	223
Figure 7.164. Time histories of accelerations of TB20 specimen tested at 50° C .	223
Figure 7.165. Displacement time history of TB30 specimen tested at 50°C	224
Figure 7.166. A1, acceleration time history of TC10 specimen tested at 50°C	224
Figure 7.167. Pore water pressure distribution of TC10 specimen tested at 50°C	225
Figure 7.168. Time histories of accelerations of TC10 specimen tested at 50° C .	225
Figure 7.169. Displacement time history of TC10 specimen tested at 50°C	226
Figure 7.170. A1, acceleration time history of TC15 specimen tested at 50°C	226
Figure 7.171. Pore water pressure distribution of TC15 specimen tested at 50°C	227

Figure 7.172.	Time histories of accelerations of TC15 specimen tested at 50° C .	227
Figure 7.173.	Displacement time history of TC15 specimen tested at 50°C	228
Figure 7.174.	A1, acceleration time history of TC20specimen tested at 50°C	228
Figure 7.175.	Pore water pressure distribution of TC20 specimen tested at 50°C .	229
Figure 7.176.	Time histories of accelerations of TC20 specimen tested at 50° C ..	229
Figure 7.177.	Displacement time history of TC20 specimen tested at 50°C	230
Figure 7.178.	A1, acceleration time history of TC30 specimen tested at 50°C	230
Figure 7.179.	Pore water pressure distribution of TC30 specimen tested at 50°C .	231
Figure 7.180.	Time histories of accelerations of TC30 specimen tested at 50° C...	231
Figure 7.181.	Displacement time history of TC30 specimen tested at 50°C	232
Figure A.1.	A1, acceleration time history of sand specimen tested under 0°C....	248
Figure A.2.	A2, acceleration time history of sand specimen tested under 0° C ..	248
Figure A.3.	A3, acceleration time history of sand specimen tested under 0° C ..	249
Figure A.4.	Displacement time history of sand specimen tested under 0° C	249
Figure A.5.	Pore water pressure distribution of sand specimen tested at 0° C	250
Figure A.6.	A1, acceleration time history of TB10 specimen tested under 0° C .	250
Figure A.7.	A2, acceleration time history of TB10 specimen tested under 0° C .	251
Figure A.8.	A3, acceleration time history of TB10 specimen tested under 0° C .	251
Figure A.9.	Displacement time history of TB10 specimen tested under 0° C	252
Figure A.10.	Pore water pressure distribution of TB10 specimen tested at 0° C .	252
Figure A.11.	A1, acceleration time history of TB15 specimen tested under 0° C ...	255
Figure A.12.	A2, acceleration time history of TB15 specimen tested under 0° C .	253
Figure A.13.	A3, acceleration time history of TB15 specimen tested under 0° C .	254
Figure A.14.	Displacement time history of TB15 specimen tested under 0° C	254
Figure A.15.	Pore water pressure distribution of TB15 specimen tested at 0° C ..	255
Figure A.16.	A1, acceleration time history of TB20 specimen tested under 0° C ..	255

Figure A.17.	A2, acceleration time history of TB20 specimen tested under 0°C ..	256
Figure A.18.	A3, acceleration time history of TB20 specimen tested under 0°C ..	256
Figure A.19.	Displacement time history of TB20 specimen tested under 0°C	257
Figure A.20.	Pore water pressure distribution of TB20 specimen tested at 0°C ..	257
Figure A.21.	A1, acceleration time history of TB30 specimen tested under 0°C .	258
Figure A.22.	A2, acceleration time history of TB30 specimen tested under 0°C ..	258
Figure A.23.	A3, acceleration time history of TB30 specimen tested under 0°C .	259
Figure A.24.	Displacement time history of TB30 specimen tested under 0°C	259
Figure A.25.	Pore water pressure distribution of TB30 specimen tested at 0°C ..	260
Figure A.26.	A1, acceleration time history of TC10 specimen tested under 0°C .	260
Figure A.27.	A2, acceleration time history of TC10 specimen tested under 0°C .	261
Figure A.28.	A3, acceleration time history of TC10 specimen tested under 0°C .	261
Figure A.29.	Displacement time history of TC10 specimen tested under 0°C	262
Figure A.30.	Pore water pressure distribution of TC10 specimen tested at 0°C ..	262
Figure A.31.	A1, acceleration time history of TC15 specimen tested under 0°C .	263
Figure A.32.	A2, acceleration time history of TC15 specimen tested under 0°C .	263
Figure A.33.	A3, acceleration time history of TC15 specimen tested under 0°C .	264
Figure A.34.	Displacement time history of TC15 specimen tested under 0°C	264
Figure A.35.	Pore water pressure distribution of TC15 specimen tested at 0°C ..	265
Figure A.36.	A1, acceleration time history of TC20 specimen tested under 0°C .	265
Figure A.37.	A2, acceleration time history of TC20 specimen tested under 0°C .	266
Figure A.38.	A3, acceleration time history of TC20 specimen tested under 0°C .	266
Figure A.39.	Displacement time history of TC20 specimen tested under 0°C	267
Figure A.40.	Pore water pressure distribution of TC20 specimen tested at 0°C ..	267
Figure A.41.	A1, acceleration time history of TC30 specimen tested under 0°C .	268
Figure A.42.	A2, acceleration time history of TC30 specimen tested under 0°C .	268

Figure A.43.	A3, acceleration time history of TC30 specimen tested under 0°C .	269
Figure A.44.	Displacement time history of TC30 specimen tested under 0°C	269
Figure A.45.	Pore water pressure distribution of TC30 specimen tested at 0°C ..	270
Figure A.46.	A1, acceleration time history of sand specimen tested at room temperature	270
Figure A.47.	A2, acceleration time history of sand specimen tested at room temperature	271
Figure A.48.	A3, acceleration time history of sand specimen tested at room temperature	271
Figure A.49.	Displacement time history of sand specimen tested at room temperature	272
Figure A.50.	Pore water pressure distribution of sand specimen tested at room temperature	272
Figure A.51.	A1, acceleration time history of TB10 specimen tested at room temperature	273
Figure A.52.	A2, acceleration time history of TB10 specimen tested at room temperature	273
Figure A.53.	A3, acceleration time history of TB10 specimen tested at room temperature	274
Figure A.54.	Displacement time history of TB10 specimen tested at room temperature	274
Figure A.55.	Pore water pressure distribution of TB10 specimen tested at room temperature	275
Figure A.56.	A1, acceleration time history of TB15 specimen tested at room temperature	275
Figure A.57.	A2, acceleration time history of TB15 specimen tested at room temperature	276
Figure A.58.	A3, acceleration time history of TB15 specimen tested at room temperature	276

Figure A.59.	Displacement time history of TB15 specimen tested at room temperature	277
Figure A.60.	Pore water pressure distribution of TB15 specimen tested at room temperature	277
Figure A.61.	A1, acceleration time history of TB20 specimen tested at room temperature	278
Figure A.62.	A2, acceleration time history of TB20 specimen tested at room temperature	278
Figure A.63.	A3, acceleration time history of TB20 specimen tested at room temperature	279
Figure A.64.	Displacement time history of TB20 specimen tested at room temperature	279
Figure A.65.	Pore water pressure distribution of TB20 specimen tested at room temperature	280
Figure A.66.	A1, acceleration time history of TB30 specimen tested at room temperature	280
Figure A.67.	A2, acceleration time history of TB30 specimen tested at room temperature	281
Figure A.68.	A3, acceleration time history of TB30 specimen tested at room temperature	281
Figure A.69.	Displacement time history of TB30 specimen tested at room temperature	282
Figure A.70.	Pore water pressure distribution of TB30 specimen tested at room temperature	282
Figure A.71.	A1, acceleration time history of TC10 specimen tested at room temperature	283
Figure A.72.	A2, acceleration time history of TC10 specimen tested at room temperature	283

Figure A.73.	A3, acceleration time history of TC10 specimen tested at room temperature	284
Figure A.74.	Displacement time history of TC10 specimen tested at room temperature	284
Figure A.75.	Pore water pressure distribution of TC10 specimen tested at room temperature	285
Figure A.76.	A1, acceleration time history of TC15 specimen tested at room temperature	285
Figure A.77.	A2, acceleration time history of TC15 specimen tested at room temperature	286
Figure A.78.	A3, acceleration time history of TC15 specimen tested at room temperature	286
Figure A.79.	Displacement time history of TC15 specimen tested at room temperature	287
Figure A.80.	Pore water pressure distribution of TC15 specimen tested at room temperature	287
Figure A.81.	A1, acceleration time history of TC20 specimen tested at room temperature	288
Figure A.82.	A2, acceleration time history of TC20 specimen tested at room temperature	288
Figure A.83.	A3, acceleration time history of TC20 specimen tested at room temperature	289
Figure A.84.	Displacement time history of TC20 specimen tested at room temperature	289
Figure A.85.	Pore water pressure distribution of TB20 specimen tested at room temperature	290
Figure A.86.	A1, acceleration time history of TC30 specimen tested at room temperature	290

Figure A.87.	A2, acceleration time history of TC30 specimen tested at room temperature	291
Figure A.88.	A3, acceleration time history of TC30 specimen tested at room temperature	291
Figure A.89.	Displacement time history of TC30 specimen tested at room temperature	292
Figure A.90.	Pore water pressure distribution of TC30 specimen tested at room temperature	292
Figure A.91.	A1, acceleration time history of sand specimen tested at 50°C	293
Figure A.92.	A2, acceleration time history of sand specimen tested at 50°C	293
Figure A.93.	A3, acceleration time history of sand specimen tested at 50°C	294
Figure A.94.	Displacement time history of sand specimen tested at 50°C	294
Figure A.95.	Pore water pressure distribution of sand specimen tested at 50°C .	295
Figure A.96.	A1, acceleration time history of TB10 specimen tested at 50°C	295
Figure A.97.	A2, acceleration time history of TB10 specimen tested at 50°C	296
Figure A.98.	A3, acceleration time history of TB10 specimen tested at 50°C	296
Figure A.99.	Displacement time history of TB10 specimen tested at 50°C	297
Figure A.100.	Pore water pressure distribution of TB10 specimen tested at 50°C	297
Figure A.101.	A1, acceleration time history of TB15 specimen tested at 50°C	298
Figure A.102.	A2, acceleration time history of TB15 specimen tested at 50°C	298
Figure A.103.	A3, acceleration time history of TB15 specimen tested at 50°C	299
Figure A.104.	Displacement time history of TB15 specimen tested at 50°C	299
Figure A.105.	Pore water pressure distribution of TB15 specimen tested at 50°C	300
Figure A.106.	A1, acceleration time history of TB20 specimen tested at 50°C	300
Figure A.107.	A2, acceleration time history of TB20 specimen tested at 50°C	301

Figure A.108.	A3, acceleration time history of TB20 specimen tested at 50°C ...	301
Figure A.109.	Displacement time history of TB20 specimen tested at 50°C	302
Figure A.110.	Pore water pressure distribution of TB20 specimen tested at 50°C	302
Figure A.111.	A1, acceleration time history of TB30 specimen tested at 50°C ...	303
Figure A.112.	A2, acceleration time history of TB30 specimen tested at 50°C ...	303
Figure A.113.	A3, acceleration time history of TB30 specimen tested at 50°C ...	304
Figure A.114.	Displacement time history of TB30 specimen tested at 50°C	304
Figure A.115.	Pore water pressure distribution of TB30 specimen tested at 50°C	305
Figure A.116.	A1, acceleration time history of TC10 specimen tested at 50°C ...	305
Figure A.117.	A2, acceleration time history of TC10 specimen tested at 50°C ...	306
Figure A.118.	A3, acceleration time history of TC10 specimen tested at 50°C ...	306
Figure A.119.	Displacement time history of TC10 specimen tested at 50°C	307
Figure A.120.	Pore water pressure distribution of TC10 specimen tested at 50°C	307
Figure A.121.	A1, acceleration time history of TC15 specimen tested at 50°C ...	308
Figure A.122.	A2, acceleration time history of TC15 specimen tested at 50°C ...	308
Figure A.123.	A3, acceleration time history of TC15 specimen tested at 50°C ...	309
Figure A.124.	Displacement time history of TC15 specimen tested at 50°C	309
Figure A.125.	Pore water pressure distribution of TC15 specimen tested at 50°C	310
Figure A.126.	A1, acceleration time history of TC20 specimen tested at 50°C ...	310
Figure A.127.	A2, acceleration time history of TC20 specimen tested at 50°C ...	311
Figure A.128.	A3, acceleration time history of TC20 specimen tested at 50°C ...	311
Figure A.129.	Displacement time history of TC20 specimen tested at 50°C	312

Figure A.130.	Pore water pressure distribution of TC20 specimen tested at 50°C	312
Figure A.131.	A1, acceleration time history of TC30 specimen tested at 50°C ...	313
Figure A.132.	A2, acceleration time history of TC30 specimen tested at 50°C ...	313
Figure A.133.	A3, acceleration time history of TC30 specimen tested at 50°C ...	314
Figure A.134.	Displacement time history of TC30 specimen tested at 50°C	314
Figure A.135.	Pore water pressure distribution of TC30 specimen tested at 50°C	315
Figure B.1.	A1, acceleration time history of sand specimen tested at 0°C	316
Figure B.2.	A2, acceleration time history of sand specimen tested at 0°C	317
Figure B.3.	A3, acceleration time history of sand specimen tested at 0°C	317
Figure B.4.	Displacement time history of sand specimen tested at 0°C	318
Figure B.5.	Pore water pressure distribution of sand specimen tested at 0°C ..	318
Figure B.6.	A1, acceleration time history of TB10 specimen tested at 0°C	319
Figure B.7.	A2, acceleration time history of TB10 specimen tested at 0°C	319
Figure B.8.	A3, acceleration time history of TB10 specimen tested at 0°C	320
Figure B.9.	Displacement time history of TB10 specimen tested at 0°C	320
Figure B.10.	Pore water pressure distribution of TB10 specimen tested at 0°C ..	321
Figure B.11.	A1, acceleration time history of TB15 specimen tested at 0°C	321
Figure B.12.	A2, acceleration time history of TB15 specimen tested at 0°C	322
Figure B.13.	A3, acceleration time history of TB15 specimen tested at 0°C	322
Figure B.14.	Displacement time history of TB15 specimen tested at 0°C	323
Figure B.15.	Pore water pressure distribution of TB15 specimen tested at 0°C ...	323
Figure B.16.	A1, acceleration time history of TB20 specimen tested at 0°C	324
Figure B.17.	A2, acceleration time history of TB20 specimen tested at 0°C	324
Figure B.18.	A3, acceleration time history of TB20 specimen tested at 0°C	325

Figure B.19.	Displacement time history of TB20 specimen tested at 0°C	325
Figure B.20.	Pore water pressure distribution of TB20 specimen tested at 0°C	...	326
Figure B.21.	A1, acceleration time history of TB30 specimen tested at 0°C	326
Figure B.22.	A2, acceleration time history of TB30 specimen tested at 0°C	327
Figure B.23.	A3, acceleration time history of TB30 specimen tested at 0°C	327
Figure B.24.	Displacement time history of TB30 specimen tested at 0°C	328
Figure B.25.	Pore water pressure distribution of TB30 specimen tested at 0°C	...	328
Figure B.26.	A1, acceleration time history of TC10 specimen tested at 0°C	329
Figure B.27.	A2, acceleration time history of TC10 specimen tested at 0°C	329
Figure B.28.	A3, acceleration time history of TC10 specimen tested at 0°C	330
Figure B.29.	Displacement time history of TC10 specimen tested at 0°C	330
Figure B.30.	Pore water pressure distribution of TC10 specimen tested at 0°C	...	331
Figure B.31.	A1, acceleration time history of TC15 specimen tested at 0°C	331
Figure B.32.	A2, acceleration time history of TC15 specimen tested at 0°C	332
Figure B.33.	A3, acceleration time history of TC15 specimen tested at 0°C	332
Figure B.34.	Displacement time history of TC15 specimen tested at 0°C	333
Figure B.35.	Pore water pressure distribution of TC15 specimen tested at 0°C	...	333
Figure B.36.	A1, acceleration time history of TC20 specimen tested at 0°C	334
Figure B.37.	A2, acceleration time history of TC20 specimen tested at 0°C	334
Figure B.38.	A3, acceleration time history of TC20 specimen tested at 0°C	335
Figure B.39.	Displacement time history of TC20 specimen tested at 0°C	335
Figure B.40.	Pore water pressure distribution of TC20 specimen tested at 0°C	...	336
Figure B.41.	A1, acceleration time history of TC30 specimen tested at 0°C	336
Figure B.42.	A2, acceleration time history of TC30 specimen tested at 0°C	337
Figure B.43.	A3, acceleration time history of TC30 specimen tested at 0°C	337
Figure B.44.	Displacement time history of TC30 specimen tested at 0°C	338

Figure B.45.	Pore water pressure distribution of TC30 specimen tested at 0°C ..	338
Figure B.46.	A1, acceleration time history of sand specimen tested at room temperature	339
Figure B.47.	A2, acceleration time history of sand specimen tested at room temperature	339
Figure B.48.	A3, acceleration time history of sand specimen tested at room temperature	340
Figure B.49.	Displacement time history of sand specimen tested at room temperature	340
Figure B.50.	Pore water pressure distribution of of sand specimen tested at room temperature	341
Figure B.51.	A1, acceleration time history of TB10 specimen tested at room temperature	341
Figure B.52.	A2, acceleration time history of TB10 specimen tested at room temperature	342
Figure B.53.	A3, acceleration time history of TB10 specimen tested at room temperature	342
Figure B.54.	Displacement time history of TB10 specimen tested at room temperature	343
Figure B.55.	Pore water pressure distribution of TB10 specimen tested at room temperature	343
Figure B.56.	A1, acceleration time history of TB15 specimen tested at room temperature	344
Figure B.57.	A2, acceleration time history of TB15 specimen tested at room temperature	344
Figure B.58.	A3, acceleration time history of TB15 specimen tested at room temperature	345
Figure B.59.	Displacement time history of TB15 specimen tested at room temperature	345

Figure B.60. Pore water pressure distribution of TB15 specimen tested at room temperature	346
Figure B.61. A1, acceleration time history of TB20 specimen tested at room temperature	346
Figure B.62. A2, acceleration time history of TB20 specimen tested at room temperature	347
Figure B.63. A3, acceleration time history of TB20 specimen tested at room temperature	347
Figure B.64. Displacement time history of TB20 specimen tested at room temperature	348
Figure B.65. Pore water pressure distribution of TB20 specimen tested at room temperature	348
Figure B.66. A1, acceleration time history of TB30 specimen tested at room temperature	349
Figure B.67. A2, acceleration time history of TB30 specimen tested at room temperature	349
Figure B.68. A3, acceleration time history of TB30 specimen tested at room temperature	350
Figure B.69. Displacement time history of TB30 specimen tested at room temperature	350
Figure B.70. Pore water pressure distribution of TB30 specimen tested at room temperature	351
Figure B.71. A1, acceleration time history of TC10 specimen tested at room temperature	351
Figure B.72. A2, acceleration time history of TC10 specimen tested at room temperature	352
Figure B.73. A3, acceleration time history of TC10 specimen tested at room temperature	352

Figure B.74. Displacement time history of TC10 specimen tested at room temperature	353
Figure B.75. Pore water pressure distribution of TC10 specimen tested at room temperature	353
Figure B.76. A1, acceleration time history of TC15 specimen tested at room temperature	354
Figure B.77. A2, acceleration time history of TC15 specimen tested at room temperature	354
Figure B.78. A3, acceleration time history of TC15 specimen tested at room temperature	355
Figure B.79. Displacement time history of TC15 specimen tested at room temperature	355
Figure B.80. Pore water pressure distribution of TC15 specimen tested at room temperature	356
Figure B.81. A1, acceleration time history of TC20 specimen tested at room temperature	356
Figure B.82. A2, acceleration time history of TC20 specimen tested at room temperature	357
Figure B.83. A3, acceleration time history of TC20 specimen tested at room temperature	357
Figure B.84. Displacement time history of TC20 specimen tested at room temperature	358
Figure B.85. Pore water pressure distribution of TC20 specimen tested at room temperature	358
Figure B.86. A1, acceleration time history of TC30 specimen tested at room temperature	359
Figure B.87. A2, acceleration time history of TC30 specimen tested at room temperature	359

Figure B.88.	A3, acceleration time history of TC30 specimen tested at room temperature	360
Figure B.89.	Displacement time history of TC30 specimen tested at room temperature	360
Figure B.90.	Pore water pressure distribution of TC30 specimen tested at room temperature	361
Figure B.91.	A1, acceleration time history of sand specimen tested at 50°C	361
Figure B.92.	A2, acceleration time history of sand specimen tested at 50°C	362
Figure B.93.	A3, acceleration time history of sand specimen tested at 50°C	362
Figure B.94.	Displacement time history of sand specimen tested at 50°C	363
Figure B.95.	Pore water pressure distribution of sand specimen tested at 50°C ..	363
Figure B.96.	A1, acceleration time history of TB10 specimen tested at 50°C	364
Figure B.97.	A2, acceleration time history of TB10 specimen tested at 50°C	364
Figure B.98.	A3, acceleration time history of TB10 specimen tested at 50°C	365
Figure B.99.	Displacement time history of TB10 specimen tested at 50°C	365
Figure B.100.	Pore water pressure distribution of TB10 specimen tested at 50°C .	366
Figure B.101.	A1, acceleration time history of TB15 specimen tested at 50°C ...	366
Figure B.102.	A2, acceleration time history of TB15 specimen tested at 50°C ...	367
Figure B.103.	A3, acceleration time history of TB15 specimen tested at 50°C ...	367
Figure B.104.	Displacement time history of TB15 specimen tested at 50°C	368
Figure B.105.	Pore water pressure distribution of TB15 specimen tested at 50°C	368
Figure B.106.	A1, acceleration time history of TB20 specimen tested at 50°C ...	369
Figure B.107.	A2, acceleration time history of TB20 specimen tested at 50°C ...	369
Figure B.108.	A3, acceleration time history of TB20 specimen tested at 50°C ...	370
Figure B.109.	Displacement time history of TB20 specimen tested at 50°C	370

Figure B.110.	Pore water pressure distribution of TB20 specimen tested at 50°C	371
Figure B.111.	A1, acceleration time history of TB30 specimen tested at 50°C ...	371
Figure B.112.	A2, acceleration time history of TB30 specimen tested at 50°C ...	372
Figure B.113.	A3, acceleration time history of TB30 specimen tested at 50°C ...	372
Figure B.114.	Displacement time history of TB30 specimen tested at 50°C	373
Figure B.115.	Pore water pressure distribution of TB30 specimen tested at 50°C	373
Figure B.116.	A1, acceleration time history of TC10 specimen tested at 50°C ...	374
Figure B.117.	A2, acceleration time history of TC10 specimen tested at 50°C ...	374
Figure B.118.	A3, acceleration time history of TC10 specimen tested at 50°C ...	375
Figure B.119.	Displacement time history of TC10 specimen tested at 50°C	375
Figure B.120.	Pore water pressure distribution of TC10 specimen tested at 50°C	376
Figure B.121.	A1, acceleration time history of TC15 specimen tested at 50°C ...	376
Figure B.122.	A2, acceleration time history of TC15 specimen tested at 50°C ...	377
Figure B.123.	A3, acceleration time history of TC15 specimen tested at 50°C ...	377
Figure B.124.	Displacement time history of TC15 specimen tested at 50°C	378
Figure B.125.	Pore water pressure distribution of TC15 specimen tested at 50°C	378
Figure B.126.	A1, acceleration time history of TC20 specimen tested at 50°C ...	379
Figure B.127.	A2, acceleration time history of TC20 specimen tested at 50°C ...	379
Figure B.128.	A3, acceleration time history of TC20 specimen tested at 50°C ...	380
Figure B.129.	Displacement time history of TC20 specimen tested at 50°C	380
Figure B.130.	Pore water pressure distribution of TC20 specimen tested at 50°C	381
Figure B.131.	A1, acceleration time history of TC30 specimen tested at 50°C ...	381

Figure B.132.	A2, acceleration time history of TC30 specimen tested at 50°C ...	382
Figure B.133.	A3, acceleration time history of TC30 specimen tested at 50°C ...	382
Figure B.134.	Displacement time history of TC30 specimen tested at 50°C	383
Figure B.135.	Pore water pressure distribution of TC30 specimen tested at 50°C	383

LIST OF TABLES

Table 2.1. Recycle, Reuse or Disposal Alternatives for Scrap Tires (UNCTAD secretariat and OECD, 1998).	11
Table 2.2. Case histories of Geotechnical Uses of Scrap Tires (WSDOT, 2003), (continued).	22
Table 4.1. Liquefaction Remediation Measures (National Research Council, 1985).	50
Table 5.1. Examples of Modelling from Previous Studies.	78
Table 6.1. Density and Relative Density values of samples.	88
Table 6.2. CBR Test Program.	90
Table 6.3. Direct Shear Test Program.	93
Table 6.4. Cyclic Triaxial Test Program.	100
Table 7.1. CBR Test Results.	109
Table 7.2. Summary of the Direct Shear Test Results of Sand-Tire Crumbs Mixtures.	137
Table 7.3. Summary of The Direct Shear Test Results of Sand-Tire Buffings Mixtures.	138
Table 7.4. The evaluation of liquefaction susceptibility of soil.	140
Table 7.5. Summary of Cyclic Triaxial Test Results.	170
Table 7.6. Results of Laboratory Tests.	245

LIST OF SYMBOLS

c	Cohesion of material
i	Initial orientation angle with respect to shear surface
k	Shear distortion ratio
R_t	Mobilized tensile strength of inclusions per unit area of soil
R_σ	Tensile stress developed in the inclusion at the shear plane
x	Horizontal shear displacement
z	Thickness of shear zone
γ	Unit weight of material
ϕ	Angle of internal friction
θ	Angle of shear distortion
Δ_{SR}	Increase in shear strength caused by the addition of reinforcement

LIST OF ACRONYMS / ABBREVIATIONS

ASTM	American Society of Testing Materials
CBR	California Bearing Ratio
EPA	Environmental Protection Agency
FEM	Finite Element Method
RMA	Rubber Manufacturers Association
TB	Tire Buffings Material
TB1	Tire buffing swith sizes between 2mm and 4mm
TB2	Tire buffings with the sizes greater than 4mm
TC	Tire Crumbs Material

1. INTRODUCTION

1.1. General

As a result of industrial developments and high demand on consumption, as other waste materials, millions tons of tire wastes are disposed all around the world. This serious problem deducts environmental affects such as air pollution, diseases caused by mosquitos and health hazards. Disposal problems of these large amounts of scrap tires make necessary to generate solutions on how to decompose them. Reuse, recycling and recovering of tire wastes partially brought solutions to this problem (RMA, 2000).

Because of its high engineering properties such as flexibility, compressibility, high strength, thermal insulation and permeability, tire wastes are evaluated in many different engineering applications. Also, the advantage of its different sizes and shapes, they are used in the direction of the targeted purposes. Thermal properties of tire wastes make possible to use them under different climatic conditions. Especially in geotechnical applications, tire wastes are used as lightweight fill material.

The aim of this thesis is to investigate the liquefaction mitigation effect of scrap tire inclusions into the sand under different thermal conditions. In this sense, an experimental study conducted with different proportions of tire buffings and tire crumbs material with sand. To determine material properties of specimens, a series of geotechnical laboratory tests are performed. In the light of laboratory test results, the liquefaction susceptibility of the soil is evaluated. Secondly, cyclic triaxial tests are conducted to determine shear modulus and damping ratio of the specimens. In the next stage, a flexible shear stack is designed and constructed in order to use in shaking table model tests. A set of shaking table tests are performed with sand and sand-tire mixtures at three different temperatures: 0°C, 50°C and room temperature. At the end of laboratory tests, shape effect, ratio and aspect ratio of tire waste material at three different temperature conditions are compared. An overall evaluation of liquefaction mitigation effect of tire waste is performed according to the test results.

1.2. Problem Statement

Since amount of tire waste deposits increased rapidly all around the world, new and applicable solutions have been carried out to decompose it. For this reason, new ways of recycling and reusing tire wastes is a new research topic in today's world. An alternative way to consume large amounts of tire wastes is using them in geotechnical applications. Use of tire wastes to overcome earthquake induced hazards at different temperature conditions is a technique which enables to improve properties of soil beside the excessive temperatural effects of extreme climatic conditions. In addition to engineering advantages, the cost effective aspects of tire waste is the other favourable point.

1.3. Objective of the Thesis

This thesis is mainly concentrated on to develop a new technique on liquefaction mitigation effect of tire waste inclusion under different temperatures. For this purpose, a set of geotechnical laboratory test is conducted with sand-tire waste mixtures. In the light of the laboratory test results, the evaluation of liquefaction susceptibility of soil is performed. Cyclic Triaxial Laboratory Tests of specimens are performed to measure shear modulus and damping ratio of specimens. A flexible shear stack is modelled and constructed. Small scale shaking table tests are performed with prepared specimens. These tests are conducted with sand, sand-tire buffings and sand-tire crumb mixtures with different proportions and aspect ratios. Small size shaking table tests were performed with earthquake ground motions under different temperatures. According to the experimantal results, the effect of optimum content, shape and aspect ratio of tire waste on the test results were determined.

1.4. Organization of Thesis

This thesis starts with general information about tire wastes and geotechnical application areas. The following section continues with experimental program in which detailed information about the conducted tests is gathered. The results of experimental program are given in further sections. Finally, summary information and conclusion of whole study is given in last section.

2. LITERATURE REVIEW

2.1. General Information About Scrap Tires

Tire wastes are normally produced in every society causing serious environmental problems. According to the Environmental Protection Agency (EPA), about 290 millions of new scrap tires are generated in the U.S. each year. In 2007, Rubber Manufacturers of Association (RMA) estimates that about 4595.7 thousand tons of tires were generated in the U.S. By comparison, in 2005, 82% of tires were consumed by weight. In 1990, only 11% of tires were consumed on a per tire basis (RMA, 2007). On the other hand, according to the Association of Rubber Industrialists of Turkey (LASDER), 180000 tons of tires are being generated in Turkey each year (2007).

Huge tire waste stockpiles are among the most important problems need to be solved. The amount of tire wastes is increasing rapidly because of the increasing population, demand on tires and also their short service life. They are generally disposed in stockpiles or landfills (Figure 2.1). Especially, some of the developed countries focused on some regulations like recycling and reuse of tire wastes as construction material in order to prevent environmental pollution.



Figure 2.1. An example of tire waste stockpile.

Since 1994 continued progress in scrap tire management practices across the nation resulting in significant reduction of scrap tire stockpiles and continued progress in putting tire wastes to new uses (RMA, 2000). Even though the amount of scrap tire stockpiles increases each year, reused and recycled amount of scrap tires increases, too. The variation of number of scrap tires in stockpiles between 1990 and 2005 is demonstrated clearly in Figure 2.2.

Figure 2.3 shows the reported recycling, reuse and disposal data for 2002 to 2008. The total amount of tire wastes generated in 2008 is over 5 million tires. An estimated total of 87.383 tons of tire wastes generated in 2008. The total reported tire disposal, recycling and reuse in Washington for 2008 is 84.895 tons. This is the total of the 26.590 tons landfilled, 40.124 tons recycled, 5.912 tons of tires bales used in construction, 8.440 tons used as energy and 3.829 tons retreaded. Reporting of tire bale use is only available after 2006 (Washington Department of Ecology). Figure 2.4 shows the process of recycle, reuse and disposal of tire wastes in schematic way.

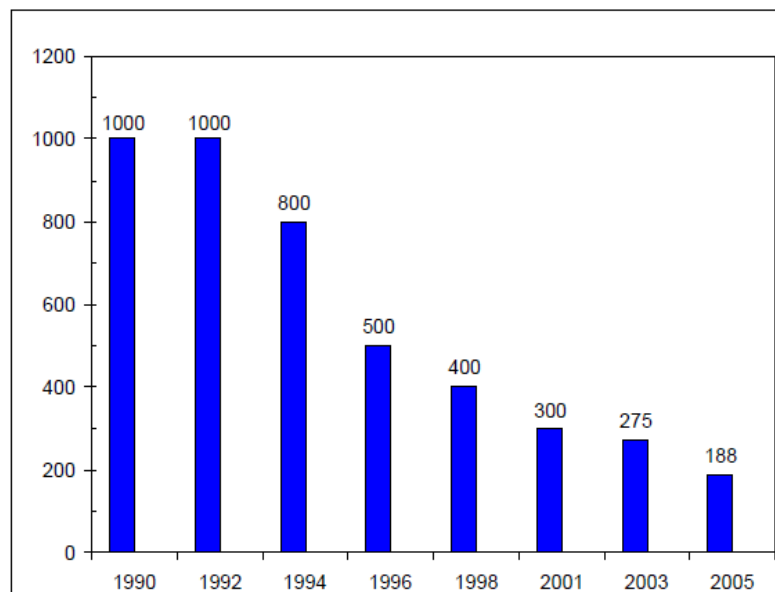


Figure 2.2. Millions of Scrap Tires Remaining in U.S. Stockpiles, 1990-2005 (RMA, 2006).

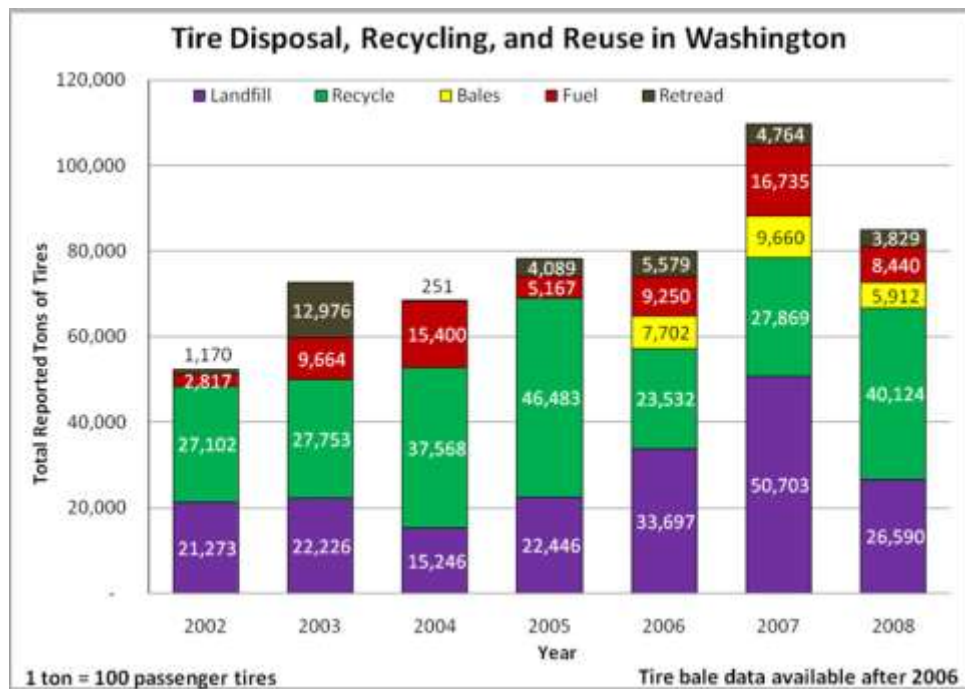


Figure 2.3. Disposal, recycled and reused amount of tire waste (Washington Department of Ecology, 2010).

2.2. Environmental Problems with Scrap Tire

2.2.1. Tire Fires

Tire waste stockpiles are difficult to ignite. However, once ignited, tires burn and it is very difficult to extinguish. That is why, smothering a tire fire with dirt or sand is perhaps the best current option for extinguishing tire fires. The sand or dirt is moved with heavy equipment to cover the burning tires. Even though, the prevention of run-off oil can not be achieved in this way but it is the cheapest and the fastest way to deflate fire. A large tire fire can smolder for several weeks or even months, sometimes with dramatic effect on the surrounding environment.

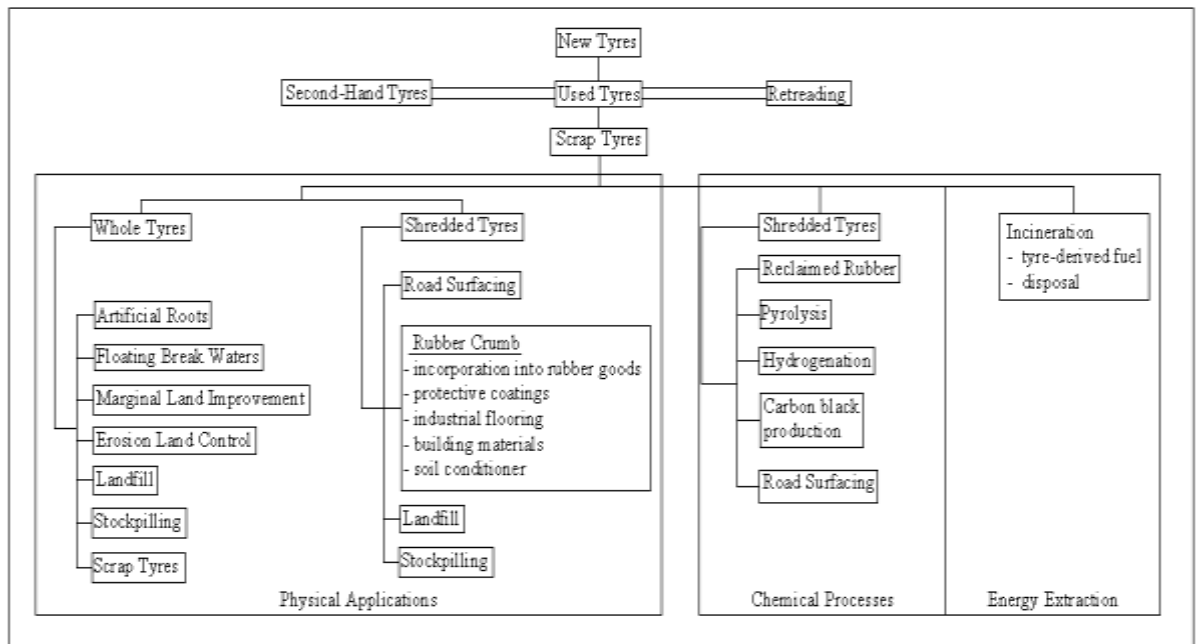


Figure 2.4. Recycle, Reuse or Disposal Alternatives for Scrap Tires (UNCTAD secretariat and OECD, 1998).

2.2.2. Health Hazards

Tire waste stockpiles are convenient breeding grounds for mosquitoes. Because of the shape of tires, they may hold water for long periods of time providing excellent site for mosquito larvae development. Tire stockpiles also have contributed to the introduction of non-native mosquito species when used tires are transported from one place to another. The new species are often more difficult to control and they spread more disease.

It is clear that the elimination of scrap tire piles will eliminate a prolific mosquito habitat along with the associated disease risks. One of the commonly known species of mosquito, the Asian Tiger Mosquito is spreaded in the past thirty years. This species have invaded many countries throughout the world by the transport of goods and increasing international travel. Many states have banned importation of scrap tires for this reason (RMA, 2006).

2.3. Material Properties of Scrap Tires

Scrap tires can be managed as a whole tire, a slit tire, a shredded or chipped tire, as ground rubber, or as a crumb rubber product. Tire chips are normally somewhat uniformly sized and tire shreds are more well-graded. Tire shreds have an irregular particle shape and relatively low unit weight. They usually orient parallel to the horizontal shear plane. Tire shred particles cannot be screened through standard sieves. The ASTM D422 states the procedures of sieve analysis for particle size distribution.

2.3.1. Physical Properties

Scrap tires can be managed as a whole tire, a slit tire, a shredded or chipped tire, as ground rubber, or as a crumb rubber product. After a processing stage, a whole tire waste can be divided into pieces with desired sizes (Figure 2.5).

2.3.1.1. Whole Tires. A typical automobile tire weighs around 9.1 kg which consists of recoverable, natural and synthetic rubber. Steel-belted radial tires are the predominant type of tire which produced in U.S. A greater type of tire, truck tire weighs averagely 18.2 kg and contains nearly 65% recoverable rubber.

2.3.1.2. Rubber Buffings. A form of readily available scrap tire is rubber buffings. Rubber buffings are produced from retreading tires or scrap tires for landfills. The tires are "buffed" by equipment. This equipment removes old tread from tires so new treads can be applied. Also it removes extra rubber from scrap tires prior to landfilling. Rubber buffings are elongated particles which are coarser than crumbs rubber particles. Scrap tire rubber buffings need to be stabilized to prevent migration by wind or water forces.

2.3.1.3. Shredded Tires. Tire shreds are basically flat, irregularly shaped tire chunks with jagged edges that may or may not contain protruding, sharp pieces of metal, which are parts of steel belts or beads. As previously noted, the size of tire shreds may range from as large as 305 mm to as small as 50 mm, with most particles within the 100 mm to 200 mm range. The average loose density of tire shreds varies according to the size of the shreds, but can be expected to be between 390 kg/m^3 to 535 kg/m^3 . The average compacted density ranges from 650 kg/m^3 to 840 kg/m^3 .

2.3.1.4. Tire Chips. Tire chips are more finely and uniformly sized than tire shreds, ranging from 50 mm down to approximately 12 mm in size. Although the size of tire chips, like tire shreds, varies with the type and condition of the processing equipment, nearly all tire chip particles can be gravel sized. The loose density of tire chips can be expected to range from 320 kg/m^3 to 490 kg/m^3 .

2.3.1.5. Ground Rubber. Ground rubber particles are intermediate in size between tire chips and crumbs rubber. The particle sizing of ground rubber ranges from 9.5 mm to 0.85 mm.

2.3.1.6. Crumbs Rubber. Crumbs rubber used in hot mix asphalt normally has 100% of the particles finer than 4.75 mm. Although, the majority of the particles used in the wet process are sized within the 1.2 mm to 0.42 mm range. Some crumbs rubber particles may be as fine as 0.075 mm. They are free of fabric, wire or other contaminants.

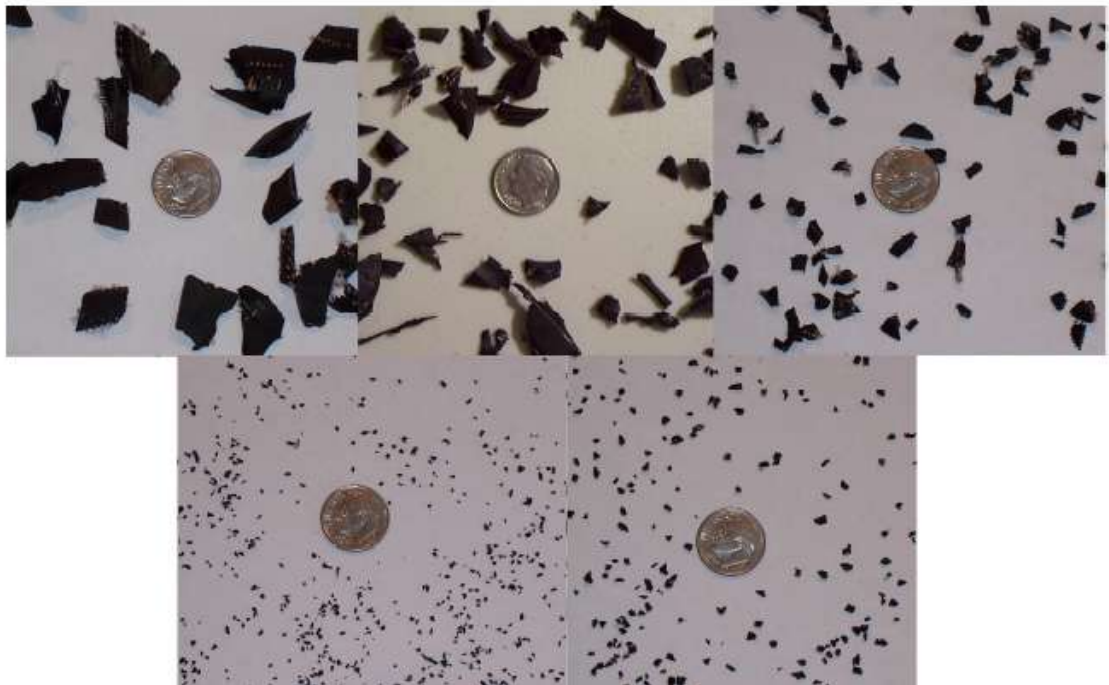


Figure 2.5. Example of different shapes and sizes of processed tires (Çağatay, 2008).

2.3.2. Chemical Properties

Scrap tire material is not reactive under normal environmental conditions. The principal chemical component of tires is a blend of natural and synthetic rubber but additional components include carbon black, sulfur, polymers, oil, paraffins, pigments, fabrics, and bead or belt materials.

2.3.3. Mechanical Properties

The available data about shear strength parameters of tire chips and tire shreds are limited. The wide range of shred size makes it difficult to find a large enough apparatus to perform a meaningful shear test. Although the shear strength characteristics of tire chips vary according to the size and shape of the chips, internal friction angles were between to range from 19° to 26° while cohesion values ranged from 4.3 kPa to 11.5 kPa.

2.3.4. Engineering Properties

2.3.4.1. Specific Gravity. The specific gravity of tire chips is expected to be in the 1.1 to 1.3 range, with higher specific gravity values for chips containing steel belts.

2.3.4.2. Unit Weight. Depending on the size of the tire material, unit weights can range from as low as 25 lb/ft^3 to as high as 53 lb/ft^3 . The coarser the size of the scrap tire particle, the lower the compacted unit weight (Table 2.1).

2.3.4.3. Shear Strength. Limited direct shear testing of tire material has been performed using a specially designed large-scale direct shear testing apparatus. The friction angle of tire material ranged from 19° to 25° . Cohesion values range from 7.6 kPa to 11.5 kPa. Tire chips with a greater amount of exposed steel belts tend to have a higher angle of internal friction

2.3.4.4. Compressibility. Tire shreds or chips are much more compressible during the initial stages of loading than soils. Final loading cycles normally result in significantly less compressibility of the tire shreds or chips. Higher amounts of exposed steel belts appear to result in higher compressibility, especially during the first loading cycle.

2.3.4.5. Young Modulus. The values of Young's modulus for tire chips range from 770 kPa to 1250 kPa. Therefore, at least 0.9 m of conventional soil is required to be placed on top of a layer of tire chips in order to prevent or minimize surface deflections.

2.3.4.6. Combustibility. Although scrap tire particles (shreds or chips) are not capable of spontaneous combustion, it does appear to be possible that, under certain circumstances, an initial exothermic reaction may occur within a tire shred or tire chip embankment or backfill that could eventually raise the temperature within the fill to a point where ignition could possibly occur.

Table 2.1. Unit Weights of Scrap Tire (WSDOT Report, 2003).

Unit Weight (lb/ft ³)	Compaction Method	Particle Size	Reference
Laboratory Compaction			
35.1 - 37.3	Modified	12 mm max.	Cecich <i>et al.</i> , 1996.
31.5 - 37.5		38 mm max.	Benda, 1995.
41	Modified		Humphrey and Manion, 1992.
40	Standard		
40	60% Standard		
38.6 - 40.1	60% Standard		Humphrey, <i>et al.</i> , 1993.
27.5 - 31.3	Shaken/vibrated in mold		Westerberg and Mascik, 2001.
43.0	Modified	400 to 50 mm	Moo-Young, <i>et al.</i> , 2001.
28.6	Loose		
31.3		D ₅₀ = 30 mm	Newcomb and Drescher, 1994.
42.8 - 46.9	Standard	16 mm max.	Youwai and Bergado, 2003.
25	Loose	5 to 25 mm	Ahmed and Lovell, 1993.
35	Modified		
In-Place or Field Compacted			
43.1 - 44.3	Walk behind, vibratory tamping foot roller compactor, static weight 2600 lb.	1.5 to 3 in 38 to 76 mm	Tweedie, Humphrey and Sandford, 1998.
33 45 53	In trucks D-8 Dozer 5.5 ft Surcharge		Upton and Machan, 1993.
42.3 - 47.6	1152 lb/ft ² Surcharge		Benda, 1995.
31.3 - 43.8	626 - 1044 lb/ft ² 8354 lb/ft ²		Westerberg and Mascik, 2001.
38	20000 lb smooth, steel wheel roller; then loaded with up to 5 ft of fill and 8 ft of surcharge that remained for 4 mo.	4.75 to 300 mm	Dickson, Dwyer and Humphrey, 2001.

2.3.5. Thermal Properties

Because of the difference of the thermal properties of sand and rubber, it is very efficient to use mixtures of these two materials in order to get good thermoelastic properties. Frost penetration combined with accessibility of water causes frost heave in especially fine grained soils. With the repeated effect of temperature changes, the bearing capacity loss can occur. The low thermal conductivity of tire wastes makes the material suitable for thermal insulation material.

Tire wastes are generally used in road constructions as thermal insulation materials. During the frozen, bearing capacity of road decreases. When the layer of tire waste itself is at freezing condition, even at low freezing index, the layer effectively insulates the layer below. The insulation effect is acting on the underlying soil and reduces the heat transfer. By the way, the bearing capacity and fatigue failures caused temperature differences can be minimised.

Pamukcu and Akbulut (2006) studied on Ottawa sand and rubber mixtures to investigate the increase of the shear modulus and damping ratio. By the performed analysis, it is concluded that the results mainly hinge on the proportion of contacts between dissimilar materials within the particulate matrix. The increment of rubber content causes more contact surfaces and by the way the stiffness and the thermoelastic damping ratio are increase. At higher volume contents than the optimal value, the proportion of dissimilar material contacts decreases in a given volume of the mixture, causing reversal of the gained stiffness and damping. The best explanation for the increase in low-strain damping ratio was found in possible thermoelastic enhancement effects at soil-to-rubber interfaces of dissimilar materials. The thermoelastic damping is known as to occur at interfaces of materials with significantly different elastic and thermal properties. The improvement was reduced at high rubber contents owing to the replacement of the soil-to-rubber interfaces with more of the similar material, or rubber-to-rubber interfaces (Pamukcu and Akbulut, 2006).

The thermal insulation enhancement of waste PET pieces and rubber material are also investigated (Yesilata *et al.*, 2007). Five different concrete samples are considered in their study. A dynamic adiabatic box was used for thermal tests. This technique is pre-estimation technique before absolute measurements with other commonly used ones.

Another thermal performance tests are performed by Turgut and Yesilata (2007). The combinations of crumbs rubber and concrete are tested. The thermal insulation performance, energy absorption capacity and resistivity to sudden brittle fractures are observed. Figure 2.6 shows the compressive strength variation before and after 50 cycles of freezing-thawing test. The curve shows that it is suitable to use crumbs rubber as a freeze – thaw resisting material. The curves which shows losses of compressive strengths of specimens before and after 50 cycles of freezing-thawing tests demonstrate us that the lower values of crumbs-rubber content is less resistant than higher crumbs rubber content (Turgut and Yesilata, 2007).

Tests which are objected to present the effect of tire crumb addition on thermal transmittance, the transiency of three rubber-brick specimens (with 20%, 40% and 60% rubber contents), showed that the largest heat loss rate occurs for no rubber case. The addition of crumbs rubber lowers the thermal transmittance of the brick, or improves its insulation property. The best insulation improvement was obtained with the specimen, which had the largest amount of crumbs rubber among the tested specimens (Turgut and Yesilata, 2007).

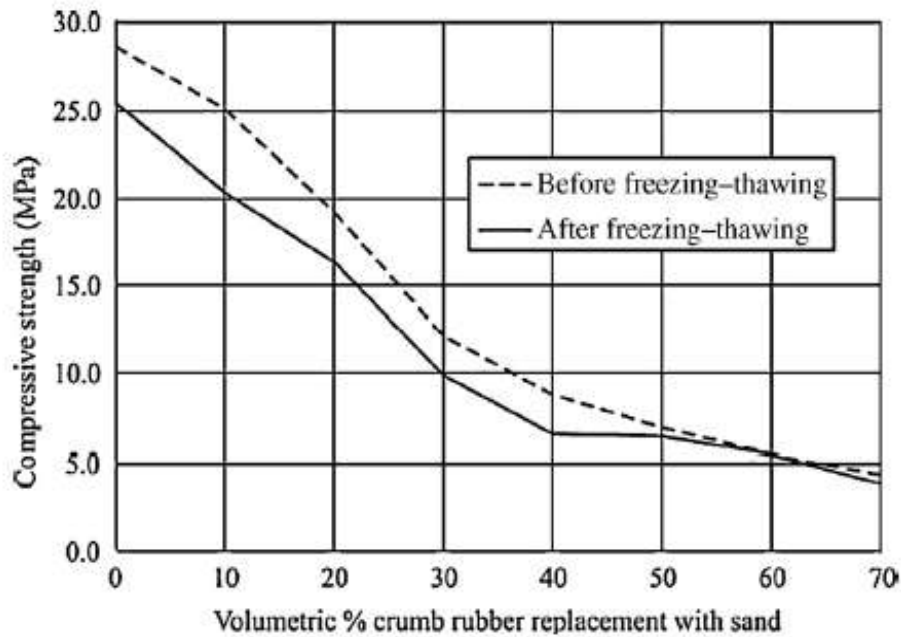


Figure 2.6. The compressive strength variation before and after 50 cycles of freezing-thawing test (Turgut and Yesilata, 2007).

2.4. Tire Waste Utilization Fields

Tire wastes have hardness and elasticity properties superior to those of rubber, good resistance to weathering that can be used for preventing impact damage of construction materials because of their low specific gravity which is lower than that of most construction materials. Moreover, it is possible to use tires in almost all environmental, in both hot and cold climate conditions. Tire wastes are modifiable and inexpensive thus, it can be reused as floor mats, belts, gaskets, shoe soles, dock bumpers, seals, muffler hangers, shims, and washers. Among all wide range of utilization fields, tire wastes can be utilized as electrical insulator, too.

The United States produces nearly 290-300 million scrap tires per year. Of these scrap tires, 14% are landfilled or dumped (legally or illegally) in stockpiles. The largest portions of scrap tires being used are burned for tire derived fuel (52%), civil engineering applications (16%) and ground rubber (12%). Figure 2.7 shows the increasing tendency of scrap tire market trend between the years of 1990 and 2005 (RMA, 2006).

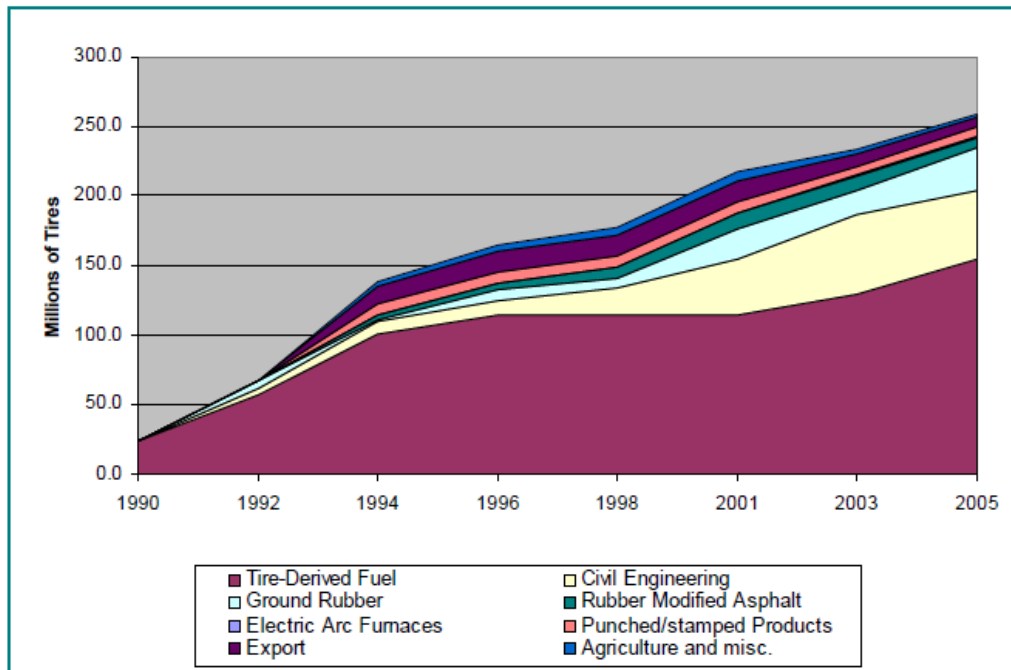


Figure 2.7. Scrap Tire Market Trends, 1990-2005, (RMA, 2006).

2.4.1. Tire Derived Fuel

Because of their high heating value, tire wastes are used as fuel. Burning tire wastes is considered as a higher use than landfilling. Tires used for fuel are shredded - known as tire-derived fuel - or whole, depending on the type of combustion device. Combustion facilities have utilized as tire derived fuel as an effective means to reduce critical criteria pollutants, to improve ash handling and to help offset the high price of energy. Tire-derived fuel is an alternative fuel source to petroleum coke, natural gas and inexpensive coals. Oftenly, the combination of modifications needed to be used as tire derived fuel, the misperceptions of tires as waste and inconsistent service by tire derived fuel suppliers allows potential end users to wait out the situation until they get their price.

Currently, the largest use for scrap tires is as a fuel in power plants, cement plants, pulp and paper mill boilers, utility boilers and other industrial boilers. At least 100 million scrap tires were used as an alternative fuel either in whole or chipped form. Figure 2.8 shows basically the process of tire derived fuel application.



Figure 2.8. Co-processing tire derived fuel.

2.4.2. Ground Rubber Applications

Nearly 10 millions scrap tires are processed into ground rubber each year in the world. Ground tire rubber is used in rubber products (such as floor mats, carpet padding, and vehicle mud guards), plastic products and as a fine aggregate addition (dry process) in asphalt friction courses. Two types of rubber playground surfacing material are on the market today: loose fill and solid mats. Loose fill generally consists of chips of rubber ranging from one half inch to three quarters inch in size.

Ground rubber also bring many advantages in the field of engineering. Some of the economic interests fear that the addition of ground rubber to asphalt will make the pavement last too long and require too little maintenance and repair. On the other hand, over-production of ground rubber affects prices and business plans. We have to understand better where and how ground rubber can be added to other polymer materials (plastics and non-tire rubber) to obtain improved performance or cost savings.

Some of the other ground rubber application examples with scrap tires are; ground cover under playground equipment, running track material, sports and playing fields, ground tire rubber blended with asphalt for road construction, molded rubber products,

brake pads and brake shoes, additive to injection molded and extruded plastics, automotive parts, agricultural and horticultural applications/soil amendments, horse arena footing.

2.4.3. Civil Engineering Applications

According to the RMA data, over 200 millions of tires were used in civil engineering applications in 2005. They were mainly used in landfill construction and operations, cap closures, alternate daily covers, leachate collection systems, gas venting systems, septic system drain fields, subgrade fill and embankments, backfill for walls and bridge abutments, subgrade insulation for roads, vibration dampening layers (RMA, 2006).

2.4.3.1. Subgrade Fill and Embankment Applications. The use of tire shreds or tire chips for the construction of embankments provides several advantages. The most important advantage is that of reduced unit weight, which is especially beneficial in situations of embankment to be constructed over an area with low bearing capacity. In addition to all good engineering properties, tire shreds and tire chips offer good thermal characteristics in resisting frost penetration and have good drainage characteristics, being as permeable as a coarse granular soil to an embankment (Figure 2.9).

For postconstruction settlements up to 0.5 m over the life of an embankment may be considered tolerable if it occurs slowly, in a long duration of time. By using flexible materials, the failure effect of settlements can be reduced. Additionally, by placing some surcharge loadings or by applying stage construction, settlements can be mitigated, too.

To use rubber-soil mixtures to construct the embankment could be better than using tire shreds or tire chips alone in order to prevent embankment settlements. It has been found that a ratio of about 40% tire chips by weight of soil may be an optimum value for the quantity of chips in a rubber-soil mix, although this may vary depending on the size of the tire chips and the type of soil. The optimum ratio of tire chips to soil is likely to yield a

compacted dry unit weight of rubber-soil mix that is roughly two-thirds the dry unit weight of soil alone.

Masad *et al.* (1996) studied on the effect of the addition of shredded tires on Ottawa sand. He concluded that the shredded tires-Ottawa sand mixture could be used as a lightweight fill material in highway embankments over weak or compressible soils.

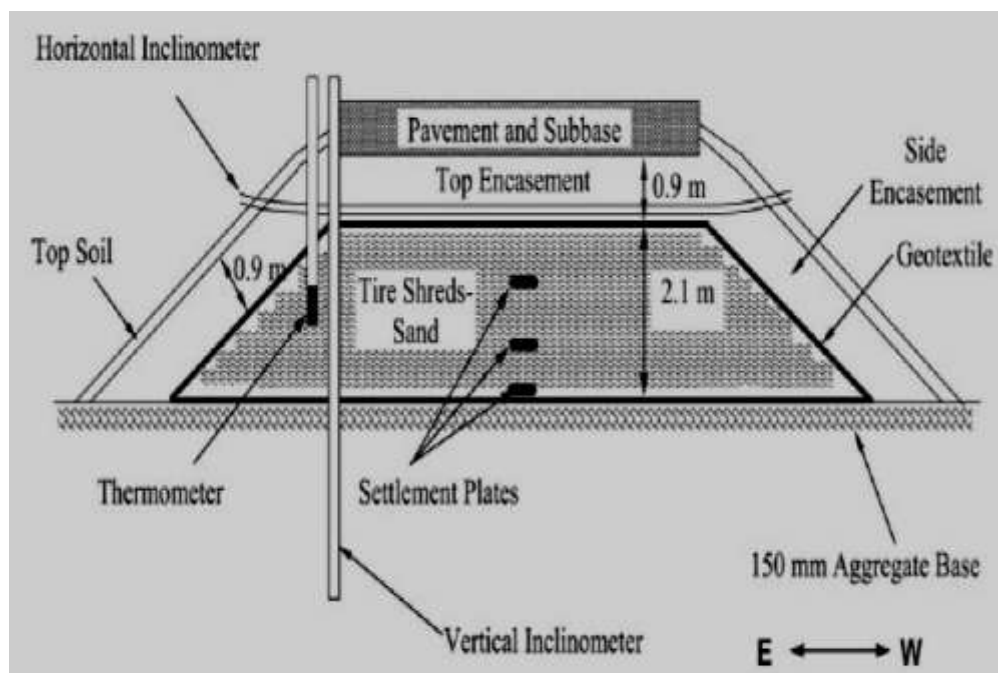


Figure 2.9. Schematic cross-section of an embankment constructed with tire shreds and sand (Yoon *et al.*, 2008).

2.4.3.2. Highway Applications. Crumbs rubber can be used to modify the asphalt binder (e.g., increase its viscosity) in a process in which the rubber is blended with asphalt binder (usually in the range of 18 to 25% rubber). This process, commonly referred to as the ‘wet process’, blends and partially reacts crumbs rubber with asphalt cement at high temperatures to produce a rubberized asphalt binder. Crumbs rubber modifier used in asphalt paving materials, consumes one to two million tires per year. Asphalt – rubber binders are used primarily in hot mix asphalt pavings, seal coat applications, stress absorbing membrane interlayer construction, crack or joint sealing and hot mixed asphalt concrete pavement construction (Figure 2.10).



Figure 2.10. Tire chip-seal construction

2.4.3.3. Landfill Applications. The use of shredded tires in landfill construction and as landfill components is beneficial by providing all performance requirements by the help of its good engineering properties. In most of the landfill applications shredded tires have been used because of their appropriateness for drainage and higher permeability. However, it is important that the shredded tires should not contain dirt clods, loose wires, or be coated with fines. Using scrap tires into landfills also has positive effect upon the markets for scrap tires. In some locations, it is the only applicable disposal option.

2.4.4. Case Histories of Geotechnical Uses of Scrap Tires

Scrap tire is one of the preferable construction material in geotechnical applications. It has been used in retaining walls, embankments, landfills, slope stability applications. Depending on the degree of compaction of soil-tire mixture, geotechnical and drainage performance of soil could be enhanced. In a construction of a retaining wall, light equipment need to be used only and to provide lateral and vertical earth pressure. Hence, tire could be an excellent choice to mix with soil in such cases.

The use of soils locally available at the construction site will usually satisfy design specifications with a significant reduction in construction costs. The filling of the tire with soil can be accomplished even by manual compaction. This type of wall does not require cement or steel. Other geotechnical applications using scrap tires have described elsewhere (Garga and O'Shaughnessy, 1995).

Lee *et al.* (1999) used numerical modeling to study the mechanical behavior of shredded tire backfill. The results of the study prove that tire shred-sand mixture is an effective example for backfill material. Bosscher and Edil (1994) found that vertically placed tire shred provide higher shear strength. Also, when pressure caused by water is taken into consideration, to use tire shred in soil mixture will bring advantages by providing good drainage performance.

Bosscher et al (1997) investigated the effect of heavy trucks on embankment constructed with outwash sand and shredded tires. It is claimed that the embankment

showed a satisfactory performance. Moreover, Bosscher stated out that over a period of 2 years the sections constructed with pure tire shreds exercised a smaller amount of settlement than the sections constructed with soil. There are several projects in the world which benefitted from shredded tires at the construction of asphalt pavement in civil engineering applications.

Case histories of geotechnical uses of scrap tires are summarised in Table 2.3.

Table 2.3. Case histories of Geotechnical Uses of Scrap Tires (WSDOT, 2003).

State	Reference(s)	Project Name	H _{max} (ft)	Type of Fill	Drainage Layer?	If Unsuccessful, Reason for Failure	FHWA 1997 ¹	Usage ²	Est. Unit Weight (lb/ft ³)	Quantity ³	Year Built	Additional Comments
Embankments Over Soft Ground												
CA	CalTrans, 2002 and 2001	I-880 Dixon Landing Road On-Ramp	<10	M			Yes	S		0.9M	2001	Embankment was constructed using at least two layers of pure tires, wrapped in geotextile and separated by a layer of soil.
ME	Humphrey, et al., 1998 and Whetten and Weaver, 1997	Topsham Brunswick Bypass (Merrymeeting Bridge, North Abutment)	14	M	No		No	S	56	0.4M	1996	Larger shreds on bottom 10ft, smaller shreds in top 4ft; impermeable clay to limit air/water access; 20 in of settlement; temp lower in larger shreds
ME	Humphrey, Dunn and Merfeld, 2000 and Humphrey, et al., 1998	Portland Jetport Embankment	10	M	No		Yes	S	49	1.2M	1997	First designed using 1997 FHWA Interim Guidelines
MN	Civil Engineering News, 1997 and Civil Engineering, 1997	Carlton Co. (CSAH 11 and Pine County 48)	14	M	No		ID ⁷	S	~20	0.52M	1996	Placed in 4ft lifts
MN	Drescher and Newcomb, 1994 and Engstrom and Lamb, 1994	Ramsey Co. Rd. No. 59 (Centerville Rd.)	3	M	No		No	S		0.1M	1990	
MN	Ibid.	Eden Prairie	9	M	No		Yes	S	---	0.2M ⁶		
MN	Ibid.	Prior Lake	3	M	No		No	S	---	0.4M ⁶	1991	Initial 6 in settlement following application of 2ft thick subbase; no further detrimental settlement. 100 % Passing 4 in
MN	Ibid.	Milaca	3	M	No		Yes	S		0.05M		
MN	Ibid.	Pine City	15	M	No		Yes	S	22	0.9M	1992	
MN	Drescher and Newcomb, 1994, Engstrom and Lamb, 1994 and Public Works, 1990	Benton Co., near Rice	3	M	?	Longitudinal cracking in wheel paths, some rutting and some cracking indicative of an embankment failure.	Yes	S	30	0.052M	1989	Computed unit weight. Maximum tire length was 12 inches.

Table 2.2. Case histories of Geotechnical Uses of Scrap Tires (WSDOT, 2003), (continued).

State	Reference(s)	Project Name	H _{max} (ft)	Type of Fill	Drainage Layer?	If Unsuccessful, Reason for Failure	FHWA 1997 ¹	Usage ²	Est. Unit Weight (lb/ft ³)	Quantity ³	Year Built	Additional Comments
MN	Engstrom and Lamb, 1994	Lake Co., near Finland, CSAH #7	4	M	No		Yes	S		0.2M ⁶	1990	4x12 in shreds; above GWT; No noticeable settlements reported.
MN	Drescher and Newcomb, 1994	Minneapolis Convention Center	3	M	---		Yes	S	---	0.13M	---	Tires used to reduce weight on below grade parking structure.
MN	Drescher and Newcomb, 1994	Scott Co.	6	M ³	?		No	S	---	---	1991	Tires used as lightweight fill over an existing water main. Maximum tire length, 3 inches.
MN	Drescher and Newcomb, 1994	Athens Twp. Rd. T194	3	M	---	---	ID	S	---	---	1991	Excavated and replaced roadway fill over soft ground. The 3 ft height was the loose lift thickness.
SD	Follow-up response to WSDOT Scrap Tire Use Survey	---	15	M	Yes		ID	S	---	0.06M	1996	Lightweight fill over a box culvert to reduce required thickness of top slab of culvert
VA	Hoppe, 1994 and ENR, 93	Rt. 646 Connector, near Williamsburg	20	X	No		No	E	71	1.7M	1993	Claimed to be largest tire fill to date. Virginia DEQ subsidized \$150000 to use tire shreds; this is about \$0.15/tire or about 1/5 - 1/6 the cost of landfill disposal.
Manitoba	Shalaby and Khan, 2002		6.4	M	No		Yes	E	63	0.3M	1999	Unit wt. estimated from geometry and number of tires used in embankment.
Common Embankments												
ME	Humphrey, 1998	Rt. 9 near Crawford	---	M	---		ID	S	---	0.3-0.7M	---	Objective in using tires was to remove them from a nearby stockpile. Maine DOT paid the equivalent cost for common borrow, the while Maine Dept. of Environmental Protection subsidized the remaining cost for the tires. No absolute cost data was given.

Table 2.3. Case histories of Geotechnical Uses of Scrap Tires (WSDOT, 2003), (continued).

State	Reference(s)	Project Name	H _{max} (ft)	Type of Fill	Drainage Layer?	If Unsuccessful, Reason for Failure	FHWA 1997 ²	Usage ²	Est. Unit Weight (lb/ft ³)	Quantity ³	Year Built	Additional Comments
IA(?)	Gebhardt, Kjartanson and Lohnes, 2001	Proposed design parameters for a scrap tire fill crossing a ravine	15	M	---		No					Authors proposed design strength parameters based on direct shear tests. For tire shreds they proposed $\phi=38^\circ$, and for scrap tires on glacial till, $c = 0.1$ psi and $\phi=33^\circ$.
NY	Dickson, et al., 2001	Rt. 17, Westbound Off Ramp to the new North Road Bridge	10	M	No		Yes	S	38	0.3M	1999	Trench drains were used below the embankment. Ground water quality was monitored.
WA	Humphrey, 1996	Falling Springs Rd., Garfield Co.	49	M	No	Fire	No	S	---	0.9M	1995	"Stringy" shreds <2in wide and 12 in long were used in bottom 20 ft of embankment. This material was described as generally steel belts encased in a minimal amount of rubber. Shreds of at least 10 in, some with both sidewalls still intact, were used in the upper portion of the embankment. Little initial settlement. Between Jan- Feb 1996, 4 to 6 ft of settlement occurred in the roadway.
WI	Bosscher, Edil and Eldin, 1993 and Eldin and Senouci, 1992	Experimental embankment; included lysimeters to monitor leachate.	5	M, L, X	No		No	E	19-35	---	1990	Embankment settlement in the section with the 2 in shreds was larger than in the section with 4 in shreds. Lower unit weights were realized in sections with larger shred size.
Landslide Remediation												
CO	Cheng, 2003	I-76 between Broadway and Huron	5	M	---		ID	S	---	---	1991	
LA	Morvant, 2003 and Technology Today, 1997	LA-8 Landslide Repair, near Harrisonburg	---	M, X	Yes.		No	S	---	0.9M	1997	DEQ subsidy of \$0.15/tire; top portion was a monofill, bottom portion was soil/tire mixture for increased weight to act as a buttress.

Table 2.3. Case histories of Geotechnical Uses of Scrap Tires (WSDOT, 2003), (continued).

State	Reference(s)	Project Name	H _{max} (ft)	Type of Fill	Drainage Layer?	If Unsuccessful, Reason for Failure	FHWA 1997 ¹	Usage ²	Est. Unit Weight (lb/ft ³)	Quantity ³	Year Built	Additional Comments
OR	Upton and Machan, 1993 and Read, Dobson and Thomas, 1991	US42 Landslide Repair, near Roseburg	12.5			Cracking, rutting in wheel path. Excavation showed soil cap was only 1.5-2 ft thick, replacement with the specified thickness of 3 ft solved the cracking problem.				0.6M	1990	
WA	Gacke, Lee and Boyd, 1997 and Humphrey, 1996	SR-100 Landslide Repair at Ilwaco	26	M	No	Fire	No	S		0.7M	1995	Used 2 – 6in tire shreds that were produced by shearing and ripping. There was more exposed steel in ripped shreds. The fill was constructed 4 ft above the ground water table, and four feet of cover was placed over the fill. There was approximately 2 in. of initial settlement.
WA	WSDOT Records	SR-101 Cosmopolis	30	M	No			S			1993	Sliver fills over existing wood chips.
WY	Hager, et al., 1998, Dahill, 1994, Scrap Tire News, 1994 and Transportation Topics, 1994	WYO 28, Near Lander (Double Nickel Landslide)	11	M	Yes		Yes	S	53	0.5M	1995	Used entire supply of scrap tires in the state.
Backfill for Retaining Walls												
CO	Humphrey, 1996	Glennwood Canyon	70	M(?)		Fire	ID	---	---	---	1995	
ME	Humphrey, et al., 1998 and Whetten and Weaver, 1997	Topsham-Brunswick Bypass (Rigid Frame Bridge)	20	M	No			S		1336 yd ³	1996	Rigid wall; lateral earth pressures reduced 40 %
ME	Tweedie, Humphrey and Sanford, 1998a,b and c	Experimental Wall	16	M	No		No	E	43.1-44.3	130 yd ³ or ~0.008M		Relative to expected pressures from granular backfill: At-rest pressures were 45% less Active pressures were 35% less

Table 2.3. Case histories of Geotechnical Uses of Scrap Tires (WSDOT, 2003), (continued).

State	Reference(s)	Project Name	H _{max} (ft)	Type of Fill	Drainage Layer ⁵	If Unsuccessful, Reason for Failure	FHWA 1997 ¹	Usage ²	Est. Unit Weight (lb/ft ³)	Quantity ³	Year Built	Additional Comments
SD	Reid, Soupir and Schaefer, 1998	Experimental Wall	5	M	No	---		E	---	2.3 yd ³	---	Reduced passive lateral earth pressure on model abutment wall.
SD	Prevention of voids below approach slabs	An experimental study utilizing tire shreds below the approach slab and behind the abutment. The use of tires for the abutment wall backfill, reduced passive pressures on the retained fill and was therefore thought to reduce the mechanism causing voids to develop	1990 (?)	Reid, Soupir and Schaefer, 1998								
TX	Tire bales	A landslide on I-30 was repaired by backfilling the failed area with tire bales. The bales contained about 100 tire each, and weighed about 2000 lb. A total of 36,000 tires were utilized.	2002	TCEQ, 2003								

1. Does the project meet the FHWA 1997 Interim Guidelines? The project received a "No" if it failed to meet any requirement of the guidelines, e.g., size distribution of shreds, maximum recommended embankment height, no measures to prevent the access of water and air to the tire fill, etc. The exception to this rule was with regard to particle size distribution. In many cases it was difficult, or impossible, to determine if the tire shreds met the size distribution specified by the Interim Guidelines. Therefore, if the project met all other guidelines, it was given a "Yes".
2. E = experimental; S = in service, i.e., the installation was intended to receive traffic
3. Unless otherwise noted, the given quantity is millions of tires.
4. Include any other significant uses such as anchors for tie back walls, whole tire walls, crash attenuators, etc.
5. Two 3 ft layers, separated by a geotextile
6. Computed using given volumes and assuming $\gamma = 40 \text{ lb/ft}^3$ and 20 pounds per tire.
7. ID = insufficient data.

2.5. Scrap Tire as a Geomaterial

In most of the geotechnical applications, tire waste can be used as lightweight material mostly as filling materials. Not only in the form of shredded chips or blended in soil but also whole tires are used especially as an embankment material. That kind of studies need to be analyzed in accordance with laboratory studies (Ahmed and Lovell, 1993; Masad et. al, 1996; Lee et. al, 1999; Tweedie et. al, 1998, Humphrey and Tweedie, 2002; and Edil, 2002).

Even though shredded chips or whole tires are efficient for most of geotechnical applications, lighter materials minimize foundation requirements, reduce land cutting for mountainous area, decrease settlements by increasing cohesion of soil and shorten construction times. In the case of retaining wall, lightweight fill will reduce the lateral earth pressure thus reducing the structural requirements of the wall including the foundations.

2.6. Improvement of Soil Properties with Scrap Tire

Tire chips can be mixed or blended with soil. As the percentage of soil increases, the unit weight of the mixture increases. To simplify blending in the field, mixed ratios are usually prepared on a volumetric basis. A maximum equal tire chip to soil ratio is suggested so that tire chip usage is not reduced too greatly. Small percentages of tire chips could improve the compactibility of the soil.

For sand-tire mixtures, it can be concluded that; increase in the percent of tire waste increases the shear strength of the sand. Also the increase in the initial dry density of the sand-tire waste mixture means higher shear strength parameters of mixture.

2.7. Unresolved Issues

There are several unresolved issues about using shredded scrap tires in fills and embankments. The first one is to determine the cause or causes of the exothermic reactions

that resulted in scrap tire embankment fires. Tire shred or tire chip embankment projects, should be more closely monitored, possibly by installing temperature probes and gas sampling wells. Gas from such wells should be periodically measured and analyzed for oxygen level, hydrogen sulfide, carbon dioxide, carbon monoxide, and hydrocarbons. The PH of any water leaching from scrap tire fills should be measured.

On the other hand, more information is needed on the basic types of tire shredding machinery currently in use and their effect on particle shape and size. The effects of mixing or blending various size shreds or chips within an embankment also need to be further evaluated in terms of resultant engineering properties such as settlement, permeability, drainage conditions, etc.

For soil improvement properties, blending of soil and tire chips or shreds must be investigated more to obtain most effective proportions of tire chips and soil. The type of soil is another variable that will influence the bulk density and compaction characteristics of the tire chip-soil mixtures. To analyze optimum proportions of tire chips and soil for different tire particle sizes and or soil types can figure out best results for all engineering applications.

2.8. Scrap Tire Management Options

The environmentally acceptable scrap tire management options are; reduction as a consequence of a technological development that improves service life, re-use as tires by retreading, recycle by cutting, to make new products such as floor mats, recycle by grinding, to make asphalt mixtures or rubber plastic compounds, recycle of tire chips in applications such as road beds and tracking fields, recover of the raw material to manufacture new products, process of the tire to make tire-derived fuel, re-use of the whole tire for civil engineering purposes.

3. GENERAL INFORMATION ABOUT TIRE WASTE INCLUSIONS

3.1. Previous Studies of Direct Shear Tests

Humphrey *et al.* (1993) has conducted large-scale direct shear tests with three different tire chips. Tire chips with length smaller than 72 mm were used. They reported that friction angles and cohesions were ranging between 19°-25° and 7.7-8.6 kPa respectively. In the study it is stated that tire chips are useful for constructing lightweight embankments over soft soils.

Tatlisoz *et al.* (1998) studied on the evaluation of the mechanical properties and behavior of tire waste chips and their mixtures with fine and coarse-grained soils. Large-scale laboratory testing equipment was used to conduct the study. Tests were conducted to evaluate shear strength, deformability and compressibility. Mixtures made with typical backfill soils such as clean sand, sandy silt and clay. Results of the tests showed that tire chips and soil-tire chip mixtures behave like soils but are more compressible and also require more deformation to mobilize their ultimate shear strength. Also, adding tire chips results a decrease in shear strength at low normal stress values. It is explained with the increase in strength which probably not obtained because of poor bonding between clay and tire chips.

Young *et al.* (2003) performed a set of direct shear tests in order to investigate physical and chemical properties of recycled tire shreds. In order to test the shear strength parameters of tire shreds, the minimum aspect ratio of the apparatus to the maximum particle size is 2 to 1. The normal force was applied by using a 1334.5 kN capacity testing machine. In conclusion, results revealed that tire shreds can be utilized in construction applications. As the particle size from 50 to 300 mm of the tire shreds increased, the shear strength of the scrap tire increased. Moreover, as the tire shred size increased, compressibility increased.

Edinçliler *et al.* (2004) conducted a set of large-scale direct shear test. The results showed that the two potential waste materials can be used in highway embankment construction: tire buffings and manufactured fly ash pellet aggregates. The results indicated that the displacement at failure values were increased by three to seven fold with tire buffings addition. Even at 10% tire–sand mixture, the deformation behaviour mixture altered considerably.

Attom (2005) investigated the effect of shredded tires on the physical properties of sands. Three types of sand was mixed with four different percentages of shredded tires: 10, 20, 30 and 40% by dry weight. Direct shear tests were conducted to study the effect of the shredded tires on the shear strength properties of sands, such as angle of internal friction and shear strength. From the tests conducted on three different gradations of sand mixed with four different percentages of shredded tire wastes. It is concluded that the increase in the percent of shredded tire waste increased both the angle of internal friction and the shear strength of the sand. The increase in the initial dry density of the sand– shredded tire waste mixture, increased the shear strength of the sand.

Ghazavi and Sakhi (2005) investigated the influence of optimized tire shred on shear strength parameters of sand. In the study, they performed direct shear tests with tire shreds contents of 15%, 30% and 50% by volume and prepared with a special cutter in three widths of 2, 3 and 4 cm and various lengths. The results show that the influencing parameters on shear strength characteristics of sand–shred mixtures are normal stress, sand matrix unit weight, shred content, shred width and aspect ratio of tire shreds. The friction angle of mixtures increases by using optimum shred aspect ratio and by increasing shred contents and mixture compaction.

Additionally, Ghazavi and Sakhi (2005) stated that the tires selected for tests by the authors were roughly smooth. If the tires had been chosen similar to those used by Foose *et al.* (1996) greater friction angles would have been obtained. As the amount tire shred material increases, the interlocking effect becomes more significant and higher cohesion appears. When shear stresses are applied to specimens, sand grains penetrate into shreds

and sample tends to dilate, volume of mixtures increase. Thus the sample thickness increase and the friction between particles decreases. Furthermore, if shred sizes optimized, the initial friction angle of mixtures increases. In small aspect ratios for tire shreds, less friction exists between materials. The shear resistance increases as the anchored length increase. On the other hand if the shreds are longer than a certain quantity, the movement of the mixture due to shear loading, causes some of these shred lengths due to their continuity, and are possibly curved and separated from sand grains and other shreds in their vicinity.

Venkatappa and Dutta (2006) studied on compressibility and strength behaviour of sand–tire chip mixtures. In this study, they performed compressibility tests in order to assess the behaviour of the admixtures by varying chip size and chip content. The results of the test figured out that sand–tyre chip mixtures up to 20% could be a potential material for highway construction and embankment construction up to 10 m height. Additionally, drained triaxial test results showed that the addition of chips causes a marginal increase of about 2° in the value of ϕ' for all types of chips. It is stated that as it is seen at Foose *et al.* (1996), different sample preparation procedure as different compaction procedures can produce various magnitudes of strength.

The summary of previous studies stated by Ayhan (2007) is modified with recent studies and given in Table 3.1.

Table 3.1. Summary of previous shear strength test results (after Ayhan, 2007), (continued).

Reference	Test	Material	$\gamma(\text{kN/m}^3)$	c (kPA)	Φ (°)
Humphrey <i>et al.</i> (1993)	Large Scale Direct Shear Test	Tire Chips 1 < 76mm	7.01	8.6	25
		Tire Chips-1 < 76 mm	6.82	11.5	19
		Tire Chips-1< 76 mm	7.24	7.7	21
		Tire Chips-2 < 76 mm	-	4.3	26
Wu <i>et al.</i> (1997)	Triaxial Compression Test	Tire Chips 38 mm-Flat	5.89	0	57
		Tire Chips 2 mm- Powder	5.69	0	45
		Tire Chips 9.5 mm-Granular	5.89	0	47
		Tire Chips 19 mm-Granular	5.69	0	54
		Tire Chips 9.5 mm Elongated	4.95	0	54
Tatlisoz <i>et al.</i> (1998)	Large Scale Direct Shear Test	Sandy Silt	18.3	11	30
		10 % Tire Chips	17.6	8	55
		20 % Tire Chips	17	38	54
		30 % Tire Chips	16.3	39	53
		Sand	16.8	2	34
		Tire Chips	5.9	0	30
		10 % Tire Chips	5.9	2	46
		20 % Tire Chips	15.6	2	50
		30 % Tire Chips	13.3	2	52
Edinçliler <i>et al.</i> (2004)	Large Scale Direct Shear Test	Sand	15.3	6.9	33
		Tire Buffings	5.1	3.1	22
		5 % Tire Buffings	15.19	10.4	28
		10 % Tire Buffings	14.89	8.7	29
		20 % Tire Buffings	14.22	15.5	5
		30 % Tire Buffings	23.56	10.7	8

Table 3.1. Summary of previous shear strength test results (after Ayhan, 2007), (continued).

Reference	Test	Material	$\gamma(\text{kN/m}^3)$	c (kPa)	Φ (°)
Zornberg <i>et al.</i> (2004)	Large Scale Triaxial Test (CD) (48.3, 103.5 and 207 kPa)	Sand	15.64	7.8	36.8
		Sand	16.21	3.8	41.0
		Tire Shred	-	22.8	21.4
		5% Tire Shred	-	7.0	36.1
		10% Tire Shred	-	21.7	35.7
		30% Tire Shred	-	30.4	35.7
		60% Tire Shred	-	18.2	34.4
		38.3% Tire Shred	-	41.2	36.1
Attom (2004)	Large Scale Direct Shear (Sand A)	Sand A	-	0	25
		10 % Tire Shred	-	0	30
		20 % Tire Shred	-	0	37
		30 % Tire Shred	-	0	41
		40 % Tire Shred	-	0	45
	Large Scale Direct Shear (Sand B)	Sand B	-	0	28
		10 % Tire Shred	-	0	35
		20 % Tire Shred	-	0	42
		30 % Tire Shred	-	0	47
		40 % Tire Shred	-	0	49
	Large Scale Direct Shear (Sand C)	Sand C	-	0	36
		10 % Tire Shred	-	0	42
		20 % Tire Shred	-	0	45
		30 % Tire Shred	-	0	48
		40 % Tire Shred	-	0	50

Table 3.1. Summary of previous shear strength test results (after Ayhan, 2007), (continued).

Reference	Test	Material	$\gamma(\text{kN/m}^3)$	c (kPa)	Φ (°)
Gotteland <i>et al.</i> (2005)	Large scale Triaxial (CD) (50, 75 and 100 kPa)	Sand	16.7	0	40.9
		Tire Chips	6.1	16.3	19
		14% Tire Chips	15.5	13.8	39
		14 % Tire Chips (H)	15.9	15	42.6
		14% Tire Chips (V)	15.9	7.5	41.7
		15% Tire Chips (H&V)	15.5	10	41.1
		22 % Tire Chips (H&V)	15.3	50	36.1
		50 % Tire Chips	11.4	7.5	41.5
Venkatappa a Rao <i>et al.</i> (2006)	Triaxial (CD) (34.5, 69, 138, 276 kPa)	Sand	16.7	0	38
		5 % Tire Chips 1	-	6.6	39.6
		10 % Tire Chips 1	-	9.1	39.7
		15 % Tire Chips 1	-	11.5	39.9
		20 % Tire Chips 1	-	13.3	40
		5 % Tire Chips 2	-	9.2	39.5
		10 % Tire Chips 2	-	11.6	39.7
		15 % Tire Chips 2	-	14.1	39.9
		Sand A	-	0	25
		10 % Tire Shred	-	0	30
		20 % Tire Shred	-	0	37
		30 % Tire Shred	-	0	41
		40 % Tire Shred	-	0	45

Table 3.1. Summary of previous shear strength test results (after Avhan, 2007). (continued).

Reference	Test	Material	$\gamma(\text{kN/m}^3)$	c (kPa)	Φ (°)	
Ayhan (2007)	Large Scale Direct Shear Test	Sand	14	0	34.20	
		Tire Crumbs	3.5	5.4	16.39	
		10% Tire Crumbs + 90% Sand	13.5	5.46	38.32	
		20% Tire Crumbs + 80% Sand	13	10.86	29.52	
		30% Tire Crumbs + 70% Sand	12	12.77	28.13	
	Large Scale Direct Shear 2mm<TB<4 mm	Tire Buffings	5.5	7.58	11.56	
		10% Tire Buffings + 90% Sand	13.5	16.53	29.79	
		20% Tire Buffings + 80% Sand	12	13.91	32.37	
		30% Tire Buffings + 70% Sand	10	17.73	25.19	
	Large Scale Direct Shear TB>4mm	Tire buffings	3.5	12.44	7.37	
		10% Tire Buffings + 90% Sand	13.5	11.46	37.4	
		20% Tire Buffings + 80% Sand	12	0.11	51.13	
		30% Tire Buffings + 70% Sand	10	13.39	32.02	
	Çağatay (2008)	Triaxial (Quick Compression) (40, 100, 200 kPa)	Sand	16.0	9.97	16.89
			Tire Crumbs	6.5	8.10	38.19
			5% Tire Crumbs	15.1	15.1	38.16
10% Tire Crumbs			14.5	21.02	35.12	
20% Tire Crumbs			13.3	24.65	31.02	
30% Tire Crumbs			12.5	14.21	31.02	
40% Tire Crumbs			11.2	9.28	28.69	
Tire Buffings			4.6	9.54	14.35	
5% Tire Buffings			14.7	11.43	41.28	
10% Tire Buffings			13.7	14.98	35.93	

Table 3.1. Summary of previous shear strength test results (after Ayhan, 2007), (continued).

Reference	Test	Material	γ (kN/m ³)	c (kPA)	Φ (°)
Çağatay (2008)	Triaxial (CD) (40, 100, 200 kPa)	20% Tire Buffings	12.1	14.04	30.99
		30% Tire Buffings	10.30	13.63	26.89
		40% Tire Buffings	9.10	11.18	24.70
		Sand	16.0	1.45	41.49
		Tire Crumbs	6.5	30.17	17.56
		5% Tire Crumbs	15.1	16.13	39.35
		10% Tire Crumbs	14.5	17.38	38.33
		20% Tire Crumbs	13.3	15.60	35.44
		30% Tire Crumbs	12.5	12.72	36.28
		40% Tire Crumbs	11.2	27.85	27.57
		Tire Buffings	4.6	29.51	16.62
		5% Tire Buffings	14.7	5.51	41.07
		10% Tire Buffings	13.7	15.64	35.10
		20% Tire Buffings	12.10	14.74	33.88
		30% Tire Buffings	10.3	11.83	30.47
		40% Tire Buffings	9.10	28.05	24.36
		Edinçliler and Ayhan (2010)	Large Scale Direct Shear Test	Tire Buffings	5.1
Sand	15.3			6.9	33
5% TB + 95% sand	15.2			10.4	28.2
10% TB + 90% sand	14.9			8.7	29
20%TB + 80% sand	14.2			15.5	5.3
30%TB + 70% sand	13.6			10.7	8.3
Tire buffings (TB1)	5.5			7.6	11.6

Table 3.1. Summary of previous shear strength test results (after Ayhan, 2007), (continued).

Reference	Test	Material	$\gamma(\text{kN/m}^3)$	c (kPA)	Φ (°)
Edinçliler and Ayhan (2010)	Large Scale Direct Shear Test	Sand (S)	14.0	0	34.2
		TB1-10 (10% TB1 + 90% sand)	13.5	16.5	29.8
		TB1-20 (20% TB1 + 80% sand)	12.0	13.9	32.4
		TB1-30 (30% TB1 + 70% sand)	10.0	17.7	25.2
		Sand (S)	14.0	0	34.2
		TB2-10 (10% TB2 + 90% sand)	13.5	11.5	37.4
		TB2-20 (20% TB2 + 80% sand)	12.0	2.2	45.4

3.2. Previous Studies on Dynamic Laboratory Tests

Feng and Sutter (2000) performed a set of torsional resonant column test to investigate the shear modulus and damping ratio of granulated rubber and sand mixtures. Specimens were constructed using different percentages of granulated tire rubber and Ottawa sand at different percentages. As a result of these set of tests, it is figured out that the shear modulus of the mixtures influenced by the percentage of the rubber inclusion. Damping ratio increased slightly with confinement pressure for the 100% rubber. This can be explained as; under increasing confining stress, the size of interparticle contacts between particles increases significantly due to the presence of rubber. Additionally, the normalized shear modulus reduction for 50% granulated rubber is close to a typical saturated cohesive soil. It is stated that the damping ratio in rubber-sand mixture is due to; (i) the friction particles and (ii) the deformation of particles. The sand particles are very stiff and thus dissipate very little energy in particle deformation. Also, the samples prepared by hand-spooning were less uniform and consequently more sand clusters existed

in samples and by the way the rubber dominates the strength behaviour of mixture which results with lower shear modulus.

Edinçliler *et al.* (2004) conducted a set of cyclic triaxial test with tire buffings, sand and tire buffing mixtures. Test results demonstrate that the dynamic shear modulus values for tire buffings are very low when compared to those of sand and tire buffing mixtures. Also, tire buffings added to the medium dense sand changed the deformation behavior and the dynamic behavior of sand–tire buffings mixture. The damping ratio of sand was increased more than three fold by the addition of tire buffings due to the fiber shape of tire buffings.

Ribay *et al.* (2004) carried out a set of laboratory cyclic triaxial and resonant column tests to investigate shear modulus and damping ratio of grouted sand. Different types of grouted sands were investigated. The results of experiments demonstrate that; the shear modulus increase with confining stress and variation of confining stress has a negligible effect on the damping ratio of specimen. Also the shear modulus increases as strain increases. The slight effect of variation in confining stress on damping ratio explained by the limited rotation and particle sliding and restricted mobilisation of sliding.

Anastasiadis *et al.* (2009) performed experimental and theoretical studies to investigate dynamic characteristics of soil-rubber mixtures using a fixed-free torsional resonant column device. Specimens were prepared with various percentages of granulated tire rubber and a medium poor graded sand. Specimens were tested under 50 and 100 kPa confining pressures. It is concluded that low amplitude resonant column results indicate a significant reduction in shear stiffness of sand/rubber specimens due to contribution of rubber solids on shear stiffness of the sand/rubber matrix. Also, low amplitude damping ratio of sand-rubber mixtures increases significantly with an increase in the percentage of rubber. The dynamic parameters of clean granulated tire rubber are unaffected by confining pressure. Saturated specimens exhibit higher damping ratio at low amplitude shear strains due to the mechanisms of viscous damping observing on saturated specimens. Low amplitude shear modulus is slightly affected by moisture content.

4. LIQUEFACTION

4.1. General Information About Liquefaction

Liquefaction is a phenomenon wherein a mass of soil loses a large percentage of its shear resistance, when subjected to monotonic, cyclic or shock loading and flows in a manner resembling a liquid until the shear stresses acting on the mass are as low as the reduced shear resistance. Soil liquefaction can be defined as the transformation from a solid state to a liquefied state as a consequence of increased pore pressure and reduced effective stress. Some ground failures attributed to soil liquefaction are more correctly described to "cyclic mobility" which results in limited soil deformations without liquid-like flow. The definition for soil liquefaction has been the subject of a geotechnical profession. Liquefaction is commonly used to describe all failure mechanisms resulting from the build-up of pore pressures during undrained cyclic shear of saturated soils (Rauch, 1997).

Liquefaction results from the tendency of soils to decrease in volume when subjected to shear stresses. The soil grains tend to rearrange into a more dense packing, with less space in the voids, as water in the pore spaces is forced out, when loose and saturated soils are sheared. If drainage of pore water is impeded, pore water pressures increase progressively with the shear load. This leads to the transfer of stress from the soil skeleton to the pore water precipitating a decrease in effective stress and shear resistance of the soil. If the shear resistance of the soil becomes less than the static, driving shear stress, the soil can undergo large deformations and is said to liquefy (Seed and Idriss 1982). Liquefaction of loose, cohesionless soils can be observed under both monotonic and cyclic shear loads.

When dense sands are monotonically sheared, the soil skeleton may first compress and then dilate as the sand particles move up and over one another. For dense, saturated sands sheared without pore water drainage, the tendency for dilation or volume increase results in a decrease in pore water pressure. When a dense sand sample is subjected to cycles of small shear strains under undrained conditions, excess pore pressure may be generated in each load cycle leading to softening and the accumulation of deformations.

However, at larger shear strains, dilation relieves the excess pore pressure resulting in an increased shear resistance.

The probability of dense, saturated sands to progressively soften under undrained cyclic shear but achieve limiting strains under subsequent static loading, is more precisely described as cyclic mobility (Castro, 1975; Castro and Poulos, 1977). Cyclic mobility is distinguished from liquefaction by the fact that a liquefied soil exhibits no appreciable increase in shear resistance regardless of the magnitude of deformation (Seed 1979). Soils subject to cyclic mobility will first soften under cyclic loading but then stiffen when monotonically loaded without drainage as the tendency to dilate reduces the pore pressures. During cyclic mobility, the residual shear resistance remains greater than the driving static shear stress and deformations accumulate only during cyclic loading.

It is possible for a dilative soil to reach a temporary condition of zero effective stress and shear resistance. When the initial static shear stress is low, cyclic loads may produce a reversal in the shear stress direction. That is, the stress path passes through a state of zero shear stress. Under these conditions, a dilative soil may accumulate sufficient pore pressures to reach a condition of zero effective stress and large deformations may develop. The deformations stabilize when cyclic loading ends because the tendency to dilate with further shear increases the effective stress and shear resistance. Unlike cyclic mobility, cyclic liquefaction involves at least some deformation occurring while static shear stresses exceed the shear resistance (when the condition of zero effective stress is approached). However, deformations do not continue after cyclic loading ends as the tendency to dilate quickly results in strain hardening. Again, this type of failure in saturated, dense cohesionless deposits is usually identified as "liquefaction" but with limited deformations.

Considering these mechanisms of ground failure, Robertson *et al.* (1997) suggested a classification system to define "soil liquefaction". This system can be summarised as;

- (i) Flow liquefaction, used for the undrained flow of a saturated, contractive soil when the static shear stress exceeds the residual strength of the soil. Failure may be triggered by cyclic or monotonic shear loading.
- (ii) Cyclic softening used to describe large deformations occurring during cyclic shear due to pore pressure build-up in soils that would tend to dilate in undrained, monotonic shear.

Cyclic softening, in which deformations do not continue after cyclic loading ceases, can be further classified as; Cyclic Liquefaction and Cyclic Mobility. Cyclic Liquefaction occurs when cyclic shear stresses exceed the initial, static shear stress to produce a stress reversal. A condition of zero effective stress may be achieved during which large deformations may occur. Cyclic Mobility occurs when cyclic loads do not yield a shear stress reversal and a condition of zero effective stress does not develop. Deformations accumulate in each cycle of shear stress.

This classification system for liquefaction recognizes that various mechanisms may be involved in a given ground failure. Yet, this definition preserves the contemporary usage of the term "liquefaction" to broadly describe the failure of saturated, cohesionless soils during earthquakes.

In most of the well known earthquakes in the world, hazardous damages often associated with liquefaction. Some of those earthquakes are Kobe Earthquake (1995), Niigata Earthquake (1964), Alaska Earthquake (1964), Loma Prieta Earthquake (1989) (Figure 4.1).



Figure 4.1. Earthquake hazards caused by liquefaction.

4.2. Liquefaction Susceptibility of Soils

Liquefaction is most commonly observed in shallow, loose, saturated deposits of cohesionless soils subjected to strong ground motions in large-magnitude earthquakes. Unsaturated soils are not liquefiable because volume compression does not generate excess pore pressures. Liquefaction and large deformations are more likely with contractive soils while cyclic softening and limited deformations are associated with dilative soils.

Since liquefaction is associated with the tendency for soil grains to rearrange when sheared, anything that impedes the movement of soil grains will increase the liquefaction resistance of a soil deposit. Particle cementation, soil fabric, and aging - all related to the geologic formation of a deposit are important factors that can hinder particle rearrangement (Seed, 1979). Soils deposited prior to the Holocene epoch (more than 10,000 years old) are usually not prone to liquefaction (Youd and Perkins, 1978), perhaps due to weak cementation at the grain contacts. However, conventional sampling techniques inevitably disturb the structure of cohesionless soils such that laboratory test specimens are usually

less resistant to liquefaction than the in-situ soil. Even with reconstituted laboratory samples, the soil fabric and resistance to liquefaction are affected by the method of preparation such as dry pluviation, moist tamping, water sedimentation, etc. After liquefaction has occurred, the initial soil fabric and cementation have very little influence on the shear strength beyond about 20% strain (Ishihara, 1993).

Stress history plays an important role in determining liquefaction resistance of a soil. Deposits subjected to past cyclic loading are usually more resistant to liquefaction as the soil grains tend to be in a more stable arrangement. Additionally, the liquefaction resistance of a soil deposit increases with depth as the effective overburden pressure increases. Characteristic of the soil grains influence the susceptibility of a soil to liquefy. Rounded soil particles of uniform size are generally the most susceptible to liquefaction. Well-graded sands with angular grain shapes are generally less prone to liquefaction. Soils with a significant plastic fines content are rarely observed to liquefy in earthquakes. Low plasticity fines may contribute to the liquefaction susceptibility of a soil. Permeability also affects the liquefaction characteristics of a soil deposit. High permeable soils are more susceptible to liquefaction than low permeable soils. Soils with 50% or more of their grain size in the range of 0.02 mm to 0.2 mm are potentially liquefiable when saturated. To initiate liquefaction local ground acceleration greater than 0.10g is required.

Seed *et al.* (1983) also stated that based on both laboratory testing and field performance, the great majority of cohesive soils will not liquefy during earthquakes. Using criteria originally stated by Seed and Idriss (1982) and subsequently confirmed by Youd and Gilstrap (1999), a soil must meet all the following three criteria to liquefy;

- The soil must have less than 15% of the particles, based on dry weight, that are finer than 0.005 mm (i.e., % finer at 0.005 mm < 15%)
- The soil must have a liquid limit (LL) that is less than 35 (that is, $LL < 35$)
- The water content of the soil must be greater than 90% of the liquid limit (that is, $w > 0.9 * LL$).

4.3. Soil Liquefaction and Ground Failures

The nature and severity of liquefaction damage is a function of the reduced shear strength and the magnitude of the static shear loads supported by the soil deposit (Ishihara *et al.* 1991). The likelihood of soil liquefaction has been identified, an engineering evaluation must focus on the mode and magnitude of ground failures that might result. Eight types of failure commonly associated with soil liquefaction in earthquakes:

- Sand boils, which usually result in subsidence and relatively minor damage.
- Flow failures of slopes involving very large down-slope movements of a soil mass.
- Lateral spreads resulting from the lateral displacements of gently sloping ground.
- Ground oscillation where liquefaction of a soil deposit beneath a level site leads to back and forth movements of intact blocks of surface soil.
- Loss of bearing capacity causing foundation failures.
- Buoyant rise of buried structures such as tanks.
- Ground settlement, often associated with some other failure mechanism.
- Failure of retaining walls due to increased lateral loads from liquefied backfill soil or loss of support from liquefied foundation soils.

4.4. Main Factors that Govern Liquefaction of The Field

There are many factors that govern liquefaction process in situ soil. The most important factors that govern liquefaction are as follows:

4.4.1. Earthquake Intensity and Duration

The character of the ground motion, such as; acceleration and duration of shaking cause contraction of soil. The potential of liquefaction increase as the earthquake and duration of shaking increase.

4.4.2. Groundwater Table

The soils are currently above the groundwater table and are highly to become saturated for given foreseeable changes in the hydrological regime, then such soils generally do not need to be evaluated for liquefaction potential. At sites where the groundwater table significantly fluctuates, the liquefaction potential also fluctuate.

4.4.3. Soil Type

Seed and Idriss (1982) stated and subsequently Youd and Gilstrap (1999) confirmed that liquefaction susceptible soil must have less than 15% of the particles, based on dry weight, that are finer than 0.005 mm (per-cent finer than 0.005 mm < 15%). Also, sand which has uniform gradation and rounded soil particles, very loose or loose density state, recently deposited with no cementation between soil grains, and no prior preloading or seismic shaking is susceptible to liquefaction.

4.4.4. Soil Relative Density

Cohesionless soils in a loose relative density state are susceptible to liquefaction. Loose nonplastic soils will contract during the seismic shaking which will cause the development of excess pore water pressures. For dense sands, the state of initial liquefaction does not produce large deformations because of the dilation tendency of the sand upon reversal of the cyclic shear stress.

4.4.5. Particle Size Gradation

Uniformly graded nonplastic soils tend to form more unstable particle arrangements and are more susceptible to liquefaction than well graded soils. Kramer (1996) states that field evidence indicates that most liquefaction failures have involved uniformly graded granular soils. Also, Tsuchida (1970) developed a chart to evaluate the liquefaction susceptibility of soils (Figure 4.2).

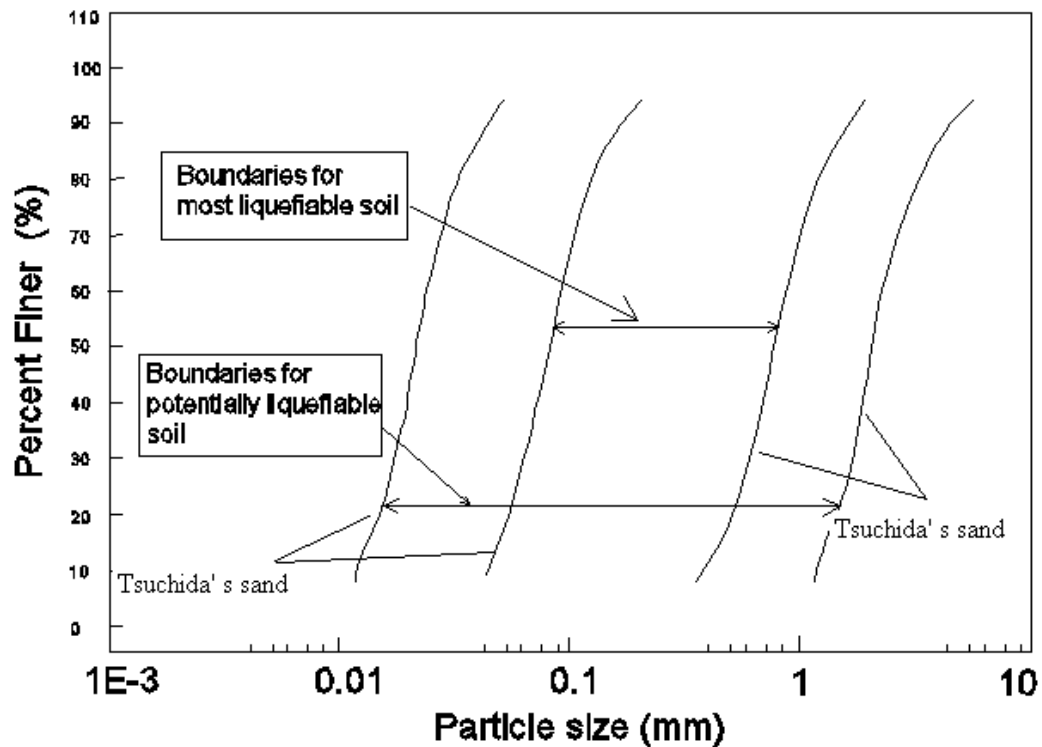


Figure 4.2. Liquefaction Susceptibility Chart of Soils (Tsuchida, 1970).

4.4.6. Placement Conditions or Depositional Environment

Hydraulic fills tend to be more susceptible to liquefaction because of the loose and segregated soil structure created by the soil particles falling through water.

4.4.7. Confining Pressure

The greater confining pressure, the less susceptible the soil is to liquefaction. Conditions that can create a higher confining pressure are a deeper groundwater table, soil that is located at a deeper depth below ground surface and a surcharge pressure applied at ground surface.

4.4.8. Particle Shape

Soils having rounded particles tend to densify more easily than angular-shape soil particles. A soil which contains rounded soil particles is more susceptible to liquefaction than a soil containing angular soil particles.

4.4.9. Aging and Cementation

Newly deposited soils tend to be more susceptible to liquefaction than older deposits of soils. The increase in liquefaction resistance with time could be due to the deformation or compression of soil particles into more stable arrangements.

4.4.10. Historical Environment

Older soil deposits that have already been subjected to seismic shaking have an increased liquefaction resistance compared to a newly formed specimen of the same soil having an identical density (Finn *et al.* 1970, Seed *et al.* 1975).

4.4.11. Building Load

The construction of a heavy building on top of a sand deposit can decrease the liquefaction resistance of the soil.

4.5. Methods to Evaluate The Liquefaction Potential of a Site

For most common structures built using the Uniform Building Code (UBC, 1927), as a minimum a probabilistically derived peak ground acceleration with a 10% probability of exceedance in 50 years (i.e. 475-year return period) should be used when site-specific analyses are performed. The factor of safety for level ground liquefaction resistance has been defined as the ratio of CSR_{liq} to CSR_{eq} where CSR_{eq} is the cyclic stress ratio generated by the anticipated earthquake ground motions at the site, and CSR_{liq} is the cyclic stress ratio required to generate liquefaction (Seed and Idriss, 1982). A factor of safety in the range of about 1.1 is generally acceptable for single family dwellings, while a higher value in the range of 1.3 is appropriate for more critical structures. Furthermore, consequences of different liquefaction hazards vary. For example, hazards caused by flow failure are often more disastrous than hazards from differential settlement.

If it is determined that the soil has the ability to liquefy during an earthquake and the soil is below or will be below, then the liquefaction analysis is performed. During the calculation of Cyclic Stress Ratio (CSR), it is assumed that there is a level ground surface and a soil column of unit width and length that the soil column will move horizontally as a rigid body in response to the maximum horizontal acceleration a maximum exerted by the earthquake at ground surface (Figure 4.3).

$$\tau_{\max} = F = \gamma \times t \times z \times \left(\frac{a_{\max}}{g} \right) = \sigma_{v0} \times \left(\frac{a_{\max}}{g} \right)$$

$$\tau_{\text{cyc.}} = 0.65 \times \tau_{\max}$$

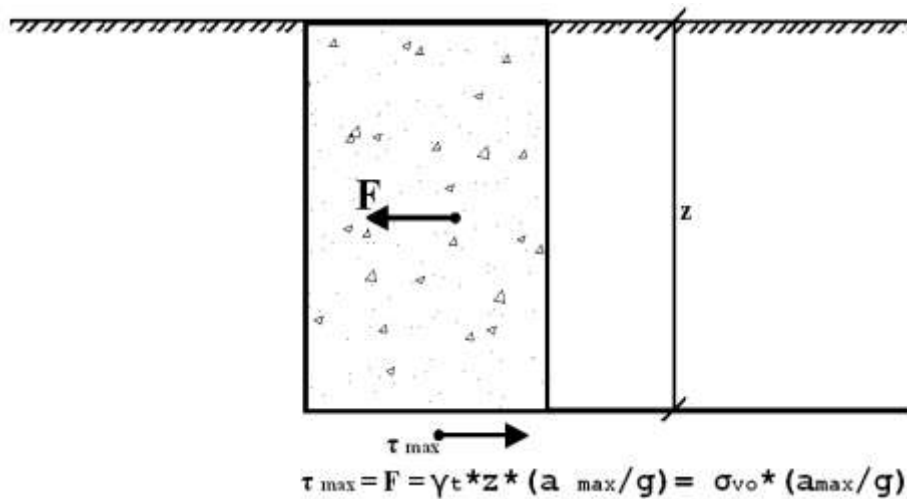


Figure 4.3. Conditions assumed for the derivation of the CSR earthquake equation

$$CSR = \frac{\tau_{\text{cyc}}}{\sigma'_{v0}} = 0.65 \times r_d \times \left(\frac{\sigma_{v0}}{\sigma'_{v0}} \right) \times \left(\frac{a_{\max}}{g} \right)$$

and

$$r_d = 1 - 0.012 \times z$$

where CSR is the cyclic stress ratio, a_{\max} is the maximum horizontal acceleration, g is the acceleration of gravity, σ_{v0} is the total vertical stress at a particular depth where the liquefaction analysis is performed, σ'_{v0} is the vertical effective stress at same depth, r_d is the depth reduction factor (dimensionless), τ_{\max} is the maximum shear stress at the depth of z , $\tau_{\text{cyc.}}$ is the shear stress occurred with the repeated loading.

4.6. Methods to Reduce Liquefaction Hazards

Liquefaction hazards have typically been mitigated using two types of techniques: Usage of specialized foundation types and in situ soil improvement techniques. Soil improvement techniques typically involve some type of soil densification process, such as vibro-compaction, deep soil mixing, dynamic compaction, or compaction grouting. These techniques tend to compact the soil, reducing the tendency for contraction during an earthquake, and thus reduce the effects of liquefaction.

If a seismic hazard assessment demonstrates that liquefaction is likely adjacent to a bridge and approach structures and geotechnical/structural limit states may be exceeded, mitigation strategies should be evaluated. Generally, seismic strengthening can be achieved by soil improvement and/or structural enhancement. Only soil improvement techniques are addressed here. The goal of remedial soil improvement is to limit soil displacements and settlements to acceptable levels.

Remedial strategies for improving the stability of slopes and embankments against to the liquefaction hazards have been well developed for both onshore and submarine slopes. Common techniques for stabilizing slopes include modifying the geometry of the slope, utilization of berms, soil replacement, soil improvement and structural techniques such as the installation of piles adjacent to the toe of the slope. Constraints imposed by existing structures will often dictate which methods, or combination of methods should be used.

Remediation objectives include increasing the soil liquefaction resistance through densification, increasing its strength, and/or improving its drainage. Table 4.1. presents the most common remediation measures. The use of these measures has limited the occurrence of liquefaction during recent earthquakes.

The monitored injection of very stiff grout into a loose sandy soil results in the controlled growth of a grout bulb mass that displaces the surrounding soils. This action

increases lateral earth pressures and compacts the soil, thereby increasing its resistance to liquefaction.

The in situ injection and mixing of cement into weak soils is becoming more common in the western United States. Recent applications include liquefaction mitigation and the strengthening of weak cohesive soils adjacent to embankments, levees and bridge abutments.

The first option to reduce liquefaction hazards is to avoid construction on liquefaction susceptible soils. By evaluating liquefaction susceptibility of soil, characterization of soil can be obtained. If the soil is in critical state, it has to be avoided.

If it is necessary to construct a structure on liquefaction susceptible soil because of space restrictions, favorable location or other reasons, it may be possible to make the structure liquefaction resistant by designing the foundation elements to resist the effects of liquefaction.

The third alternative is to reduce earthquake hazard by improving soil. There are many improvement techniques to improve soil such as; preloading, vertical drains, in-situ densification, grouting, stabilization by using mixtures, reinforcement, etc. The engineering properties of the soil such as; strength, density, drainage characteristics can be improved against to the hazardous effect of earthquakes by these set of techniques.

Table 4.1. Liquefaction Remediation Measures (National Research Council, 1985).

METHOD	PRINCIPLE	Most Suitable Soil Conditions	Maximum Effective Depth	Relative Costs
Vibratory Probe a) Terraprobe b) Vibrorods c) Vibrowing	Densification by vibration; liquefaction-induced settlement and settlement in dry soil under overburden to produce a higher density.	Saturated or dry clean sand; sand.	20 m routinely (ineffective above 3-4 m depth); > 30 m sometimes; vibrowing, 40 m.	Moderate
Vibro-compaction a) Vibrofloat b) Vibro-Composer system.	Densification by vibration and compaction of backfill material of sand or gravel.	Cohesionless soils with less than 20% fines.	> 20 m	Low to moderate
Compaction Piles	Densification by displacement of pile volume and by vibration during driving, increase in lateral effective earth pressure.	Loose sandy soil; partly saturated clayey soil; loess.	> 20 m	Moderate to high
Heavy tamping (dynamic compaction)	Repeated application of high-intensity impacts at surface.	Cohesionless soils best, other types can also be improved.	30 m (possibly deeper)	Low
Displacement (compaction grout)	Highly viscous grout acts as radial hydraulic jack when pumped in under high pressure.	All soils.	Unlimited	Low to moderate
Surcharge or buttress	The weight of a surcharge/buttress increases the liquefaction resistance by increasing the effective confining pressures in the foundation.	Can be placed on any soil surface.	Dependent on size of surcharge/buttress	Moderate if vertical drains are used

Table 4.1. Liquefaction Remediation Measures (National Research Council,1985), (continued).

METHOD	PRINCIPLE	Most Suitable Soil Conditions	Maximum Effective Depth	Relative Costs
Electrokinetic injection	Stabilizing chemical moved into and fills soil pores by electro-osmosis or colloids in to pores by electrophoresis.	Saturated sands, silts, silty clays.	Unknown	Expensive
Drains a) Gravel b) Sand c) Wick d) Wells (for permanent dewatering)	Relief of excess pore water pressure to prevent liquefaction. Primarily gravel drains; sand/wick may supplement gravel drain or relieve existing excess pore water pressure. Permanent dewatering with pumps.	Sand, silt, clay.	Gravel and sand > 30 m; depth limited by vibratory equipment; wick, > 45 m	Moderate to high
Particulate grouting	Penetration grouting-fill soil pores with soil, cement, and/or clay.	Medium to coarse sand and gravel.	Unlimited	Lowest of grout methods
Chemical grouting	Solutions of two or more chemicals react in soil pores to form a gel or a solid precipitate.	Medium silts and coarser.	Unlimited	High
Pressure injected lime	Penetration grouting – fill soil pores with lime.	Medium to coarse sand and gravel.	Unlimited	Low
Jet grouting	High-speed jets at depth excavate, inject and mix a stabilizer with soil to form columns or panels.	Sands, silts, clays.	Unknown	High
Mix-in-place piles and walls	Lime, cement or asphalt introduced through rotating auger or special in-place mixer.	Sands, silts, clays, all soft or loose inorganic soils.	> 20 m (60 m obtained in Japan)	High

4.7. Sample Preparation Methods applied in Liquefaction Tests

Considerable experience has been gained in the past two decades on the preparation of sand specimens for dynamic testing. Methods for preparing fine grained soils are still being developed.

Water content, unit weight of soil, relative density, degree of saturation, void ratio are the controlling factors in preparing representative samples. Dry and wet pluviation, moist tamping, sedimentation, rodding and consolidating from slurry are the methods currently employed to prepare samples (Figure 4.4). The basic requirements for any of the methods are firstly to obtain homogeneous samples with uniform distribution of void ratio and secondly to be able to prepare samples having the lowest possible density. The second requirement is needed to cover a wide range of density in the sample reconstituted by an identical method (Ishihara, 1994).

In wet tamping method, five equal portions of sand are mixed with water at a water content of about 5%. A membrane is stretched to the inside face of a split mould which is attached to the base pedestal of the test apparatus. Each portion of the slightly moist sand is strewed with fingers to a predetermined height in five lifts. At each lift stage, tamping is gently applied with a small flat-bottomed tamper. The tamping energy need to be adjusted so that the volume contraction upon saturation would be about 5% for preparing the loosest specimen by this method. After the sample is enclosed by the membrane with the top cap, a vacuum is applied and the mould is dismantled. Carbon dioxide gas is percolated through the sample and de-aired water flushed. The void ratio measured after saturation under vacuum pressure is taken as the initial void ratio of the sample. Consolidation is then performed to the desired confining stress. One of the advantages of this method is the versatility in permitting any sample to be prepared within a wide range of void ratios. Therefore the sample could be very loose and highly contractive or dilative in subsequent loading, depending upon the void ratio at the time of sample preparation.

Another sample preparation method is dry deposition method. Oven-dried sand is filled in a cone shaped slender funnel. The sand is spread in the forming mould with zero

height of fall at a constant speed until the mould becomes filled with the dry sand. Tapping energy is applied by hitting the side of the mould to obtain a desired density. After the sample is encased in the membrane with the top cap, a vacuum is applied and carbon dioxide gas is percolated through the sample. De-aired water is then flushed making the sample saturated. Any state of a sample could be produced by this method by adjusting the tapping energy during the process of sample preparation. The sample prepared by this method is generally denser as compared to that prepared by the moist placement method. With this sample preparation method, the sample could be only slightly contractive in its behaviour in the subsequent application of shear stress. Therefore this method is not adequate to prepare samples with highly contractive characteristics. This method is different from what is generally called air pluviation in which dry sand is discharged vertically in air from a small nozzle into the mould. The air pluviation method is known to produce samples which are always dilative and has not been used in the present study.

In wet sedimentation method, sand is mixed with de-aired water and put in a funnel with a plastic tube attached to the end. The mixture of sand and water is poured, through the plastic tube, in four layers, in the sample forming mould at zero height of fall at a constant speed, so that the surface of water is always held coincident with that of the sand sediment. By the way, the sand is deposited continuously under water without causing appreciable segregation of the material. If a denser sample is to be prepared, compacting energy is applied by hitting the side of the mould stepwise during the process of sample placement. In a special method, a predetermined amount of sand is dumped into water and some length of time, from 30 minutes to 24 hours, is allowed to elapse until the material has completely settled. In this episode of deposition, coarse-grained material sediments at the bottom, grading to fines upwards. On top of this layer, an equal amount of the same soil is poured again and let to sediment under water in the same fashion as before. This stepwise deposition is repeated 4 to 5 times to construct a complete test sample. If a denser specimen is to be prepared, the side of the sample forming mould is hit with a hammer as many times as desired.

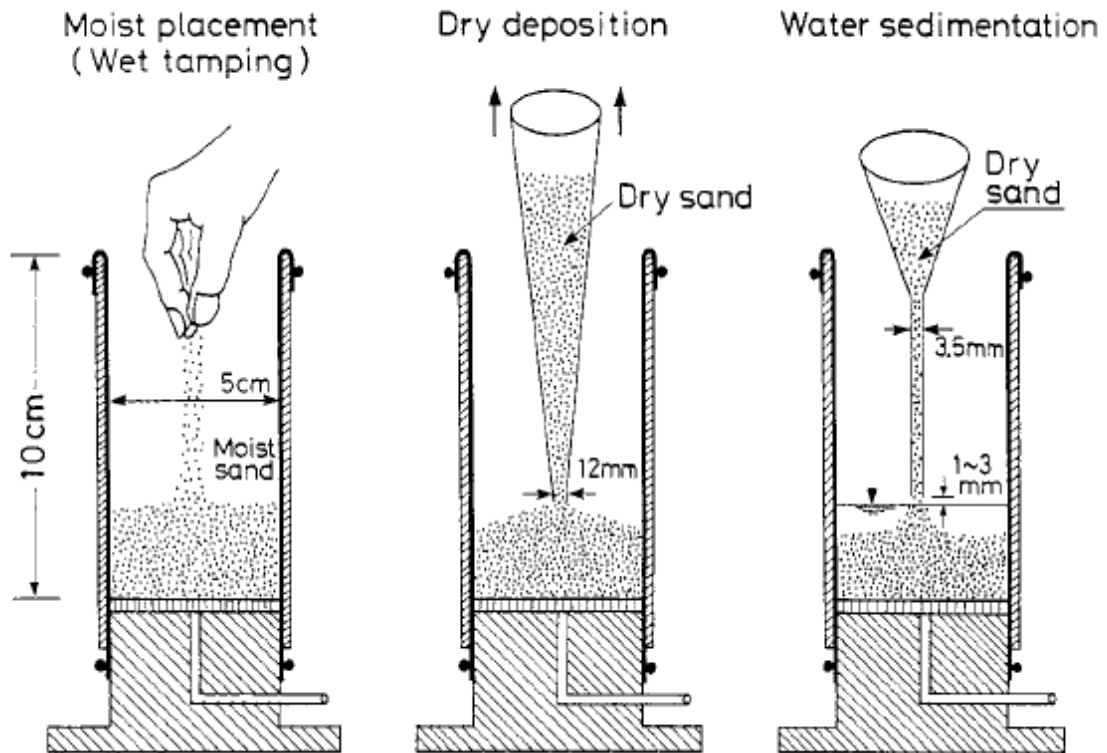


Figure 4.4. Sample Preparation Methods (Ishihara, 1994).

4.8. Background on Liquefaction Tests

Sitharam *et al.* (2004) studied on dynamic properties and liquefaction potential of soil by performing a set of laboratory tests. In the specimen preparation of dry pluviation method, it is essential to create a grain structure similar to that of naturally deposited river sand. Cylindrical soil specimens of size 50 mm diameter and 100 mm height were prepared by placing the sand in a funnel with a tube. The tube was placed at the bottom of mould. The tube was slowly raised along the axis of symmetry of the specimen. For relatively higher densities, the mould was tapped in a symmetrical pattern. After the specimen preparation normal pressure applied to reduce the disturbance using the removal of mould. Then the specimens were saturated with deaired water by using backpressure saturation. The saturation of the specimens was checked by checking Skempton's pore pressure parameter.

Ueng *et al.* (2006) developed a large biaxial shear box for shaking table test to study behaviour of saturated sand against to the liquefaction. The shear box is composed of 15 layers with a specimen size 1880 by 1880 by 1520 mm. Two dimensional wave action induced by the shaking table. The sand specimen inside the shear box is prepared by the wet sedimentation method from a large pluiviation device (Figure 4.5). A special pluivator was designed for preparing the sand specimen inside the shear box by raining method. This special pluivator composed of a container for the needed volume of sand, a motor driven perforated plate which is exchangeable for holes, a diffuser comprised of four layers of sieves. The wet sedimentation method was used for the specimen preparation in the study. The dry sand was rained down into the laminar box filled with water to a precalculated depth. The saturation of the specimen achieved by measuring P-wave velocity across the specimen horizontally at different depths. P-wave velocities between 1500 and 1700 m/s at various depths is the indication of well saturated specimen. Also, they measured the density and uniformity of specimen with short thin-walled tube samples which were taken at various locations.

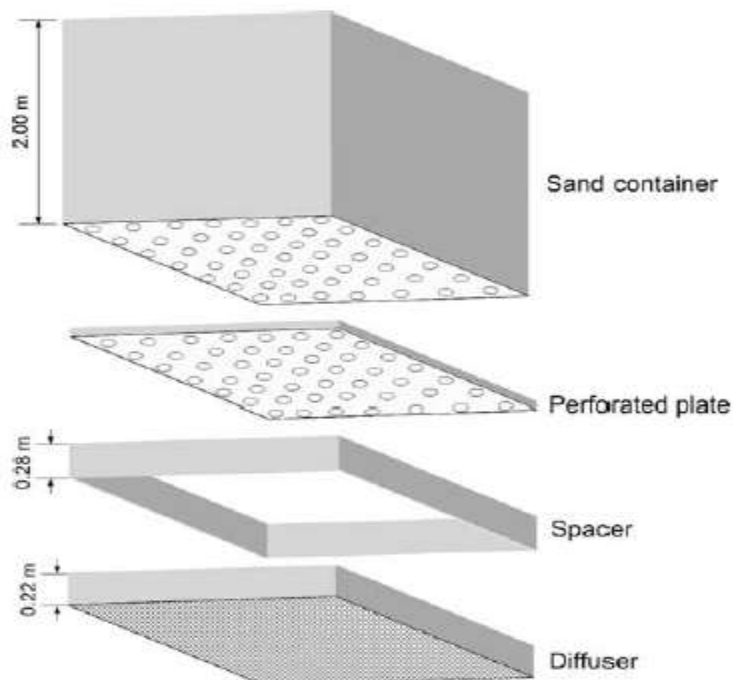


Figure 4.5. Pluivator for specimen preparation (Ueng *et al.* 2006).

Ueng *et al.* (2010) studied on settlements of saturated clean sand deposits in shaking table tests. A large scale laminar shear box with the dimension of 1880x1880x1520 mm was used in the study. The settlements of sand specimens was measured and evaluated during and after each shaking test. The specimen is prepared with wet sedimentation method. A pluviator designed to prepare sand specimens inside the shear box. Sand was rained down into the shear box filled with water to a precalculated depth. The uniformity and density of sand specimens were evaluated using a tube after pluviation. The saturation of the specimen was checked by measuring P-wave velocity across the soil specimen at different depths. After the shaking table tests the settlements measured by manual measurement of the height of the sand surface (Figure 4.6).



Figure 4.6. Measurement of the settlements after liquefaction test (Ueng *et al.* 2009).

Bayat *et al.* (2009) studied on a new liquefaction mitigation method. The study explores two different methods to introduce air/gas in the fully saturated sands. In this study set of uniform cyclic simple shear tests were performed and a shaking table was used to demonstrate that air/gas entrapment reduces the pore pressure build-up significantly, thus to prevent initial liquefaction. In the study, pluviation which is a sample preparation method to prepare soil samples with different relative densities and gradation is used.

Pluviation in water is favored over dry pluviation in that it results initially fully saturated sand samples. Fully saturated specimens were prepared by raining dry sand very slowly from a specific height into a predetermined amount of water placed in the liquefaction box. The sand used was Ottawa sand, which is uniform sand with rounded particle shape. The volume of the specimen was obtained by carefully measuring the average height and using a height versus volume chart that was prepared for the box. The experimental results demonstrate that small reduction in the degree of a fully saturated specimen can lead to significant reduction in excess pore pressures generated in loose liquefaction susceptible sand. Induced partial saturation can be a potential inexpensive liquefaction mitigation measure at sites where using conventional mitigation techniques are prohibitive.

Yegian *et al.* (2006) studied on partially saturated sands. A liquefaction box was designed and tested on a shaking table. In the specimen preparation part of experimental study, electrolysis technique was used to generate oxygen and hydrogen gases uniformly within the specimen without causing any change in the density of the loose sand. During the process of electrolysis, generation of bubbles could be observed. The entrapped bubbles could be seen by the accumulation of free water on top of the originally fully saturated specimen. The amount of displaced water was used together with phase relationships to compute the degree of saturation of a specimen at the end of electrolysis (Figure 4.7).

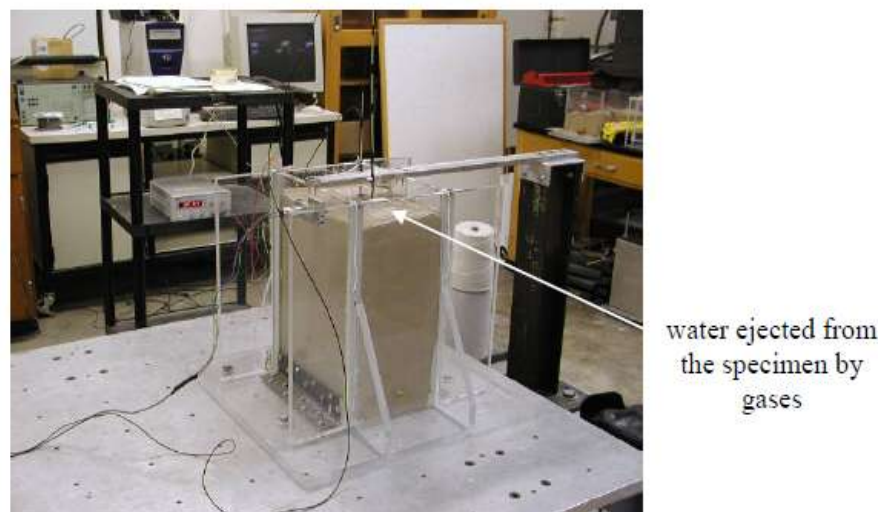


Figure 4.7. Example of partially saturated specimen (Yegian *et al.* 2006).

Özener *et al.* (2009) made investigations of liquefaction in layered sands by means of shaking table tests. In the study, layered sand columns and uniform sand columns were prepared by pouring dry sand into water in a plexiglass tube of 24 cm in diameter and 60 cm in height. They achieved the pluviation operation by a special designed sand pluviation system (Figure 4.8). It is designed for preparing desired target relative densities. For the layered sand columns; after the pluviation of the first sand layer a thin silt seam was formed and waited until the end of its sedimentation before starting the next pluviation step for the formation of the upper sand layer. The water level was kept between 4–6 cm above the surface of the sand layer in all the tests.



Figure 4.8. Sand pluviation system and model sand column seated on shaking table (Özener *et al.*, 2009).

Yegian *et al.* (2007) made experimental investigations about liquefaction mitigation of induced-partial saturated sands. In this study they designed a flexible liquefaction box. Using a shaking table, cyclic shear strain controlled tests were performed on fully and partially saturated loose sand specimens to determine the effect of partial saturation on the generation of excess pore water pressure. A device used to detect the partial saturation and a setup of a deep sand column was prepared and the long-term sustainability of air entrapped in the voids of the sand was investigated. As a result of set of shaking table tests it is concluded that partial saturation can be achieved by gas generation using electrolysis or by drainage-recharge of the pore water without influencing the void ratio of the specimen. Cyclic tests also showed that a small reduction in the degree of saturation can prevent the occurrence of initial liquefaction.

5. MODELLING TECHNIQUES

A model is a simplified representation of the actual system. The success of modelling depends on the extent to which it promotes. The skill in modelling is to spot the appropriate level of simplification to recognise those features which are important and those which are unimportant. Since all models are simplifications of reality there is always a trade-off as to what level of detail is included in the model. If too little detail is included in the model, it is a risk of missing relevant interactions and the resultant model does not promote understanding. If too much detail is included in the model, it becomes overly complicated and actually prevents the development of understanding. One simply cannot develop all models in the context of the entire the natural problems.

Modelling forms an implicit part of all engineering designs but few engineers are aware of the fact that they are making assumptions as part of the modelling or real conditions and consequences of those assumptions. During this modelling, many of them may not have stopped to think about the approximations and assumptions that are implicit in that modelling still less about the nature of the constitutive models that may have been invoked. They are probably not aware of the possibilities and implications of physical modelling either at single gravity or on a centrifuge at multiple gravities (Wood, 2004).

For a soil problem, to estimate the dynamic behaviour of a soil-structure, a proper model has to be carried out. The numerical system which will be conducted has to be in synchronized with physical model in order to take similar responses from analysis. In this sense, physical and numerical model can be considered complementary to each other. Muir *et al.* (2002) stated that the observation forms are indispensable part of the reflective practice loop which underpins engineering and scientific progress during the modelling (Figure 5.1).

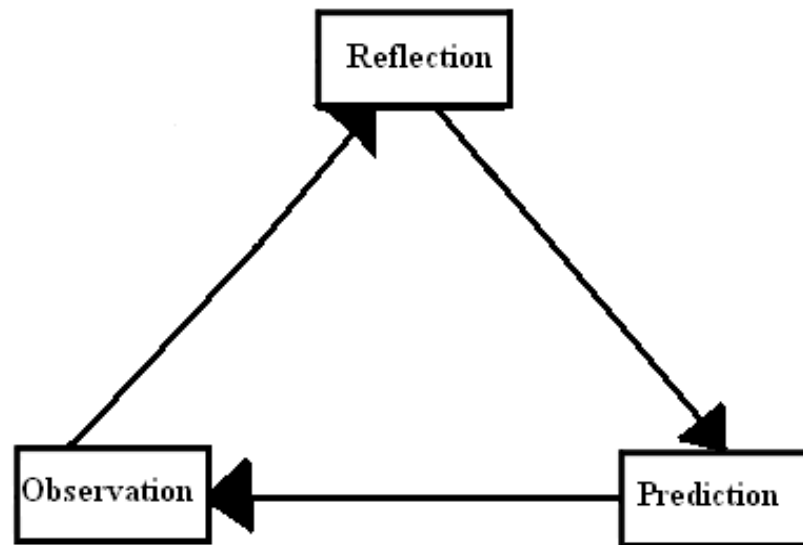


Figure 5.1. Reflective practice loop (Blockley, 1992) .

The first important subject of modelling process is theoretical modelling. The correct observation of soil behaviour and to fit it into the framework is the initial stage of theoretical modeling. Then it has to be formulated correctly. During the formulation of the theoretical modelling, to set boundary conditions and to develop numerical solutions are necessary. Also, for numerical modelling to simulate the physics of the real problem is a need to idealise the material characterisation and the representation of the boundary conditions of the problem. The chronology of the modelling is as important as excellent observation.

On the other hand, physical modelling is the next important stage of modelling process. Physical modelling is performed in order to validate theoretical or empirical hypotheses. Physical models needs visualization, from examining the model, of information about the thing the model represents. The geometry of the model and the object must be similar in the sense that one is a rescaling of the other. For that reason the scale is an important characteristic. However, in many cases the similarity is only approximate or even intentionally distorted. Physical models can be built in two cases: Full scale and small scale models. In the field of engineering, the scale model is ususally smaller than the original and used as a guide of the object in full size.

5.1. Numerical Modelling

In numerical modelling, to understand the controlling physical constraints on each problem is important. The idealisation of the material characterisation and the representation of the boundary conditions of the problem need to be completed before starting to modelling. Exact, closed-form solutions are in general only obtainable for a rather limited set of conditions. There will always be a strong temptation to convince oneself that a problem can be fitted into one of these limited sets. It is always necessary to consider whether the massaging of the problem to fit these constraints removes any key characteristics of the problem. Where the departure from the ideal situation is clearly too great, there is the possibility of using numerical techniques to obtain a solution, retaining the elegance of an underlying simple and widely accepted theoretical description of the physics of the problem on a local scale.

Numerical solution usually implies the replacement of a continuous description of a problem by one in which the solution is only obtained at a finite number of points in space and time. The quality of the numerical modelling result depends on the quality of the numerical approximation. If key quantities are changing very rapidly with position or with time, it is necessary either to increase the density of the discretisation used in the numerical modelling in order to be able to follow the changes or else to incorporate within the numerical description some mathematical interpolation which is able to follow the real variation between discrete modelling points. The speed and cost of the numerical modelling is directly proportional with the density of the modelling points. If the exact answer of a problem is known, it is highly probable to take correct results from a procedure that is developed for numerical solution. It can then be applied with greater confidence to the problem of concern (Wood, 2004).

In geotechnical engineering problems, computer programs highly capable to represent the numerical model of problems being studied by researchers. QUAD4M is one of the most commonly used computer program employs the equivalent linear method, in which the nonlinear characteristics of soils can be captured by two strain-compatible material parameters, shear modulus G and damping ratio ξ . (Kavazanjian E., 2006). It is

also a dynamic, time domain, equivalent linear two-dimensional computer program. It has been used by geotechnical engineers since it is a two-dimensional finite element program (Xu *et al.*, 2009).

The other well known computer program in the field of geotechnical engineering FLAC has been used by engineers to develop numerical models of geotechnical problems (Zarnani and Bathurst, 2008; Bathurst *et al.*, 2006). It is possible to model 2D geomechanical problems that consist of several stages, such as sequential excavations, backfilling and loading. Also it is possible to simulate the large strain behaviour of 3D structures of soil, rock or other continual materials that undergo plastic flow when their yield limits are reached. It can be used in a mixed discretization scheme to model plastic flow and collapse. Although it is programmed as a finite difference code, the spatial discretisation is handled in essentially the same way as for constant strain finite element triangles and we can deduce that reliable results will require a mesh containing large number of small elements. The advantage, for nonlinear problems, is that the computational processes involved in each time step are extremely simple.

Diana SWANDYNE numerical analysis program has been used for seismic geotechnical problems (Taylor *et al.*, 1995; Crewe *et al.*, 1995). It is a dynamic interaction and nonlinear 2D (plane strain and axi-symmetric) program which uses the fully coupled biot dynamic equation with the assumptions.

5.2. Physical Modelling

Physical modelling is necessary to study particular aspects of the behaviour of prototypes. Full-scale testing is in a way an example of physical modelling where all features of the prototype being studied and reproduced at full scale. However, most physical models will be constructed at much smaller scales than prototype because it is desired to obtain information about expected patterns of response more rapidly and with closer control over model details than would be possible with full-scale testing. This usually implies that parametric studies should be performed in which key parameters of models are varied in order to discover their effect. To get exact results from an analysis of a model test, it is necessary to perform individual tests over and over (Wood, 2004).

If the model is not built at a full scale then we need to have idea about how to extrapolate the observations that we make at model scale to the prototype scale. If the material behaviour is entirely linear and homogeneous for the loads that we apply to the model and expect in the prototype then it may be a simple matter to scale up the model observations and details of the model may not be particularly important but, this still depends on the details of the underlying theoretical model which informs our physical modelling (Wood, 2004).

However, if the material behaviour is nonlinear or if the structure to be studied contains several materials which interact with each other, then the development of the underlying theoretical model will become more difficult. It then becomes even more vital to consider and understand the nature of the expected behaviour so that the details of the model can be correctly established and the rules to be applied for extrapolation of observations are clear (Wood, 2004).

One of the physical modelling method; dimensional analysis is a method for understanding theoretical relationship of elements consisted with variables and parameters. The underlying premise is simply that any phenomenon can be described by a dimensionally consistent equation linking the controlling variables. Dimensional analysis of a problem then leads to a reduction in the number of variables that must be studied in order to understand the problem. The important point is to seek to create dimensionally homogeneous equations whose form does not depend on the units of measurement. All equations must come from an underlying insight into the phenomenon that is being modelled. If dimensional homogeneity appears difficult to capture then this is probably an indication that some key variables or parameters have been neglected (Wood, 2004).

There are various different ways in which dimensions of variables can be defined but the most commonly used fundamental system reduces everything to combinations of length [L], mass [M], time [T]. Where thermal effects are important then it is necessary also to add in temperature and charge but those additions will not concern us here. For many geotechnical problems we are concerned with forces and stresses rather than masses and the dimension of time only comes in through the conversion of mass to force.

5.2.1. Centrifuge Model Tests

Centrifuge test is one of the most common type of physical modelling test which the mechanical principle of centrifuge modelling is; if a body of mass m is rotating at constant radius r about an axis with steady speed ' v ' then in order to keep it in that circular orbit it must be subjected to a constant radial centripetal acceleration. In order to produce this acceleration, the body must experience a radial force, mrw^2 , directed towards the axis (Wood, 2004).

In order to replicate the gravity-induced stresses of a prototype in a $1/n$ reduced model, it is necessary to test the model in a gravitational field n times larger than that of prototype. A centrifuge is the most convenient tool to make a high acceleration field in a model. This idea was applied for the first time in 1930's, in the field of the geotechnical engineering. From that time, a number of geotechnical centrifuges have been installed in research institutes all over the world. By the way, centrifuge modelling has become one of the powerful tools for physical modelling (Wood, 2004).

There are two types of centrifuge machine that are in common use: beam and drum (Figure 5.2 and 5.3). In a beam centrifuge the model is rotated about a vertical axis at the end of a strong beam which at its other end carries some sort of a balancing mass or counterweight in order to prevent damaging out of balance rotatory forces on the centrifuge bearings. In many beam centrifuges the model is placed on a swinging platform so that the local gravitational acceleration field in the model is always coincident with the model vertical as the centrifuge speed is increased. This has obvious advantages for preparation of models. The power of the centrifuge is usually quoted in g-tonnes a given device may be able to tolerate a larger model but with lower permissible maximum acceleration (Wood, 2004).

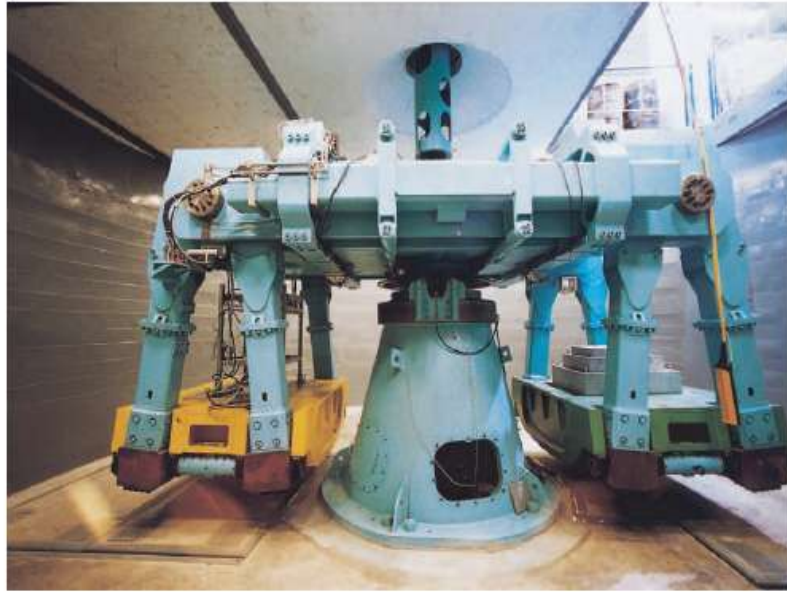


Figure 5.2. Beam Centrifuge Test Machine.



Figure 5.3. Drum Centrifuge Test Machine.

5.2.2. Shaking Table Model Tests

Shaking table tests have the advantage of well controlled large amplitude, multi-axis input motions and easier experimental measurements and their usage is justified if the purpose of the test is to validate the numerical model or to understand the basic failure

mechanisms. Shaking table research has provided valuable insight into liquefaction, post-earthquake settlement, foundation response and lateral earth pressure problems. For the models used in shaking tables, soil can be placed, compacted and instrumented relatively easily. Though higher gravitational stresses cannot be produced in a shaking table test, the contractive behaviour associated with high normal stresses at significant depths can be simulated by placing soil very loosely during model preparations (Figure 5.4).



Figure 5.4. Shaking Table Test Machine.

In shaking table tests, the similarity rule in terms of stress and strain against the prototype cannot be satisfied because of the stress dependency of the stress–strain soil behaviour. Thus the model tests can be considered to be small prototype test. A number of works have been carried out to understand the failure mechanisms and behaviour of earth structures using shaking table tests. Koga and Matsuo (1990) carried out shaking table tests on reduced scale embankment models founded on saturated sandy ground. They investigated the cyclic stress strain behaviour of soil in the ground by using the acceleration and pore pressure records. Kokusho (2003) has explained the use of 1 g shaking table tests in understanding the mechanism of flow failure in liquefied deposits. He retrated that use of torsional simple shear tests, in situ soil investigation, case histories including shaking table tests were essential to understand and develop the lateral flow

mechanism during liquefaction. Orense *et al.* (2003) stated the importance of 1 g shaking table tests in understanding the behaviour of underground structures during soil liquefaction. They have reviewed several shaking table test results from different authors on the behaviour of buried structures and possible mitigation measures against liquefaction failure using gravel drains. In order to reproduce actual earthquake data, a six degree of freedom shaking table is essential. It is a very complex electro-hydraulic system which is very expensive and requires high maintenance and operational costs. If the response and failure mechanisms are eliminated, single degree of freedom of shaking tables are sufficient. The increase of payload causes the increase in cost of motion starters.

5.3. Modelling in Earthquake Geotechnical Engineering

Subsurface geological features or units can be considered as forming “geo-objects”. Features, such as a rock layer or a fault plane, whose position in space can be better identified with additional samples, are termed “sampling-limited geo-objects”. For a geotechnical model, the object of any analysis is to break down a problem into sufficiently small elements. By the way, the behaviour of which can be characterised to a satisfactory level of accuracy so as to represent the problem as a whole. To achieve this rationalisation in geotechnical problems one must attempt to predict the behaviour of a given soil in the most appropriate manner available.

Theoretically, a proper ground description for a geotechnical calculation to determine the behaviour of a soil or rock mass and engineering structure should include all properties in the mass including all spatial variations of these properties. It is unrealistic to describe and test every single piece of ground material. Therefore, to divide a mass into assumed homogeneous geotechnical units is necessary. Then, a part of the mass in which the mechanical properties of the soil or intact rock material are assumed to be uniform. This includes also direction-dependent features such as discontinuities, of which the orientation and properties are uniform within the same geotechnical unit. Figure 5.5 shows a schematic visualization of a ground mass and its division in geotechnical units. In practice, homogeneity is seldom found and material and discontinuity properties vary within a selected range of values within every unit. The allowable variation of the properties within one geotechnical unit depends on the degree of variability of the properties within a mass and the context in which the geotechnical unit is used. A ground mass with a large

variation of properties over small distances necessarily results in geotechnical units with wider variations in properties. The smaller the allowed variability of the properties means more accurate calculation. Smaller variability of the properties of the geotechnical units involves collecting more data, however, and is thus more costly. The higher accuracy obtained for a calculation based on more data, therefore, has to be balanced against the economic and environmental value of the engineering structure to be built and the possible risks for the engineering structure, environment or human life. The allowable variations within a geotechnical unit for the foundation of a highly sensitive engineering structure will be smaller than for a geotechnical unit in a calculation for the foundation of a standard house. There is no specific standards for dividing a mass into units. It just depends on experience and ‘engineering judgment’ of geotechnical engineers. However, features such as changes in lithology, faults, shear zones, etc., are often the boundaries of a geotechnical unit (Hack *et al.* 2006).

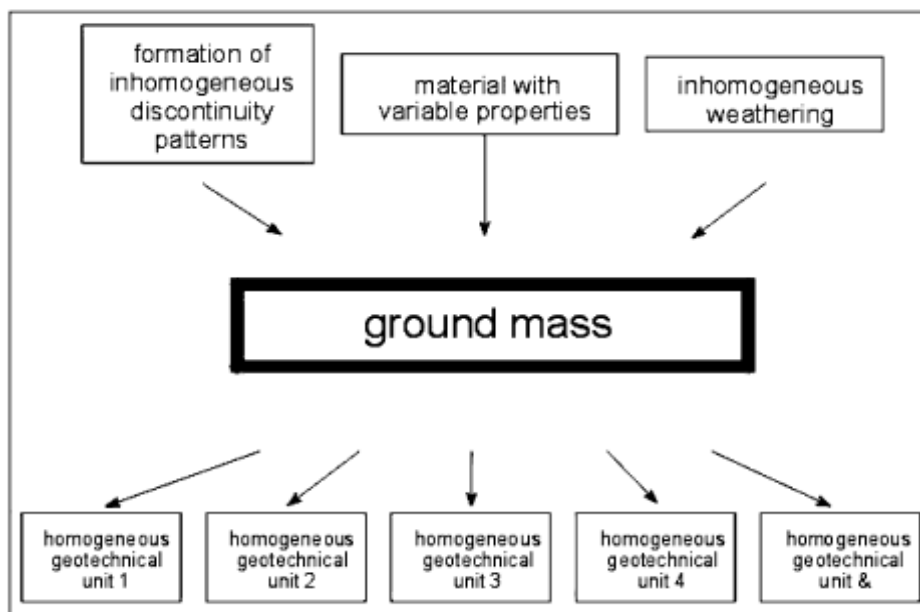


Figure 5.5. Mass Components (Hack *et al.*, 2006).

In traditional methods of design, it has been necessary to neglect or restrict one or more of the soil behaviours in order to make useful estimations with the parameters and methods available. Although each of the methods restricts different requirements, the constitutive behaviour is always idealised in a variety of manners, none of which are a true representation of actual soil behaviour. That is why, the ability of full numerical analyses,

such as those using the finite element or finite difference method, to represent all of these characteristics, including a wide range of constitutive soil models, which sets it apart as a uniquely powerful tool for the modern engineer. To be benefitted from such methods correctly, it is important to fully understand their specific applications and limitations and their theory.

Uncertainty of the model in geo-engineering work should be common practice to make an estimation of the errors in the geotechnical properties of the subsurface and the influence of these errors on the engineering structure to be built in or on it. Different methodologies are applied to give a certain amount of quantification of possible errors in the design of an engineering structure due to uncertainty regarding the subsurface properties. The geotechnical expert knowledge used to make the subsurface model and the division of the subsurface layers in geotechnical units are addressed in only a very rudimentary way or not addressed at all in these analyses. To understand that it is necessary to go back to the basics of geo-engineering. The likelihood of the distribution or the inherent error in estimating a property at a certain location in space, is well defined if appropriate statistical routines are used. However, depends on the correctness of the boundaries of the geotechnical units which itself is related to (i) the geology and (ii) the variation in properties allowed for each in geotechnical unit.

Geotechnical engineers make use of a main knowledge of the geological environment to which the subsurface geology will adhere. The quality of this information, is essential in the interpretation and it cannot in general, be quantified at present. The establishment of geotechnical units, as well as the definition of their boundaries and the allowed variation of properties within each unit. Generally, it will be based on a balance between improved detail against higher costs. It is known that no decent analysis of hazard and risk can be made if the quality of the expert knowledge and the definition of the geotechnical units cannot be quantified. Any up-to-date analysis describes all sorts of uncertainties in measurable properties, but is totally lacking one of these two main parameters governing, to a large extent, the correctness of the subsurface model.

5.3.1. Physical Modelling of Flexible Shear Boxes

A soil layer under a level ground surface is usually in a K_0 condition, while, during an earthquake, the soil at different depths may move differently in the horizontal plane following the upward shear wave propagation. To provide such flexible but unyielding side boundaries as in the field, shear boxes composed of layers of frames are commonly used in the tests. For horizontal two dimensional earthquake shaking, every layer of the frames should be able to move freely in every direction, i.e., multidirectionally, in a horizontal x-y plane that follows the movement of the soil in the container. This can be accomplished if the frames are allowed to move biaxially in both X and Y axes simultaneously. To allow biaxial motions, the laminar shear box requires a special mechanism design. Firstly, the center of mass of every layer of soil and frame is unlikely at the geometrical center of the horizontal cross section. Secondly, the centers of mass of different layers will not be aligned on the same vertical line, particularly when there are shear deformations. Therefore, the inertia force due to shaking will then produce some torque on every layer of soil about a vertical axis due to the eccentricity of the mass center. Without adequate restraints, this would introduce torsional motions of the soil, which in turn cause different shear stress and strain conditions at different locations on the same horizontal plane. The interpretation and analysis of the test results thus become very complicated and inaccurate. Therefore, not only the shear box provide free movements in multiple directions but also it must ensure non-torsional motion of the soil specimen during shaking (Figure 5.6) (Ueng *et al.*, 2006).

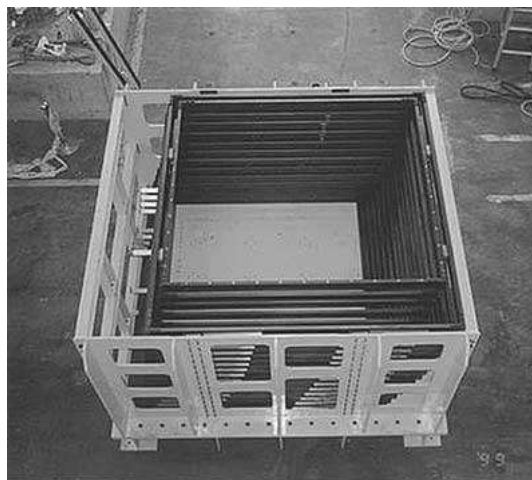


Figure 5.6. Laminar Shear Box (Ueng *et al.*, 2006).

The physical model tests in geotechnical earthquake engineering have been developed as a method between element and in situ tests. This kind of tests is being used for the study of seismic behavior of level or inclined grounds in liquefiable soils or soft clays, soil-structure systems like shallow or deep foundations, retaining walls and embankments. Using the model test results in controlled conditions considering material type and boundary conditions, we can simply identify the failure mechanisms, optimize the design methods and determine the validity of the constitutive models and analytical methods. The physical model tests in earthquake geotechnical engineering are conducted in 1g gravity field on shaking table, or the augmented gravity field in geotechnical centrifuge. Considering the necessity of correspondence for stress levels in real situation and the model case, use of centrifuge in modeling of earthquake geotechnical problems lead to more applicable results, although there are still some deficiencies and without minimizing the induced errors, the results of centrifuge tests are not reliable (Wood, 2004).

5.3.2. Design of a Flexible Shear Box

The main design principle of the shear stack is to provide a condition which the soil in the shear stack behave as it is in real nature. A soil sample in the nature neither surrounded with restrictive boundary conditions nor it is completely free to move without any control. Such important conditions have to be provided during the designation of shear stack. That is why the flexible shear stack consists of a rectangular, laminar box made from aluminium rectangular hollow section rings separated by rubber layers (Figure 5.7). These aluminium rings provide lateral rigidity and rubber layers allows the stack of rings to deform in the direction of the lateral movement. The mass and stiffness characteristics of the shear stack, natural frequencies and mode shapes in horizontal plane are compatible with those of the soil it contains (Crewe *et al.*, 1995).

The soil which will be filled into the box have to be glued to the base of the shear stack and also to the end walls to generate the necessary complementary shear stresses. The side walls have to be covered internally by a greased rubber membrane to prevent friction between the sand and inside of the wall (Taylor *et al.*, 1995).

Ideally, there should be no friction between aluminium rings. Also, the interaction between soil mass and inside wall of shear stack must be zero. When the shear stack dynamically loaded, no additional effect should affect to the soil mass. That is why, the shape and material characteristics of box should be chosen carefully and the stack should have same dynamic characteristic as the soil specimen has.

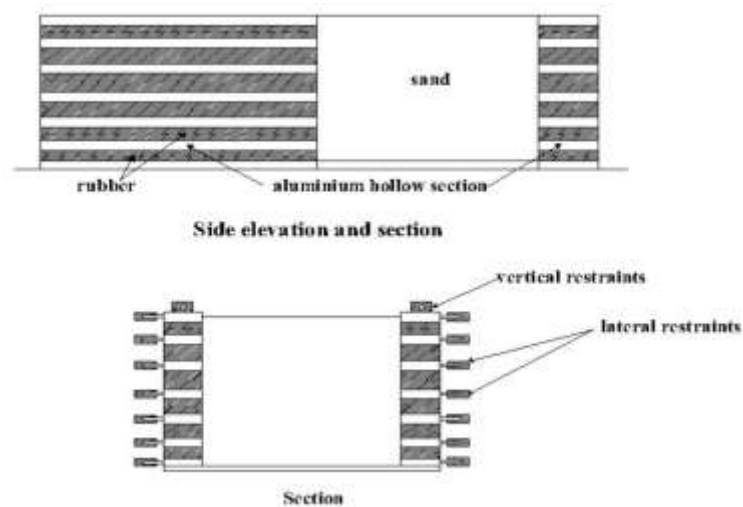


Figure 5.7. Shear Stack concept (Crewe *et al.*, 1995).

5.3.3. Performance Criteria of the Flexible Shear Stack

Two essential performance criteria that the shear stack had to meet during the dynamic loadings are;

- (i) Lateral motions should be uniform on any horizontal plane through the sand and the shear stack itself,
- (ii) Lateral motions over the depth of the stack should follow a near sinusoidal profile (Gazetas, 1982).

The soil specimen in the shear stack has to represent an element from a deposit of uniform soil of infinite lateral extent, founded on a rigid base rock. By the way the soil will deform in a sinusoidal profile (Crewe *et al.*, 1995) (Figure 5.8).

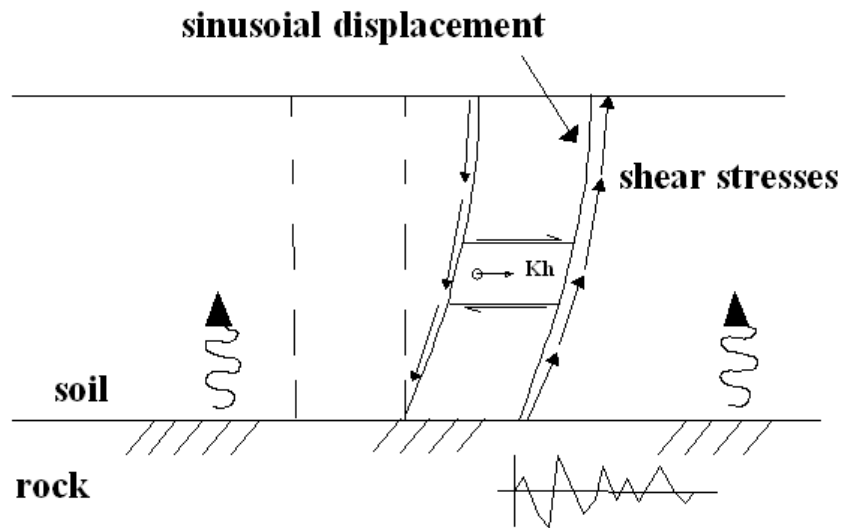


Figure 5.8. Semi-infinite soil deposit movement (Crewe *et al.*, 1995).

5.3.4. Previous Studies of Shaking Table Model Tests

Taylor *et al.* (1995) designed shaking table model of geotechnical problem. In this study, flexible shear stack for shaking table is described. The flexible shear stack designed in the dimensions of 1.20x0.55x0.78 mm. Dry Leighton Buzzard Sand with 53° friction angle were used in the tests. It is seen that tests on dense dry sand specimens are consistent with the basic concepts of initial and general fluidization proposed by Richards *et al.* (1991).

Gajo and Wood (1998) performed numerical analysis of shear stack under dynamic loadings. They modelled a flexible shear stack in the dimensions of 120x55x78 cm. Three models have been considered; the linear elastic, the Mohr-Coulomb and Pastor Zienkiewicz models. Numerical analysis are performed with the finite element program DIANA-SWANDYNE II (Chan 1988). 1D and 2-D analysis are performed and it is concluded that small accelerations it is possible to consider the soil as linear elastic and larger accelerations hard to produce peak accelerations (1D). Measured horizontal displacements are smaller than compute ones (2D).

Maugeri *et al.* (2000) performed shaking table tests on shallow foundations subjected to an eccentric load. In the study, flexible laminar box is modelled with the dimensions of 5x1x1.2 m. Leighton Buzzard sand with 15.4 kN/m³ dry unit weight is used. A shallow foundation is modelled and subjected to eccentric load and sine sweep accelerations on shaking table with the dimensions of 3x3 m. The foundation consisted from two parts; steel and plate with 1.43 m width. Also, in this study, static and dynamic bearing capacity of shallow foundation was calculated. As a result of this study, the reduction of soil inertia forces on bearing capacity is about 24% for the simplified Coulomb analysis mechanism. The reduction of bearing capacity due to the eccentric load is 57% and it is bigger than the reduction of 22% due to soil inertia forces.

Wood *et al.* (2004) studied on shaking table testing of geotechnical models. They concentrated on the application of scaling and modelling laws, the development of containers for testing for geotechnical systems and the control of seismic motion. The flexible shear stack designed with 480x120x100 cm dimensions. A retaining wall is designed in 90x40 cm dimensions. Both shear stack and retaining wall is dynamically loaded with shaking table. In the experiments, the Leighton Buzzard Sand is used and the Mohr-Coulomb analysis is performed. As a result of this study it is found that the coupling between models and experimental results are reassuring.

Prasad *et al.* (2004) performed shaking table tests in earthquake geotechnical engineering. They developed and used analytical and numerical models to simulate ground behaviour. A laminar container in the dimensions of 100x50x100 cm is designed. The Toyoura Sand is used in the experiments. 1-G shaking table tests are performed. Uni-axial, harmonic and sinusoidal vibrations are subjected to model. It is concluded that laminar box can be used both under normal gravitational and centrifuge environments.

Zarnani and Bathurst (2005) made investigations on geofoam seismic buffers with using FLAC numerical code. They performed physical and numerical tests of wall models with a seismic geofoam buffer inclusion. In this study, large shaking table with 1x1.4x2 m dimensions. The reduced scale wall is modeled with 2m long and 1 m width. The thickness

of the EPS geof foam was taken as 150 mm with 1 m height to match both at numerical and physical models. As a result of set of numerical and physical analysis, it is concluded that the numerical simulation results are also shown to be in quantitative agreement with the relative reduction of the earthquake-induced dynamic earth forces generated against the rigid wall structures with an EPS geof foam seismic buffer compared to the control case without seismic protection.

Bathurst *et al.* (2006) performed shaking table tests with geof foam seismic buffers. The tests were carried out using 1m high models mounted on a large shaking table. Three different geof foam buffer material used with 16, 14 and 6 kg/m³ densities. A rigid box is modelled with 2.5x1.4x1.3 m dimensions and dynamically tuned over 2.7x2.7 m shaking table platform. As a result of this study, it is concluded that the reduction in dynamic load increased with decreasing seismic buffer density. It is found that the maximum dynamic force reduction was 31% at a peak base acceleration of 0.7g.

Bathurst *et al.* (2006) studied on a model for response analysis of EPS geof foam seismic buffers. A wall is modelled with EPS geof foam seismic buffer as a linear elastic material. Four physical reduced-scale model shaking table tests were performed. The dimensions of the shaking table platform was 2.7x2.7 m and the EPS geof foam was taken as 150 mm thickness with 1 m height. The numerical analyses were performed with FLAC numerical code. Four type of EPS geof foam wall were used with 16, 12, 14 and 6 kg/m³. As a result of this investigations, it is seen that the measured peak horizontal force acting on the wall was less for the most compressible buffer compared to the stiffest material. At accelerations higher than 0.7g, there are likely more complex system responses that cannot be captured by the simple displacement model employed. All in all, it is concluded that the model is simple and provides a possible framework for the development of advanced models that can accommodate more complex constitutive laws for the component materials and a wider range of problem geometry.

Zarnani and Bathurst (2008) studied on numerical modeling of EPS seismic buffer shaking table tests. In the numerical analysis, FLAC numerical code was used. Five physical tests constructed with EPS geofoam materials with different material properties. The density of EPS materials were; 16, 14, 12, 6 and 1.32 kg/m³. The dimensions of shaking table was 1x1.4x2 m and the EPS geofoam was taken as 150 mm thickness with 1 m height. As a result of the study it is seen that the numerical model was able to capture the trend in earth forces with increasing base acceleration for all six models and in most cases quantitative dynamic load–time response of the numerical simulations was in good agreement with measured values.

Pitilakis *et al.* (2008) made investigations on numerical simulation of dynamic soil-structure interaction in shaking table. In this study, they designed a shear stack in 1.2 m long, 0.55 m wide and 0.8 m deep. A shaking table with 3m by 3m cast-aluminium seismic platform capable of carrying a maximum payload of 21 tons is used. The uniformly graded Dry Hostun S28 sand is used for as test material. The numerical code MISS3D is used to simulate the shaking table tests. The numerical analysis is performed in the frequency range up to 100 Hz with a step of 0.1 Hz. It is concluded that in the higher-frequency range, above 20 Hz, the numerical tool overestimated the response particularly in the vicinity of the resonant frequency of the deposit. The laboratory data exhibited higher damping, primarily within the uppermost soil layers. A close match is found for the response at the top of the structure particularly when converted to spectral accelerations, assuring the correct spectral design. The numerical simulation is not affected by the inability to reliably simulate the soil response above 20 Hz.

Literature study on numerical and experimental modelling tests for geotechnical application under earthquake loadings are summarized in Table 5.1. Also, information on shaking table tests and centrifuge tests are given.

Table 5.1. Examples of Experimental and Numerical Modelling from Previous Studies.

Examples of Modelling From Previous Studies									
Reference(s)	Research Name	Objective of Study	Centrifuge/ Shaking	Type of Box	Size of Box/ model	Method-Programme	Type of Soil Deposit	Numerical/Physical Model	Result
Taylor <i>et al.</i> (1995)	Shaking Table Modelling of Seismic Geotechnical Problems	To investigate the performance of dynamically tuned flexible shear stack	Shaking Table	Flexible Shear Stack	120x55x78 cm box	Mohr-Coulomb	Leighton Buzzard Sand	Physical Model	Results from dense dry sand specimens are consistent with the basic concepts of initial and general fluidization propose by Richards <i>et al.</i>
Crewe <i>et al.</i> (1995)	Development of a large flexible shear stack for testing dry sand and simple direct foundations on a shaking table	To investigate simple direct foundations subjected to seismic loading by developing large flexible shear stack	Shaking Table	Flexible Shear Stack	500x100x120 cm box	Mohr-Coulomb	Leighton Buzzard Sand	Numerical and Physical	Performance of the shear stack is good and the results are represents consistency with free field experiments.
Gajo and Wood (1998)	Numerical analysis of Shear stack Under dynamic Loading	To evaluate the reliability of shear stack in reproducing an infinite layer of soil, testing and comparing three constitutive models and analyzing the dynamic interaction soil and shallow footing	Shaking Table	Flexible Shear Stack	120x55x78 cm box	Linear Elastic, Mohr Coulomb, Pastor Zienkiewicz Model	Leighton Buzzard Sand (0.425-0.600 mm)	Numerical	At small accelerations it is possible to consider the soil as linear elastic and larger accelerations hard to produce peak accelerations (1D). Measured horizontal displacements are smaller than computer ones (2D)
Zeng (1999)	Several important issues related to liquefaction study using centrifuge modelling	To figure out the boundary effects of model containers, use of viscous fluids in model tests and the accuracy of using centrifugal acceleration to simulate gravity	Centrifugal Acceleration	Equivalent Shear Beam Container	560x250x226 cm box	Linear Elastic and Cam-Clay Nonlinear Analysis (Schofield and Wroth, 1968)	Ottawa Sand	Numerical and Physical	An equivalent-shear-beam model container is an applicable to reduce boundary effect of box and viscous fluid in centrifuge modelling is not appropriate choosing. Moreover, size of the centrifuge model and centrifuge must be reasonable.

Table 5.1. Examples of Experimental and Numerical Modelling from Previous Studies, (continued).

Examples of Modelling From Previous Studies									
Reference(s)	Research Name	Objective of Study	Centrifuge/ Shaking	Type of Box	Size of Box/ model	Method-Programme	Type of Soil Deposit	Numerical/Physical Model	Result
Bathurst <i>et al.</i> (2006)	A simple displacement model for response analysis of EPS geofoam	to compute the compression-load-time response of an idealized seismic buffer	Shaking Table	Rigid Strong Box	1.4 m wide, 2 m long and 1m height model	FLAC Code	Artificial sintered silica-free synthetic olivine sand	Numerical and Physical	At accelerations higher than 0.7g, there are likely more complex system responses that cannot be captured by the simple displacement model employed.
Bathurst and Zarnani (2008)	Numerical Modelling of EPS Seismic Buffers	placed against a rigid wall and used to attenuate earthquake-induced dynamic loads	Shaking Table	Strongbox with Plexiglass constructed sidewalls.	1.4 m wide, 2 m long and 1m height model	(a) simple sliding wedge (block); (b) dynamic finite difference method (FLAC) using linear-elastic plastic Mohr- Coulomb model with Raleigh damping, and (c) as (b) but using the equivalent-linear method (ELM)	Sand material with 46° residual frictional angle	Numerical and Physical	The simple linear elastic-plastic constitutive model adopted in this study was judged to be sufficient since the measured compressive strains in the physical models were less than the elastic strain limit of 1% determined from rapid uniaxial compression tests.
Zarnani and Bathurst (2008)	Numerical modeling of EPS seismic buffer shaking table tests	To investigate the details and verification of a FLAC numerical code that was used to simulate the results of an experimental program of reduced-scale wall models constructed with a seismic geofoam buffer inclusion and loaded using a large shaking table.	Shaking Table	Strongbox with Plexiglass constructed sidewalls.	1.4 m wide, 2 m long and 1m height model	Finite Element analysis with FLAC Code	Sand material with 46° residual frictional angle	Numerical and Physical	The numerical model was able to capture the trend in earth forces with increasing base acceleration for all six models and in most cases quantitative dynamic load-time response of the numerical simulations was in good agreement with measured values.
Maugeri <i>et al.</i> (2000)	Shaking table test of failure of a shallow foundation subjected to an eccentric load	to analyse the real failure mechanism of a shallow foundation, to make a comparison with the analytical results and at the same time to provide a database for	Shaking Table	Shear Stack	3x3 m.	Limit Analysis with Coulomb type Mechanism	Leighton Buzzard Sand	Numerical and Physical	The reduction of soil inertia forces on bearing capacity is about 24% for the simplified Coulomb analysis mechanism. The reduction of bearing capacity due to the eccentric load is 57% and it is bigger than the reduction of 22% due to soil inertia forces.

Table 5.1. Examples of Experimental and Numerical Modelling from Previous Studies, (continued).

Examples of Modelling From Previous Studies									
Reference(s)	Research Name	Objective of Study	Centrifuge/ Shaking Table	Type of Box	Size of Box/ model	Method-Programme	Type of Soil Deposit	Numerical/Physic al Model	Result
Wood et al. (2002)	Shaking Table Testing of Geotechnical Models	To concentrate on; the application of scaling and modelling laws, the development of containers for testing for geotechnical systems and the control of seismic motion.	Shaking Table	Flexible Shear Stack and Gravity Retaining Wall	480x120x100 shear stack and 90x40 retaining wall	Mohr-Coulomb	Leighton Buzzard Sand	Numerical and Physical	The coupling between models and experimental results are reassuring.
Prasad et al. (2004)	Shaking Table tests in earthquake geotechnical engineering.	To develop and use analytical/numerical model to simulate ground behaviour.	Shaking Table	Laminar Container	100x50x100 cm box.		Dry Toyoura Sand	Numerical and Physical	Effect of boundary is negligible. Possible to test larger size particles. It was not possible to control stress and strain during the test. Achiving high confining pressure and study of liquefaction problems was difficult.
Zarnani and Bathurst (2005)	Numerical Investigation of Geofoam Seismic Buffers Using FLAC	To investigate the attenuation effect of EPS geofoam material	Shaking Table	Rigid Strong Box	1.4 m wide, 2 m long and 1m height model	Mohr-Coulomb Analysis with FLAC Code	Sand Backfill	Numerical and Physical	The numerical simulation results are in quantitative agreement with the relative reduction of the earthquake-induced dynamic earth forces generated against the rigid wall structures with an EPS geofoam seismic buffer compared to the control case without seismic protection.

6. EXPERIMENTAL PROGRAM

6.1. General

The main purpose of the experimental program is to investigate the liquefaction hazard mitigation effect of tire material in saturated sand (S) at different temperature conditions. In this sense, a set of geotechnical laboratory tests were performed to evaluate the liquefaction potential of soil. Also Direct Shear Tests and CBR Tests were performed with sand and sand-tire mixtures. Specimens are named with abbreviations such as TB10, TC15, TC, S, etc. These abbreviations are referenced to type of specimen and its proportion. For example; TB10 refers to a mixture with 90% sand and 10% tire buffings by weight. Secondly, Cyclic Triaxial Tests were performed with sand and sand-tire mixtures with different tire percentages to obtain shear modulus and damping ratio of specimens. All tests were conducted in accordance with ASTM standards. After, static and dynamic laboratory tests, a Flexible Shear Box was designed and constructed. Shaking Table Model Tests were performed with constructed Flexible Shear Box. A set of shaking table tests were performed to evaluate the earthquake mitigation effect of tire material at different temperatures. Shaking table tests are performed with Small Shaking Table with Thermal Cabin. The earthquake ground motions which recorded on Small Shaking Table with Thermal Cabin is applied to the specimens during the tests. A1 is the base input acceleration.

6.1.1. Geotechnical Laboratory Tests

A set of Geotechnical Laboratory Tests is performed to define the engineering properties of materials which will be used in shaking table tests. In this part of laboratory test program, grain size distribution, direct shear tests, California Bearing Ratio (CBR) Tests, Specific gravity and Unit Weight Determination tests of all specimens were performed individually. Based on the tests, physical properties of the specimens are figured out. The material properties are used to evaluate the classification of materials and liquefaction susceptibility of soil. All the tests are performed in accordance with related ASTM Standards.

6.2. Materials Used in Experiments

6.2.1. Sand

The sand used is called as Silivri Sand, which is widely found in Istanbul. Sieve analysis of sand performed according to the ASTM D422. The grain size distribution of sand is shown in Figure 6.1. The coefficient of uniformity (C_u) is calculated as 2.4 and the coefficient of curvature (C_c) is calculated as 1.35. According Unified Classification System (UCS), sand can be classified as SP, poorly graded rounded sand. Sand used in this study is shown in Figure 6.2.

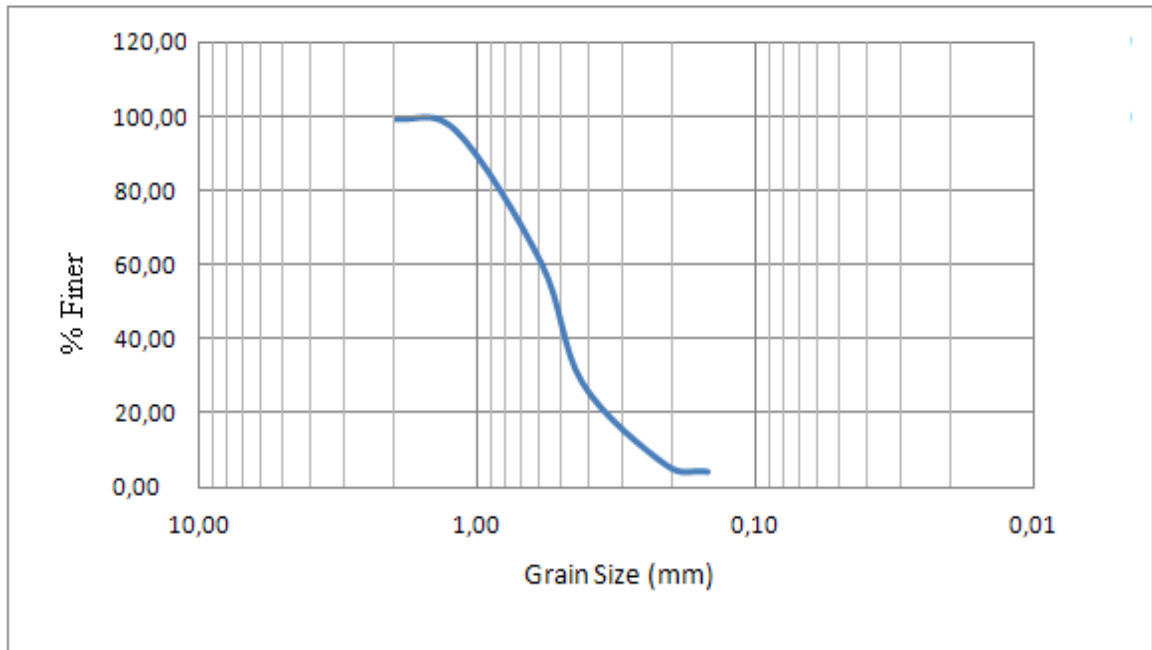


Figure 6.1. Grain size distribution of the sand.



Figure 6.2. Sand used in experiments.

6.2.2. Tire Waste Material

6.2.2.1. Tire Crumbs. Tire Crumbs material used in this study obtained from a company in Istanbul and the grain size distribution curve is shown in Figure 6.3 and tire crumbs used in the tests demonstrated in Figure 6.4.

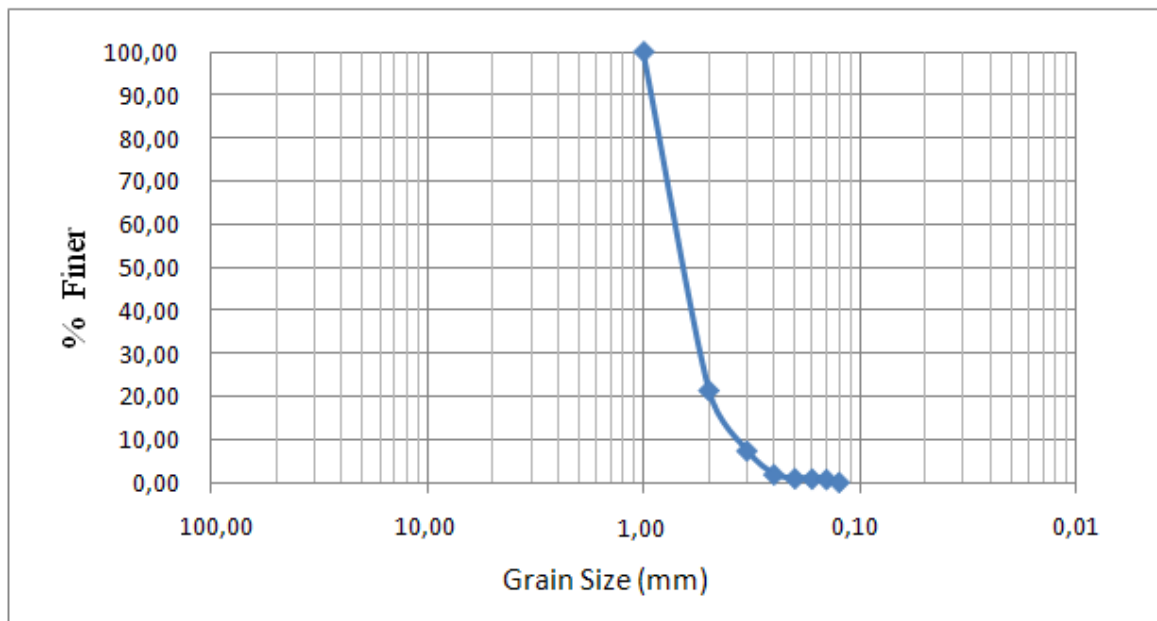


Figure 6.3. Grain size distribution of the Tire Crumbs Material.



Figure 6.4. Tire Crumbs material

6.2.2.2. Tire Buffings. Tire buffings material is obtained as a result of retreading process. It is purchased from a company in Istanbul. The grain size distribution of tire buffings material is shown in Figure 6.5. The sieve analysis is performed according to ASTM D4767-04 Standards. The dimension of material varied between 1-9 mm. Dust material and particles greater than 1 cm was removed in order to have 1/5 aspect ratio. The tire buffings is shown in Figure 6.6. and a comparison of tire buffings and tire crumbs materials is shown in Figure 6.7.

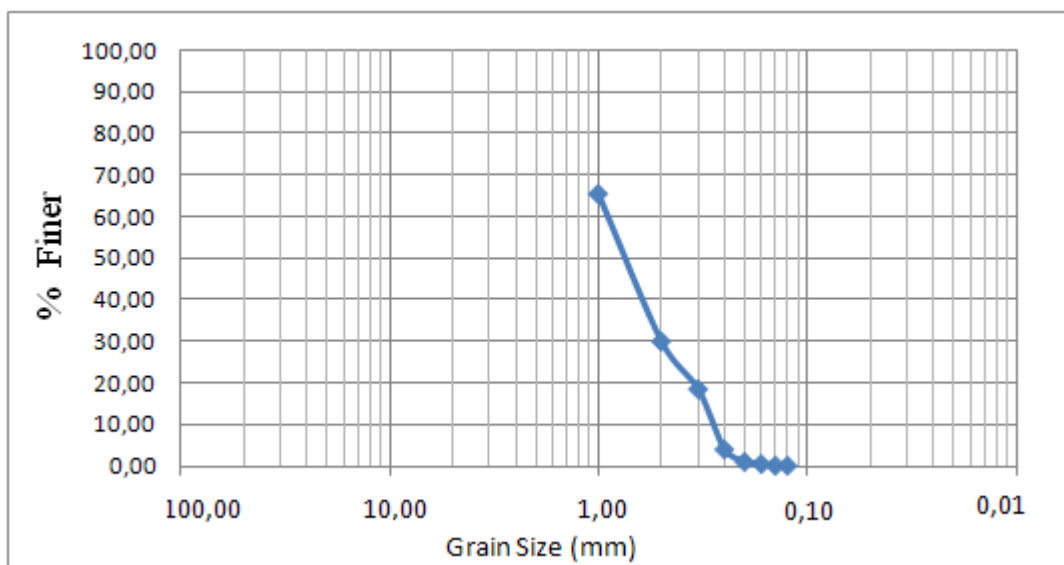


Figure 6.5. Grain size distribution of Tire Buffings.



Figure 6.6. Tire Buffings used in the experiments.



Figure 6.7. Tire Buffings and Tire Crumbs materials.

Sieves sizes with 1, 2 and 4 mm are used to distinguish the tire buffings into two sizes and get rid of the tire dust. The used sieves are shown in Figure 6.8.



Figure 6.8. Sieves used in experiments.

6.2.3. Unit Weight Determination Tests

Unit weight determination tests are performed to determine the state of density of soil with respect to its maximum and minimum densities. In this test; sand, sand-tire buffings mixtures and sand-tire crumbs mixtures were tested. A standart compaction mold and compaction hammer are used and test is performed in accordance with ASTM D4253-83 (Figure 6.9.)



Figure 6.9. Compaction Mold and Hammer.

6.2.3.1. Sample Preparation. Within the scope of this test, minimum and maximum density of materials are determined. Tests are conducted with sand, sand-tire crumbs mixtures and sand-tire buffings mixtures. Sand-tire buffings and sand-tire crumbs materials were prepared at seven tire contents of 5%, 10%, 15%, 20%, 30%, 40%, 50% by weight. Also only sand, only tire buffings and only tire crumbs are tested too. For all specimens, the weight of the sand and both tire buffings and tire crumbs materials were calculated and materials mixed uniformly. The uniformity of specimen was controlled by eye observation. Materials are filled into the mold in loose state to obtain minimum density. Secondly, same material is filled into the same mold in five layers and each layer hammered with fifteen blows. The mold weighed again and maximum density of material is obtained. With the minimum and maximum density values, the relative density of specimens were calculated. After calculating minimum and maximum densities, a density between these values is selected. The maximum, minimum and selected density values are shown in Table 6.1.

Table 6.1. Density and Relative Density values of samples.

Sample	Min. (kN/m³)	Max. (kN/m³)	Used (kN/m³)	Dr
%100 Sand-S	14.40	15.70	14.90	0.38
% 5 Crumbs (TC5)	12.90	14.30	13.30	0.32
% 10 Crumbs (TC10)	12	13.80	12.60	0.37
% 15 Crumbs (TC15)	11.30	13.10	12.00	0.42
% 20 Crumbs (TC20)	10.60	12.40	11.20	0.37
% 30 Crumbs (TC30)	9.90	11.30	10.30	0.34
% 40 Crumbs (TC40)	9.40	10.40	9.80	0.44
% 50 Crumbs (TC50)	8.40	9.90	8.90	0.41
% 100 Crumbs (TC)	5.50	7.30	6.10	0.38
% 5 Buffings (TB5)	12.10	14.80	13	0.40
% 10 Buffings (TB10)	11.10	13.30	11.80	0.35
% 15 Buffings (TB15)	10.20	12.20	10.80	0.33
% 20 Buffings (TB20)	8.90	11.00	9.50	0.31
% 30 Buffings (TB30)	7.80	9.70	8.50	0.44
% 40 Buffings (TB40)	6.50	8.20	7.20	0.47
% 50 Buffings (TB50)	6	7.10	6.40	0.40
% 100 Buffings (TB)	3.50	5.40	4.10	0.43

6.2.4. California Bearing Ratio (CBR) Tests

A set of CBR test are performed with sand and sand-tire mixtures. The mixtures are prepared at tire contents of 5, 10, 15, 20, 30 and 40% tire waste by weight. Sand is used with a unit weight of 14.90 kN/m³. The effect of tire content and tire shape is observed. The CBR values evaluated for measuring the load-bearing capacity of specimen. The higher the CBR rating, the harder the surface.

Tests are performed in the Geotechnical Laboratory of Bogazici University using a standard CBR machine with a penetration speed of 1.27 mm/min. as described in ASTM D1883-07, a standard CBR mold with a diameter of 15.2 cm, a standard compaction hammer, a spacer disk with a diameter 15.1 cm and 6.14 cm height, a displacement measuring device and a load measuring device (Figure 6.10).

6.2.4.1. Sample Preparation. Sand-tire buffings and sand-tire crumbs mixtures are prepared at seven tire contents of 5%, 10%, 15%, 20%, 30% and 40% by weight. For all specimens, the weight of the sand and both tire buffings and tire crumbs materials were calculated and mixed uniformly. Specimens were placed in the CBR mold in three equal layers and each layer compacted with hammer by 36 blows. The load readings were recorded at penetrations of 0.5, 1.0, 1.5, 2.0, 2.5, 3.0, 4.0, 5.0, 7.5, 10 and 12.5 mm. CBR tests are conducted on unsoaked specimens only. The maximum load and corresponding penetration value noted for a penetration less than 12.5 mm. The test program is summarised in Table 6.2.

Table 6.2. CBR Test Program.

Specimen	Material	Tire Size (mm)
S	% 100 Sand	-
TC5	Sand + 5% Tire Crumbs	1 - 2
TC10	Sand + 10% Tire Crumbs	1 - 2
TC15	Sand + 15% Tire Crumbs	1 - 2
TC20	Sand + 20% Tire Crumbs	1 - 2
TC30	Sand + 30% Tire Crumbs	1 - 2
TC40	Sand + 40% Tire Crumbs	1 - 2
TB5 - No.1	Sand + 5% Tire Buffings No.1	1 - 2
TB10 - No.1	Sand + 10% Tire Buffings No.1	1 - 2
TB15 - No.1	Sand + 15% Tire Buffings No.1	1 - 2
TB20 - No.1	Sand + 20% Tire Buffings No.1	1 - 2
TB30 - No.1	Sand + 30% Tire Buffings No.1	1 - 2
TB40 - No.1	Sand + 40% Tire Buffings No.1	1 - 2
TB5 - No.2	Sand + 5% Tire Buffings No.2	2 - 4
TB10 - No.2	Sand + 10% Tire Buffings No.2	2 - 4
TB15 - No.2	Sand + 15% Tire Buffings No.2	2 - 4
TB20 - No.2	Sand + 20% Tire Buffings No.2	2 - 4
TB30 - No.2	Sand + 30% Tire Buffings No.2	2 - 4
TB40 - No.2	Sand + 40% Tire Buffings No.2	2 - 4



Figure 6.10. CBR Machine.

6.2.5. Direct Shear Tests

A set of direct shear test is performed to find the shear strength parameters of sand and sand-tire waste mixtures. Tests are performed on only sand, only tire buffings, only tire crumbs materials and sand-tire buffings and sand-tire crumbs contents of 5, 10, 15, 20, 30 and 40% by weight. All tests are repeated under three different normal stress of 10, 20 and 40 kPa to determine shear strength parameters. Tests are performed at the Geotechnical Laboratory of Bogazici University in accordance with ASTM D3080. The direct shear test machine is shown in Figure 6.11.

6.2.5.1. Sample Preparation. Test specimen is prepared at defined proportions and mixed carefully. All samples are filled into the box carefully. The shear box with 10x10 cm dimensions has two stacked rings to hold sample. The contact interface of sample is approximately at the mid-height of shear box. A normal stress is applied vertically to the specimen during the test. The samples are horizontally loaded with a strain rate of 0.5mm/min. The upper ring is pulled laterally until the sample fails or through a specified strain. The stress value is recorded at frequent intervals and the shear strain-stress curve of the specimens are drawn. The direct shear test program is summarised in Table 6.3.

The dial readings of device refer to; 1 Horizontal Displacement equals to 0.01mm/div., 1 Vertical Displacement equals to 0.01mm/div. and 1 Horizontal Loading equals to 0.00203 kN/div.



Figure 6.11. Direct Shear Test Machine.

Table 6.3. Direct Shear Test Program.

Specimen	Material	Tire Size	Normal Stress (kPa)
S	% 100 Sand	-	40 - 100 - 200
TC5	Sand + 5% Tire Crumbs	1 - 2 mm	40 - 100 - 200
TC10	Sand + 10% Tire Crumbs	1 - 2 mm	40 - 100 - 200
TC15	Sand + 15% Tire Crumbs	1 - 2 mm	40 - 100 - 200
TC20	Sand + 20% Tire Crumbs	1 - 2 mm	40 - 100 - 200
TC30	Sand + 30% Tire Crumbs	1 - 2 mm	40 - 100 - 200
TC40	Sand + 40% Tire Crumbs	1 - 4 mm	40 - 100 - 200
TB5	Sand + 5% Tire Buffings	1 - 4 mm	40 - 100 - 200
TB10	Sand + 10% Tire Buffings	1 - 4 mm	40 - 100 - 200
TB15	Sand + 15% Tire Buffings	1 - 4 mm	40 - 100 - 200
TB20	Sand + 20% Tire Buffings	1 - 4 mm	40 - 100 - 200
TB30	Sand + 30% Tire Buffings	1 - 4 mm	40 - 100 - 200
TB40	Sand + 40% Tire Buffings	1 - 4 mm	40 - 100 - 200

6.2.6. Specific Gravity Test

Specific gravity values of sand, tire crumbs and tire buffings were calculated. During the experiment, a volumetric flask with 500 ml is used for all three materials (Figure 6.12). A vacuum pump used to remove air included in mixtures.

Sand, tire buffings and tire crumbs materials were prepared and weighed. Each material is filled in a volumetric flask individually. Then, mass of water filled into the flask up to the specified line and the air in the flask is discharged. The final volume and mass of volumetric flask is measured. To correct the test values for 19 C° temperature, correction factor α found as 1.0002. Tests are conducted in accordance with ASTM D 854. Specific gravity of sand is found as 2.67. Specific gravity of unsieved tire buffings and tire crumbs are found as 1.08 and 1.04, respectively.



Figure 6.12. Volumetric flask with sand-water, tire crumbs-water and tire buffings-water mixtures.

6.3. Dynamic Laboratory Tests

Dynamic triaxial tests are performed to obtain shear modulus and damping ratio of sand, sand-tire buffings and sand-tire crumbs mixtures. Specimens are prepared at different content of tire material and the tests are conducted under three different confining pressure values; 40, 100 and 200 kPa. Only sand and all tire waste materials are mixed with sand at 10%, 20% and 30% proportions. The shear modulus and damping ratio values of all specimens are determined. The variation of shear modulus and damping ratio with increasing confining pressure and tire content is investigated. The optimum proportion and type of tire material are obtained as a result of these set of dynamic tests. Tests are performed according to ASTM D3999 (1991) standards.

Cyclic triaxial test results are used for evaluating the ability of a soil to resist against to the shear stresses induced in a soil mass due to earthquake or other cyclic loading. Also it provides the determination of the cyclic strength of saturated soils in either undisturbed or reconstituted states by the load-controlled cyclic triaxial technique. In this case, a series of cyclic triaxial tests are performed on sand and sand-tire waste mixtures. Total amount of 19 cyclic triaxial tests are conducted at three different confining pressures. The Cyclic Triaxial Test program is summarised in Table 6.4. The specimens are prepared at a constant volume with a diameter of 35 mm and a height of 70 mm. All tests are carried out in the Geotechnical Laboratory of the Istanbul Technical University. The Cyclic Triaxial Test Machine is shown in Figure 6.13.



Figure 6.13. Triaxial Test Machine.

6.3.1. Principles of Cyclic Triaxial Test

Cyclic triaxial test may be evaluated under different values of confining pressures. During this evaluation, the data obtained to understand the stability of soil. Cyclic strength depends upon different factors such as; confining pressure, applied cyclic shear stress, stress history, grain structure, age of soil deposit, specimen preparation procedure, and the frequency, uniformity and shape of the cyclic wave form. The evaluation may be investigated by taking into account the development of axial strain, magnitude of applied cyclic stress, number of cycles of stress application, development of excess pore-water pressure and state of effective stress. The test can be performed under undrained conditions to figure out undrained field conditions during earthquakes or rapid repeated loadings. Test processes may be interrupted because of failures. Generally these failures caused by excess pore pressures.

Cyclic triaxial tests are appropriate to determine shear modulus and damping ratio of soils. Also additional soil types may be tested to ensure that soil problems receive special consideration when tested and when test results are evaluated. Like all of the laboratory tests, this test has some restrictions, too. First of all; nonuniform stress conditions can cause a redistribution of void ratio within the specimen during the test. The interaction between soil and all other test equipments has effect on cyclic behavior. Change in water pressures can cause changes in membrane penetration in specimens of cohesionless soils. These changes can significantly influence the test results.

For an isotropically consolidated contractive (volume decreasing) specimen tested in cyclic compression, the maximum cyclic shear stress that can be applied to the specimen is equal to one-half of the initial total axial pressure. Cohesionless soils are not working against to the tensile stresses. That is why cyclic shear stresses greater than this value tend to lift the top platen from the soil specimen. To get best results from cyclic triaxial test, it is better to reconstitute soil specimens. To reconstitute specimens to the same density may result in significantly different cyclic strengths. Also, undisturbed specimens will almost always be stronger than reconstituted specimens.

6.3.2. Cyclic Triaxial Test Apparatus

The apparatus is composed of a load frame, top drainage, filter paper for side drainages, porous stone, membrane, back pressure and pore water pressure channels, 'O' rings, a triaxial cell, strain controlling compression machine, specimen trimmer, wire saw, vacuum source, rubber membrane, water distribution channels, pressure controlling panel, displacement, load and pressure controlling panel. The used equipments are rubber membranes, filter paper, porous stones, two-way split mold, and rubber 'O' rings (Figure 6.14). In the apparatus, a pneumatic stress controlled system is capable of generating cyclic axial stresses at frequencies between 0.001 Hz and 2 Hz. The testing system individually enables the measure and the record of axial vertical load, axial vertical displacement, pore water pressure and the specimen volume change. The triaxial cell has a diameter of 50 mm, a maximum piston load of 45 kN. and a working pressure limit of 1.700 kPa. The general

components of the cyclic triaxial test and the test equipment used in this study are shown in Figure 6.15.



Figure 6.14. Triaxial Test Apparatus.

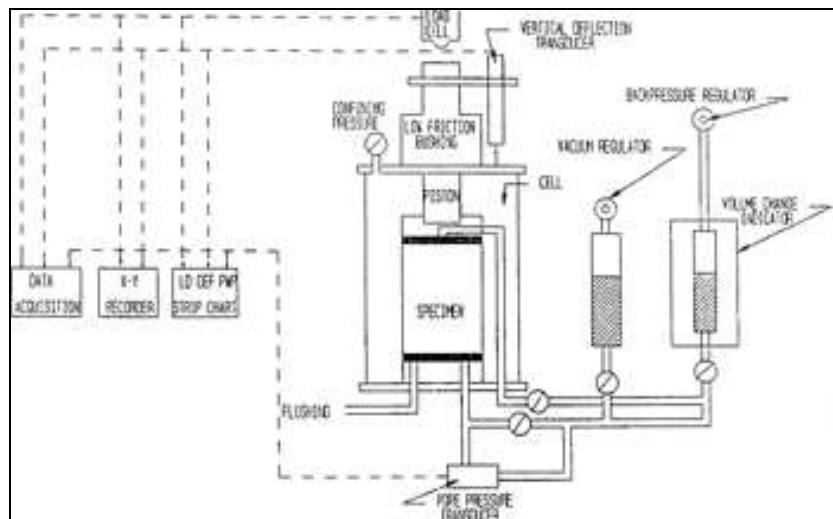


Figure 6.15. Schematic figure of Triaxial Test Machine

6.3.3. Sample Preparation

Tests are conducted with sand, sand-tire crumbs and sand-tire buffings materials. Sand-tire buffings and sand-tire crumbs materials were prepared at three tire contents of 10%, 20% and 30% by weight. Testing program is summarised in Table 6.4. For all mixtures, the weight of the sand and both tire buffings and tire crumbs material were

calculated and mixed uniformly. The uniformity of specimen was controlled by eye evaluation. To create a homogenous distribution of tire orientation of sand and fibers, mixtures were placed with a spoon regularly. The sample placed and base of the pressure cell is closed. Rubber membrane is placed inside the membrane tube and ends of membrane folded over the outside of the tube slide. The membrane sealed to the base pedestal using two rubber 'O' rings and air pockets removed. The vacuum between the tube and membrane removed and membrane rolled ends of the application tube onto the foot piece and it is capped.

6.3.4. Cyclic Triaxial Test Procedure

For cyclic triaxial tests, the drainage vent is closed during the test. After the specimen placed, desired pressure in the cell with the air regulator cell pressure and control panel is given to the water in the flexiglass cell. The strain gauge brought in to contact with the datum bar on the top of the cell and it is adjusted to read zero. The dynamometer adjusted to read zero and the compression machine for a strain rate about 0.5% per minute arranged and turned on. The tested specimen from the cell is removed. The same test has repeated at three times for 40, 100 and 200 kPa confining pressure (ASTM D3999). The cyclic triaxial test program is summarised in Table 6.4.

Table 6.4. Cyclic Triaxial Test Program.

Specimen	Materials by weight	Tire Size	γ(kN/m³)	Confining Pressures (kPa)
S	% 100 Sand	-	16.5	40 - 100 - 200
TC10	Sand + 10% Tire Crumbs	1 - 2 mm	14.7	40 - 100 - 200
TC20	Sand + 20% Tire Crumbs	1 - 2 mm	16.0	40 - 100 - 200
TC30	Sand + 30% Tire Crumbs	1 - 2 mm	15.3	40 - 100 - 200
TB10	Sand + 10% Tire Buffings	1 - 4 mm	15.3	40 - 100 - 200
TB20	Sand + 20% Tire Buffings	1 - 4 mm	15.5	40 - 100 - 200
TB30	Sand + 30% Tire Buffings	1 - 4 mm	15.4	40 - 100 - 200

6.4. Numerical Design of Shear Stack

In the modelling of flexible shear stack, SAP2000 finite element program is used. SAP2000 analysis program is a general purpose finite element program which performs the static or dynamic, linear or nonlinear analysis of structural systems. It is used to model, analyze, design, and display the flexible shear stack geometry, material properties and analysis results. The analysis procedure of flexible shear stack is divided into three parts: preprocessing, solving and postprocessing. In preprocessing part, the geometry of flexible shear stack is set up. Then the material and member section properties are assigned. Load cases, load magnitudes and restraints are defined at the last step of preprocessing part. In the analysis part, Flexible Shear Stack dynamically tuned with previously defined load

cases. In the postprocess part, the deformed shape of flexible shear stack is displayed. The member forces of all shear stack elements are figured out in a diagram of forces. The design criteria of shear stack are controlled. The geometry and material properties of flexible shear stack are modified if the performance criteria are not provided.

The designed shear stack is illustrated in Figure 6.16. Its dimensions are; 250 mm long by 150 mm wide by 180 mm deep. The shear stack consists of three rigid rectangular rings (made from welded 20x20 mm aluminium rings, weighing 1.53 kg/mm) and three rectangular rubber blocks. At the bottom of the shear stack, an aluminium sheet element with 1 mm thickness is used. The bottom aluminium ring is rigidly bolted to aluminium sheet and it is fixed to the shaking table.

6.5. Shaking Table Tests

In this part of laboratory tests, only sand and sand-tire mixtures are tested on shaking table at different temperature conditions. Shaking table tests are performed first at room temperature. Secondly, all tests are performed under low and high temperature conditions. Sand, sand-tire buffings and sand-tire crumbs composites are tested individually. During the shaking table tests, earthquake ground motions are applied to the specimens. To measure acceleration, displacement and pore pressure values of specimens, three accelerometers, a pore pressure transducer and a laser displacement sensor are used. Two accelerometers are placed in the specimen and one accelerometer is fixed on the surface of the shaking table. The submersible accelerometers are placed at different height of specimen in order to observe the effect of acceleration changes at different heights. Pore Pressure transducer is located at mid-height of the specimen. A laser displacement sensor is fixed at the top layer of flexible shear stack to observe the displacement variation of shear stack at all earthquake motions.



Figure 6.16. View of Flexible Shear Stack used in tests.

6.5.1. Sample Preparation

Shaking Table Tests are performed on sand, sand-tire buffings and sand-tire crumbs mixtures with the contents of 10, 15, 20 and 30 % by weight. The aspect ratio of tire material is 1/5. Also the dust material inside tire buffings are removed. Tire buffings materials are weighed for determined percentages. All mixtures are prepared in a large bowl carefully and saturated with water. Specimen is filled into the box carefully. Accelerometers and pore water pressure transducer (PPT) are located in specimen with an order. The first layer, 20 mm of specimen filled into the box and the first accelerometer located over the specimen without compaction. The second layer of the specimen, 70 mm, filled into the box and PPT is located at mid center of the shear stack. The last layer of specimen is filled carefully as 70 mm and the second accelerometer is located. Since the height of the flexible shear box is 18 cm, to prevent overflowing of material during the movement, 17 cm of box filled carefully. The specimen is filled into the box with $D_r = 0.40$. Each layer filled into the box properly without compaction to provide the uniformity of specimen (Table 6.5).

6.5.2. Preparation of Test Set Up

Shaking table tests are performed with the sand and tire waste material which the material properties are determined with the previous studies. The flexible shear box with 150x250x180 mm dimensions are filled with the test specimen and 3 accelerometers; Acc.1, Acc.2 and Acc.3 and a Pore Pressure Transducer (PPT) and a laser displacement sensor

(LVDT) are located at different locations of flexible shear box and shaking table. To get all accelerometer data from different locations of shear box, three accelerometers which two of them are put inside of shear box and the other one fixed directly on shaking table surface. Accelerometers are positioned inside of flexible shear box and fixed at bottom layer and top layer of specimen respectively adjacent to side wall. The third accelerometer is fixed on the surface of the shaking table. Also PPT was located at the mid height and center of test sample. To get the displacement values of shear box under dynamic loading the laser displacement sensor fixed on the box. The instrumentation of shaking table is shown in Figure 6.17. During the performed tests, one laser temperature sensor was used to adjust the temperature.

6.5.3. Shaking Table Test Procedure

Three different types of motions; İzmit E-W, Sakarya N-S and Tabas E-W earthquake motions were applied to shaking table. During the experiments, the temperature of thermal cabin varied between 0°C, room temperature and 50°C. Specimens are cooled in shaking table cabin for one day to reach 0°C temperature. Five different types of data were obtained from 3 accelerometers, a pore pressure transducer and a laser displacement sensor. The temperature of shaking table cabin was kept under control in order to prevent any damage of high temperature to data cables. As the first motion applied to shaking table, the temperature value was 0°C. When a set of motion is applied to shaking table, the temperature of shaking table cabin increased up to room temperature and then 50°C with small increments. As the temperature of shaking table cabin reached to 50°C, the temperature value of specimen measured with laser temperature sensor from various points of specimen.

Table 6.5. Summary of Specimen Preparation and Testing Program.

Specimen Preparation and Testing Program						
Test No.	Sample	Preparation Method	Unit Weight (kN/m ³)	Dr	Temperature	Type of Motion (1-D)
Test 1-2-3	100 % Sand	Sand saturated with water. Then filled into the shear box.	16.34	0.40	(i) 0 °C (ii) 50 °C (iii) Room Temp.	İzmit E-W
						Tabas E-W
						Sakarya N-S
Test 4-5-6	TB10	Sand mixed with 10% tire buffings material in a bowl and saturated with water. Then filled into the shear box.	12.50	0.40	(i) 0 °C (ii) 50 °C (iii) Room Temp.	İzmit E-W
						Tabas E-W
						Sakarya N-S
Test 7-8-9	TB15	Sand mixed with 15% tire buffings material in a bowl and saturated with water. Then filled into the shear box.	11.40	0.40	(i) 0 °C (ii) 50 °C (iii) Room Temp.	İzmit E-W
						Tabas E-W
						Sakarya N-S
Test 10-11-12	TB20	Sand mixed with 20% tire buffings material in a bowl and saturated with water. Then filled into the shear box.	10.30	0.40	(i) 0 °C (ii) 50 °C (iii) Room Temp.	İzmit E-W
						Tabas E-W
						Sakarya N-S
Test 13-14-15	TB30	Sand mixed with 30% tire buffings material in a bowl and saturated with water. Then filled into the shear box.	8.90	0.40	(i) 0 °C (ii) 50 °C (iii) Room Temp.	İzmit E-W
						Tabas E-W
						Sakarya N-S

Table 6.5. Summary of Specimen Preparation and Testing Program, (continued).

Specimen Preparation and Testing Program						
Test No.	Sample	Preparation Method	Unit Weight (kN/m ³)	Dr	Temperature	Type of Motion (1-D)
Test 16-17-18	TC10	Sand mixed with 10% tire crumb material in a bowl and saturated with water. Then filled into the shear box.	12.50	0.40	(i) 0 °C (ii) 50 °C (iii) Room Temp.	İzmit E-W
						Tabas E-W
						Sakarya N-S
Test 19-20-21	TC15	Sand mixed with 15% tire crumb material in a bowl and saturated with water. Then filled into the shear box.	11.90	0.40	(i) 0 °C (ii) 50 °C (iii) Room Temp.	İzmit E-W
						Tabas E-W
						Sakarya N-S
Test 22-23-24	TC20	Sand mixed with 20% tire crumb material in a bowl and saturated with water. Then filled into the shear box.	10.00	0.40	(i) 0 °C (ii) 50 °C (iii) Room Temp.	İzmit E-W
						Tabas E-W
						Sakarya N-S
Test 25-26-27	TC30	Sand mixed with 30% tire crumb material in a bowl and saturated with water. Then filled into the shear box.	8.50	0.40	(i) 0 °C (ii) 50 °C (iii) Room Temp.	İzmit E-W
						Tabas E-W
						Sakarya N-S

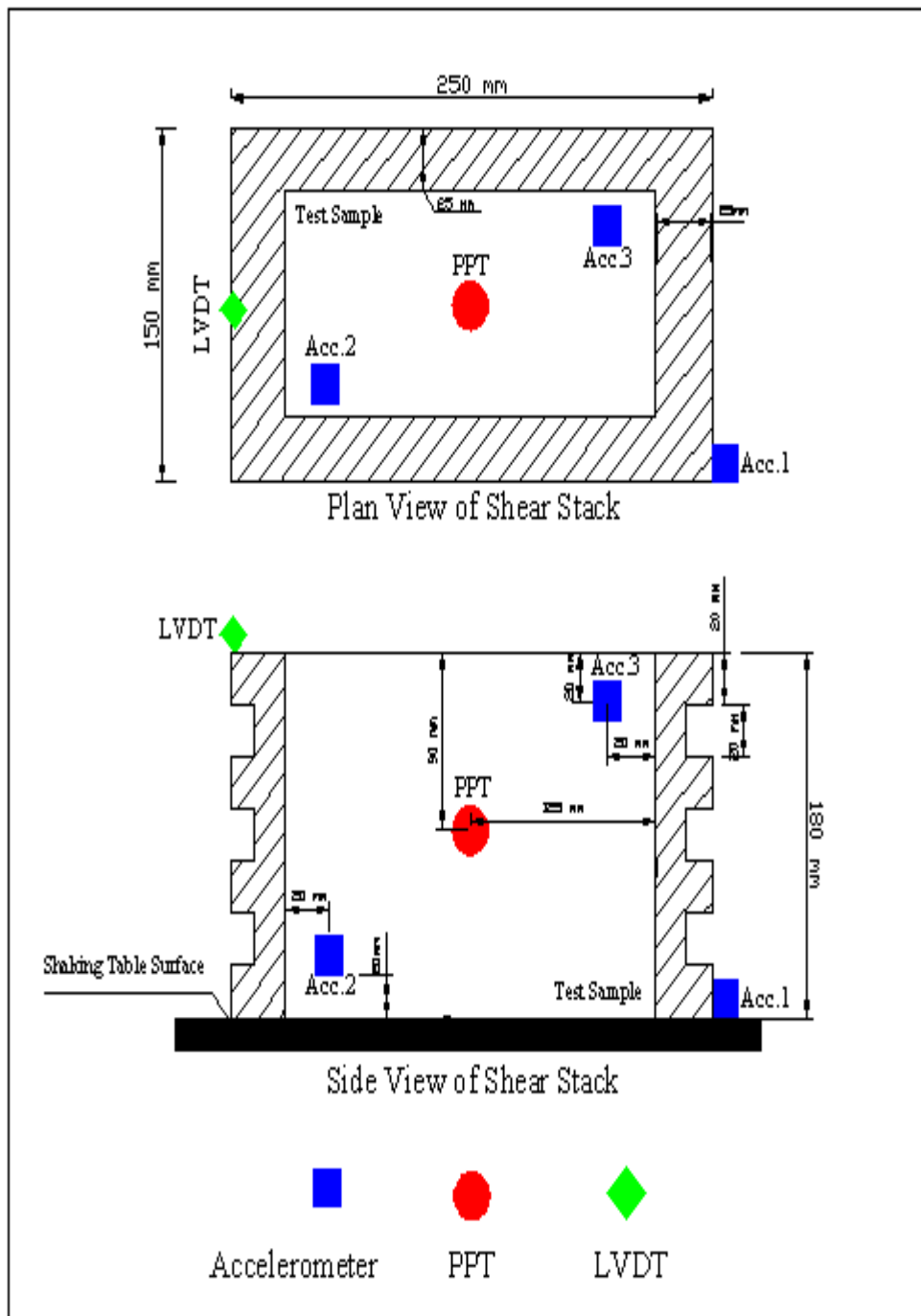


Figure 6.17. Instrumentation on Shaking table Test Setup.

7. EXPERIMENTAL RESULTS

7.1. California Bearing Ratio (CBR) Test Results

A set of CBR tests are performed with sand and sand-tire mixtures at varying contents by weight. Tire buffings material is used at two different sizes; Tire Buffings No 1. (TB1) and Tire Buffings No 2. (TB2). The dimensions of TB1 material is between 1-2 mm and the dimensions of TB2 varies between 2-4 mm. Tire Crumbs material have an aspect ratio of 1-1.5. At the beginning of tests, only sand material is tested without any inclusion. Then, mixtures are prepared at 5, 10, 20, 30, and 40% tire waste by weight. The CBR tests were conducted according to the ASTM D1883-07 standards. Test results are summarised in Table 7.1.

7.1.1. Analysis of California Bearing Ratio Test Results

The CBR value of the sand obtained as 7 and it is rated as 'Fair' according to the ASTM D1883-07 Standards. It is observed that the inclusion of tire crumbs decreases the CBR value of the sand. The CBR value of sand is 7. It is decreased to minimum value as 4.13 for sand-tire crumbs mixture with 40%. On the other hand, it is increased up to 12 for TB2. For TB1 the maximum CBR value observed as 12. The maximum CBR value, increased more than 60% with respect to CBR value of sand. Ghazavi and Sakhi (2005) stated that the influencing parameters on shear strength characteristics of sand-shred mixtures are normal stress, sand matrix unit weight, shred content, shred width and aspect ratio of tire shreds. The addition of TB1 increases the CBR value of the sand and it is not as high as TB2. It can be concluded that in small aspect ratios of tire waste, less friction exists between materials. Additionally, the anchored length of tire elements which are distributed randomly is short. The anchored elements lengths increase the shear resistance along the shear zone.

The other influencing parameter is tire content. It can be easily seen that the CBR value of all specimens increases until a peak value with increasing content of tire and then it decreases. It is also found that the shear resistance of sand-tire mixtures increased for optimum tire contents. In general, the whole test results showed that the CBR value does not increase as the tire content increase. The CBR value of specimens usually increases up

to optimum tire content and it reaches its peak value. After the optimum percent of tire content, the CBR value decreases (Table 7.1).

Table 7.1. CBR Test Results.

Sample	Unit Weight (kN/m³)	Water Content (%)	CBR Value	General Rating
S	15.1	16	7	Fair
TC5	13.0	15	6	Poor to Fair
TC10	12.1	14	6	Poor to Fair
TC15	11.5	12	6	Poor to Fair
TC20	10.7	10	5	Poor to Fair
TC30	9.9	10	4	Poor to Fair
TC40	9.4	14	4	Poor to Fair
TB5 - No.1	12.2	14	7	Fair
TB10 - No.1	11.2	13	8	Fair
TB15 - No.1	10.3	12	9	Fair
TB20 - No.1	9.0	11	10	Fair
TB30 - No.1	7.9	11	10	Fair
TB40 - No.1	6.6	10	10	Fair
TB5 - No.2	13.9	15	8	Fair
TB10 - No.2	13.0	14	9	Fair
TB15 - No.2	12.5	14	10	Fair
TB20 - No.2	11.8	13	12	Fair
TB30 - No.2	11.0	12	11	Fair
TB40 - No.2	10.5	12	11	Fair

Figure 7.1 shows the CBR vs. Tire percentage graph of the sand-tire waste materials. The CBR values of sand-tire crumbs mixtures reached to its minimum for 40% content. The correlation between these two materials does not provide sufficient frictional surface. The few frictional surface produces lower shear resistance and tensile forces. The sand-tire crumbs mixture for 10% content provides maximum CBR value and it decreases even the tire crumbs content continues to increase.

Benson and Khire (1994) stated that the addition of high-density polyethylene (HDPE) strips to Portage sand increased its CBR by as much as a factor of 5, with the largest increase occurring for strip contents of 4%. Additionally, peak values of CBR were obtained at an aspect ratio of 8. Also, Çağatay (2008) figured out that the addition of tire crumbs which is a granular material with an aspect ratio about 1-1.5 do not have an important effect on the CBR value, however, the addition of tire buffings which is a fiber shaped material increases the CBR value. Tire buffings material having an aspect ratio of 7.5-8 increases the CBR value of soil higher compared to tire buffings having an aspect ratio of 3.5-4.

In conclusion, test results are in agreement with both Benson and Khire (1994) and Çağatay (2008). The results of the experiments demonstrate that the addition of tire crumbs material with an aspect ratio 1-1.5 causes a slight decrease in CBR value of sand. On the other hand the addition of tire buffings which is a fiber shaped material increases the CBR value for optimum content. TB1 with an aspect ratio 4.5-5, increase the CBR value up to 43%. The TB2 material with an aspect ratio higher than 5 increases the CBR value of the sand 61% to 12. To optimize the dimension and content of the mixture for the highest CBR value, it can be easily seen that the TB2 material with 20% content by weight has the best performance of shear resistance. As it is seen, tire crumbs material which has an angular shape decrease the CBR value of sand while tire buffings material which has a fiber shape increase the CBR value of sand. All of these test results obtained with the materials used in this study and further investigations should be initiated to provide assurance of these results with any other material.

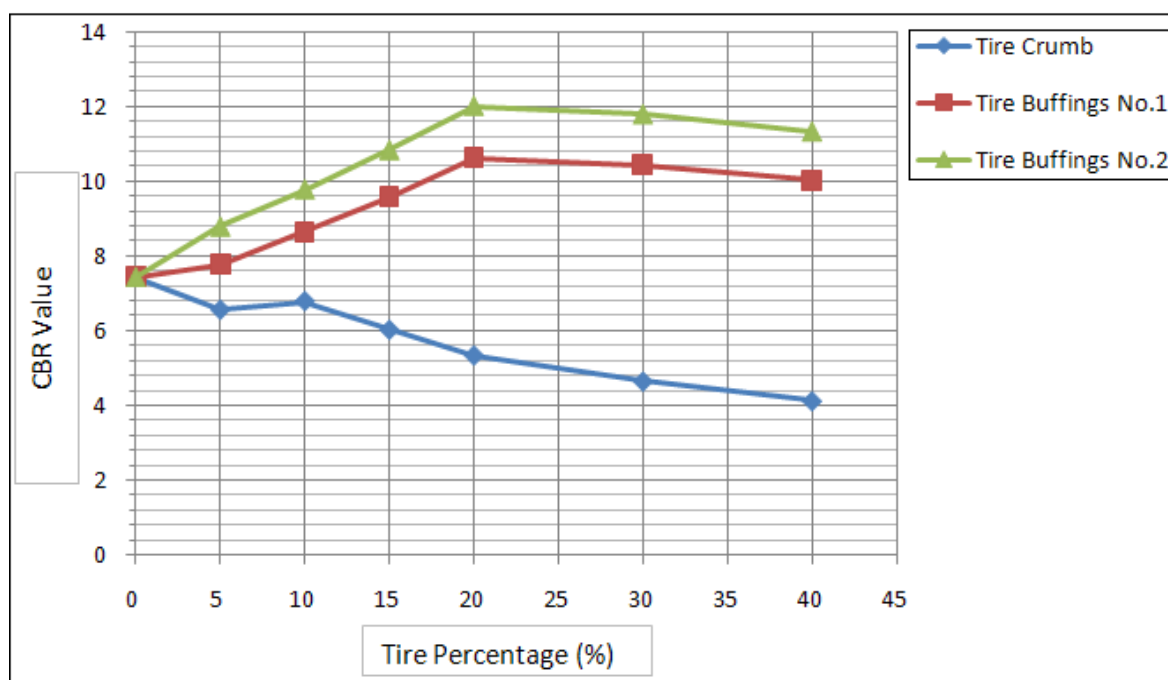


Figure 7.1. CBR vs. Tire percentage of materials.

7.1.2. Direct Shear Test Results

Tire crumbs, tire buffings materials and their mixtures with sand are tested at different compositions. Sand-tire waste mixtures having 5, 10, 15, 20, 30 and 40% by weight are tested. Tests are repeated under normal stresses of 10, 20 and 40 kPa. These tests are named as Test#1, Test#2 and Test#3. The direct shear tests were conducted to evaluate shear strength parameters of specimens. Tire waste material was used at different shapes and contents to determine the optimum behaviour of mixtures.

7.1.3. 100% Sand

The only sand material is tested first. As it is seen, sand displayed a rise in shear stress until the horizontal displacement reached a value of 3 cm. (Figure 7.2.). For only sand material, shear stress first increased then reached to steady state. During the whole of the test, no distinct peak occurs. The maximum shear stress value obtained as 38 kPa at 4 cm horizontal displacement. The relationship between shear stress and normal stress figured out in Figure 7.3. The failure envelope is drawn, apparent cohesion and angle of internal friction values are found. The apparent cohesion value is found as 0 and the angle of friction is found as 24°.

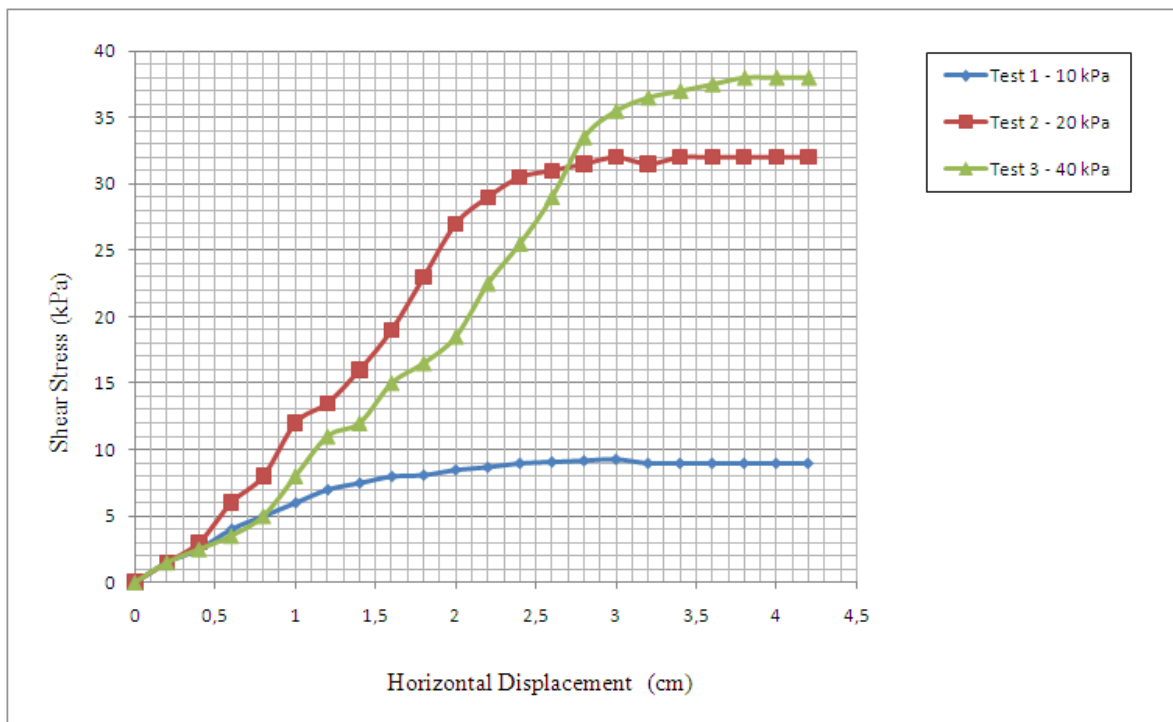


Figure 7.2. Shear Stress vs. Horizontal Displacement Graph of Sand.

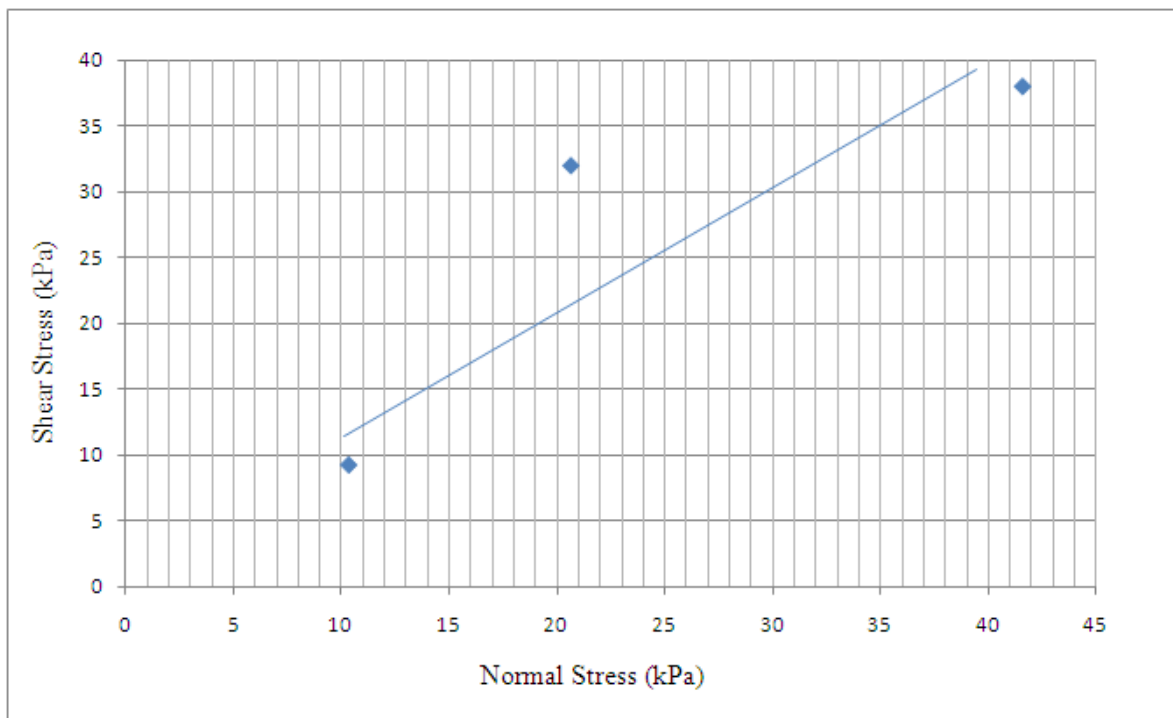


Figure 7.3. Shear Stress vs. Normal Stress graph of Sand.

7.1.4. 100% Tire Crumbs

Only tire crumbs sample is tested and test data are recorded. Shear stress vs. horizontal displacement graph is drawn (Figure 7.4). Shear stress values increased without reaching any constant value. The failure envelope gave results of a apparent cohesion value of 5.75 kPa and the internal friction angle found as 11.30° (Figure 7.5).

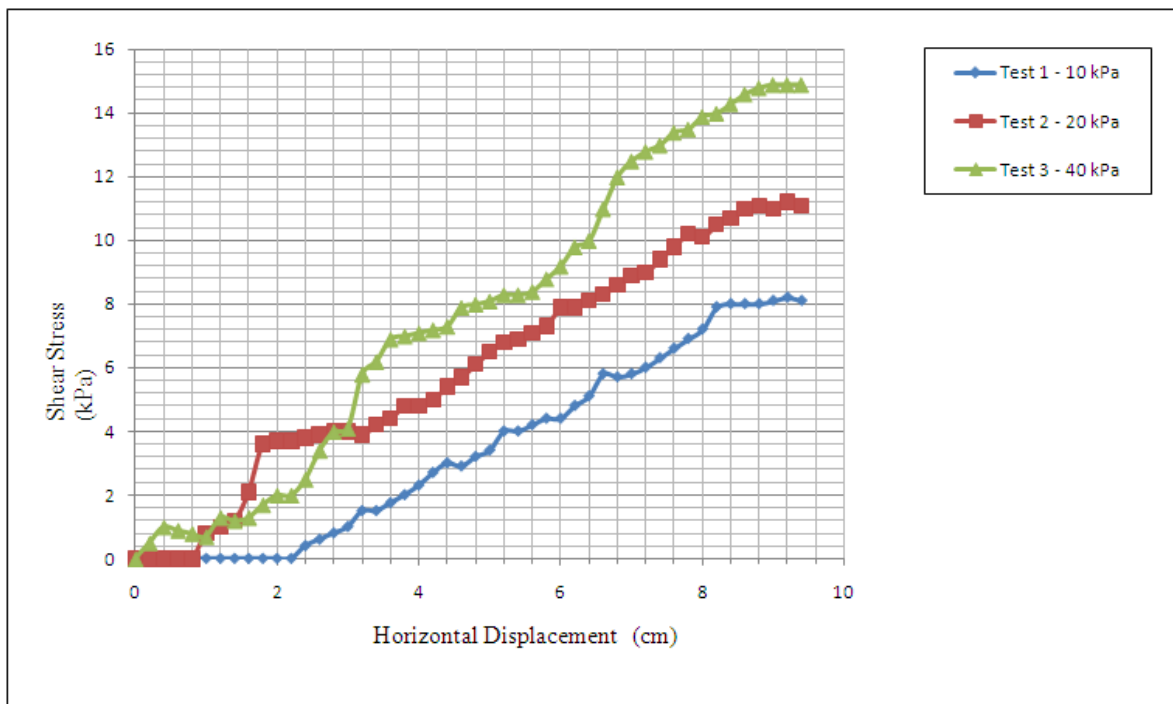


Figure 7.4. Shear Stress vs. Horizontal Displacement Graph of TC.

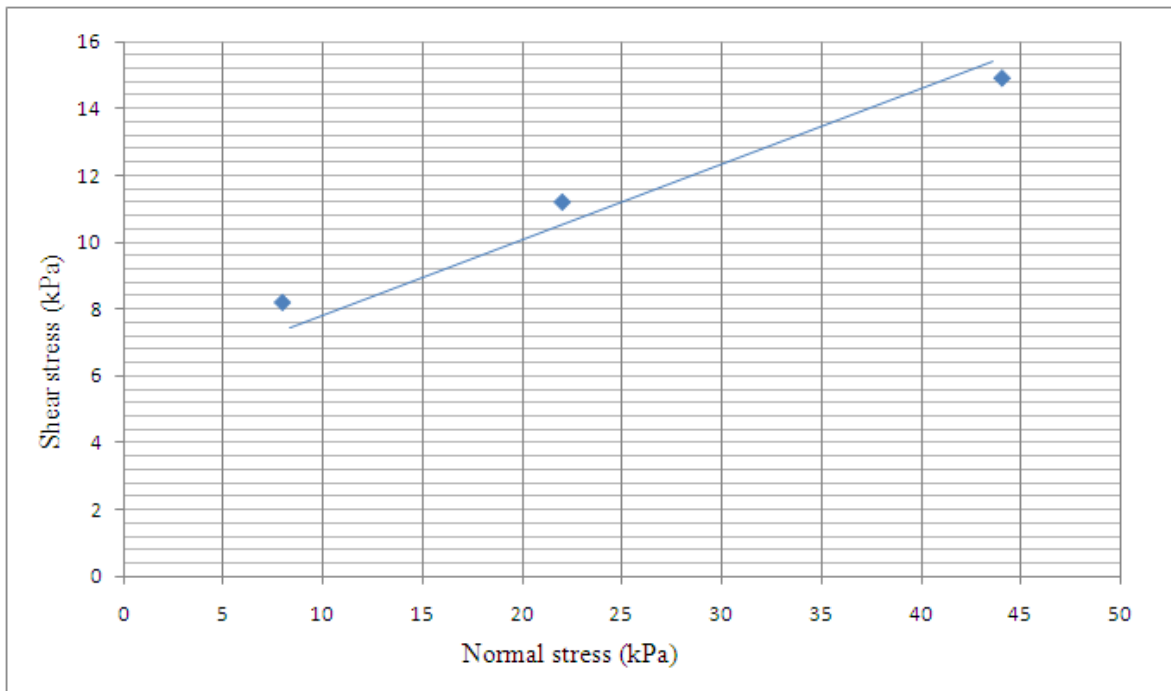


Figure 7.5. Shear Stress vs. Normal Stress graph of TC.

7.1.5. 5% Tire Crumbs

5% tire crumbs by weight is mixed with sand and tested. The unit weight of the sample is found as 13.7 kN/m^3 . The shear stress vs. horizontal displacement and shear stress vs. normal stress graphs are given in Figure 7.6. and Figure 7.7. Shear stress value reaches constant value at 3 cm horizontal displacement. As the normal stress increases the shear stress value increases. The apparent cohesion value is found as 2.1 kPa and the angle of internal friction is found as 26.10° .

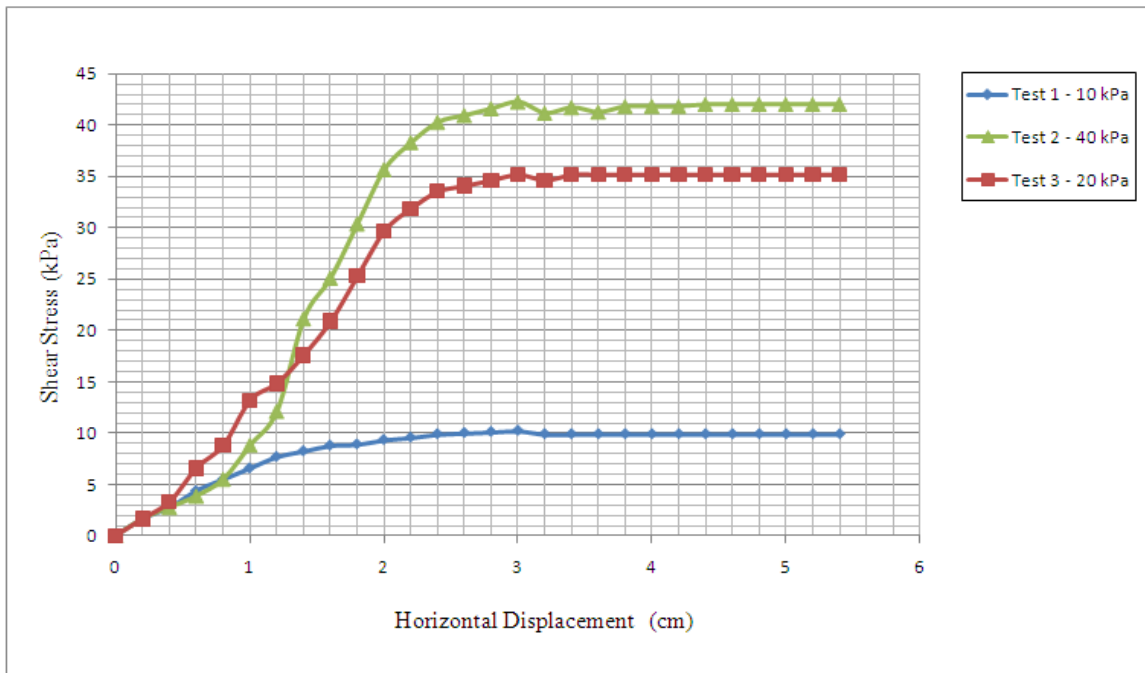


Figure 7.6. Shear Stress vs. Horizontal Displacement Graph of TC5.

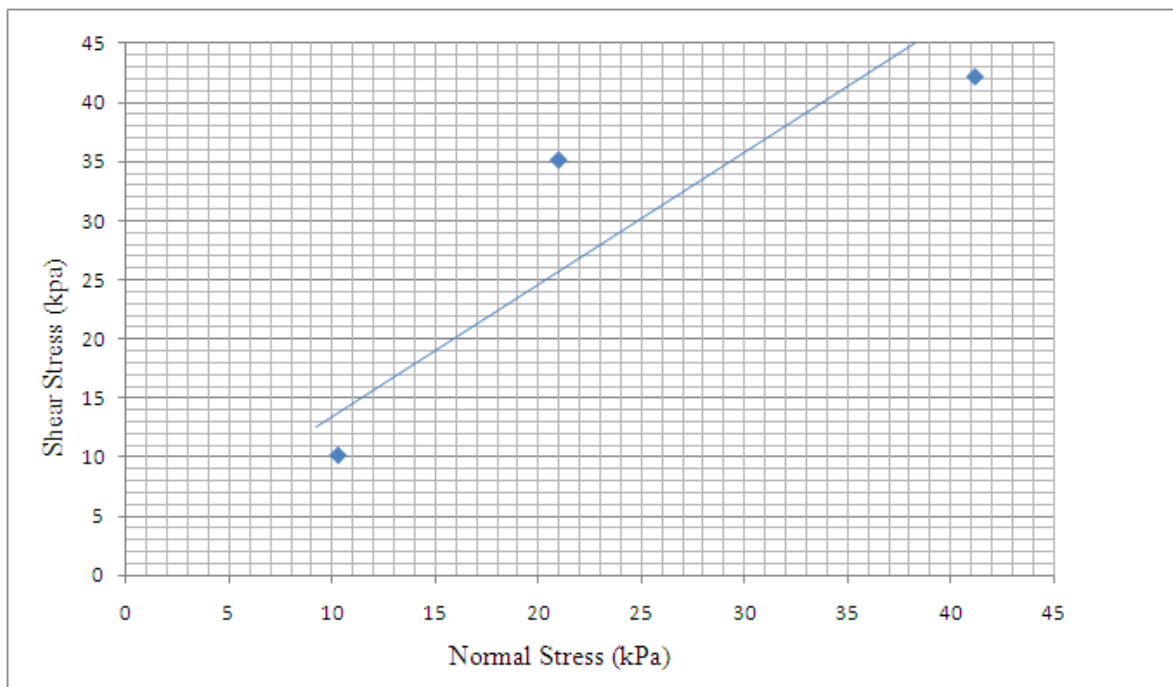


Figure 7.7. Shear Stress vs. Normal Stress graph of TC5.

7.1.6. 10% Tire Crumbs

10% tire crumbs by weight is mixed with the sand and tested. The shear stress vs. horizontal displacement and shear vs. normal stress graphs are given in Figure 7.8 and Figure 7.9. As the normal stresses increases, the difference between the ultimate shear stresses of three tests increases. The maximum shear stress value of the specimen found as 46.27 kPa under 40 kPa normal stresses while it is found as 33.01 kPa under 20 kPa normal stresses and 14.62 kPa under 10 kPa normal stresses. The apparent cohesion value is found as 3.50 kPa and the angle of internal friction is found as 35.80° .

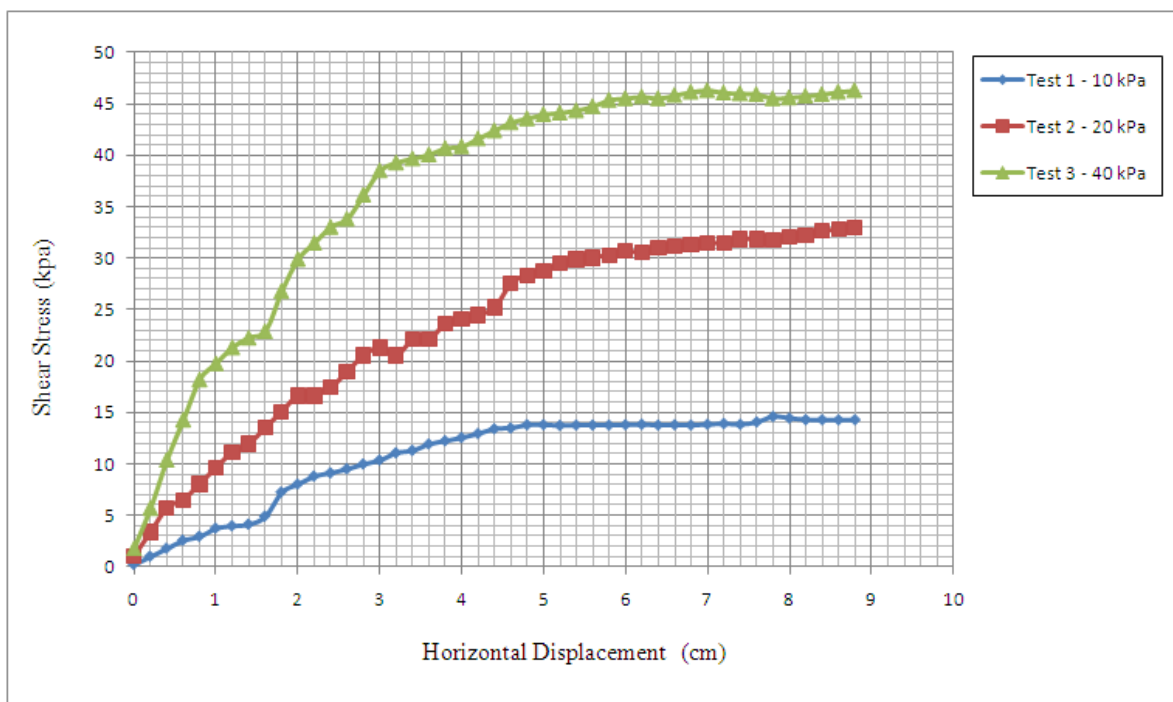


Figure 7.8. Shear Stress vs. Horizontal Displacement Graph of TC10.

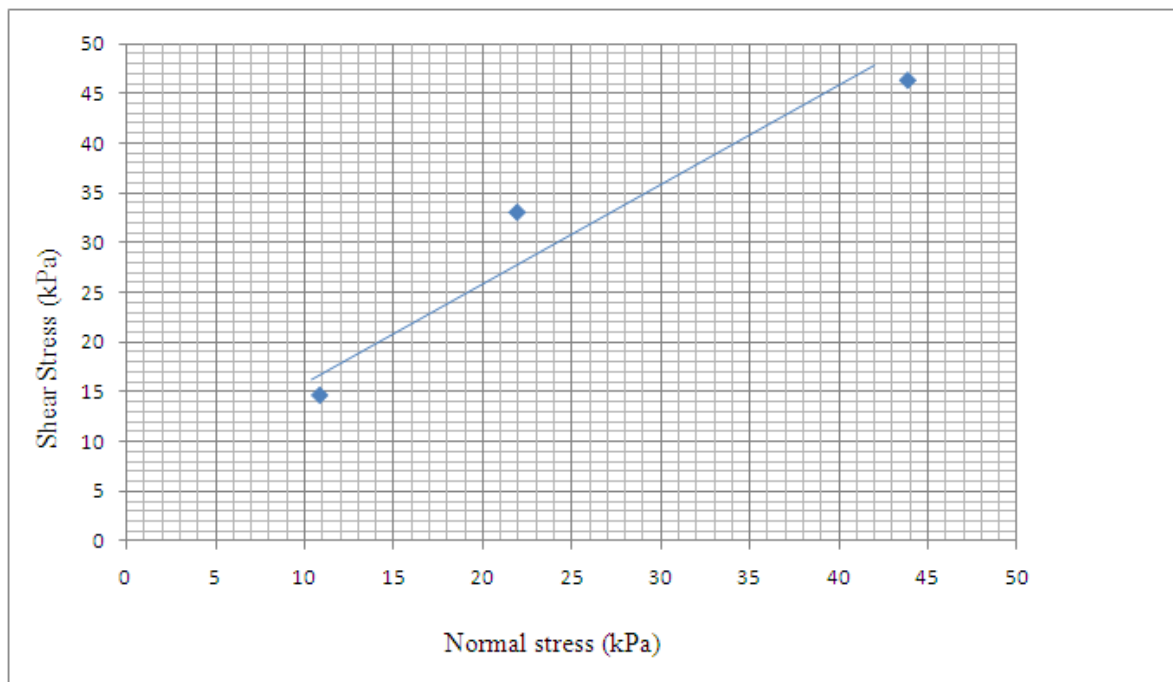


Figure 7.9. Shear Stress vs. Normal Stress graph of TC10.

7.1.7. 15% Tire Crumbs

15% tire crumbs by weight is mixed with sand and tested. The unit weight of the sample is found as 12.5 kN/m^3 . The shear stress vs. horizontal displacement and shear vs. normal stress graphs are given in Figure 7.10 and Figure 7.11. All of the three specimens reach maximum shear stress at 8 cm horizontal displacement. The shear stress values are; 17.33 kPa, 37.96 kPa and 53.21 kPa under 10, 20 and 40 kPa normal stresses. The apparent cohesion value is found as 5.2 kPa and the angle of internal friction is found as 34.20° .

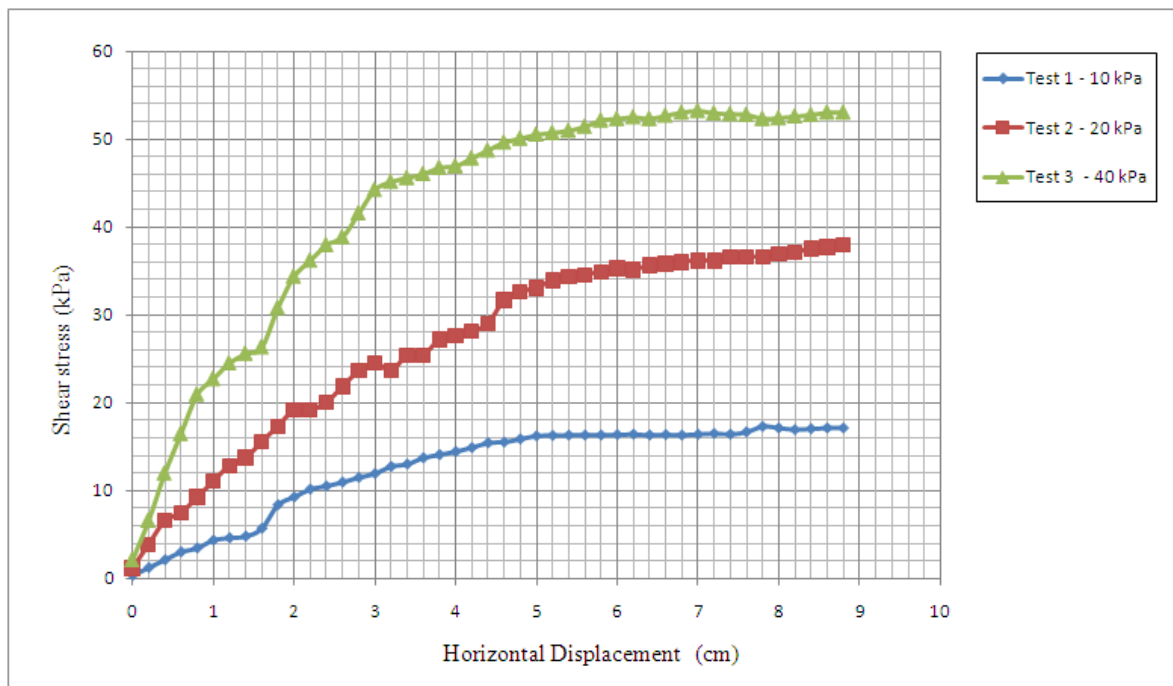


Figure 7.10. Shear Stress vs. Horizontal Displacement Graph of TC15.

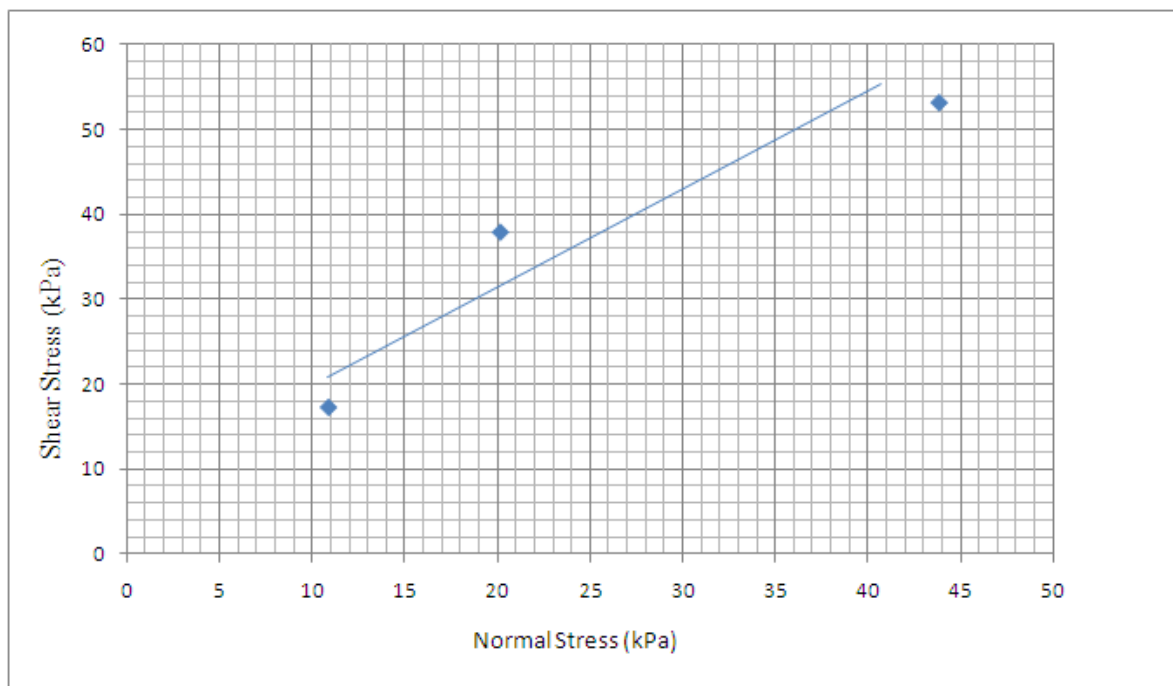


Figure 7.11. Shear Stress vs. Normal Stress graph of TC15.

7.1.8. 20% Tire Crumbs

20% tire crumbs by weight is mixed with sand and tested. The unit weight of the sample is 11.8 kN/m^3 . The shear stress vs. horizontal displacement and shear vs. normal stress graphs are given in Figure 7.12. and Figure 7.13. According to the shear stress vs. horizontal displacement curves, it is recorded that the maximum shear stress values are; 19 kPa 42 kPa and 59 kPa under 10, 20 and 40 kPa normal stresses, respectively. The apparent cohesion value is found as 4.15 kPa and the angle of internal friction is found as 30.40° .

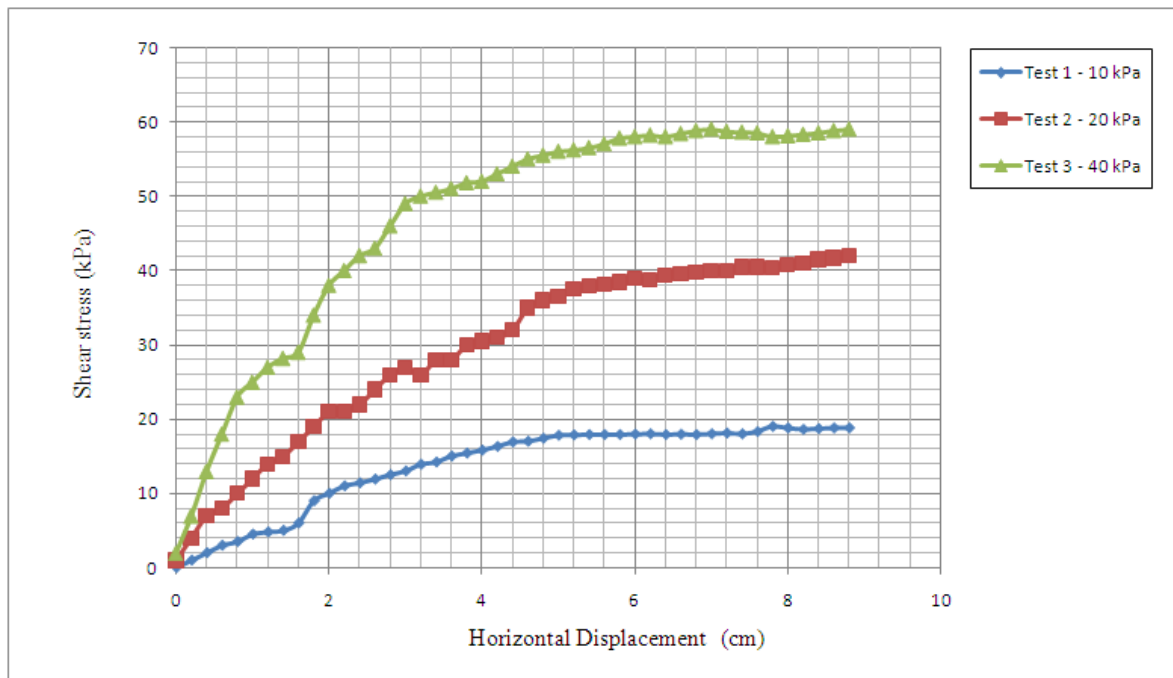


Figure 7.12. Shear Stress vs. Horizontal Displacement Graph of TC20.

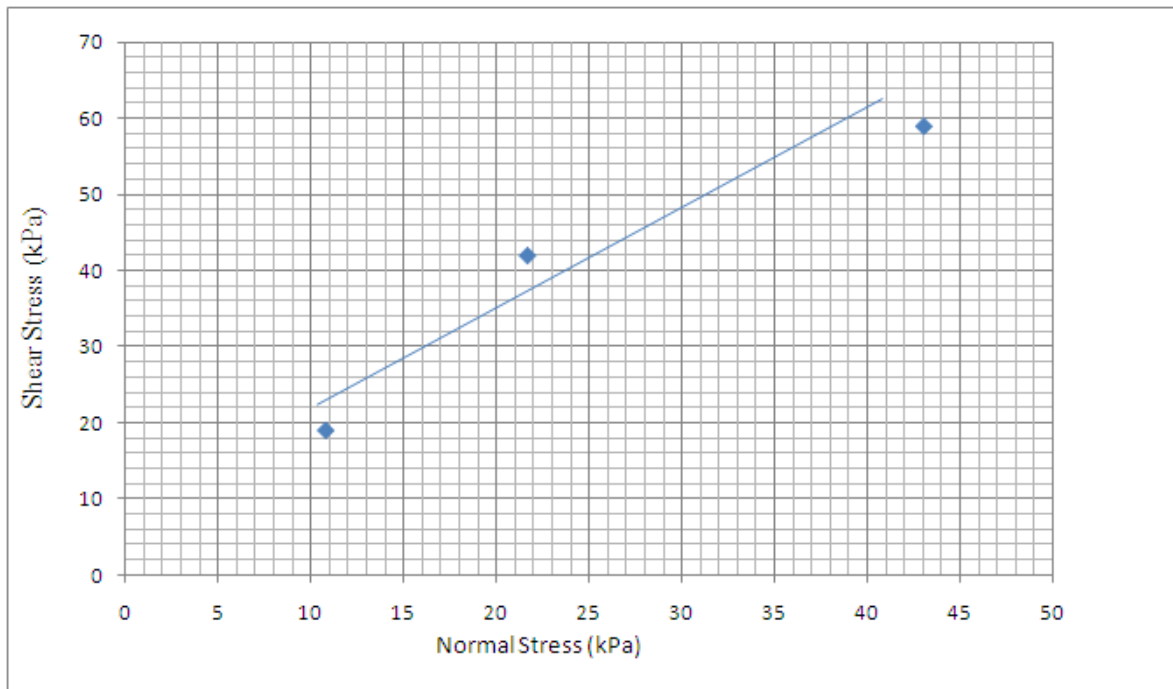


Figure 7.13. Shear Stress vs. Normal Stress graph of TC20.

7.1.9. 30% Tire Crumbs

30% tire crumbs by weight is mixed with sand. The unit weight of the sample is $10,75 \text{ kN/m}^3$. The shear stress vs. horizontal displacement and shear vs. normal stress graphs are given in Figure 7.14 and Figure 7.15. Shear stress value of specimens are; 15.61 kPa, 42.97 kPa and 60.31 kPa under 10, 20 and 40 kPa normal stresses respectively. The apparent cohesion value is found as 4.20 kPa and the angle of internal friction is found as 29.50° .

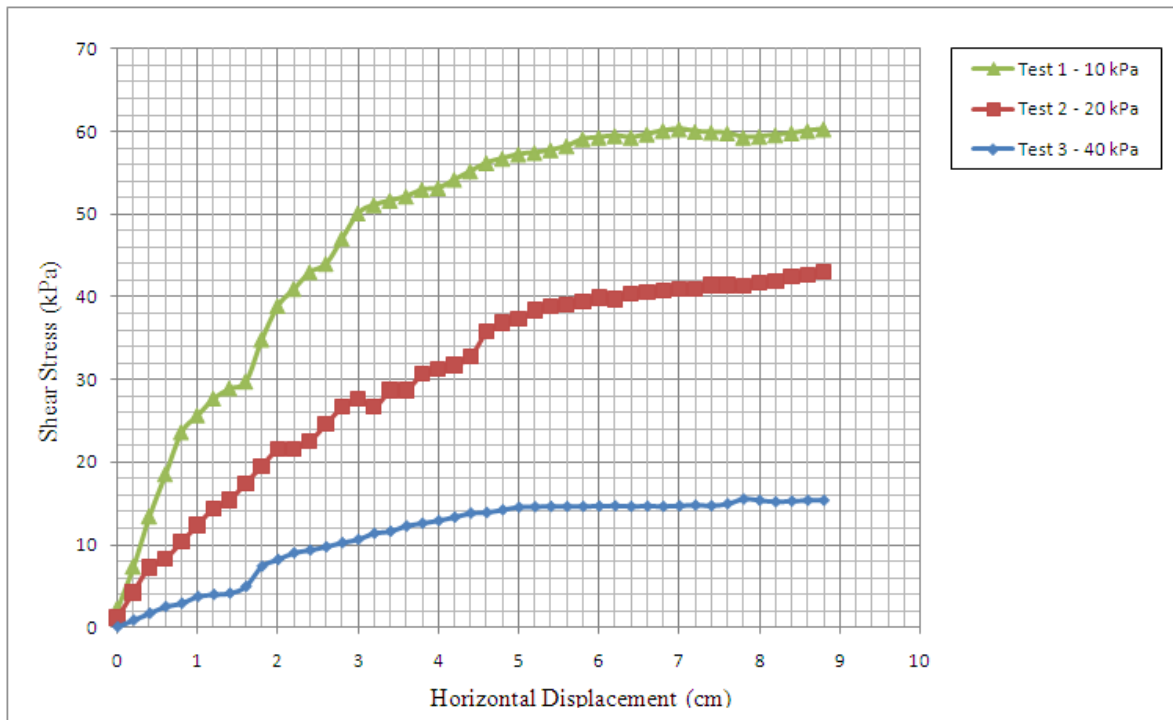


Figure 7.14. Shear Stress vs. Horizontal Displacement Graph of TC30.

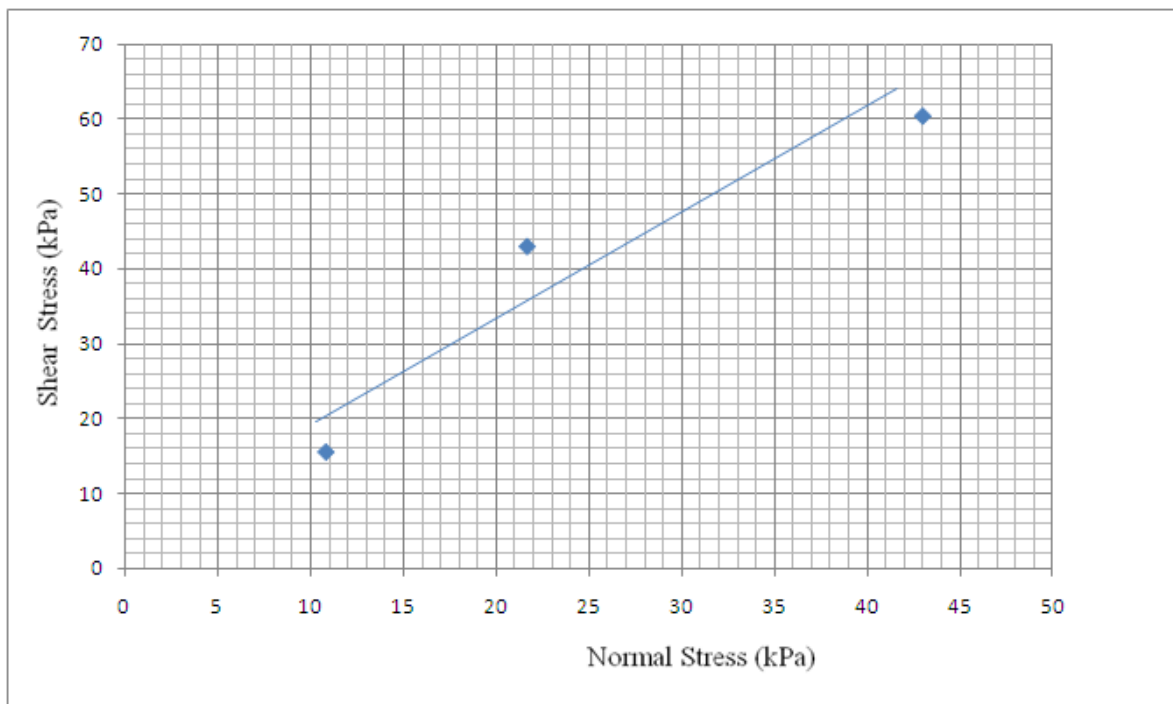


Figure 7.15. Shear Stress vs. Normal Stress graph of TC30.

7.1.10. 40% Tire Crumbs

40% tire crumbs by weight is mixed with sand and tested. The shear stress vs. horizontal displacement and shear stress vs. normal stress graphs are given in Figure 7.16. and Figure 7.17. The apparent cohesion value is found as 3,85 kPa and the angle of internal friction is found as 33°. The shear stress value of the specimen tested under 40 kPa confining pressure is 62 kPa.

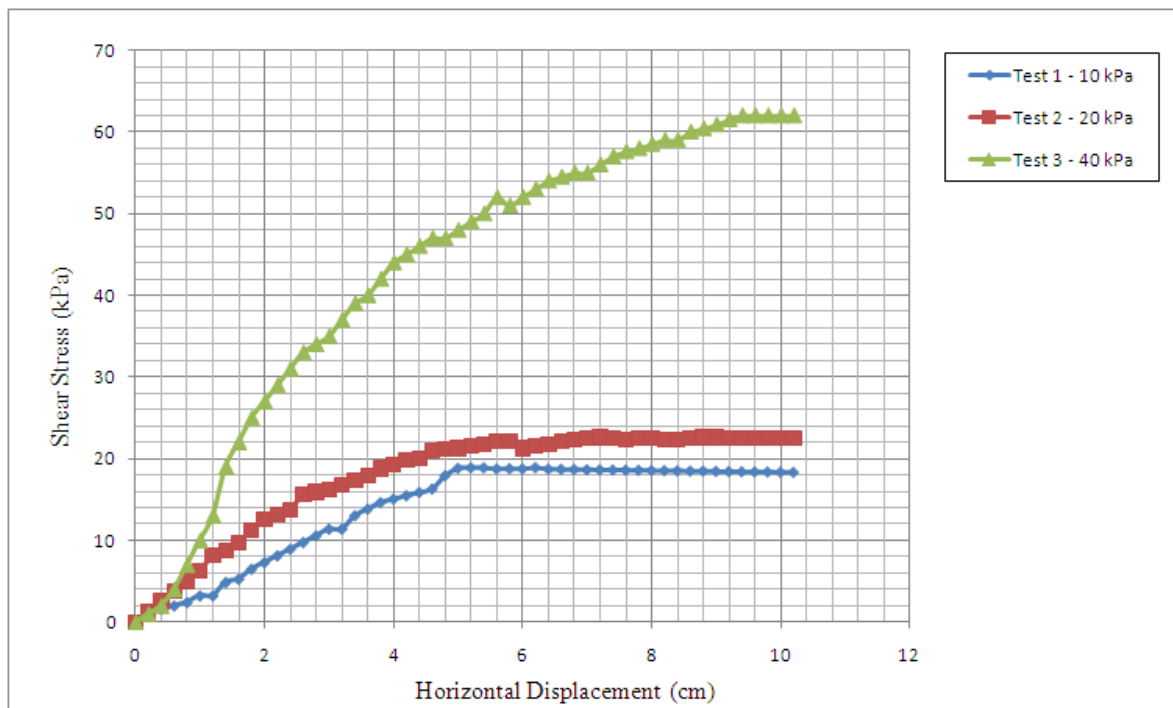


Figure 7.16. Shear Stress vs. Horizontal Displacement Graph of TC40.

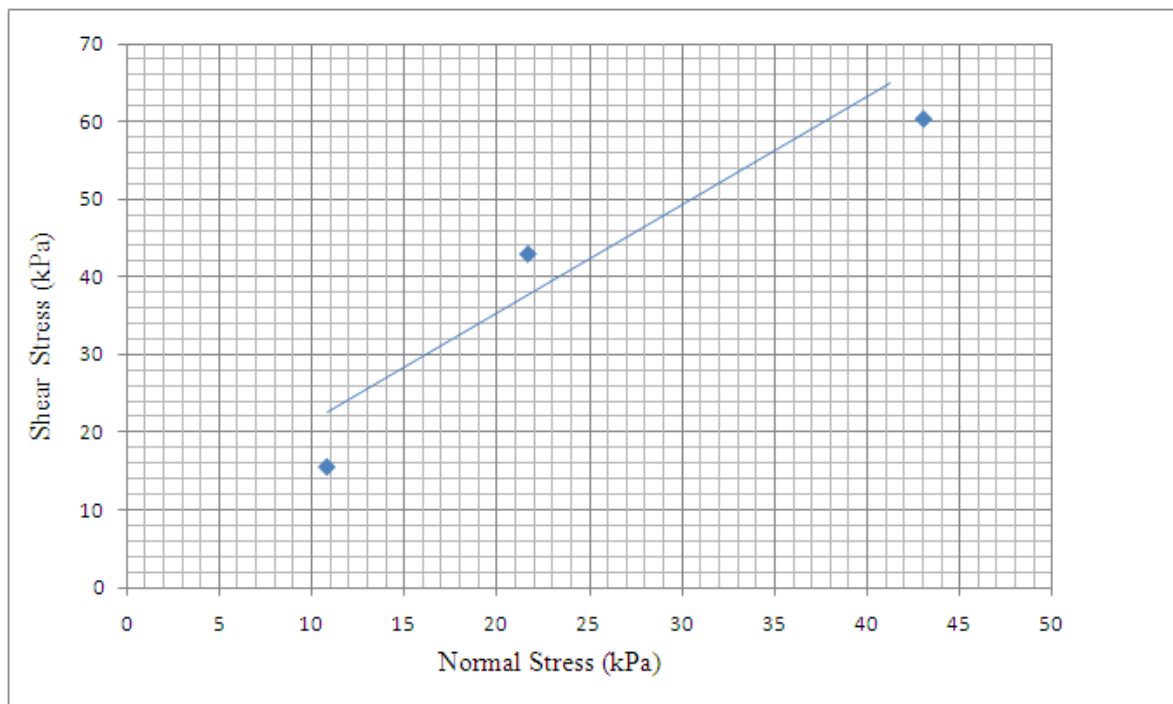


Figure 7.17. Shear Stress vs. Normal Stress graph of TC40.

7.1.11. 100% Tire Buffings

The tire buffings specimen is prepared and direct shear tests were conducted. Shear strain vs. horizontal displacement graph is drawn (Figure 7.18). The shear stress value increases without reaching any constant value. The failure envelope (Figure 7.19.) gave results of a apparent cohesion value of 5.3 kPa and the internal friction angle of 28°. The tire buffings material has a high compressibility than a soil, hence, the shear stress vs. horizontal displacement curve did not reach to steady state.

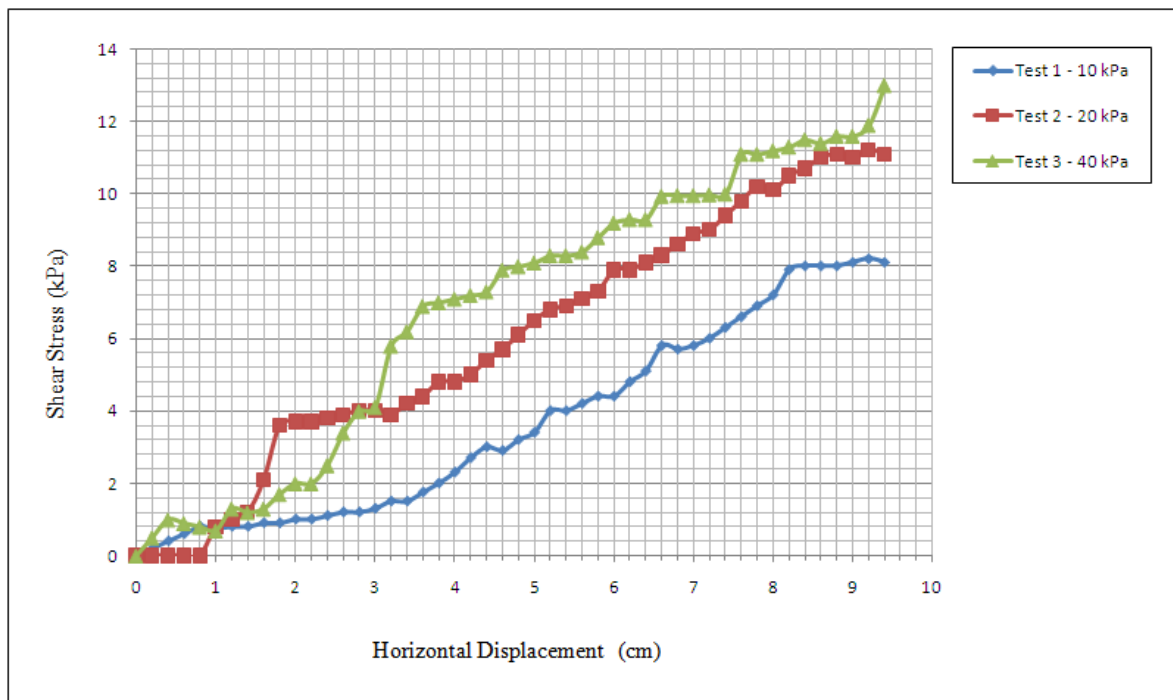


Figure 7.18. Shear Stress vs. Horizontal Displacement Graph of TB.

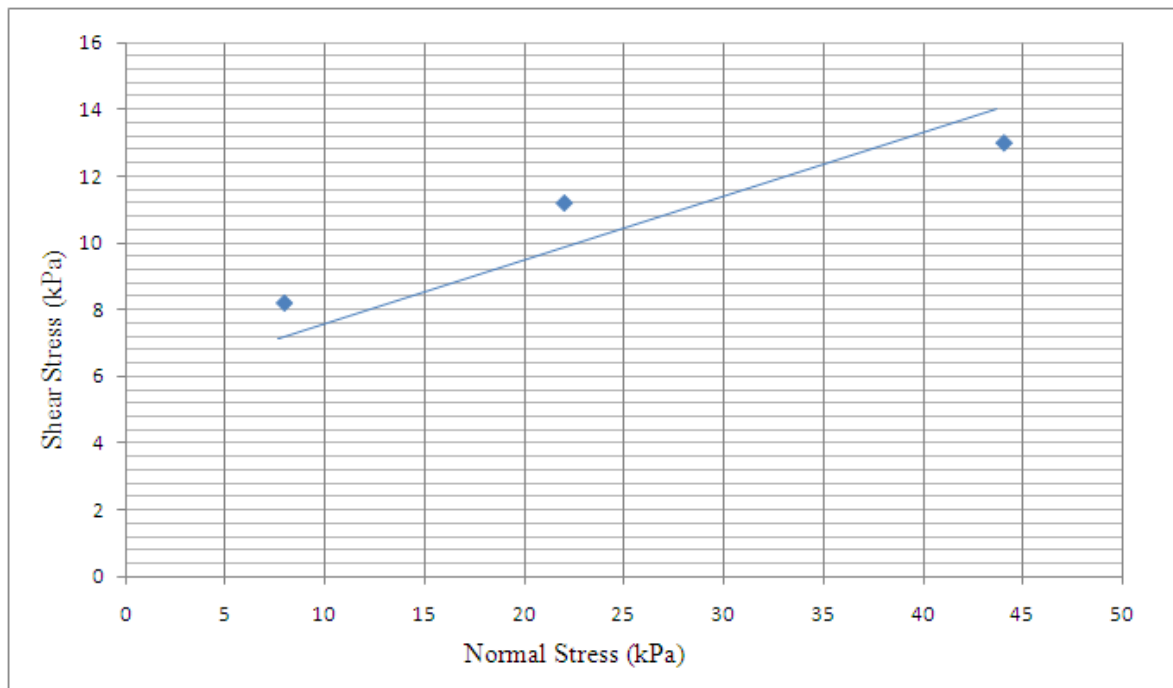


Figure 7.19. Shear Stress vs. Normal Stress graph of TB.

7.1.12. 5% Tire Buffings

5% tire buffings by weight is mixed with sand and placed into the shear box (Figure 7.20). The shear stress vs. horizontal displacement and shear stress vs. normal stress graphs are given in Figure 7.21. and Figure 7.22. Shear stress value reaches constant value at 3 cm horizontal displacement. As the normal stresses increases the maximum shear stress value increases. The unit weight of specimen is 13.20 kN/m^3 . The apparent cohesion value is found as 12.1 kPa and the angle of internal friction is found as 31° .



Figure 7.20. 20% tire buffings-sand specimen tested in direct shear test machine.

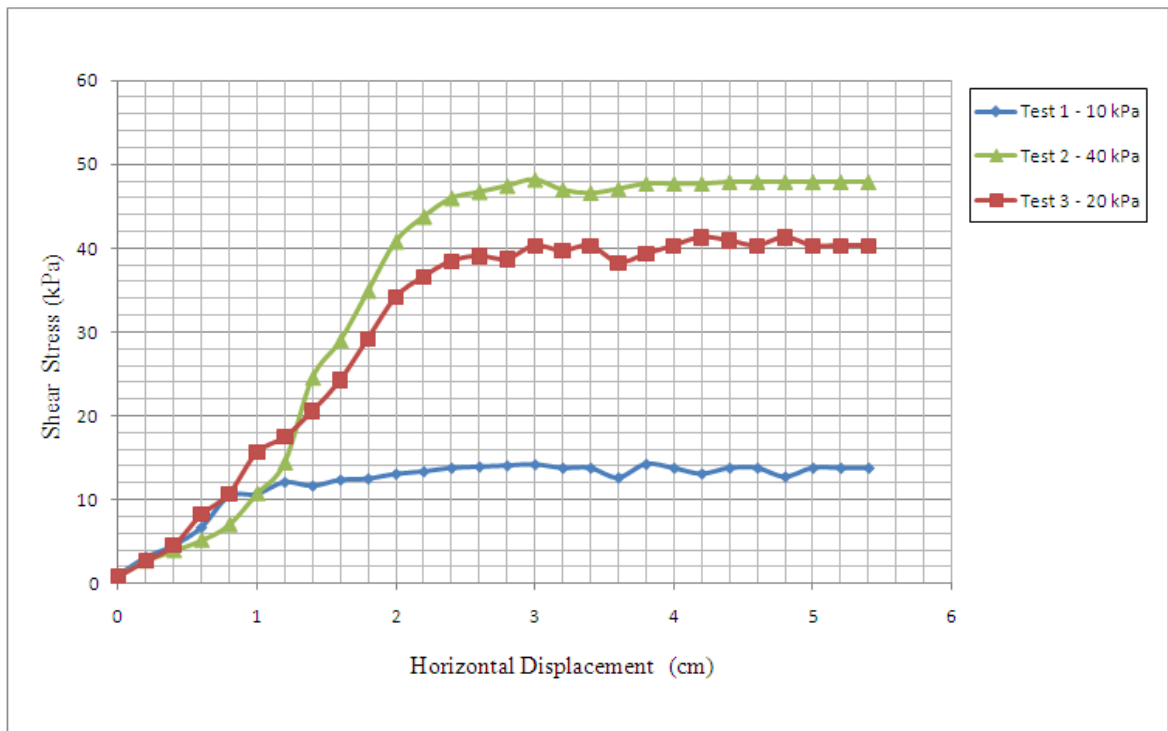


Figure 7.21. Shear Stress vs. Horizontal Displacement Graph of TB5.

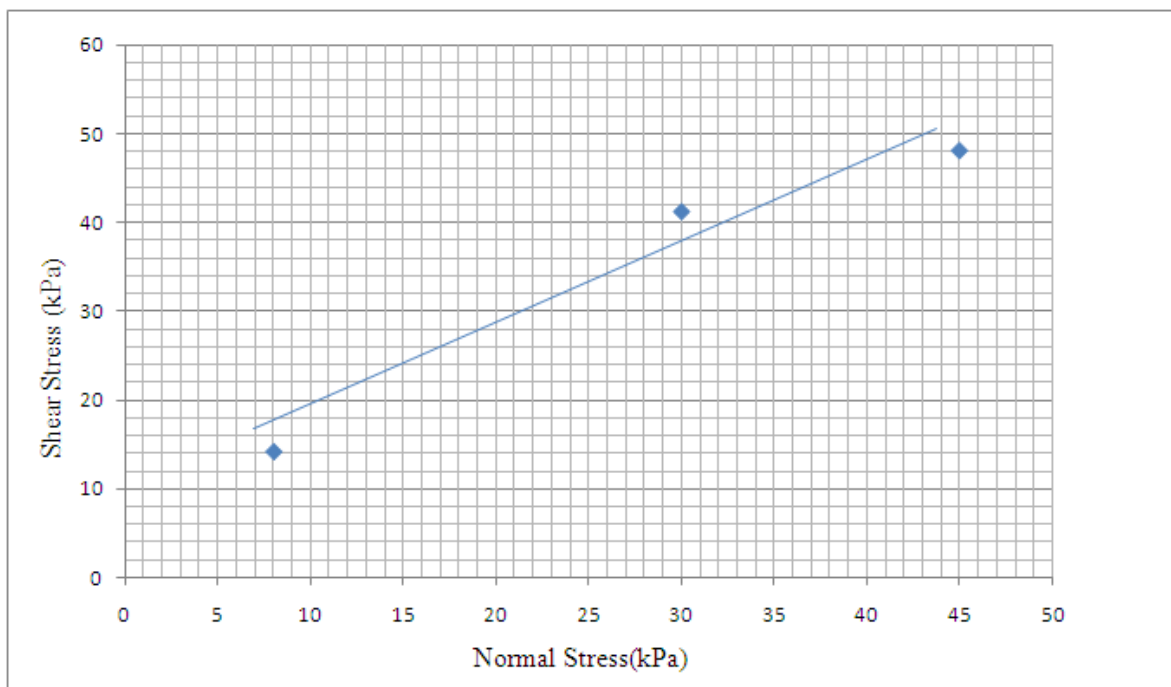


Figure 7.22. Shear Stress vs. Normal Stress graph of TB5.

7.1.13. 10% Tire Buffings

10% tire buffings by weight is mixed with sand and tested. The shear stress vs. horizontal displacement graph and shear vs. normal stress graph are given in Figure 7.23. and Figure 7.24. The maximum shear stress values of material are; 16.52 kPa, 42.15 kPa and 52.29 for specimens tested under 10 kPa, 20 kPa and 40 kPa normal stresses respectively. The apparent cohesion value is found as 13.2 kPa and the angle of internal friction is found as 27.4° .

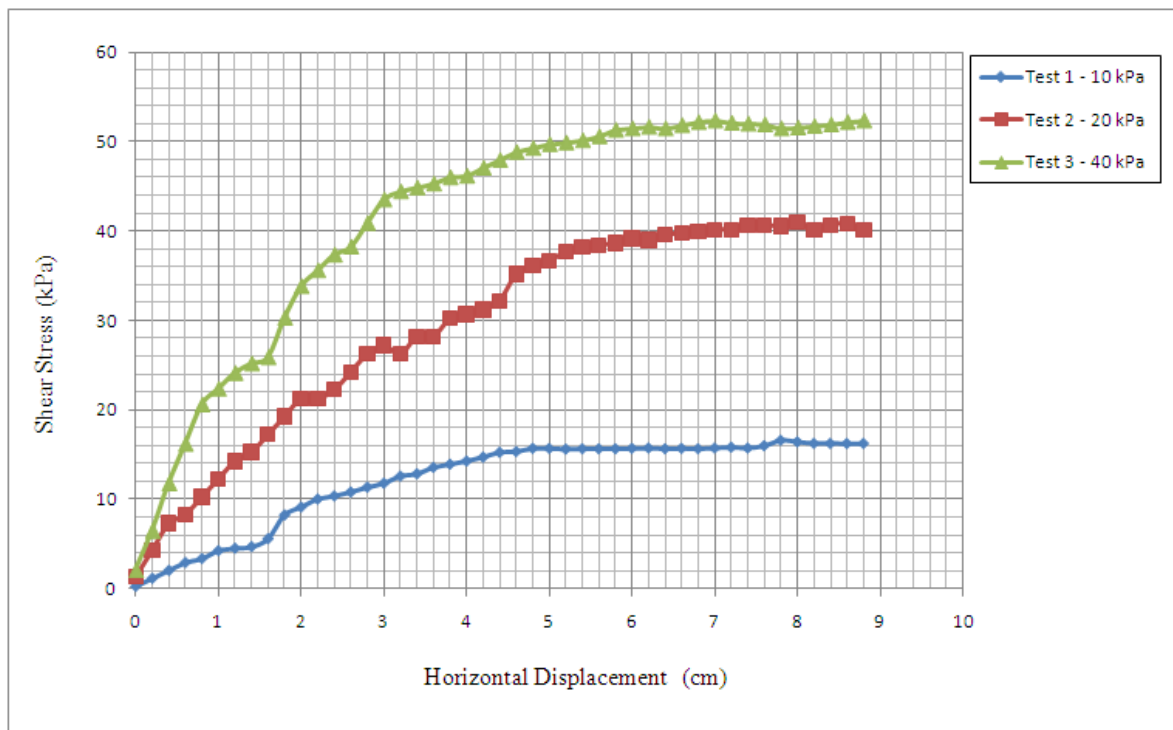


Figure 7.23. Shear Stress vs. Horizontal Displacement Graph of TB10.

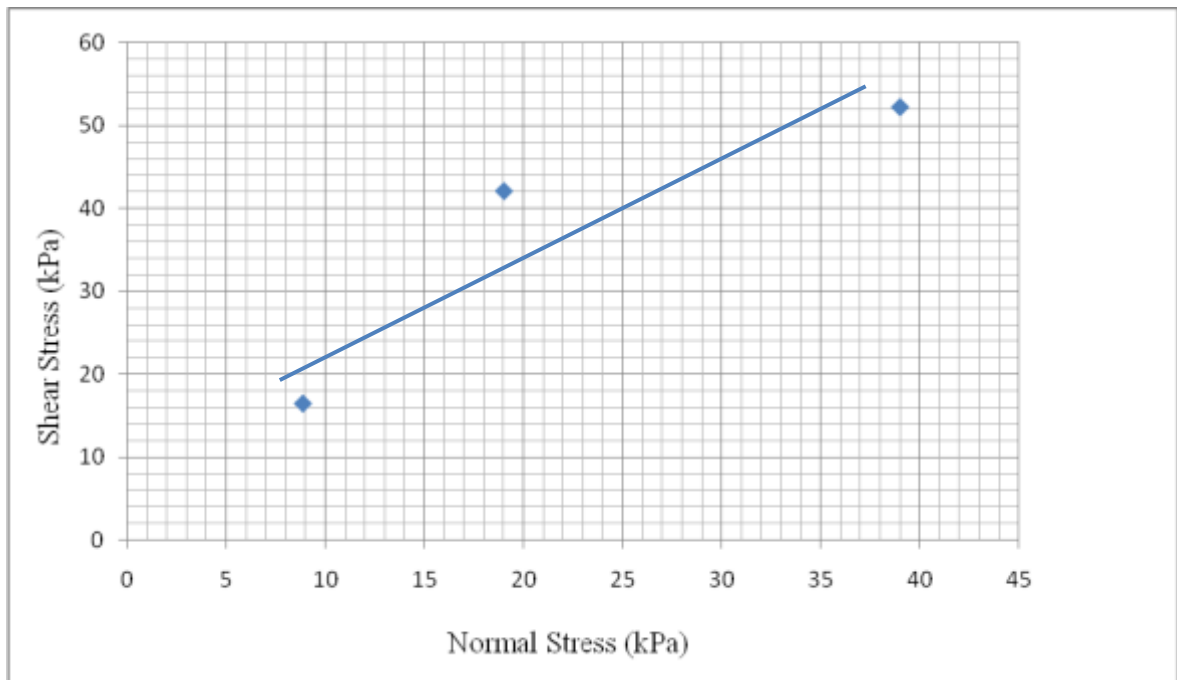


Figure 7.24. Shear Stress vs. Normal Stress graph of TB10.

7.1.14. 15% Tire Buffings

15% tire buffings by weight mixed with sand. The shear stress vs. horizontal displacement and shear vs. normal stress graphs are given in Figure 7.25. and Figure 7.26. The shear stress values are found as 19.06 kPa, 41.76 kPa and 54.43 kPa for the specimens tested under 10 kPa, 20 kPa and 40 kPa normal stresses, respectively. The apparent cohesion value is found as 14.9 kPa and the angle of internal friction is found as 22.2° .

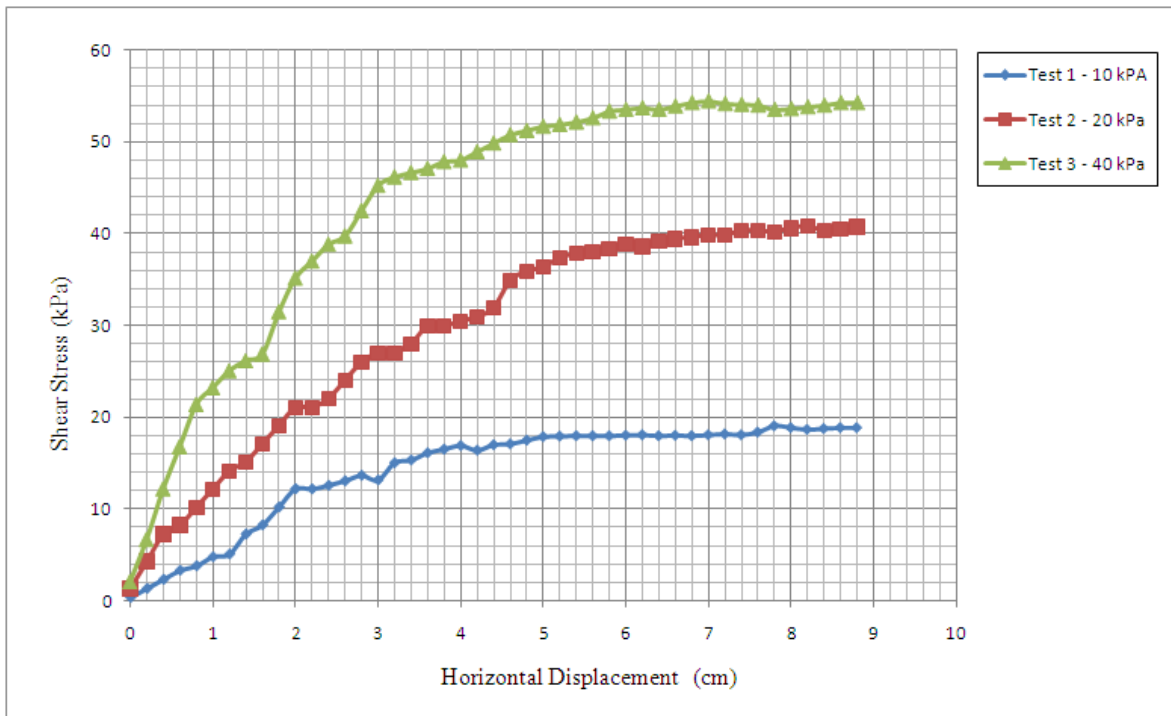


Figure 7.25. Shear Stress vs. Horizontal Displacement Graph of TB15.

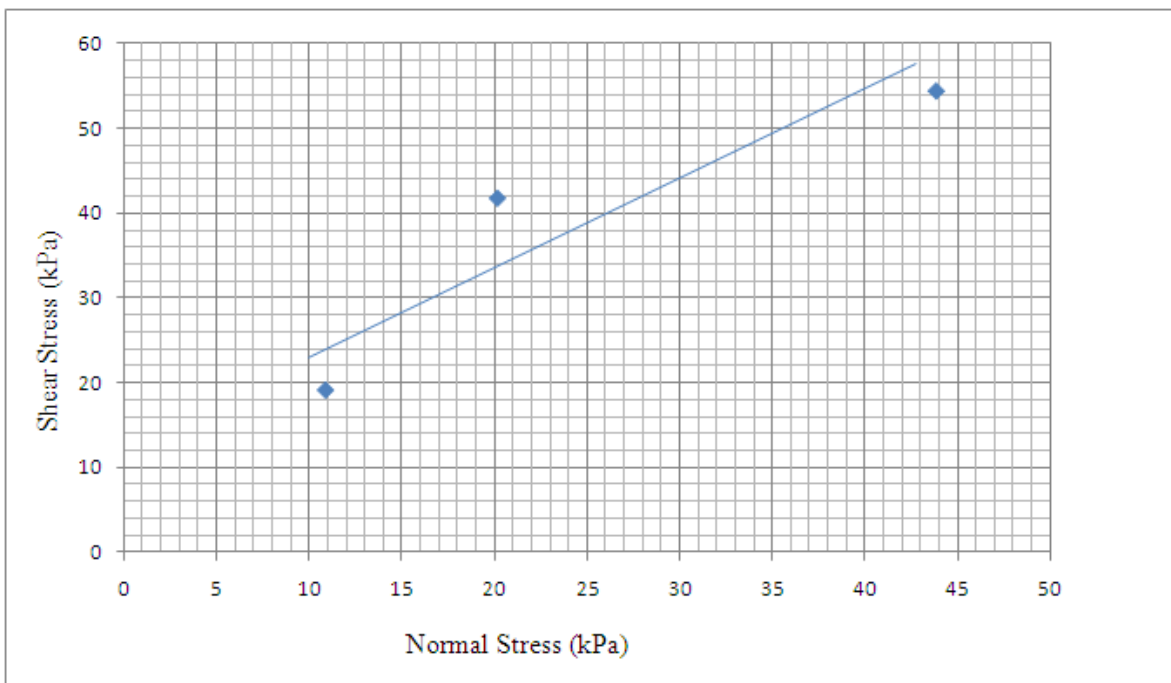


Figure 7.26. Shear Stress vs. Normal Stress graph of TB15.

7.1.15. 20% Tire Buffings

20% tire buffings by weight was mixed with sand and tested. The shear stress vs. horizontal displacement and shear vs. normal stress graphs are given in Figure 7.27. and Figure 7.28. The shear stress values are found as 16.53 kPa, 31.06 kPa and 43.63 kPa for the specimens tested under 10 kPa, 20 kPa and 40 kPa normal stresses respectively. The apparent cohesion value is found as 14.5 kPa and the angle of internal friction is found as 34° .

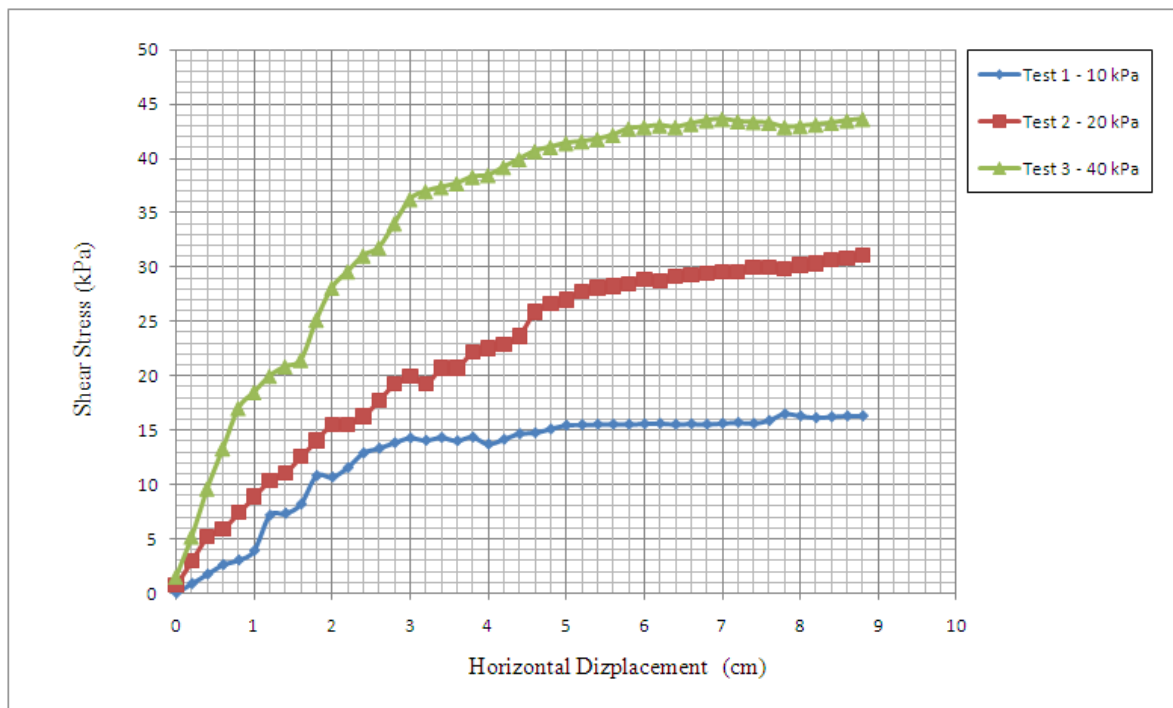


Figure 7.27. Shear Stress vs. Horizontal Displacement Graph of TB20.

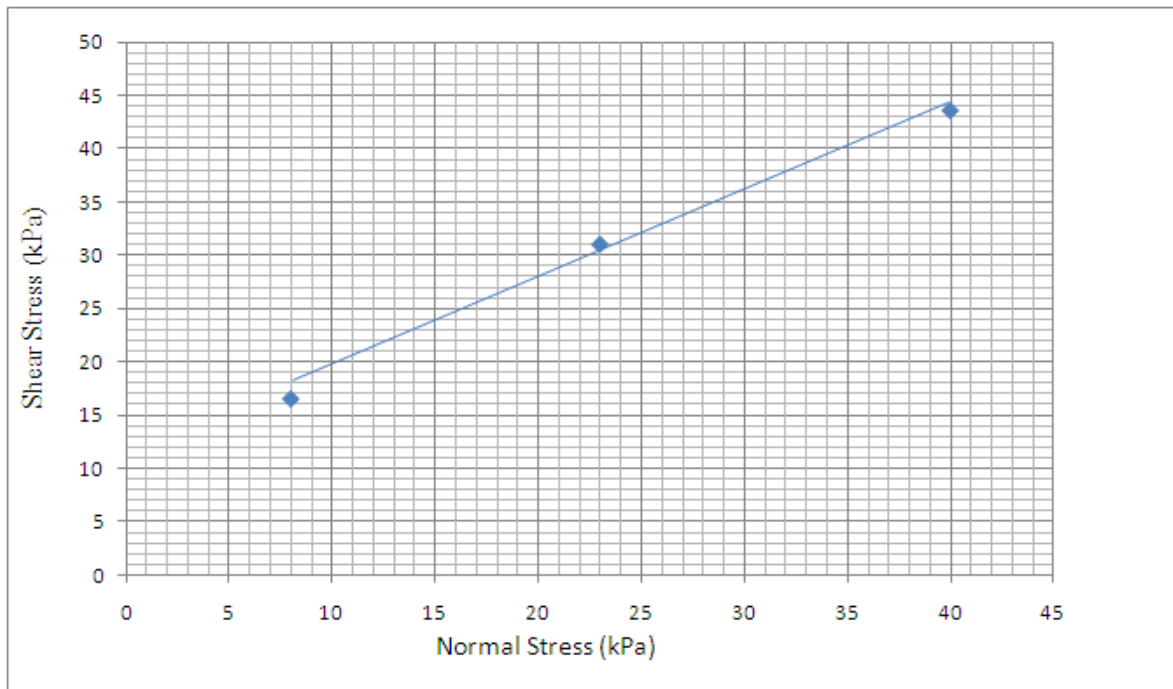


Figure 7.28. Shear Stress vs. Normal Stress graph of TB20.

7.1.16. 30% Tire Buffings

30% tire buffings by weight was mixed with sand and tested. The shear stress vs. horizontal displacement and shear stress vs. normal stress graphs are given in Figure 7.29. and Figure 7.30. The maximum shear stress values are found as 16.2 kPa, 28.7 kPa and 38.4 kPa for the specimens tested under 10 kPa, 20 kPa and 40 kPa normal stresses respectively. The apparent cohesion value is found as 12 kPa and the angle of internal friction is found as 30.5° .

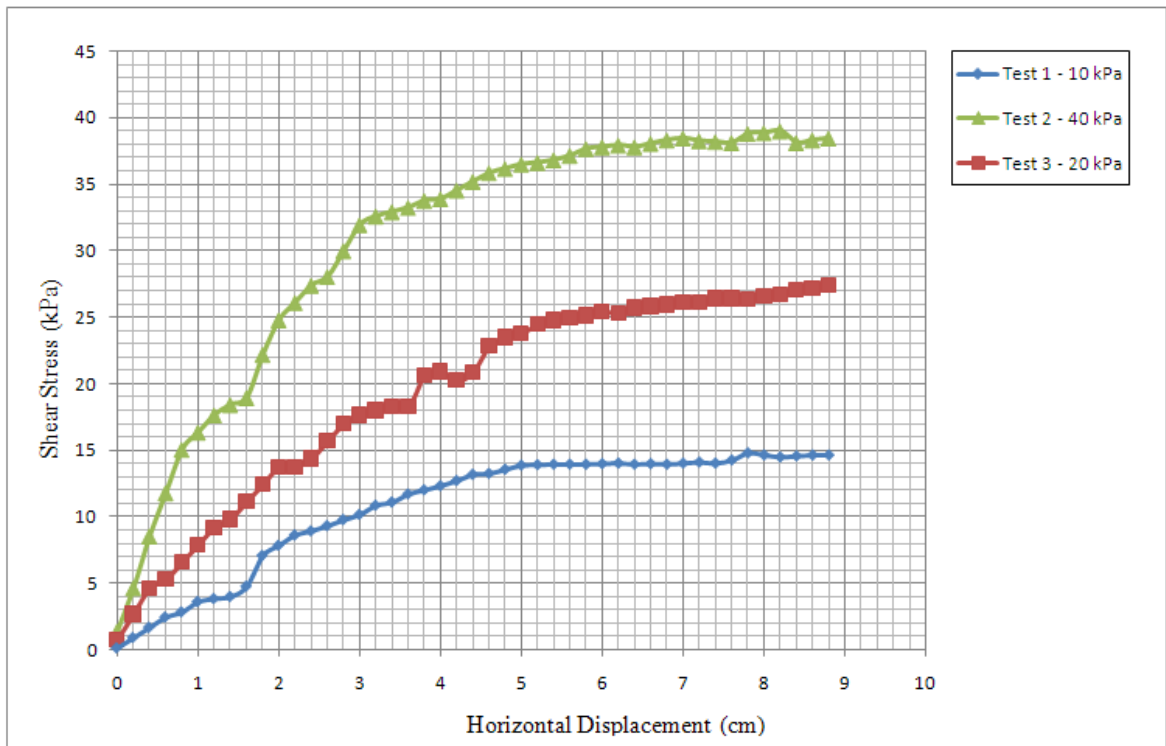


Figure 7.29. Shear Stress vs. Horizontal Displacement Graph of TB30.

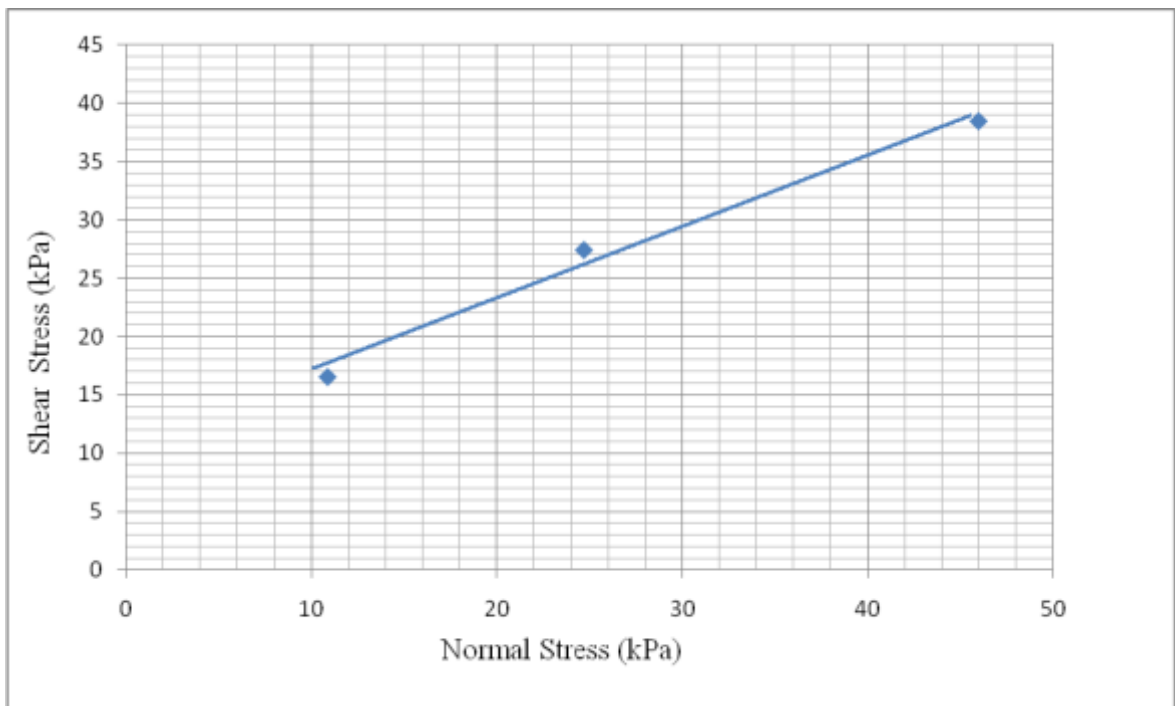


Figure 7.30. Shear Stress vs. Normal Stress graph of TB30.

7.1.17. 40% Tire Buffings

40% tire buffings by weight is mixed with sand and tested. The unit weight of the sample is 7.5 kN/m^3 . The shear stress vs. horizontal displacement graph and shear vs. normal stress graph are given in Figure 7.31. and Figure 7.32. Shear stress values are found as 18.86 kPa, 27.15 kPa and 49.60 kPa for the specimens tested under 10 kPa, 20 kPa and 40 kPa normal stresses, respectively. The apparent cohesion value is found as 8.2 kPa and the angle of internal friction is found as 24° .

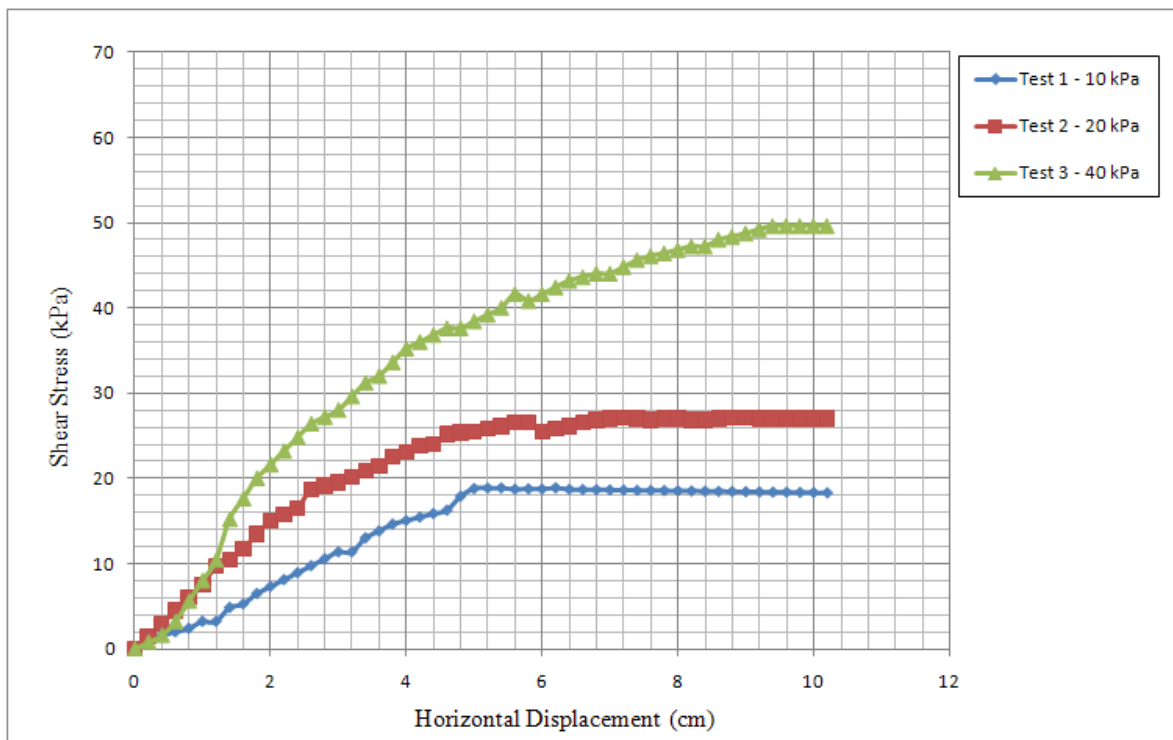


Figure 7.31. Shear Stress vs. Horizontal Displacement Graph of TB40.

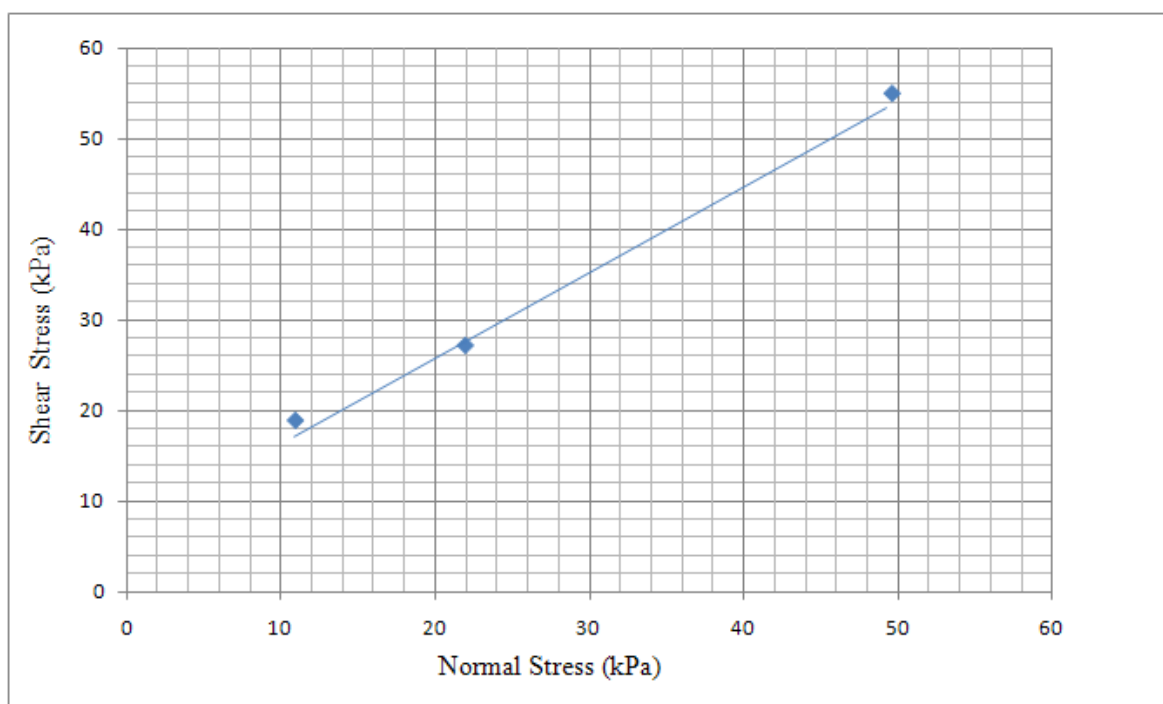


Figure 7.32. Shear Stress vs. Normal Stress graph of TB40.

7.1.18. Analysis of Direct Shear Test Results

In this set of experiments, a total of 15 tests were performed. Two types of waste material was used; tire buffings and tire crumbs material. All of the tests were performed in accordance with ASTM-D3080. Tests are conducted under three normal pressure values; 10, 20, and 40 kPa. Direct shear tests with only sand, only tire crumbs, only tire buffings and tire waste-sand mixtures were prepared. Sand-tire buffings and sand-tire crumbs mixtures prepared with 5%, 10%, 15%, 20%, 30% and 40% tire waste by weight. Direct shear tests were conducted to study the effect of tire materials on shear strength parameters of sands. Test results are summarised in Table 7.2. and Table 7.3.

First of all, a relatively uniform sand has been tested without inclusion of materials. The sand tested under three normal loads and shear stresses obtained as 9.3 kPa, 32 kPa and 38 kPa. The apparent cohesion of sand is 0° , internal friction angle is 24° and its unit weight is 16.52 kN/m^3 . As tire crumbs mixed with sand, shear strength parameters of sand material have changed.

The internal friction angle of sand-tire crumbs is increasing with tire crumbs inclusion and it reaches its peak value at sand-tire crumbs mixtures 10% by weight and then it decreases. On the other hand, as tire content increases the apparent cohesion value of the sand irregularly increases. It reaches its peak value at TC15.

The other additive material, tire buffings tested with same procedure. The test results are summarised in Table 7.3. The maximum shear stress values are observed for TB15. Also, the maximum apparent cohesion value of the sand-tire buffings mixtures obtained with same specimen as 14.8° . It reached peak value for 15% TB specimen and then decreased. At lower contents of tire buffings material, sand material predominantly defines the behaviour of mixture. When the tire content increases, the contributive effect of tire material increases up to optimum value. For that reason, it is better to increase tire content with small increments in order to obtain the best proportion for optimum shear strength parameters. On the other hand, maximum friction angle is 34° for TB20. The unit weight of the specimen is 10.30 kN/m^3 .

To compare the results of tire buffings and tire crumbs mixtures, it is easily seen that the apparent cohesion value of tire buffings material is higher than crumbs material considerably. (Figure 7.33). The difference between apparent cohesion values can be explained with the different geometrical shape, aspect ratio and density of tire buffings and tire crumbs materials. The unit weight of tire crumbs material is 6.5 kN/m^3 while it is 4.5 kN/m^3 for tire buffings material. When the shear resistance of tire crumbs material increases, it displays a good performance against to the normal loading. The buffings material has a 1/5 aspect ratio and it behaves as a fiber material. It produces frictional surfaces against to the shear forces. The longer reinforcement element have long contact areas with sand particles and provides shear resistance. The frictional angle values are scattered in a wide range for both tire crumbs and tire buffings materials (Figure 7.34).

According to these test results, it is concluded that both tire buffings and tire crumbs inclusion improves the shear strength of the composite materials. The internal friction angle of the sand-tire crumbs material with 10% by weight obtained as 35.8° while

it is 24° for unreinforced material. In all specimens, the apparent cohesion value is greater than only sand.

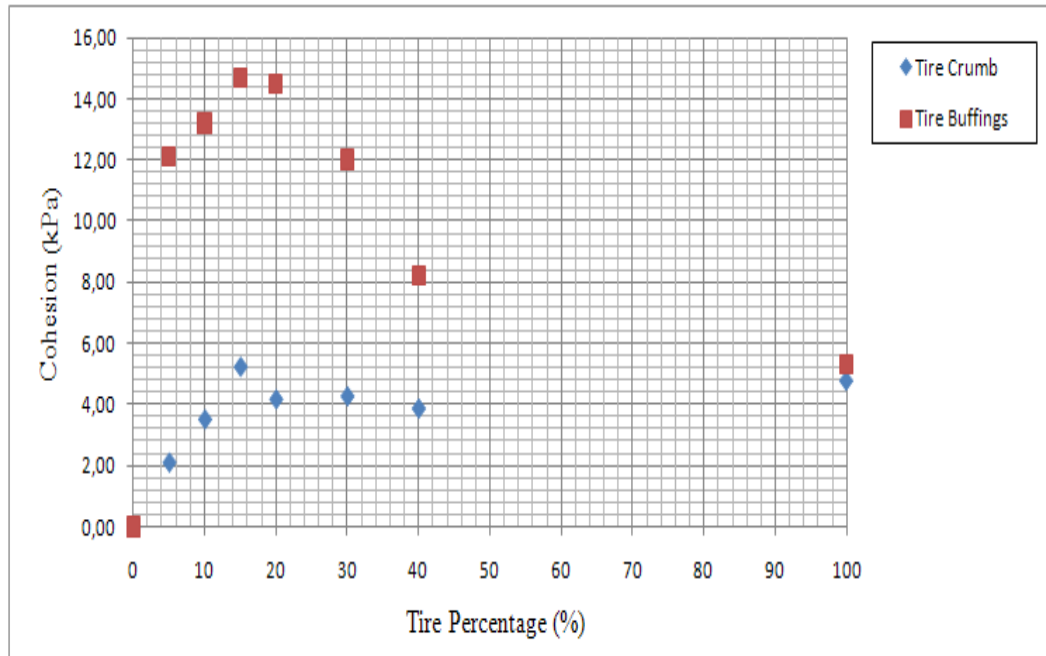


Figure 7.33. Cohesion vs. Tire percentages for all samples.

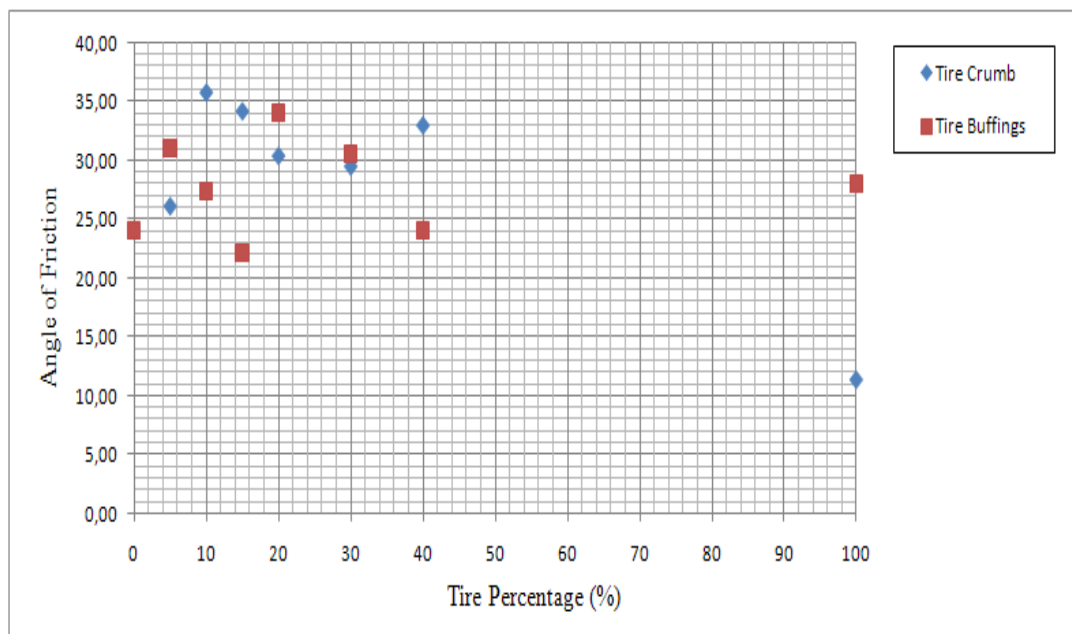


Figure 7.34. Internal Friction Angle vs. Tire percentages for all samples.

Table 7.2. Summary of the Direct Shear Test Results of Sand-Tire Crumbs Mixtures.

	Normal Stress (kPa)	Shear Stresses (kPa)							
		S	TC5	TC10	TC15	TC20	TC30	TC40	TC
1st	10	9,3	10,2	14,6	17,3	19	15,6	18,8	8,2
2nd	20	32	35,2	33,0	37,9	42	42,9	22	11,5
3rd	40	38	42,2	46,3	53,2	59	60,3	62	14,9
internal friction angle (°)		24	26,1	35,8	34,2	30,4	29,5	33	11,3
cohesion (kPa)		0	2,1	3,5	5,2	4,2	4,2	3,8	5,8
unit weight (kN/m³)		16,5	13,7	13	12,5	11,8	10,7	10	6,5

Table 7.3. Summary of The Direct Shear Test Results of Sand-Tire Buffings Mixtures.

	Normal Stress (kPa)	Shear Stresses (kPa)							
		S	TB5	TB10	TB15	TB20	TB30	TB40	TB
1st	10	9,3	14,2	14,6	19,1	16,5	16,2	18,9	8,2
2nd	20	32	41,3	42,2	41,8	31,0	28,7	27,2	11,2
3rd	40	38	48,2	52,6	54,4	43,6	38,4	49,6	13

internal friction angle (°)	24	31	27,4	22,2	34	30,5	24	28
cohesion (kPa)	0	12,1	13,2	14,9	14,5	12	8,2	5,3
unit weight (kN/m³)	16,5	13,2	12,5	11,5	10,3	8,9	7,5	4,5

7.2. Analysis of Geotechnical Laboratory Tests

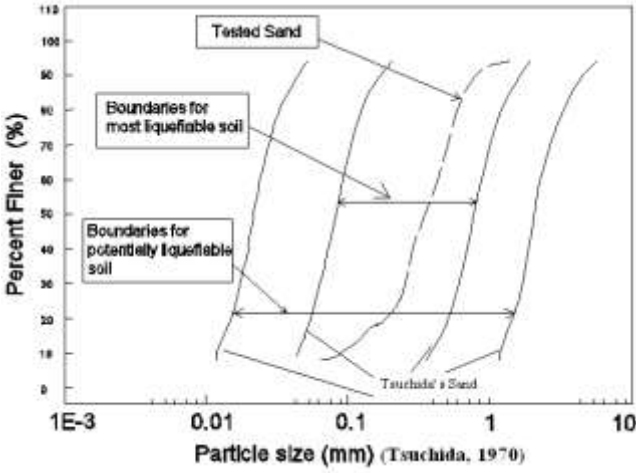
In the geotechnical laboratory tests, sieve analysis of all specimens; S, TB and TC are performed. As a result of the sieve analysis of sand material, the coefficient of uniformity, $C_u=2.4$ and $C_c=1.35$. The particles of sand material is rounded shape and according to the Unified Soil Classification System (or USCS), the soil which will be used in shaking table tests classified as SP, poorly graded sand.

Ishihara (1985) stated that, non plastic soil fines with a dry surface texture do not create adhesion and do not provide significant resistance to particle rearrangement and liquefaction. Moreover, low plasticity fines may contribute to the liquefaction susceptibility of soil.

Liquefaction is usually associated with sands or silts and gravelly soils have also been known to liquefy. Rounded particles of uniform sizes are generally most susceptible to liquefaction (Poulos *et al.* 1985). Well graded sands with angular shapes are less prone to liquefy because of a more stable interlocking of soil grains.

If a cohesive soil does not meet all three criteria, then it is generally considered to be not susceptible to liquefaction. The summary of evaluation of sand which the static laboratory tests are given in Table 7.4. It is seen that all material properties of sand are satisfied to liquefaction except the coefficient of uniformity. The soil specimen is not enough resistant against to the liquefaction. Hence, during a dynamic motion, a failure caused by liquefaction can be seen most probably.

Table 7.4. The evaluation of liquefaction susceptibility of soil.

Mechanical Properties	Susceptible	Not Susceptible
Water Content, ω	$w > 0.9*LL$	$w < 0.9*LL$
	30	
Soil Relative Density, D_r	Loose	Dense
	0.40	
Particle Shape	Rounded Shape	Angular Shape
	Rounded	
Particle Size	Poorly Graded	Well Graded
	$C_u = 2.4 - C_c = 1.35$	
Grain Size Distribution	 <p>The graph plots Percent Finer (%) on the y-axis (0 to 100) against Particle size (mm) on a logarithmic x-axis (1E-3 to 10). It shows several curves representing different soil types. A specific curve is labeled 'Tested Sand'. Two sets of curves are labeled 'Boundaries for most liquefiable soil' and 'Boundaries for potentially liquefiable soil'. A curve at the bottom is labeled 'Tsuchida's Sand'.</p>	

7.3. Cyclic Triaxial Test Results

A set of cyclic triaxial compression test are performed with only sand, mixtures of sand-tire buffings and sand-tire crumbs materials at different contents. Tire waste-sand mixtures are prepared at 10, 20 and 30% of tire waste by weight. Two different processed tire wastes were used: tire crumbs (TC) and fiber-shaped tire buffings (TB). Specimens are named with abbreviations such as TB10, TC15, TC, S, etc. These abbreviations are reference to type of specimen and its proportion. For example; TB20 refers to a mixture with 80% sand and 20%% tire buffings. Each test is repeated under three different confining presssures as; 40, 100 and 200 kPa. The rate of strain is selected as 0.5 mm/min. The tests were conducted in general accordance with ASTM-D3999 (2003). Cyclic triaxial tests were conducted on samples to study the dynamic soil properties of sand-tire waste mixtures. The shear modulus and damping ratio values are determined for samples using different shear amplitudes and confining pressures. By the way, the dynamic properties of waste materials can be used for a successful geotechnical design against earthquakes. The tested cyclic triaxial test samples are given in Table 7.5.

Table 7.5. Cyclic Triaxial Test Samples.

Test No.	Specimen No	Confining Pressure	γ (kN/m³)
Test 1	TC10	40 kPa	15.8
Test 2	TC10	100 kPa	15.8
Test 3	TC10	200 kPa	15.8
Test 4	TC20	40 kPa	15.5
Test 5	TC20	100 kPa	15.5
Test 6	TC20	200 kPa	15.5
Test 7	TC30	40 kPa	15.0
Test 8	TC30	100 kPa	15.0
Test 9	TC30	200 kPa	15.0
Test 10	S	200 kPa	16.5
Test 11	TB10	40 kPa	15.5
Test 12	TB10	100 kPa	15.5
Test 13	TB10	200 kPa	15.5
Test 14	TB20	40 kPa	15.5
Test 15	TB20	100 kPa	15.5
Test 16	TB20	200 kPa	15.5
Test 17	TB30	40 kPa	15.3
Test 18	TB30	100 kPa	15.3
Test 19	TB30	200 kPa	15.3

7.3.1. Sand Material

The cyclic triaxial test of sand material is performed under three different confining pressures. The unit weight of specimen is 16.5 kN/m^3 . As a result of these set of cyclic triaxial tests, damping ratio-shear strain and shear modulus-shear strain relationships were plotted. Figure 7.35 and Figure 7.36 show the effect of confining pressure on shear modulus and damping ratio of the specimen. It is noticed that when the confining pressure increases, shear modulus increases with increasing shear strain. Damping ratio of all three specimens are nearly constant between 0.0005% and 0.005% shear strain. The increasing tendency of the damping ratio values begin at 0.01% shear strain and they increase nearly linear. The shear modulus of sand decreases as the confining pressure decreases.

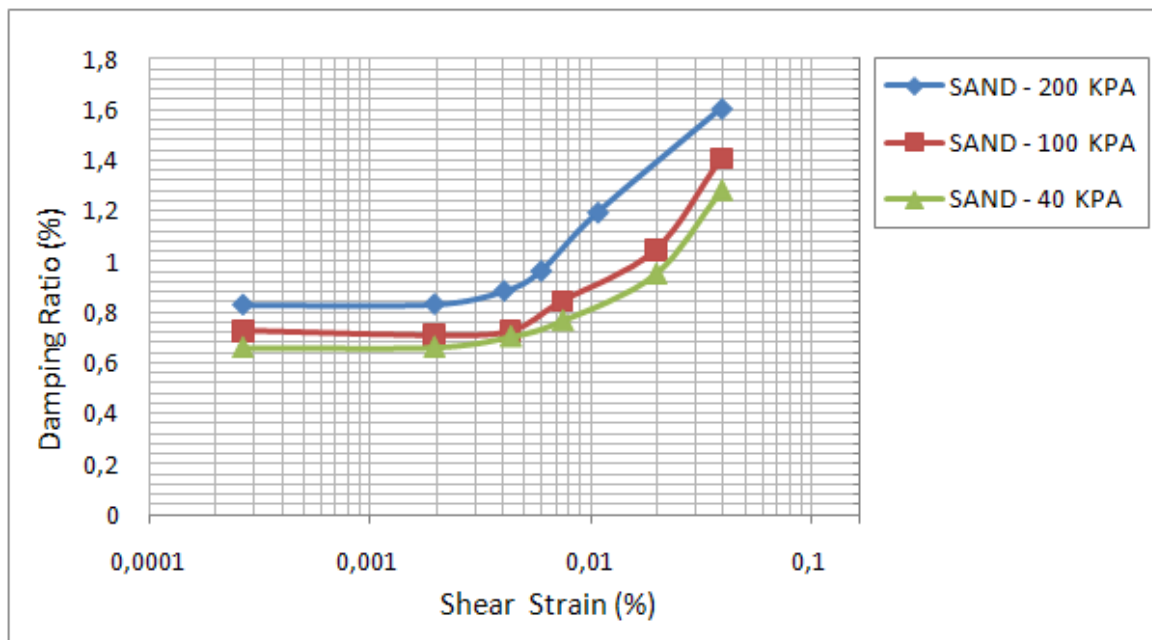


Figure 7.35. Damping Ratio vs. Shear Strain curve for only sand.

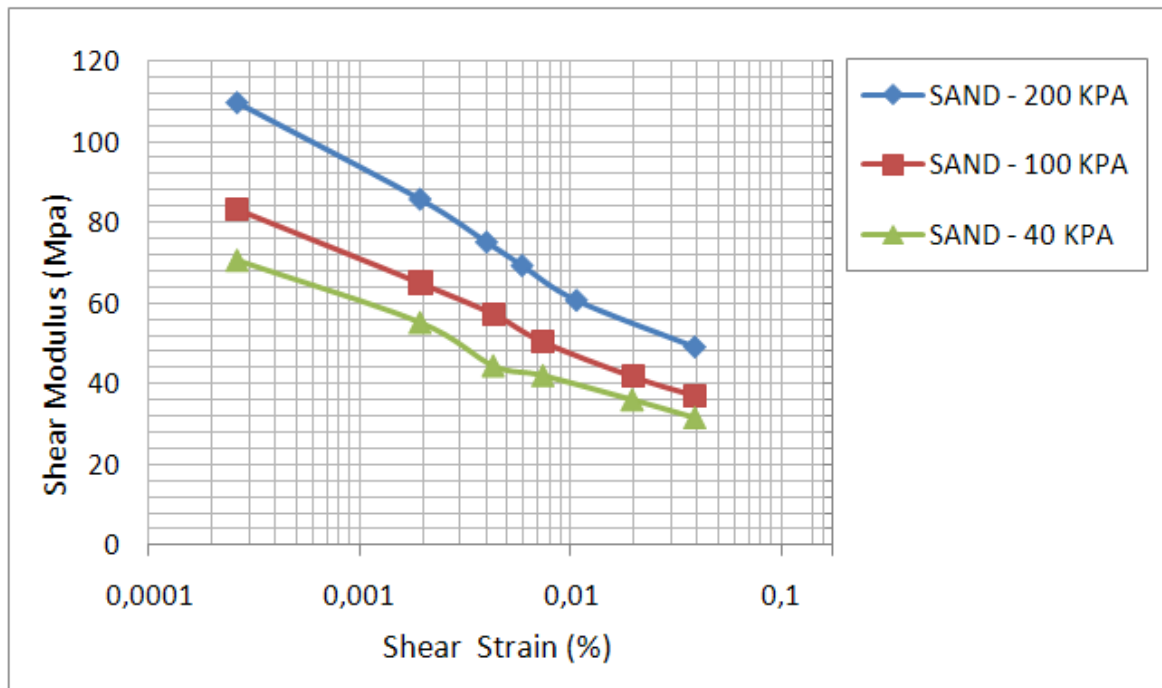


Figure 7.36. Shear Modulus vs. Shear Strain curve for only sand.

7.3.2. TB-Sand Mixtures

7.3.2.1. 10% Tire Buffings-Sand (TB10). Figure 7.37 shows the damping ratio vs. shear strain curve of TB10 specimen (sand with 10% tire buffings mixture). The unit weight of specimen which is tested under 40, 100 and 200 kPa. is 15.5 kN/m^3 . In general, the damping ratio of specimen have increasing tendency with increasing shear strain under all three confining pressure values. The damping ratio value decreases as the confining pressure increases. The sand particles are very stiff and thus dissipate very little energy in particle deformation. In contrast, the tire consumes energy through the deformation of tire particles themselves. To examine the entire behaviour of all three curves it can be seen that they are not completely smooth. All of the curves show steeper and linear behaviour after 0.005% shear strain value up to maximum damping ratio values.

The shear modulus of tire waste is very low relative to that of a sand, hence the contribution of rubber to shear modulus in the mixture is not significant. The shear modulus-shear strain relationship of mixtures are plotted in Figure 7.38. The initial shear modulus of sand is 110 MPa. under 200 kPa. The inclusion of 10% tire buffings material

decrease the shear modulus down to 44 MPa. At higher shear strain, final shear modulus values are getting closer to each other but the slight difference can be seen.

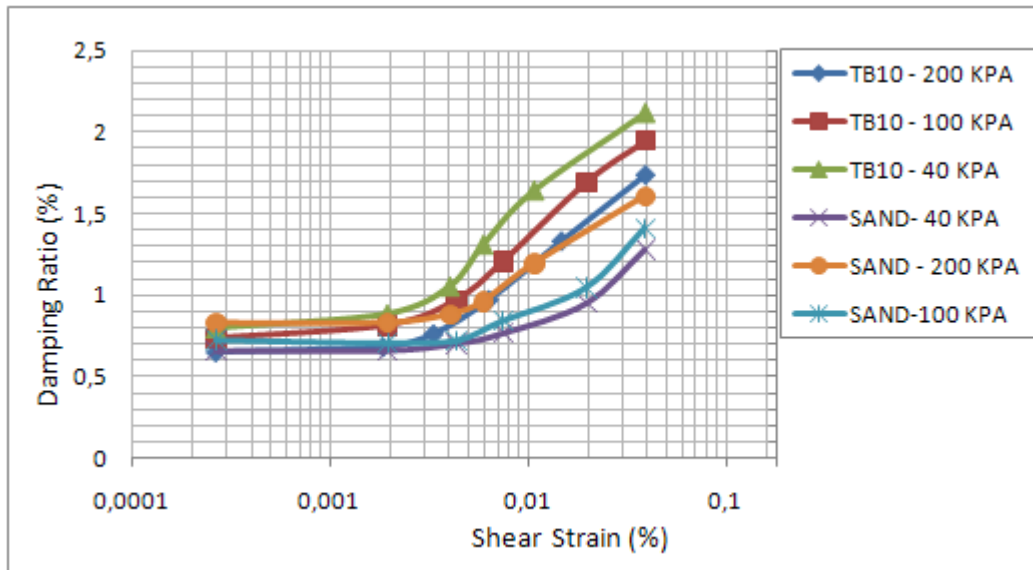


Figure 7.37. Damping Ratio vs. Shear Strain curve for TB10 specimen.

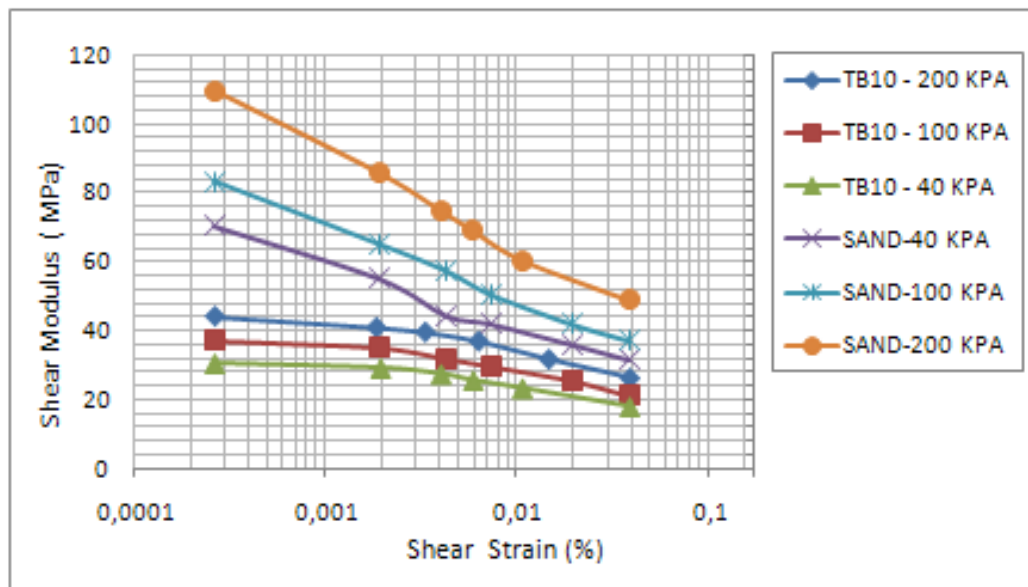


Figure 7.38. Shear Modulus vs. Shear Strain curve for TB10 specimen.

7.3.2.2. 20% Tire Buffings-Sand Mixture (TB20). Figure 7.39. demonstrates the damping ratio vs. shear strain curve of sand-tire buffings mixture with 20% content. The unit weight of specimen which is tested under 40, 100 and 200 kPa. confining pressure is 15.5 kN/m^3 . The damping ratio of specimen have increasing tendency with increasing shear strain for all three confining pressure values. Especially between the range of 0.0005-0.005% shear strain, damping ratio increases with slower rate and then increases more rapidly. The effect of mean confining pressure and 20% tire content on shear modulus of sand-tire buffings mixture has a similar trend like on sand-tire mixture with the 10% content. The shear modulus of sand-tire buffings mixture is lower than of only sand approximately three times (Figure 7.40). The shear modulus of the mixture is strongly influenced by the percentage of tire waste inclusion.

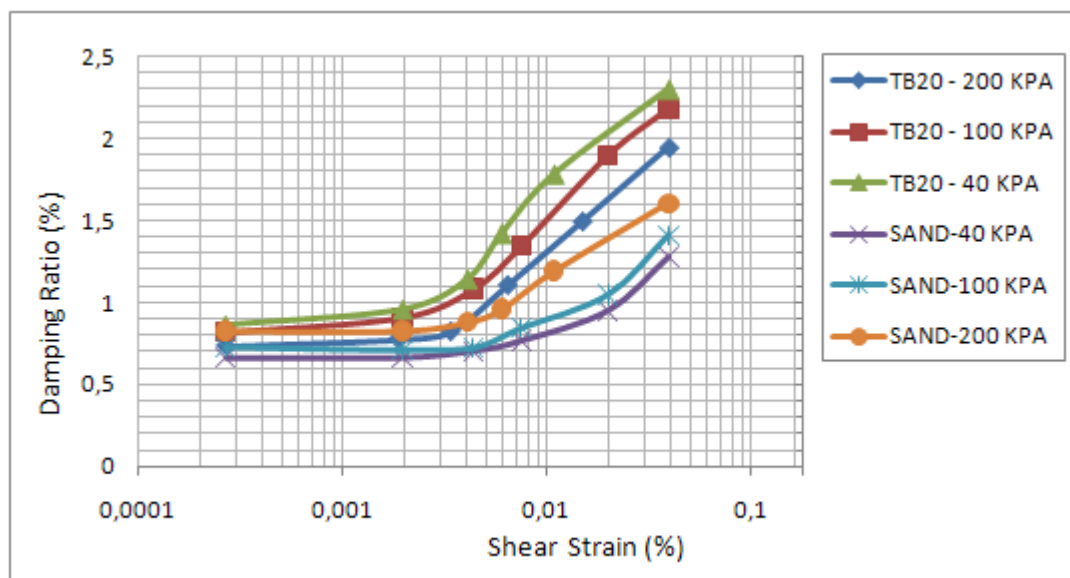


Figure 7.39. Damping Ratio vs. Shear Strain curve for TB20.

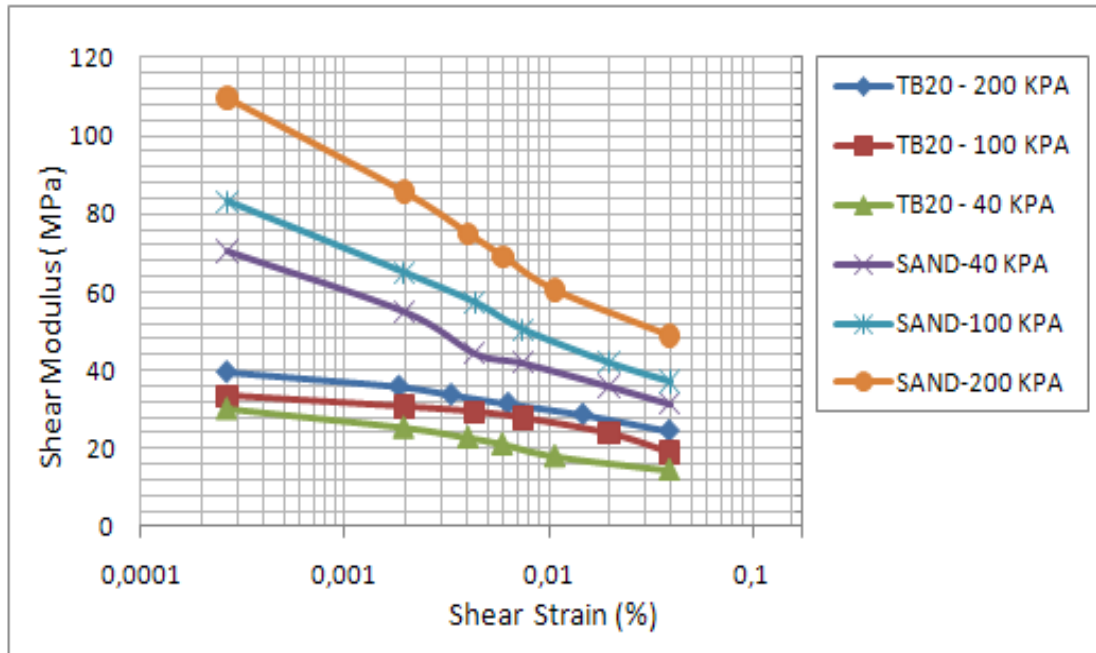


Figure 7.40. Shear Modulus vs. Shear Strain curve for TB20.

7.3.2.3. 30% Tire Buffings-Sand Mixture (TB30). The specimen is prepared by mixing sand with 30% tire buffings by weight (TB30). The unit weight of specimen which is tested under 40, 100 and 200 kPa. is 15.3 kN/m^3 . The damping ratio increases as the shear strain increases (Figure 7.41). The effect of confining pressure can be noticed very clearly. As the confining pressure increases both the initial and final damping ratio increase. As shear strain increases, shear modulus decreases (Figure 7.42).

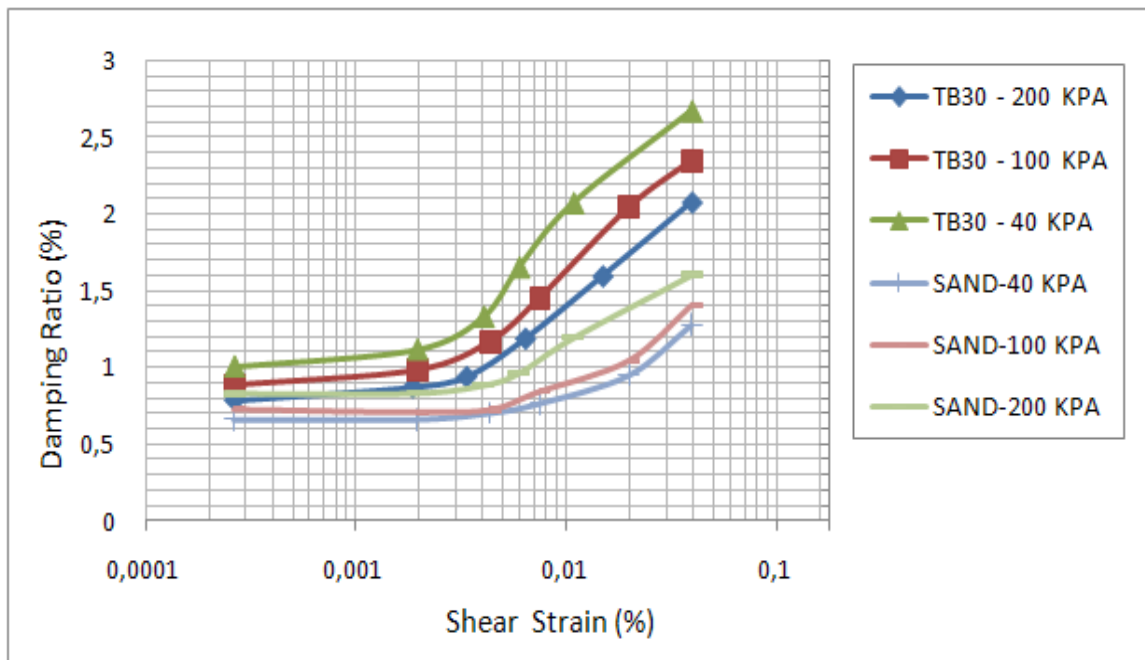


Figure 7.41. Damping Ratio vs. Shear Strain curve for TB30.

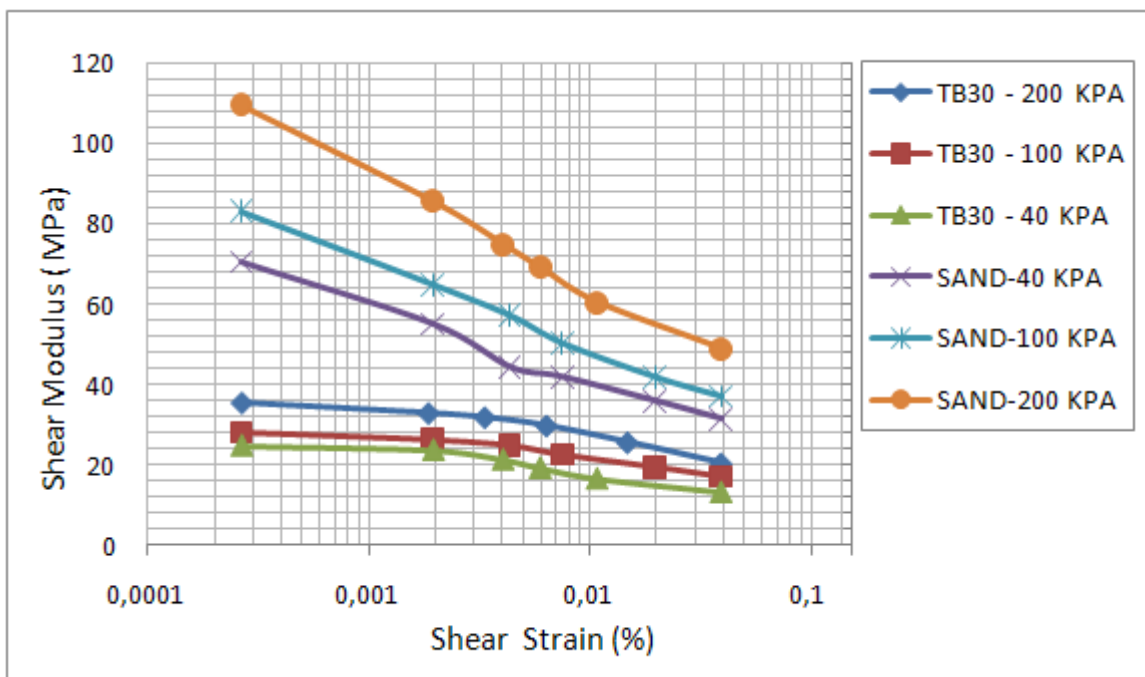


Figure 7.42. Shear Modulus vs. Shear Strain curve for TB30.

7.3.2.4. All Tire Buffings-Sand Mixtures. Tests performed with sand-tire buffings materials under three different confining pressures (Figure 7.43 and Figure 7.44). The damping ratio of TB30 which is tested under 40 kPa. reaches the highest value among all specimens (Figure 7.43). The higher confining pressure for the specimens of all tire buffings contents exhibited higher performance of damping ratio compared to specimens tested under lower confining pressures. Additionally, it is proved that the damping ratio is getting higher as the percentage of tire increases, mainly due to the significant effect of tire percentage. The shear modulus of TB10 tested under 200 kPa. is the highest among all tests performed with only sand and tire buffings material addition (Figure 7.44). As the tire buffings content increases and confining pressure decreases, shear modulus decreases. The maximum difference of shear modulus values observed between TB10 tested under 200 kPa. and TB30 tested under 40 kPa. confining pressure.

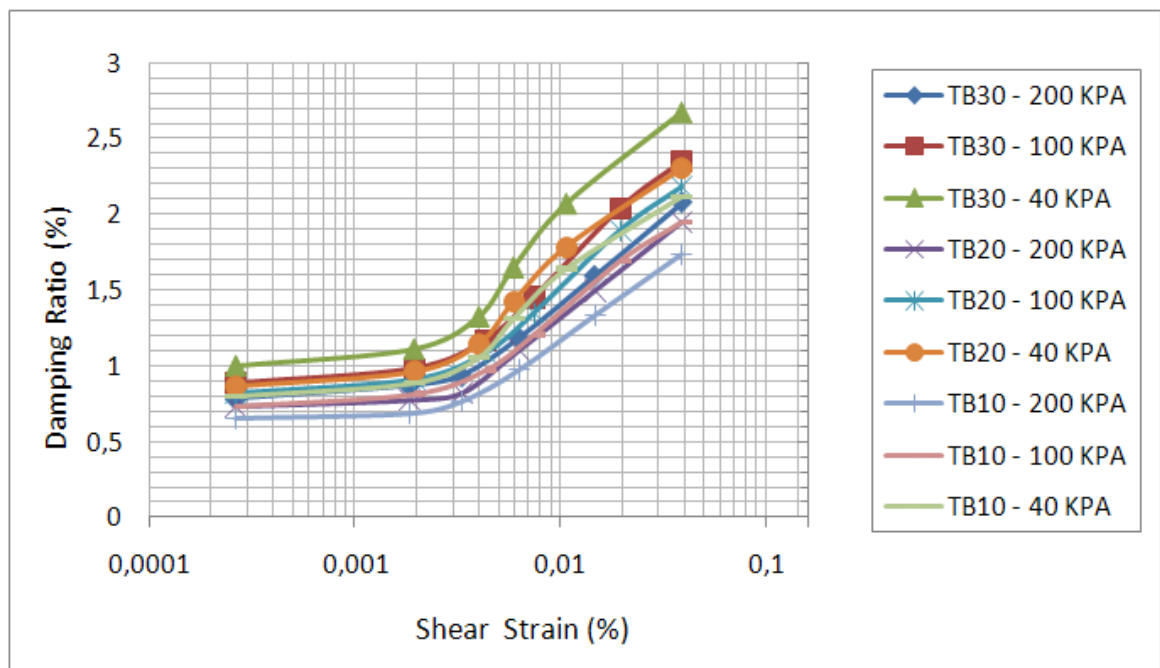


Figure 7.43. Damping Ratio vs. Shear Strain curves for all tire buffings-sand mixtures.

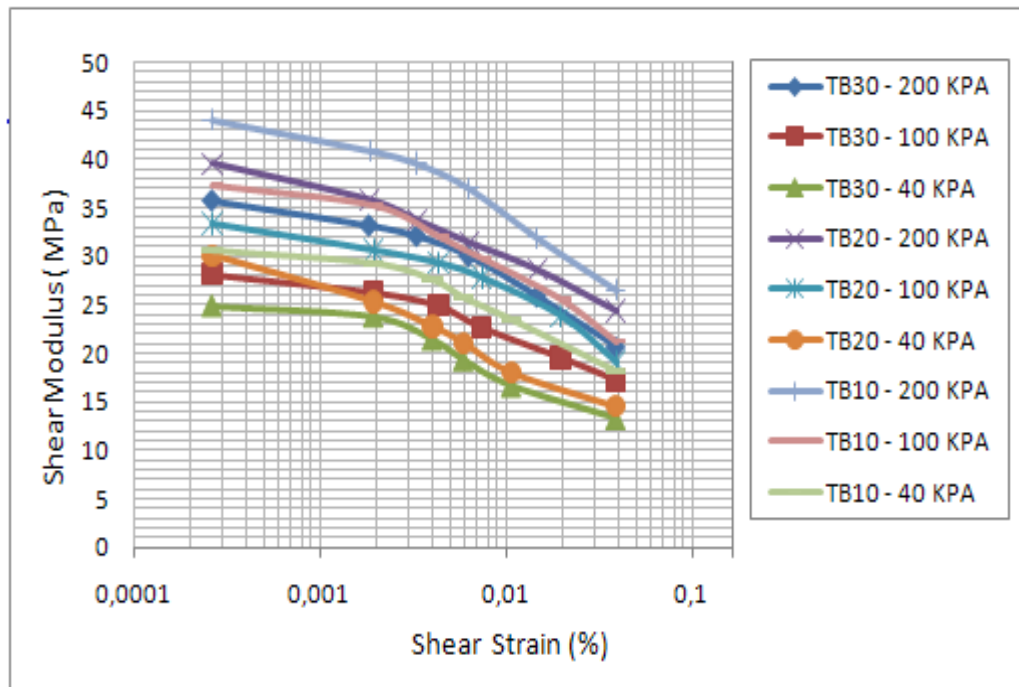


Figure 7.44. Shear Modulus vs. Shear Strain curve for all tire buffings-sand mixtures.

7.3.2.5. Damping Ratio vs. Shear Strain curves for TB10, TB20 and TB30 (40 kPa.).

Figure 7.45. shows the damping ratio vs. shear strain curves of all sand-tire buffings mixtures which are tested under 40 kPa confining pressure. It is seen that the final damping ratio values increases as the tire waste content decreases. There is significant difference between the damping ratio values of only sand and tire waste-sand materials. However, at relatively high shear strains, the damping ratio curves of specimens have more upright tendency. This trend is explained by the fact that an increase in shear strain, the behaviour of damping ratio curves are more steep. The shear modulus behaviour of sand with tire buffings and only sand materials under 40 kPa. is demonstrated in Figure 7.46.

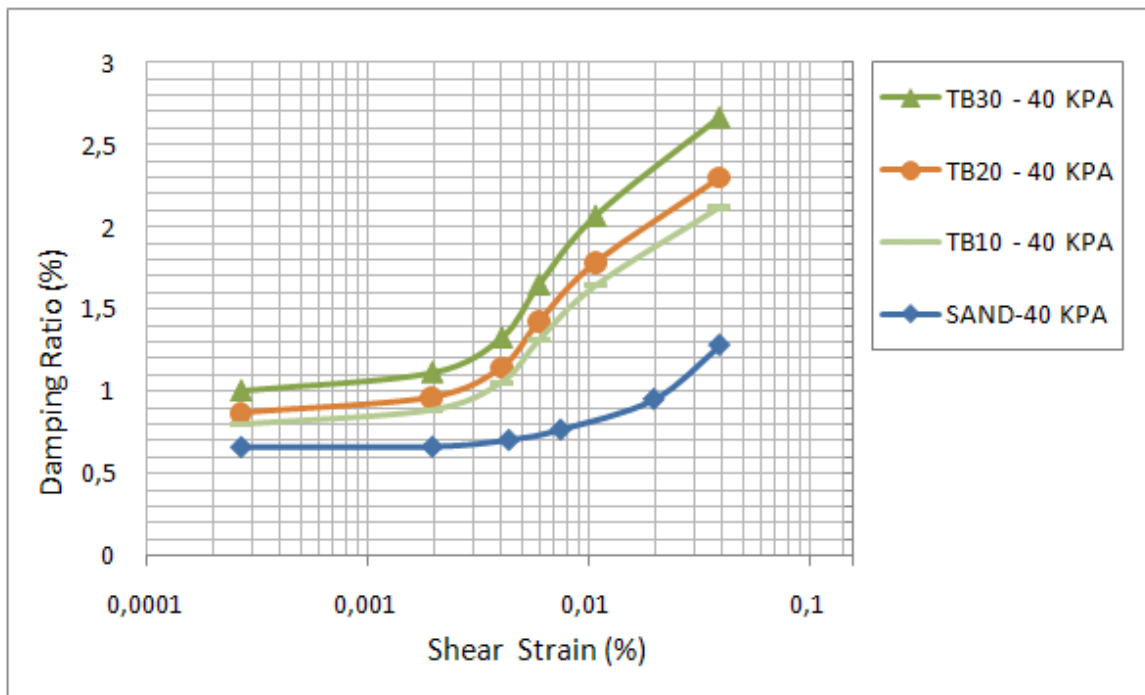


Figure 7.45. Damping Ratio vs. Shear Strain curves for tire buffings –sand mixtures under 40 kPa. confining pressure.

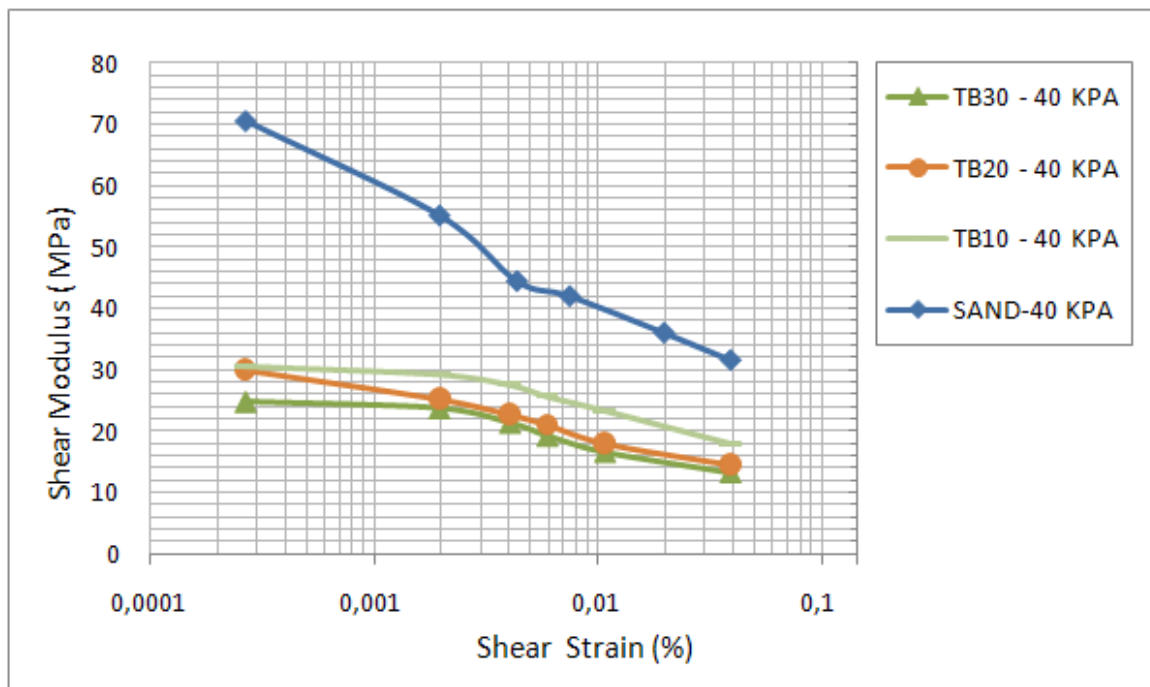


Figure 7.46. Shear Modulus vs. Shear Strain curves for tire buffings –sand mixtures under 40 kPa. confining pressure.

7.3.2.6. Damping Ratio vs. Shear Strain curves TB10, TB20 and TB30 (100 kPa). The result of cyclic triaxial tests which are performed with sand-tire buffings mixtures under 100 kPa confining pressure shown in Figure 7.47. To compare all tire included specimens, the maximum damping ratio value at TB30 which is tested under 100 kPa. confining pressure. Damping ratio value of only sand is at the lowest value among all four specimens. On the other hand, the effect of tire inclusion on shear modulus of sand material is visible in Figure 7.48. The maximum shear modulus value obtained from only sand and the minimum one obtained with TB30 specimen which is tested under 100 kPa. confining pressure. Even though the initial shear modulus values are different from each other, final values are relatively closer. The addition of each 10% tire buffings material decreased the shear modulus, while it causes a major increase in damping ratios.

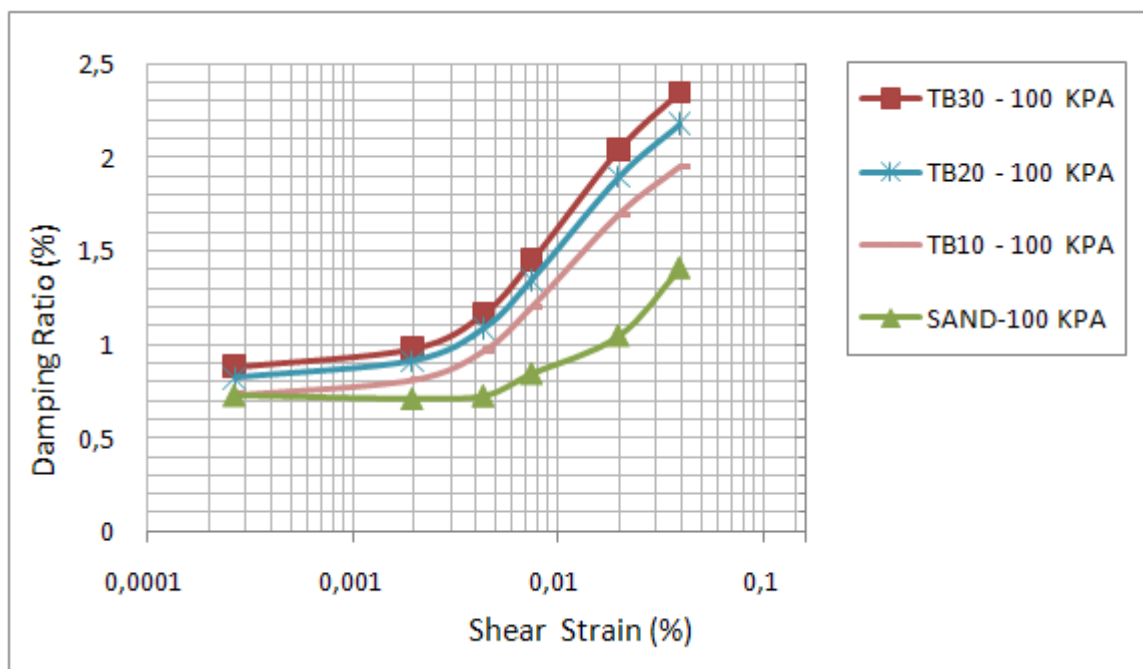


Figure 7.47. Damping Ratio vs. Shear Strain curves for tire buffings –sand mixtures under 100 kPa. confining pressure.

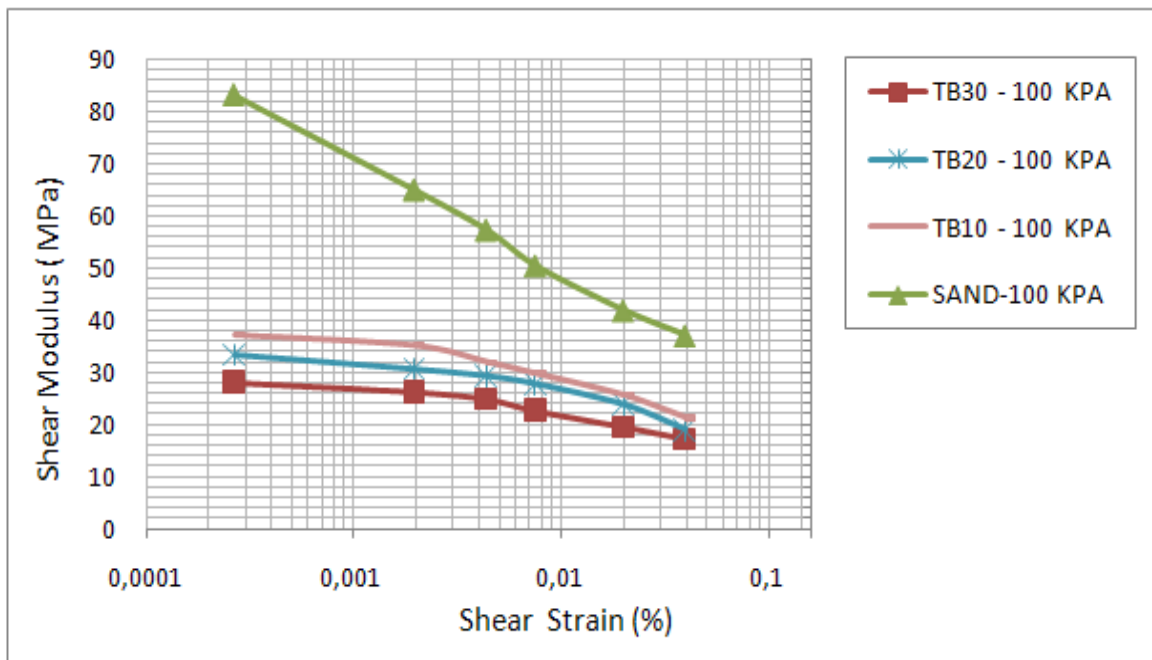


Figure 7.48. Shear Modulus vs. Shear Strain curves for tire buffings –sand mixtures under 100 kPa. confining pressure.

7.3.2.7. Damping Ratio vs. Shear Strain curves TB10, TB20 and TB30 (200 kPa.). The performance of only sand and tire included specimens are showed at the highest value of confining pressure, 200 kPa. (Figure 7.49). As the shear strain increases, the increasing tendency of curves forms in two steps. At lower shear strain values, damping ratio of all specimens increase slowly. Between the range of 0.005% and 0.05% the upward trend of curves become more distinctive. Throughout the whole strain values, the maximum damping ratio observed with TB30. The shear modulus of sand is the highest one. The initial shear modulus values of TB30, TB20, TB10 specimens are respectively 42 MPa., 40 MPa. and 38 MPa (Figure 7.50).

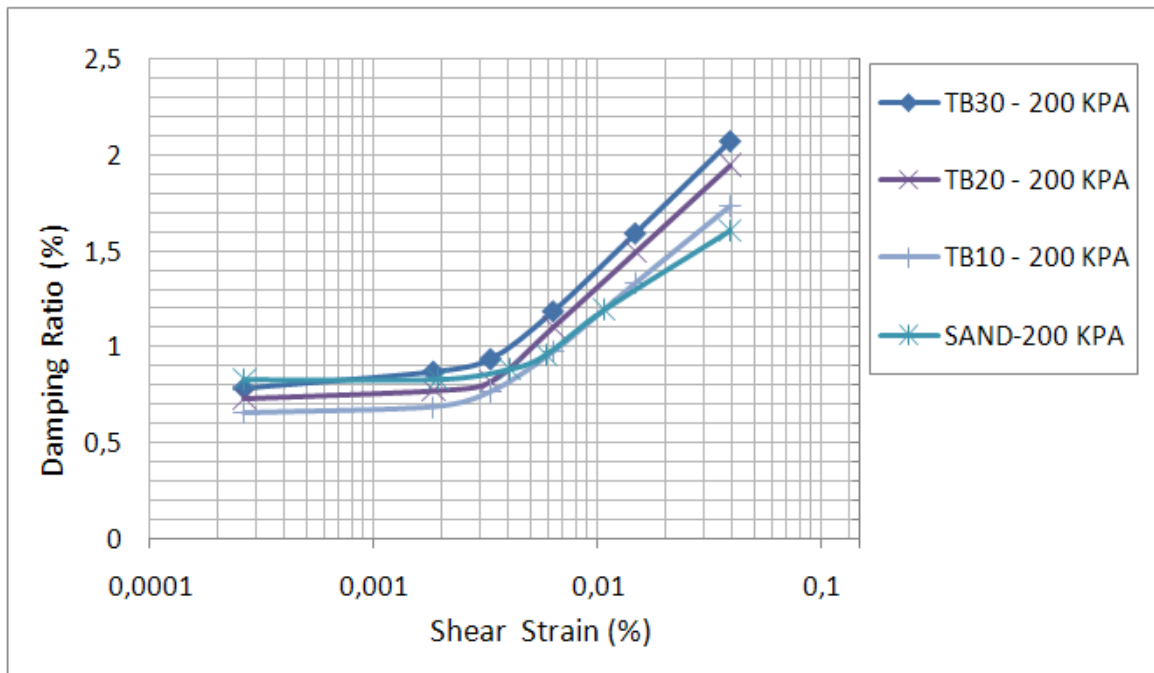


Figure 7.49. Damping Ratio vs. Shear Strain curves for tire buffings –sand mixtures under 200 kPa. confining pressure.

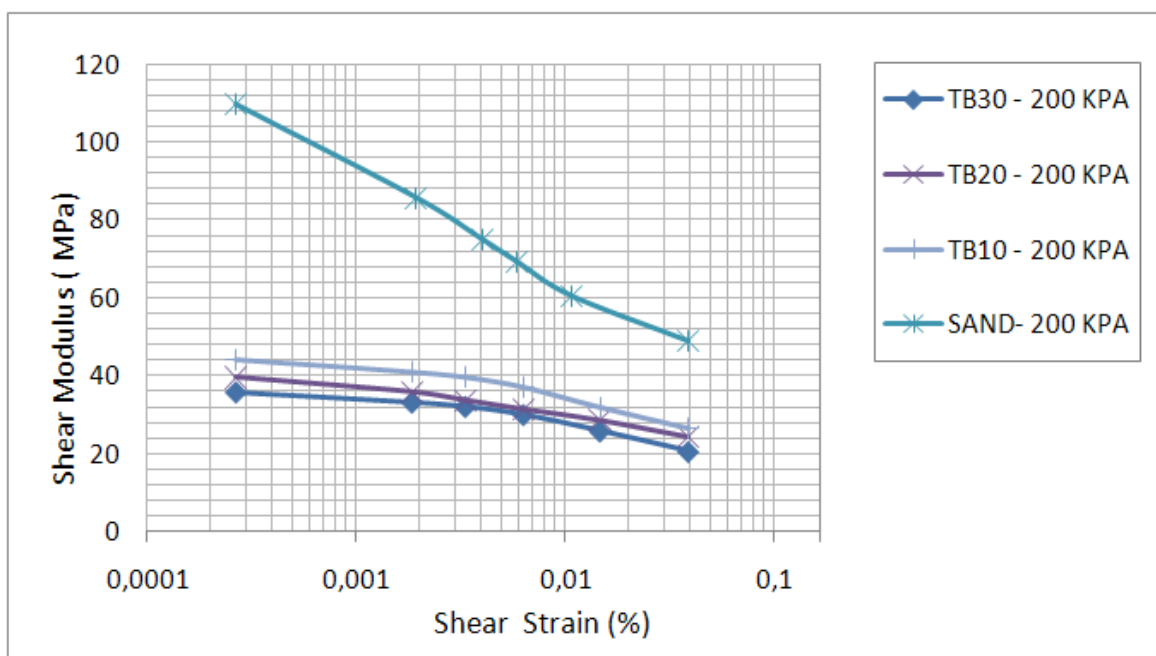


Figure 7.50. Shear Modulus vs. Shear Strain curves for tire buffings –sand mixtures under 200 kPa. confining pressure.

7.3.3. TC-Sand Mixtures

7.3.3.1. 10% Tire Crumbs -Sand Mixture (TC10). Figure 7.51. shows the damping ratio vs. shear strain curves of sand-tire crumbs mixture with 10% content by weight. The unit weight of specimen which is tested under 40, 100 and 200 kPa is 15.8 kN/m^3 . In general, the damping ratio of specimen have increasing tendency with increasing shear strain under all three confining pressure values (Figure 7.52). The damping ratio values decrease as the confining pressure increases. The initial damping ratio value of the TC10 specimen under 40 kPa confining pressure is 1.15%. As the confining pressure increases, the initial damping ratio value decreases. The final damping ratio value of the TC10 specimen under 40 kPa confining pressure is higher than the ones specimen tested under 100 and 200 kPa. All of the curves show steeper and linear behaviour after 0.005% shear strain value up to maximum damping ratio values. The shear modulus-shear strain relationship of mixtures are plotted in Figure 7.52. The initial shear modulus of only sand is 110 MPa under 200 kPa. The inclusion of 10% tire crumbs decrease the shear modulus to 38 MPa. The reduction of shear modulus is at lesser extent for lower confining pressure. At higher shear strain, shear modulus values are getting closer to each other as it is similar with the test results of TB10 specimen.

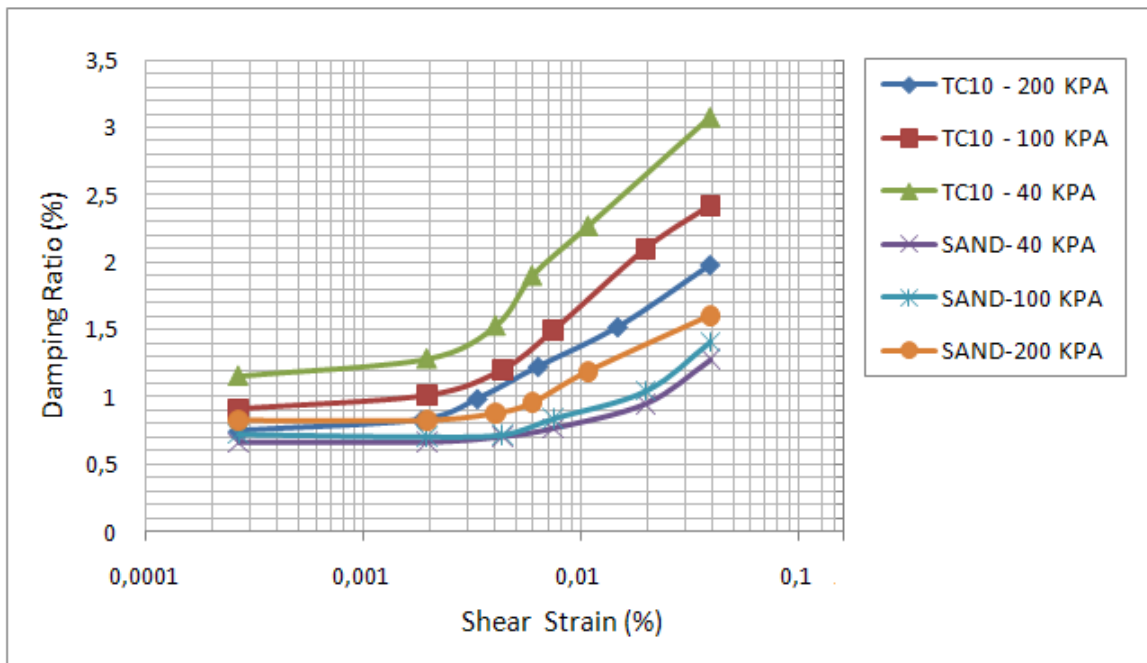


Figure 7.51. Damping Ratio vs. Shear Strain curve for TC10.

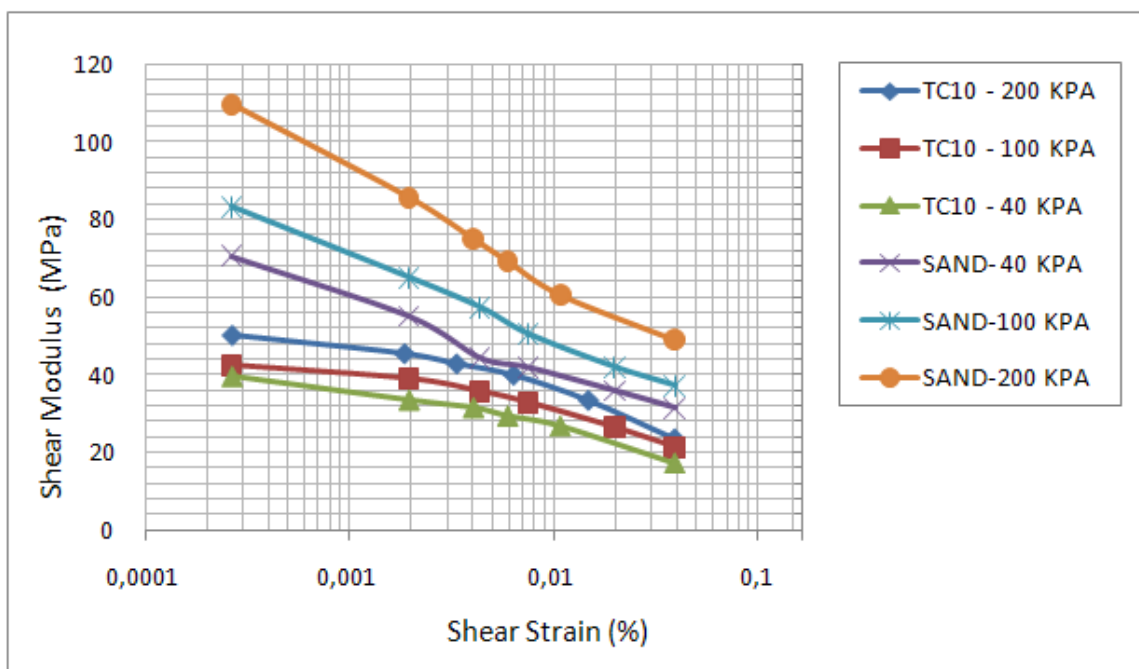


Figure 7.52. Shear Modulus vs. Shear Strain curve for TC10.

7.3.3.2. 20% Tire Crumbs -Sand Mixture (TC20). Figure 7.53. shows the damping ratio vs. shear strain curves of sand-tire crumbs mixture with 20% content (TC20). The unit weight specimen which is tested under 40, 100 and 200 kPa. is 15.5 kN/m^3 . The damping ratio of specimen have increasing tendency with increasing shear strain under all three confining pressure values (Figure 7.53). Especially between the range of 0.0005-0.005% shear strain, damping ratio first increases with slow rate, then continue to increase more rapidly. The initial damping ratio values of sand are 1% and with the inclusion of tire crumbs material, it is increased to 1.5%. The effect of confining pressure and 20% tire crumbs content on the shear modulus of specimen has a similar trend like sand-tire buffings mixtures. Three times the shear modulus of sand-tire crumbs mixture is lower than of only sand approximately (Figure 7.54). At the same shear strain, shear modulus of sand-tire crumbs mixture is 42 MPa under 200 kPa confining pressure while it is 34 MPa and 30 MPa under 100 kPa. and 40 kPa confining pressures, respectively. As the shear strain increase, the distinct between shear modulus of only sand and sand-tire crumbs mixtures gets closer.

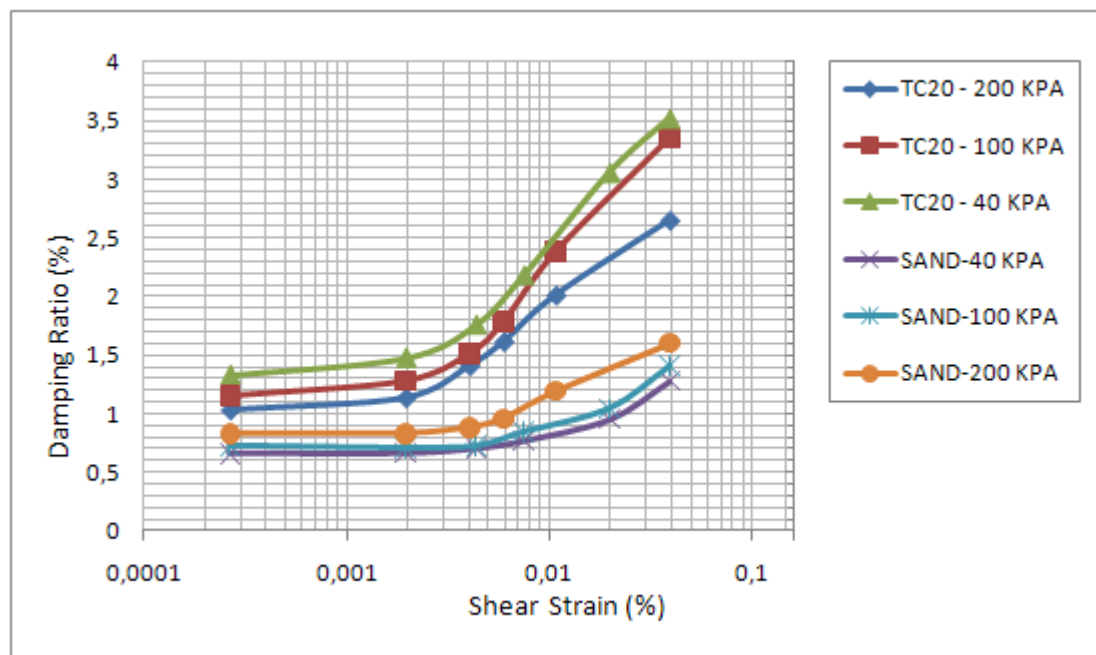


Figure 7.53. Damping Ratio vs. Shear Strain curve for TC20.

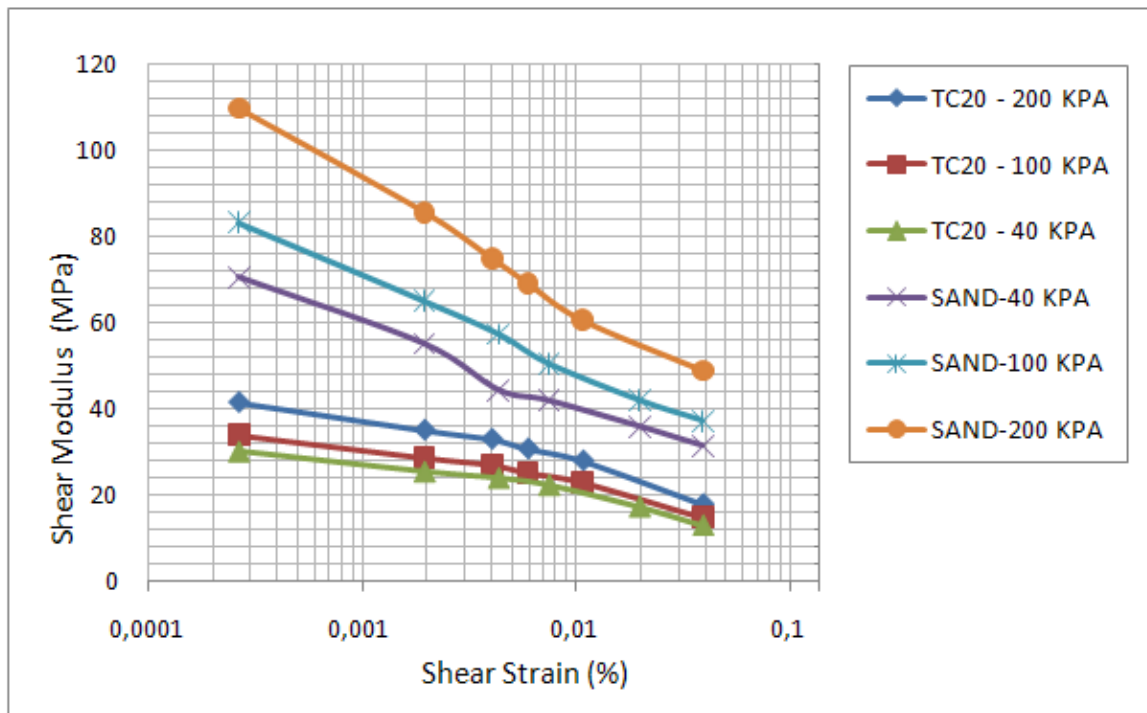


Figure 7.54. Shear Modulus vs. Shear Strain curve for TC20.

7.3.3.3. % 30 Tire Crumbs-Sand Mixture (TC30). The specimen is prepared by mixing sand and 30% tire crumbs by weight (TC30). The unit weight of specimen which is tested under 40, 100 and 200 kPa. is 15 kN/m^3 . The effect of confining pressure on damping ratio can be noticed clearly (Figure 7.55). As the confining pressure increases both the initial and final damping ratio values decrease. As the damping ratio increases, shear strain increases. The increasing tendency of curves of mixtures and only sand samples are nearly the same. The shear modulus of sand tested under 200 kPa. confining pressure is 110 kPa. at 0.0005% shear strain and 48 kPa. at 0.055% shear strain. Under the same confining pressure, the shear modulus values of TC30 specimens are 36 kPa. and 18 kPa. respectively. The shear modulus of only sand is three times greater than TC30 at the beginning of the test (Figure 7.56).

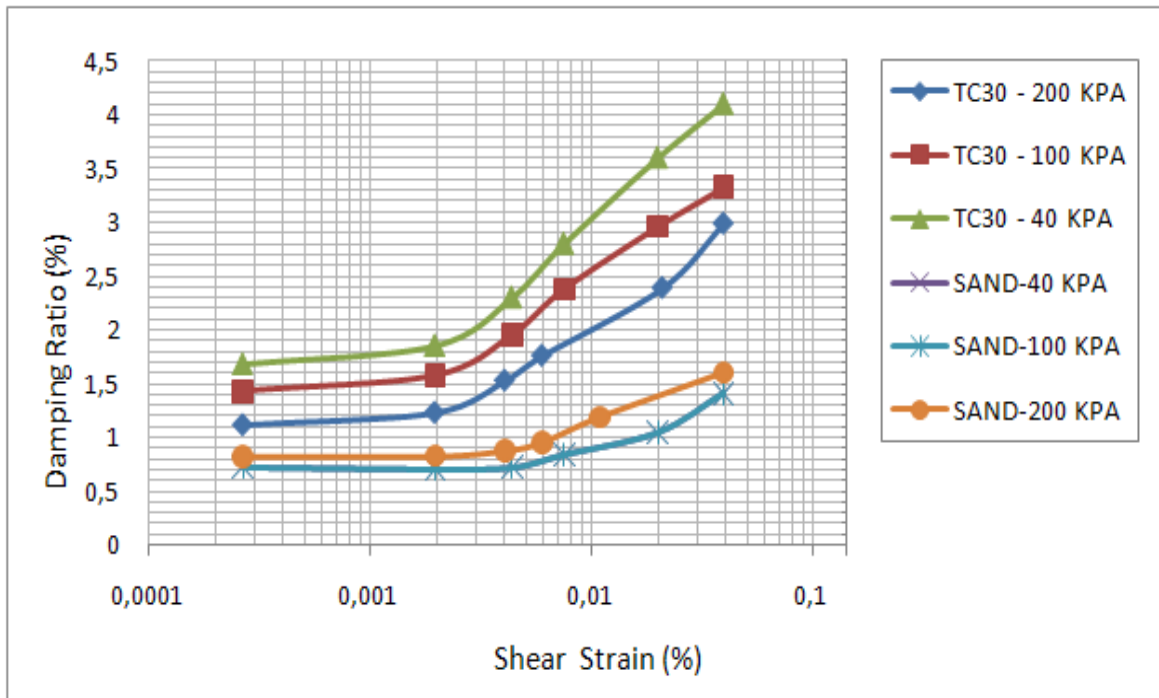


Figure 7.55. Damping Ratio vs. Shear Strain curve for TC30.

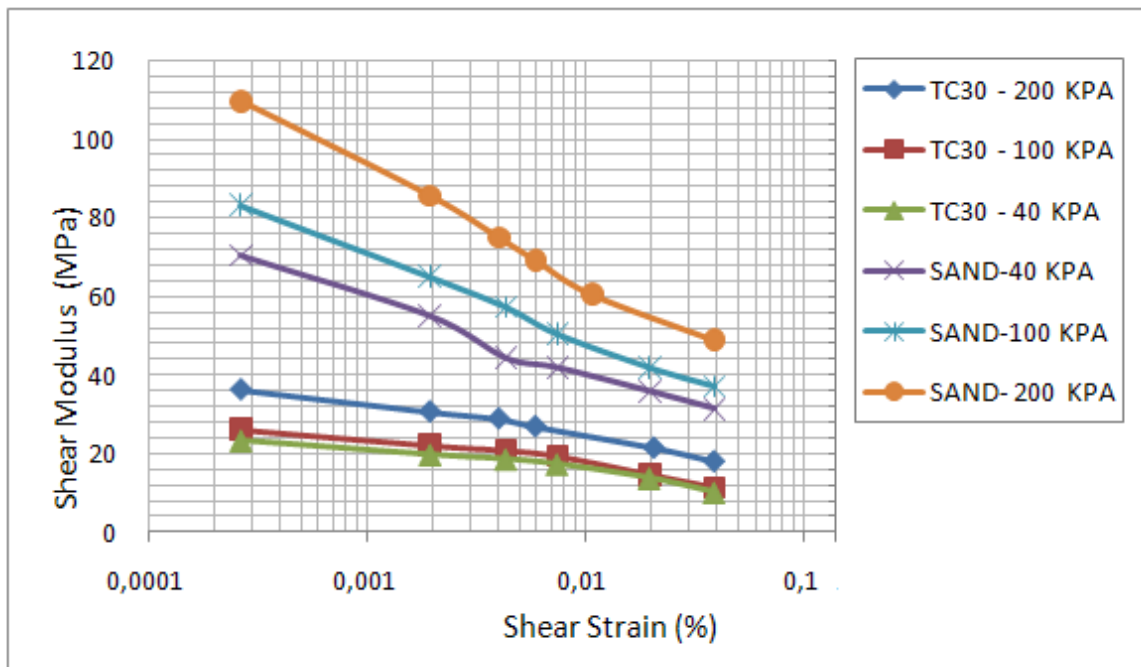


Figure 7.56. Shear Modulus vs. Shear Strain curve for TC30.

7.3.3.4. All Tire Crumbs-Sand Mixtures. From the comparison of tests performed with sand-tire crumbs materials under three different confining pressures, it is seen that the TC specimen which is tested under high confining pressure reached high damping ratio value (Figure 7.58). Additionally, it is noticed that the damping ratio is getting higher as the percentage of tire waste increases. At relatively high shear strains, the damping ratio curves of different mixtures in consistency with the ones at low shear strain values. The shear modulus of TC10 specimen which is tested under 200 kPa. is the highest one among all tests performed with only sand and sand-tire crumbs mixtures. As the tire crumbs content increases and confining pressure decreases, shear modulus decreases (Figure 7.58). The decisive effect of tire content and confining pressure is seen clearly. The characters of curves are nearly the same for all three types of mixtures but the effect of all TC specimens are different from each other.

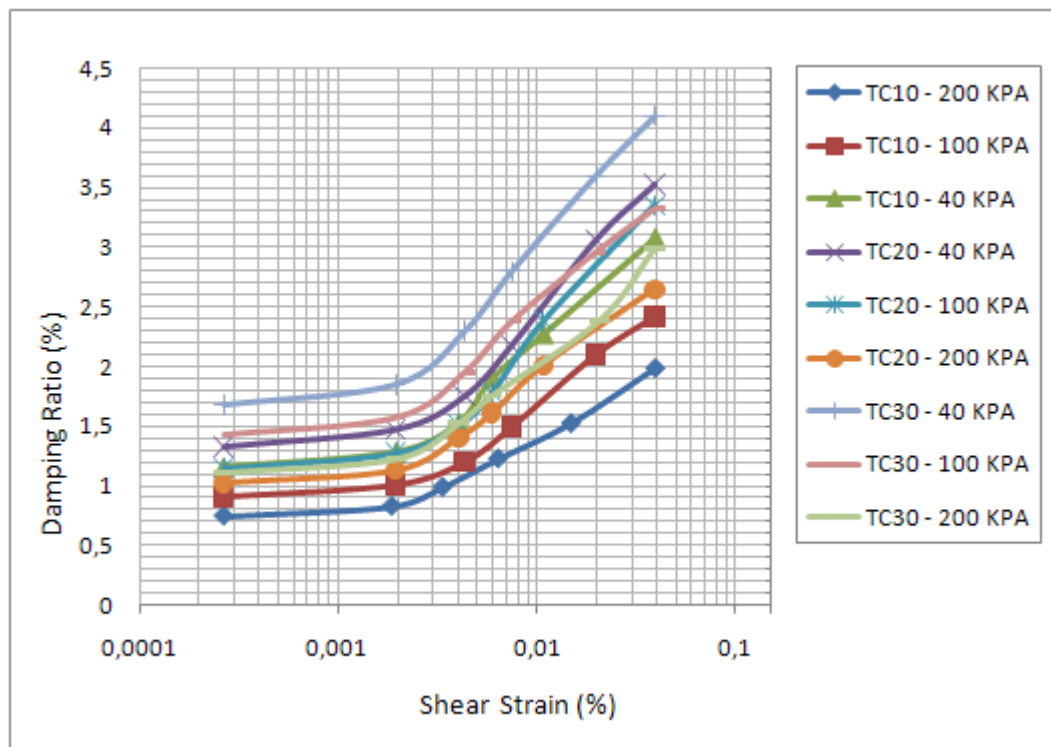


Figure 7.57. Damping Ratio vs. Shear Strain curves for tire Crumbs-sand mixtures.

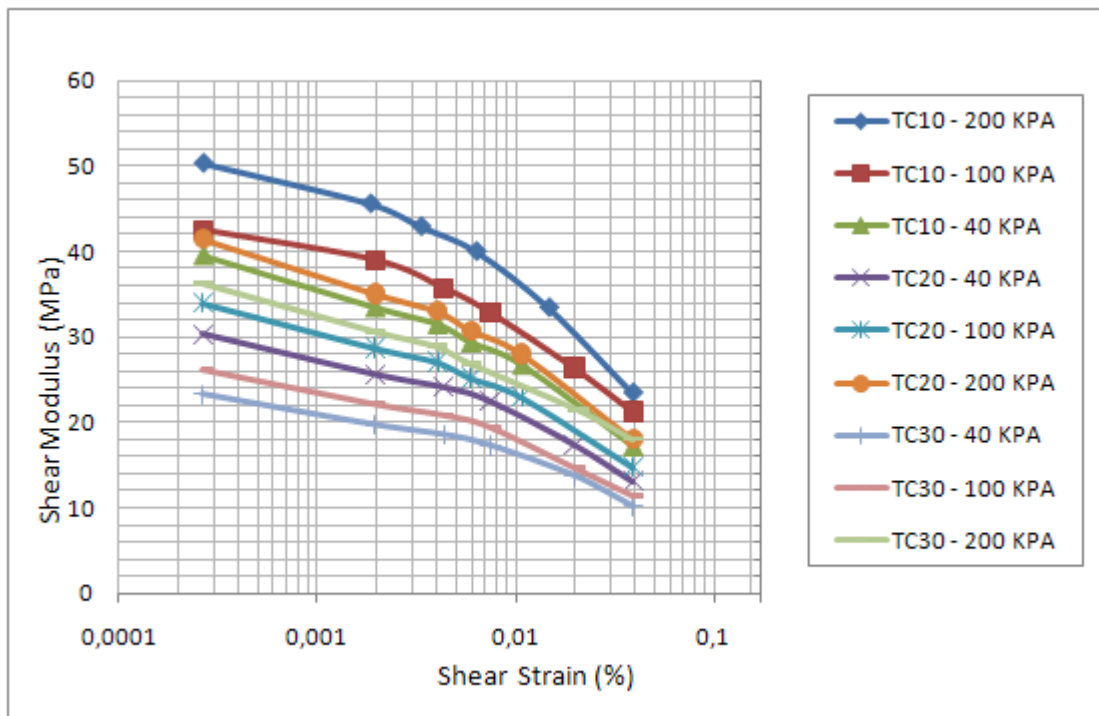


Figure 7.58. Shear Modulus vs. Shear Strain curves for tire Crumbs–sand mixtures.

7.3.3.5. Damping Ratio vs. Shear Strain curves TC10, TC20 and TC30 (40 kPa). Figure 7.59. shows the damping ratio vs. shear strain curves of all sand-tire crumbs mixtures which are tested under 40 kPa. confining pressure. When the results of specimens tested under other confining pressures are not considered, only the effect of tire content over dynamic properties of specimens can be evaluated. It is concluded that the final damping ratio values increases as the tire crumbs content decreases. There is a considerable difference between the damping ratio values of only sand and sand-tire mixtures. At low shear strains, the increasing tendency of damping ratio curves are less steep. However, at relatively high shear strains, the damping ratio curves of specimens have more upright tendency. The shear modulus behaviour of sand with tire crumbs mixture and only sand materials under 40 kPa. was shown in Figure 7.60. Tire inclusion effected the shear modulus value of sand up to 1.75 times.

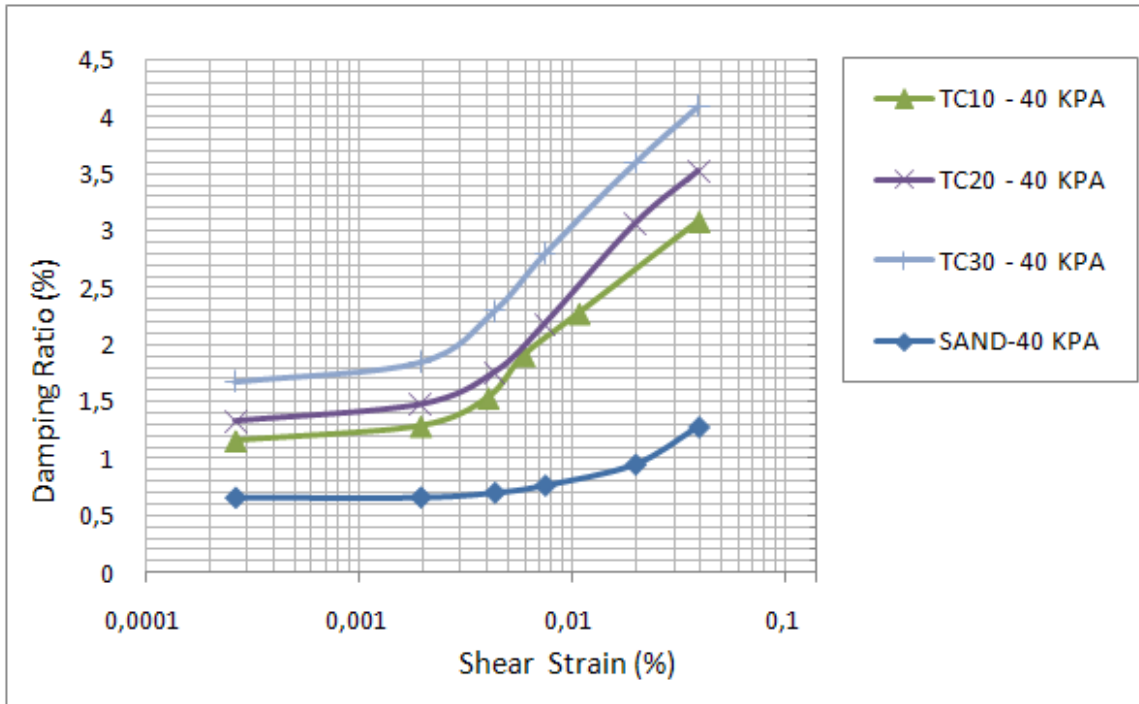


Figure 7.59. Damping Ratio vs. Shear Strain curves for tire Crumbs –sand mixtures under 40 kPa confining pressure.

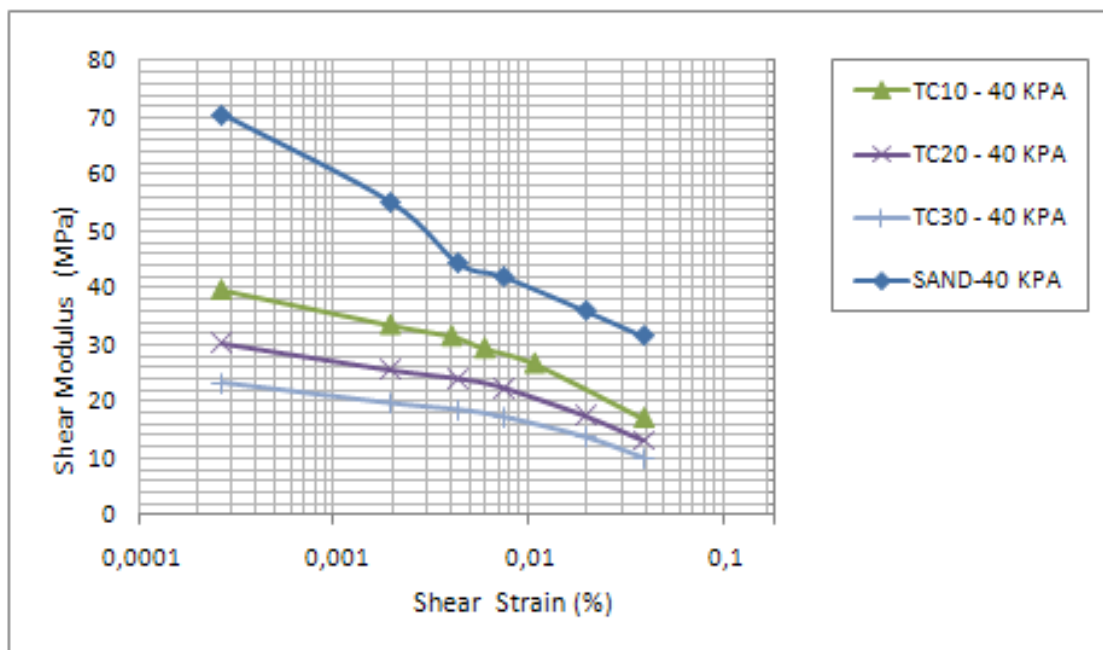


Figure 7.60. Shear Modulus vs. Shear Strain curves for tire Crumbs–sand mixtures under 40 kPa confining pressure.

7.3.3.6. Damping Ratio vs. Shear Strain curves TC10, TC20 and TC30 (100 kPa). The results of cyclic triaxial tests which are performed under 100 kPa confining pressure is shown in Figure 7.61. To compare all tire included specimens, the maximum damping ratio value occurred with TC30 which is tested under 100 kPa confining pressure (Figure 7.61). Damping ratio of only sand is at the lowest value among all four specimens. Final damping ratio values are nearly at same proportions. On the other hand, the effect of tire inclusion on shear modulus of sand material is noticeable (Figure 7.62). The maximum shear modulus obtained with only sand and the lowest one observed with TC30 specimen which is tested under 100 kPa confining pressure. The addition of each ten percent tire crumbs material caused to decrease in shear modulus and causes major increase in damping ratio. In conclusion, under the same confining pressure, as tire crumbs content increases, damping ratio increases and shear modulus decreases.

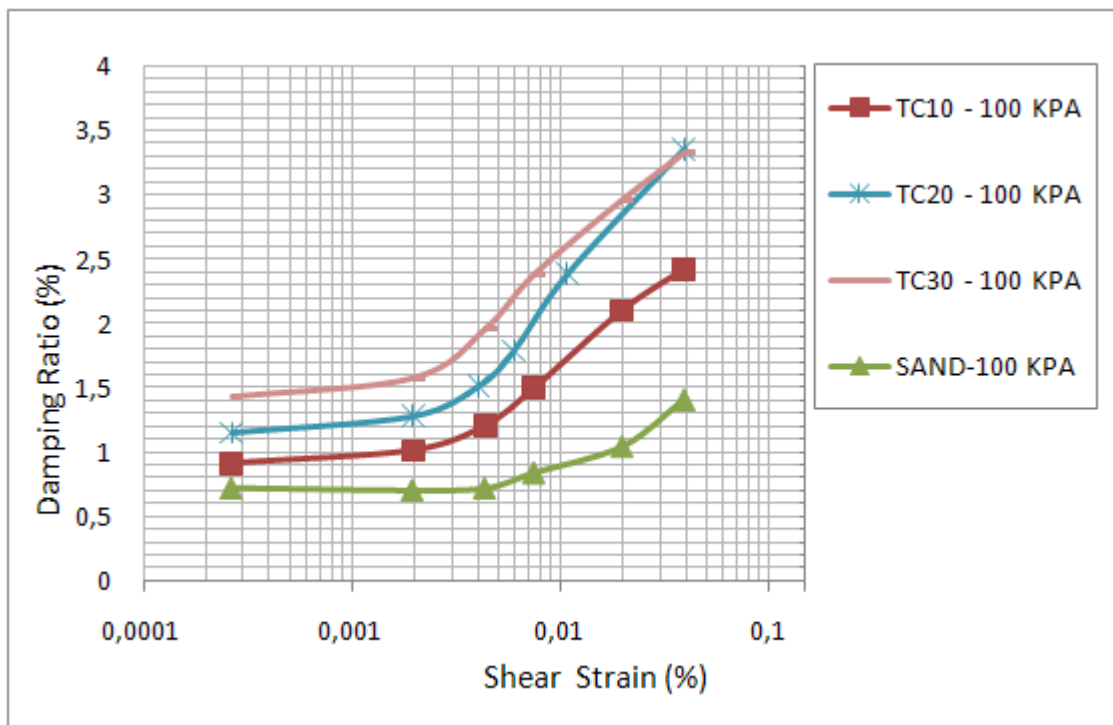


Figure 7.61. Damping Ratio vs. Shear Strain curves for tire crumbs –sand mixtures under 100 kPa confining pressure.

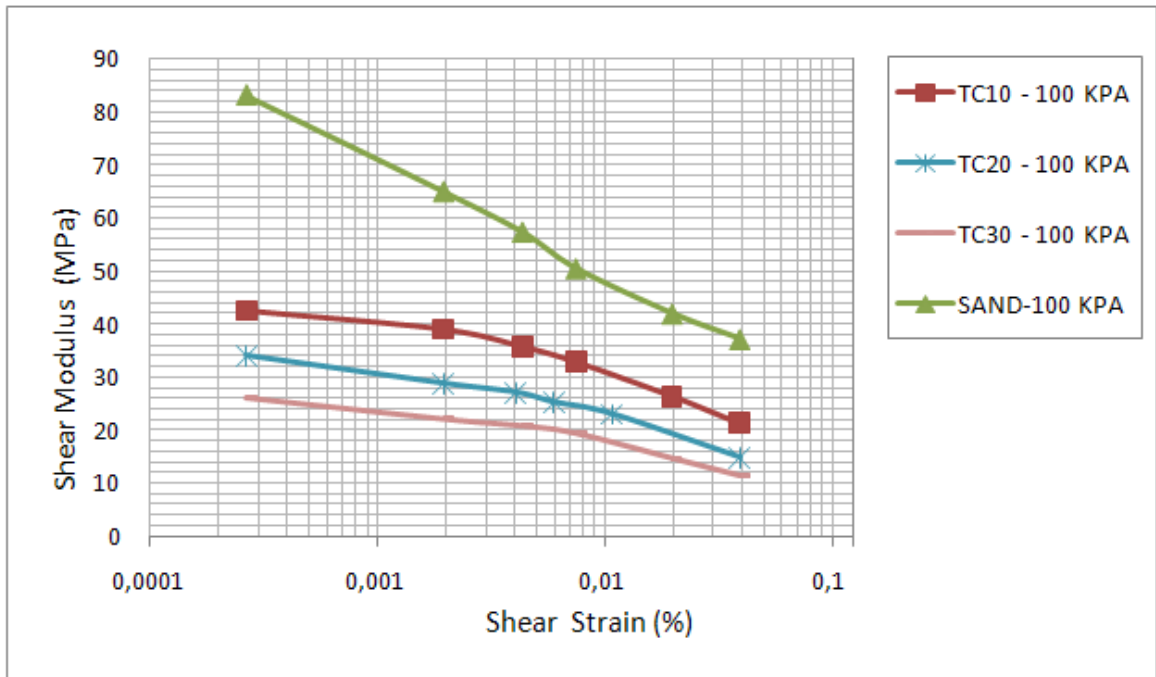


Figure 7.62. Shear Modulus vs. Shear Strain curves for tire crumbs –sand mixtures under 100 kPa confining pressure.

7.3.3.7. Damping Ratio vs. Shear Strain curves TC10, TC20 and TC30 (200 kPa). The performance of only sand and tire included specimens are demonstrated at the highest value of confining pressure, 200 kPa. (Figure 7.63). At lower shear strain values, damping ratio of all specimens increases slowly. Between the range of 0.005% and 0.05% the upward trend of curves become more distinctive. The maximum damping ratio obtained from TC30. According to the test results, the shear modulus of sand is the highest one among all four specimens. (Figure 7.64). The decreasing tendency of damping ratio vs. shear strain curve is linear. The shear modulus values of TC30, TC20, TC10 specimens are 50 MPa., 46 MPa. and 40 MPa., respectively. The effect of tire crumbs inclusion increased the shear modulus around 5%.

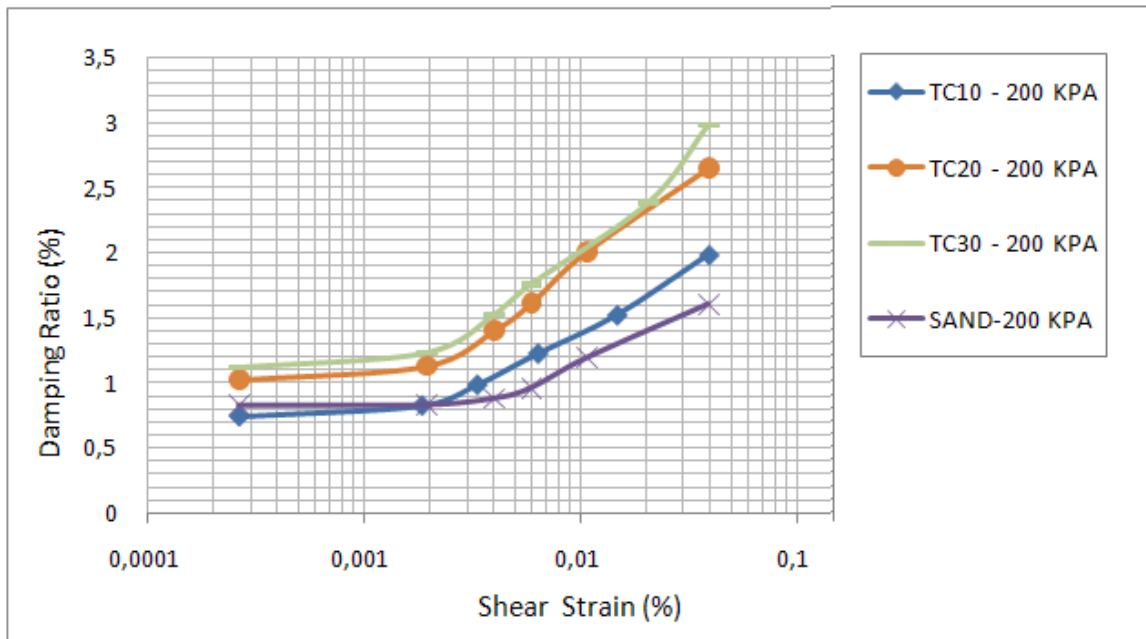


Figure 7.63. Damping Ratio vs. Shear Strain curves for Tire Crumbs–Sand Mixtures under 200 kPa confining pressure.

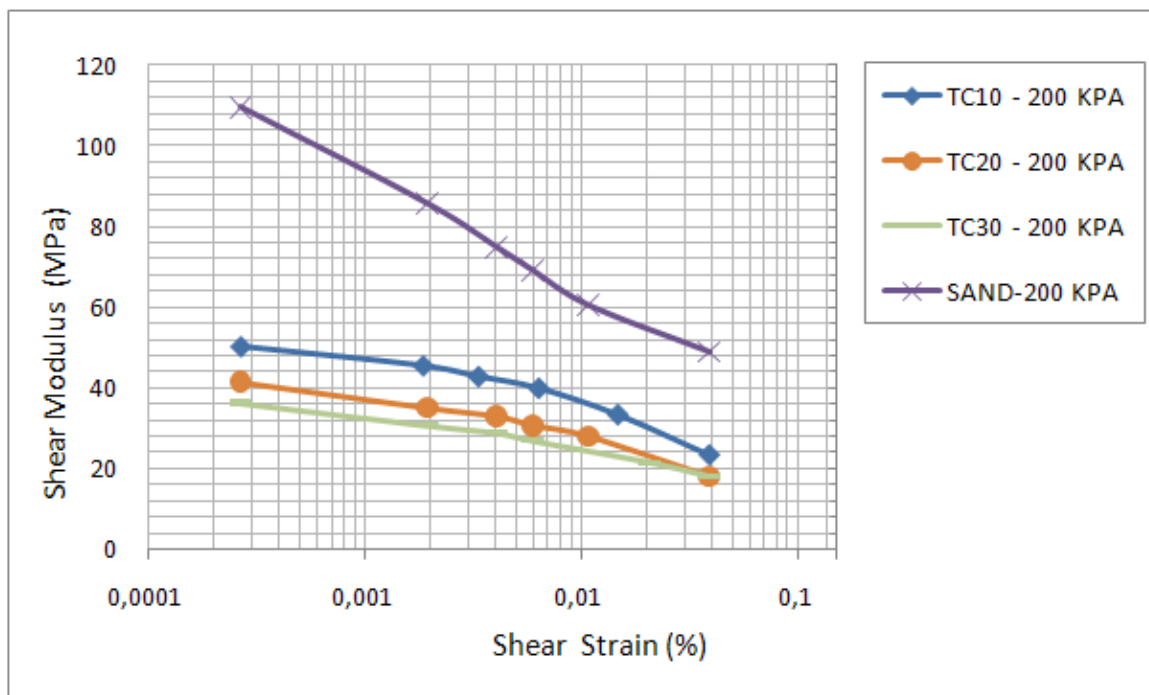


Figure 7.64. Shear Modulus vs. Shear Strain curves for tire crumbs–sand mixtures under 200 kPa confining pressure.

7.3.4. Analysis of Cyclic Triaxial Laboratory Tests

A set of cyclic triaxial compression test are performed with only sand, mixtures of sand-tire buffings and sand-tire crumbs materials at different contents. Tire waste-sand mixtures are prepared at 10, 20 and 30% of tire waste by weight. Each test is repeated under three different confining pressures as; 40, 100 and 200 kPa. The rate of strain is selected as 0.5 mm/min. The tests were conducted in general accordance with ASTM-D3999 (2003). The shear modulus and damping ratio values are determined for samples under different confining pressures.

Figure 7.65 and Figure 7.66 show graphs of the test results of all specimens. With each 10% tire waste content, it is observed that the damping ratio of specimens increases considerably. The damping ratio value observed with TC30 specimen which is tested under 40 kPa confining pressure is the maximum one, 4.10%. The minimum damping ratio is observed with only sand specimen which is tested under 40 kPa. as 1.25%. To compare the performance of the buffings and crumbs material, it can be seen that at same shear strains, damping ratio of tire crumbs mixtures are higher than tire buffings mixtures. Additionally, TB30 specimens which is tested under 40 kPa. confining pressure displayed the maximum damping ratio values among all tire buffings-sand mixtures (Figure 7.65).

The damping ratio of specimens are nearly constant at lower shear strain values. At higher shear strain values, as the shear strain increases, the damping ratio of the specimens increases. Damping in a tire-sand mixture is due to the friction of the particle contacts and the deformation of particles. Shear modulus of sand decreases as tire content increases. The maximum shear modulus value observed with only sand material tested under 200 kPa. The test which is performed with TC30 specimen under 200 kPa confining pressure displayed the highest shear modulus value among all tire waste-sand mixtures (Figure 7.66). The maximum shear modulus value measured from TC10 specimen tested under 200 kPa confining pressure.

The confining pressure has an important effect on dynamic properties of specimens. For all specimens, as the confining pressure increases, shear modulus increases and

damping ratio decreases. As Ribay *et al.* (2004) stated, it is proved with the experiment results that whatever the type of material, confining stress improves the shear modulus whereas it has negligible effect on the damping ratio. The shear modulus of specimen increases as confining pressure increases.

The initial shear modulus values of specimens are varied in a wider range of scale while the final shear modulus values are scattered in a narrow band. As the specimens reach the maximum shear strain value, the differences between the shear modulus values are decreased. In contrast to shear modulus values, final damping ratio values of specimens are not very close to each other at maximum shear strain values. The increasing shear strain value causes higher damping ratio and lower shear modulus.

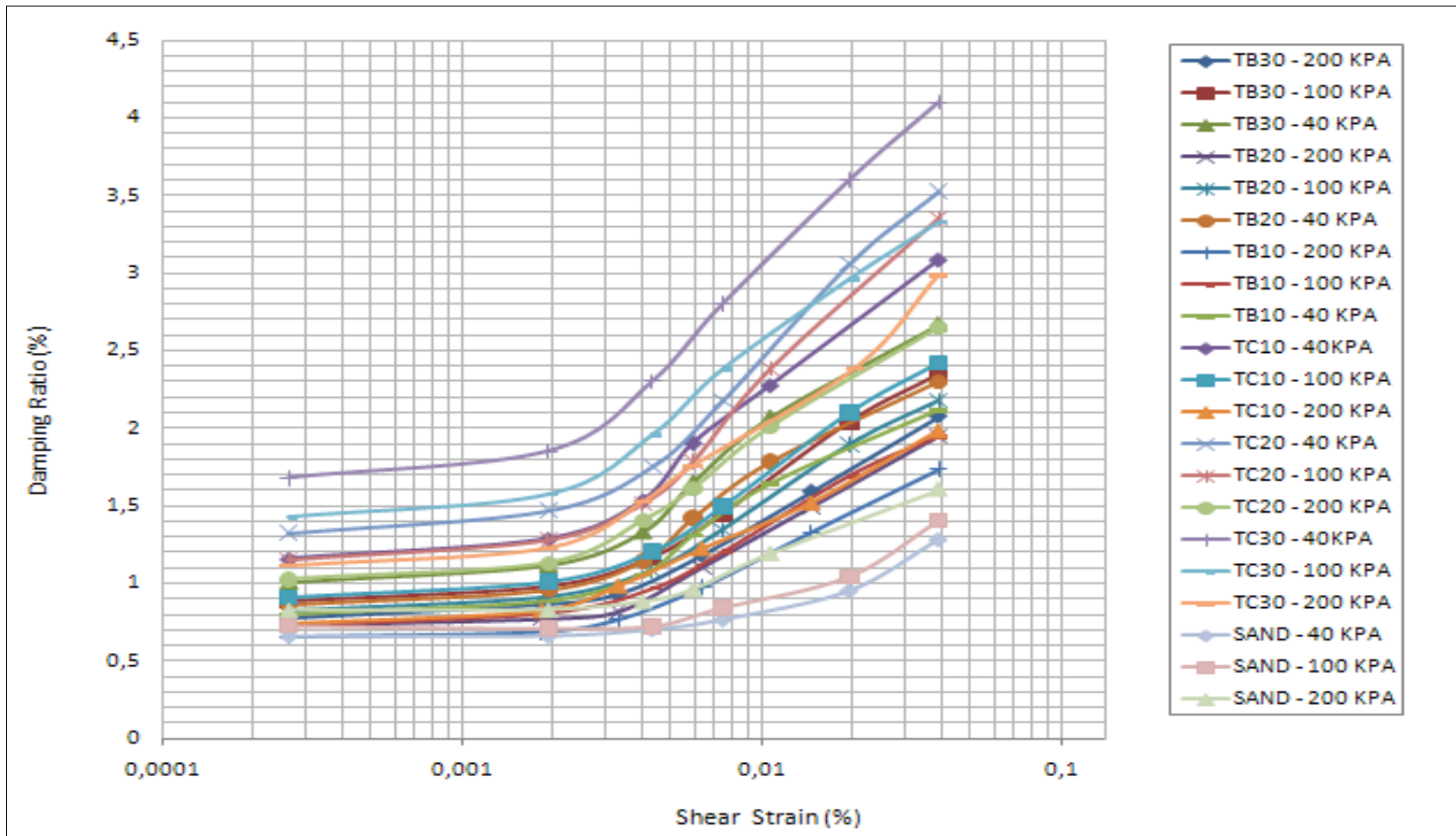


Figure 7.65. Damping Ratio vs. Shear Strain curves for all tests.

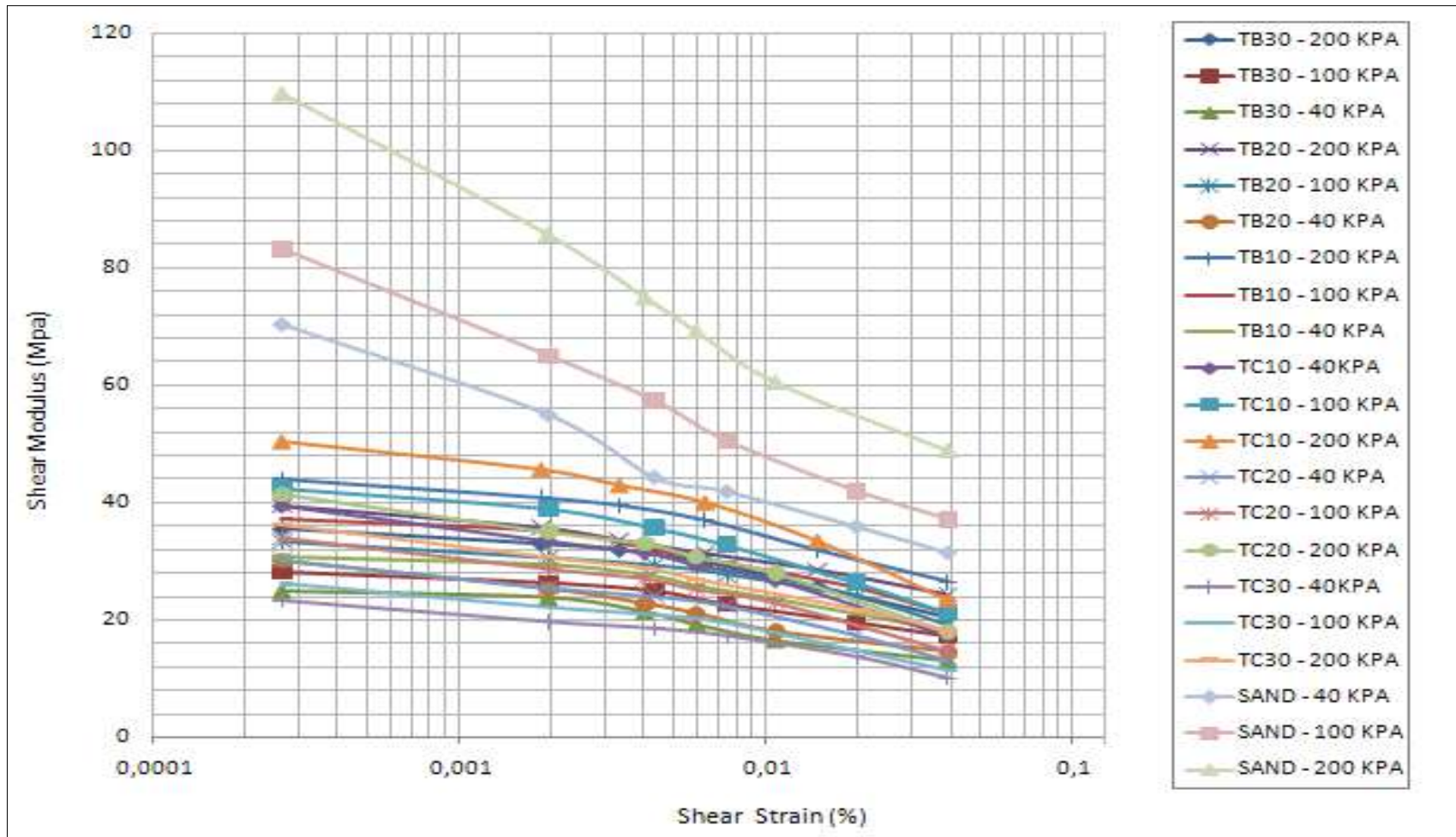


Figure 7.66. Shear Modulus vs. Shear Strain curves for all tests.

Table 7.5. Summary of Cyclic Triaxial Test Results.

Specimen	Damping Ratio (%)			Shear Modulus (MPa)			Shear Strain (%)
	Confining Pressures			Confining Pressures			
	40 kPa	100 kPa	200 kPa	40 kPa	100 kPa	200 kPa	
S	0.64 - 1.24	0.78 - 1.40	0.83 - 1.60	70 - 31	83 - 37	109 - 48	0.00027 - 0.0390
TB10	0.80 - 2.12	0.73 - 1.94	0.65 - 1.74	30.64 - 18.05	37.19 - 21.24	44.06 - 26.49	0.00027 - 0.0390
TB20	0.87 - 2.30	0.82 - 2.18	0.73 - 1.95	30.07 - 14.50	33.36 - 19.05	39.52 - 24.38	0.00027 - 0.0390
TB30	1.00 - 2.67	0.88 - 2.35	0.78 - 2.08	24.82 - 13.19	28.13 - 17.21	35.69 - 20.60	0.00027 - 0.0390
TC10	1.16 - 3.08	0.91 - 2.42	0.75 - 1.98	39.56 - 17.19	42.48 - 21.26	50.32 - 23.40	0.00027 - 0.0390
TC20	1.33 - 3.53	1.15 - 3.35	1.03 - 2.65	30.26 - 13.15	34.00 - 14.00	41.48 - 18.00	0.00027 - 0.0390
TC30	1.68 - 4.10	1.43 - 3.32	1.11 - 2.98	23.30 - 10.12	26.18 - 11.37	36.29 - 18.07	0.00027 - 0.0390

7.4. Shaking Table Test Results

All mixtures; sand, tire buffings and tire crumbs are prepared in a large bowl carefully and saturated with water. The aspect ratio of tire buffings (TB) material is 1/5 and the aspect ratio of tire crumb (TC) is 1-1.5. The dust material inside of tire buffings are removed. Specimens are prepared with $D_r = 0.40$ relative density. The water content of the specimens are 30%. Only sand, TB10, TB15, TB20, TB30, TC10, TC15, TC20 and TC30 specimens are used in the tests. Since the height of the shear stack is 18 cm, to prevent overflowing of material during the movement, 17 cm of box filled carefully. The material filled into the box with three layers. Three accelerometers (A1, A2, A3), a pore pressure transducer, a laser displacement sensor are used in the experiments. Accelerometer A1 is fixed on the shaking table surface to measure acceleration value. Submersible accelerometer A2 is placed in lower layer of specimen. Other submersible accelerometer is placed in the upper layer of specimen. Pore pressure transducer is placed at mid-height of the specimen. Laser displacement sensor is fixed at top layer of shear stack (Figure 6.17). Three different earthquake ground motions which recorded on Small Shaking Table with Thermal Cabin as; İzmit (E-W), Sakarya (N-S) and Tabas (E-W) are applied to the specimens during the tests. A1 is the base input acceleration. These three ground motions recorded on small Shaking Table with Thermal Cabin are given in Figure 7.67, Figure 7.68 and Figure 7.69. Each specimen is tested under 0°C, 20°C and 50°C. To control the temperature of specimen, laser temperature sensor is used. The tests are performed with İzmit (E-W) earthquake motion and summarised in the following section. Also, the shaking table test results of Tabas (E-W) and Sakarya (N-S) earthquake ground motions are given in Appendixes.

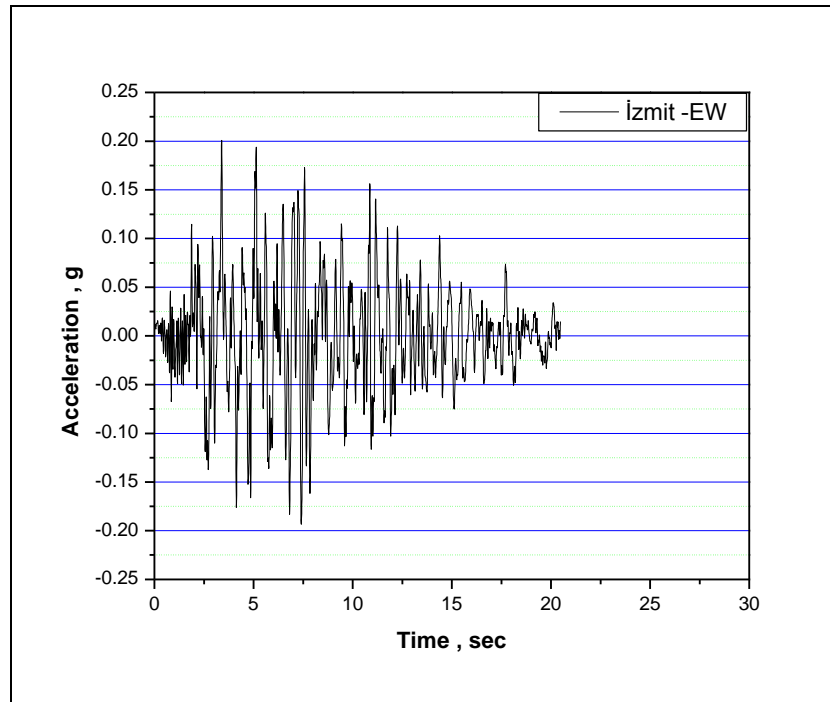


Figure 7.67. Acceleration time history of İzmit (E-W) (1999) Earthquake Ground Motion.

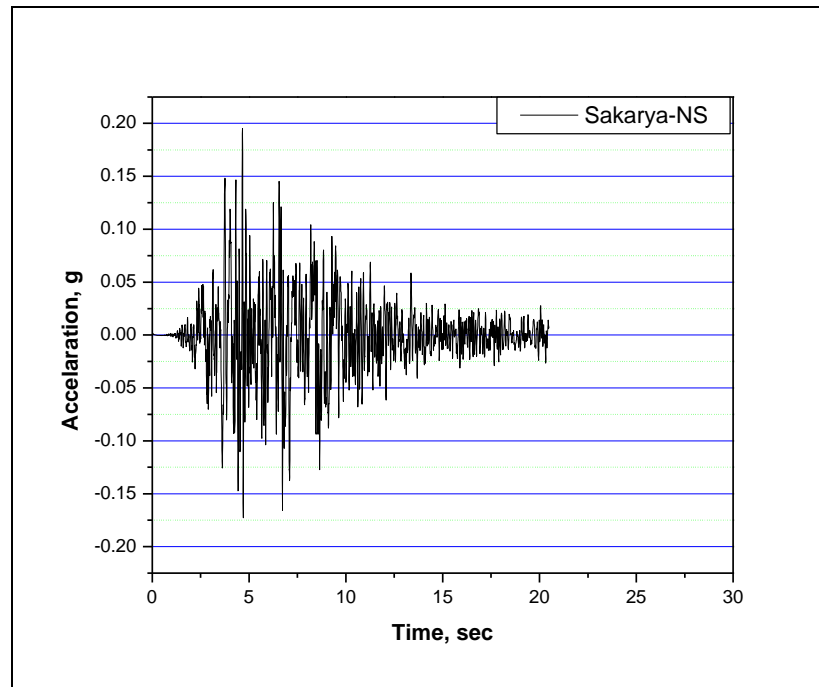


Figure 7.68. Acceleration time history of Sakarya (N-S) (1967) Earthquake Ground Motion.

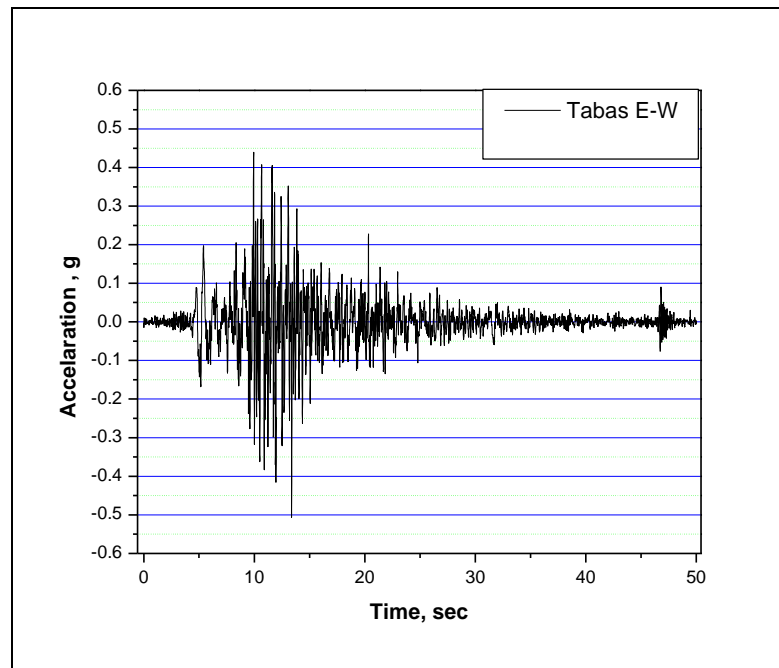


Figure 7.69. Acceleration time history of Tabas (E-W) (1978) Earthquake Ground Motion.

7.4.1. Tests Performed Under 0°C Temperature

7.4.1.1. İzmit (E-W) Earthquake - 100% Sand Specimen (S). The test specimen is prepared in a large bowl and saturated with water. It is filled into the shear box. The earthquake record of İzmit (E-W) is applied to the specimen. Tests are performed below 0°C temperature (Figure 7.71). The acceleration, pore water pressure and lateral displacement values were measured carefully. The acceleration time history, displacement time history and pore water pressure change graphs are obtained.

The acceleration time history of A1 base accelerometer which is fixed on the shaking table surface is given in Figure 7.70. Maximum acceleration value of A1 accelerometer is 0.15g.

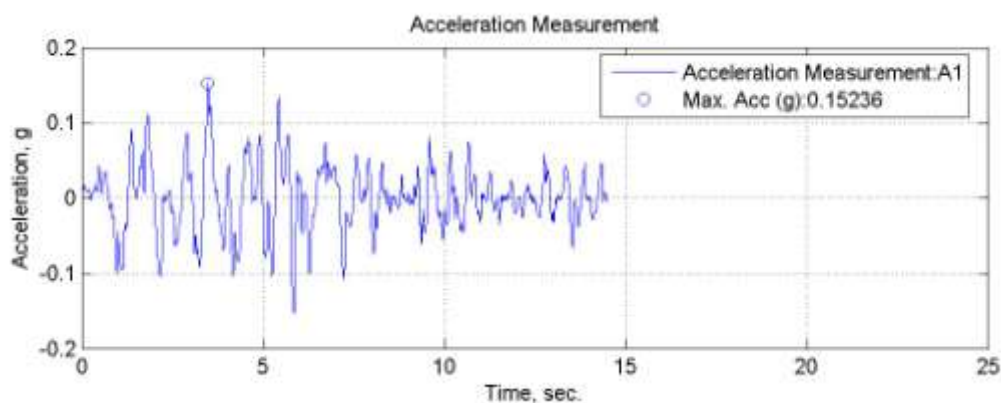


Figure 7.70. A1, acceleration time history of sand specimen tested under 0°C.



Figure 7.71. Sand specimen tested under 0°C.

The pore water pressure change of sand specimen is shown in Figure 7.72. It is observed that the pore water pressure value is zero during the test. The pore water pressure change of the specimen can be explained as; the water particles are frozen and thus no upward motion occurred. The acceleration time history of A2 is shown in Figure 7.73. A3 is the accelerometer placed at upper layer of soil. The acceleration values are measured by the submersible accelerometers. The maximum A2 acceleration value is measured as 0.16g, and the maximum A3 acceleration value is measured as 0.15g. The maximum lateral displacement value is measured as 3,02 cm. (Figure 7.74). The rigidity of specimen affects the behaviour of displacement.

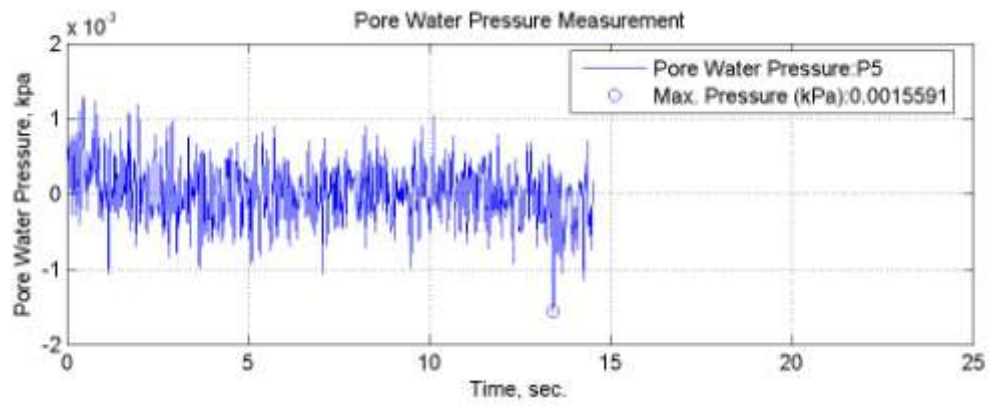


Figure 7.72. Pore water pressure change of sand specimen tested under 0°C .

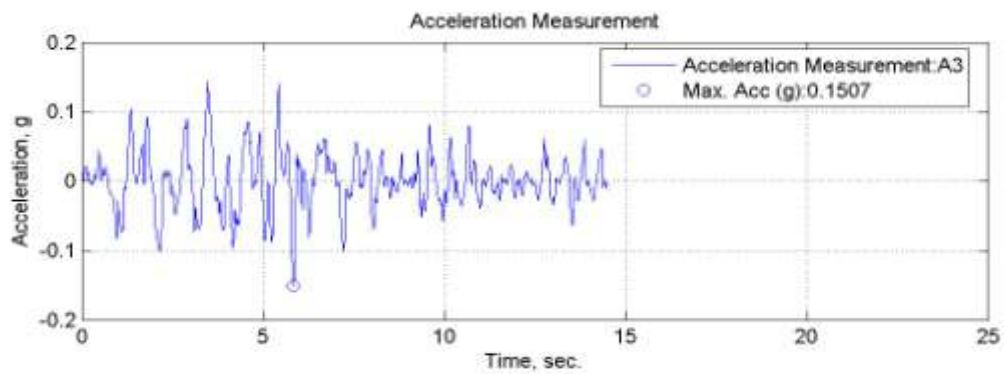
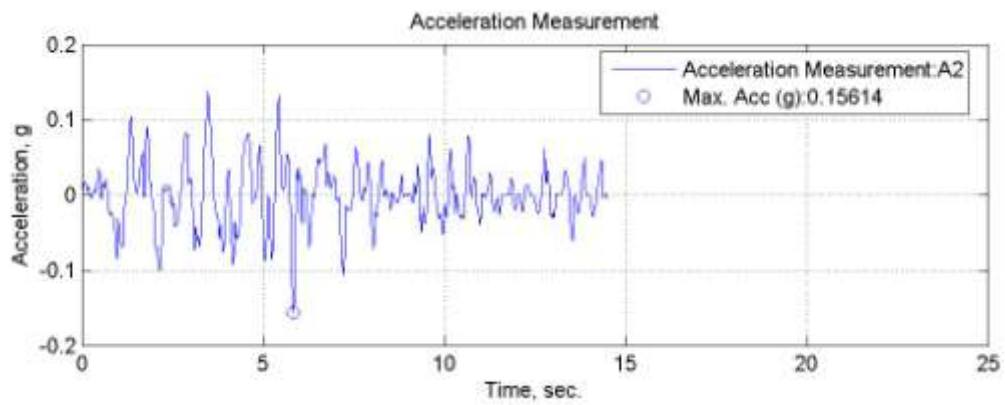


Figure 7.73. Time histories of accelerations of sand specimen tested under 0°C .

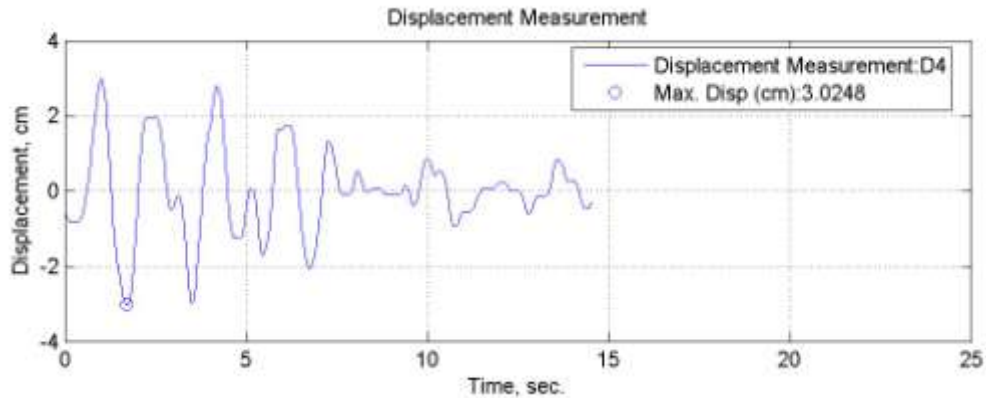


Figure 7.74. Lateral displacement time history for sand specimen tested under 0°C.

7.4.1.2. İzmit (E-W) Earthquake - TB10 Specimen. Same specimen preparation method was used to prepare 10% tire buffings-sand specimen. The mixture is prepared in a large bowl and saturated with water. Specimen is prepared with $D_r = 0.40$ relative density. Then it is filled into the shear box and İzmit (E-W) earthquake record is applied to the table. Maximum acceleration value of A1 base accelerometer is 0.15g (Figure 7.75).

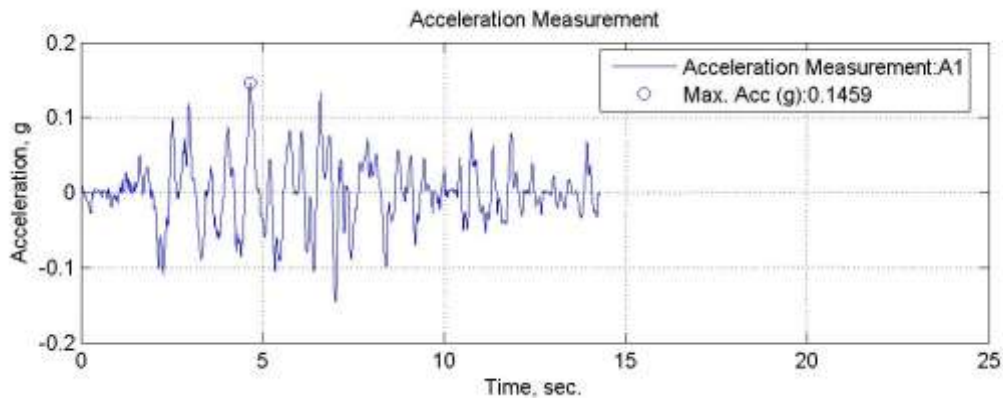


Figure 7.75. A1, acceleration time history of TB10 specimen tested under 0°C.

The pore water pressure change of the specimen is shown in Figure 7.76. It is observed that the pore water pressure value is almost zero during the test. The acceleration time histories of A2 and A3 accelerometers are shown in Figure 7.77. The maximum acceleration value of A3 is measured as 0.15g, and the maximum acceleration value of A2 is measured as 0.16g. The maximum lateral displacement value is measured as 3.12 cm. (Figure 7.78).

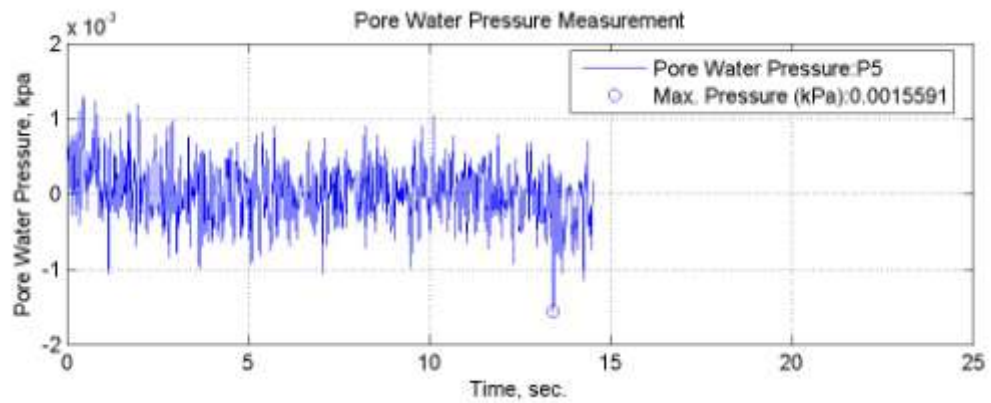


Figure 7.76. Pore water pressure change of TB10 specimen tested under 0°C.

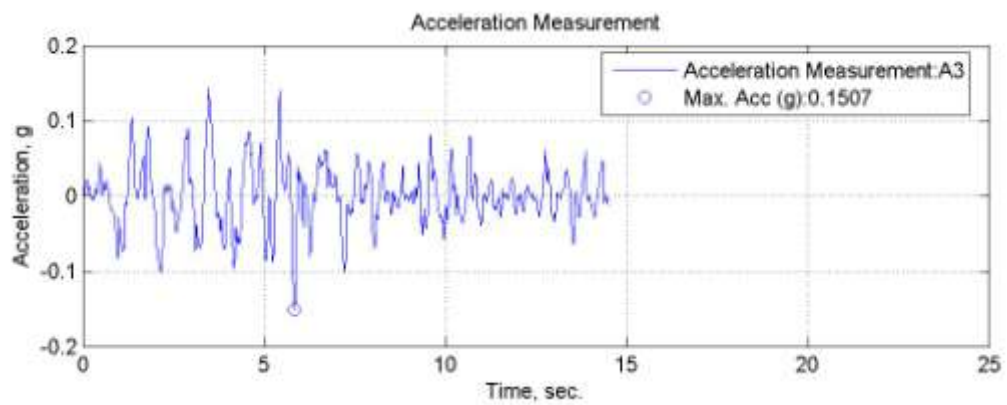
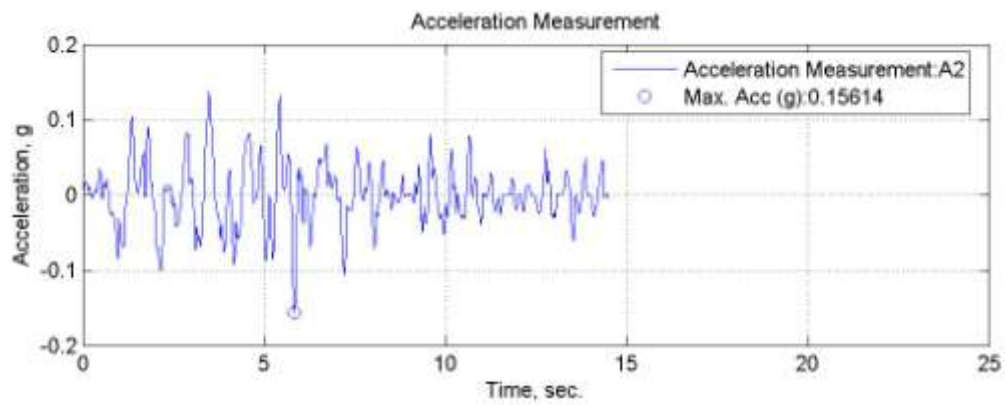


Figure 7.77. Time histories of accelerations of TB10 specimen tested under 0°C.

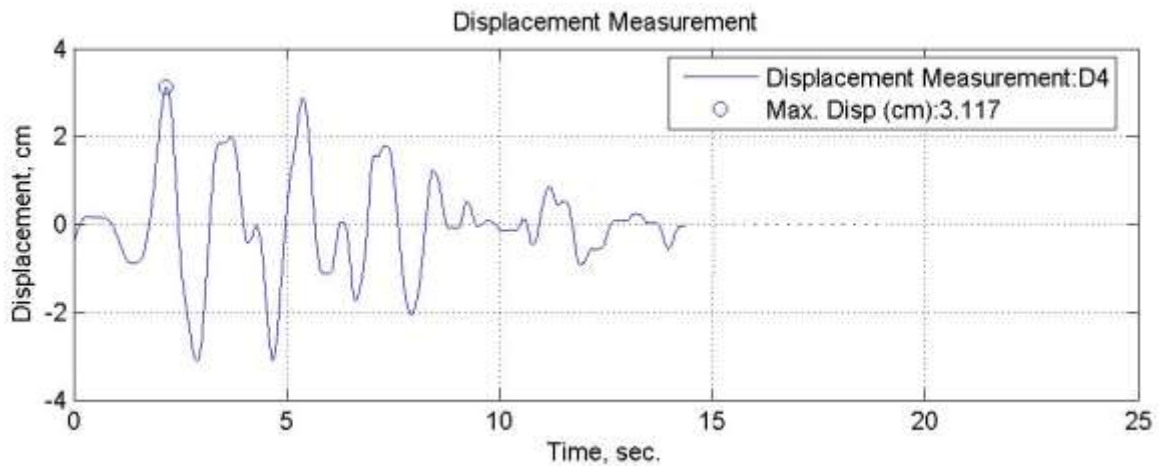


Figure 7.78. Lateral displacement time history for TB10 specimen tested under 0°C.

7.4.1.3. İzmit (E-W) Earthquake - TB15 Specimen. TB15 specimen is prepared in a large bowl and saturated with water. Specimen is prepared with $D_r = 0.40$ relative density. The temperature of specimen is arranged as 0°C (Figure 7.79). Then it is filled into the shear box and İzmit (E-W) earthquake ground motion is applied to the table. The acceleration time history, displacement time history and pore water pressure change graphs are obtained. The A1 base input acceleration time history is given in Figure 7.80. The maximum acceleration value of A1 accelerometer is 0.15g.



Figure 7.79. TB15 specimen tested on shaking table below 0°C.

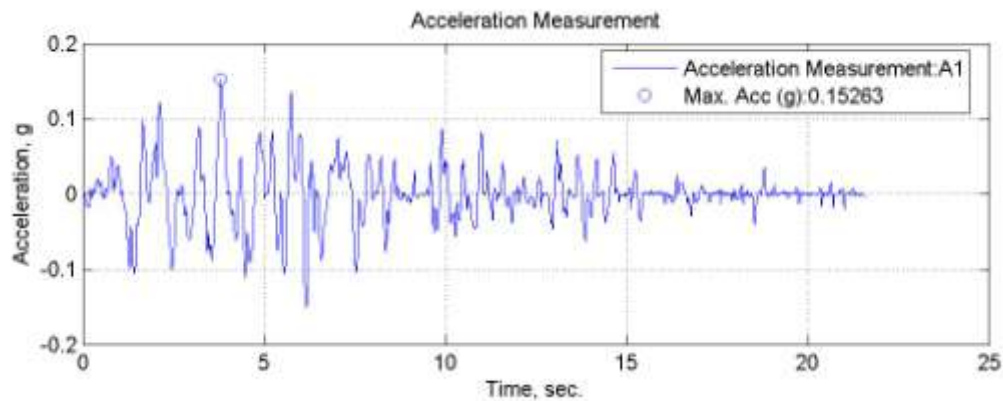


Figure 7.80. A1, acceleration time history of TB15 specimen tested under 0°C.

The pore water pressure change of the specimen is shown in Figure 7.81. It is observed that the pore water pressure value is almost zero during the test. The acceleration time histories of A2 and A3 accelerometers are shown in Figure 7.82. The acceleration values are measured by the accelerometers A2 and A3 within the soil and compared with A1 base input acceleration. The maximum acceleration value of A3 is measured as 0.15g, and the maximum acceleration value of A2 is measured as 0.43g. The maximum lateral displacement value of shear box is measured as 3.13 cm. (Figure 7.83).

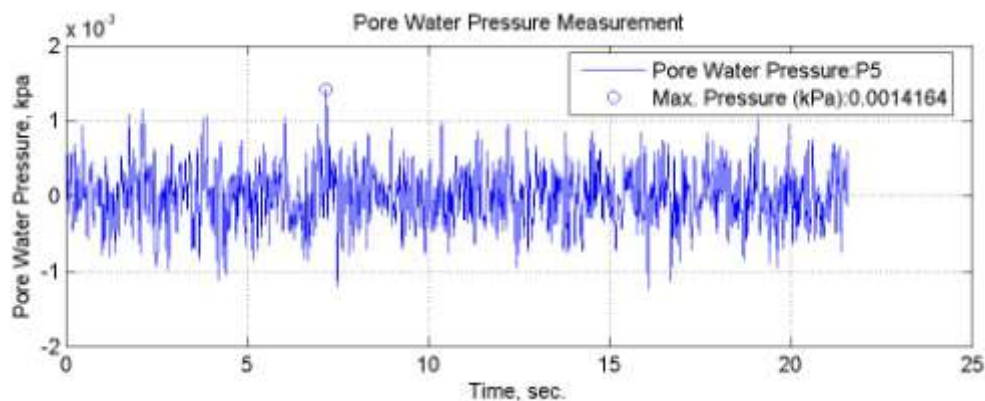


Figure 7.81. Pore water pressure change of TB15 specimen tested under 0°C.

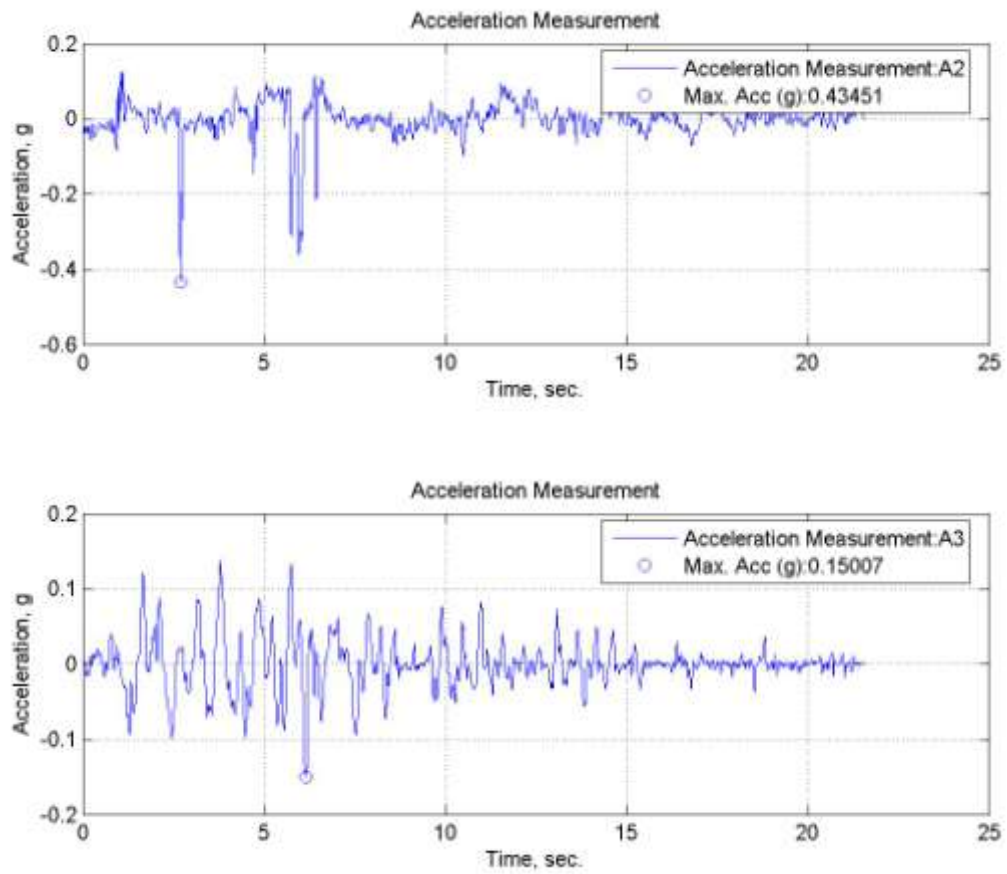


Figure 7.82. Time histories of accelerations of TB15 specimen tested under 0°C.

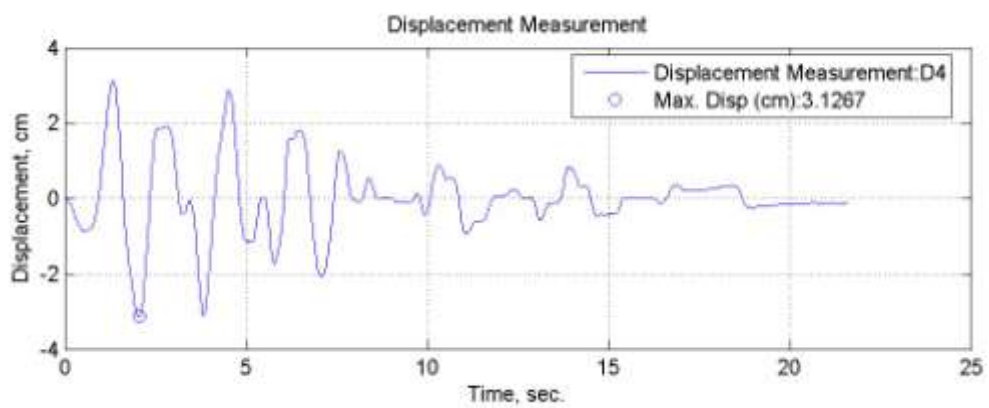


Figure 7.83. Lateral displacement time history for TB15 specimen tested under 0°C.

7.4.1.4. İzmit (E-W) Earthquake - TB20 Specimen. TB20 specimen is prepared in a large bowl and saturated with water. Specimen is prepared with $D_r = 0.40$ relative density. Then it is filled into the shear box. The specimen is cooled in shaking table cabin for one day to reach 0°C temperature. İzmit (E-W) earthquake motion is applied to the table. The acceleration time history, displacement time history and pore water pressure change graphs are obtained. The acceleration time history of A1 accelerometer is given in Figure 7.84. Maximum A1 base input acceleration value is $0.16g$.

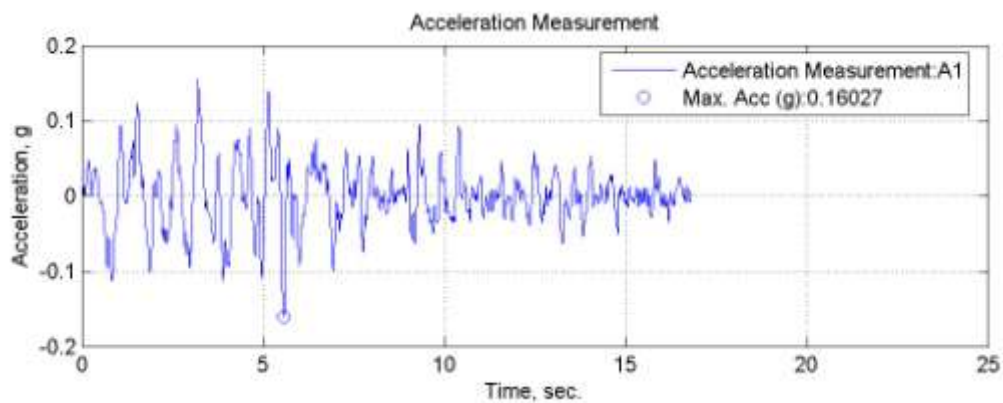


Figure 7.84. A1, acceleration time history of TB20 specimen tested under 0°C .

The pore water pressure change of the specimen is shown in Figure 7.85. It is observed that the pore water pressure value is almost zero during the test. The acceleration time histories of A2 and A3 accelerometers are shown in Figure 7.86. The A2 and A3 acceleration values are measured by the accelerometers within the soil and compared with A1 base input acceleration. The maximum A3 acceleration value is measured as $0.17g$, and the maximum A2 acceleration value is measured as $0.21g$. The maximum acceleration value of A1 is $0.180g$. The maximum lateral displacement value is measured as 3.13 cm . (Figure 7.87).

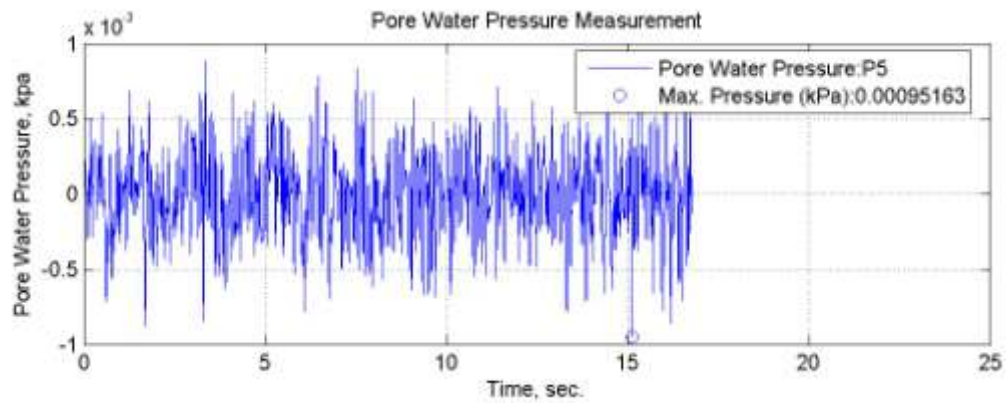


Figure 7.85. Pore water pressure change of TB20 specimen tested under 0°C .

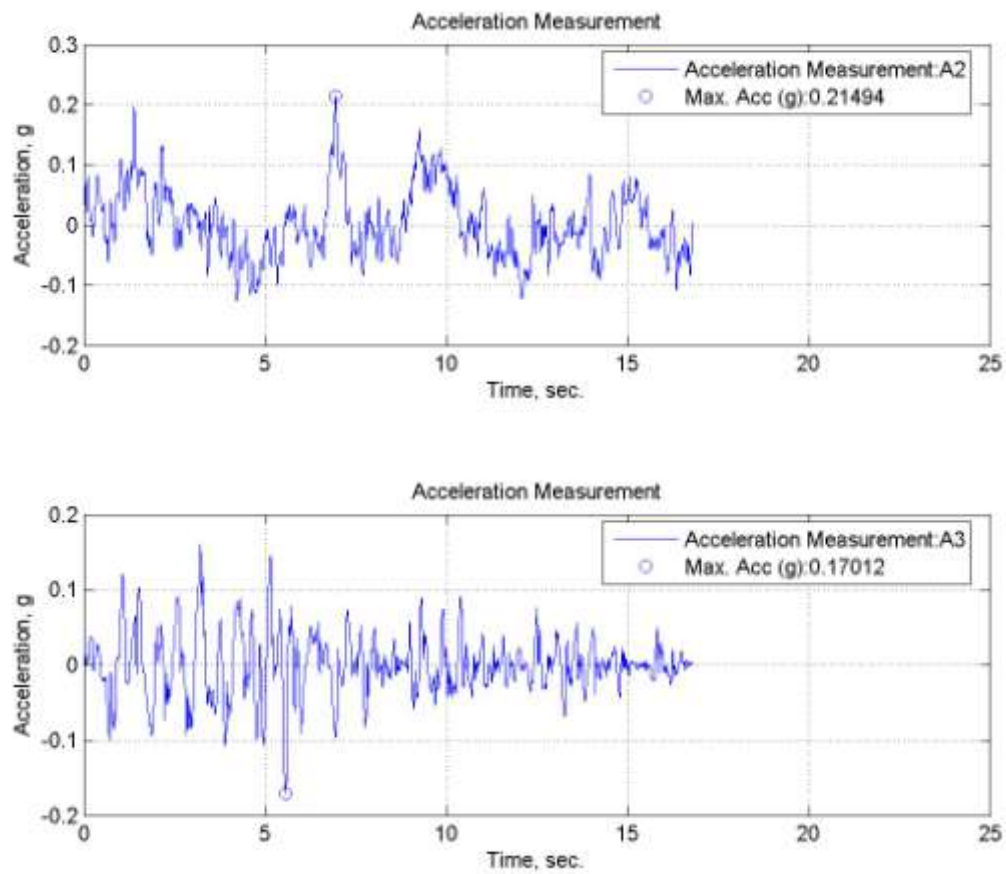


Figure 7.86. Time histories of accelerations of TB20 specimen tested under 0°C .

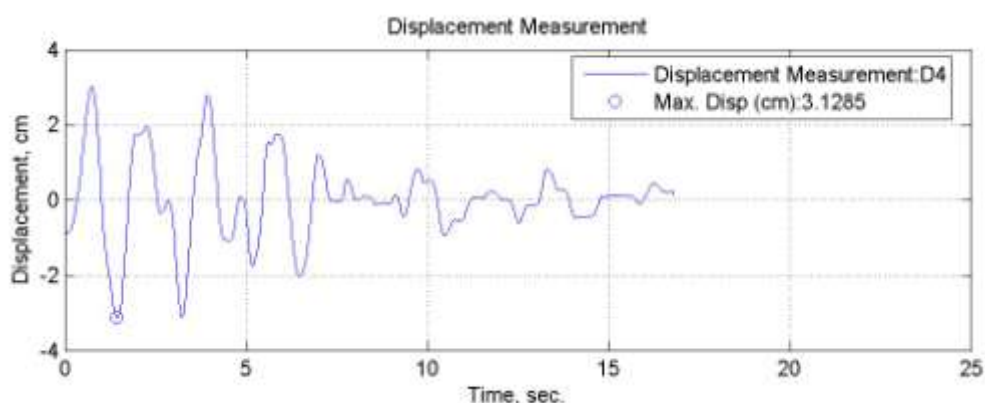


Figure 7.87. Lateral displacement time history for TB20 specimen tested under 0°C.

7.4.1.5. İzmit (E-W) Earthquake - TB30 Specimen. TB30 specimen is prepared in a large bowl and saturated with water. Specimen is prepared with $D_r = 0.40$ relative density. Then it is filled into the shear box. The temperature of specimen is arranged as 0°C. İzmit (E-W) earthquake ground motion is applied to the table. The acceleration time history, displacement time history and pore water pressure change graphs are obtained. The acceleration time history of A1 base input accelerometer is given in Figure 7.88. Maximum acceleration value of A1 accelerometer is 0.17g.

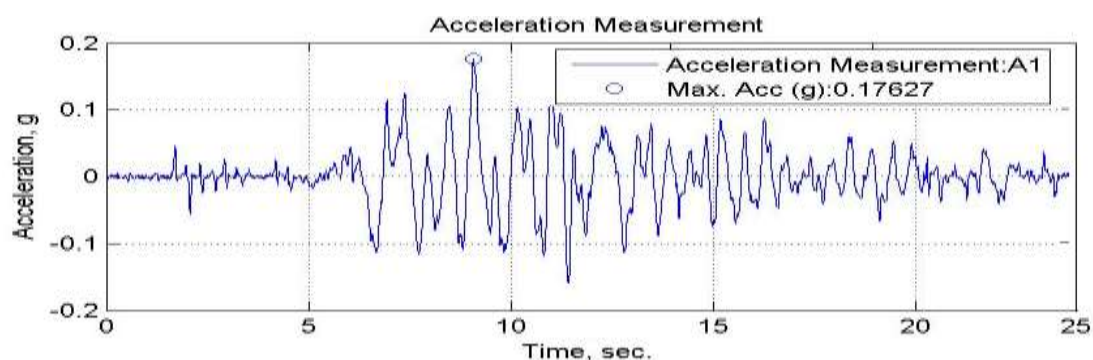


Figure 7.88. A1, acceleration time history of TB30 specimen tested under 0°C.

The pore water pressure change of the specimen is shown in Figure 7.89. It is observed that the pore water pressure value is almost zero during the test. The acceleration time histories of A2 and A3 accelerometers are shown in Figure 7.90. The maximum acceleration value of A3 is measured as 0.19g and the maximum A2 acceleration value is

measured as 0.19g. It is seen that the maximum acceleration value of A1 is 0.18g. The maximum lateral displacement value is measured as 4.50 cm. (Figure 7.91).

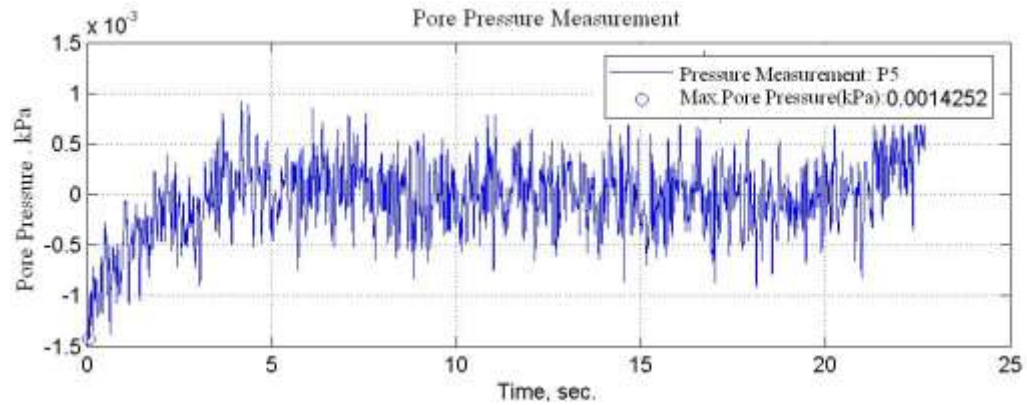


Figure 7.89. Pore water pressure change of TB30 specimen tested under 0°C.

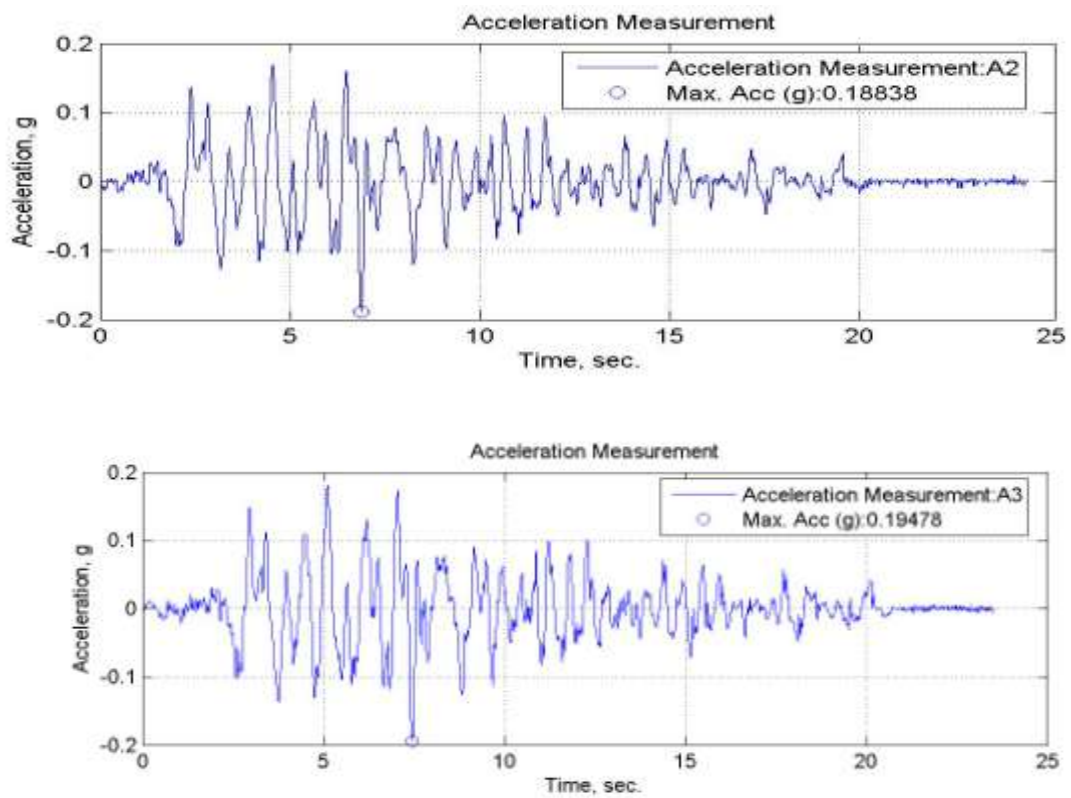


Figure 7.90. Time histories of accelerations of TB30 specimen tested under 0°C.

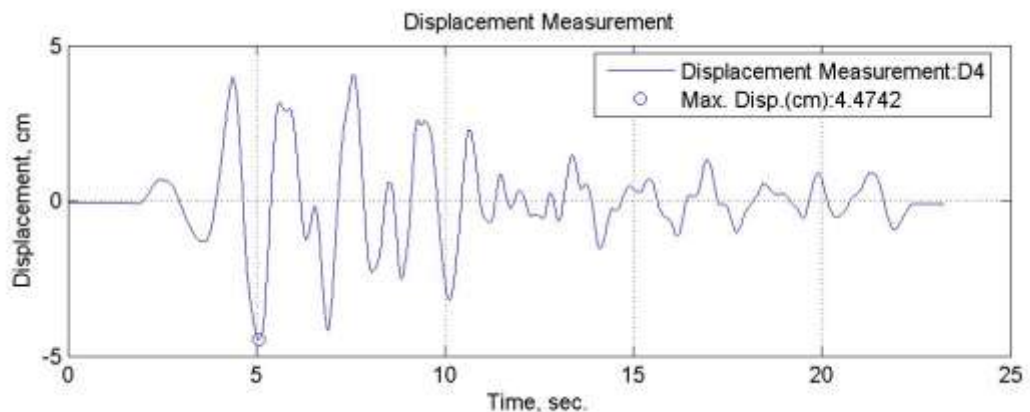


Figure 7.91. Lateral displacement time history for TB30 specimen tested under 0°C.

7.4.1.6. İzmit (E-W) Earthquake - TC10 Specimen. TC10 specimen is prepared in a large bowl and saturated with water. Specimen is prepared with $D_r = 0.40$ relative density. Then it is filled into the shear box. The temperature of specimen is arranged as 0°C and İzmit (E-W) earthquake ground motion is applied to the table. The acceleration, pore water pressure change and displacement graphs are drawn. The acceleration time history of A1 accelerometer is given in Figure 7.92. Maximum acceleration value of A1 accelerometer is 0.17g.

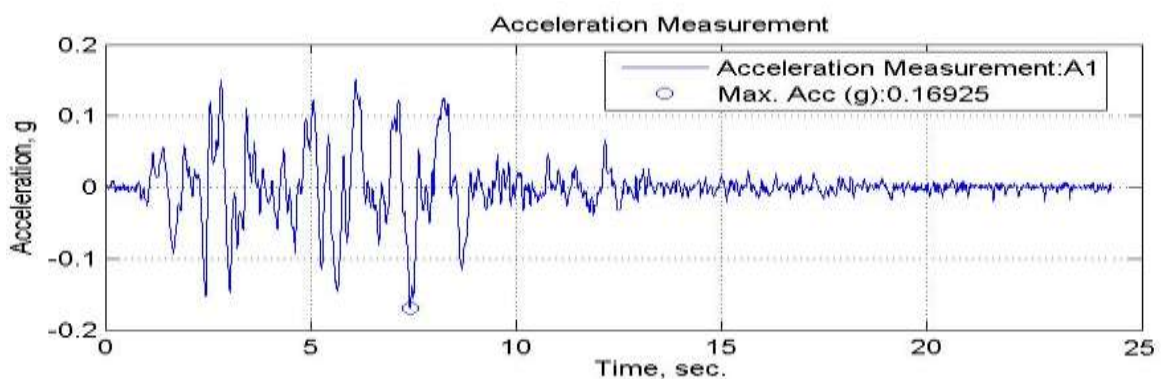


Figure 7.92. A1, acceleration time history of TC10 specimen tested under 0°C.

The pore water pressure change of the specimen is shown in Figure 7.93. It is observed that the pore water pressure value is almost zero during the test. The acceleration time histories of A2 and A3 accelerometers are shown in Figure 7.94. The acceleration values of A2 and A3 are recorded and compared with A1 base input accelerations. A3 is

the accelerometer placed at upper layer of soil. The maximum A3 acceleration value is measured as 0.18g. and the maximum A2 acceleration value is measured as 0.16g. The maximum A1 base input acceleration is 0.17g. The maximum lateral displacement value is measured as 4.03 cm. (Figure 7.95).

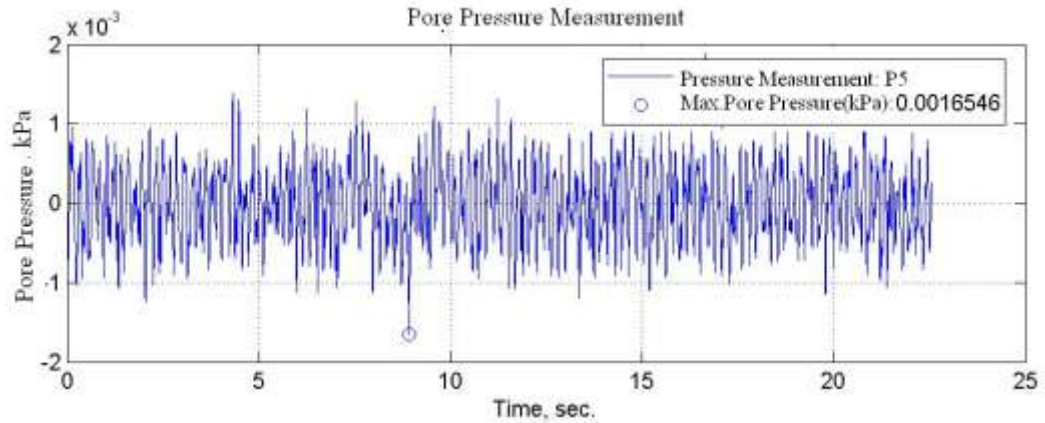


Figure 7.93. Pore water pressure change of TC10 specimen tested under 0°C.

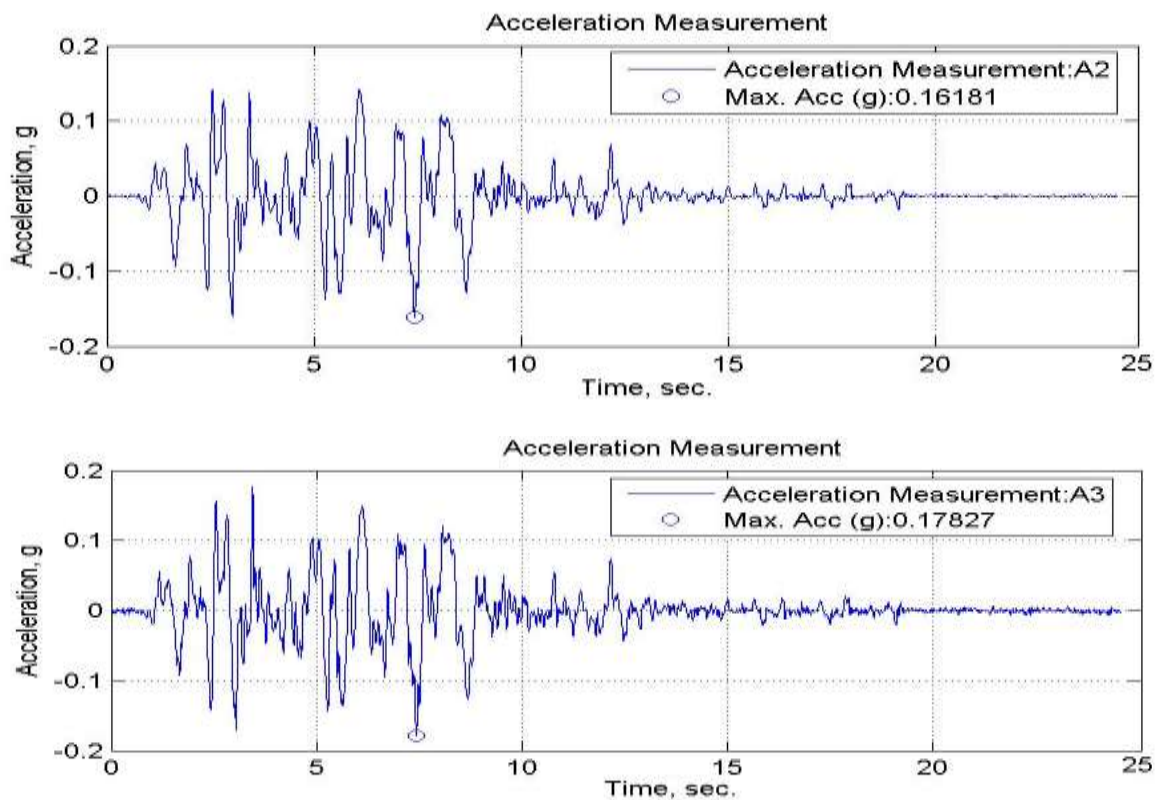


Figure 7.94. Time histories of accelerations of TC10 specimen tested under 0°C.

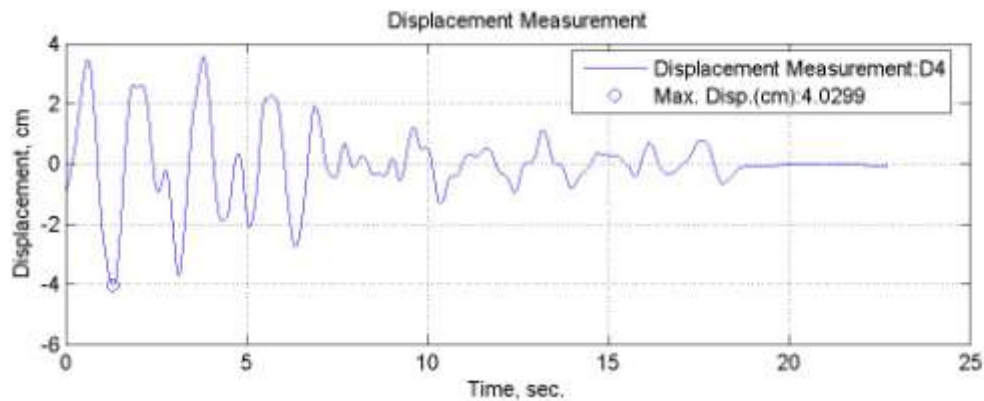


Figure 7.95. Displacement time history of TC10 specimen tested under 0°C.

7.4.1.7. İzmit (E-W) Earthquake - TC15 Specimen. TC15 specimen is prepared in a large bowl and saturated with water. Specimen is prepared with $D_r = 0.40$ relative density. The temperature of specimen is arranged as 0°C. İzmit (E-W) earthquake motion is applied to the table. The acceleration time history, displacement time history and pore water pressure change graphs are obtained. The acceleration time history of A1 base input acceleration is given in Figure 7.96. Maximum acceleration value of A1 accelerometer is 0.16g.

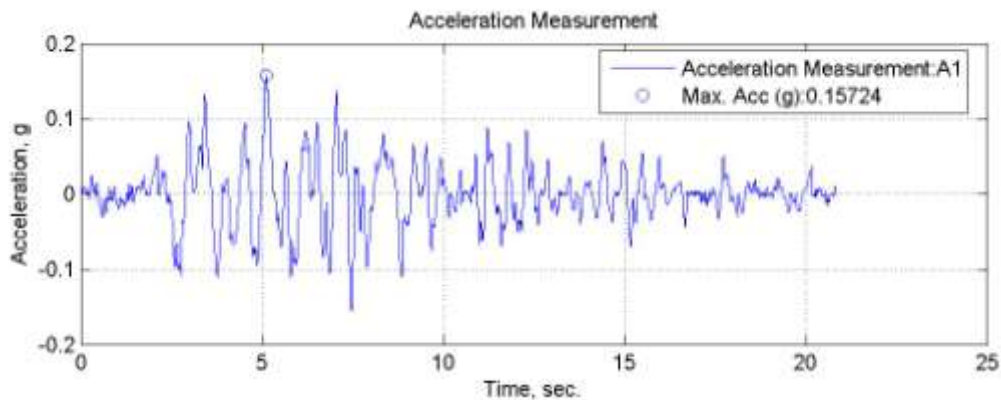


Figure 7.96. A1, acceleration time history of TC15 specimen tested under 0°C.

The pore water pressure change of TC15 specimen is shown in Figure 7.97. It is observed that the pore water pressure value is almost zero during the test. The acceleration time histories of A2 and A3 accelerometers are shown in Figure 7.98. The A2 and A3 acceleration values measured by the accelerometers within the soil and compared with A1 base input acceleration. The maximum A3 acceleration value is measured as 0.14g, and the

maximum A2 acceleration value is measured as 0.09g. The maximum lateral displacement value is measured as 3.44 cm. (Figure 7.99).

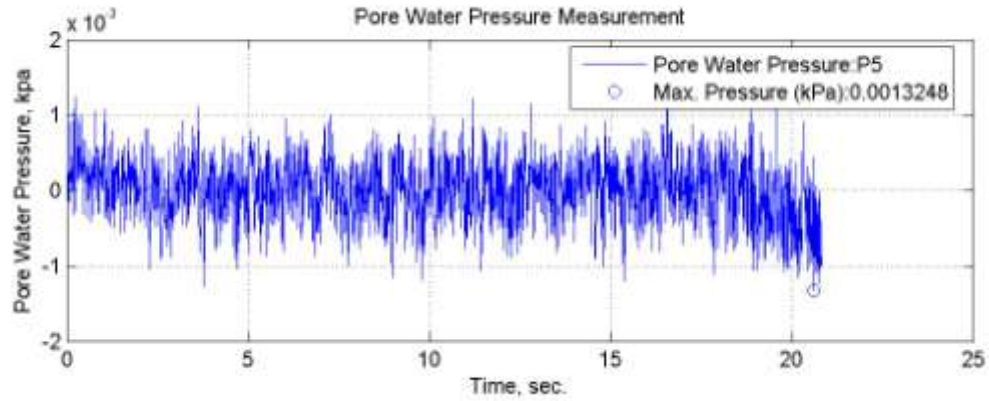


Figure 7.97. Pore water pressure change of TC15 specimen tested under 0°C.

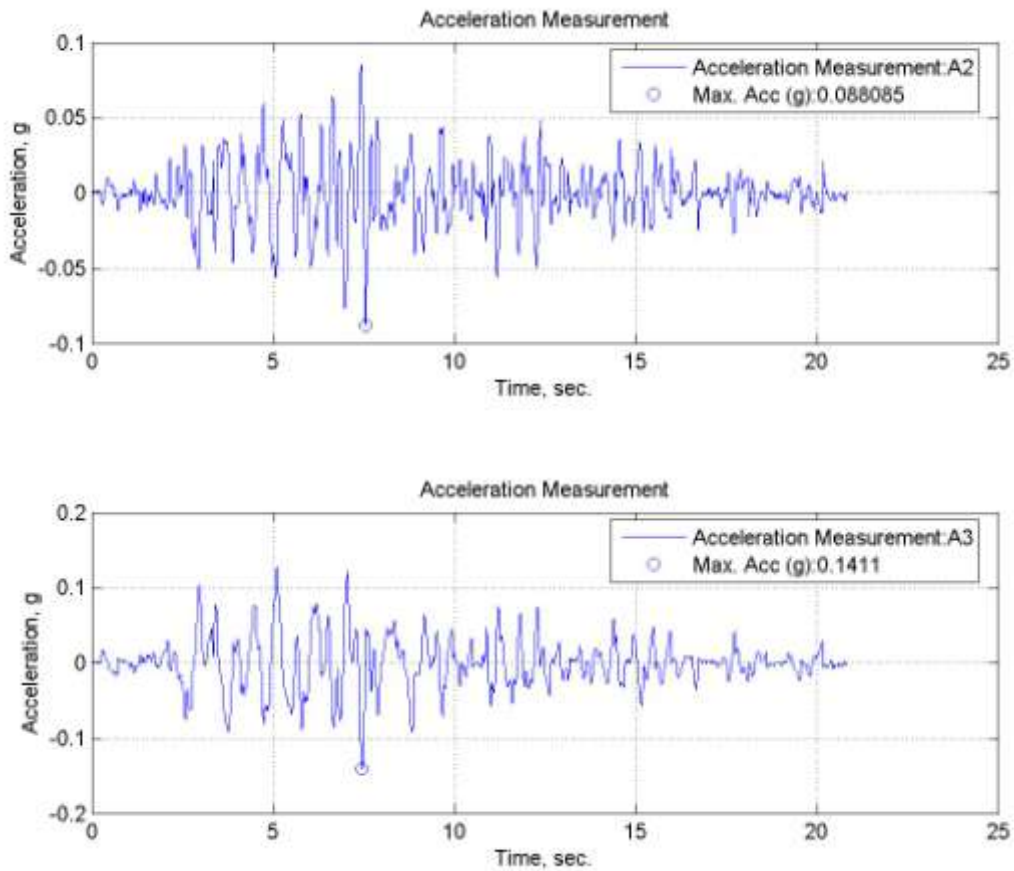


Figure 7.98. Time histories of accelerations of TC15 specimen tested under 0°C.

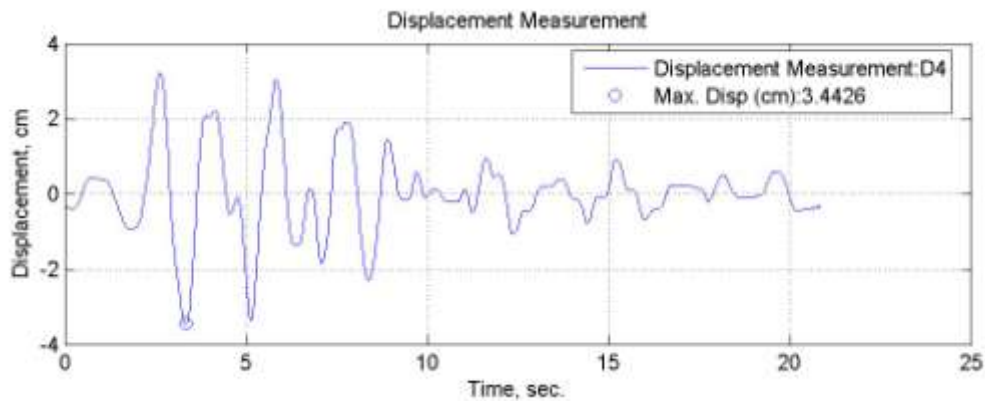


Figure 7.99. Lateral displacement time history for TC15 specimen tested under 0°C.

7.4.1.8. İzmit (E-W) Earthquake - TC20 Specimen. TC20 specimen is prepared in a large bowl and saturated with water. Then it is filled into the shear box. Specimen is prepared with $D_r = 0.40$ relative density. The temperature of specimen is arranged as 0°C. and İzmit (E-W) earthquake motion is applied to the table. The acceleration time history, displacement time history and pore water pressure change graphs are obtained. The acceleration time history of A1 accelerometer is given in Figure 7.100. Maximum acceleration value of A1 base input accelerometer is 0.18g.

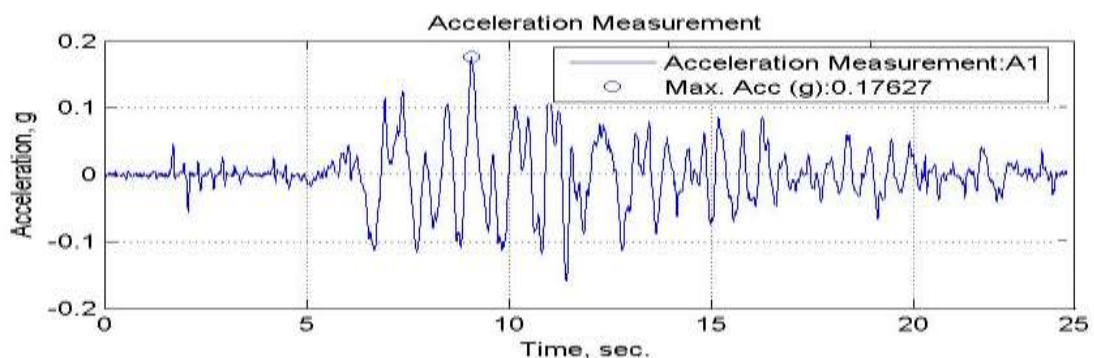


Figure 7.100. A1, acceleration time history of TC20 specimen tested under 0°C.

The pore water pressure change of the specimen is shown in Figure 7.101. It is observed that the pore water pressure value is almost zero during the test. The acceleration time histories of A2 and A3 accelerometers are shown in Figure 7.102. The acceleration values are measured by A2 and A3 accelerometers and compared with A1 base input

acceleration. A3 is the accelerometer placed at upper layer of soil. The maximum A3 acceleration value is measured as 0.50g, and the maximum A2 acceleration value is measured as 0.13g. The maximum A1 base input acceleration is 0.18g. The maximum lateral displacement value is measured as 4.47 cm. (Figure 7.103).

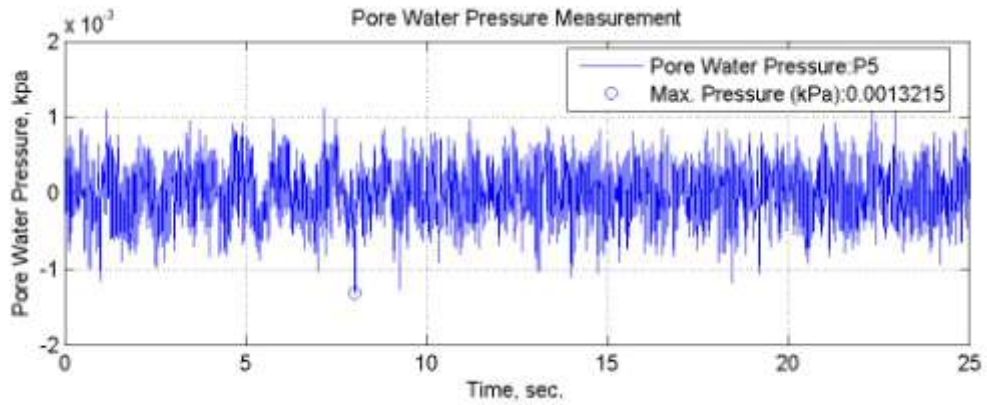


Figure 7.101. Pore water pressure change of TC20 specimen tested under 0°C.

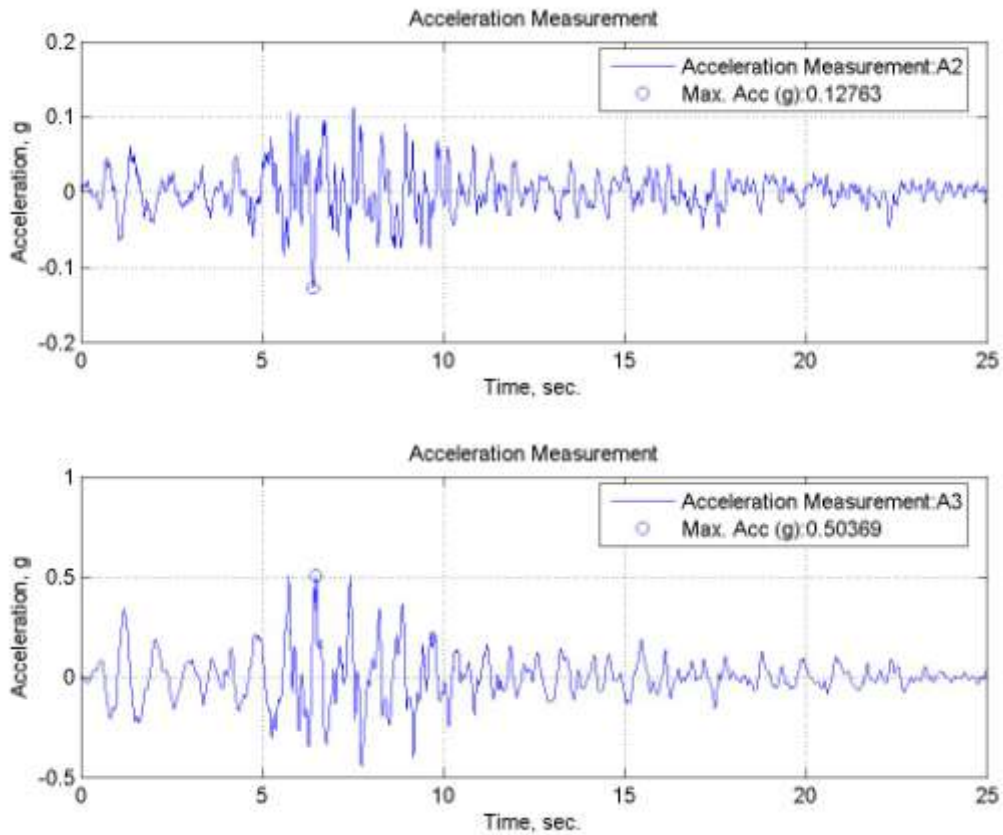


Figure 7.102. Time histories of accelerations of TC20 specimen tested under 0°C.

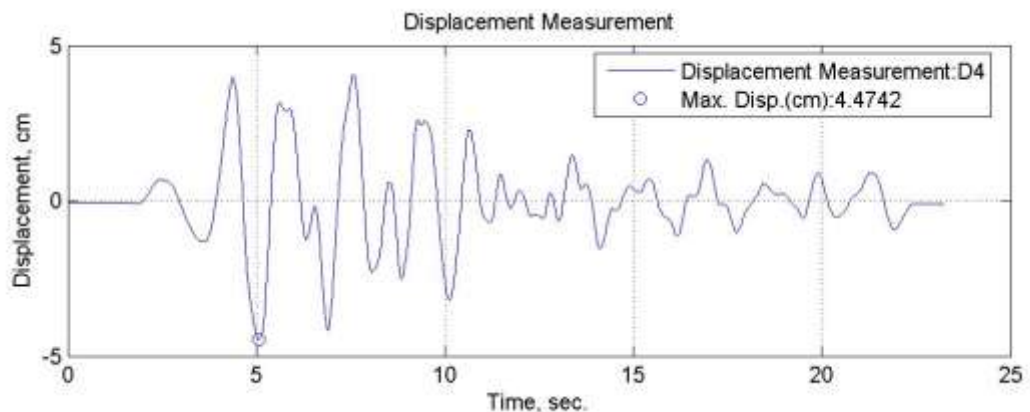


Figure 7.103. Lateral displacement time history for TC20 specimen tested under 0°C.

7.4.1.9. İzmit (E-W) Earthquake - TC30 Specimen. TC30 specimen is prepared in a large bowl and saturated with water. Then it is filled into the shear box. Specimen is prepared with $D_r = 0.40$ relative density. The temperature of specimen is arranged as 0°C. and İzmit (E-W) earthquake motion is applied to the table. The acceleration time history, displacement time history and pore water pressure change graphs are obtained. The acceleration time history of A1 accelerometer is given in Figure 7.104. Maximum acceleration value of A1 base input accelerometer is 0.15g.

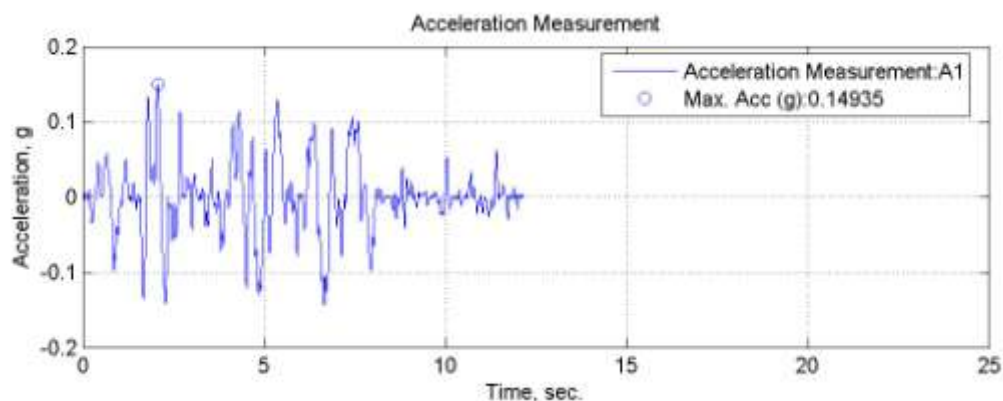


Figure 7.104. A1, acceleration time history of TC30 specimen tested under 0°C.

The pore water pressure change of the specimen is shown in Figure 7.105. It is observed that the pore water pressure value is almost zero during the test. The acceleration time histories of A2 and A3 accelerometers are shown in Figure 7.106. The acceleration

values are measured by the accelerometers within the soil and compared with A1 base input acceleration. A3 is the accelerometer placed at upper layer of soil. The maximum A3 acceleration value is measured as 0.14g. and the maximum A2 acceleration value is measured as 0.13g. The maximum lateral displacement value is measured as 4.38 cm. (Figure 7.107).

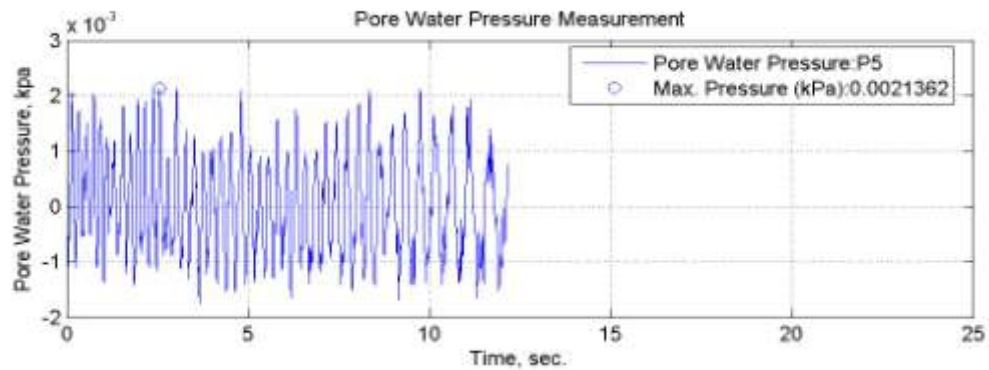


Figure 7.105. Pore water pressure change of TC30 specimen tested under 0°C.

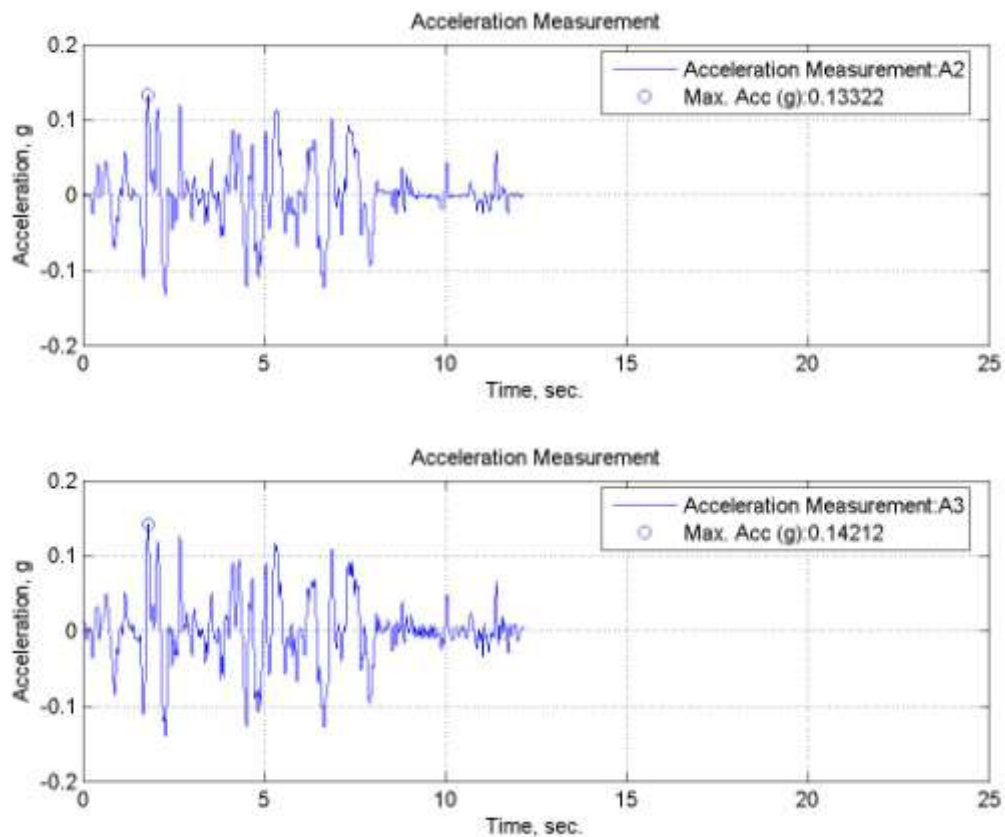


Figure 7.106. Time histories of accelerations of TC30 specimen tested under 0°C.

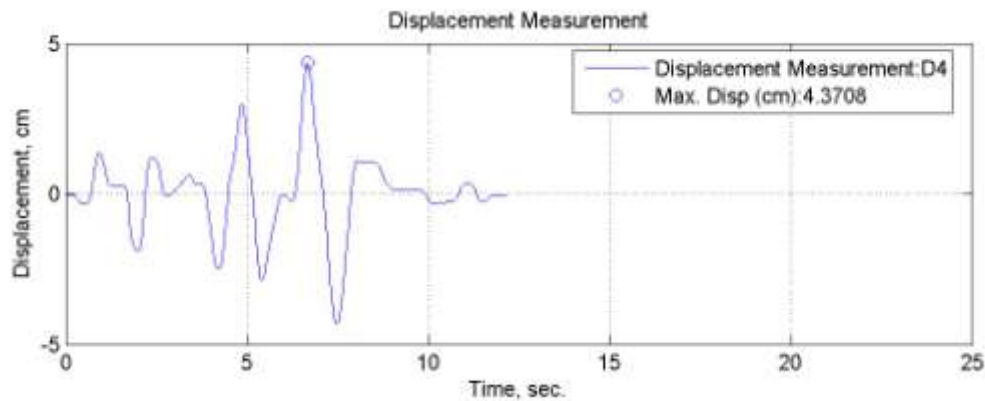


Figure 7.107. Lateral displacement time history for TC30 specimen tested under 0°C.

7.4.2. Tests Performed Under Room Temperature

7.4.2.1. İzmit (E-W) Earthquake - 100% Sand Specimen (S). Shaking Table Tests are performed with only sand at room temperature. The specimen is prepared in a large bowl and saturated with water. Then it is filled into the shear box. The earthquake record of İzmit (E-W) is applied to the specimen. The acceleration, pore water pressure and lateral displacements values were determined carefully. The acceleration time history of A1 accelerometer on shaking table surface is given in Figure 7.108. Maximum acceleration value of A1 base input accelerometer is 0.18g.

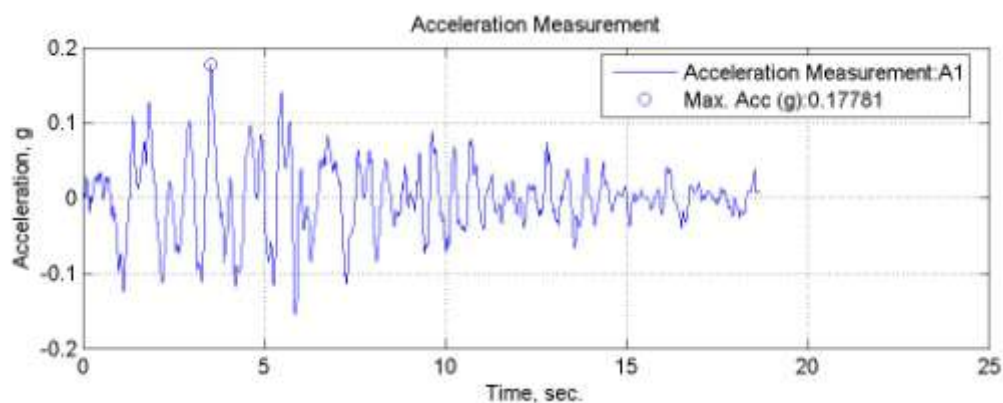


Figure 7.108. A1, acceleration time history of sand specimen tested at room temperature.

The pore water pressure change of the specimen is shown in Figure 7.109. The acceleration time histories of A2 and A3 accelerometers are shown in Figure 7.110. A3 is

the accelerometer placed at upper layer of soil. The acceleration values are measured by the submersible accelerometers within the soil and compared with A1 base input acceleration. The maximum A2 acceleration value is measured as 0.17g, and the maximum A3 acceleration value is measured as 0.06g. The maximum lateral displacement value is measured as 3.97 cm. (Figure 7.111).

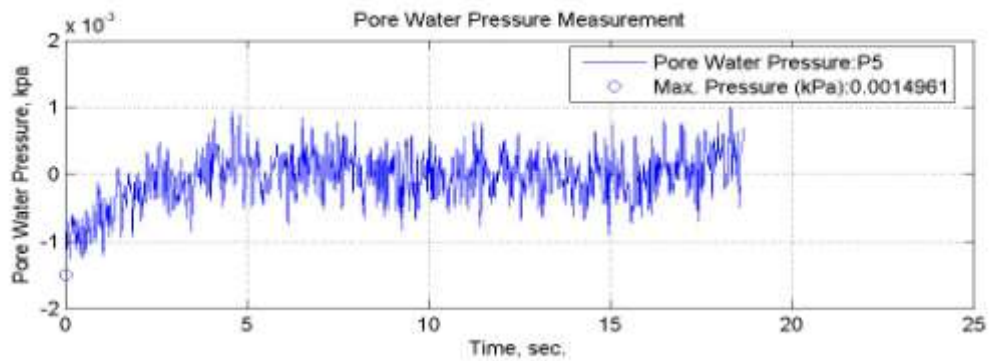


Figure 7.109. Pore water pressure change of sand specimen tested at room temperature.

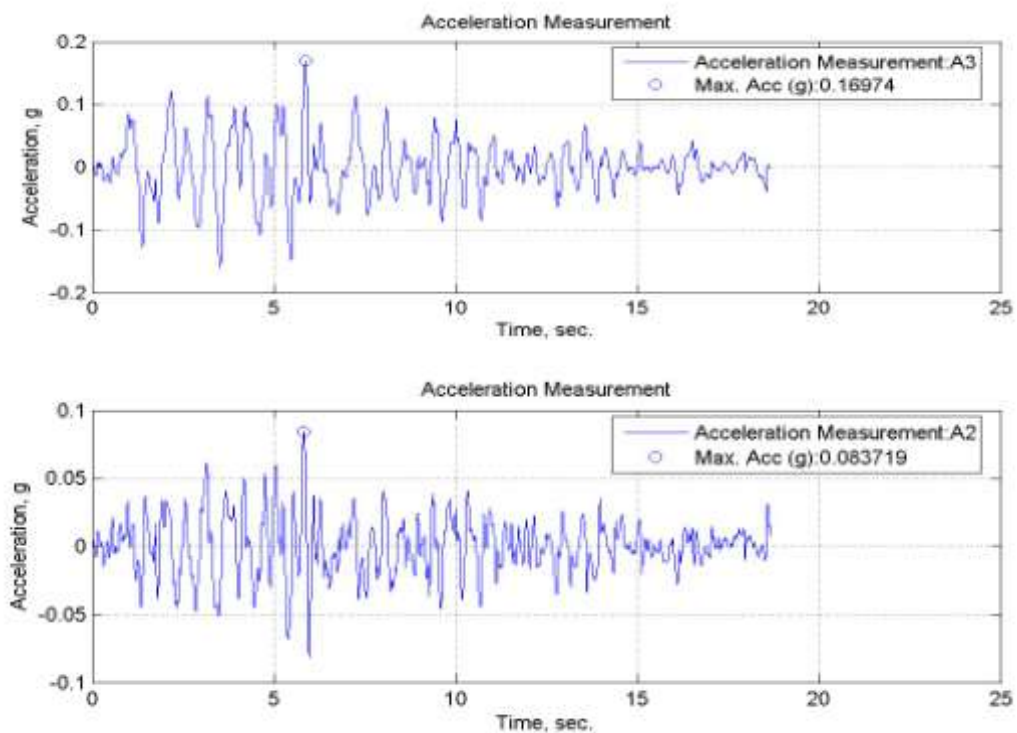


Figure 7.110. Time histories of accelerations of sand specimen tested at room temperature.

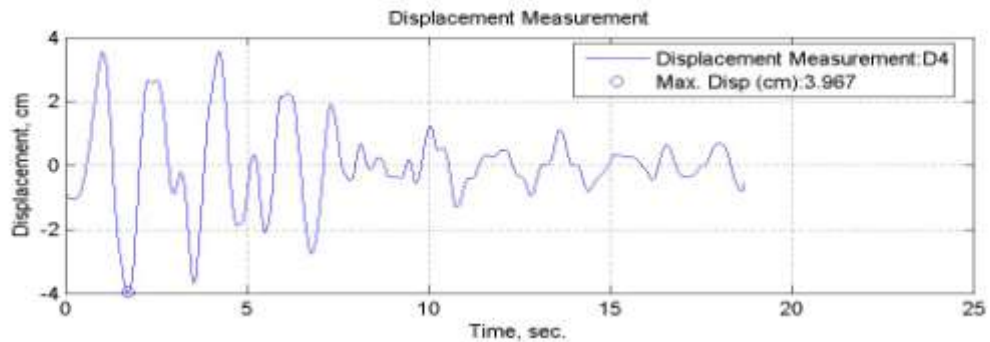


Figure 7.111. Lateral displacement time history for sand specimen tested at room temperature.

7.4.2.2. İzmit (E-W) Earthquake - TB10 Specimen. TB10 specimen is prepared in a large bowl and saturated with water. Then it is filled into the shear box. Specimen is prepared with $D_r = 0.40$ relative density. The temperature of specimen is arranged as 20°C room temperature (Figure 7.112) and İzmit (E-W) earthquake motion is applied to the table. The acceleration time history, displacement time history and pore water pressure change graphs are obtained. The acceleration time history A1 accelerometer is given in Figure 7.113. Maximum acceleration value of A1 accelerometer is $0.18g$.



Figure 7.112. TB10 specimen tested on shaking table at room temperature.

The pore water pressure change of the specimen is shown in Figure 7.114. It is observed that the pore water pressure value is almost zero during the test. The acceleration time histories of A2 and A3 accelerometers are shown in Figure 7.115. The acceleration values are measured by the accelerometers within the soil and compared with A1 base input acceleration. A3 is the accelerometer placed at upper layer of soil. The maximum A3 acceleration value is measured as 0.19g, and the maximum A2 acceleration value is measured as 0.18g. The maximum lateral displacement value is measured as 4.27 cm. (Figure 7.116).

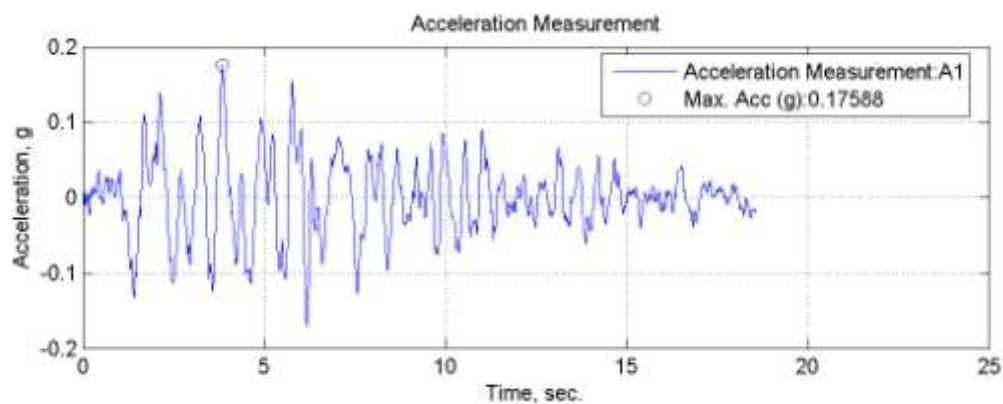


Figure 7.113. A1, acceleration time history of TB10 specimen tested at room temperature.

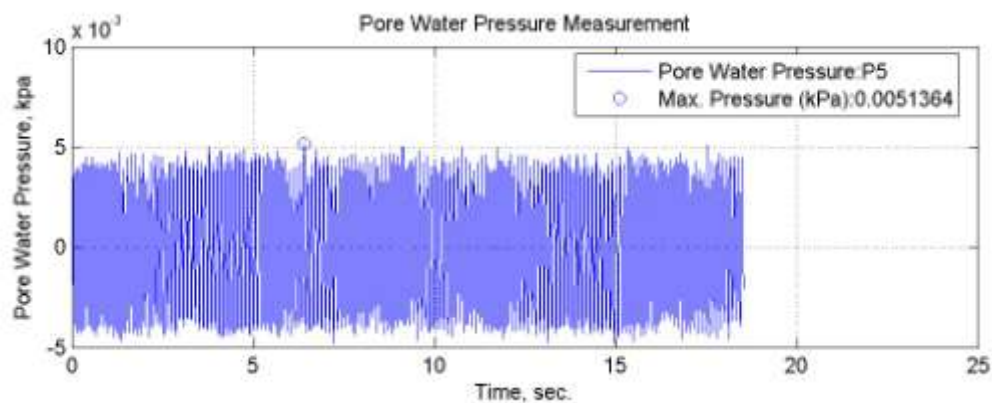


Figure 7.114. Pore water pressure change of TB10 specimen tested at room temperature.

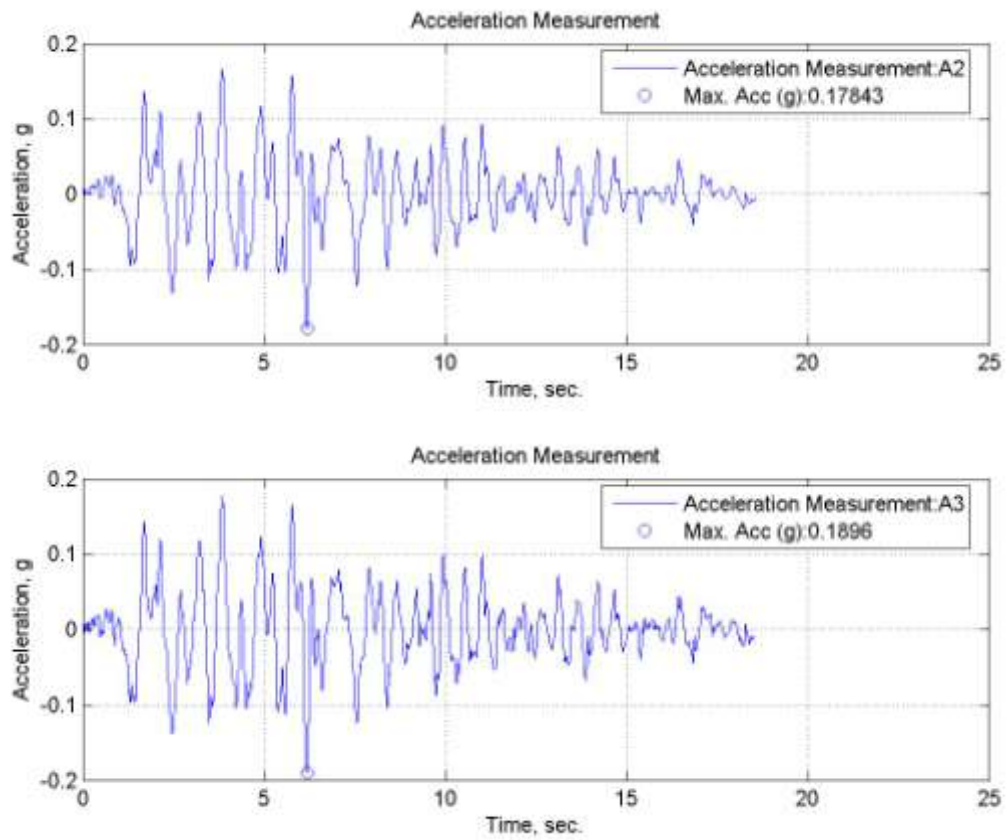


Figure 7.115. Time histories of accelerations of TB10 specimen tested at room temperature.

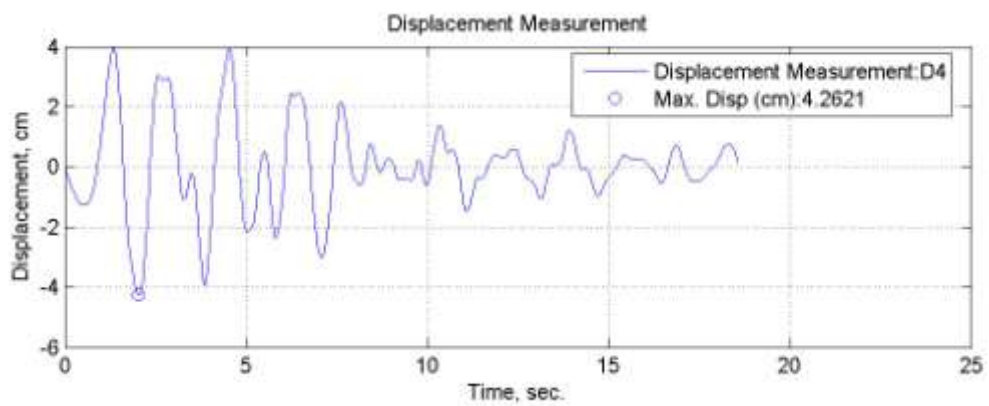


Figure 7.116. Lateral displacement time history for TB10 specimen tested at room temperature.

7.4.2.3. İzmit (E-W) Earthquake - TB15 Specimen. TB15 specimen is prepared in a large bowl and saturated with water. Then it is filled into the shear box. Specimen is prepared with $D_r=0.40$ relative density. The temperature of specimen is arranged as 20°C room temperature. and İzmit (E-W) earthquake motion is applied to the table. The acceleration time history, displacement time history and pore water pressure change graphs are obtained. The acceleration time history of A1 is given in Figure 7.117. Maximum acceleration value of A1 accelerometer is $0.17g$.

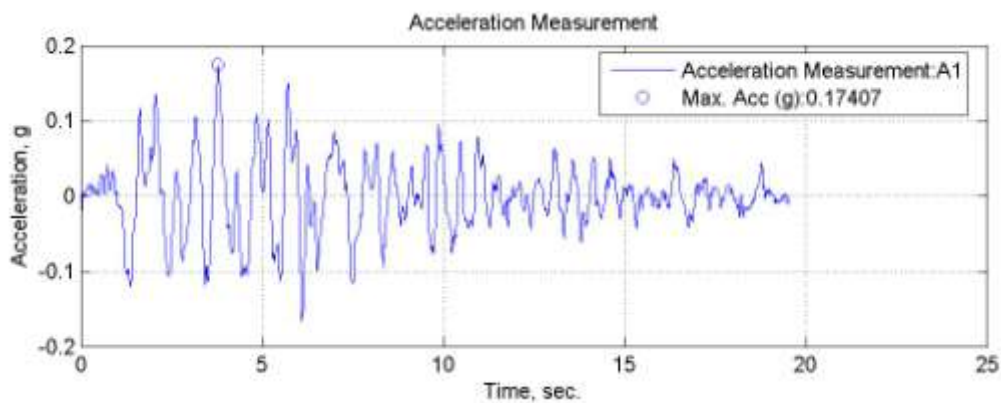


Figure 7.117. A1, acceleration time history of TB15 specimen tested at room temperature.

The pore water pressure change of the specimen is shown in Figure 7.118. It is observed that the pore water pressure value is almost zero during the test. The acceleration time histories of A2 and A3 accelerometers are shown in Figure 7.119. The maximum A3 acceleration value is measured as $0.20g$. and the maximum A2 acceleration value is measured as $0.16g$. The maximum lateral displacement value is measured as 4.22 cm . (Figure 7.120).

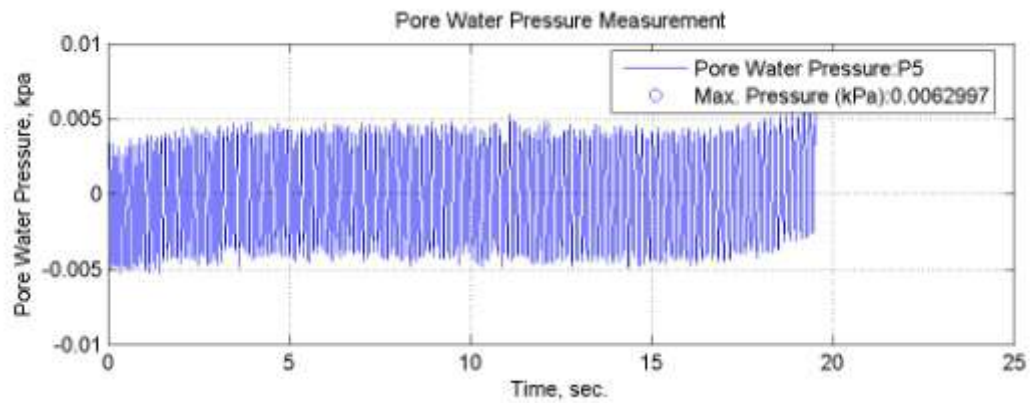


Figure 7.118. Pore water pressure change of TB15 specimen tested at room temperature.

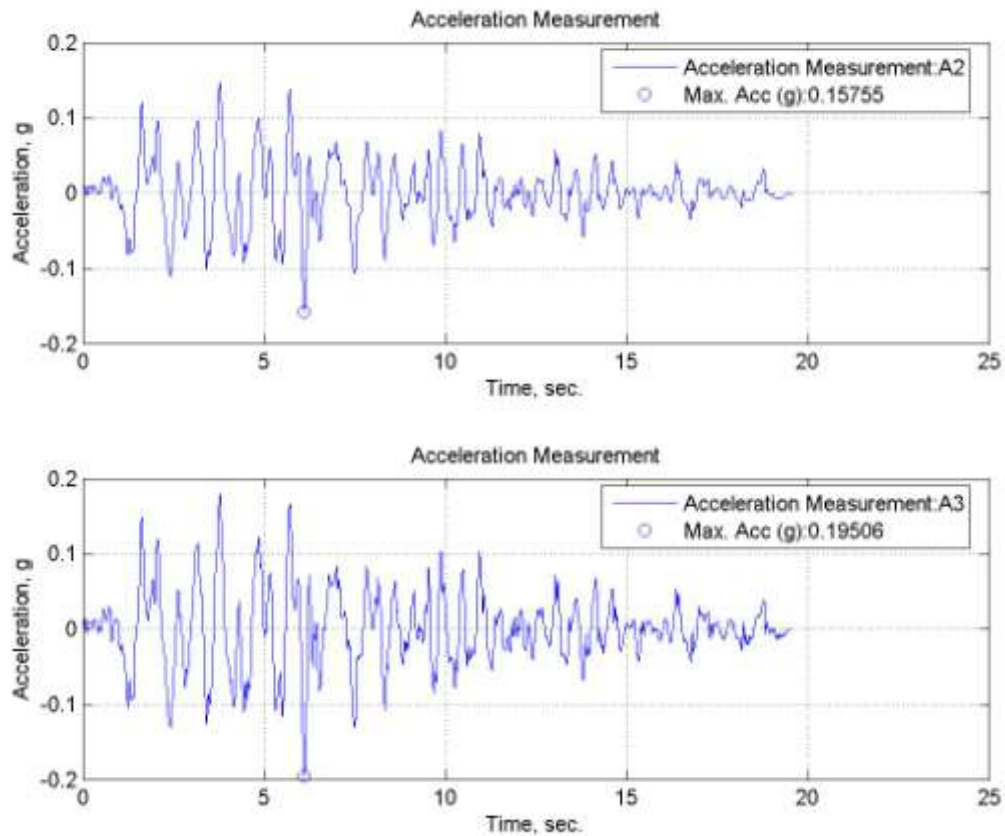


Figure 7.119. Time histories of accelerations of TB15 specimen tested at room temperature.

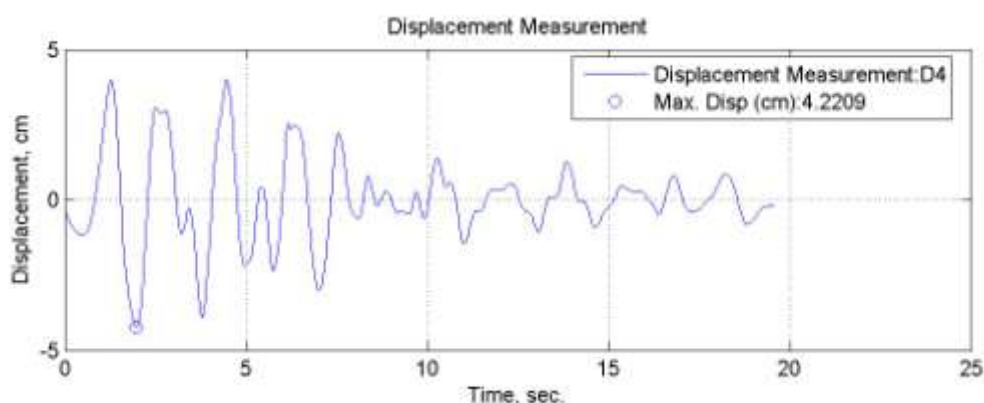


Figure 7.120. Lateral displacement time history for TB15 specimen tested at room temperature.

7.4.2.4. İzmit (E-W) Earthquake - TB20 Specimen. TB20 specimen is prepared in a large bowl and saturated with water. Then it is filled into the shear box. Specimen is prepared with $D_r = 0.40$ relative density. The temperature of specimen is arranged as 20°C room temperature. İzmit (E-W) earthquake motion is applied to the table. The acceleration time history, displacement time history and pore water pressure change graphs are obtained. The acceleration time history of A1 accelerometer which is fixed over shaking table surface is given in Figure 7.121. Maximum acceleration value of A1 accelerometer is $0.18g$.

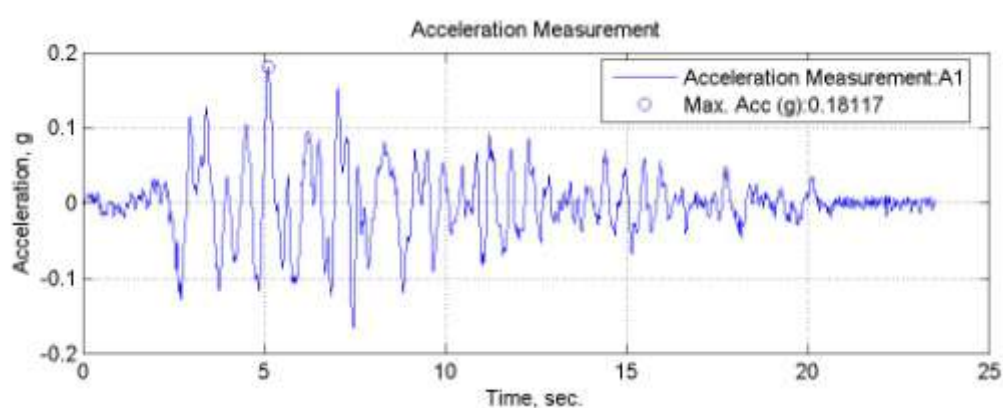


Figure 7.121. A1, acceleration time history of TB20 specimen tested at room temperature.

The pore water pressure change of the specimen is shown in Figure 7.122. It is observed that the pore water pressure value is almost zero during the test. The acceleration time histories of A2 and A3 accelerometers are shown in Figure 7.123. A3 is the

accelerometer placed at upper layer of soil. The maximum A3 acceleration value is measured as 0.19g. and the maximum A2 acceleration value is measured as 0.17g. The maximum lateral displacement value is measured as 4.02 cm. (Figure 7.124).

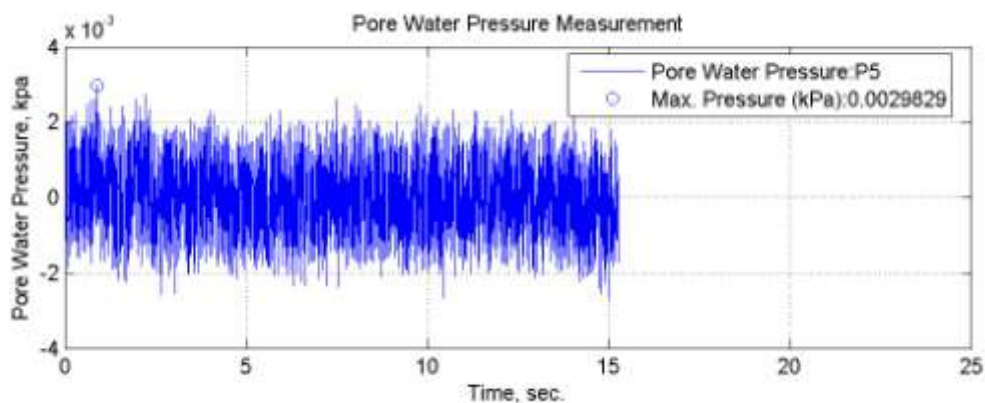


Figure 7.122. Pore water pressure change of TB20 specimen tested at room temperature.

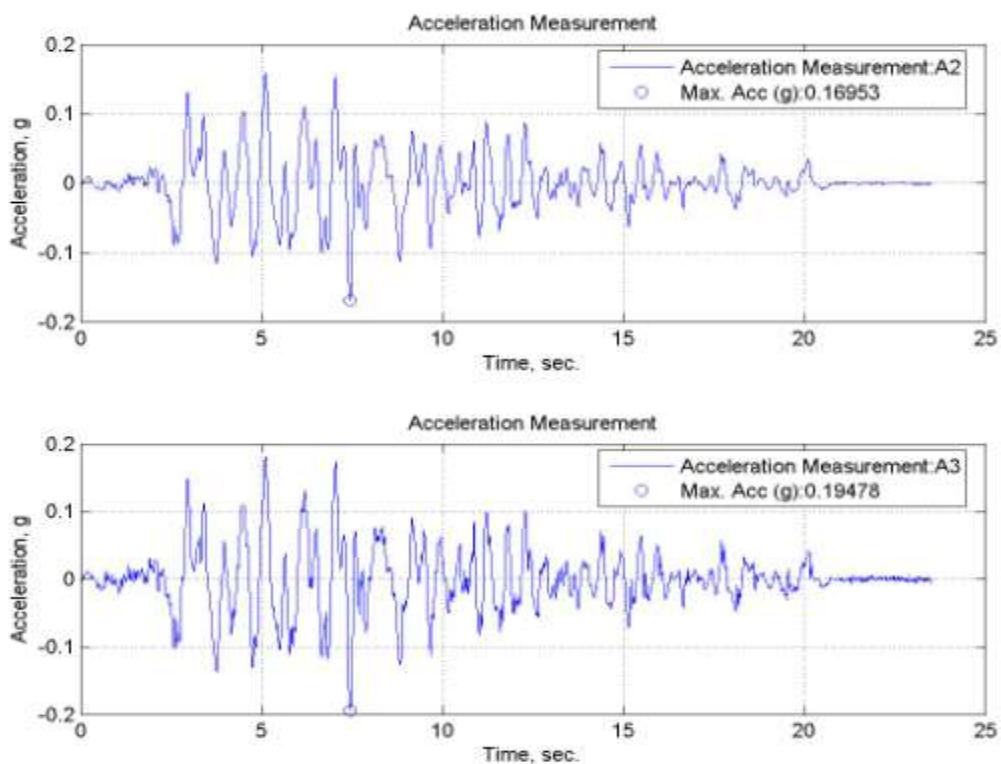


Figure 7.123. Time histories of accelerations of TB20 specimen tested at room temperature.

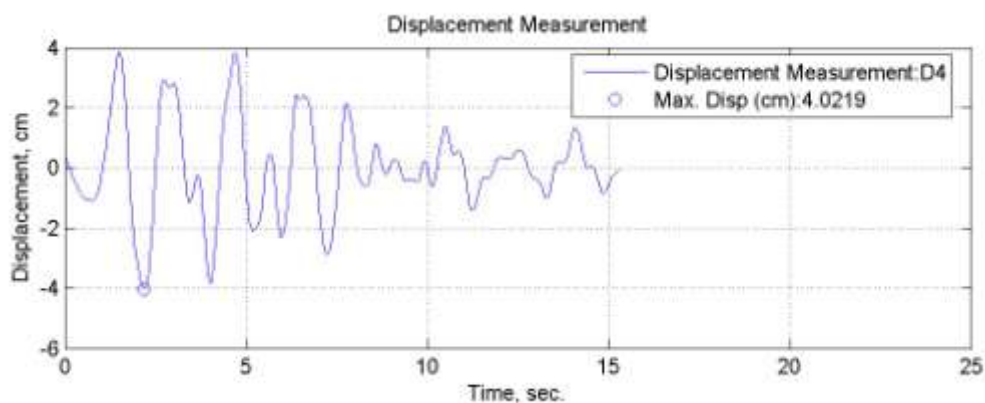


Figure 7.124. Lateral displacement time history for TB20 specimen tested at room temperature.

7.4.2.5. İzmit (E-W) Earthquake - TB30 Specimen. TB30 specimen is prepared in a large bowl and saturated with water. Then it is filled into the shear box. Specimen is prepared with $D_r = 0.40$ relative density. The temperature of specimen is arranged as 20°C room temperature. İzmit (E-W) earthquake motion is applied to the table. The acceleration time history, displacement time history and pore water pressure change graphs are obtained. The acceleration time history of A1 base accelerometer which is fixed over shaking table surface is given in Figure 7.125. Maximum acceleration value of A1 accelerometer is 0.17g.

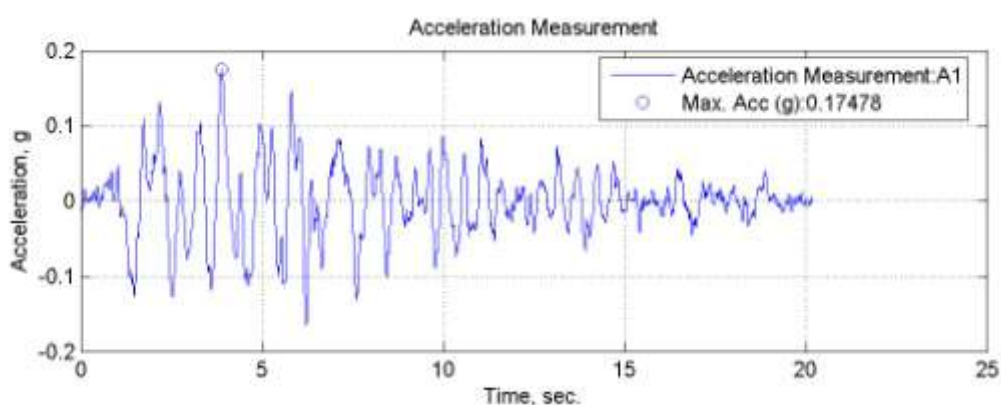


Figure 7.125. A1, acceleration time history of TB30 specimen tested at room temperature.

The pore water pressure change of TB30 specimen is shown in Figure 7.126. It is observed that the pore water pressure value is almost zero during the test. The acceleration

time histories of A2 and A3 accelerometers are shown in Figure 7.127. The maximum A3 acceleration value is measured as 0.20g, and the maximum A2 acceleration value is measured as 0.18g. The maximum lateral displacement value is measured as 4.30 cm. (Figure 7.128).

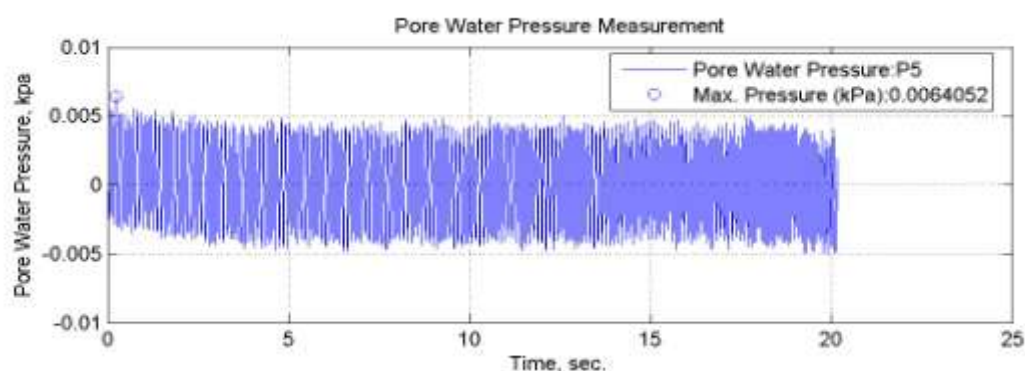


Figure 7.126. Pore water pressure change of TB30 specimen tested at room temperature.

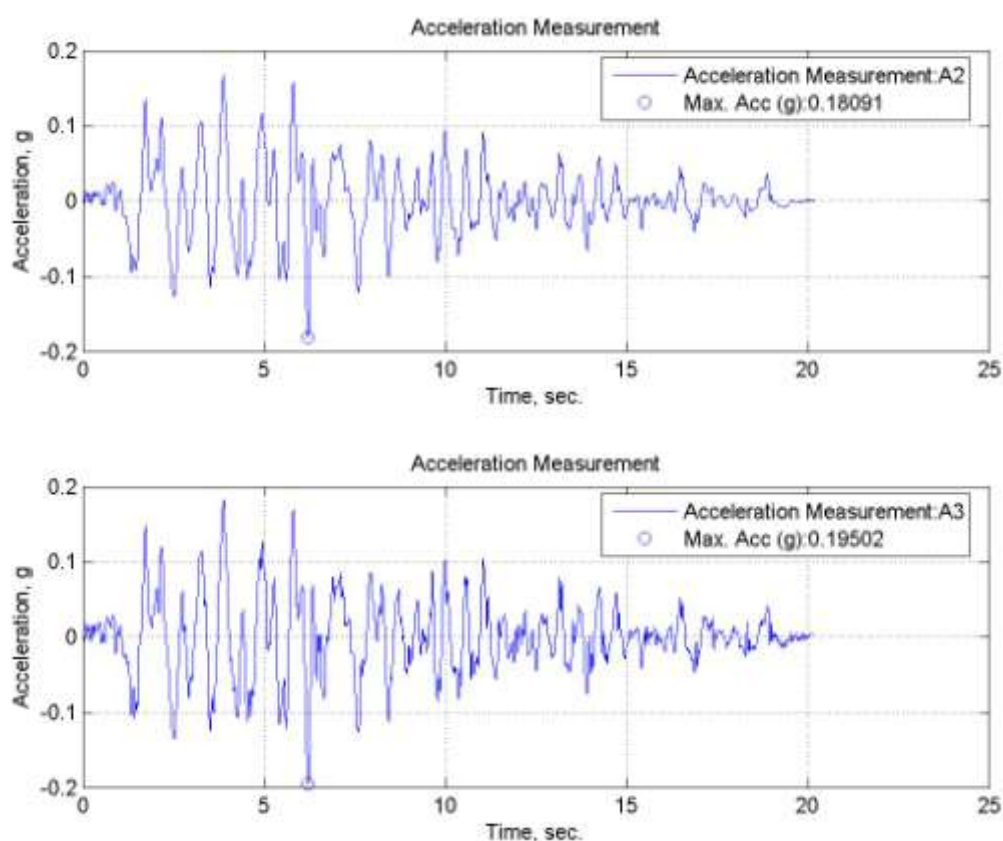


Figure 7.127. Time histories of accelerations of TB30 specimen tested at room temperature.

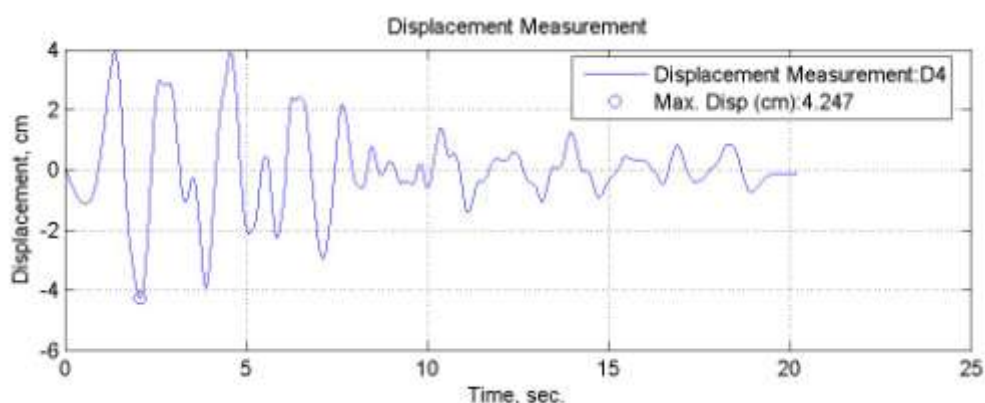


Figure 7.128. Lateral displacement time history for TB30 specimen tested at room temperature.

7.4.2.6. İzmit (E-W) Earthquake - TC10 Specimen. TC10 specimen is prepared in a large bowl and saturated with water. Then it is filled into the shear box. Specimen is prepared with $D_r = 0.40$ relative density. The temperature of specimen is arranged as 20°C room temperature. İzmit (E-W) earthquake motion is applied to the table. The acceleration time history, displacement time history and pore water pressure change graphs are obtained. The acceleration time history of A1 accelerometer which is fixed over shaking table surface is given in Figure 7.129. Maximum acceleration value of A1 accelerometer is 0.190g.

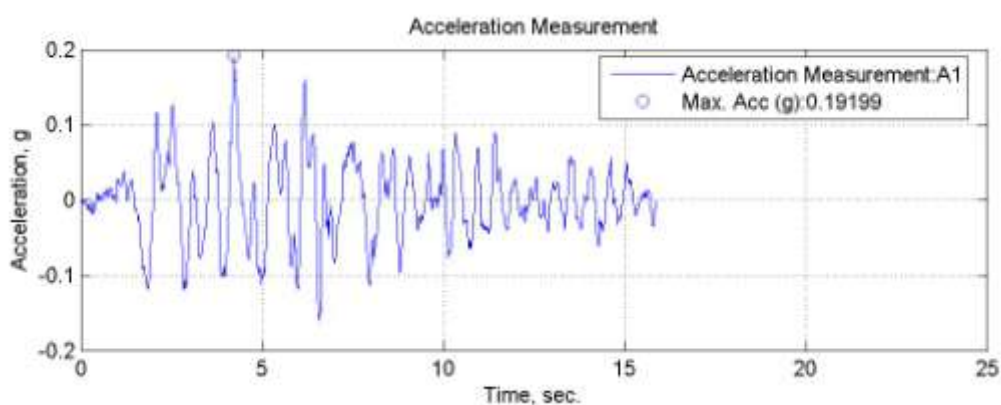


Figure 7.129. A1, acceleration time history of TC10 specimen tested at room temperature.

The pore water pressure change of the specimen is shown in Figure 7.130. It is observed that the pore water pressure value is almost zero during the test. The acceleration time histories of A2 and A3 accelerometers are shown in Figure 7.131. The acceleration

values are measured by the accelerometers A2 and A3 within the soil and compared with A1 base input acceleration. The maximum A3 acceleration value is measured as 0.19g, and the maximum A2 acceleration value is measured as 0.18g. The maximum lateral displacement value is measured as 3.93 cm. (Figure 7.132).

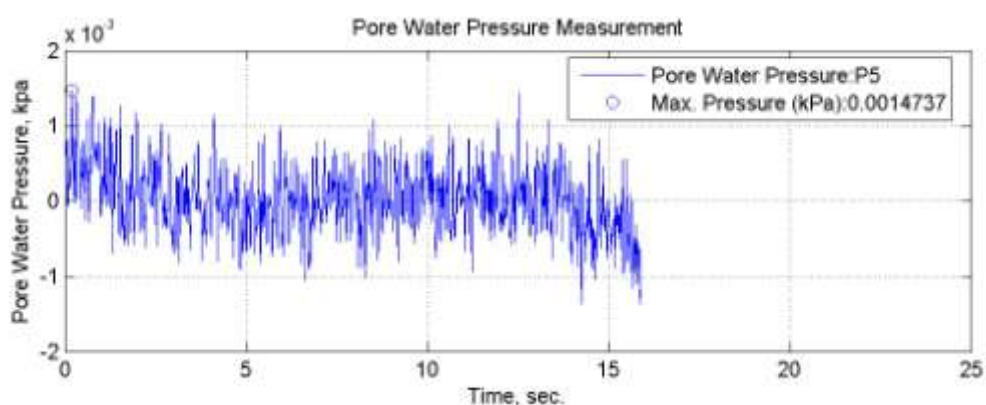


Figure 7.130. Pore water pressure change of TC10 specimen tested at room temperature.

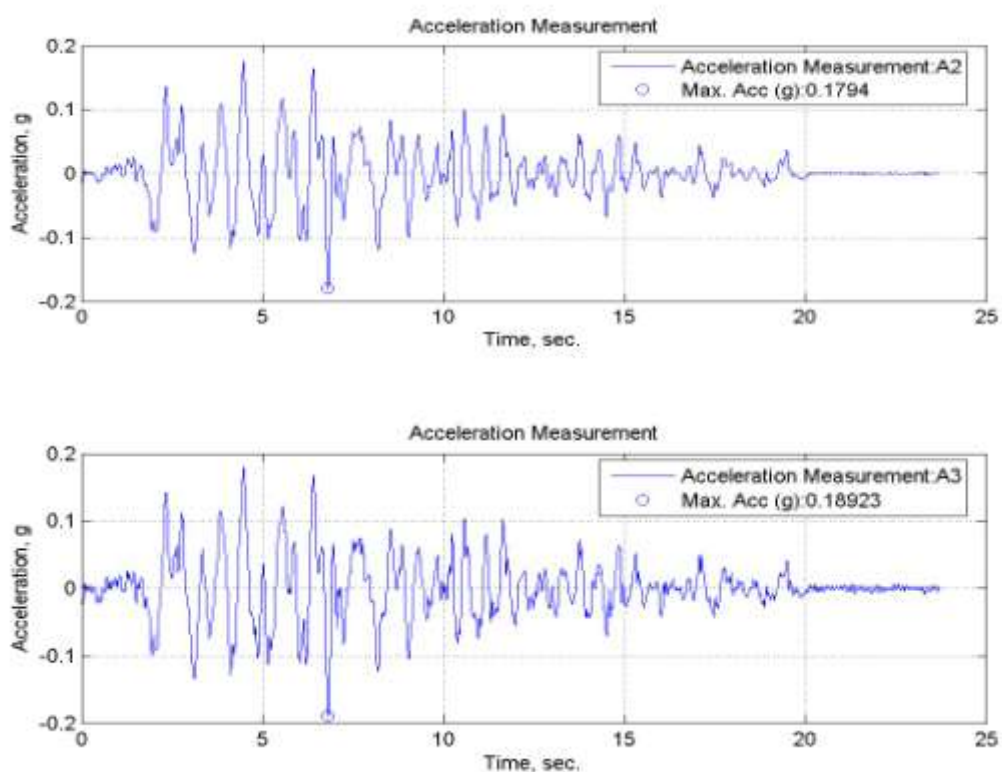


Figure 7.131. Time histories of accelerations of TC10 specimen tested at room temperature.

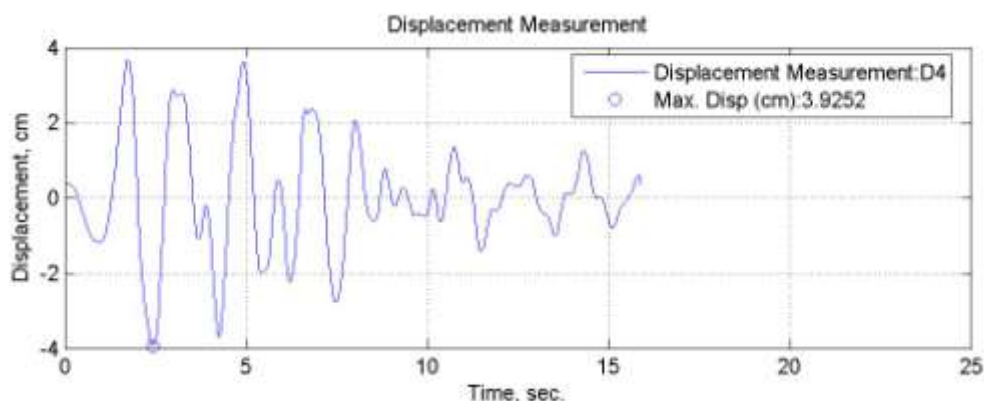


Figure 7.132. Lateral displacement time history for TC10 specimen tested at room temperature.

7.4.2.7. İzmit (E-W) Earthquake - TC15 Specimen. TC15 specimen is prepared in a large bowl and saturated with water. Then it is filled into the shear box. Specimen is prepared with $D_r = 0.40$ relative density. The temperature of specimen is arranged as 20°C room temperature. and İzmit (E-W) earthquake motion is applied to the table. The acceleration time history, displacement time history and pore water pressure change graphs are obtained. The acceleration time history of A1 accelerometer is given in Figure 7.133. Maximum acceleration value of A1 accelerometer is 0.18g.

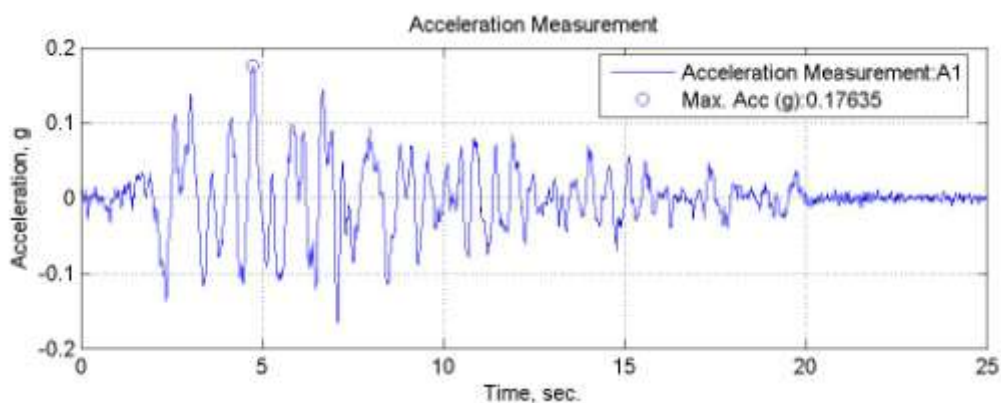


Figure 7.133. A1, acceleration time history of TC15 specimen tested at room temperature.

The pore water pressure change of the specimen is shown in Figure 7.134. It is observed that the pore water pressure value is almost zero during the test. The acceleration time histories of A2 and A3 accelerometers are shown in Figure 7.135. The acceleration

time histories are measured by the accelerometers within the soil and compared with A1 base input acceleration. The maximum A3 acceleration value is measured as 0.19g, and the maximum A2 acceleration value is measured as 0.17g. The maximum lateral displacement value is measured as 4.00 cm. (Figure 7.136).

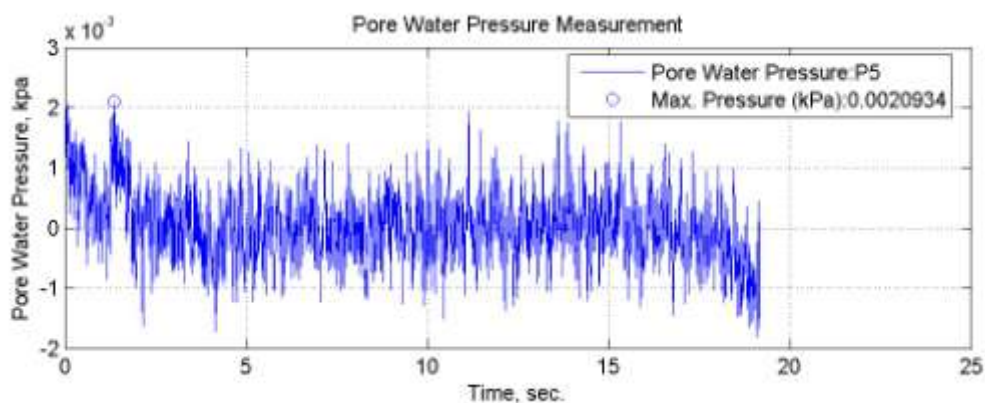


Figure 7.134. Pore water pressure change of TC15 specimen tested at room temperature.

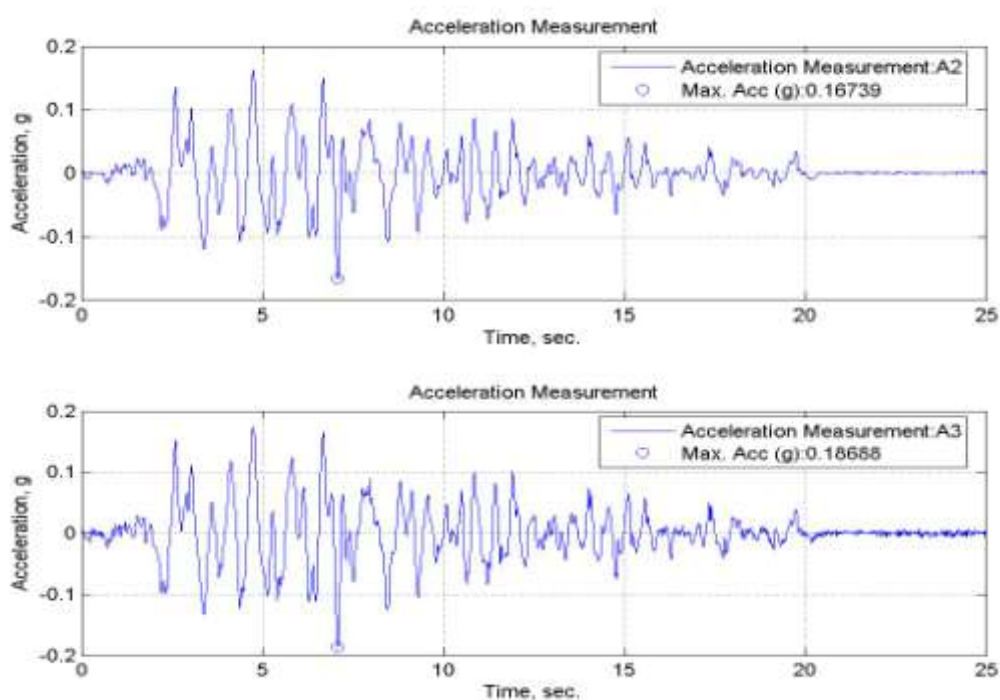


Figure 7.135. Time histories of accelerations of TC15 specimen tested at room temperature.

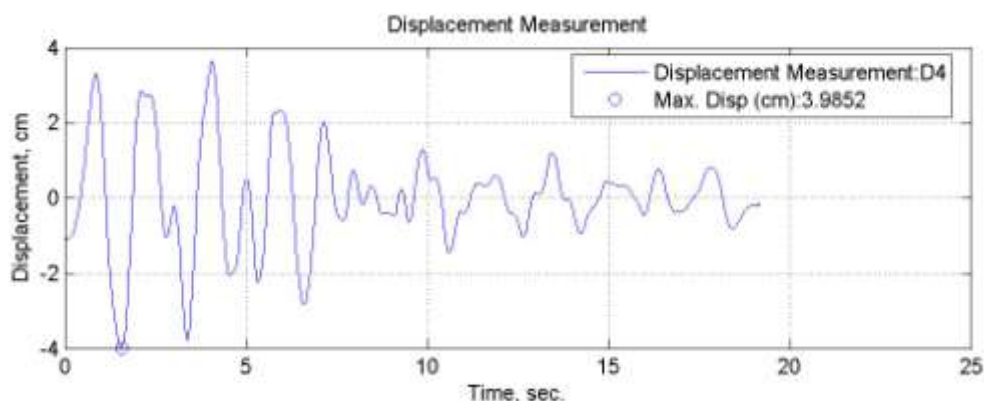


Figure 7.136. Lateral displacement time history for TC15 specimen tested at room temperature.

7.4.2.8. İzmit (E-W) Earthquake - TC20 Specimen. TC20 specimen is prepared in a large bowl and saturated with water. Then it is filled into the shear box. Specimen is prepared with $D_r = 0.40$ relative density. The temperature of specimen is arranged as 20°C room temperature. and İzmit (E-W) earthquake motion is applied to the table. The acceleration time history, displacement time history and pore water pressure change graphs are obtained. The acceleration time history of A1 accelerometer over shaking table surface is given in Figure 7.137. Maximum acceleration value of A1 accelerometer is 0.17g.

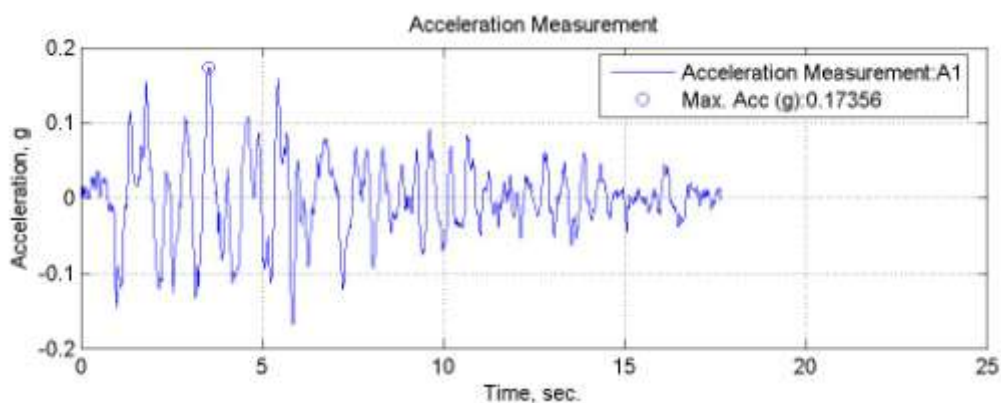


Figure 7.137. A1, acceleration time history of TC20 specimen tested at room temperature.

The pore water pressure change of the specimen is shown in Figure 7.138. It is observed that the pore water pressure value is almost zero during the test. The acceleration time histories of A2 and A3 accelerometers are shown in Figure 7.139. The acceleration values are measured by the accelerometers within the soil and compared with A1 base

input acceleration. The maximum A3 acceleration value is measured as 0.20g, and the maximum A2 acceleration value is measured as 0.18g. The maximum lateral displacement value is measured as 4.13 cm. (Figure 7.140).

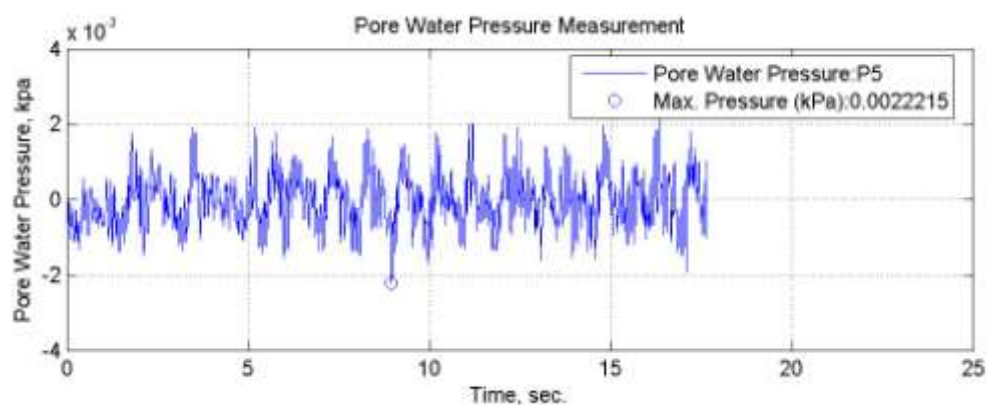


Figure 7.138. Pore water pressure change of TC20 specimen tested at room temperature.

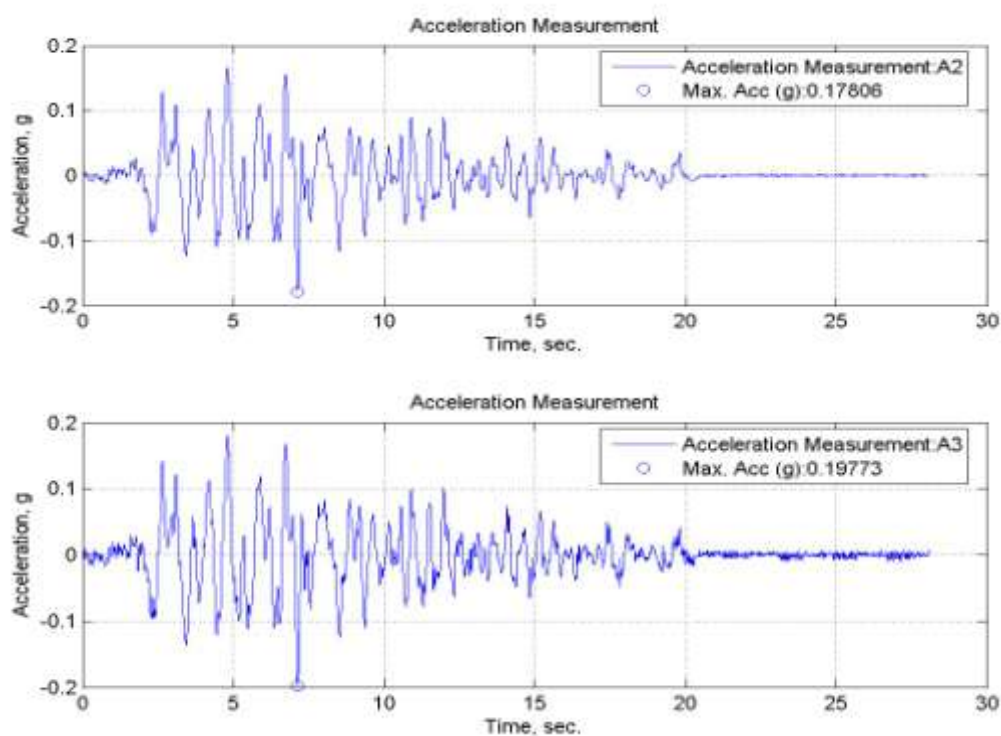


Figure 7.139. Time histories of accelerations of TC20 specimen tested at room temperature.

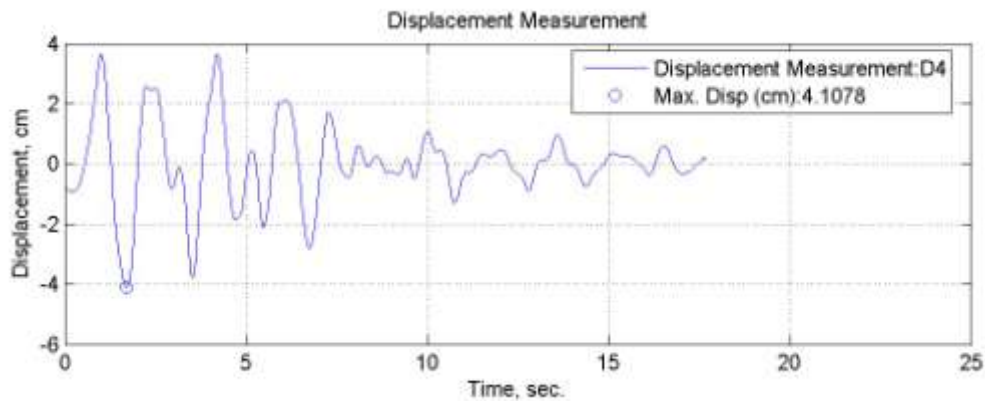


Figure 7.140. Displacement time history of TC20 specimen tested at room temperature.

7.4.2.9. İzmit (E-W) Earthquake - TC30 Specimen. TC20 specimen is prepared in a large bowl and saturated with water. Then it is filled into the shear box. Specimen is prepared with $D_r = 0.40$ relative density. The temperature of specimen is arranged as 20°C room temperature. and İzmit (E-W) earthquake ground motion is applied to the table. The acceleration time history, displacement time history and pore water pressure change graphs are obtained. The acceleration time history of A1 accelerometer which is fixed on the shaking table is given in Figure 7.141. Maximum acceleration value of A1 accelerometer is $0.18g$.

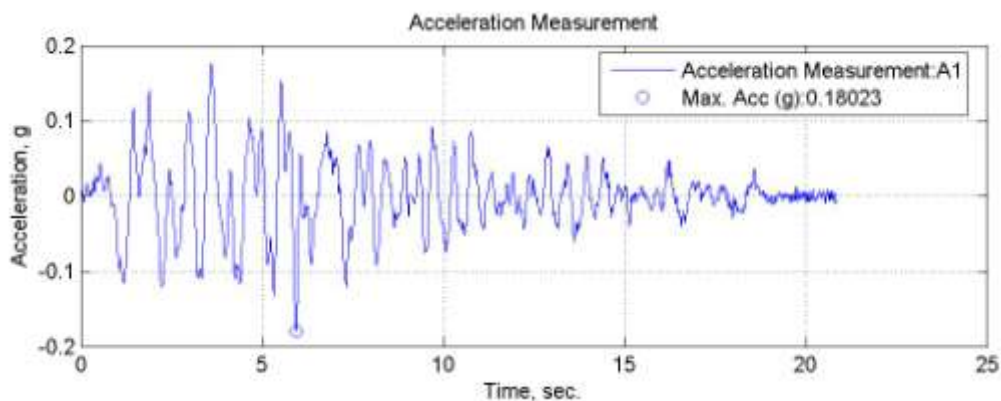


Figure 7.141. A1, acceleration time history of TC30 specimen tested at room temperature.

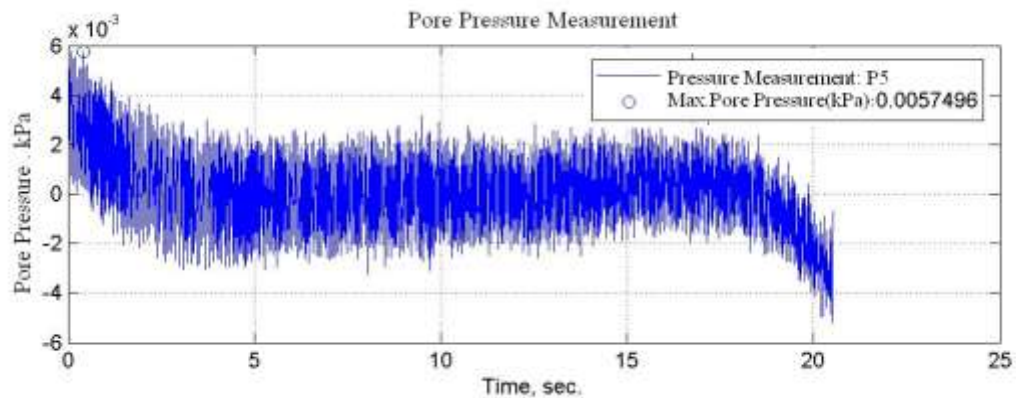


Figure 7.142. Pore water pressure change of TC30 specimen tested at room temperature.

The pore water pressure change of the specimen is shown in Figure 7.142. It is observed that the pore water pressure value is almost zero during the test. The acceleration time histories of A2 and A3 accelerometers are shown in Figure 7.143. The maximum A3 acceleration value is measured as 0.20g, and the maximum A2 acceleration value is measured as 0.18g. The maximum lateral displacement value is measured as 4.24 cm. (Figure 7.144).

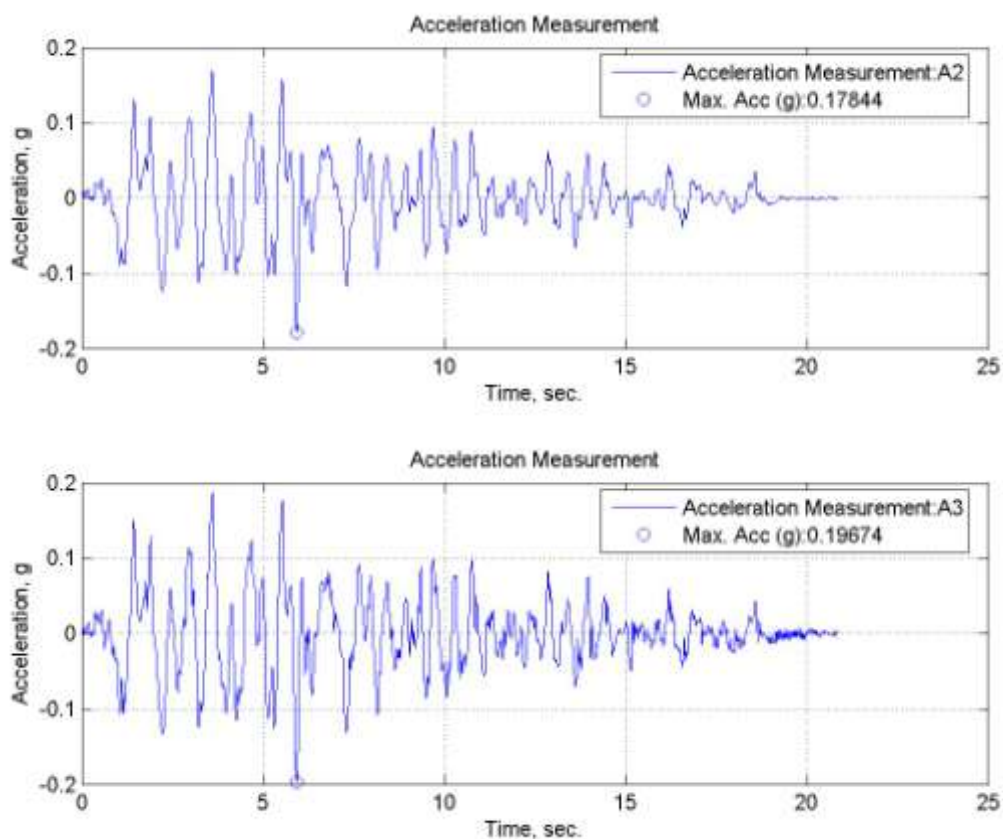


Figure 7.143 Time histories of accelerations of TC30 specimen tested at room temperature.

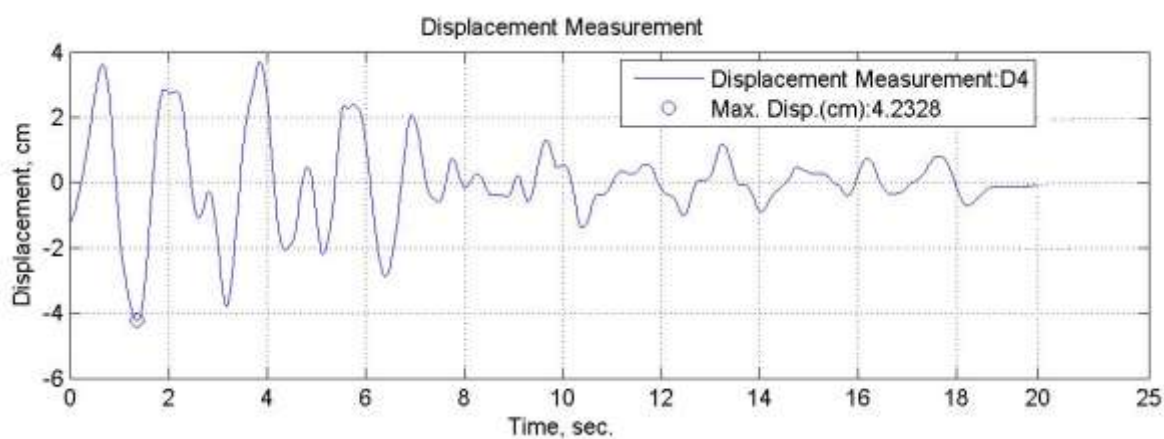


Figure 7.144. Lateral displacement time history for TC30 specimen tested at room temperature.

7.4.3. Tests Performed at 50°C

7.4.3.1. İzmit (E-W) Earthquake - 100% Sand Specimen (S). Shaking Table Tests are performed with only sand at 50°C temperature. The specimen is prepared in a large bowl and saturated with water. Then it is filled into the shear box (Figure 7.145). The earthquake record of İzmit (E-W) is applied to the specimen. The acceleration, pore water pressure and lateral displacements values were measured carefully. The acceleration time history of A1 accelerometer is given in Figure 7.146. Maximum acceleration value of A1 accelerometer is 0.18g.



Figure 7.145. Only Sand Specimen tested at 50°C.

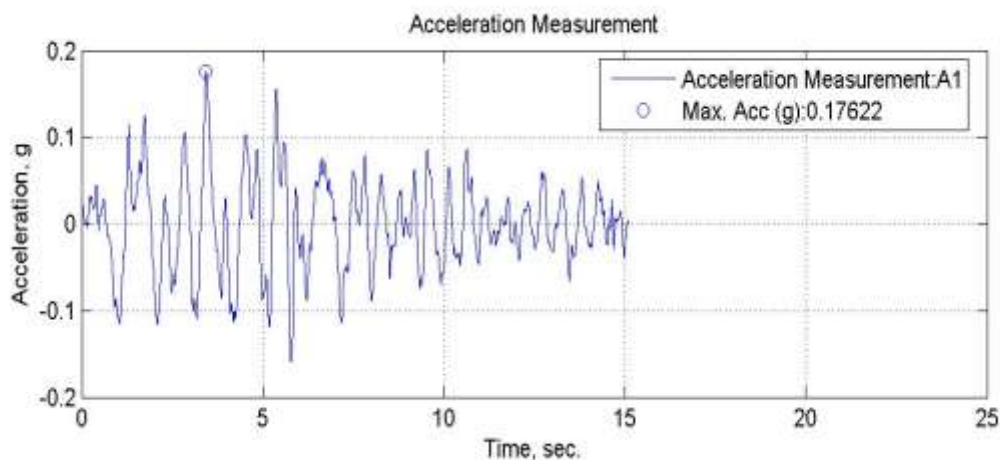


Figure 7.146. A1, acceleration time history of sand specimen tested at 50°C.

The pore water pressure change of the specimen is shown in Figure 7.147. It is observed that the pore water pressure value is zero during the test. The behaviour of pore water pressure can be explained as; the water particles are frozen and thus no upward motion occurred. The acceleration time histories of A2 and A3 accelerometers are shown in Figure 7.148. The acceleration values are measured by the submersible accelerometers within the soil and compared with A1 base input acceleration. The maximum acceleration value of A2 is measured as 0.16g, and the maximum A3 acceleration value is measured as 0.19g. The maximum lateral displacement value is measured as 4.23 cm. (Figure 7.149).

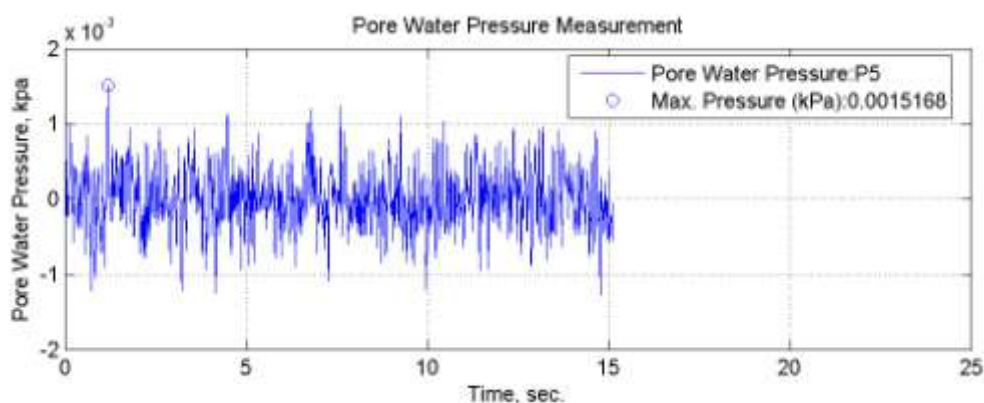


Figure 7.147. Pore water pressure change of TC30 specimen tested at room temperature.

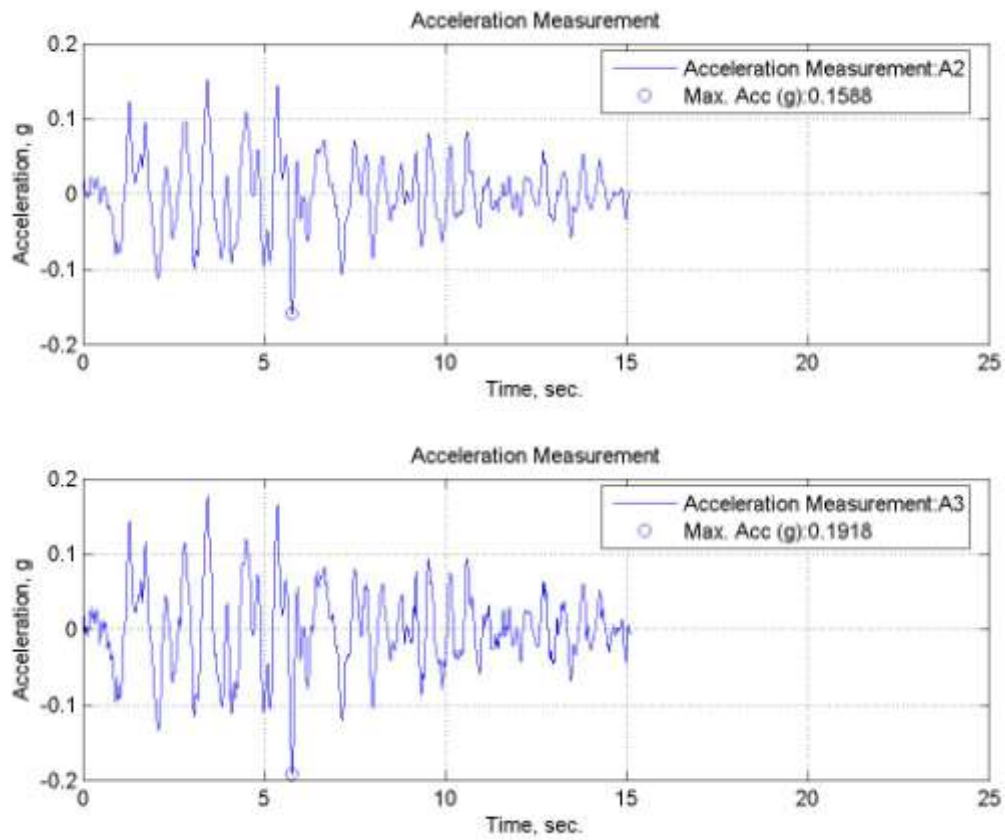


Figure 7.148. Time histories of accelerations of sand specimen tested at 50°C.

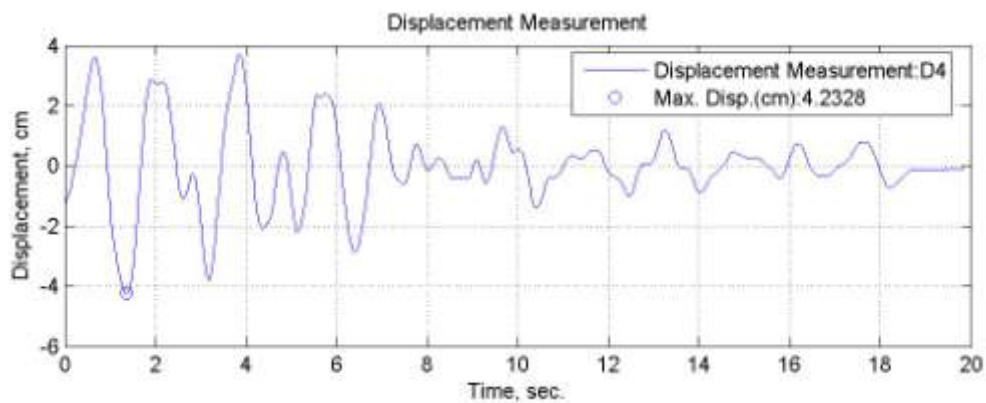


Figure 7.149. Lateral displacement time history for sand specimen tested at room temperature tested at 50°C.

7.4.3.2. İzmit (E-W) Earthquake - TB10 Specimen. TB10 specimen is prepared in a large bowl and saturated with water. Then it is filled into the shear box. Specimen is prepared with $D_r = 0.40$ relative density. The temperature of specimen is arranged as 50°C temperature. İzmit (E-W) ground earthquake motion is applied to the table. The acceleration time history, displacement time history and pore water pressure change graphs are obtained. The acceleration time history of A1 is given in Figure 7.150. Maximum acceleration value of A1 accelerometer is $0.18g$.

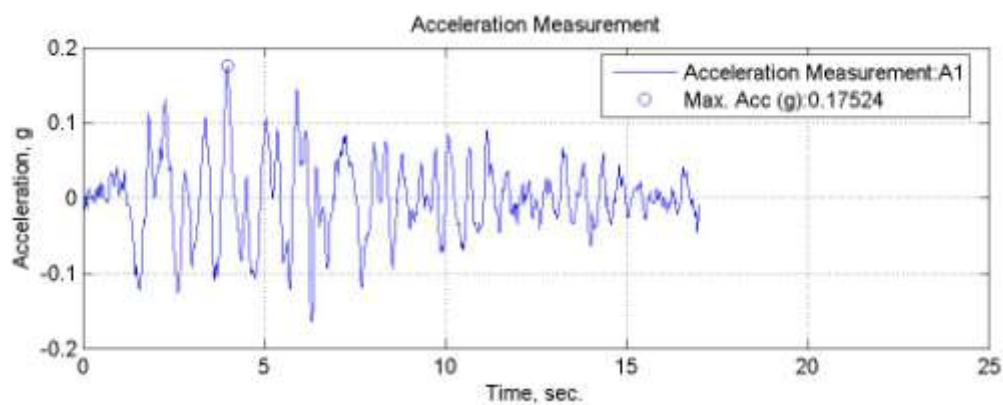


Figure 7.150. A1, acceleration time history of TB10 specimen tested at 50°C .

The pore water pressure change of the specimen is shown in Figure 7.151. It is observed that the pore water pressure value is almost zero during the test. The acceleration time histories of A2 and A3 accelerometers are shown in Figure 7.152. The acceleration values are measured by the accelerometers A2 and A3 within the soil and compared with A1 base input acceleration. The maximum A3 acceleration value is measured as $0.19g$, and the maximum A2 acceleration value is measured as $0.19g$. The maximum lateral displacement value is 4.12 cm . (Figure 7.153).

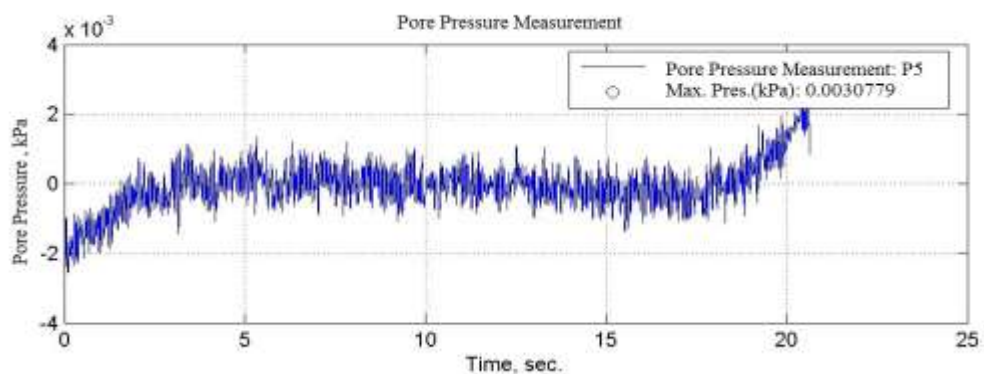


Figure 7.151. Pore water pressure change of TB10 specimen tested at 50°C.

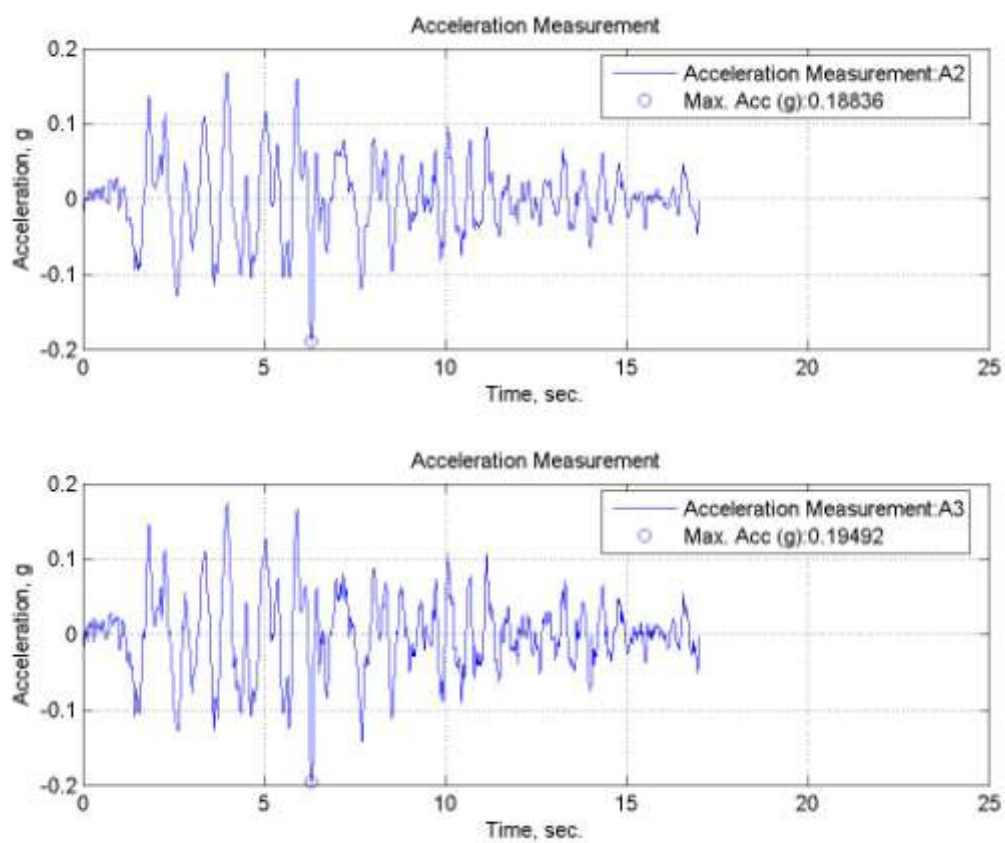


Figure 7.152. Time histories of accelerations of TB10 specimen tested at 50° C.

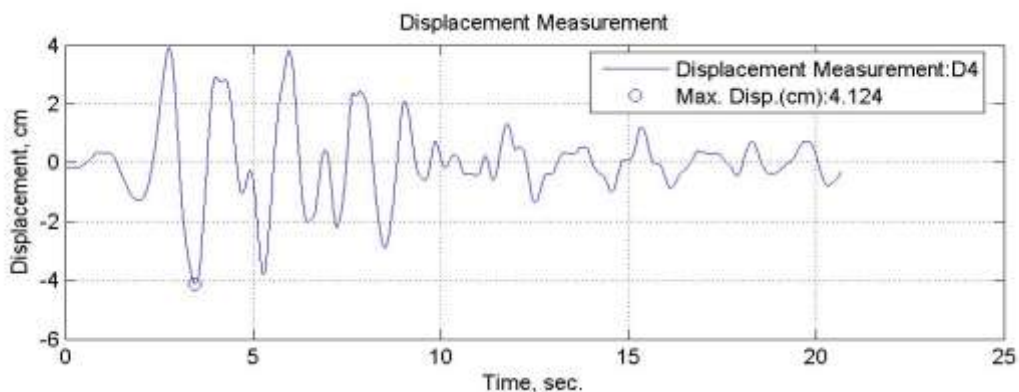


Figure 7.153. Lateral displacement time history for TB10 specimen tested at 50°C.

7.4.3.3. İzmit (E-W) Earthquake - TB15 Specimen. TB15 specimen is prepared in a large bowl and saturated with water. Then it is filled into the shear box. Specimen is prepared with $D_r = 0.40$ relative density. The temperature of specimen is arranged as 50°C temperature. İzmit (E-W) earthquake motion is applied to the table. The acceleration time history, displacement time history and pore water pressure change graphs are obtained. The acceleration time history of A1 is given in Figure 7.154. Maximum acceleration value of A1 is 0.19g.

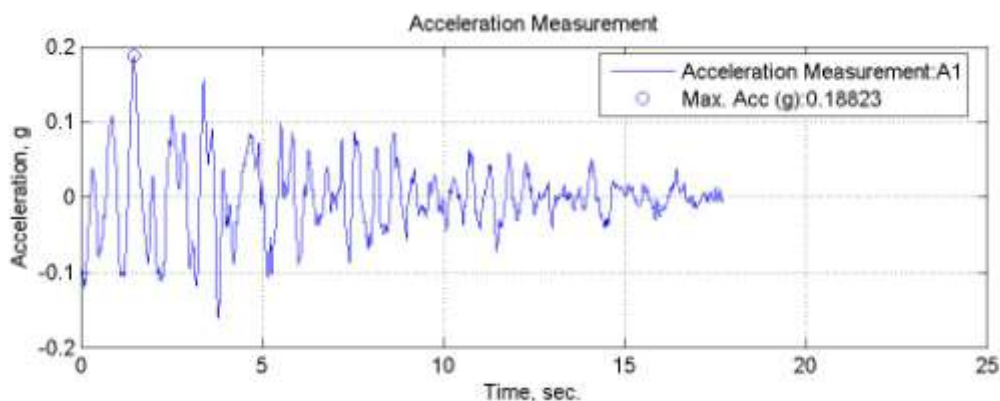


Figure 7.154. A1, acceleration time history of TB15 specimen tested at 50°C.

The pore water pressure change of the specimen is shown in Figure 7.155. It is observed that the pore water pressure value is almost zero during the test. The acceleration time histories of A2 and A3 accelerometers are shown in Figure 7.156. The acceleration values are measured by the accelerometers A2 and A3 within the soil and compared with A1 base input acceleration. The maximum acceleration value of A3 is measured as 0.18g.

and the maximum A2 acceleration value is measured as 0.20g. The maximum lateral displacement value is measured as 4.08 cm. (Figure 7.157).

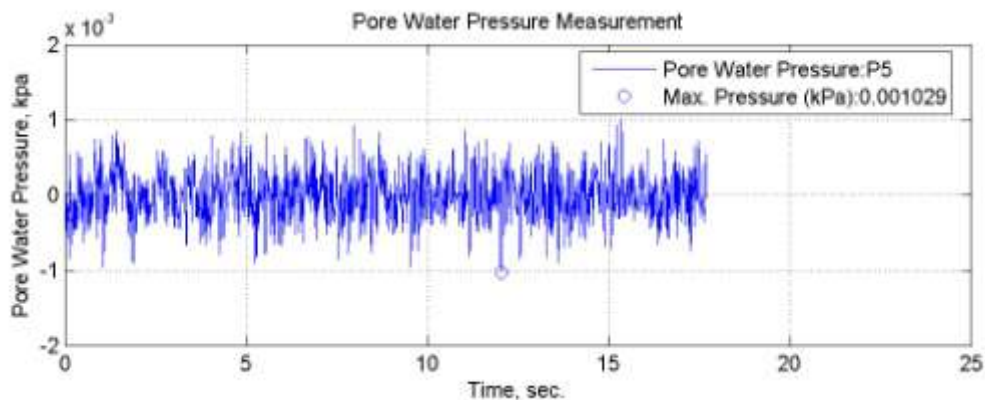


Figure 7.155. Pore water pressure change of TB15 specimen tested at 50°C.

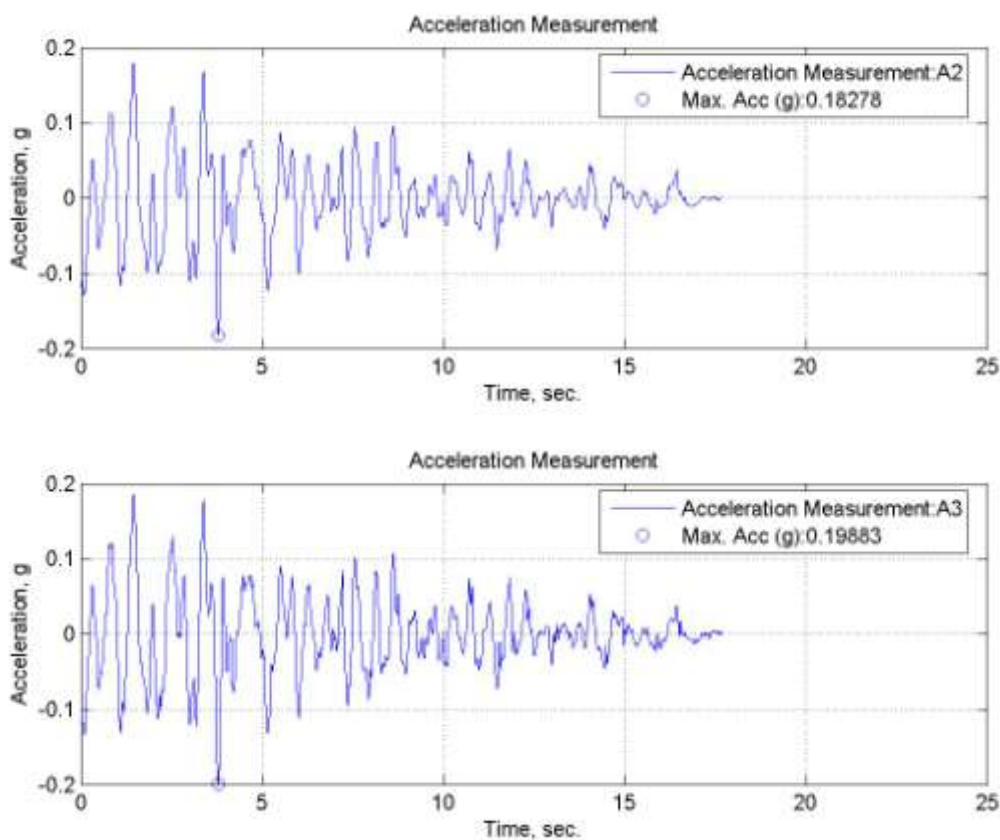


Figure 7.156. Time histories of accelerations of TB15 specimen tested at 50° C.

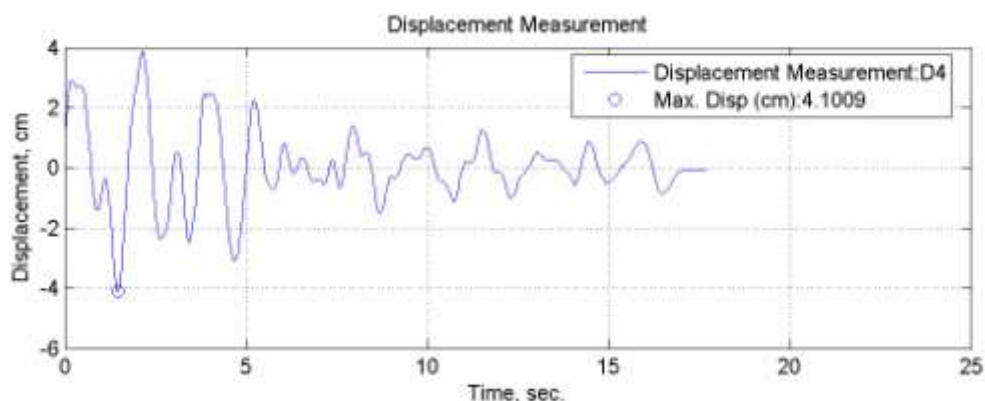


Figure 7.157. Lateral displacement time history for TB15 specimen tested at 50°C.

7.4.3.4. İzmit (E-W) Earthquake - TB20 Specimen. TB20 specimen is prepared in a large bowl and saturated with water. Then it is filled into the shear box. Specimen is prepared with $D_r = 0.40$ relative density. The temperature of specimen is arranged as 50°C temperature. İzmit (E-W) earthquake motion is applied to the table. The acceleration time history, displacement time history and pore water pressure change graphs are obtained. The acceleration time history of A1 accelerometer is given in Figure 7.158. Maximum acceleration value of A1 accelerometer is 0.18g.

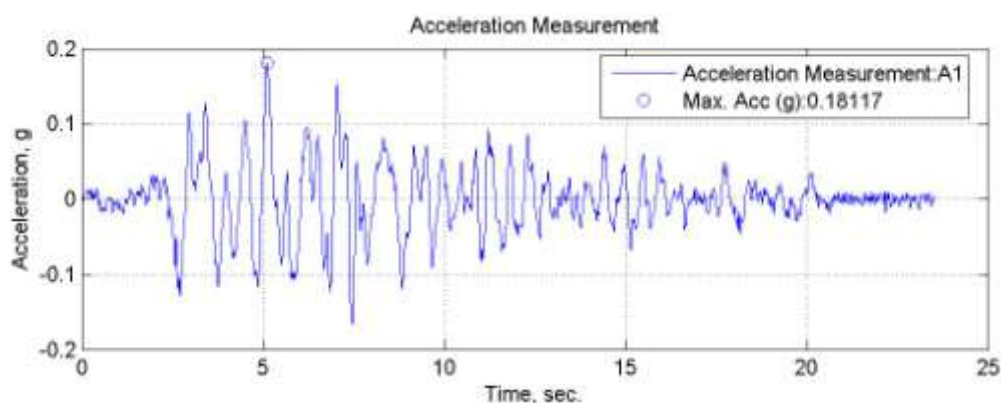


Figure 7.158. A1, acceleration time history of TB 20 specimen tested at 50°C.

The pore water pressure change of the specimen is shown in Figure 7.159. It is observed that the pore water pressure value is almost zero during the test. The acceleration time histories of A2 and A3 accelerometers are shown in Figure 7.160. The acceleration values are measured by the accelerometers A2 and A3 within the soil and compared with

A1 base input acceleration. The maximum A3 acceleration value is measured as 0.19g, and the maximum A2 acceleration value is measured as 0.17g. The maximum lateral displacement value is measured as 3.94 cm. (Figure 7.161).

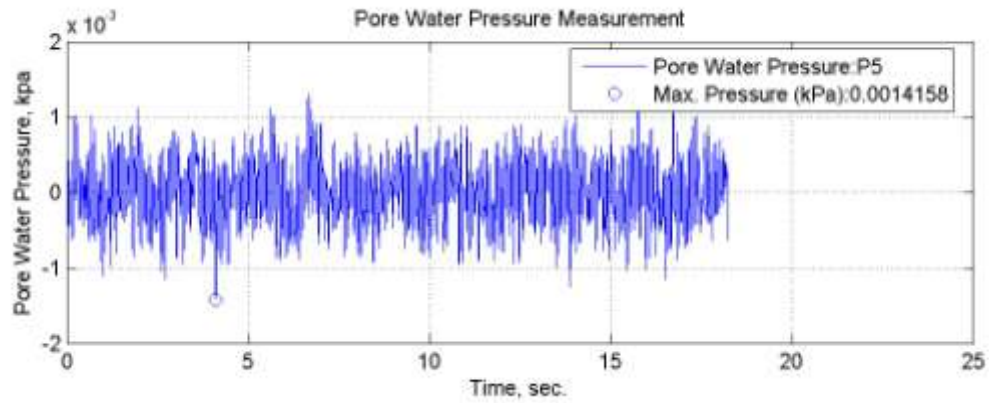


Figure 7.159. Pore water pressure change of TB20 specimen tested at 50°C.

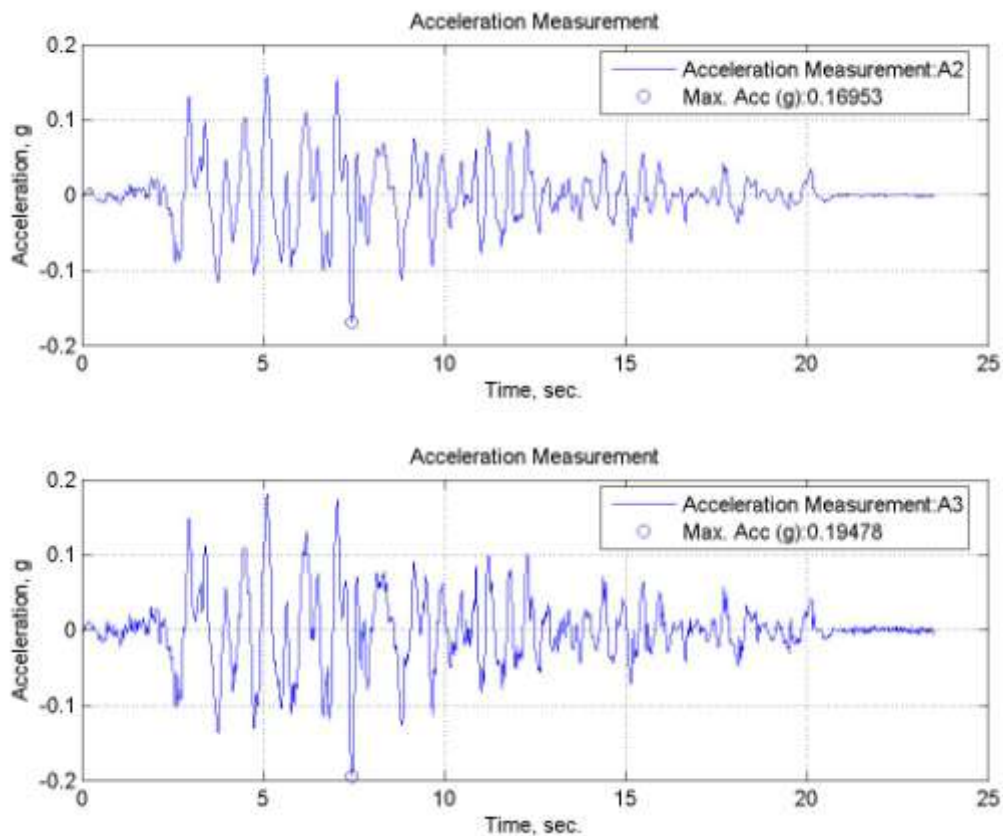


Figure 7.160. Time histories of accelerations of TB20 specimen tested at 50°C.

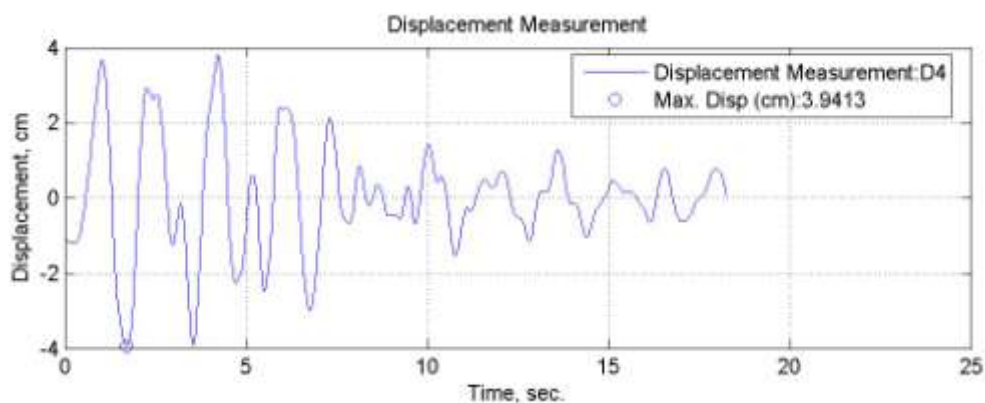


Figure 7.161. Lateral displacement time history for TB20 specimen tested at 50°C.

7.4.3.5. İzmit (E-W) Earthquake - TB30 Specimen. TB30 specimen is prepared in a large bowl and saturated with water. Then it is filled into the shear box. Specimen is prepared with $D_r = 0.40$ relative density. The temperature of specimen is arranged as 50°C temperature. and İzmit (E-W) earthquake motion is applied to the table. The acceleration time history, displacement time history and pore water pressure change graphs are obtained. The acceleration time history of A1 is given in Figure 7.162. Maximum acceleration value of A1 is 0.19g.

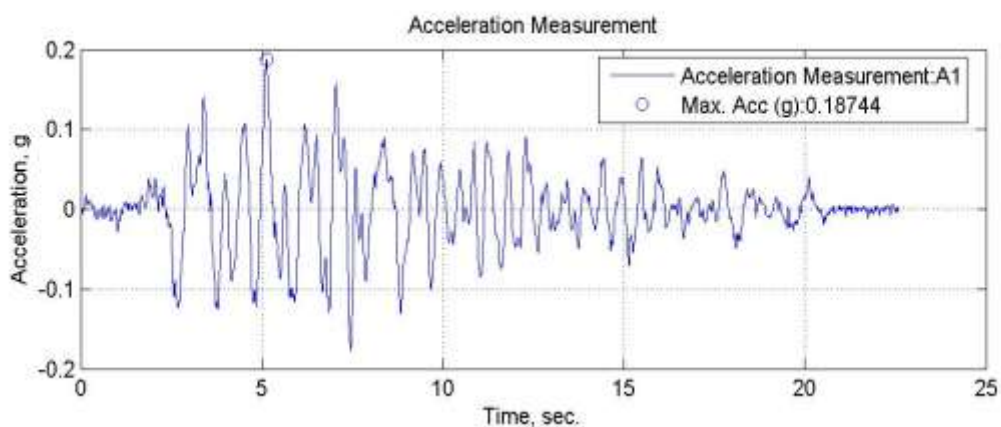


Figure 7.162. A1, acceleration time history of TB 30 specimen tested at 50°C.

The pore water pressure change of the specimen is shown in Figure 7.163. It is observed that the pore water pressure value is almost zero during the test. The acceleration time histories of A2 and A3 accelerometers are shown in Figure 7.164. The acceleration values are measured by the accelerometers A2 and A3 within the soil and compared with

A1 base input acceleration. The maximum A3 acceleration value is measured as 0.20g, and the maximum A2 acceleration value is measured as 0.20g. The maximum lateral displacement value is measured as 4.47 cm. (Figure 7.165).

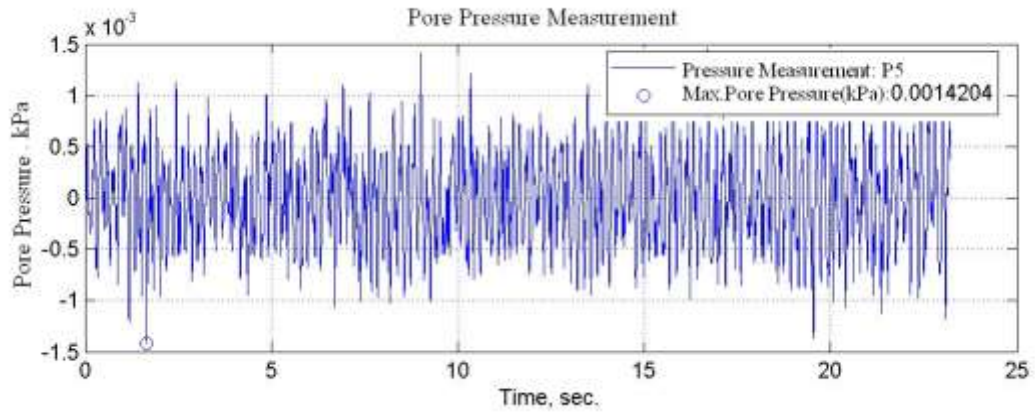


Figure 7.163. Pore water pressure change of TB30 specimen tested at 50°C.

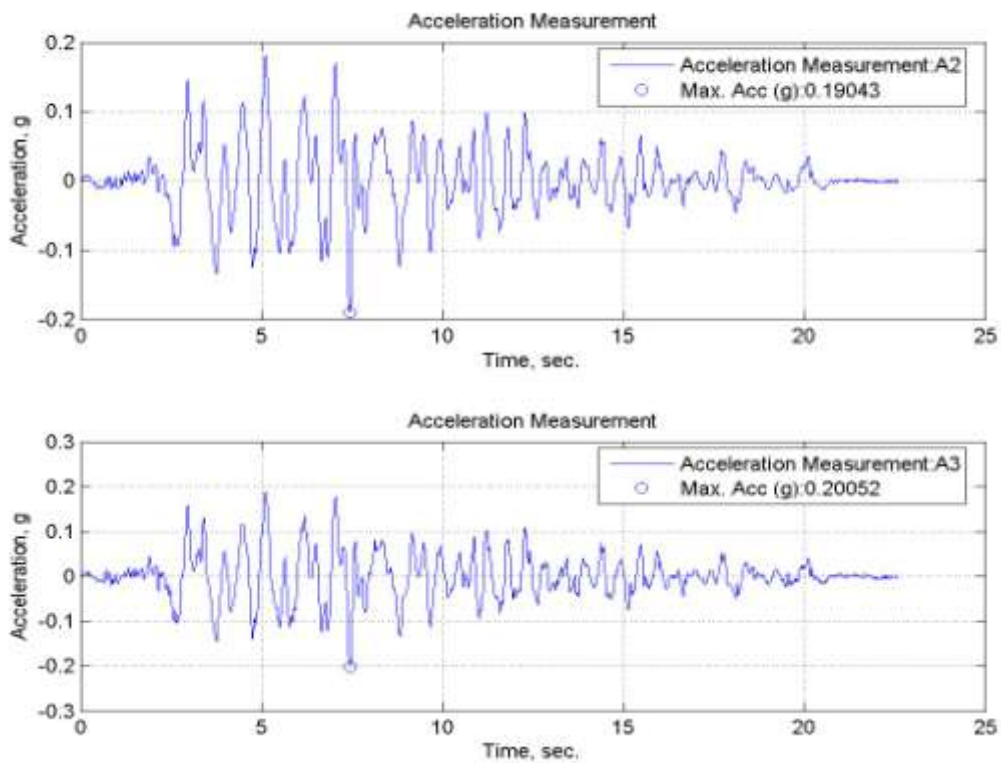


Figure 7.164. Time histories of accelerations of TB20 specimen tested at 50° C.

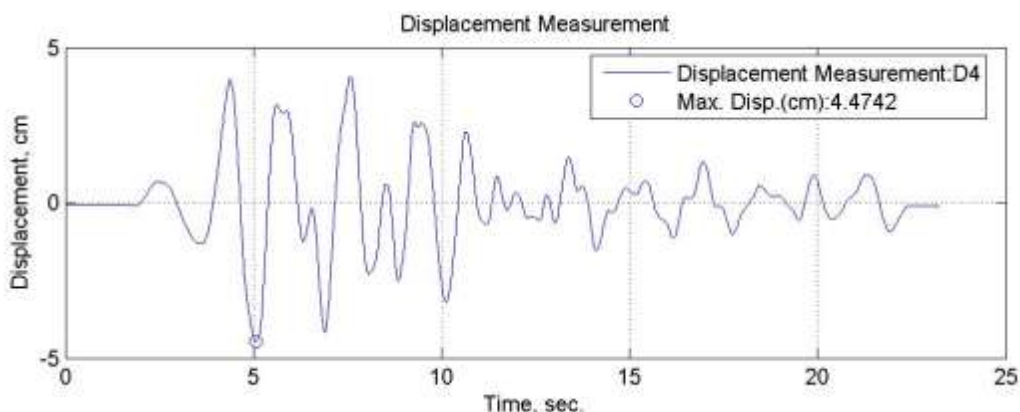


Figure 7.165. Lateral displacement time history for TB30 specimen tested at 50°C.

7.4.3.6. İzmit (E-W) Earthquake - TC10 Specimen. TC10 specimen is prepared in a large bowl and saturated with water. Then it is filled into the shear box. Specimen is prepared with $D_r = 0.40$ relative density. The temperature of specimen is arranged as 50°C temperature. and İzmit (E-W) earthquake motion is applied to the table. The acceleration time history, displacement time history and pore water pressure change graphs are obtained. The acceleration time history of A1 accelerometer which is fixed over shaking table surface is given in Figure 7.166. Maximum acceleration value of A1 accelerometer is 0.18g.

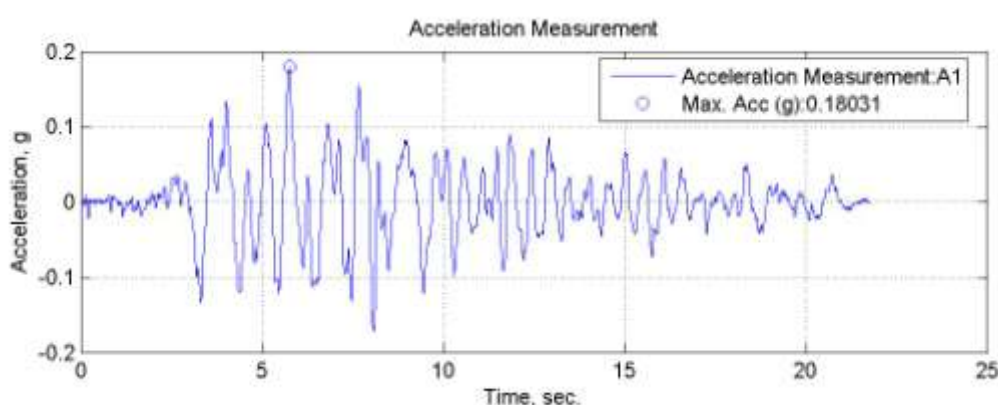


Figure 7.166. A1, acceleration time history of TC10 specimen tested at 50°C.

The pore water pressure change of the specimen is shown in Figure 7.167. It is observed that the pore water pressure value is almost zero during the test. The acceleration

time histories of A2 and A3 accelerometers are shown in Figure 7.168. The acceleration values are measured by the accelerometers A2 and A3 within the soil and compared with A1 base input acceleration. The maximum A3 acceleration value is measured as 0.17g, and the maximum A2 acceleration value is measured as 0.20g. The maximum lateral displacement value is measured as 4.28 cm. (Figure 7.169).

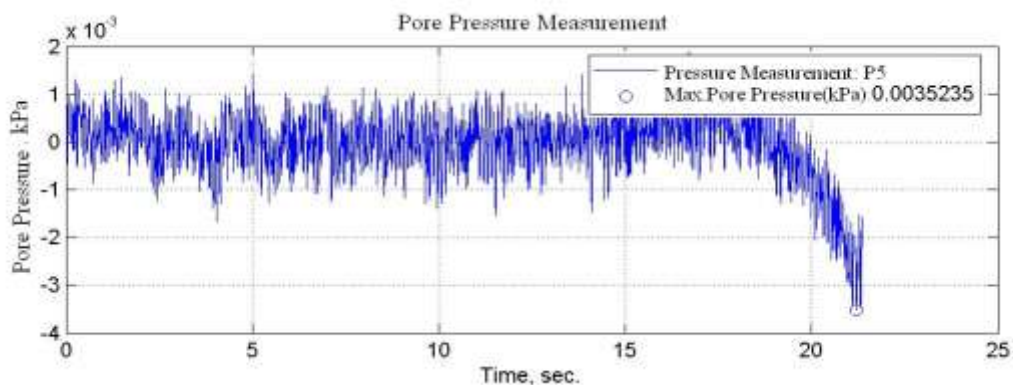


Figure 7.167. Pore water pressure change of TC10 specimen tested at 50°C.

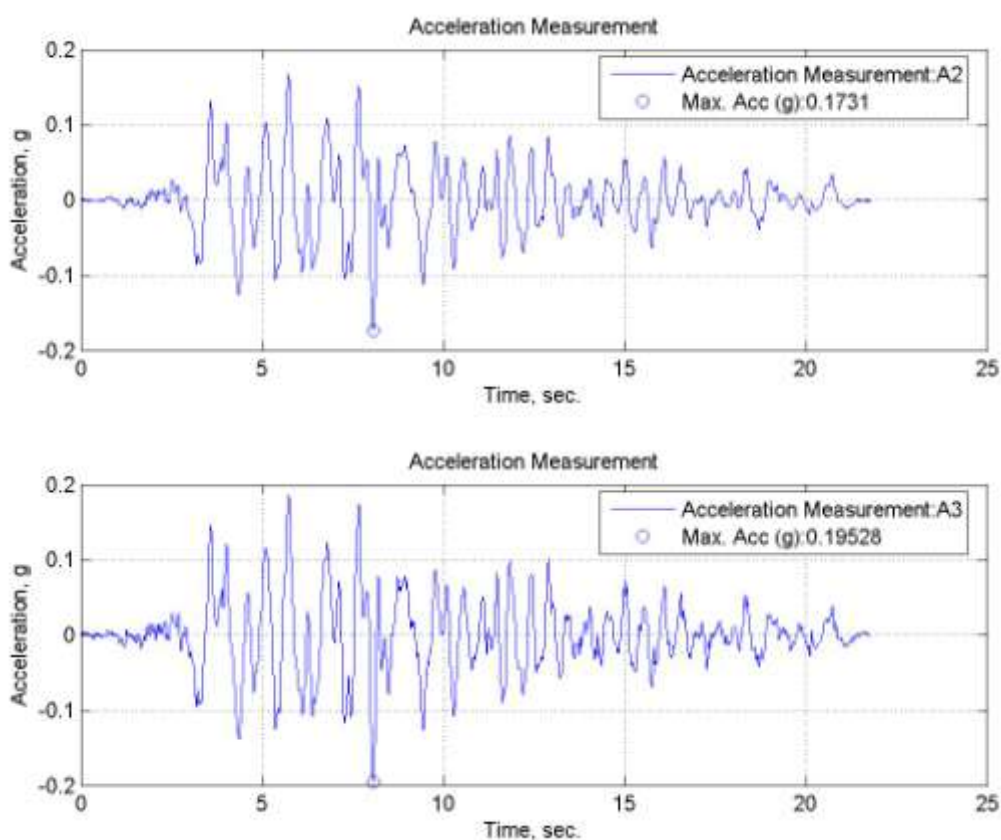


Figure 7.168. Time histories of accelerations of TC10 specimen tested at 50° C.

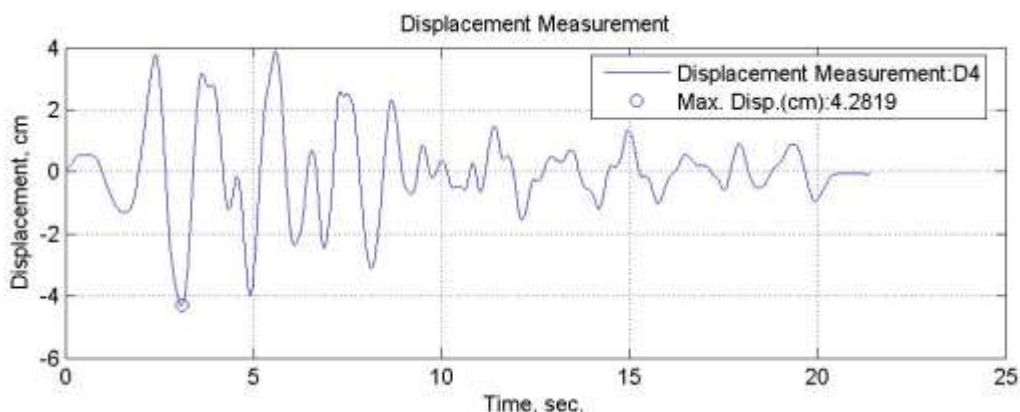


Figure 7.169. Lateral displacement time history for TC10 specimen tested at 50°C.

7.4.3.7. İzmit (E-W) Earthquake - TC15 Specimen. TC15 specimen is prepared in a large bowl and saturated with water. Then it is filled into the shear box. Specimen is prepared with $D_r = 0.40$ relative density. The temperature of specimen is arranged as 50°C temperature. İzmit (E-W) earthquake motion is applied to the table. The acceleration time history, displacement time history and pore water pressure change graphs are obtained. The acceleration time history of A1 accelerometer is given in Figure 7.170. Maximum acceleration value of A1 accelerometer is 0.18g.

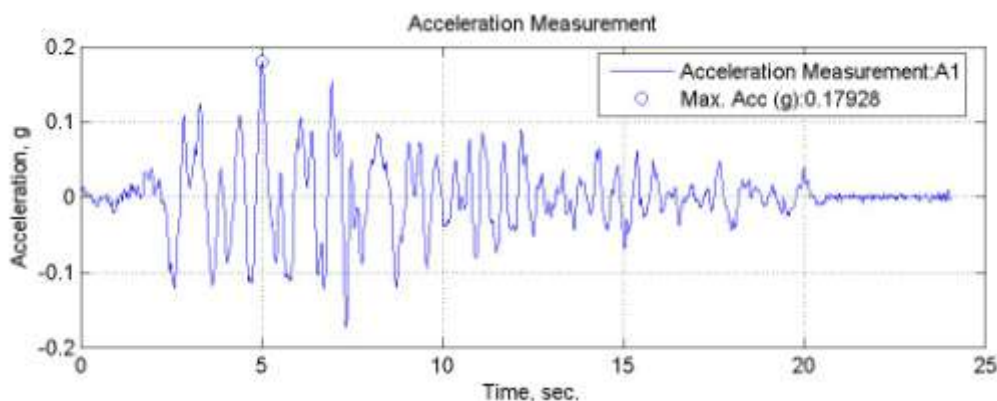


Figure 7.170. A1, acceleration time history of TC15 specimen tested at 50°C.

The pore water pressure change of the specimen is shown in Figure 7.171. It is observed that the pore water pressure value is almost zero during the test. The acceleration time histories of A2 and A3 accelerometers are shown in Figure 7.172. The acceleration

values are measured by the accelerometers A2 and A3 within the soil and compared with A1 base input acceleration. The maximum A3 acceleration value is measured as 0.20g, and the maximum A2 acceleration value is measured as 0.19g. The maximum lateral displacement value is measured as 4.19 cm. (Figure 7.173).

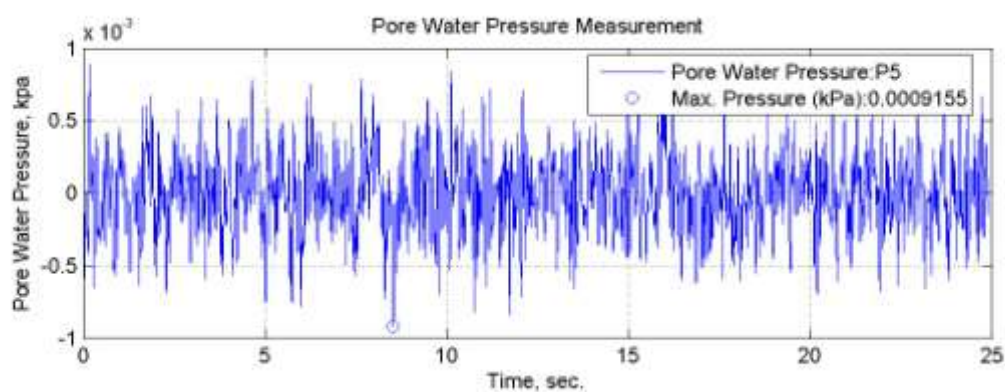


Figure 7.171. Pore water pressure change of TC15 specimen tested at 50°C.

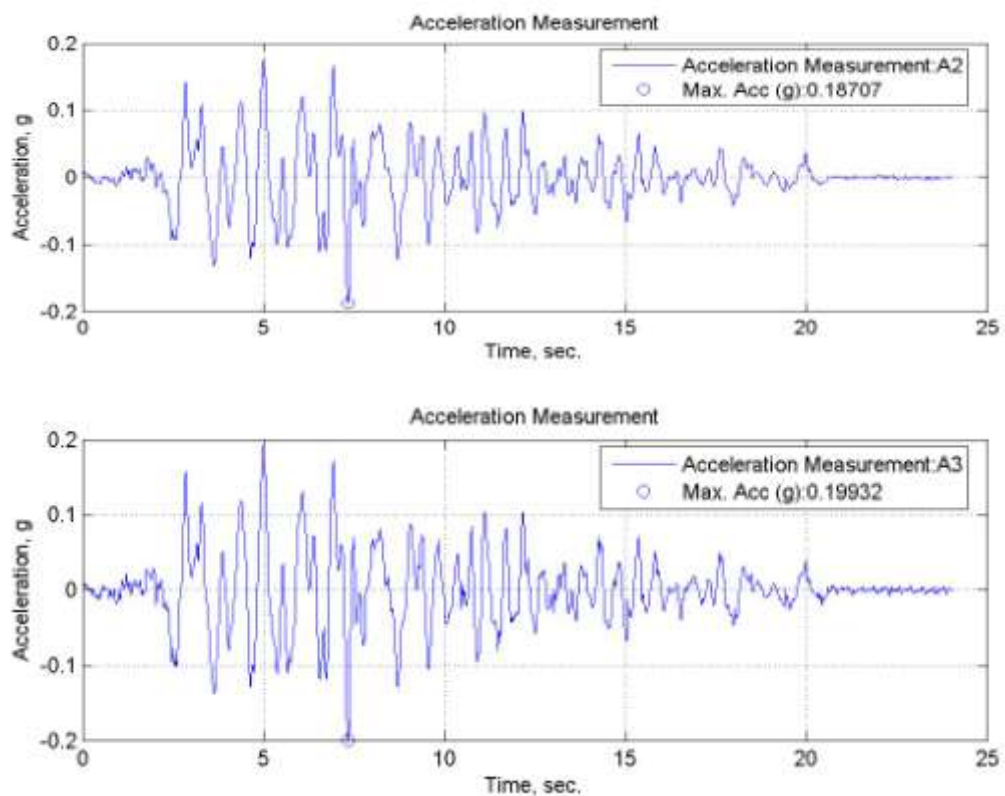


Figure 7.172. Time histories of accelerations of TC15 specimen tested at 50° C.

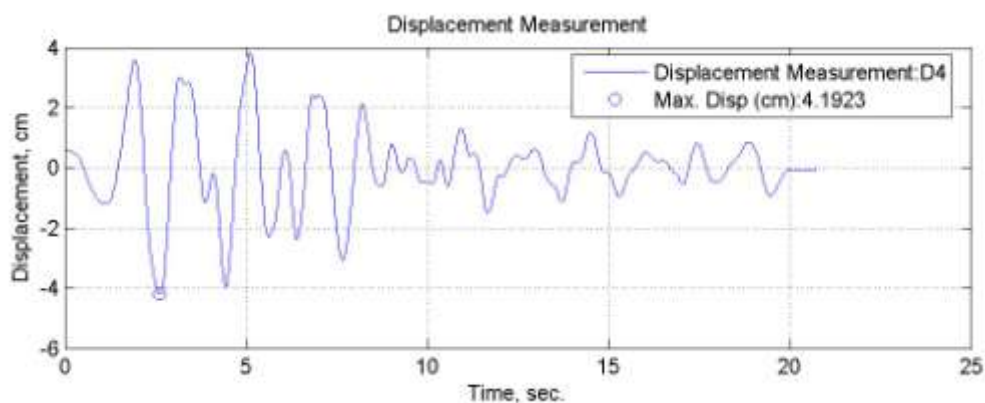


Figure 7.173. Lateral displacement time history for TC15 specimen tested at 50°C.

7.4.3.8. İzmit (E-W) Earthquake - TC20 Specimen. TC20 specimen is prepared in a large bowl and saturated with water. Then it is filled into the shear box. Specimen is prepared with $D_r = 0.40$ relative density. The temperature of specimen is arranged as 50°C temperature. İzmit (E-W) earthquake motion is applied to the table. The acceleration time history, displacement time history and pore water pressure change graphs are obtained. The acceleration time history of A1 accelerometer is given in Figure 7.174. Maximum acceleration value of A1 accelerometer is 0.18g.

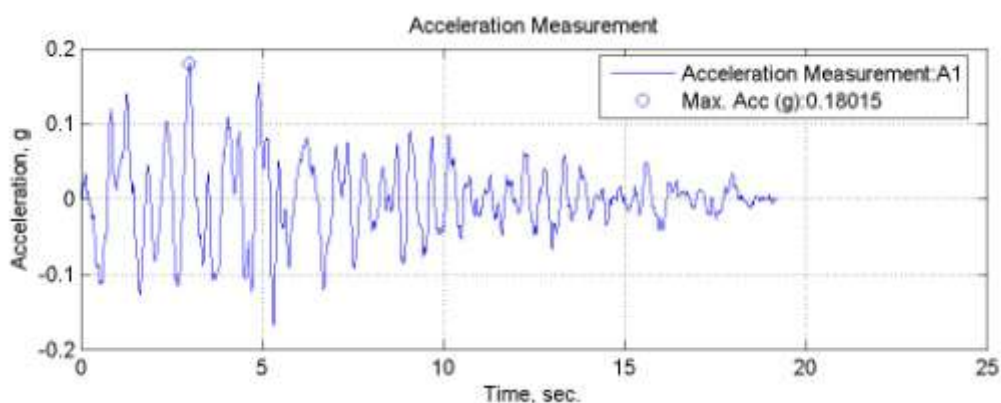


Figure 7.174. A1, acceleration time history of TC20 specimen tested at 50°C.

The pore water pressure change of the specimen is shown in Figure 7.175. It is observed that the pore water pressure value is almost zero during the test. The acceleration time histories of A2 and A3 accelerometers are shown in Figure 7.176. The acceleration values are measured by the accelerometers A2 and A3 within the soil and compared with

A1 base input acceleration. The maximum A3 acceleration value is measured as 0.18g, and the maximum A2 acceleration value is measured as 0.19g. The maximum lateral displacement value is measured as 4.35 cm. (Figure 7.177).

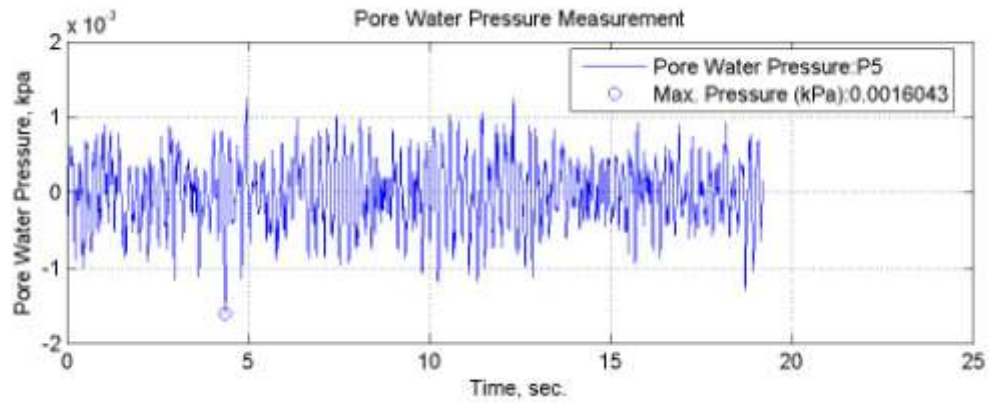


Figure 7.175. Pore water pressure change of TC20 specimen tested at 50°C.

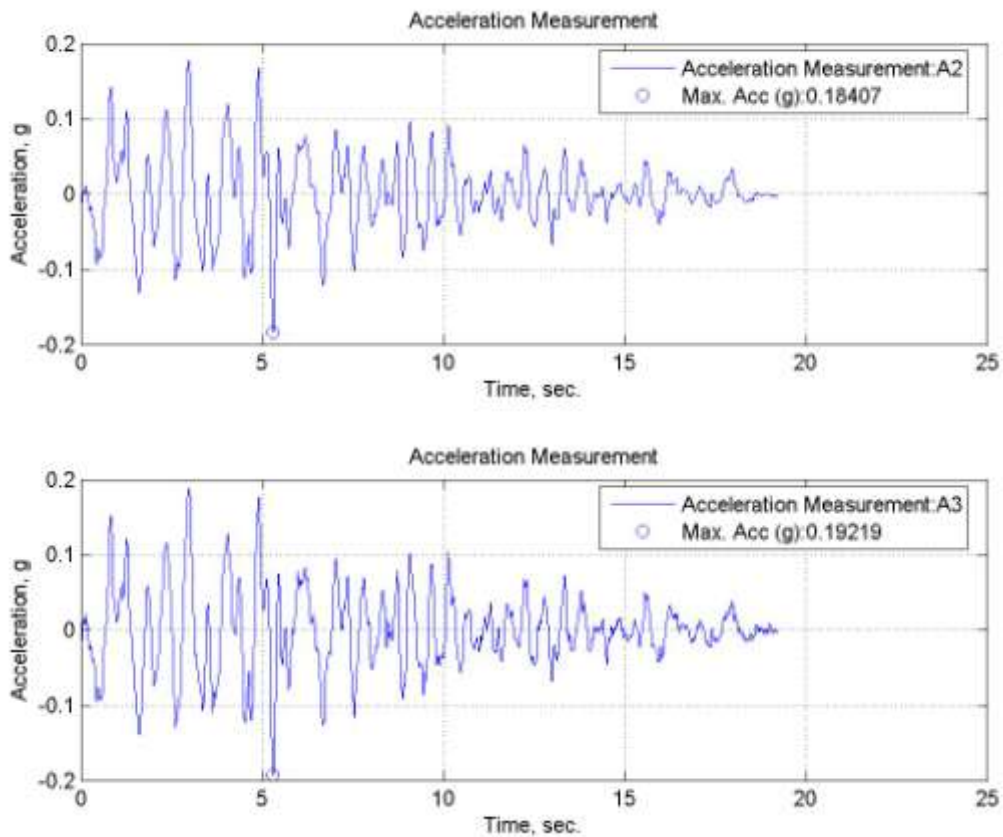


Figure 7.176. Time histories of accelerations of TC20 specimen tested at 50° C.

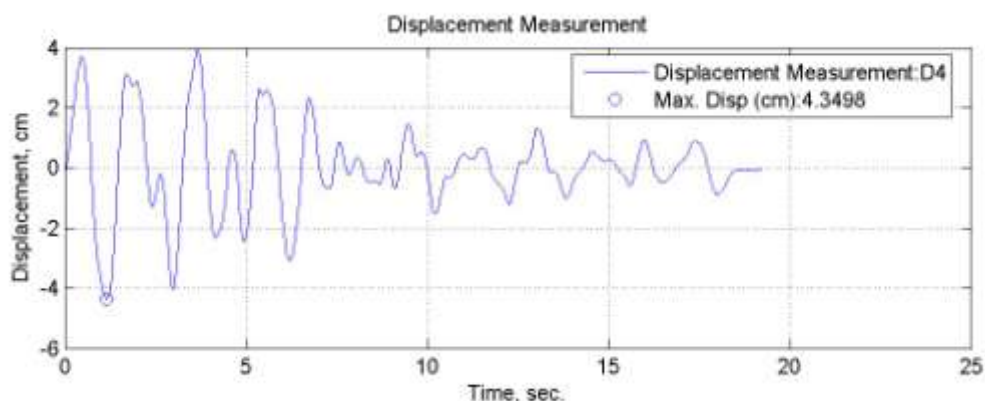


Figure 7.177. Lateral displacement time history for TC20 specimen tested at 50°C.

7.4.3.9. İzmit (E-W) Earthquake - TC30 Specimen. TC30 specimen is prepared in a large bowl and saturated with water. Then it is filled into the shear box. Specimen is prepared with $D_r = 0.40$ relative density. The temperature of specimen is arranged as 50°C temperature. İzmit (E-W) earthquake motion is applied to the table. The acceleration time history, displacement time history and pore water pressure change graphs are obtained. The acceleration time history of A1 accelerometer is given in Figure 7.178. Maximum acceleration value of A1 accelerometer is 0.18g.

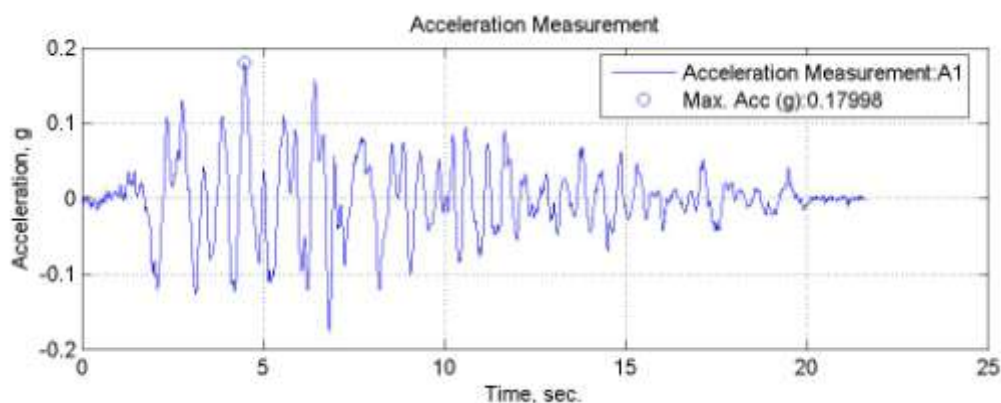


Figure 7.178. A1, acceleration time history of TC30 specimen tested at 50°C.

The pore water pressure change of the specimen is shown in Figure 7.179. It is observed that the pore water pressure value is almost zero during the test. The acceleration time histories of A2 and A3 accelerometers are shown in Figure 7.180. The acceleration values are measured by the accelerometers A2 and A3 within the soil and compared with A1 base input acceleration. The maximum A3 acceleration value is measured as 0.20g, and

the maximum A2 acceleration value is measured as 0.19g. The maximum lateral displacement value is measured as 4.31 cm. (Figure 7.181).

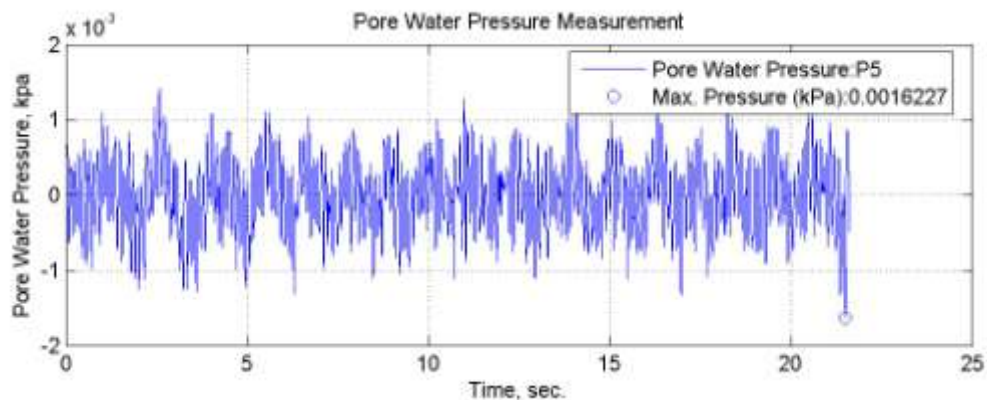


Figure 7.179. Pore water pressure change of TC30 specimen tested at 50°C.

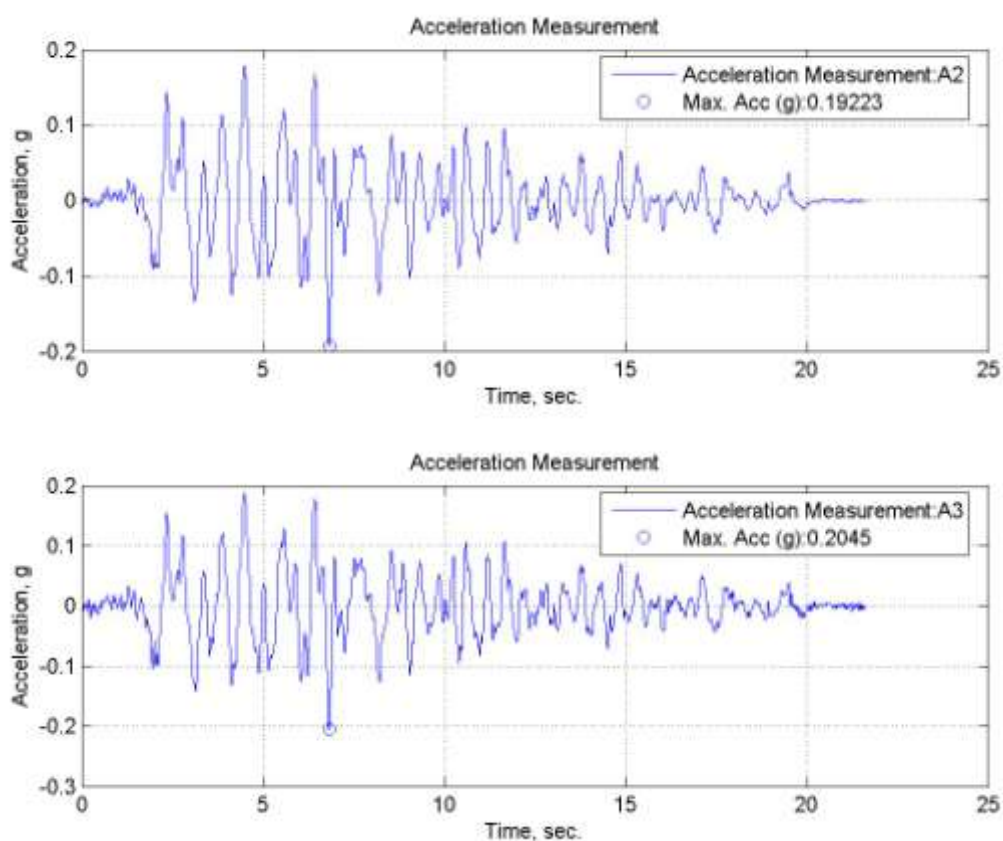


Figure 7.180. Time histories of accelerations of TC30 specimen tested at 50° C.

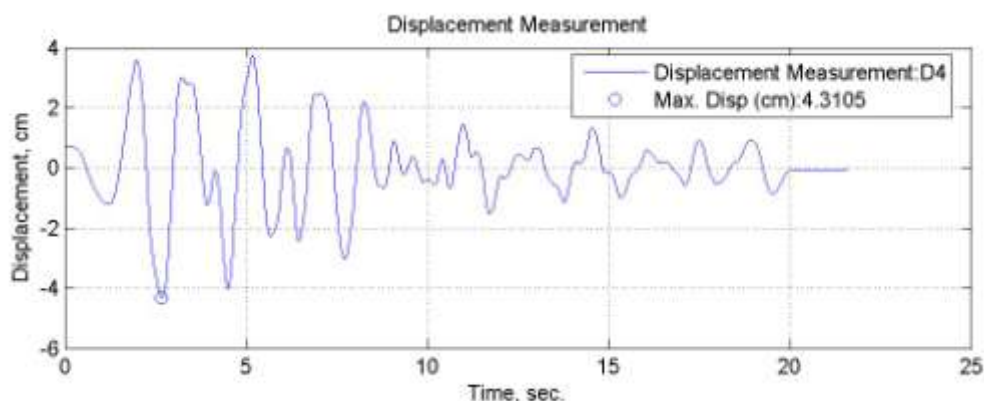


Figure 7.181. Lateral displacement time history for TC30 specimen tested at 50°C.

7.4.4. Analysis of Shaking Table Test Results

A set of shaking table tests are performed with sand and tire waste materials. Two different types of tire waste material, tire buffings and tire crumbs are used. The aspect ratio of tire buffings (TB) material is 1/5 and the aspect ratio of tire crumbs (TC) is 1-1.5. Specimens are prepared at $D_r = 0.40$ relative density. The water content of the specimens were prepared as 30%. Only sand, TB10 TB15, TB20, TB30, TC10, TC15, TC20 and TC30 specimens are used in the tests. A normal and two submersible accelerometers, a pore pressure transducer, a laser displacement sensor are used in the experiments. Three different types of earthquake motions; İzmit (E-W), Sakarya (N-S) and Tabas (E-W) were chosen as input motions during the experiments. Each specimen is tested under 0°C, room temperature as 20°C and 50°C.

The effect of three factors; tire content, tire shape and temperature are investigated during the shaking table tests. Amplification factors are calculated as the ratio of accelerations measured by A2 and A3 to the A1. Shaking Table test results are summarized in Table 7.8.

TB30 specimen reduced A2 acceleration down to 0.19g and increased A3 acceleration up to 0.42g under Tabas (E-W) ground motion at 0°C while A1 base input acceleration is 0.40g. At same temperature, TC15 reduced both A2 and A3 acceleration values down to 0.25g and 0.36g, respectively while A1 base input acceleration is 0.45g.

Also, TB30 specimen showed good performance under İzmit (E-W) ground motion. A1 base input motion is 0.47g. TB30 specimen reduced A2 and A3 accelerations down to 0,18g and 0,20g respectively under İzmit (E-W) ground motion at 20°C. On the other hand, TC15 specimen reduced A2 and A3 accelerations down to 0.09g and 0.14g respectively under same ground motion at 0°C.

TB15 and TC10 specimens displayed best performances under Sakarya (N-S) ground motions at 0°C. A1 base input motion is 0.16g for both specimens. TB15 specimen reduced A2 and A3 accelerations down to 0.10g and 0.14g while TC10 specimen reduced same acceleration values down to 0.10g and 0.13g respectively.

The maximum lateral displacement values are obtained from TB15 and TC20 specimens. The displacement values are measured as 6.83 cm from TB15 specimen at 50°C and 8.80 cm from TC20 specimen at 0°C, tested under Tabas (E-W) ground motion. The pore water pressure values of all specimens are very low.

Among all specimens tested under ground motions at three temperature values, TB30 and TC15 specimens displayed best performances under Tabas (E-W) ground motion under 0°C temperature.

Liquefaction did not observed from any of the specimens tested under 0°C temperature. Also, liquefaction did not observed from TB20 and TB30 specimens tested at 20°C temperature. Specimens tested at 50°C temperature are liquefied except TB20 and TB30 specimens. Among all of the specimens, TB20 and TB30 specimens showed best performance against to the liquefaction.

7.4.4.1. Effect of Tire Content. The inclusion of tire material changed the seismic performance of mixtures but there is not any consistency between seismic behaviour of specimens. Some of the acceleration and displacement values increased with the increasing tire content but in general, increasing tire content reduced acceleration values. Especially, TB15 and TC15 specimens tested under Tabas (E-W) ground motion demonstrated that as the tire content increased, the energy absorption effect of rubber increased.

7.4.4.2. Effect of Tire Shape. Two different types of tire material used in the tests. Generally, acceleration values recorded by A3 accelerometer which is placed at upper layer of specimen is higher than records taken by A2 accelerometer from lower layer. Also, both for TB and TC specimens, some of the acceleration values recorded at lower layer of soil are lower than acceleration values of A1 acceleration. Pore water pressure of all TB and TC specimens are at very low range. Displacement values of specimens varied between 3.00 and 8.80 cm for both of tire materials.

7.4.4.3. Effect of Temperature. To take all of the shaking table test results into evaluation, it is obvious that specimens tested at 0°C and 20°C temperatures displayed highest performance among all of the specimens. Pore water pressure values are at very low ranges. The amplification factors of the most of the specimens tested under 0°C are lower than those obtained at 20°C and 50°C temperature. The lateral displacement values of most of the specimens recorded under 0°C are lower than those recorded at 20°C and 50°C temperature values. Liquefaction did not observed at the tests performed under 0°C. The liquefaction observed from the tests performed with all of the TC and TB10 specimens.

Table 7.8. Summary of Shaking Table Test Results.

Summary of Shaking Table Test Results									
Specimen No	A1 (base motion)	A2 (lower level)		A3 (upper level)		Displacement (cm)	Pore Water Pressure (10^{-3}) (kpa)	Temperature	Type of Motion
	Acc. (g)	Acc. (g)	Factor	Acc. (g)	Factor				
Sand	0,40	0,39	0,98	0,38	0,95	5,12	2	0°C	Tabas
TB10	0,40	0,29	0,73	0,41	1,03	5,00	2		
TB15	0,40	0,36	0,90	0,40	1,00	5,09	2		
TB20	0,42	0,29	0,69	0,54	1,29	4,80	1		
TB30	0,40	0,19	0,48	0,42	1,05	6,81	0		
Sand	0,16	0,11	0,69	0,17	1,06	5,21	1	20°C	Tabas
TB10	0,42	0,44	1,05	0,49	1,17	6,59	0		
TB15	0,42	0,40	0,95	0,50	1,19	6,65	1		
TB20	0,42	0,43	1,02	0,51	1,21	6,50	0		
TB30	0,42	0,45	1,07	0,51	1,21	6,62	0		
Sand	0,41	0,41	1,00	0,48	1,17	6,40	2	50°C	Tabas
TB10	0,43	0,45	1,05	0,49	1,14	6,46	0		
TB15	0,42	0,47	1,12	0,53	1,26	6,83	1		
TB20	0,44	0,45	1,02	0,53	1,20	6,56	1		
TB30	0,43	0,49	1,14	0,53	1,23	6,82	1		

Table 7.8. Summary of Shaking Table Test Results, (continued).

Summary of Shaking Table Test Results									
Specimen No	A1 (base motion)	A2 (lower level)		A3 (upper level)		Displacement (cm)	Pore Water Pressure (10^{-3}) (kpa)	Temperature	Type of Motion
	Acc. (g)	Acc. (g)	Factor	Acc. (g)	Factor				
Sand	0,15	0,16	1,07	0,15	1,00	3,00	2	0°C	İzmit
TB10	0,15	0,16	1,07	0,15	1,00	3,12	2		
TB15	0,15	0,44	2,93	0,15	1,00	3,13	2		
TB20	0,16	0,21	1,31	0,17	1,06	3,13	1		
TB30	0,17	0,19	1,12	0,19	1,12	4,50	0		
Sand	0,18	0,17	0,94	0,06	0,33	3,97	0	20°C	İzmit
TB10	0,18	0,18	1,00	0,19	1,06	4,27	0		
TB15	0,17	0,16	0,94	0,20	1,18	4,22	0		
TB20	0,18	0,17	0,94	0,19	1,06	4,02	1		
TB30	0,47	0,18	0,38	0,20	0,43	4,30	0		
Sand	0,18	0,16	0,89	0,19	1,06	4,23	2	50°C	İzmit
TB10	0,18	0,19	1,06	0,19	1,06	4,12	0		
TB15	0,19	0,18	0,95	0,20	1,05	4,20	1		
TB20	0,18	0,17	0,94	0,19	1,06	3,94	1		
TB30	0,19	0,19	1,00	0,20	1,05	4,47	1		

Table 7.8. Summary of Shaking Table Test Results, (continued).

Summary of Shaking Table Test Results									
Specimen No	A1 (base motion)	A2 (lower level)		A3 (upper level)		Displacement (cm)	Pore Water Pressure (10^{-3}) (kpa)	Temperature	Type of Motion
	Acc. (g)	Acc. (g)	Factor	Acc. (g)	Factor				
Sand	0,16	0,14	0,88	0,16	1,00	4,37	2	0°C	Sakarya
TB10	0,16	0,14	0,88	0,22	1,38	4,25	2		
TB15	0,16	0,10	0,63	0,14	0,88	4,23	2		
TB20	0,16	0,16	1,00	0,18	1,13	4,28	1		
TB30	0,15	0,10	0,67	0,15	1,00	4,04	0		
Sand	0,40	0,10	0,25	0,13	0,33	6,18	1	20°C	Sakarya
TB10	0,17	0,16	0,94	0,18	1,06	5,68	0		
TB15	0,16	0,14	0,88	0,18	1,13	5,74	0		
TB20	0,16	0,16	1,00	0,19	1,19	5,53	1		
TB30	0,17	0,16	0,94	0,20	1,18	5,70	0		
Sand	0,16	0,15	0,94	0,18	1,13	5,36	2	50°C	Sakarya
TB10	0,18	0,19	1,06	0,19	1,06	4,10	1		
TB15	0,16	0,17	1,06	0,20	1,25	5,77	1		
TB20	0,17	0,17	1,00	0,20	1,18	5,67	1		
TB30	0,18	0,18	1,00	0,20	1,11	5,92	1,5		

Table 7.8. Summary of Shaking Table Test Results, (continued).

Summary of Shaking Table Test Results									
Specimen No	A1 (base motion)	A2 (lower level)		A3 (upper level)		Displacement (cm)	Pore Water Pressure (10^{-3}) (kpa)	Temperature	Type of Motion
	Acc. (g)	Acc. (g)	Factor	Acc. (g)	Factor				
Sand	0,40	0,39	0,98	0,38	0,95	5,03	2	0°C	Tabas
TC10	0,38	0,17	0,45	0,36	0,95	5,10	2		
TC15	0,45	0,25	0,56	0,36	0,80	0,54	2		
TC20	0,41	0,13	0,32	0,51	1,24	8,80	1		
TC30	0,16	0,39	2,44	0,40	2,50	5,15	0		
Sand	0,46	0,11	0,24	0,16	0,35	5,21	2	20°C	Tabas
TC10	0,42	0,44	1,05	0,51	1,21	6,28	2		
TC15	0,43	0,44	1,02	0,48	1,12	6,46	1		
TC20	0,42	0,44	1,05	0,50	1,19	6,57	2		
TC30	0,44	0,45	1,02	0,51	1,16	6,66	1		
Sand	0,41	0,40	0,98	0,48	1,17	6,40	1	50°C	Tabas
TC10	0,43	0,43	1,00	0,52	1,21	6,59	0		
TC15	0,43	0,46	1,07	0,50	1,16	6,71	1		
TC20	0,43	0,47	1,09	0,51	1,19	6,67	1		
TC30	0,43	0,48	1,12	0,53	1,23	6,68	1		

Table 7.8. Summary of Shaking Table Test Results, (continued).

Summary of Shaking Table Test Results									
Specimen No	A1 (base motion)	A2 (lower level)		A3 (upper level)		Displacement (cm)	Pore Water Pressure (10^{-3}) (kpa)	Temperature	Type of Motion
	Acc. (g)	Acc. (g)	Factor	Acc. (g)	Factor				
Sand	0,15	0,16	1,07	0,15	1,00	3,00	2	0°C	İzmit
TC10	0,17	0,16	0,94	0,18	1,06	4,03	2		
TC15	0,16	0,09	0,56	0,14	0,88	3,44	2		
TC20	0,18	0,13	0,72	0,50	2,78	4,47	1		
TC30	0,15	0,13	0,87	0,14	0,93	4,38	0		
Sand	0,18	0,17	0,94	0,06	0,33	3,97	2,5	20°C	İzmit
TC10	0,19	0,18	0,95	0,19	1,00	3,93	2		
TC15	0,18	0,17	0,94	0,19	1,06	4,00	2		
TC20	0,17	0,18	1,06	0,20	1,18	4,10	2		
TC30	0,18	0,18	1,00	0,20	1,11	4,24	0		
Sand	0,18	0,16	0,89	0,19	1,06	4,23	2	50°C	İzmit
TC10	0,18	0,17	0,94	0,20	1,11	4,28	0		
TC15	0,18	0,19	1,06	0,20	1,11	4,19	1		
TC20	0,18	0,18	1,00	0,19	1,06	4,35	1		
TC30	0,18	0,19	1,06	0,20	1,11	4,31	1		

Table 7.8. Summary of Shaking Table Test Results, (continued).

Summary of Shaking Table Test Results									
Specimen No	A1 (base motion)	A2 (lower level)		A3 (upper level)		Displacement (cm)	Pore Water Pressure (10 ⁻³) (kpa)	Temperature	Type of Motion
	Acc. (g)	Acc. (g)	Factor	Acc. (g)	Factor				
Sand	0,16	0,14	0,88	0,16	1,00	4,37	2	0°C	Sakarya
TC10	0,16	0,10	0,63	0,13	0,81	4,29	2		
TC15	0,17	0,12	0,71	0,13	0,76	4,52	2		
TC20	0,16	0,10	0,63	0,17	1,06	5,59	1		
TC30	0,15	0,10	0,67	0,14	0,93	4,37	0		
Sand	0,16	0,10	0,63	0,13	0,81	6,19	0	20°C	Sakarya
TC10	0,17	0,17	1,00	0,18	1,06	5,40	2		
TC15	0,18	0,16	0,89	0,18	1,00	5,51	2		
TC20	0,18	0,15	0,83	0,18	1,00	5,59	2		
TC30	0,17	0,16	0,94	0,19	1,12	5,71	2		
Sand	0,16	0,15	0,94	0,18	1,13	5,48	2	50°C	Sakarya
TC10	0,17	0,16	0,94	0,19	1,12	5,71	0		
TC15	0,18	0,18	1,00	0,19	1,06	5,86	1		
TC20	0,17	0,17	1,00	0,19	1,12	5,73	1		
TC30	0,18	0,17	0,94	0,19	1,06	5,72	1		

7.5. Discussion of Results

In the experimental study, static, dynamic and shaking table tests are performed. For shaking table tests, the Numerical Analysis of the flexible shear stack is performed. According to the all results of laboratory tests, the liquefaction hazard mitigation effect of tire material inclusion into the sand is investigated. Tests are repeated under different temperature values and liquefaction mitigation effect of the specimens are investigated.

The experimental program began with static laboratory tests. In these set of tests, sieve analysis of materials is performed. The unit weight and specific gravity of all specimens are determined. A set of small scale direct shear test is performed with only sand, tire material and also its mixtures with different proportions. California Bearing Ratio (CBR) tests are performed with the same materials. In the light of the static laboratory tests, the liquefaction susceptibility of soil is investigated. According to the liquefaction criterias stated by Tsuchida (1970), Seed and Idriss (1982) and subsequently confirmed by Youd and Gilstrap (1999), the evaluation of liquefaction susceptibility of soil is investigated. Additionally, cyclic triaxial tests are performed under three different confining pressures. Shear modulus and damping ratio values of specimens are obtained. The numerical analysis of flexible shear stack is conducted with SAP2000 finite element program. Based on the design criteria stated by Gazetas (1982), the model of flexible shear stack is created. The physical model of flexible shear stack is constructed by a company in Istanbul. Shaking table tests with only sand and sand-tire waste mixtures are performed at Shaking Table Laboratory of Boğaziçi University Kandilli Observatory and Earthquake Research Institute. Tests are conducted under different temperature values with diferent proportions of tire material. The liquefaction mitigation effect of tire material inclusion figured out the optimum tire content and temperature value.

As a result of static laboratory tests, the coefficient of uniformity (C_u) is calculated as 2.4 and the coefficient of curvature (C_c) is calculated as 1.35. Sand is classified as SP, poorly graded. Specific gravity determination. tests are conducted in accordance with ASTM D 854. The specific gravity of sand, tire buffings and tire crumbs materials are found as 2.67, 1.08 and 1.04 respectively.

The CBR value of the sand obtained as 7 and it is rated as 'Fair' according to the ASTM D1883-07. It is observed that the inclusion of tire crumbs material decreases the CBR value of sand. The CBR value of only sand is obtained as 7. It is decreased to 4 as minimum value for sand-tire crumbs mixture with 40%. On the other hand, it is increased up to 12 for TB2. For TB1, the maximum CBR value observed as 12. The CBR value of TB2 is higher than TB1. Less frictional surfaces occurred at mixtures with small aspect ratios of Tire Buffings material. When the anchored length of tire elements are small, the shear resistance of mixtures increases. To optimize the dimension and content of the mixture for the highest CBR value, it is concluded that the CBR value of only sand is better compared to granular tire inclusions. Also, the CBR test results indicated that as the aspect ratio increases, the effectiveness of tire waste increases.

Direct shear tests are conducted to obtain shear strength parameters of samples. Small scale direct shear tests are performed with two types of tire waste materials as tire buffings and tire crumbs. All of the tests were performed under three normal pressure values; 10, 20, and 40 kPa. According to direct shear test results, it is concluded that both tire buffings and tire crumbs inclusion improves the shear strength of the composite material. The internal friction of the sand-tire crumbs material with 10% by weight obtained as 36° while it is 24° for only sand. Direct Shear Tests with only sand, only tire crumbs, only tire buffings and tire waste included sand mixtures are performed. Sand-tire buffings and sand-tire crumbs mixtures are prepared at 5%, 10%, 15%, 20%, 30% and 40% content by weight.

As it is shown in Table 7.4 (p.147), the water content (ω) of sand is 30% and percent finer at 0.005 mm is 10%. According to these results, soil is accepted as liquefiable soil and it has to be improved against to liquefaction.

In the next step, a set of cyclic triaxial compression test is performed with only sand, mixtures of sand-tire buffings and sand-tire crumbs materials at different contents. Tire waste-sand mixtures are prepared at 10, 20 and 30% of tire waste by weight. Each test is repeated under three different confining pressures as; 40, 100 and 200 kPa.

As a result of cyclic triaxial tests, it is observed that as the confining pressure increases, shear modulus increases and damping ratio decreases. Increasing confining pressure increases the shear modulus whereas it has negligible effect on the damping ratio. Additionally, shear modulus of sand decreases as tire content increases. The maximum shear modulus value observed with only sand material tested under 200 kPa. It can also be seen that at same shear strains, damping ratio of tire crumbs mixtures are higher than tire buffings mixtures. Additionally, TB30 specimens which are tested under 40 kPa. confining pressure displayed the maximum damping ratio value among all TB specimens.

Shaking table tests are performed with only sand and sand-tire waste mixtures. Three different types of motions; İzmit (E-W), Sakarya (N-S) and Tabas (E-W) were applied to specimens during the experiments. The temperature of shaking table cabin arranged as 0°C, 20°C and 50°C. Five different types of data were obtained from accelerometers, pore pressure transducer and laser displacement sensor. To control the temperature of specimen, a laser temperature sensor is used. The amplification factors of each specimen are obtained by the division of acceleration values to A1 base input acceleration value. Each of parameters; tire shape, temperature and tire content effected the performance of specimens during the motion.

Shaking table tests are performed under three different temperature values; 0°C, room temperature and 50°C. The pore water pressure of the specimens tested under 0°C are constant and very small. Due to the freezing effect of temperature, the upward motion of water is minimized. Hence, the pore pressure value of specimens tested under 0°C was very low. Additionally, displacement values of specimens tested under all three temperatures are very close to each other.

The inclusion of tire material changed the performance of soil specimens irregularly. The increasing content of tire material changed the both pore water pressure, displacement and acceleration values of specimens. TC and TB specimens tested under the three earthquake ground motions demonstrated that the energy absorption effect of rubber increased as the tire content increased.

Both, TB and TC inclusion changed the acceleration values of A1 base input motion. The acceleration reduction factors of TB and TC specimens are very close to each other. Generally, acceleration values recorded by A3 accelerometer which is fixed from upper layer of specimen is higher than records taken by A2 accelerometer from lower layers. Also, the acceleration values recorded at lower layer of soil are lower than the base input motion accelerations both for TB and TC specimens. Pore water pressure of all TB and TC specimens are at very low range. The upward motion of water is limited for both TB and TC specimens. Displacement values of specimens varied between 3 and 7cm for both of tire materials. Evidently, the effect of tire shape included in sand is insignificant in comparison to other affecting parameters

To take all of the shaking table test results of TC specimens into evaluation, it is obvious that TC15 specimen tested at 0°C temperatures displayed highest performance among all of TC specimens. The amplification factor of the accelerometers A2 and A3 are 0.56 and 0.80 respectively for the test performed at 0°C under Tabas (E-W) ground motion. Also, the amplification factor of the accelerometers A2 and A3 are 0.56 and 0.88 respectively for the test performed at 0°C under Tabas (E-W) ground motion.

TC specimens under Tabas (E-W) ground motion and TB specimens under İzmit (E-W) ground motion displayed best performance. It is noteworthy that, the amplification factor of TB30 specimen is 0.82 and 0.75 for A2 and A3 accelerometers. Smaller acceleration ratio means higher effectiveness in reducing ground acceleration to which an increasing attention has been paid by earthquake engineering (Tsang *et. al.*, 2010).

Specimens tested at 0°C are more resistant against to the liquefaction than the ones tested at 20°C and 50°C. Liquefaction did not observed from TB20 and TB30 specimens at three temperature values. All of the TC specimens are liquefied at tests performed at 20°C and 50°C temperature values. The less liquefaction resistant TB specimen is TC10 specimen.

The results of laboratory tests are summarized in Table 7.6.

Table 7.6. Results of Laboratory Tests.

RESULTS OF LABORATORY TESTS															
SPECIMEN	γ (kn/m ³)	Dr	Test Name		Test Name		Test Name						Test Name		
			Direct Shear Test		CBR Test		Cyclic Triaxial Test						Shaking Table Test		
			c	ϕ	CBR	General Rating	Damping Ratio			Shear Modulus			Liquefaction Observed?		
							40 kPa	100 kPa	200 kPa	40 kPa	100 kPa	200 kPa	0°C	Room Temp.	50°C
S	14,85	0,38	0,00	24,00	7,34	Fair	0,64 - 1,24	0,78 - 1,40	0,83 - 1,60	31 - 70	37 - 83	48 - 109	NO	YES	YES
TC	6,10	0,38	5,75	11,30	-	-	-	-	-	-	-	-			
TB	4,10	0,43	5,30	28,00	-	-	-	-	-	-	-	-			
TC10	12,60	0,37	3,50	35,80	6,78	Poor to Fair	1,16 - 3,08	0,91 - 2,42	0,75 - 1,98	39,56 - 17,19	42,48 - 21,26	50,32 - 23,40	NO	YES	YES
TC20	11,20	0,36	4,15	30,40	5,34	Poor to Fair	1,33 - 3,53	1,15 - 3,35	1,03 - 2,65	30,26 - 13,15	34,00 - 14,00	41,48 - 18,00	NO	YES	YES
TC30	10,30	0,34	4,25	29,50	4,65	Poor to Fair	1,68 - 4,10	1,43 - 3,32	1,11 - 2,98	23,30 - 10,12	26,18 - 11,37	36,29 - 18,07	NO	YES	YES
TC40	9,80	0,44	3,85	33,00	4,13	Poor to Fair	-	-	-	-	-	-			
TB10	11,80	0,35	13,20	27,40	8,65	Fair	0,80 - 2,12	0,73 - 1,94	0,65 - 1,74	30,64 - 18,05	37,19 - 21,24	44,06 - 26,49	NO	YES	YES
TB20	10,80	0,31	14,50	34,00	10,63	Fair	0,87 - 2,30	0,82 - 2,18	0,73 - 1,95	30,07 - 14,50	33,36 - 19,05	39,52 - 24,38	NO	NO	NO
TB30	9,50	0,44	12,00	30,50	10,43	Fair	1,00 - 2,67	0,88 - 2,35	0,78 - 2,08	24,82 - 13,19	28,13 - 17,21	35,69 - 20,60	NO	NO	NO
TB40	7,20	0,47	8,20	24	10,02	Fair	-	-	-	-	-	-			

8. CONCLUSION AND RECOMMENDATIONS

To investigate the liquefaction mitigation effect of tire material, a set of laboratory test is conducted. In this sense, the inclusion of tire material with different percentages and shapes were investigated. Direct shear and cyclic triaxial tests at three different confining pressures and CBR tests are performed. The liquefaction susceptibility of soil is investigated according to the static laboratory test results. After static laboratory tests, Cyclic Triaxial Tests are performed with sand and sand-tire composites at different tire percentages by weight. Cyclic Triaxial Tests are performed to obtain shear modulus and damping ratio values of specimens. Then a set of shaking table tests are performed at different temperature values with different type and content of tire waste materials. All geotechnical laboratory tests are conducted in accordance with ASTM standards.

The evaluation of liquefaction mitigation effect of tire material is done according to the laboratory test results which are summarised in Table 7.6. Both tire buffings and tire crumbs materials provide advantages on soil in the use of geotechnical applications. The bearing capacity, shear resistancy and liquefaction resistancy of soil specimens are improved with the addition of tire material. The temperature affected dynamic performance of specimens. TB specimens showed best performance at 0°C.

The validity of the proposed method has been shown by a series of laboratory tests. The results of the Shaking Table Tests indicate that the use of tire waste additive improves the performance of soil against to the earthquake induced liquefaction hazards. Also, to observe the liquefaction mitigation effect of tire material in more detail, the inclusion of tire material should be done with small increments of percentages. Moreover, to figure out the behaviour of tire material under different climatic conditions, tests should be conducted under different temperature values.

On the basis of the results of experimental study, the following conclusions are made:

- The bearing capacity, shear resistancy, and liquefaction resistancy of soil specimens should be improved with the addition of tire material.
- Maximum angle of internal friction is measured as 35.80° from TC10.
- The highest CBR value obtained from TB20 specimen as 10.63.
- The damping ratio value of the TC30 specimen tested under 40 kPa confining pressure is the highest one as 4.10%. The damping ratio value of only sand specimen tested under 40kPa confining pressure is 1.24%.
- The shear modulus value of TC10 specimen which is tested under 200 kPa is the maximum one as 50.32 MPa. The shear modulus value of only sand specimen tested under 200 kPa confining pressure is 109 MPa.
- During the shaking table tests, none of the specimens tested at 0°C is liquefied.
- TC15 and TB30 specimens displayed the best seismic performance under Tabas (E-W) earthquake ground motion at 0°C .
- TC15 and TB30 specimens displayed the best seismic performance under İzmit (E-W) earthquake ground motion at 0°C and 20°C .
- TB15 and TC10 specimens displayed the best seismic performance under Sakarya (N-S) earthquake ground motion at 0°C .
- TB15 and TC20 specimens displayed the best seismic performance under Tabas (E-W) earthquake ground motion at 50°C and 0°C respectively.
- Among all specimens tested under earthquake ground motions at three different temperature values, TB30 and TC15 specimens displayed the best performances under Tabas (E-W) ground motion under 0°C temperature.

APPENDIX A: SHAKING TABLE TEST RESULTS OF SAKARYA (N-S) GROUND MOTIONS

A.1. Sand Specimen subjected to Sakarya (N-S) Earthquake Motion at 0°C

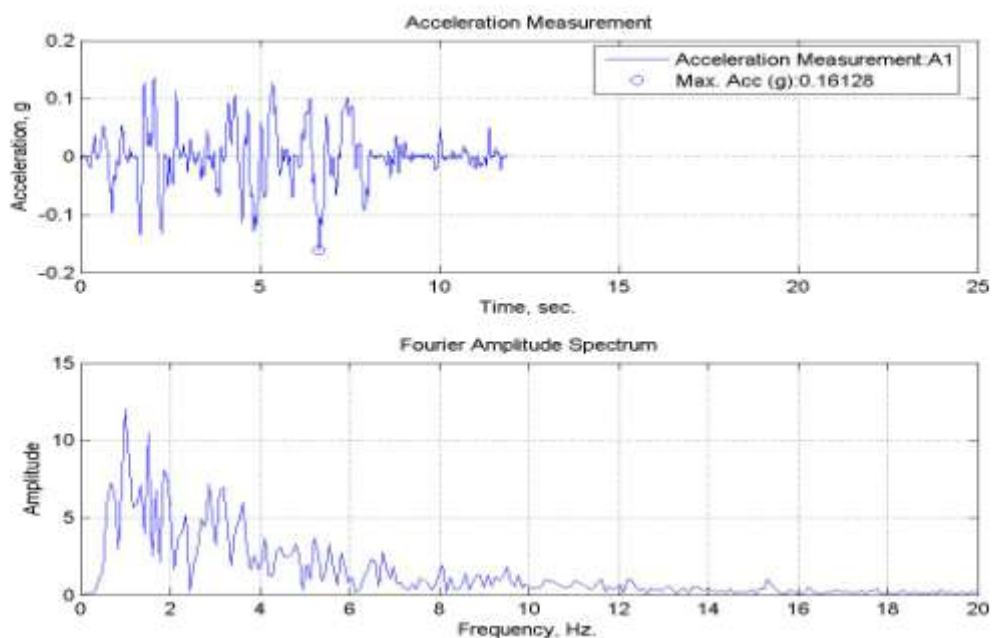


Figure A.1. A1, acceleration time history of sand specimen tested under 0°C.

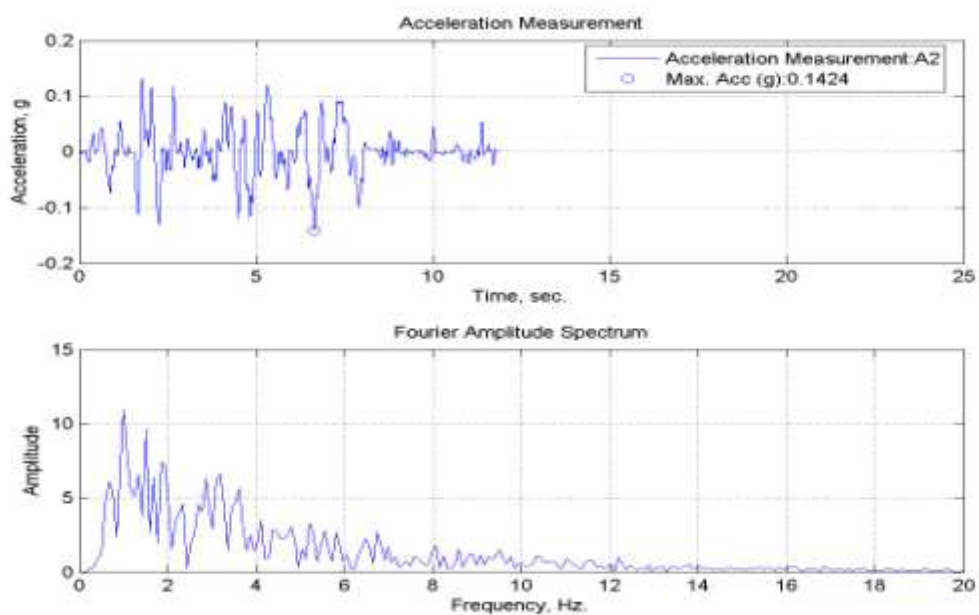


Figure A.2. A2, acceleration time history of sand specimen tested under 0°C.

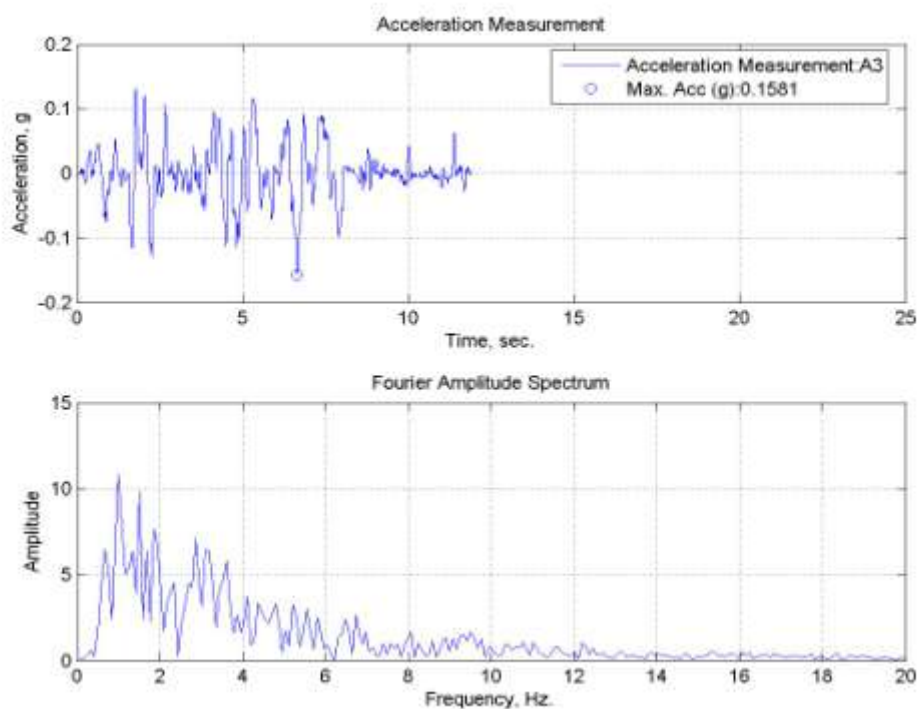


Figure A.3. A3, acceleration time history of sand specimen tested under 0°C.

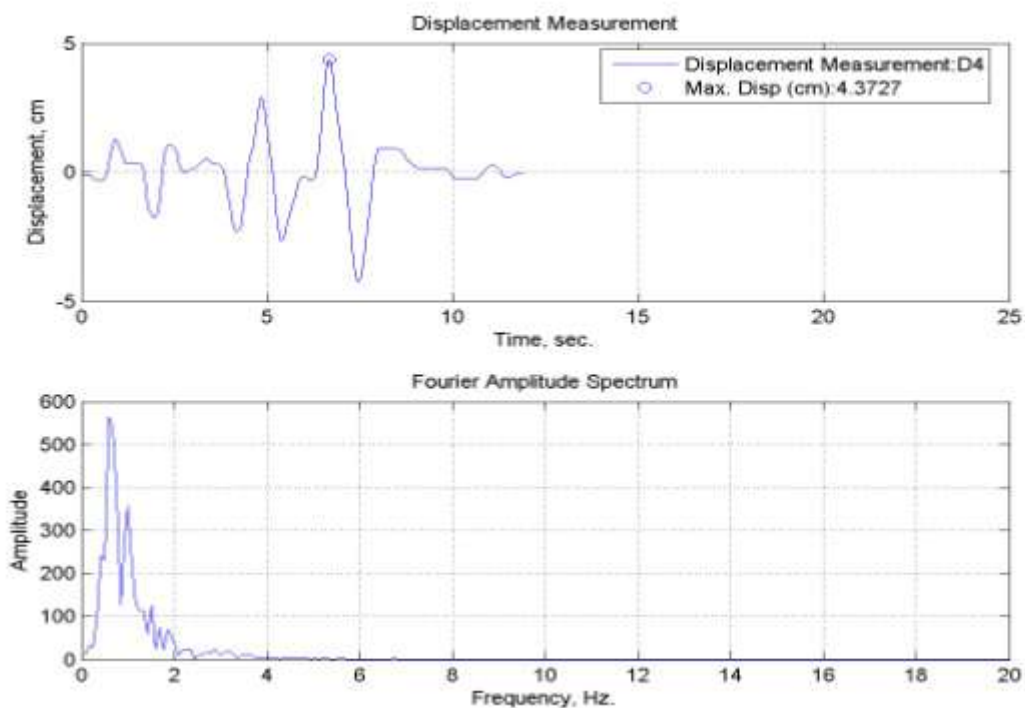


Figure A.4. Lateral displacement time history for sand specimen tested under 0°C.

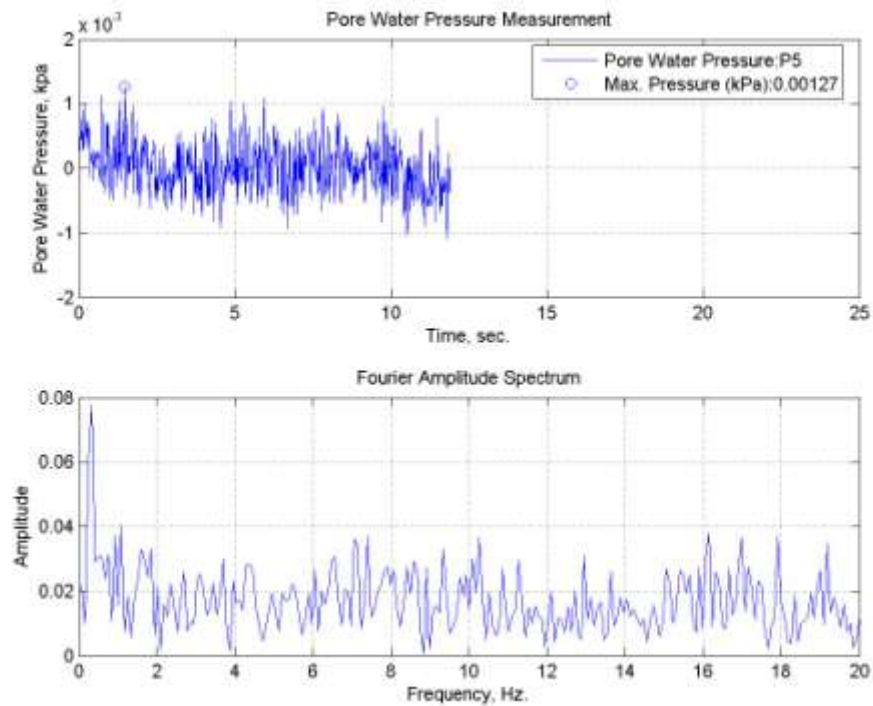


Figure A.5. Pore water pressure change of sand specimen tested at 0°C.

A.2. TB10 Specimen subjected to Sakarya (N-S) Earthquake Motion at 0°C

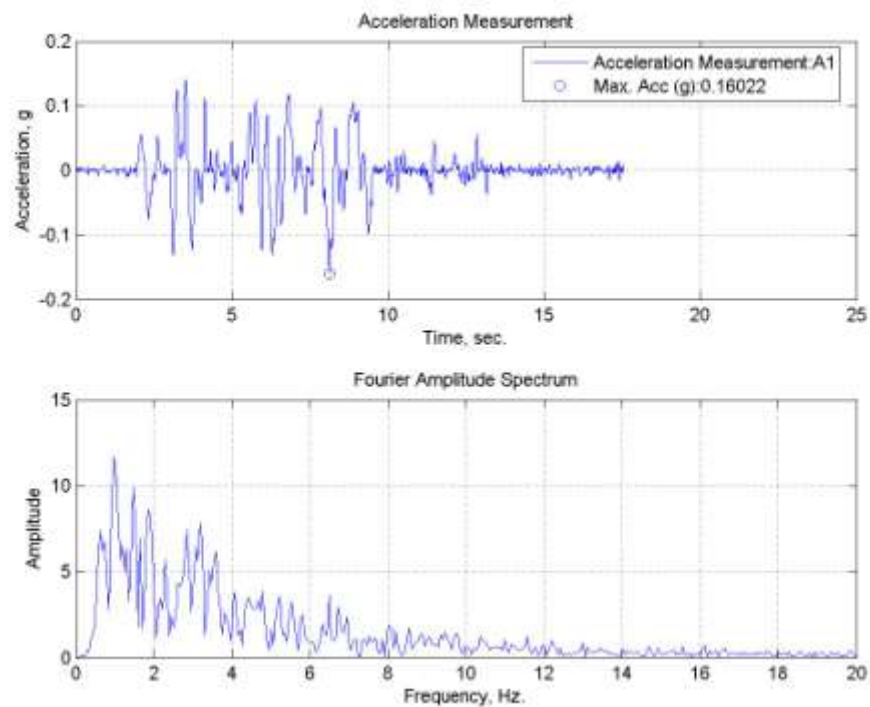


Figure A.6. A1, acceleration time history of TB10 specimen tested under 0°C.

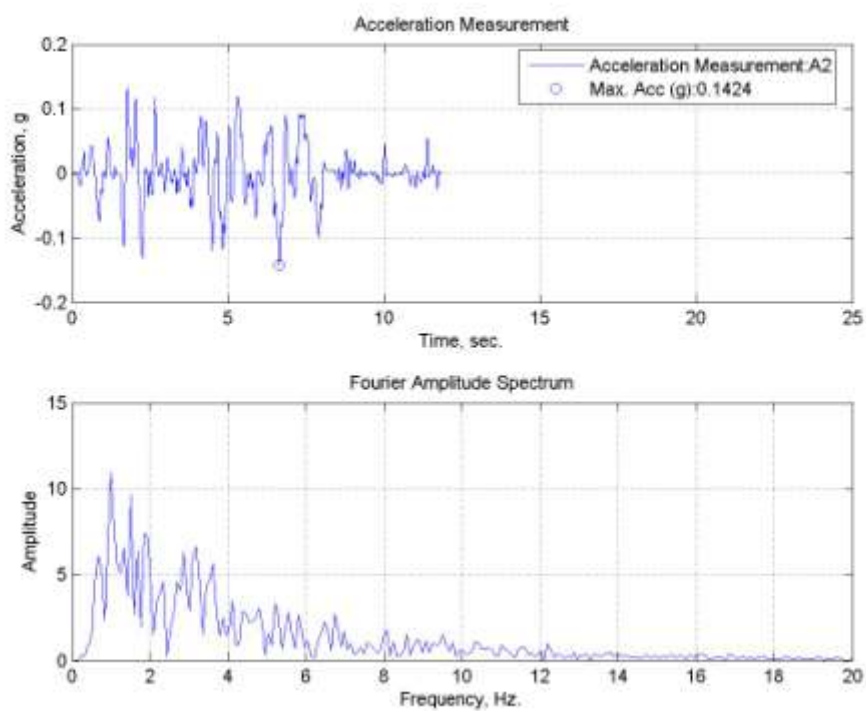


Figure A.7. A2, acceleration time history of TB10 specimen tested under 0°C.

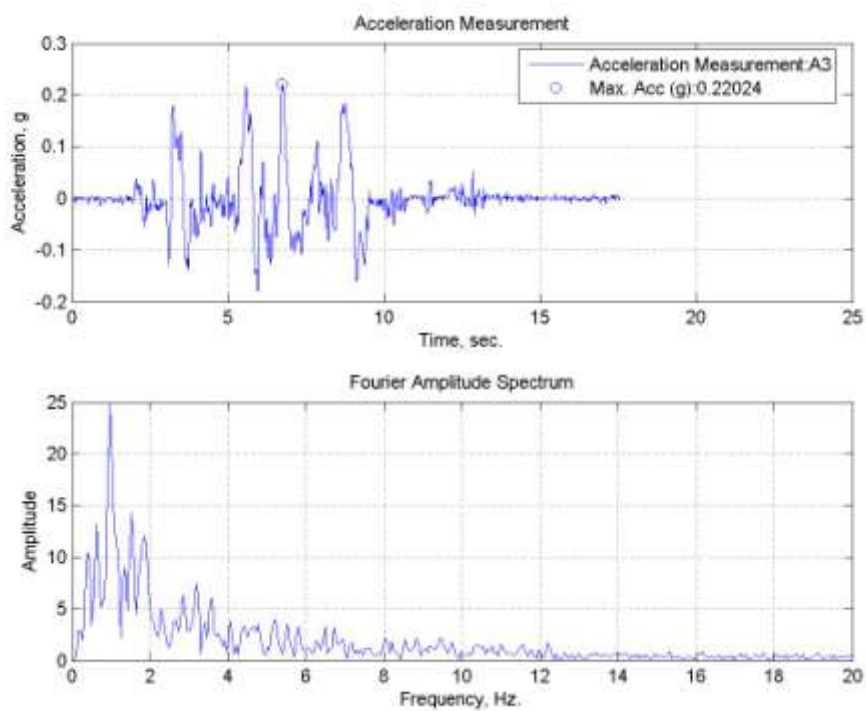


Figure A.8. A3, acceleration time history of TB10 specimen tested under 0°C.

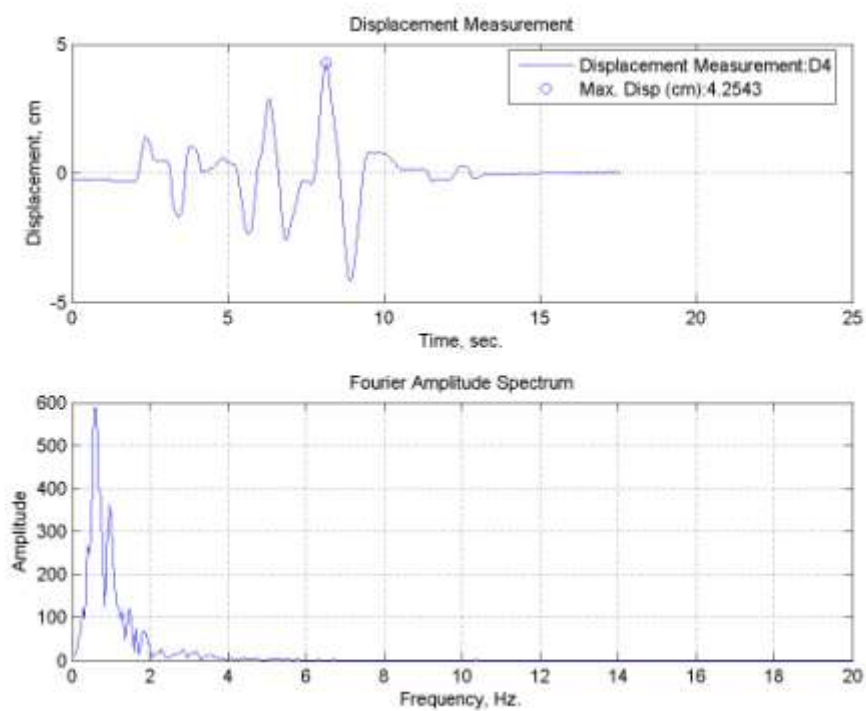


Figure A.9. Lateral displacement time history for TB10 specimen tested under 0°C.

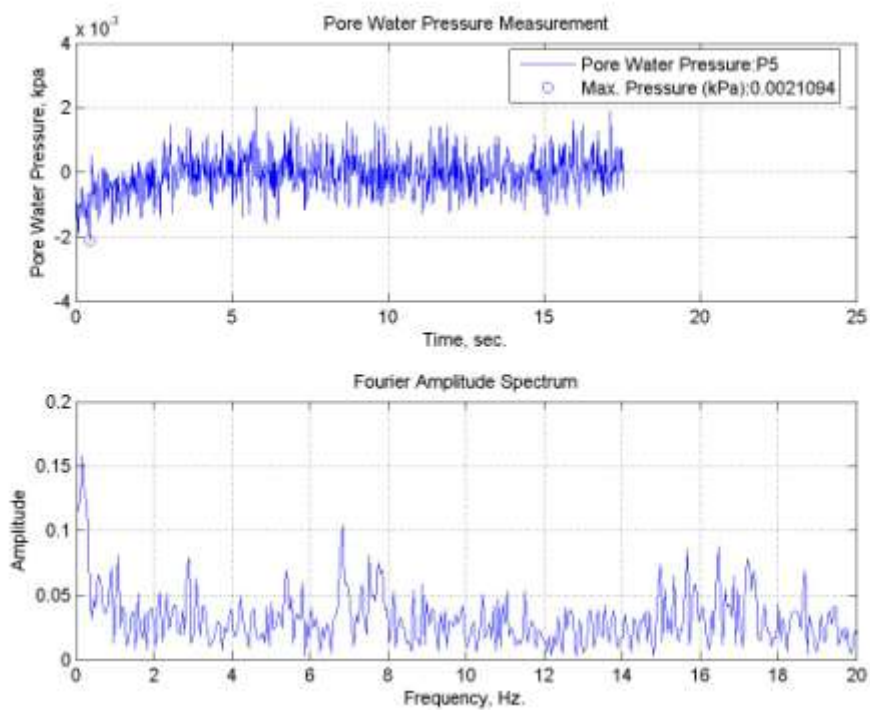


Figure A.10. Pore water pressure change of TB10 specimen tested at 0°C.

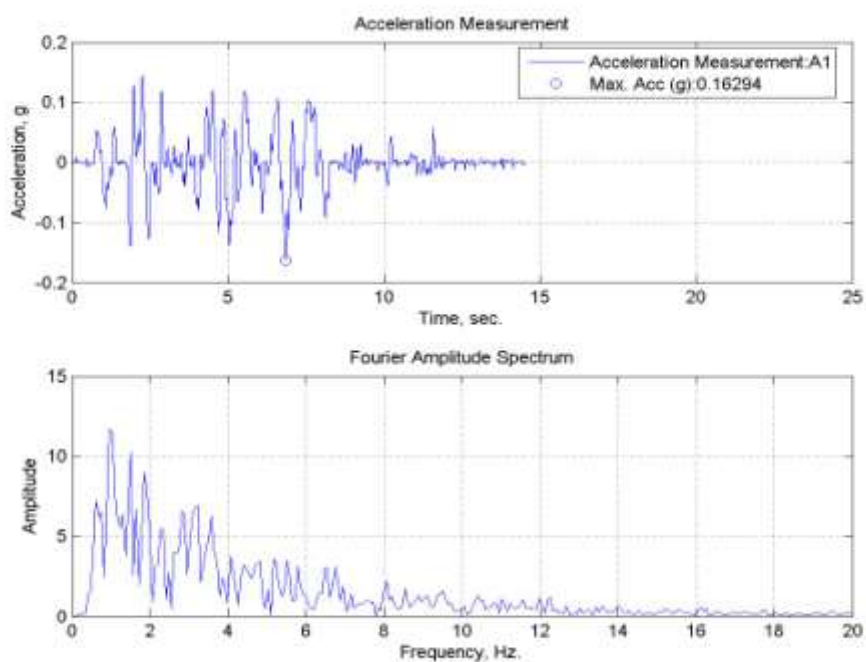
A.3. TB15 Specimen subjected to Sakarya (N-S) Earthquake Motion at 0°C

Figure A.11. A1, acceleration time history of TB15 specimen tested under 0°C.

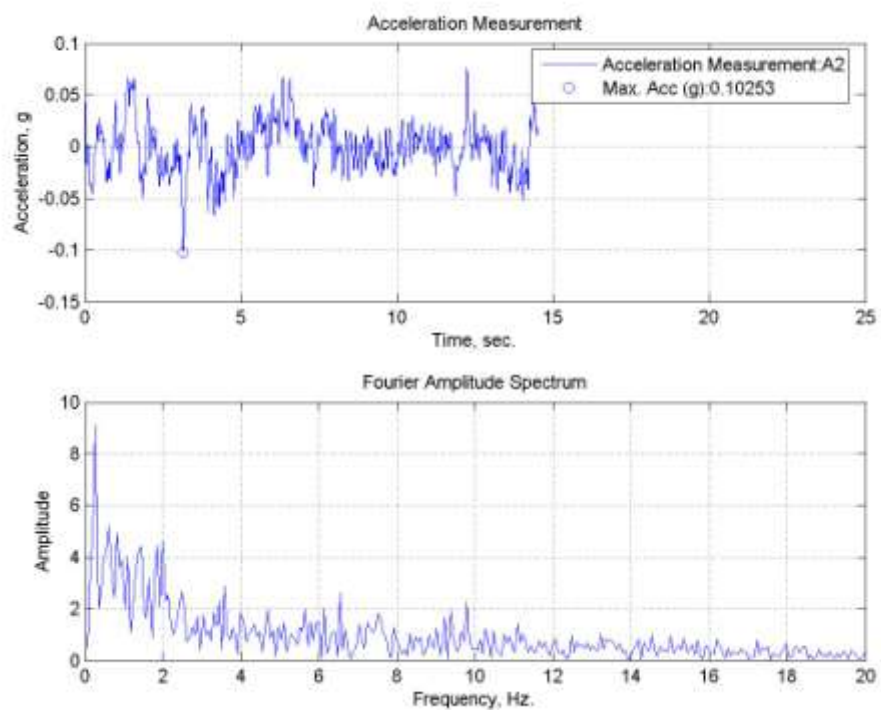


Figure A.12. A2, acceleration time history of TB15 specimen tested under 0°C.

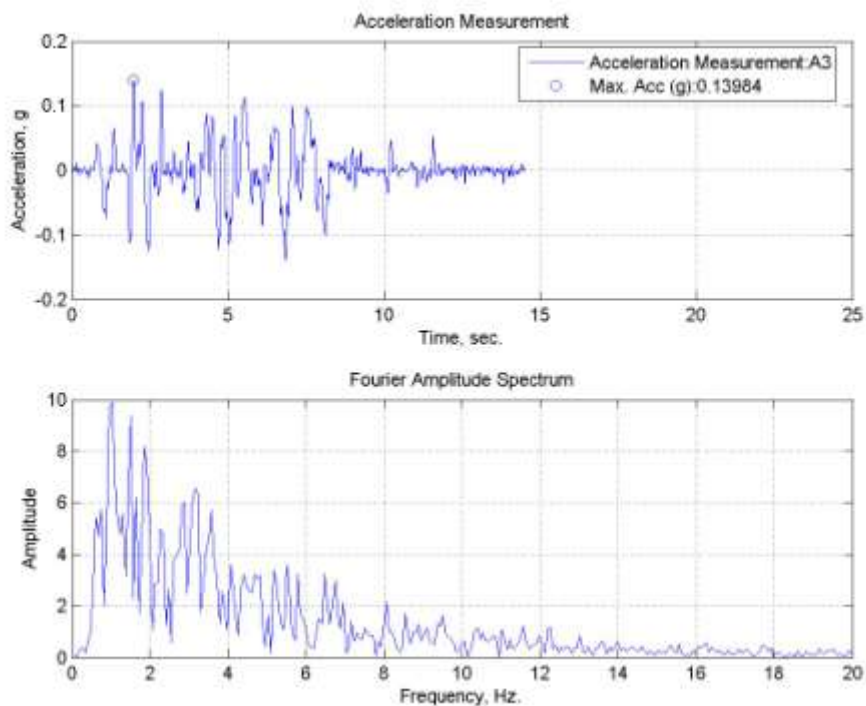


Figure A.13. A3, acceleration time history of TB15 specimen tested under 0°C.

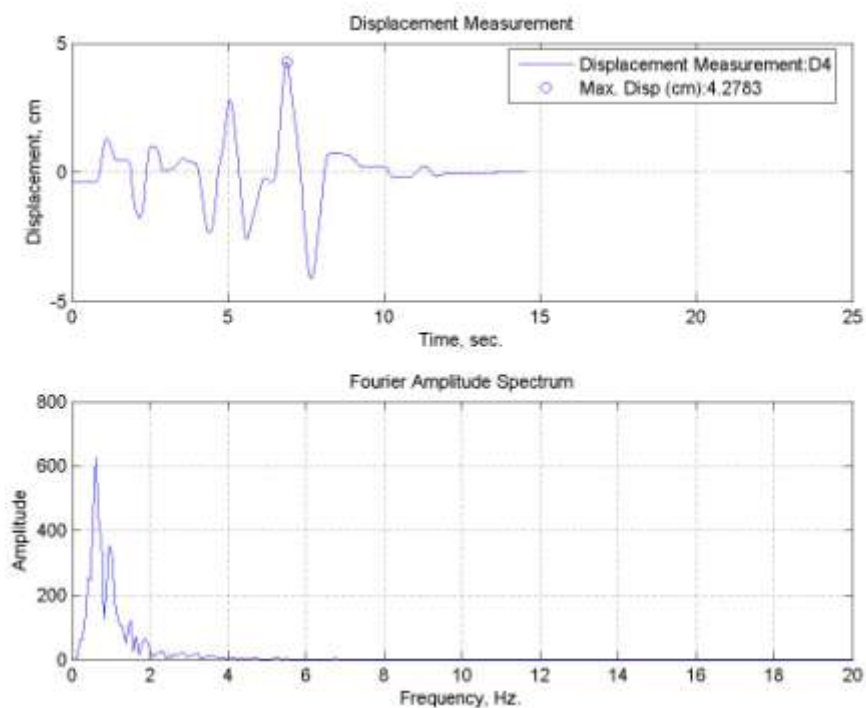


Figure A.14. Lateral displacement time history for TB15 specimen tested under 0°C.

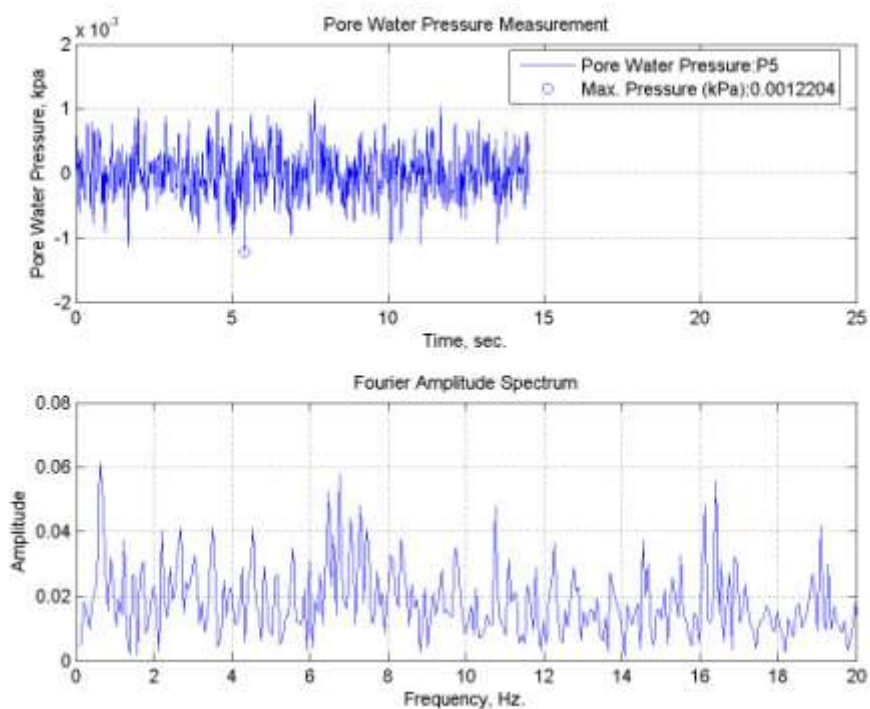


Figure A.15. Pore water pressure change of TB15 specimen tested at 0°C.

A.4. TB20 Specimen subjected to Sakarya (N-S) Earthquake Motion at 0°C

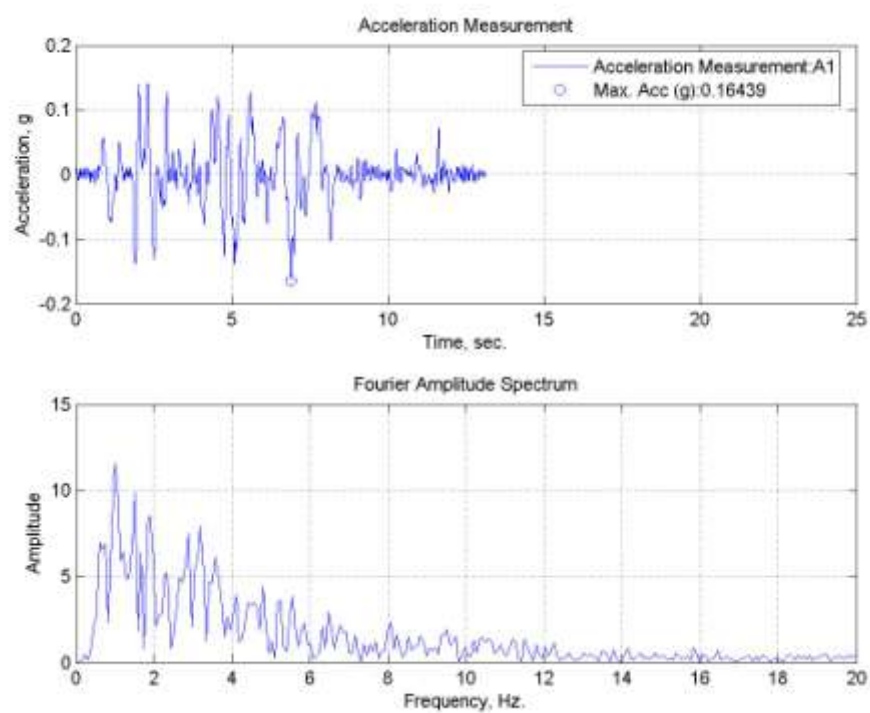


Figure A.16. A1, acceleration time history of TB20 specimen tested under 0°C.

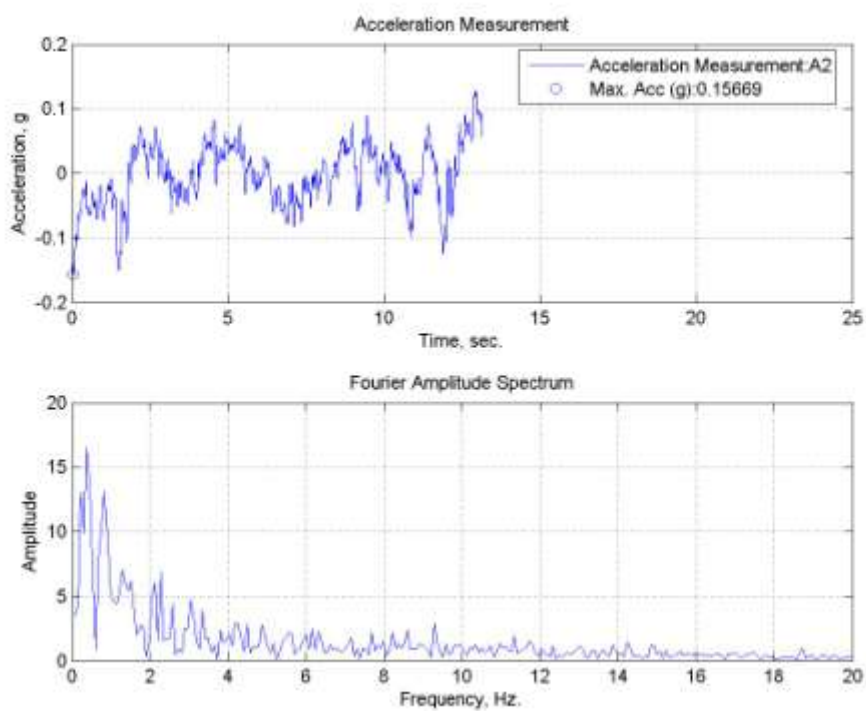


Figure A.17. A2, acceleration time history of TB20 specimen tested under 0°C.

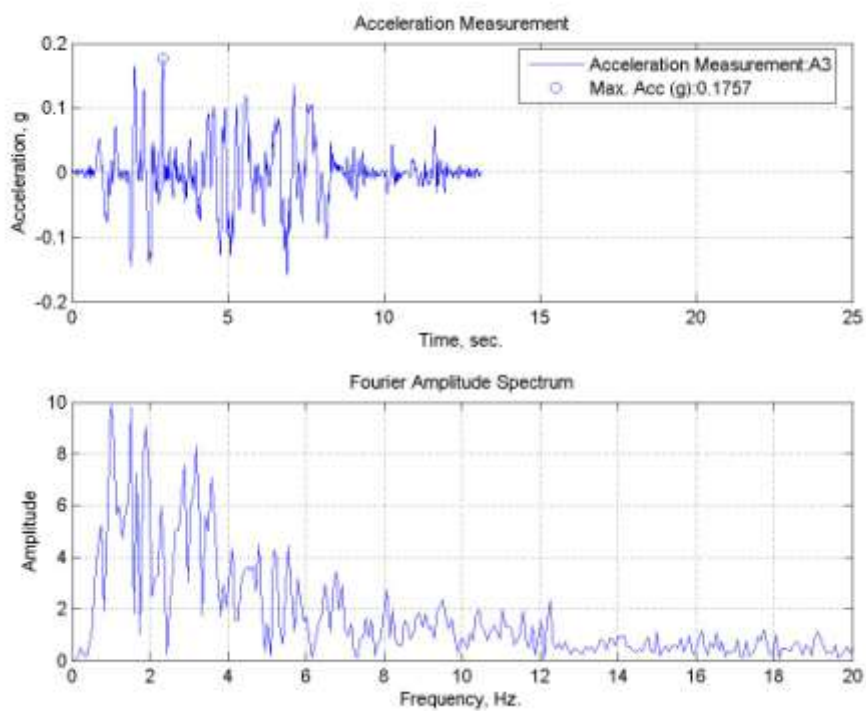


Figure A.18. A3, acceleration time history of TB20 specimen tested under 0°C.

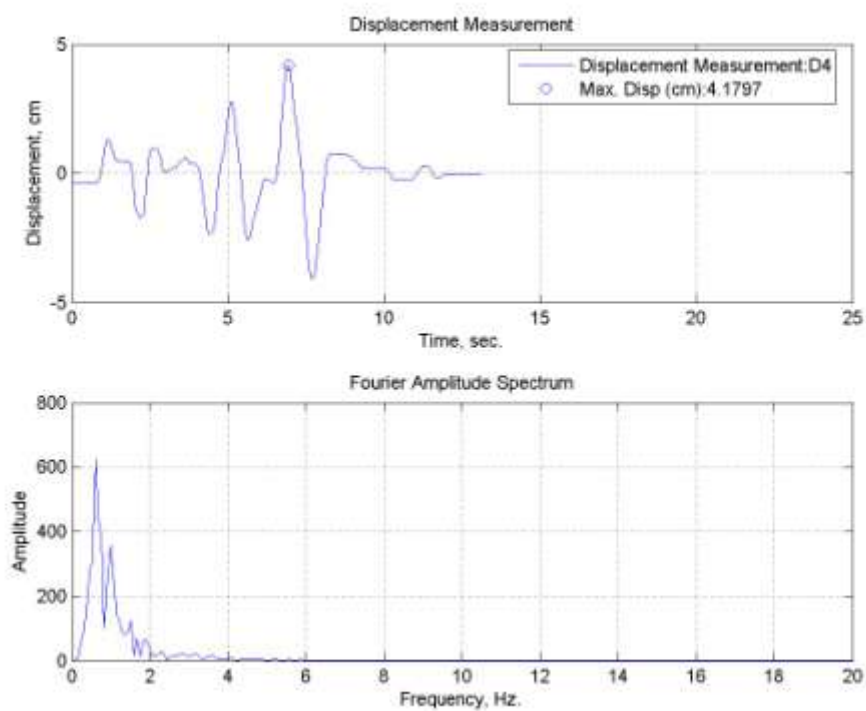


Figure A.19. Lateral displacement time history for TB20 specimen tested under 0°C.

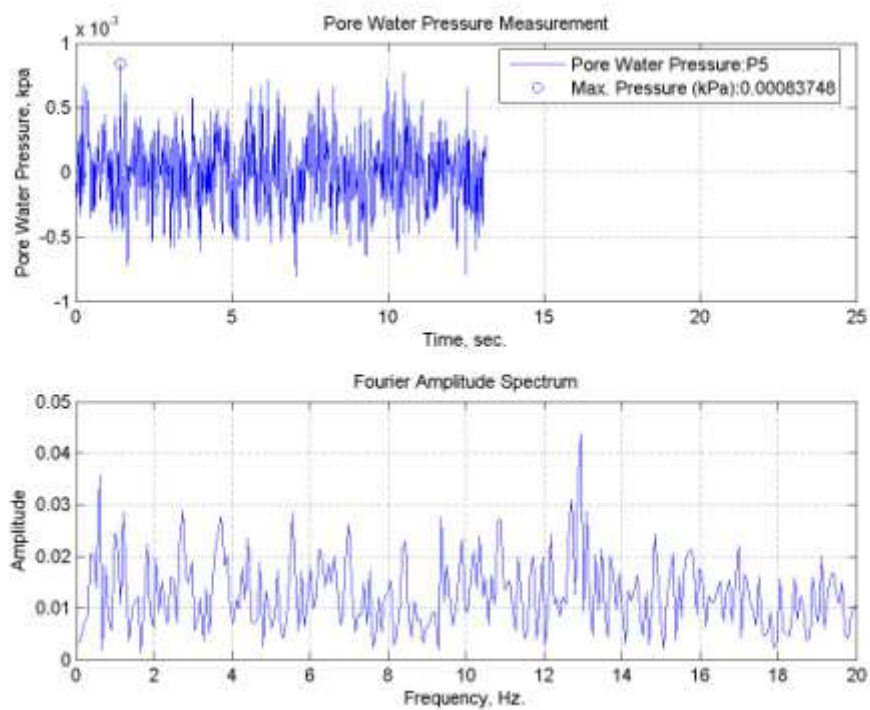


Figure A.20. Pore water pressure change of TB20 specimen tested at 0°C

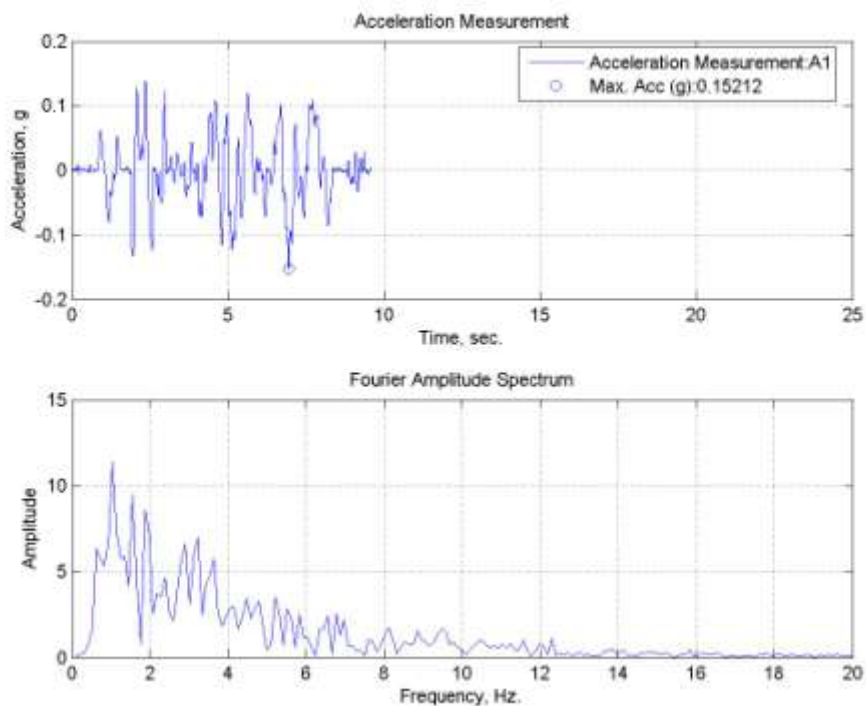
A.5. TB30 Specimen subjected to Sakarya (N-S) Earthquake Motion at 0°C

Figure A.21. A1, acceleration time history of TB30 specimen tested under 0°C.

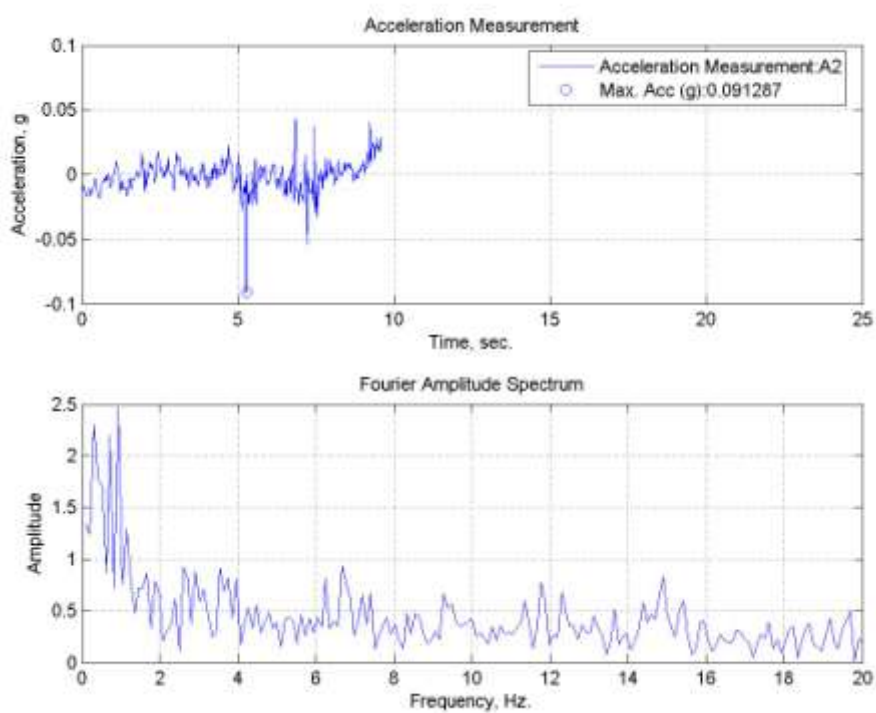


Figure A.22. A2, acceleration time history of TB30 specimen tested under 0°C.

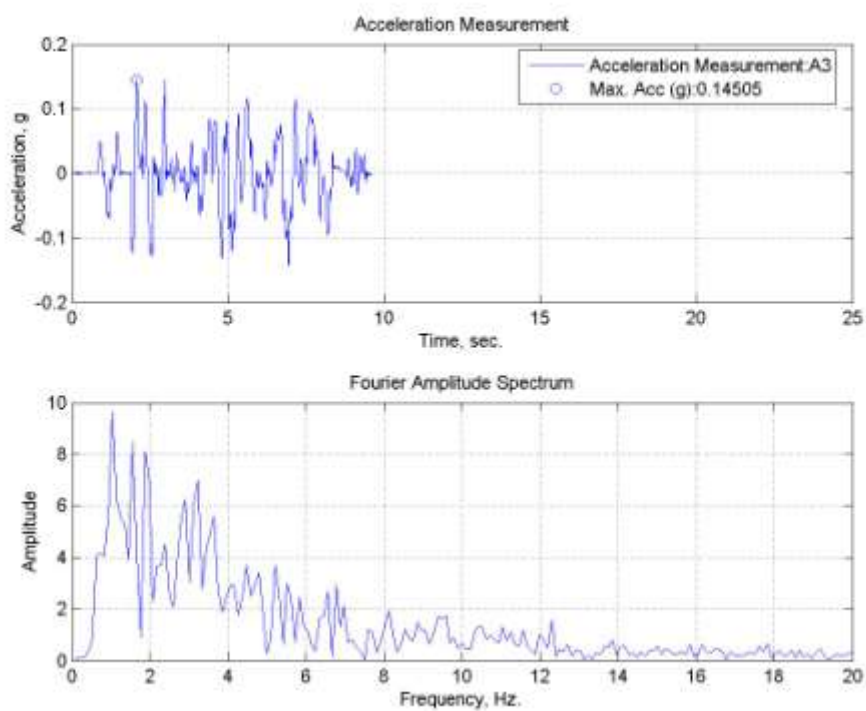


Figure A.23. A3, acceleration time history of TB30 specimen tested under 0°C.

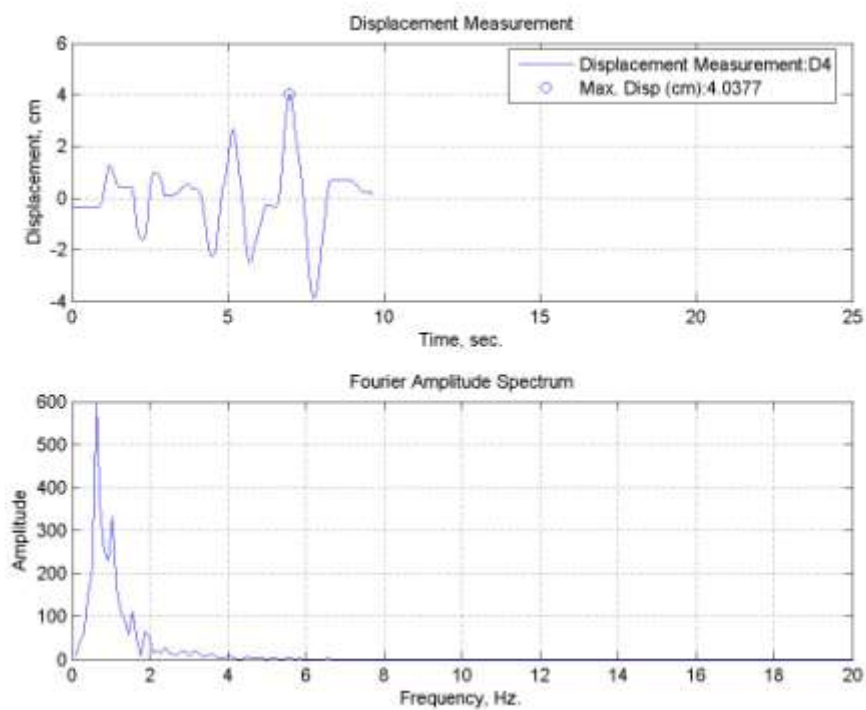


Figure A.24. Lateral displacement time history for TB30 specimen tested under 0°C.

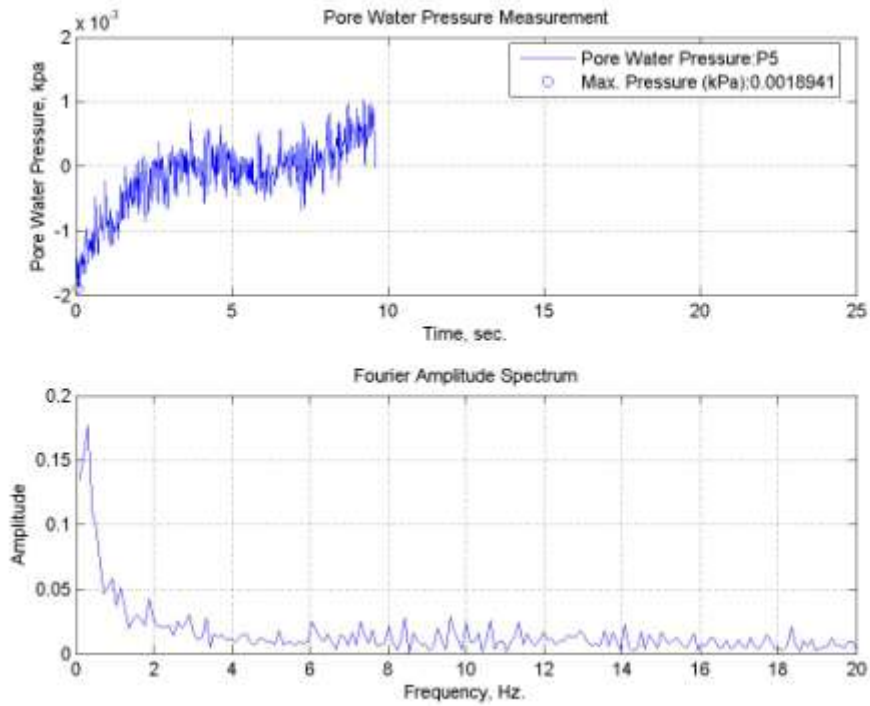


Figure A.25. Pore water pressure change of TB30 specimen tested at 0°C.

A.6. TC10 Specimen subjected to Sakarya (N-S) Earthquake Motion at 0°C

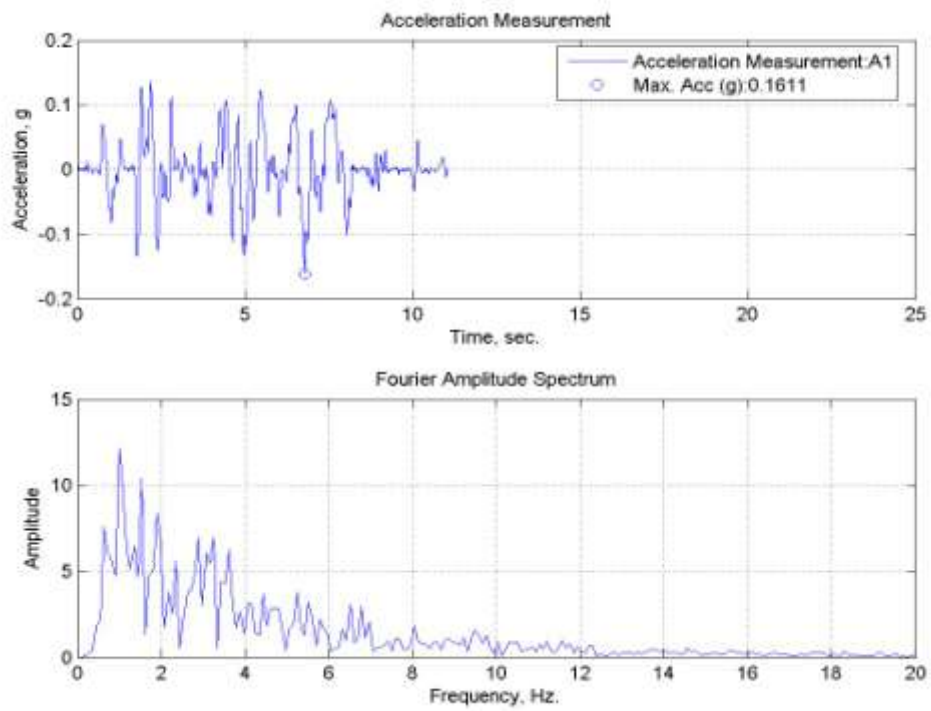


Figure A.26. A1, acceleration time history of TC10 specimen tested under 0°C.

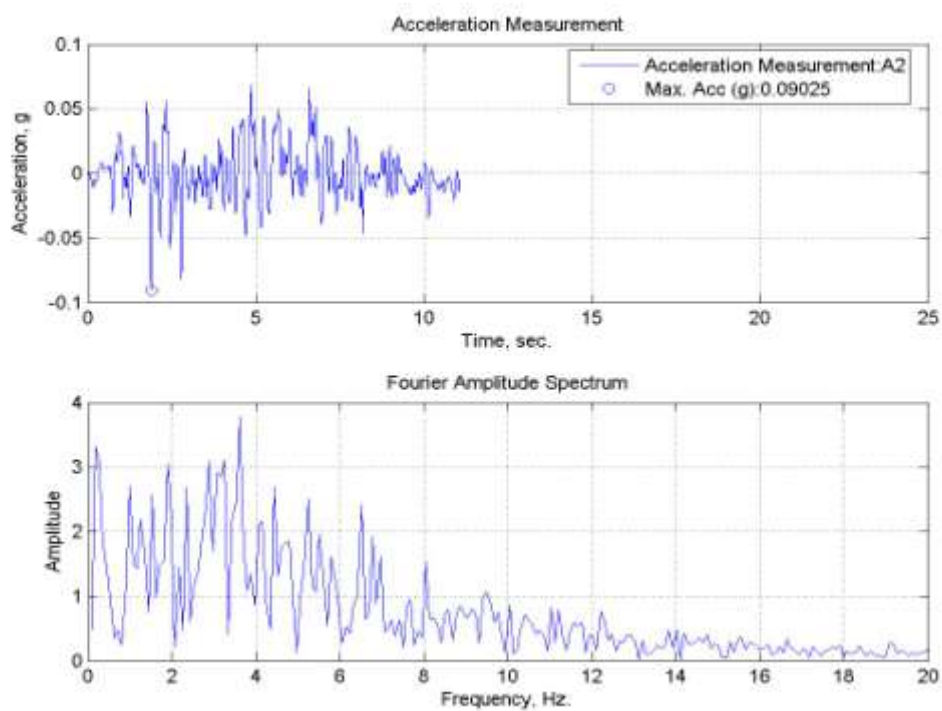


Figure A.27. A2, acceleration time history of TC10 specimen tested under 0°C.

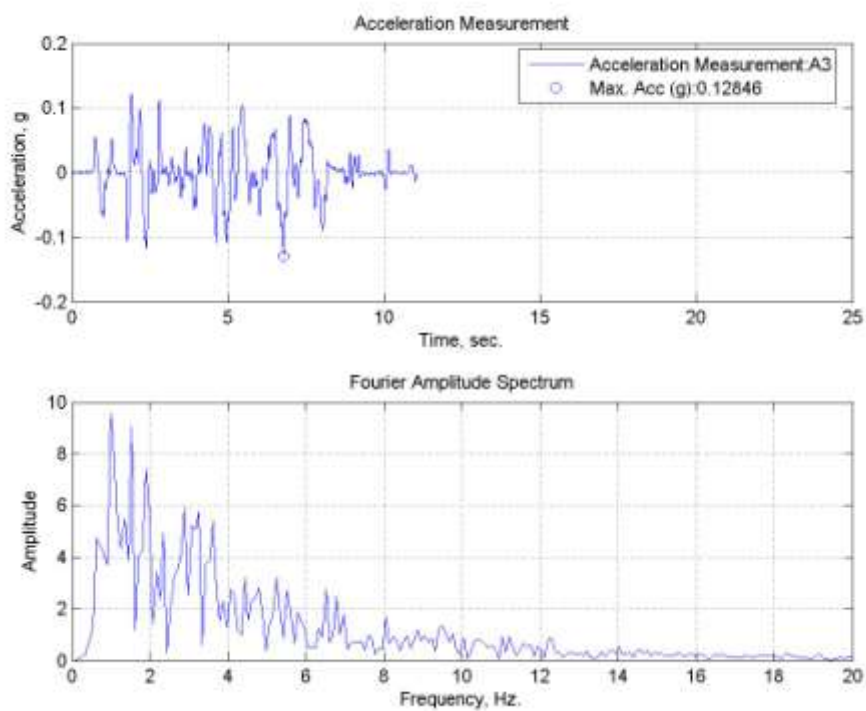


Figure A.28. A3, acceleration time history of TC10 specimen tested under 0°C.

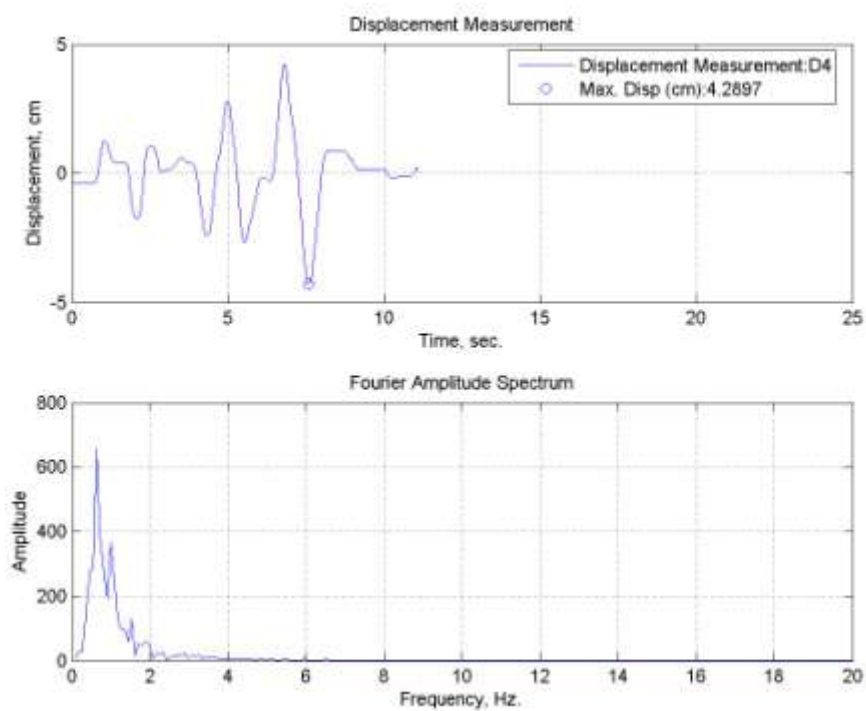


Figure A.29. Lateral displacement time history for TC10 specimen tested under 0°C.

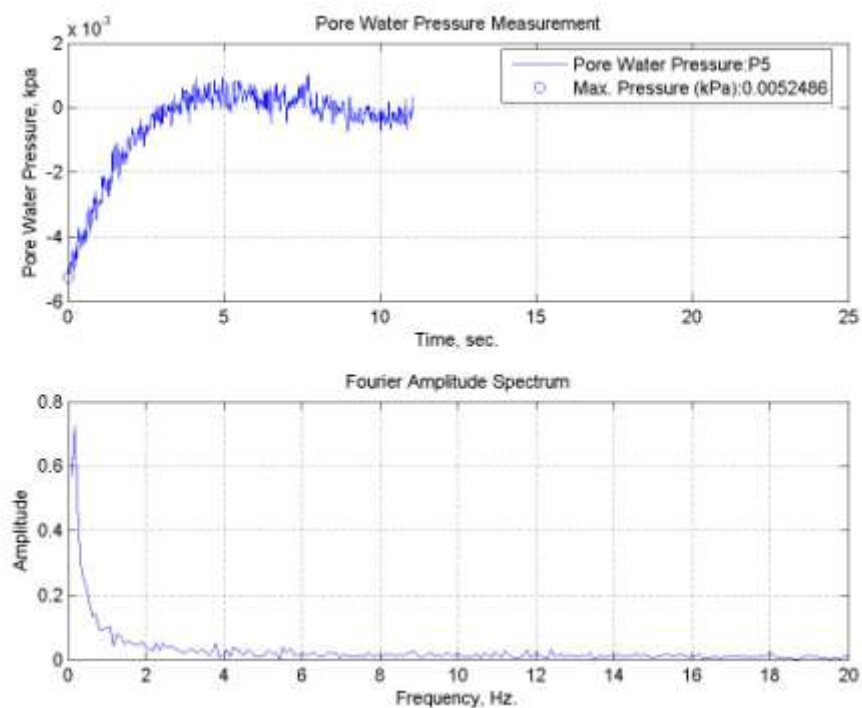


Figure A.30. Pore water pressure change of TC10 specimen tested at 0°C.

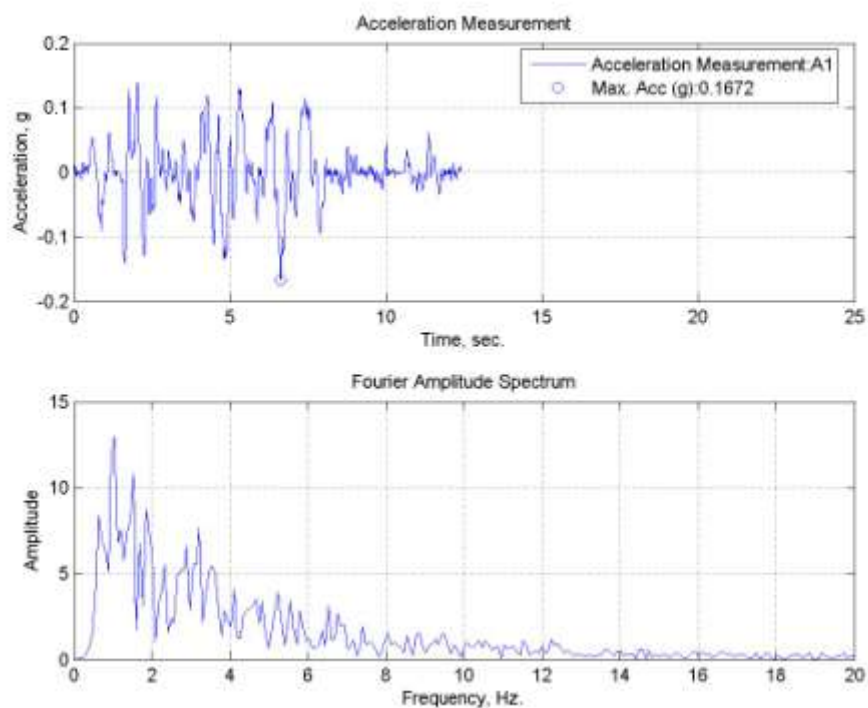
A.7. TC15 Specimen subjected to Sakarya (N-S) Earthquake Motion at 0°C

Figure A.31. A1, acceleration time history of TC15 specimen tested under 0°C.

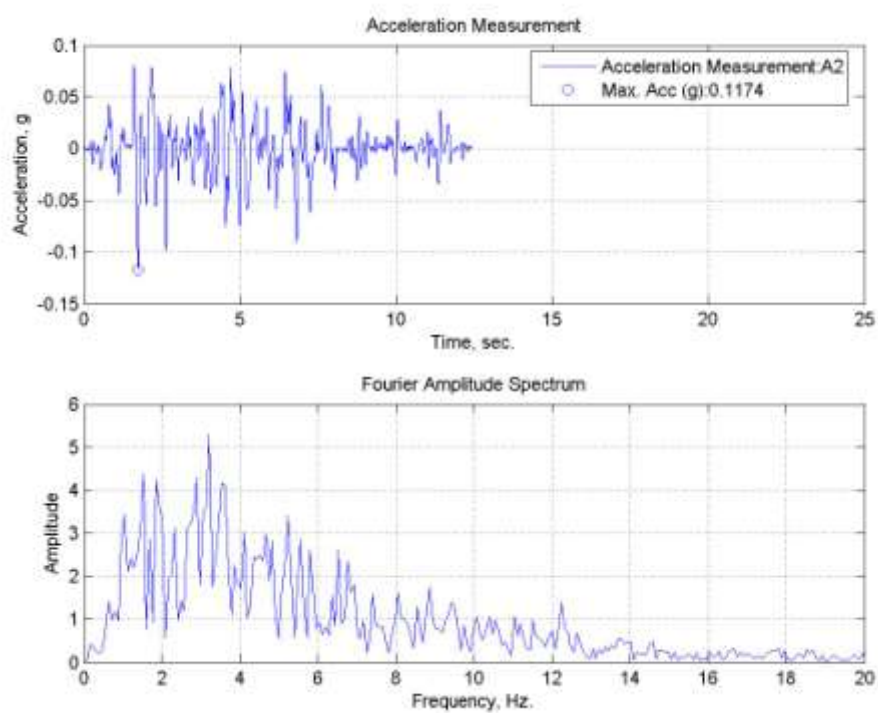


Figure A.32. A2, acceleration time history of TC15 specimen tested under 0°C.

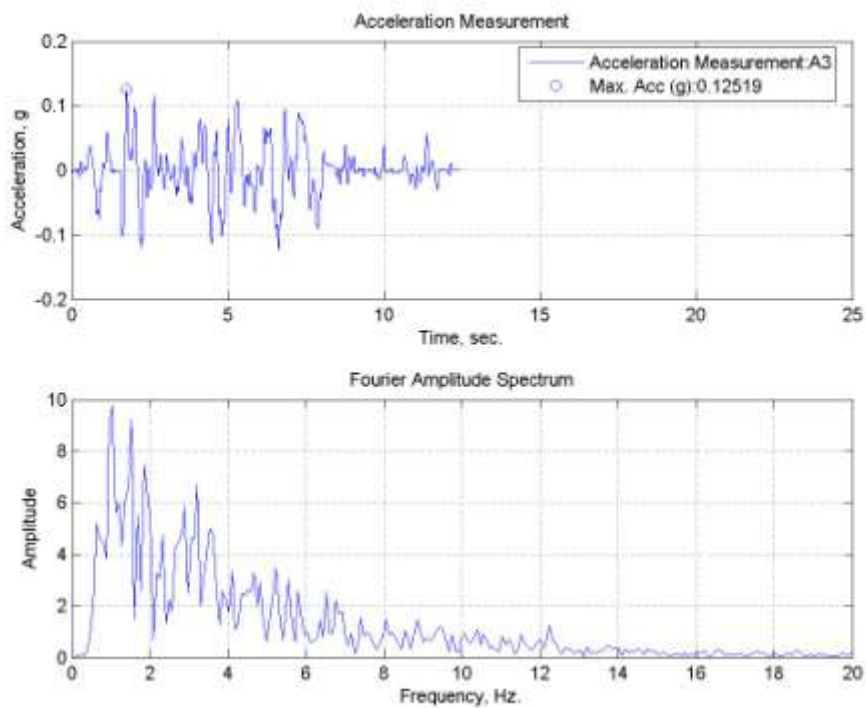


Figure A.33. A3, acceleration time history of TC15 specimen tested under 0°C.

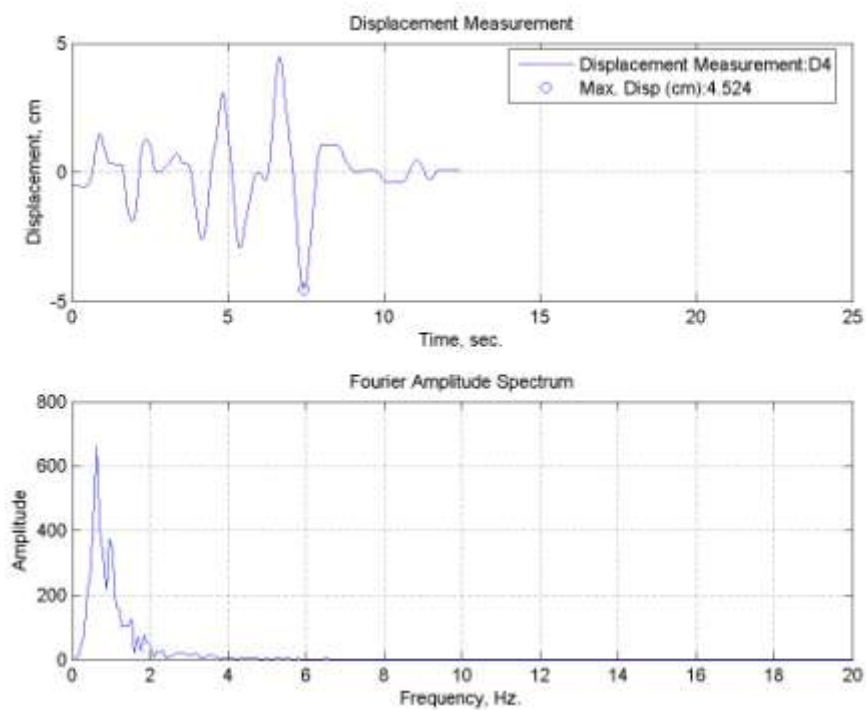


Figure A.34. Lateral displacement time history for TC15 specimen tested under 0°C.

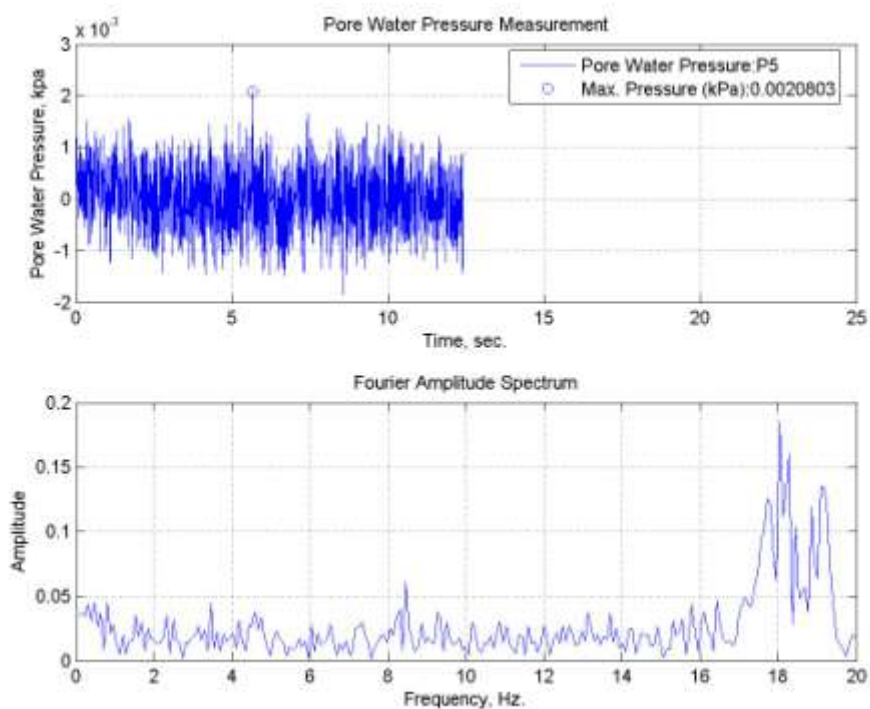


Figure A.35. Pore water pressure change of TC15 specimen tested at 0°C.

A.8. TC20 Specimen subjected to Sakarya (N-S) Earthquake Motion at 0°C

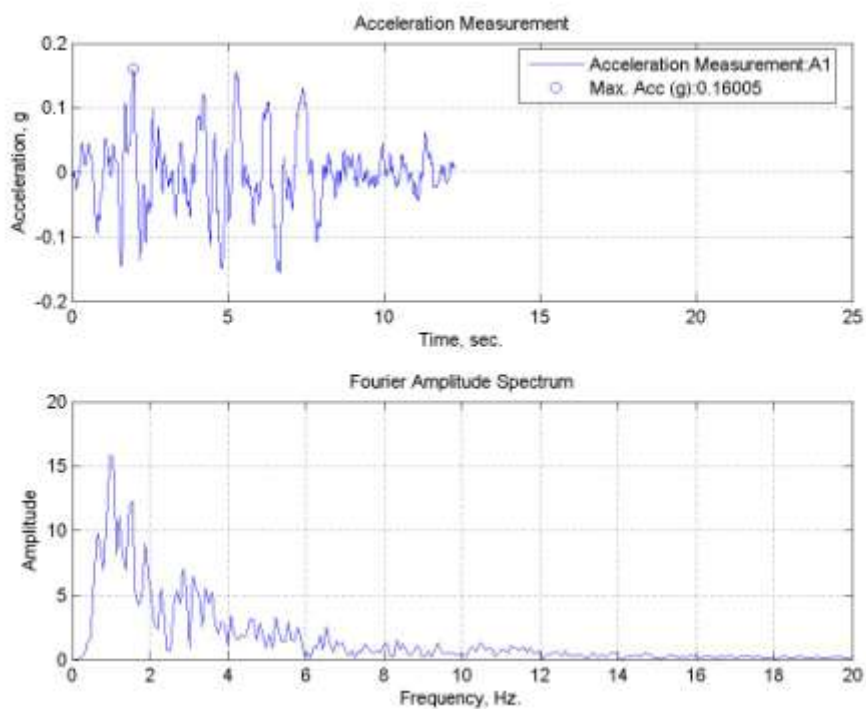


Figure A.36. A1, acceleration time history of TC20 specimen tested under 0°C.

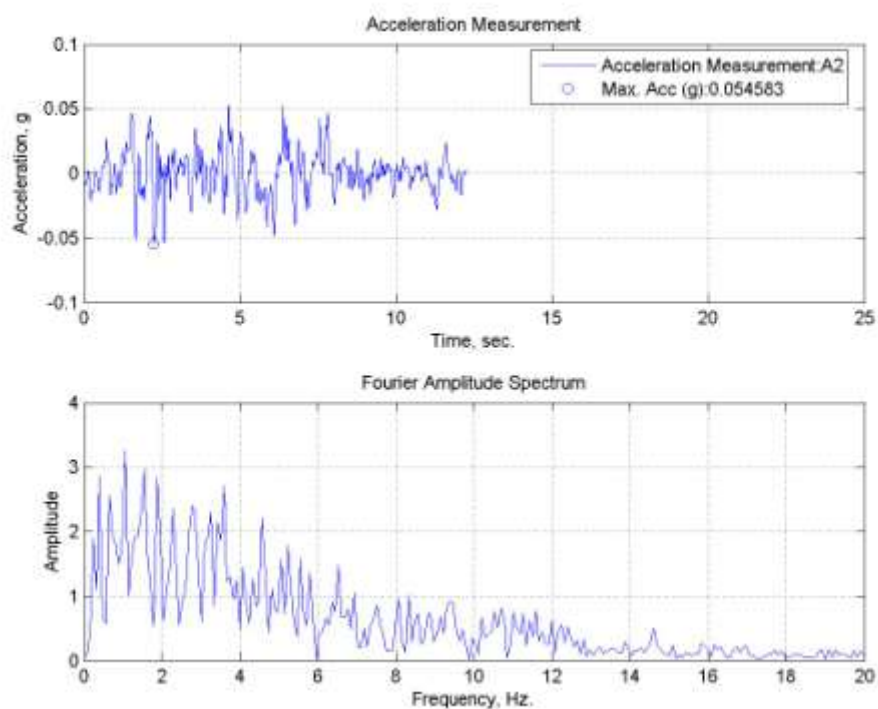


Figure A.37. A2, acceleration time history of TC20 specimen tested under 0°C.

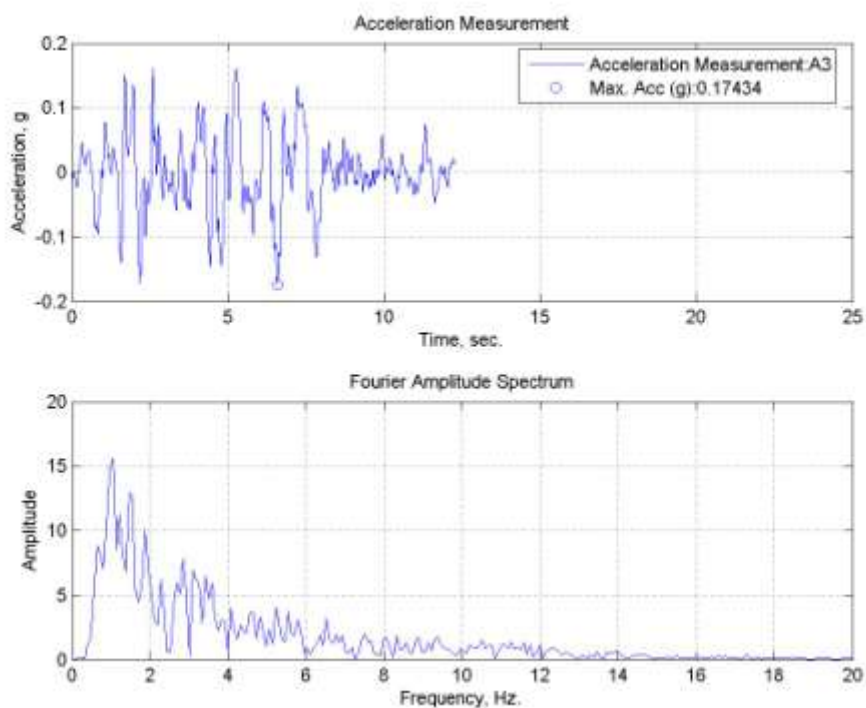


Figure A.38. A3, acceleration time history of TC20 specimen tested under 0°C.

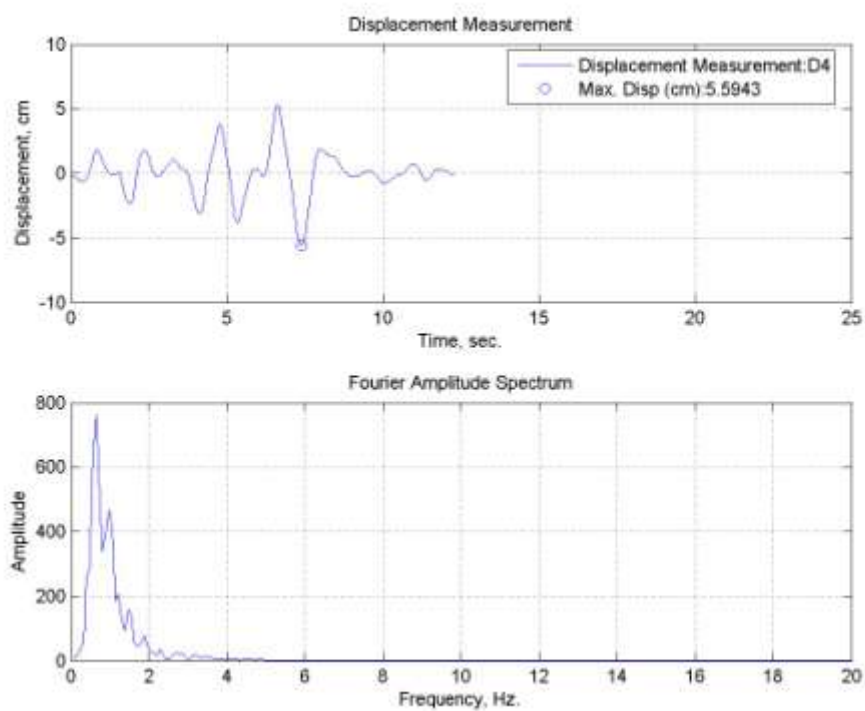


Figure A.39. Lateral displacement time history for TC20 specimen tested under 0°C.

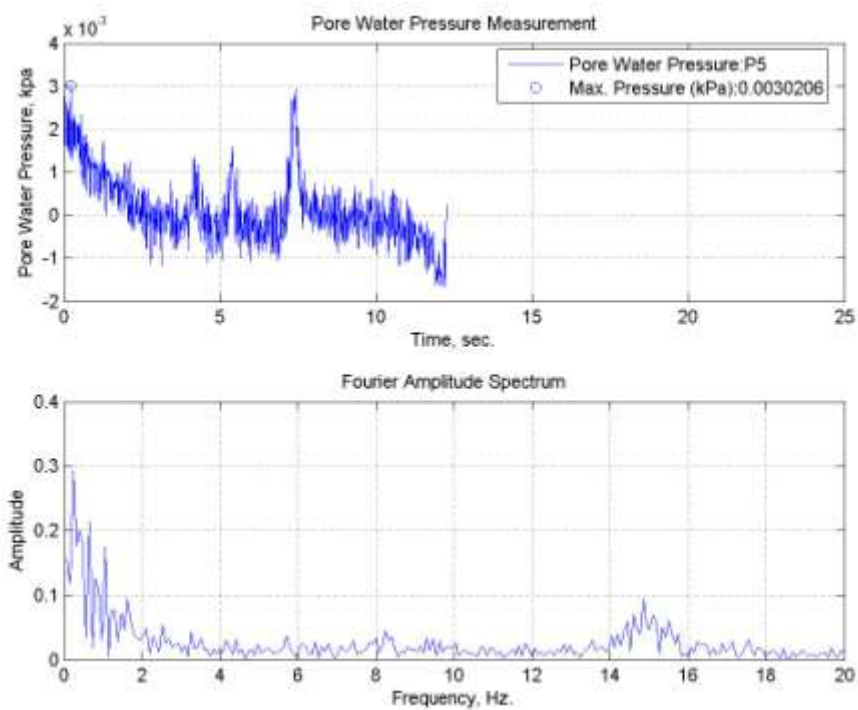


Figure A.40. Pore water pressure change of TC20 specimen tested at 0°C.

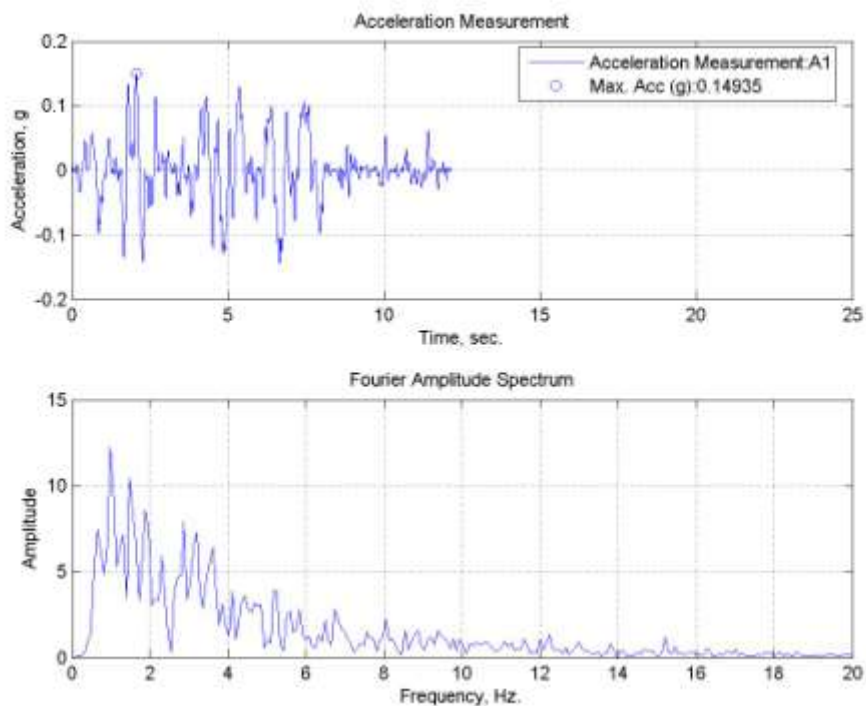
A.9. TC30 Specimen subjected to Sakarya (N-S) Earthquake Motion at 0°C

Figure A.41. A1, acceleration time history of TC30 specimen tested under 0°C.

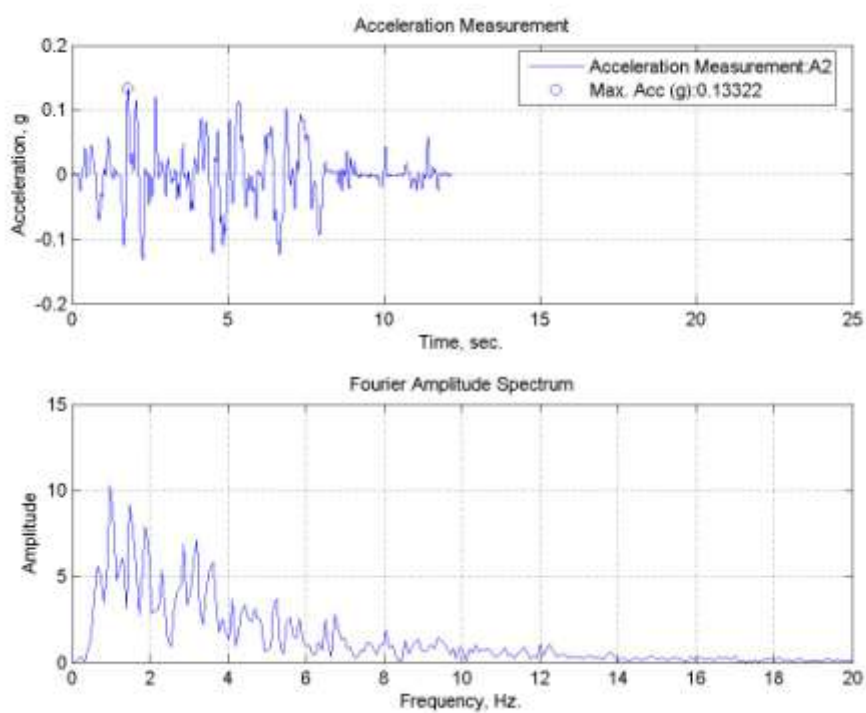


Figure A.42. A2, acceleration time history of TC30 specimen tested under 0°C.

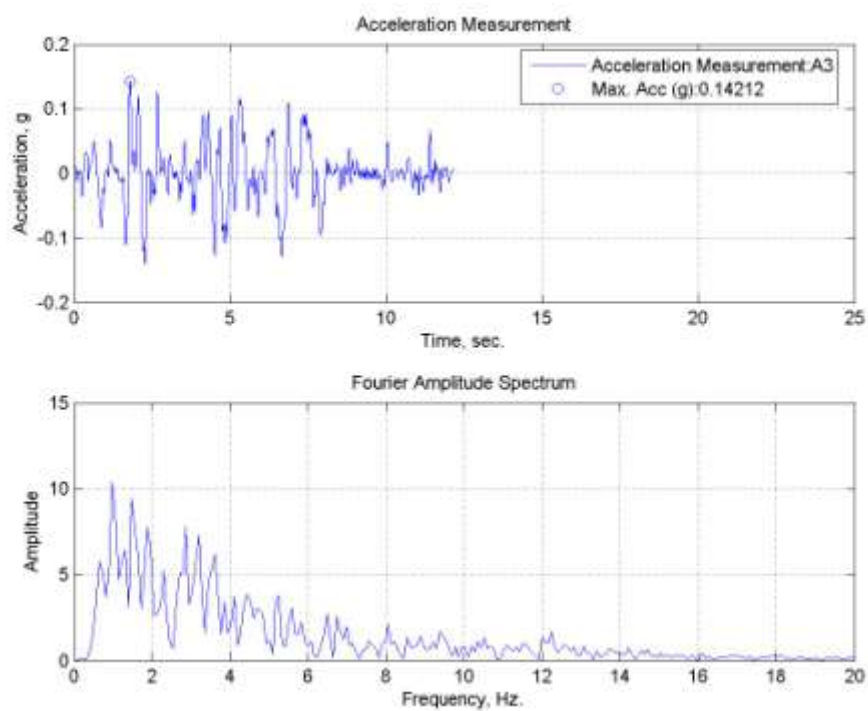


Figure A.43. A3, acceleration time history of TC30 specimen tested under 0°C.

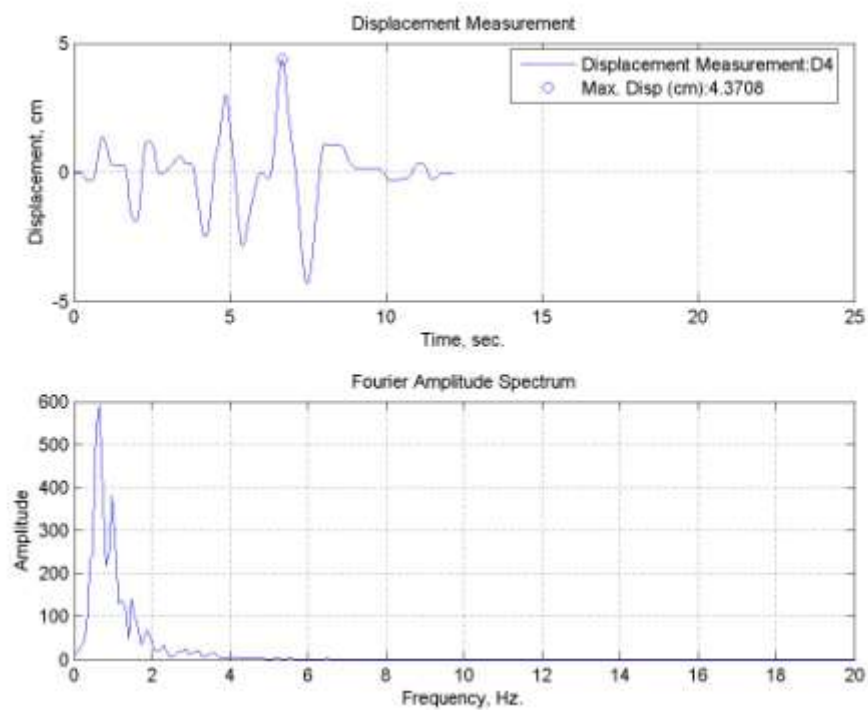


Figure A.44. Lateral displacement time history for TC30 specimen tested under 0°C.

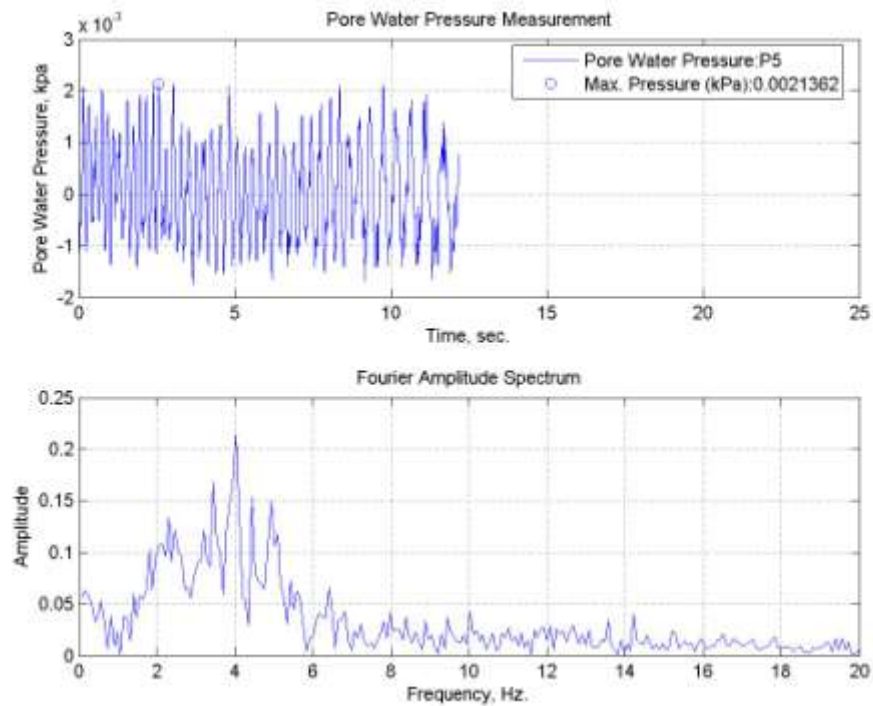


Figure A.45. Pore water pressure change of TC30 specimen tested at 0°C.

A.10. Sand Specimen subjected to Sakarya (N-S) Earthquake Motion at Room Temperature

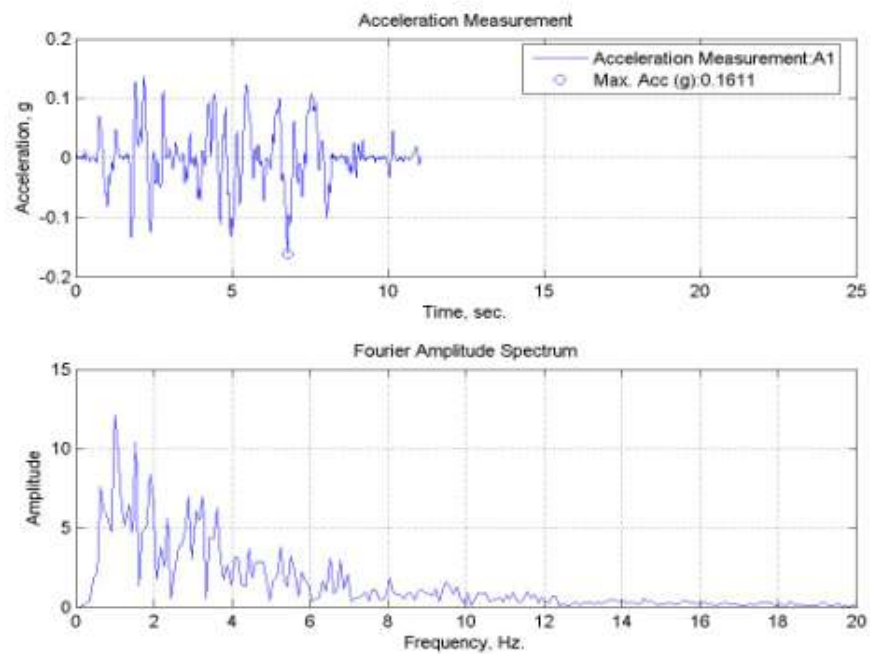


Figure A.46. A1, acceleration time history of sand specimen tested at room temperature.

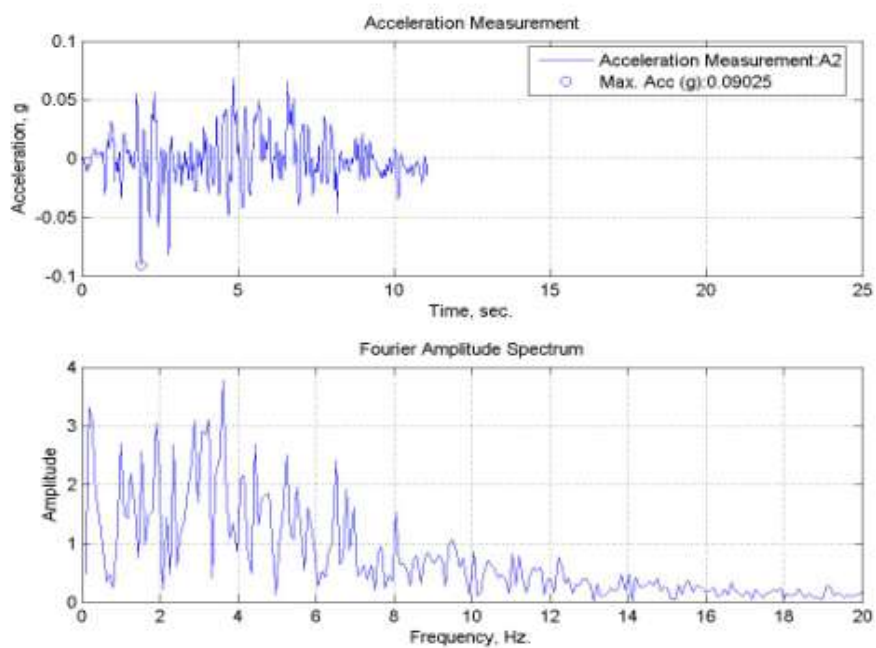


Figure A.47. A2, acceleration time history of sand specimen tested at room temperature.

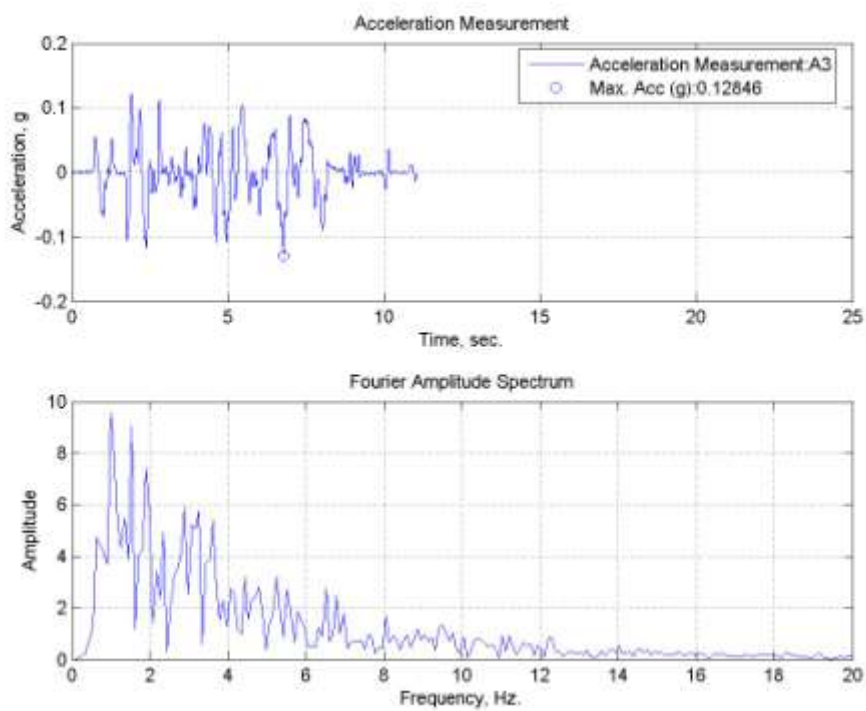


Figure A.48. A3, acceleration time history of sand specimen tested at room temperature.

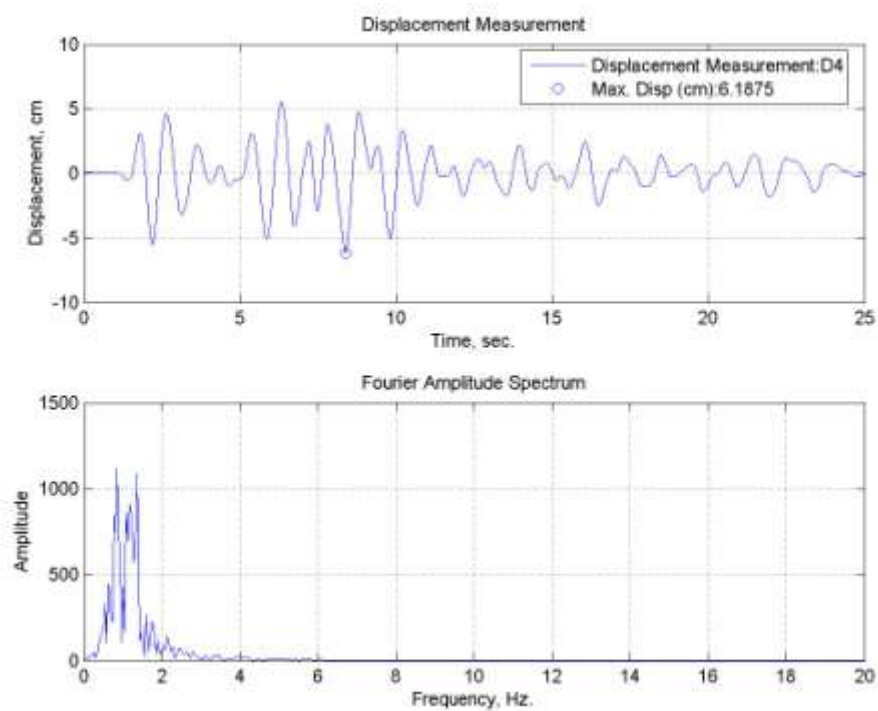


Figure A.49. Lateral displacement time history for sand specimen tested at room temperature.

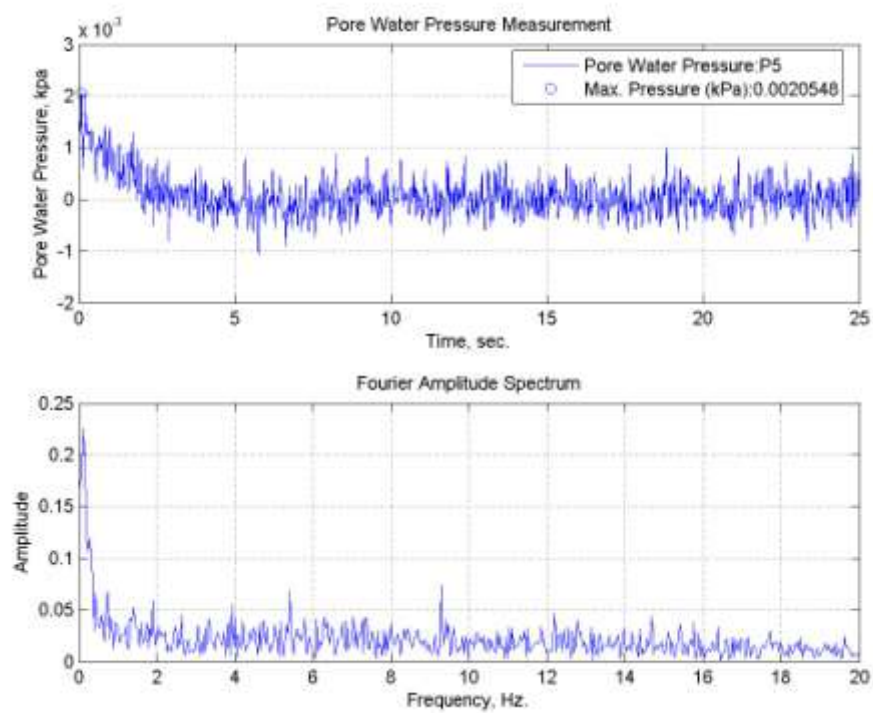


Figure A.50. Pore water pressure change of sand specimen tested at room temperature.

A.11. TB10 Specimen subjected to Sakarya (N-S) Earthquake Motion at Room Temperature

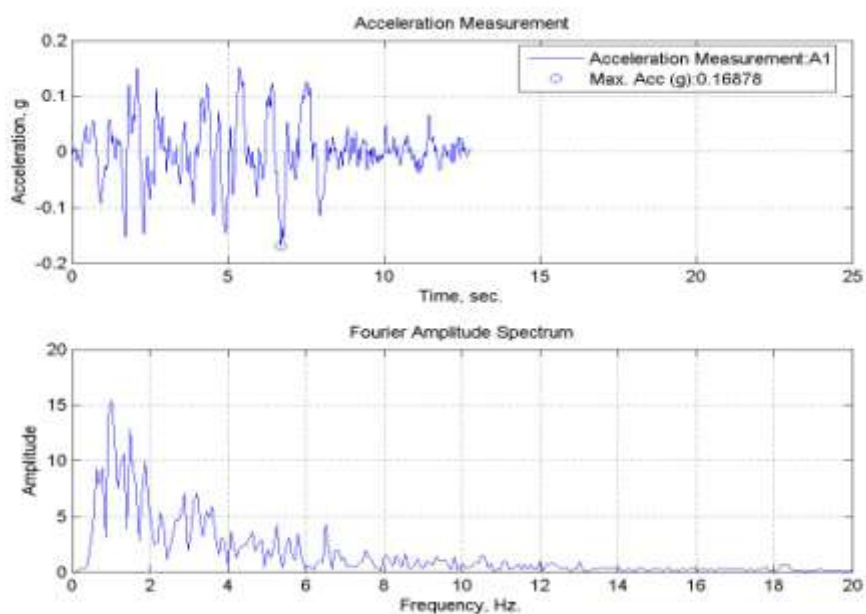


Figure A.51. A1, acceleration time history of TB10 specimen tested at room temperature.

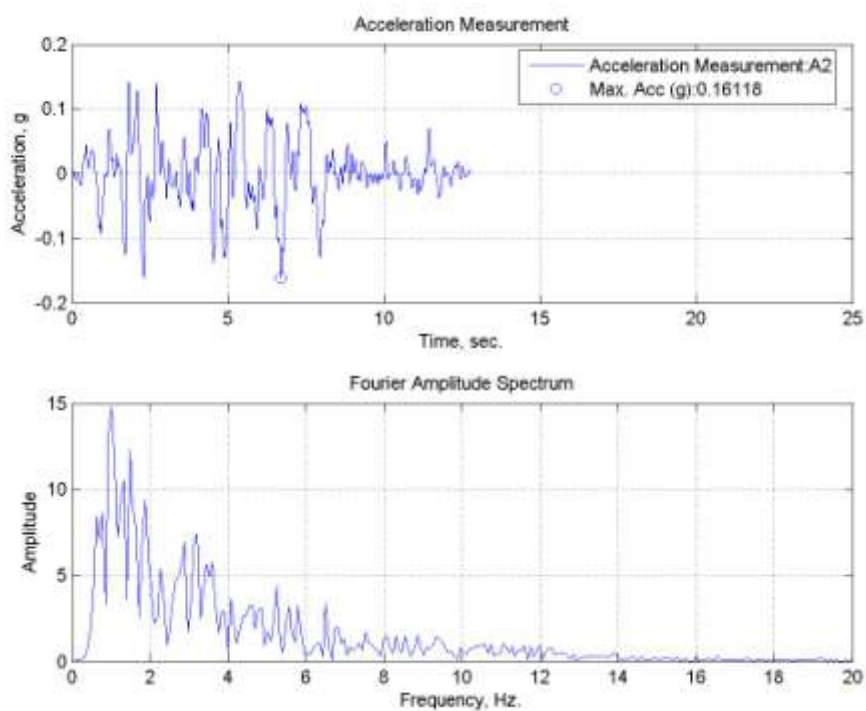


Figure A.52. A2, acceleration time history of TB10 specimen tested at room temperature.

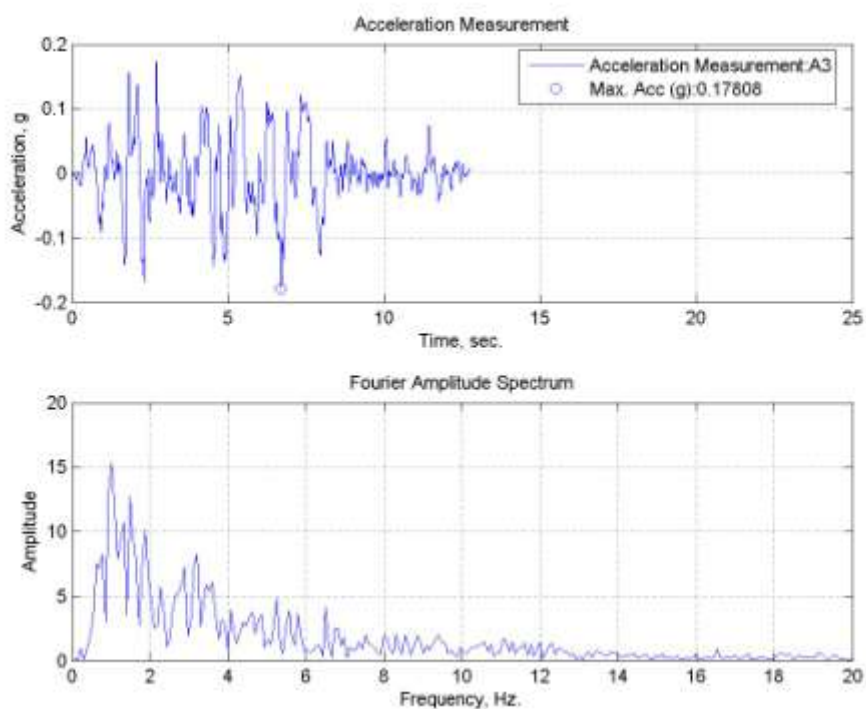


Figure A.53. A3, acceleration time history of TB10 specimen tested at room temperature.

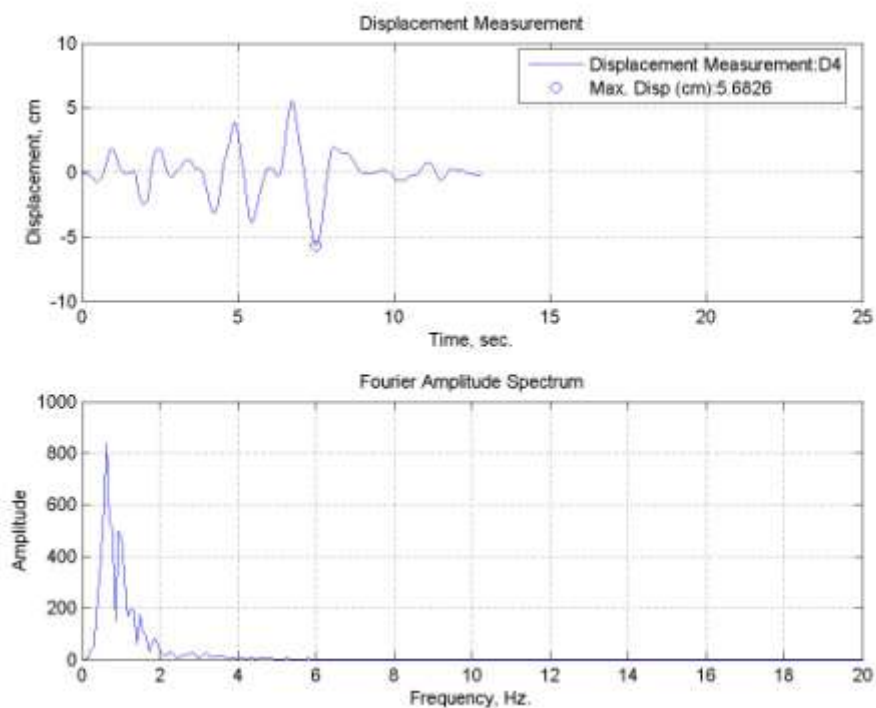


Figure A.54. Lateral displacement time history for TB10 specimen tested at room temperature.

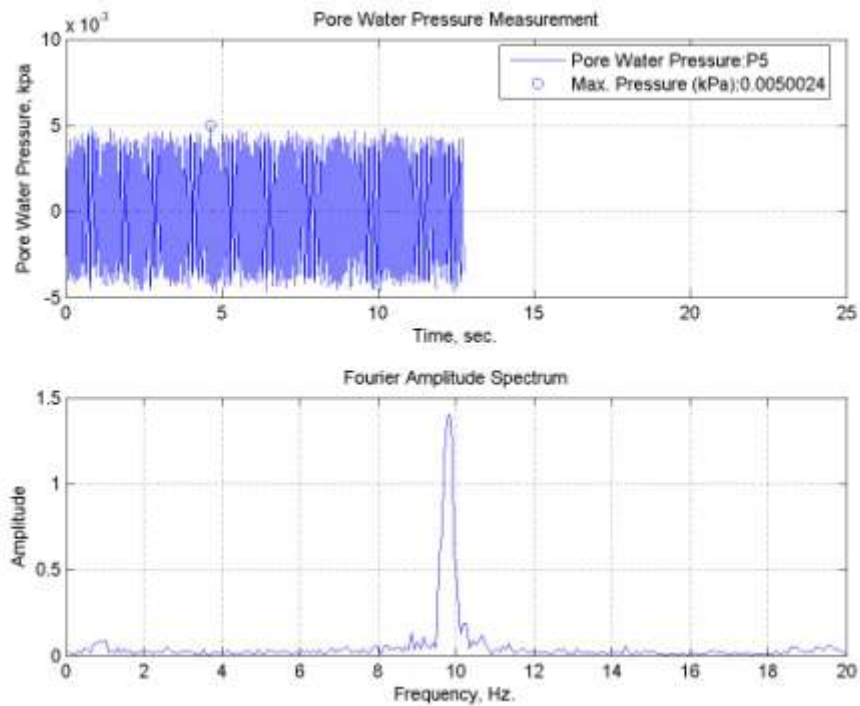


Figure A.55. Pore water pressure change of TB10 specimen tested at room temperature.

A.12. TB15 Specimen subjected to Sakarya (N-S) Earthquake Motion at Room Temperature

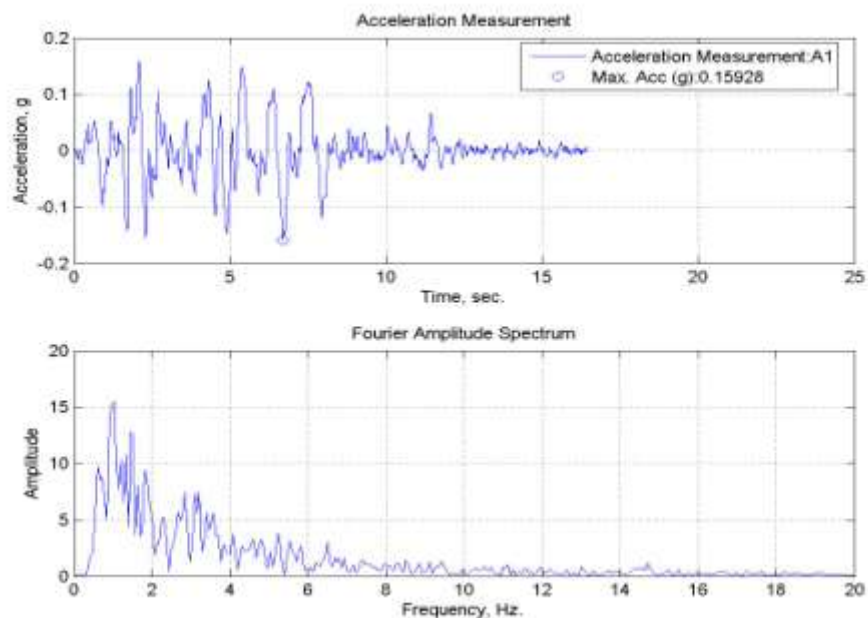


Figure A.56. A1, acceleration time history of TB15 specimen tested at room temperature.

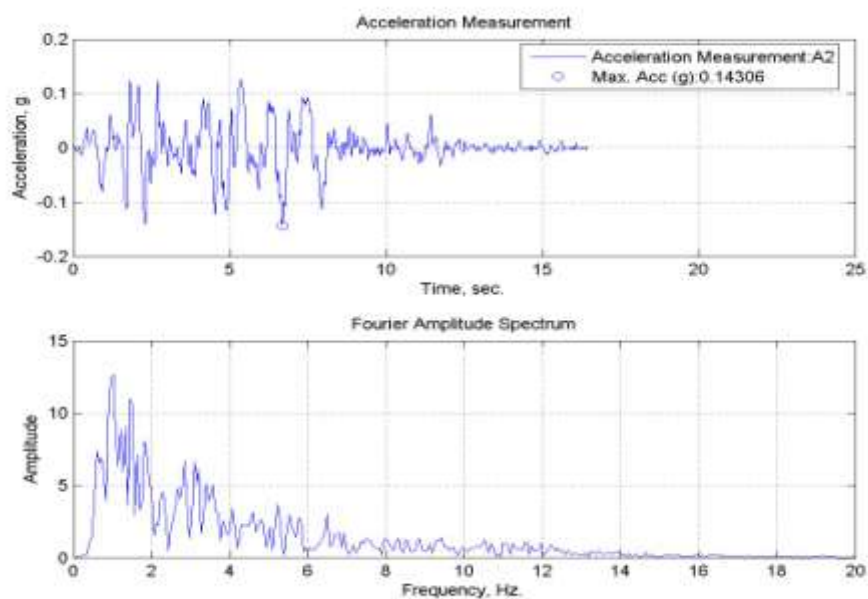


Figure A.57. A2, acceleration time history of TB15 specimen tested at room temperature.

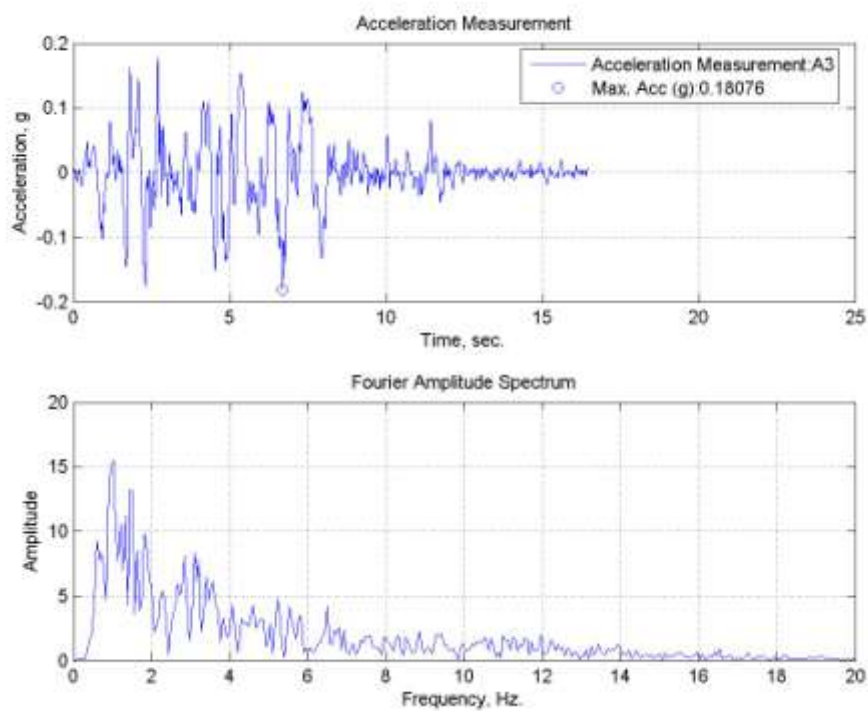


Figure A.58. A3, acceleration time history of TB15 specimen tested at room temperature.

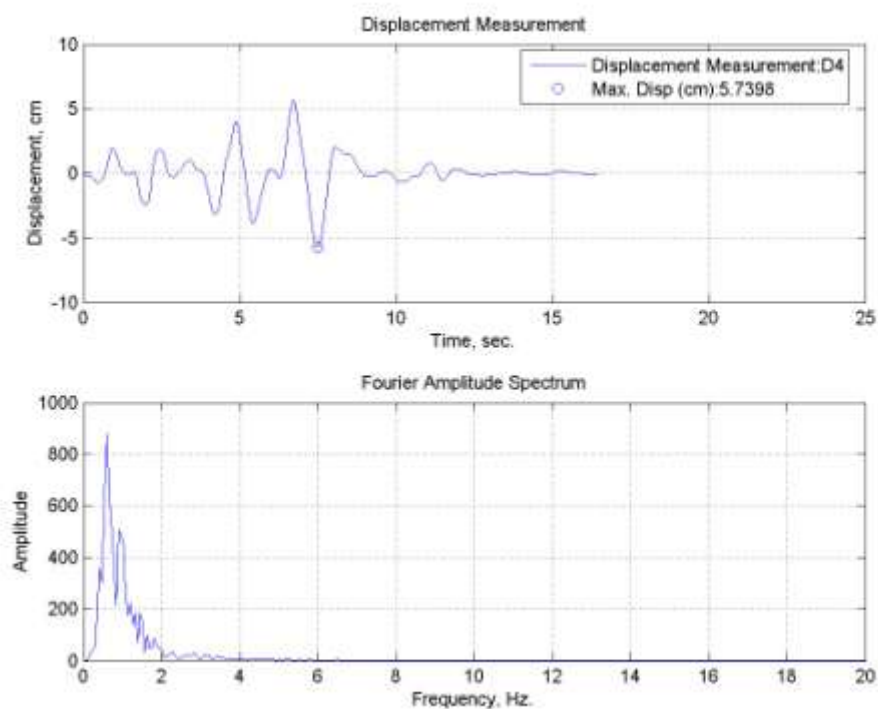


Figure A.59. Lateral displacement time history for TB15 specimen tested at room temperature.

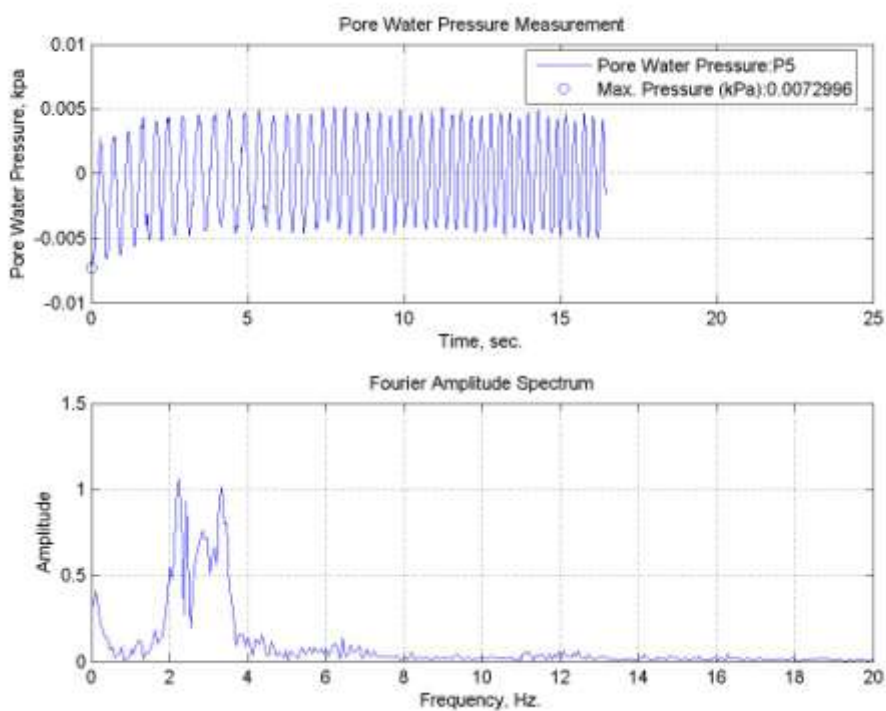


Figure A.60. Pore water pressure change of TB15 specimen tested at room temperature.

A.13. TB20 Specimen subjected to Sakarya (N-S) Earthquake Motion at Room Temperature

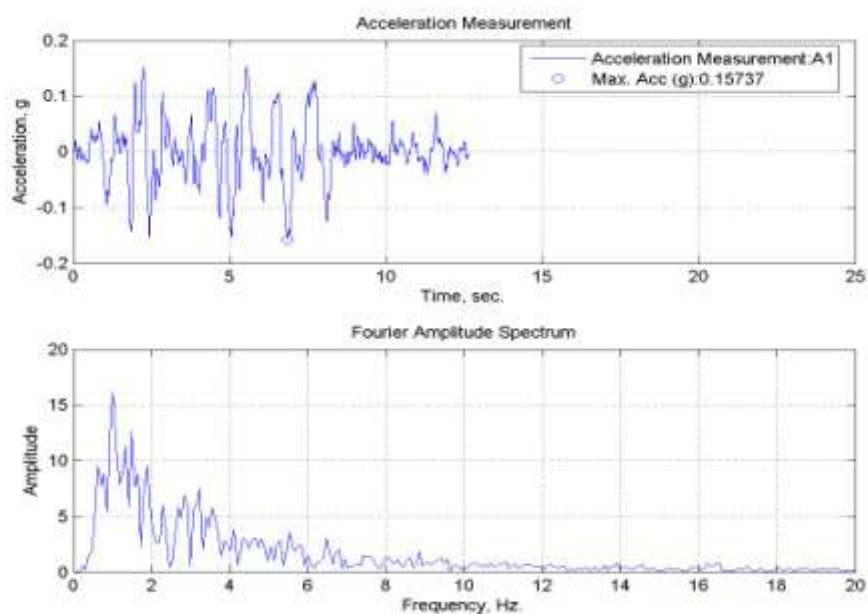


Figure A.61. A1, acceleration time history of TB20 specimen tested at room temperature.

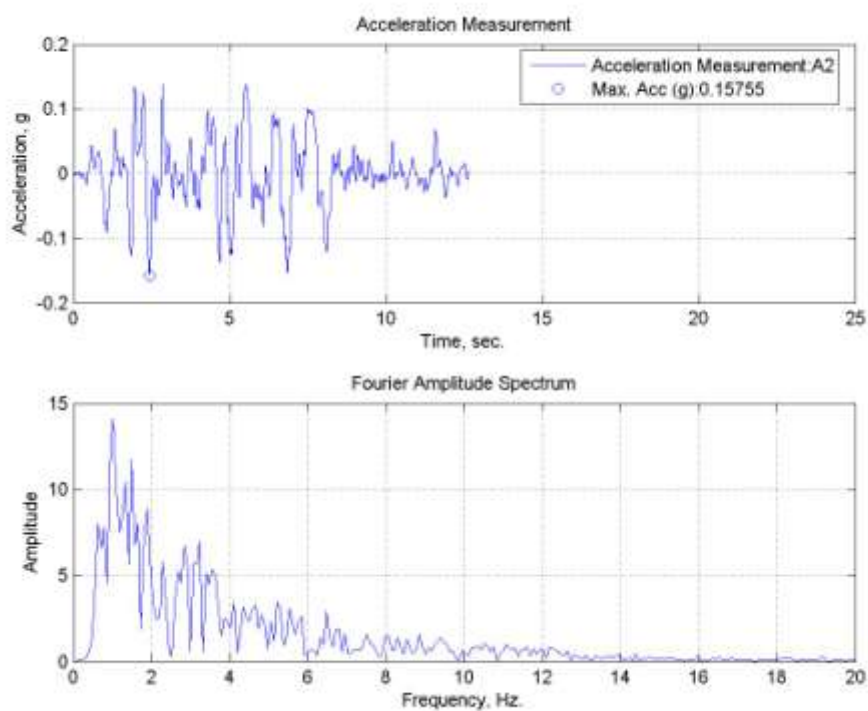


Figure A.62. A2, acceleration time history of TB20 specimen tested at room temperature.

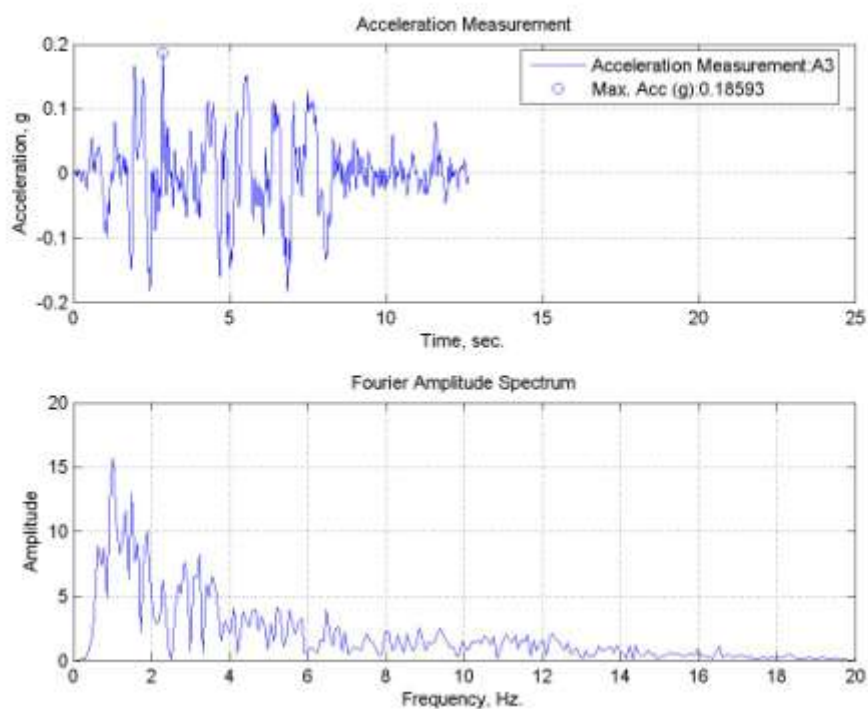


Figure A.63. A3, acceleration time history of TB20 specimen tested at room temperature.

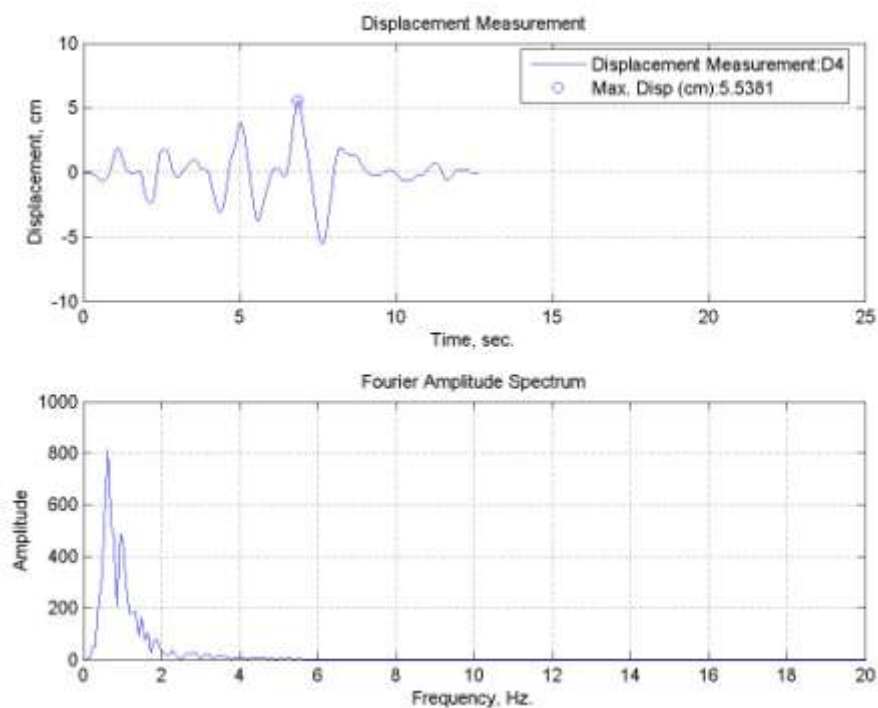


Figure A.64. Lateral displacement time history for TB20 specimen tested at room temperature.

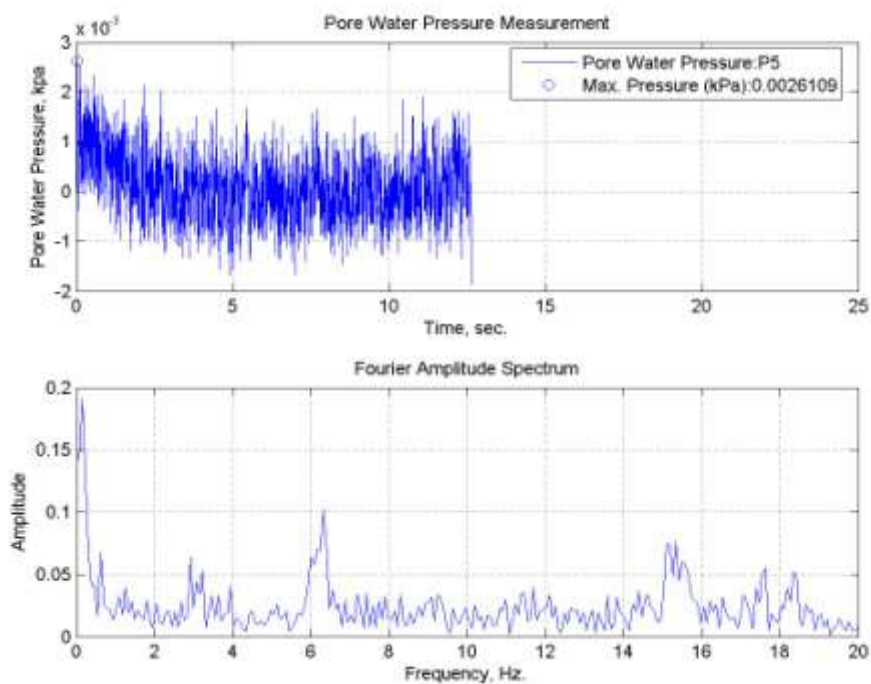


Figure A.65. Pore water pressure change of TB20 specimen tested at room temperature.

A.14. TB30 Specimen subjected to Sakarya (N-S) Earthquake Motion at Room Temperature

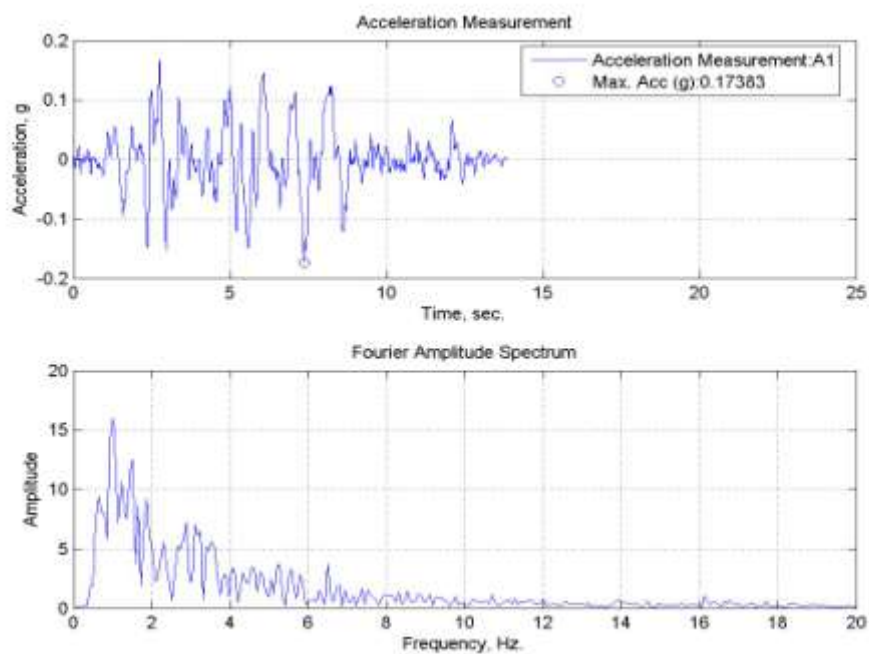


Figure A.66. A1, acceleration time history of TB30 specimen tested at room temperature.

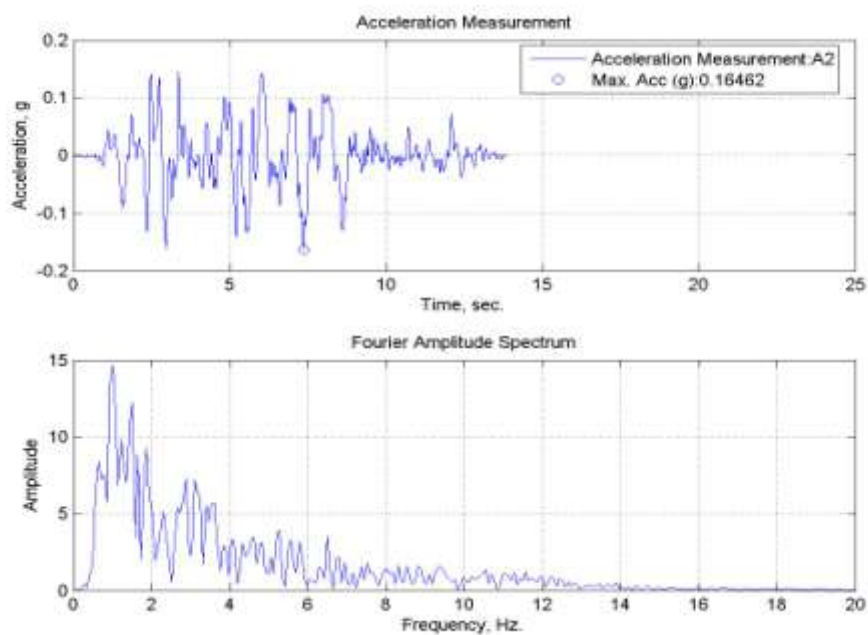


Figure A.67. A2, acceleration time history of TB30 specimen tested at room temperature.

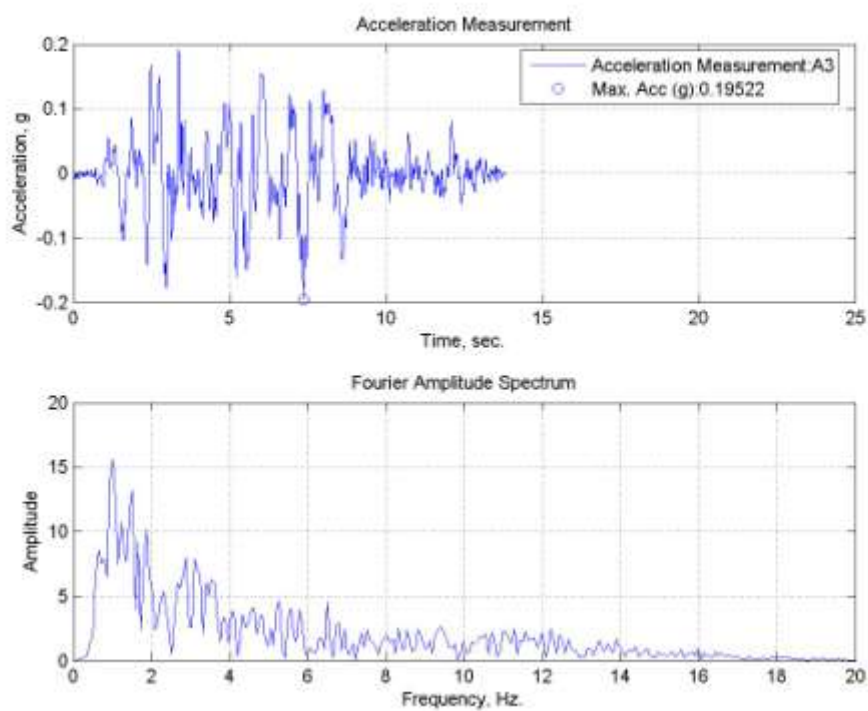


Figure A.68. A3, acceleration time history of TB30 specimen tested at room temperature.

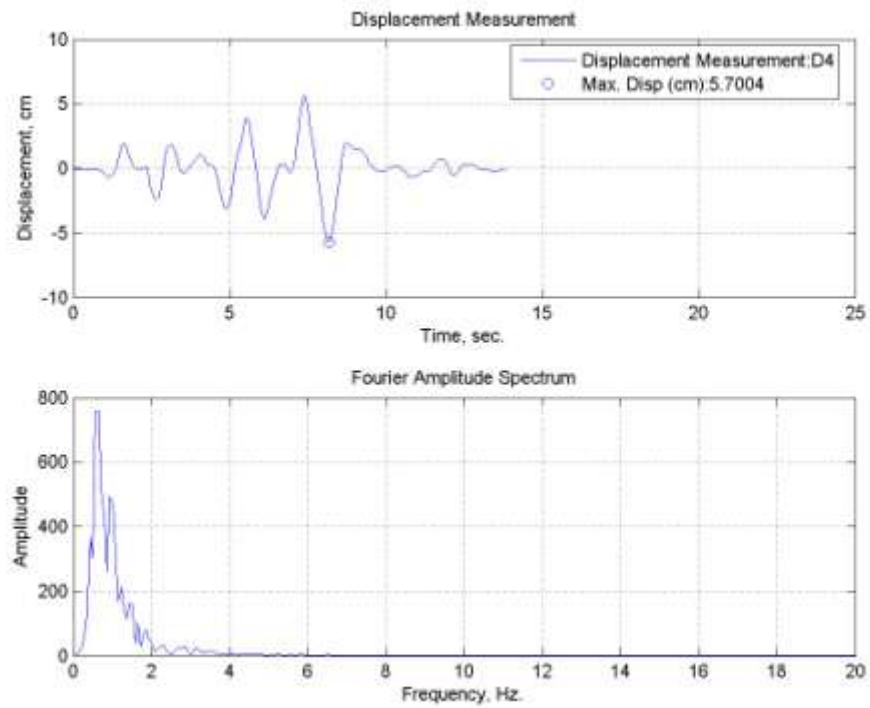


Figure A.69. Lateral displacement time history for TB30 specimen tested at room temperature.

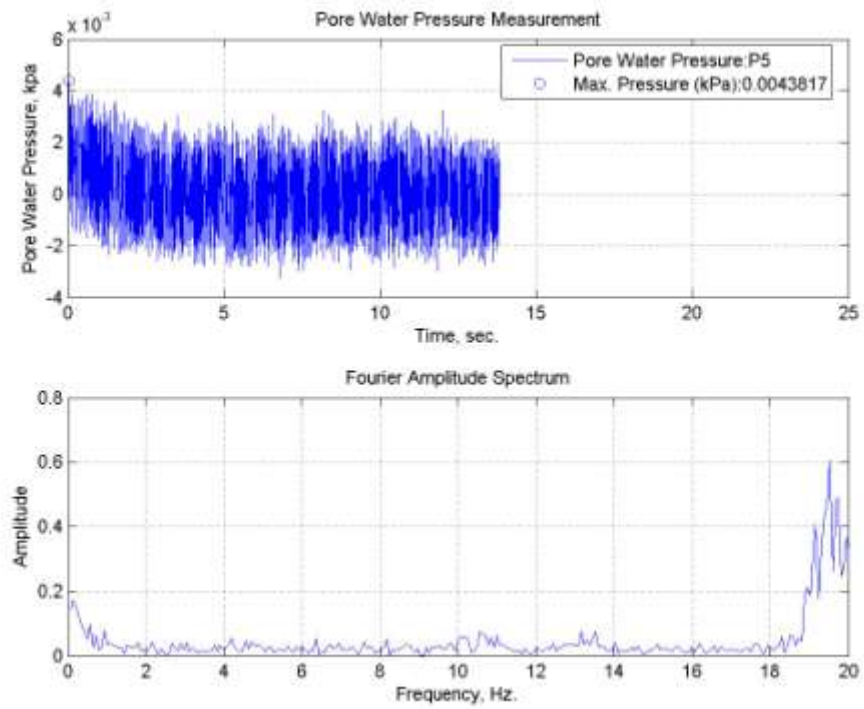


Figure A.70. Pore water pressure change of TB30 specimen tested at room temperature.

A.15. TC10 Specimen subjected to Sakarya (N-S) Earthquake Motion at Room Temperature

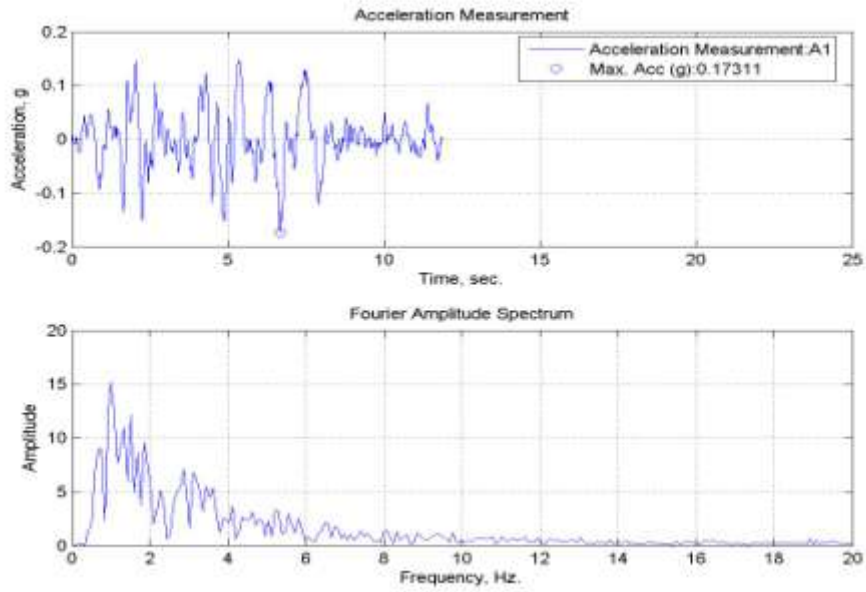


Figure A.71. A1, acceleration time history of TC10 specimen tested at room temperature.

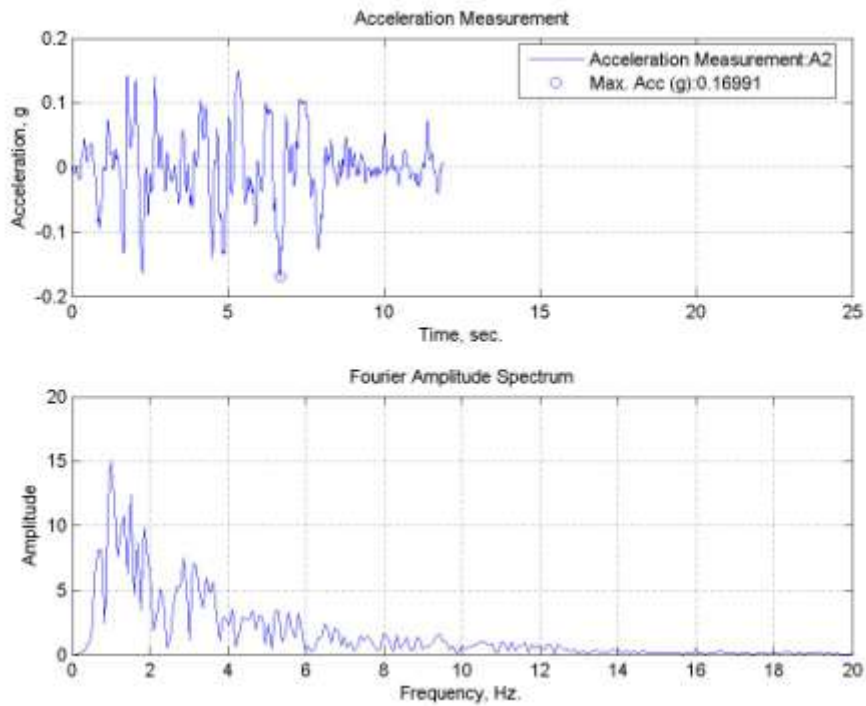


Figure A.72. A2, acceleration time history of TC10 specimen tested at room temperature.

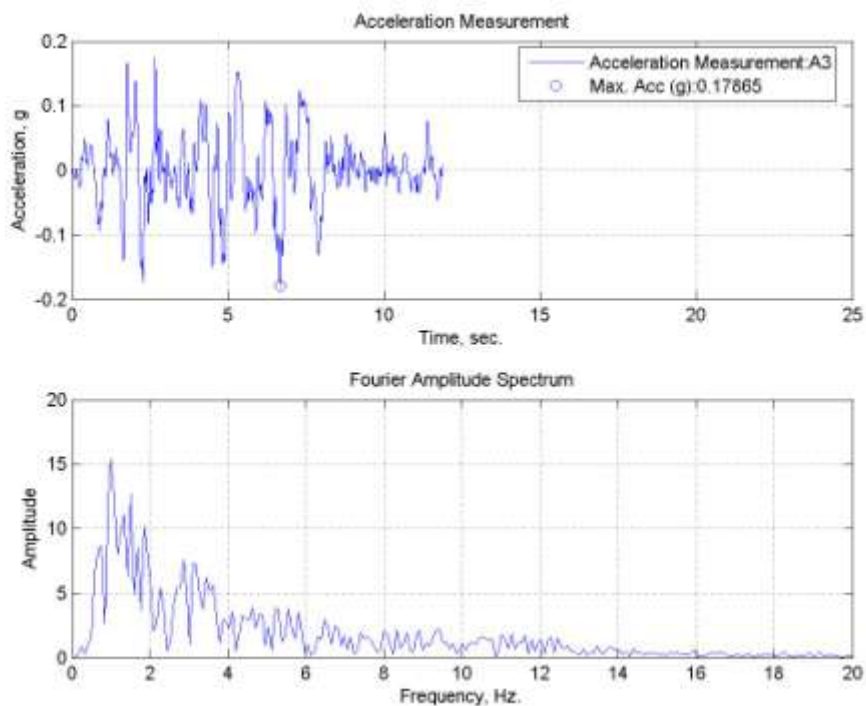


Figure A.73. A3, acceleration time history of TC10 specimen tested at room temperature.

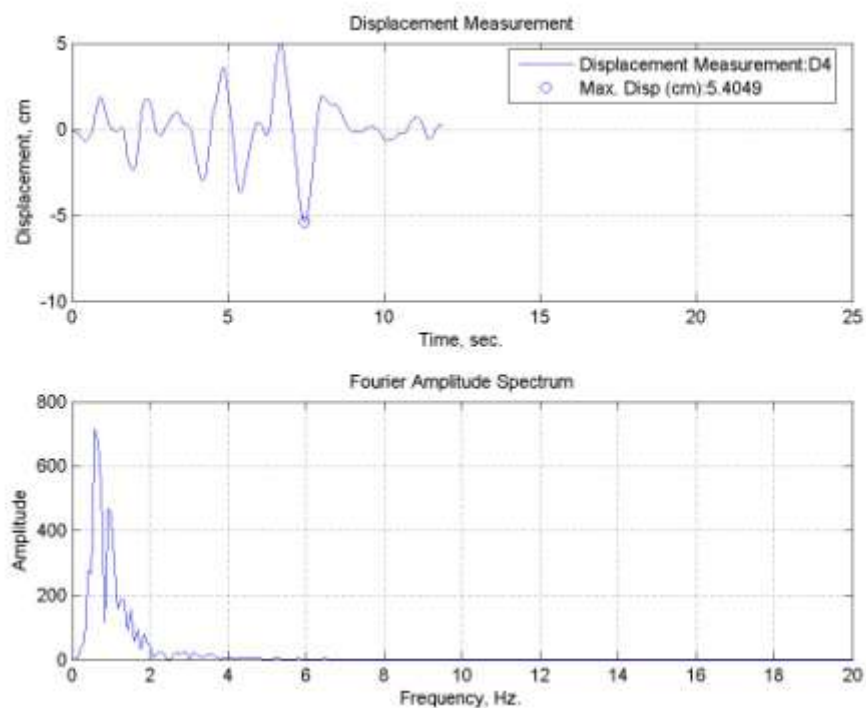


Figure A.74. Lateral displacement time history for TC10 specimen tested at room temperature.

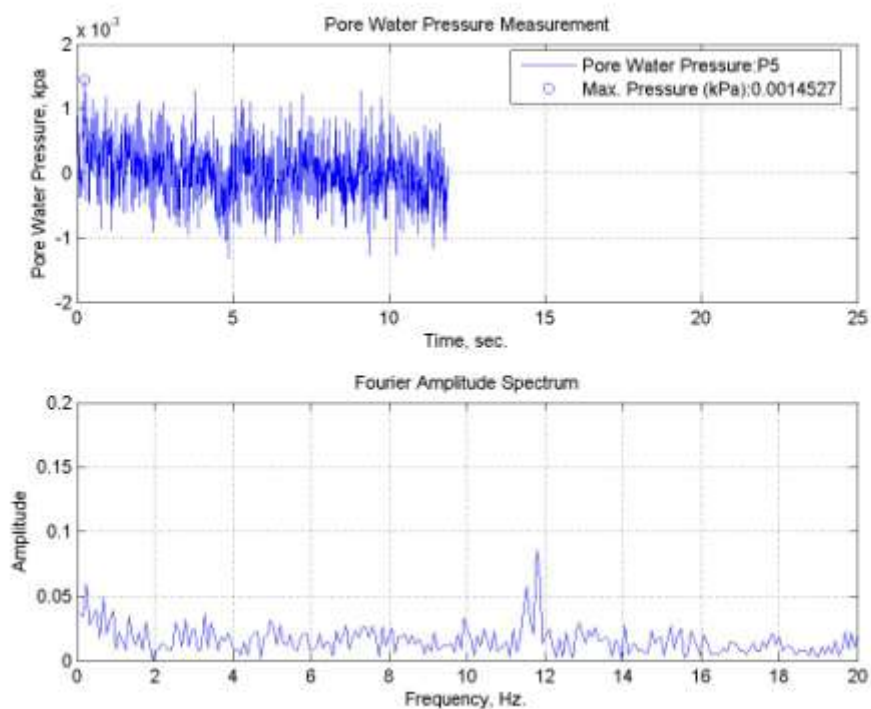


Figure A.75. Pore water pressure change of TC10 specimen tested at room temperature.

A.16. TC15 Specimen subjected to Sakarya (N-S) Earthquake Motion at Room Temperature

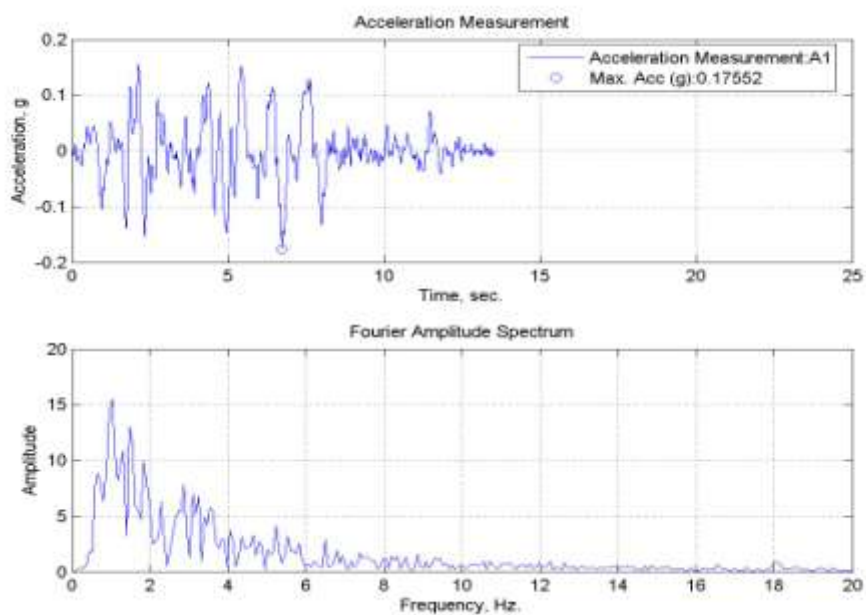


Figure A.76. A1, acceleration time history of TC15 specimen tested at room temperature.

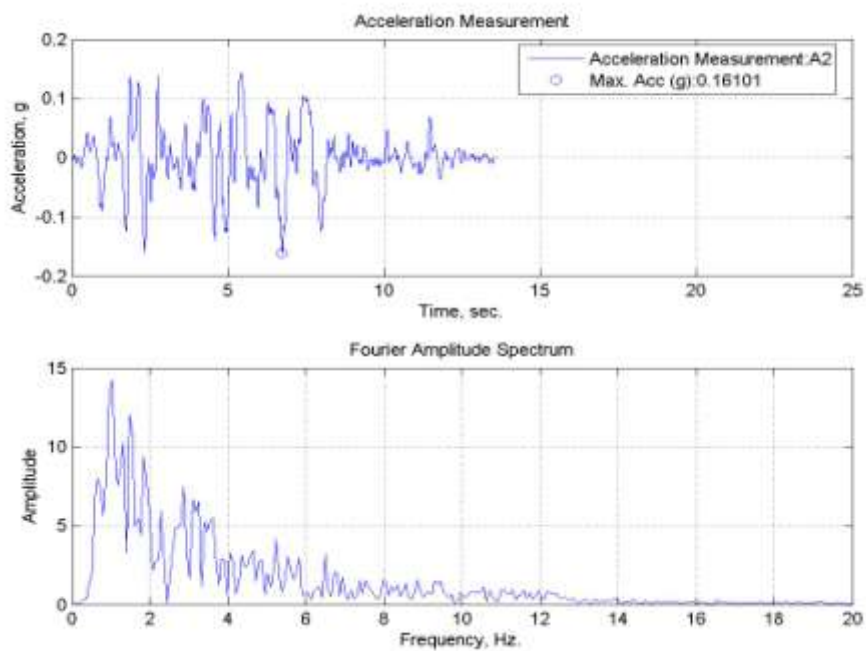


Figure A.77. A2, acceleration time history of TC15 specimen tested at room temperature.

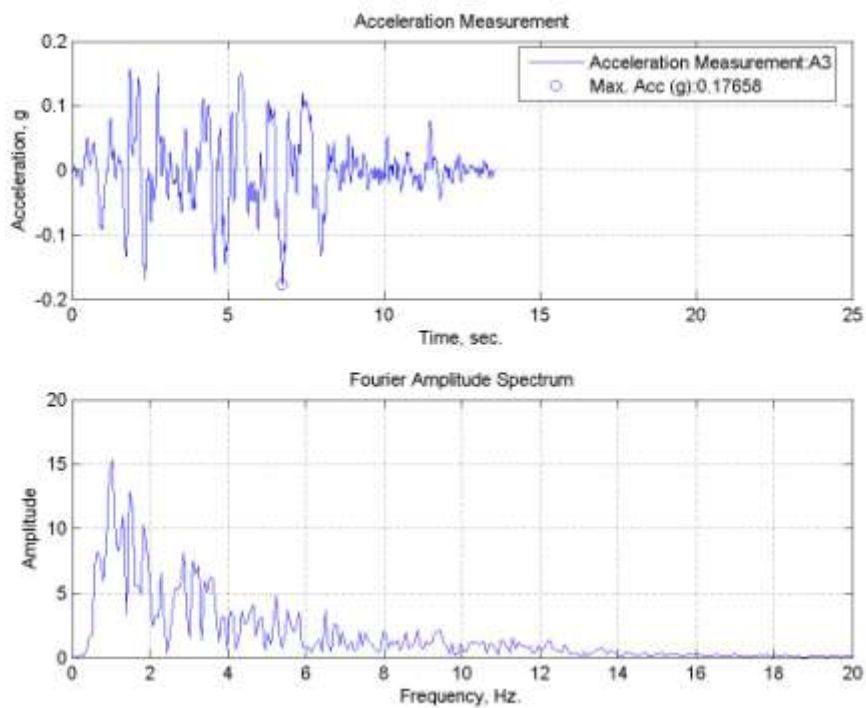


Figure A.78. A3, acceleration time history of TC15 specimen tested at room temperature.

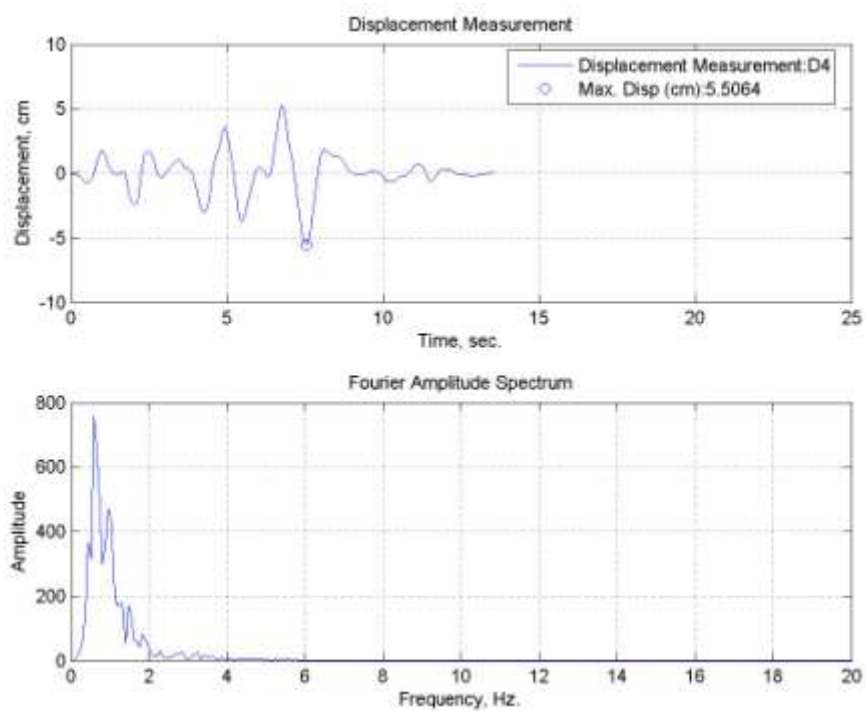


Figure A.79. Lateral displacement time history for TC15 specimen tested at room temperature.

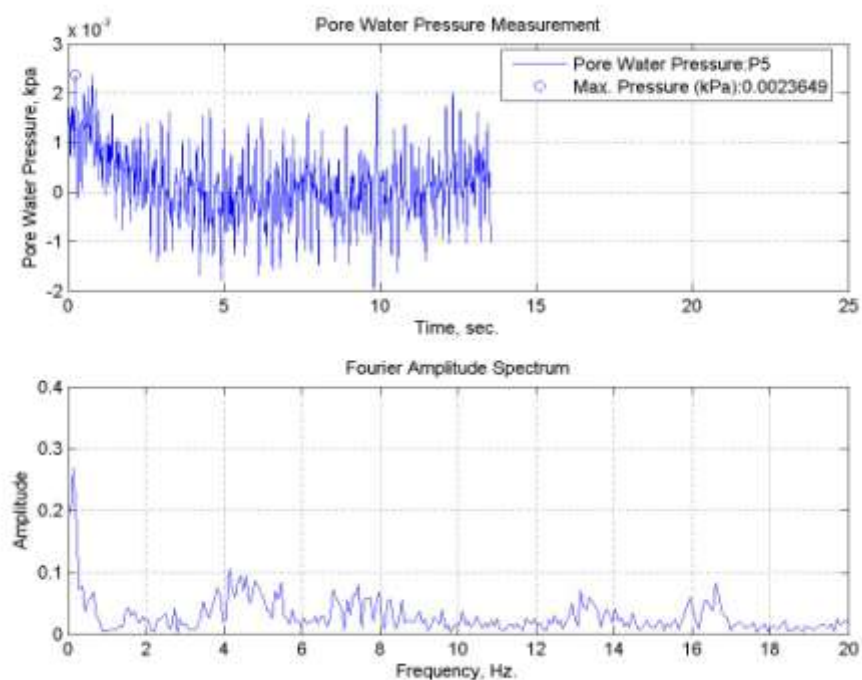


Figure A.80. Pore water pressure change of TC15 specimen tested at room temperature.

A.17. TC20 Specimen subjected to Sakarya (N-S) Earthquake Motion at Room Temperature

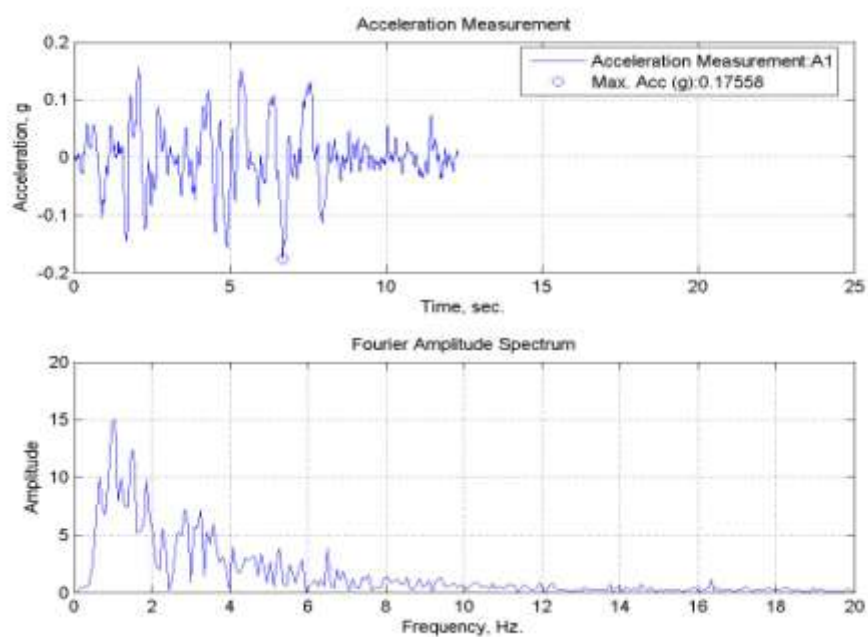


Figure A.81. A1, acceleration time history of TC20 specimen tested at room temperature.

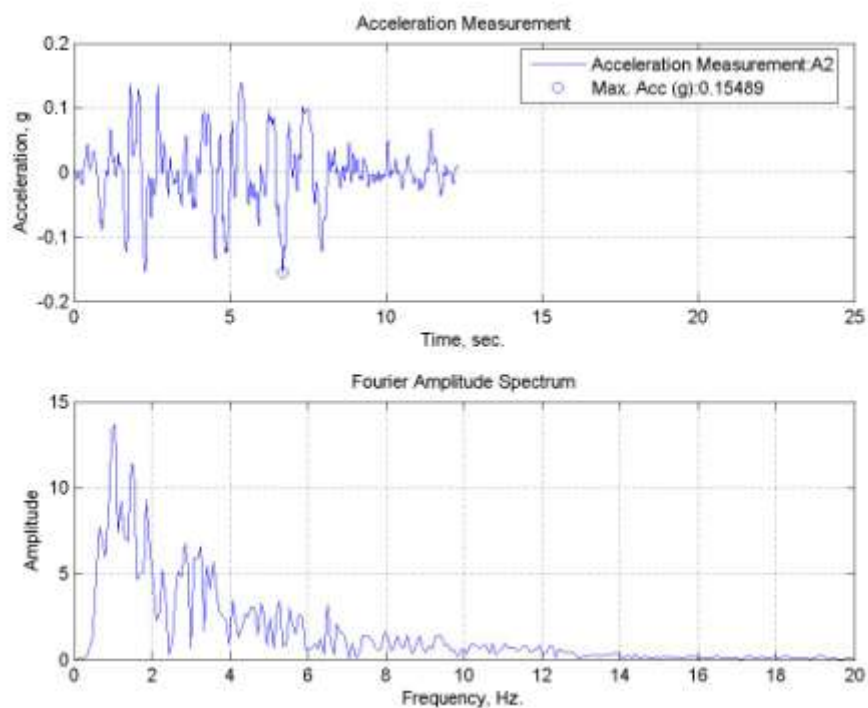


Figure A.82. A2, acceleration time history of TC20 specimen tested at room temperature.

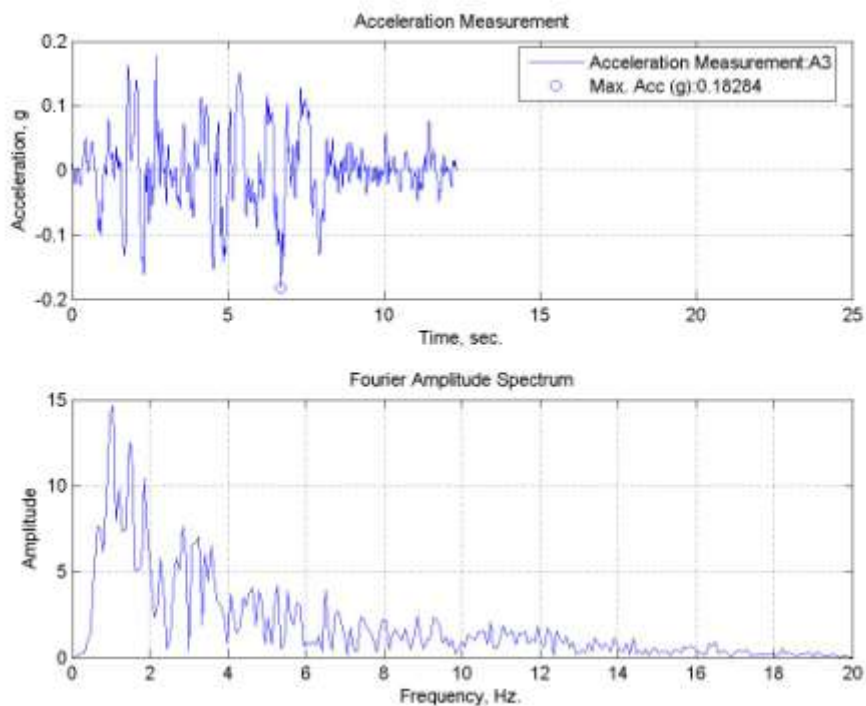


Figure A.83. A3, acceleration time history of TC20 specimen tested at room temperature.

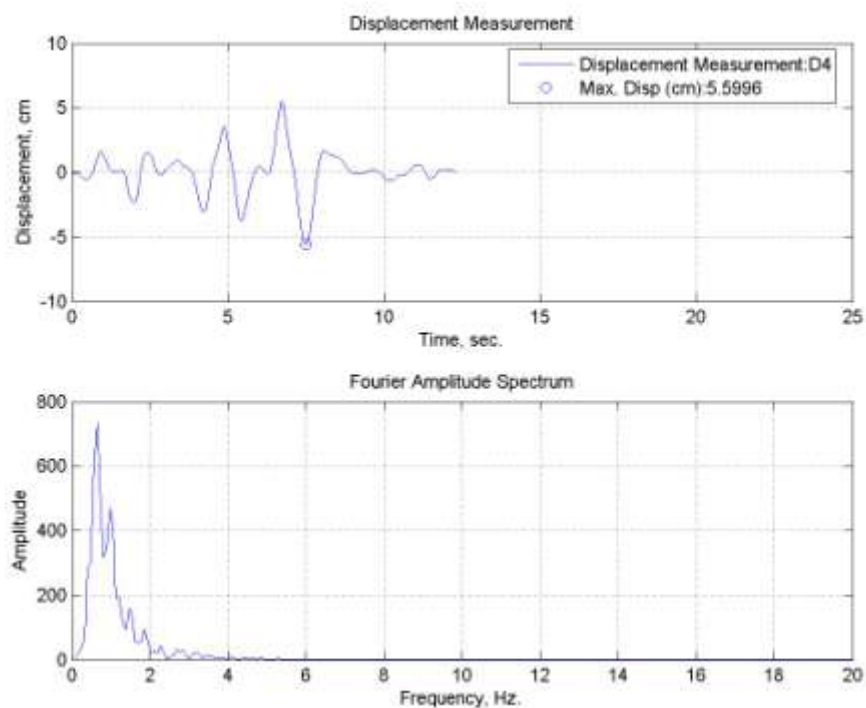


Figure A.84. Lateral displacement time history for TC20 specimen tested at room temperature.

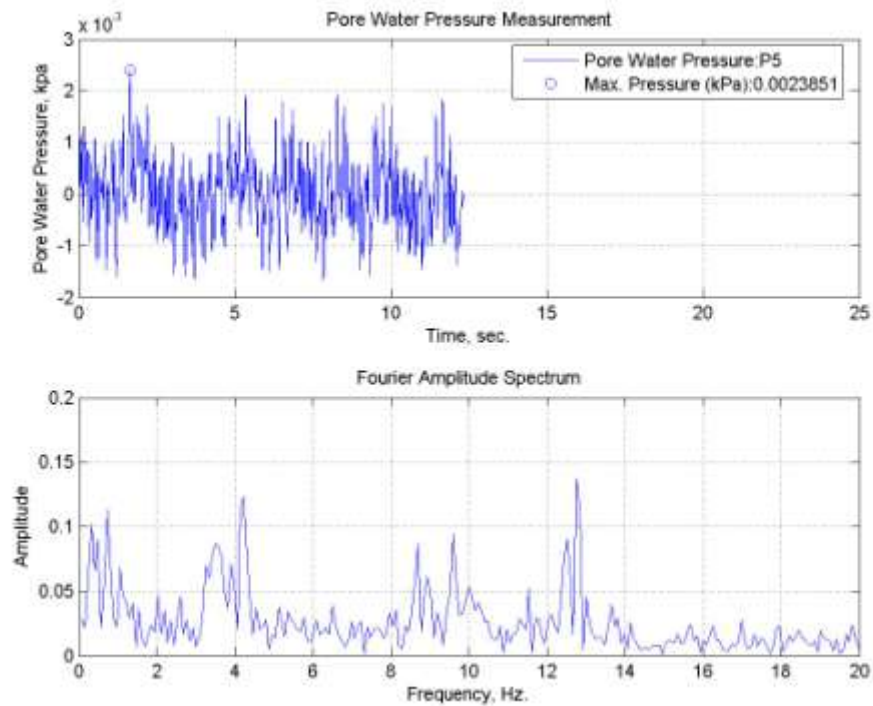


Figure A.85. Pore water pressure change of TB20 specimen tested at room temperature.

A.18. TC30 Specimen subjected to Sakarya (N-S) Earthquake Motion at Room Temperature

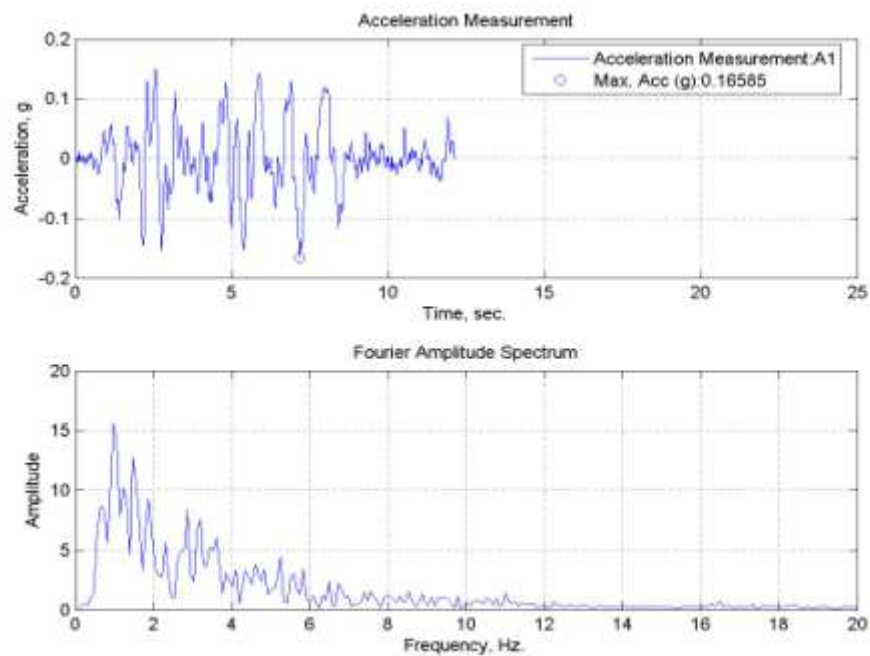


Figure A.86. A1, acceleration time history of TC30 specimen tested at room temperature.

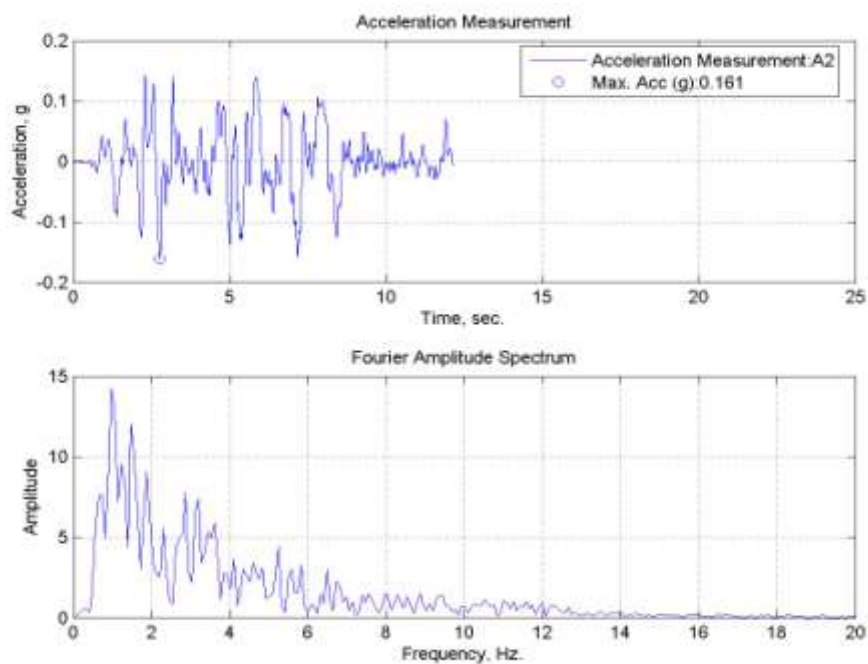


Figure A.87. A2, acceleration time history of TC30 specimen tested at room temperature.

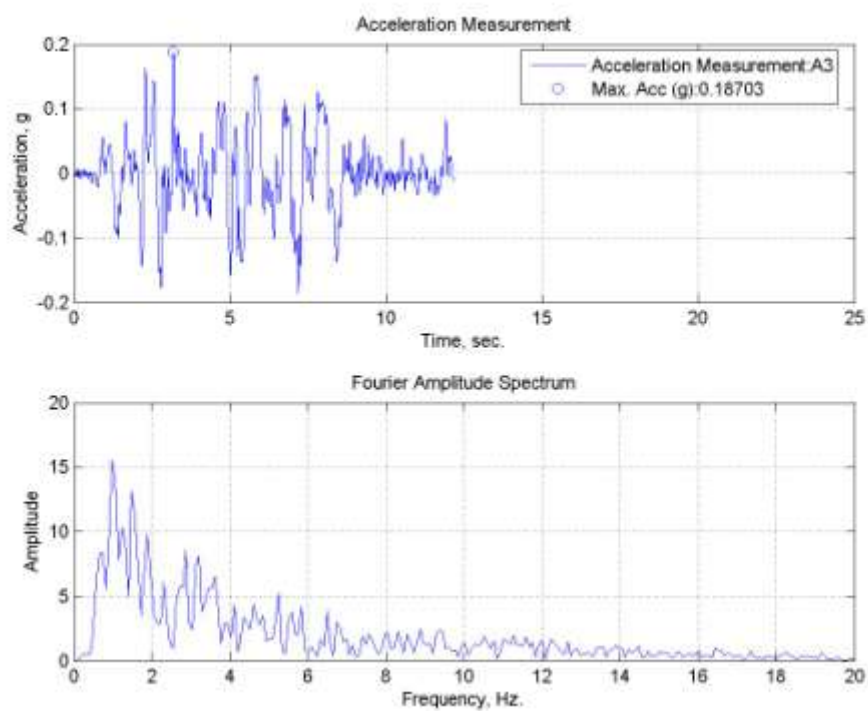


Figure A.88. A3, acceleration time history of TC30 specimen tested at room temperature.

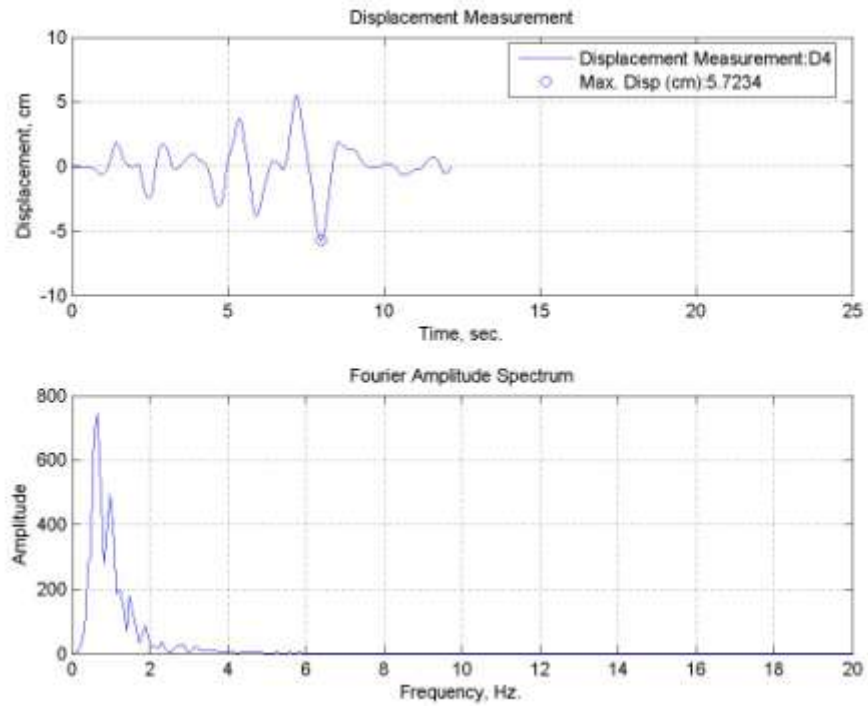


Figure A.89. Lateral displacement time history for TC30 specimen tested at room temperature.

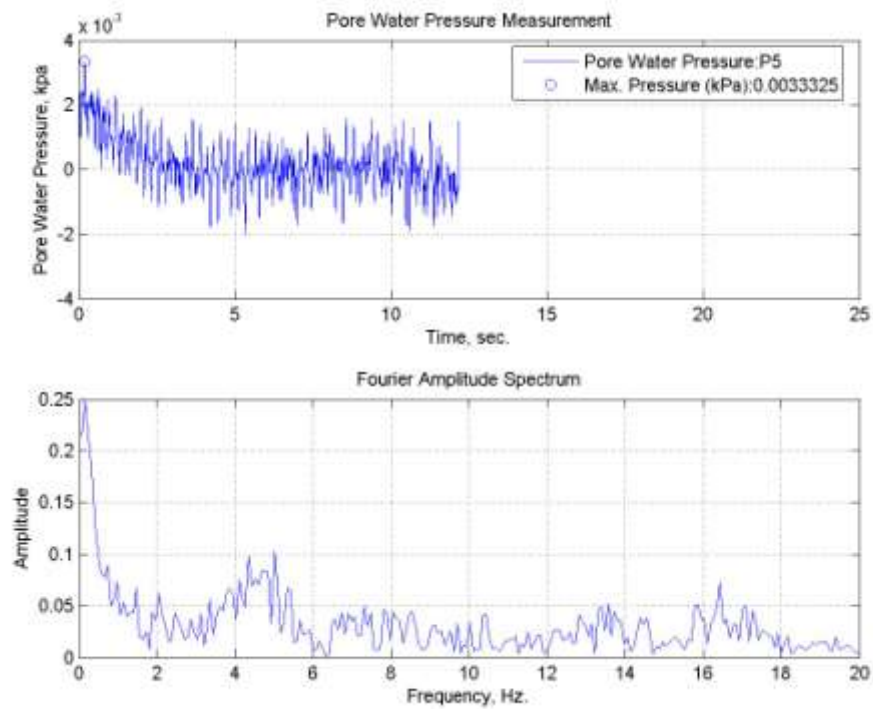


Figure A.90. Pore water pressure change of TC30 specimen tested at room temperature.

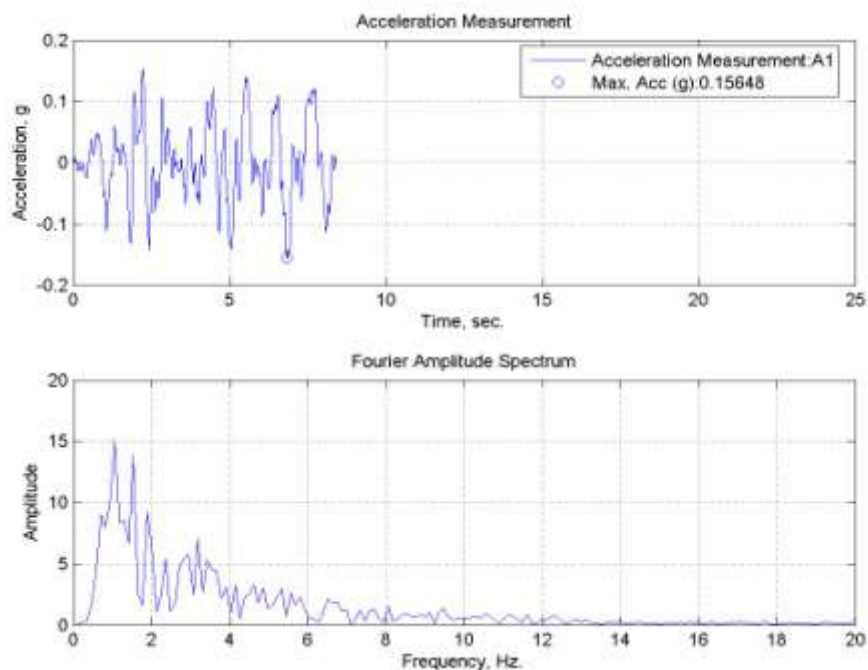
A.19. Sand Specimen subjected to Sakarya (N-S) Earthquake Motion at 50°C

Figure A.91. A1, acceleration time history of sand specimen tested at 50°C.

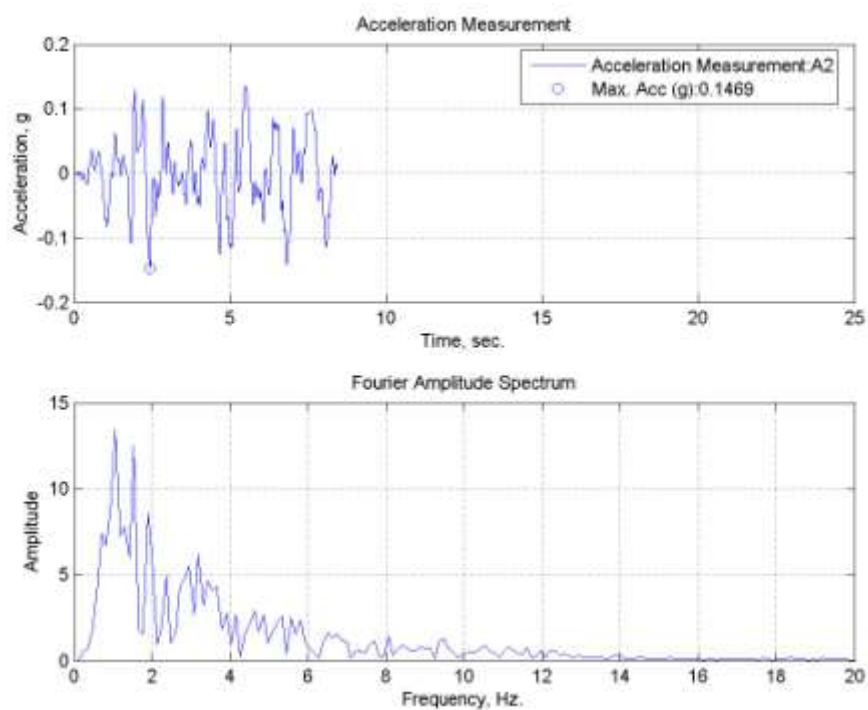


Figure A.92. A2, acceleration time history of sand specimen tested at 50°C.

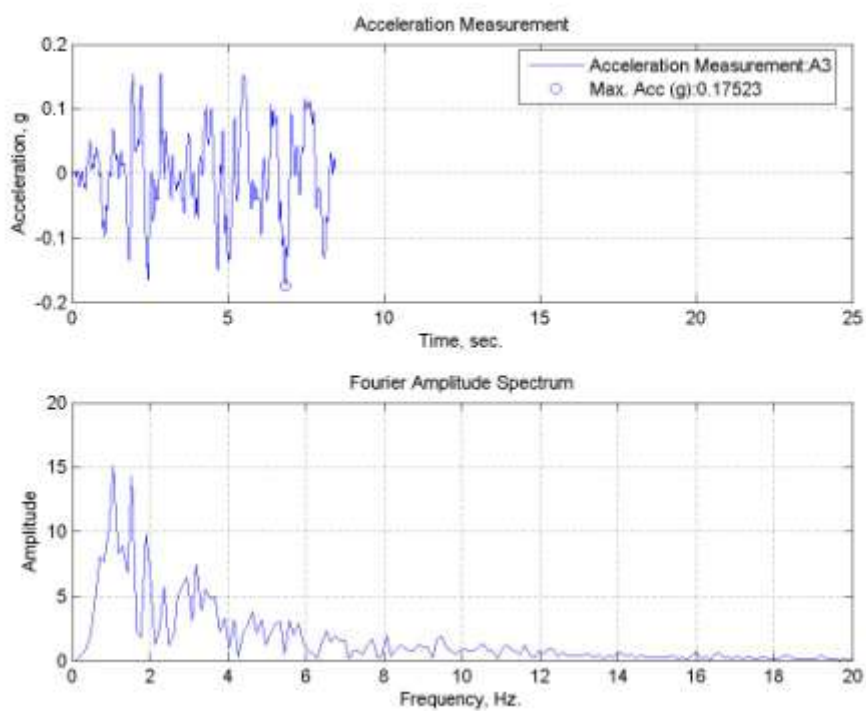


Figure A.93. A3, acceleration time history of sand specimen tested at 50°C.

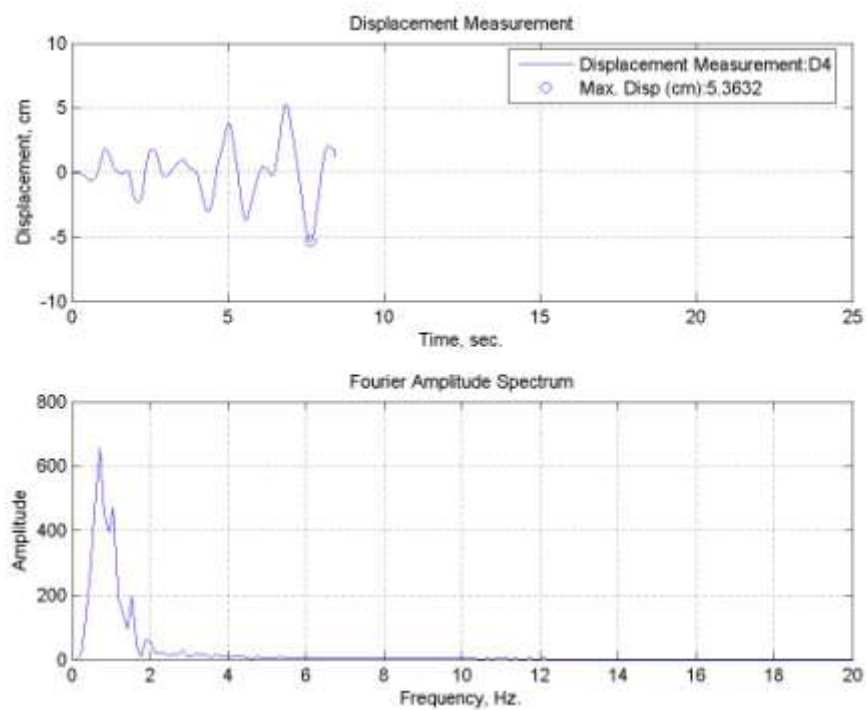


Figure A.94. Lateral displacement time history for sand specimen tested at 50°C.

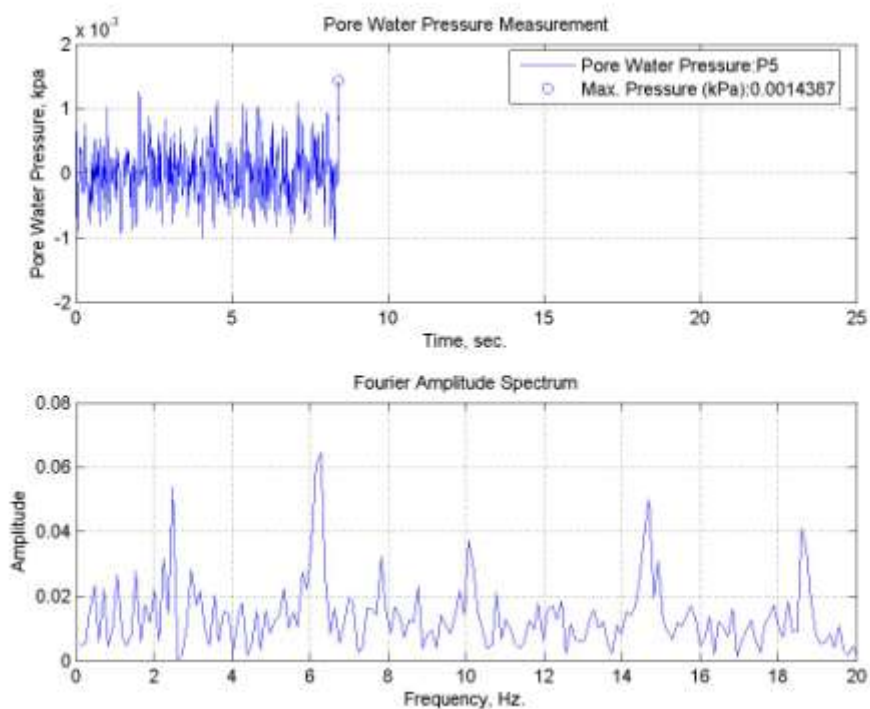


Figure A.95. Pore water pressure change of sand specimen tested at 50°C.

A.20. TB10 Specimen subjected to Sakarya (N-S) Earthquake Motion at 50°C

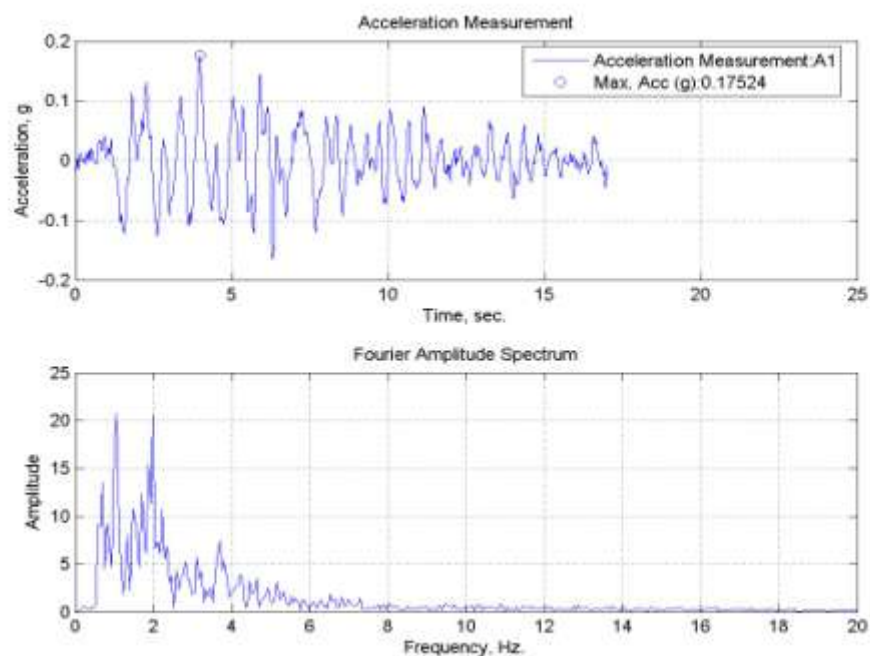


Figure A.96. A1, acceleration time history of TB10 specimen tested at 50°C.

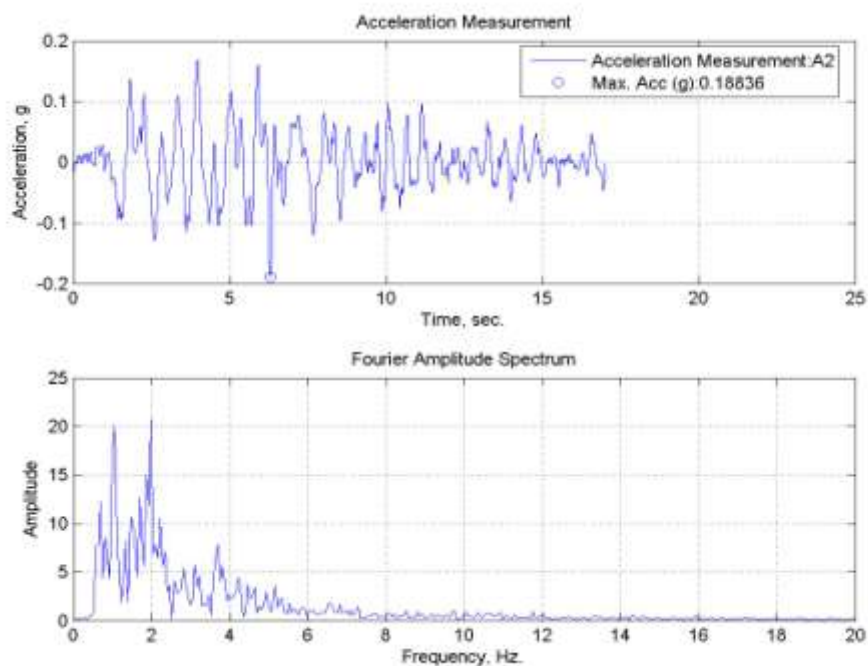


Figure A.97. A2, acceleration time history of TB10 specimen tested at 50°C.

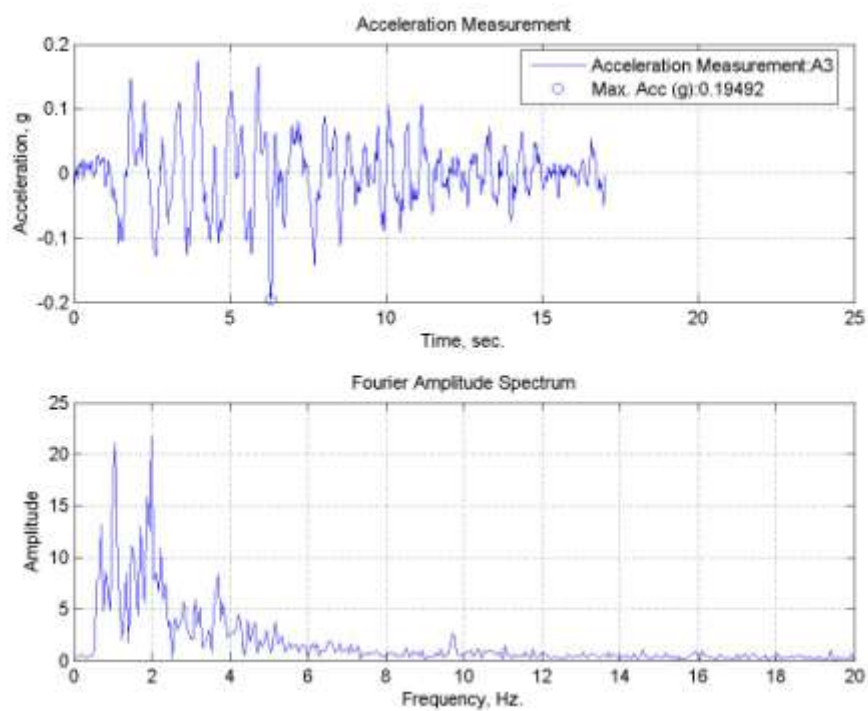


Figure A.98. A3, acceleration time history of TB10 specimen tested at 50°C.

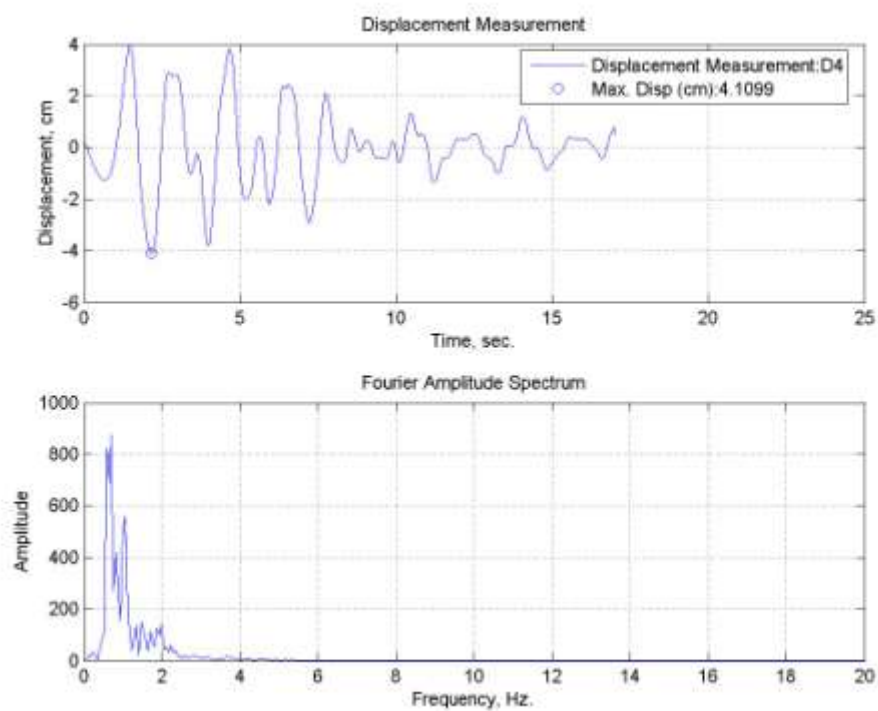


Figure A.99. Lateral displacement time history for TB10 specimen tested at 50°C.

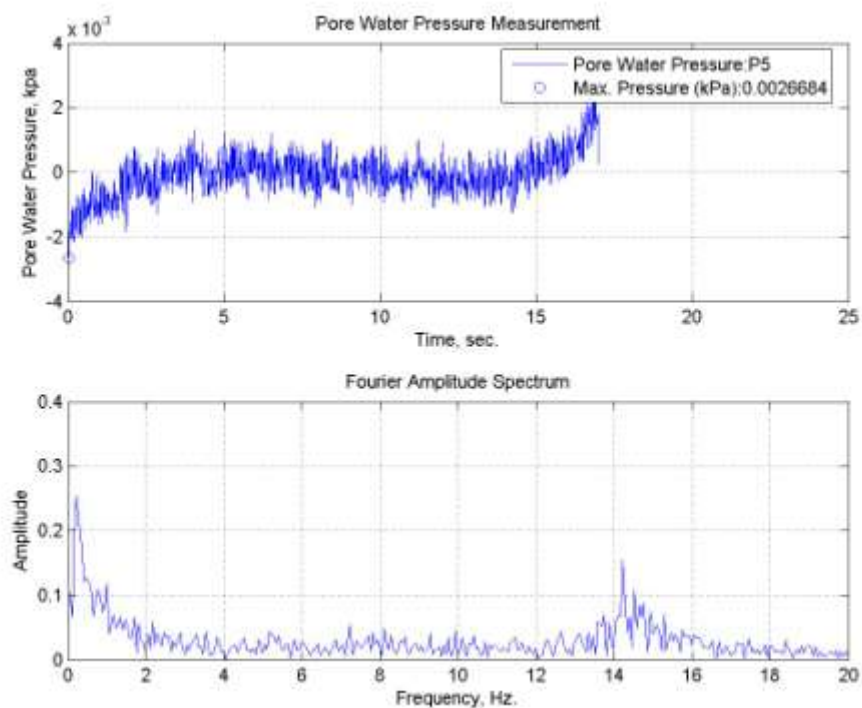


Figure A.100. Pore water pressure change of TB10 specimen tested at 50°C.

A.21. TB15 Specimen subjected to Sakarya (N-S) Earthquake Motion at 50°C

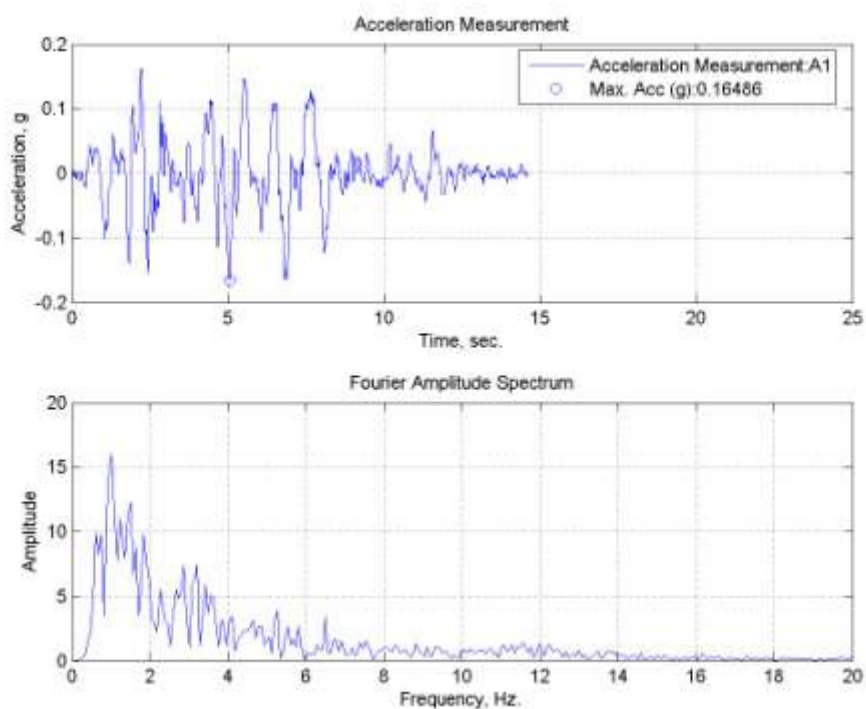


Figure A.101. A1, acceleration time history of TB15 specimen tested at 50°C.

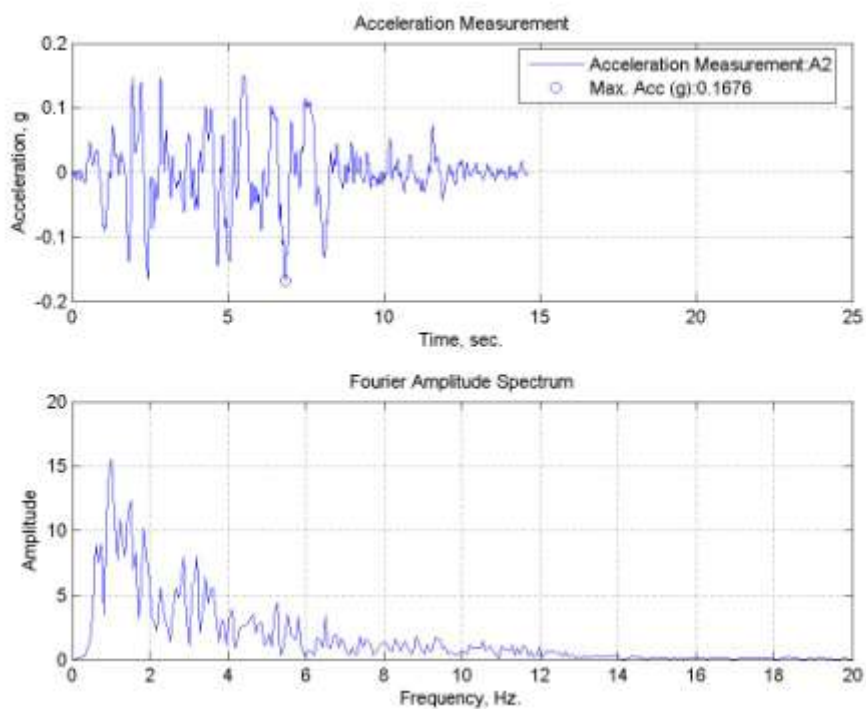


Figure A.102. A2, acceleration time history of TB15 specimen tested at 50°C.

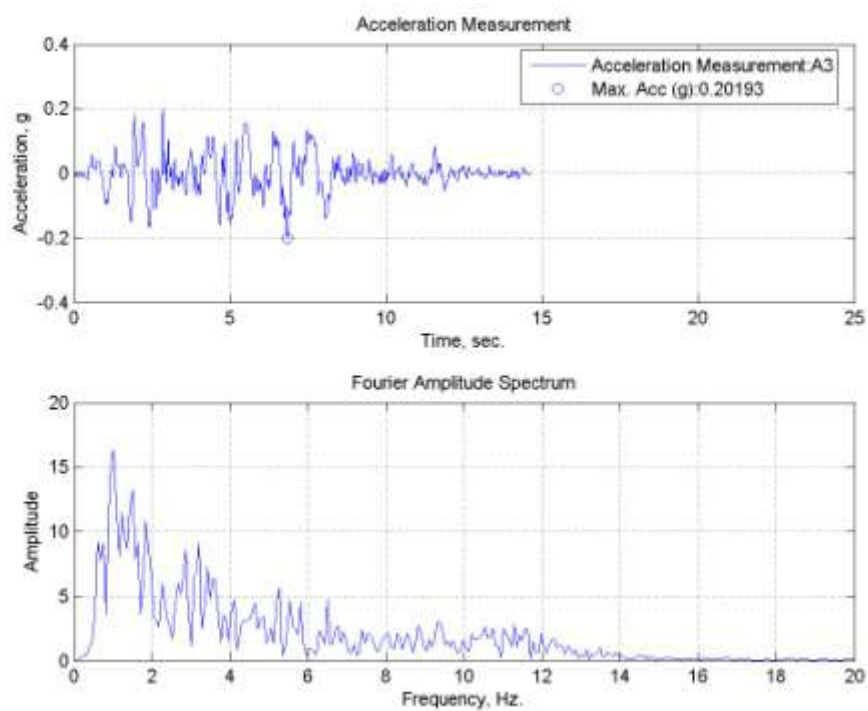


Figure A.103. A3, acceleration time history of TB15 specimen tested at 50°C.

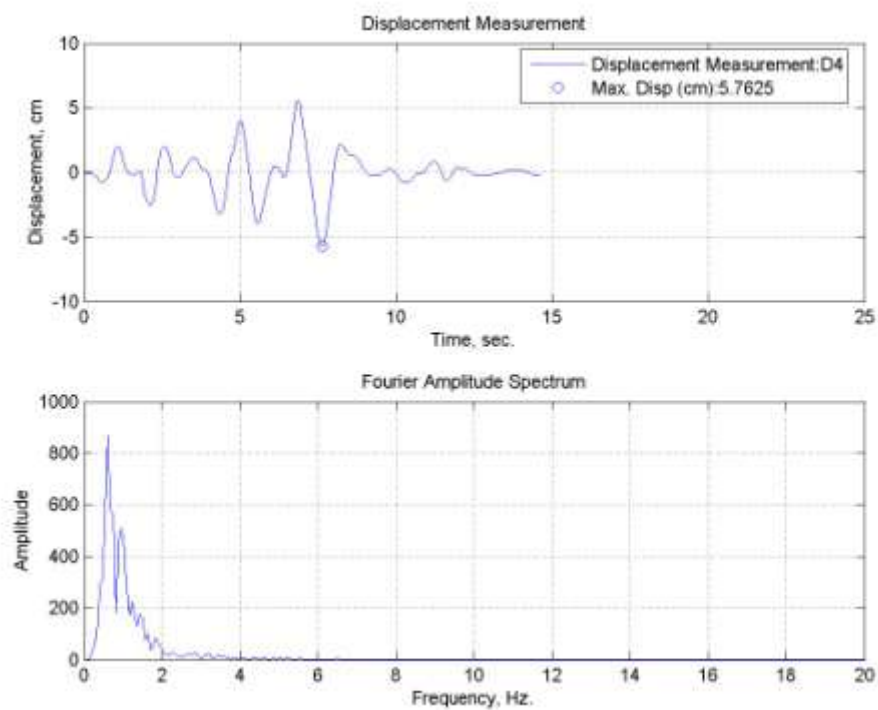


Figure A.104. Lateral displacement time history for TB15 specimen tested at 50°C.

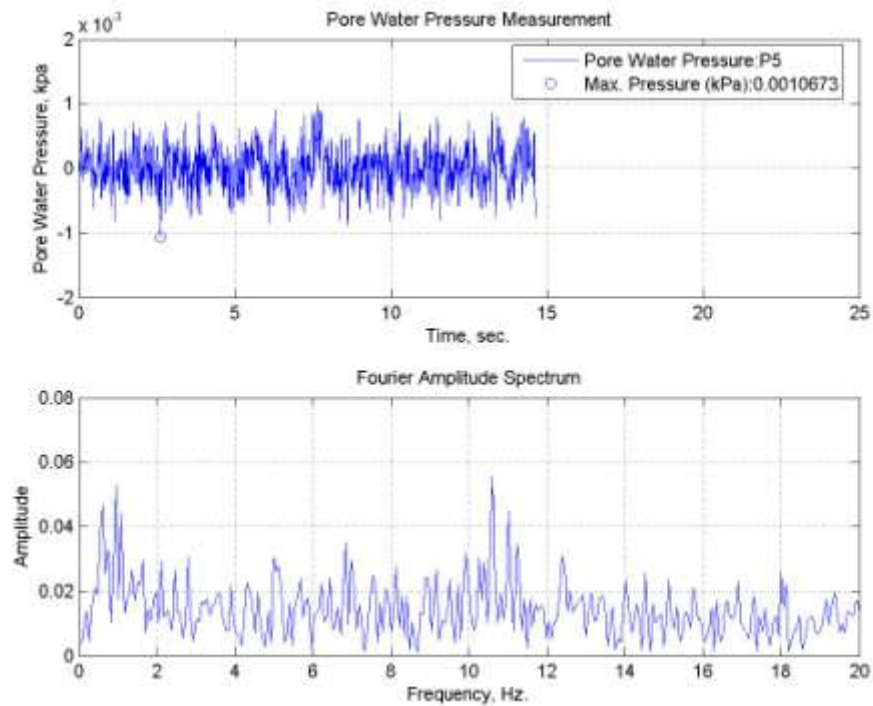


Figure A.105. Pore water pressure change of TB15 specimen tested at 50°C.

A.22. TB20 Specimen subjected to Sakarya (N-S) Earthquake Motion at 50°C.

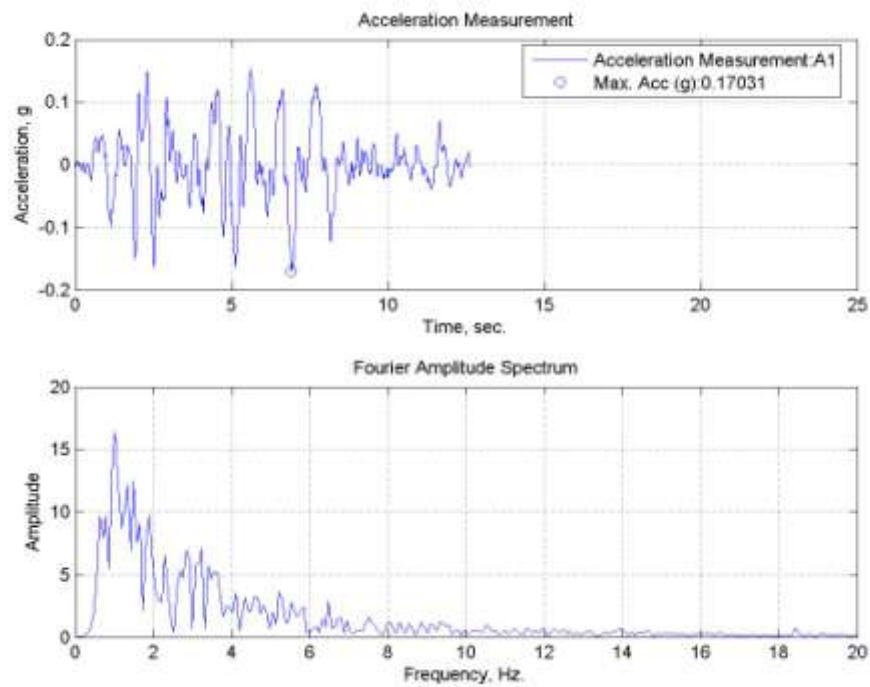


Figure A.106. A1, acceleration time history of TB20 specimen tested at 50°C.

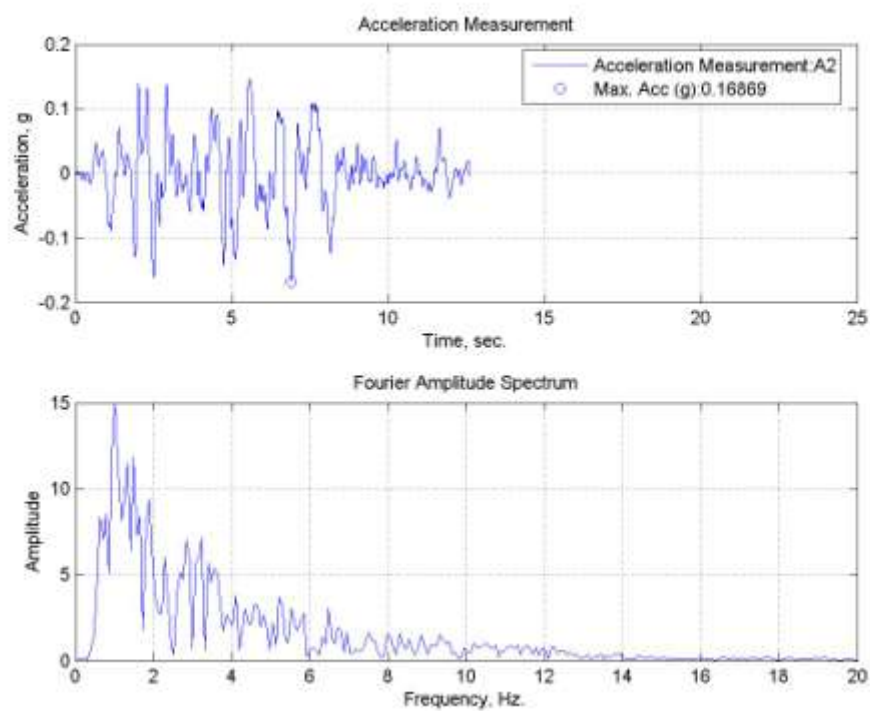


Figure A.107. A2, acceleration time history of TB20 specimen tested at 50°C.

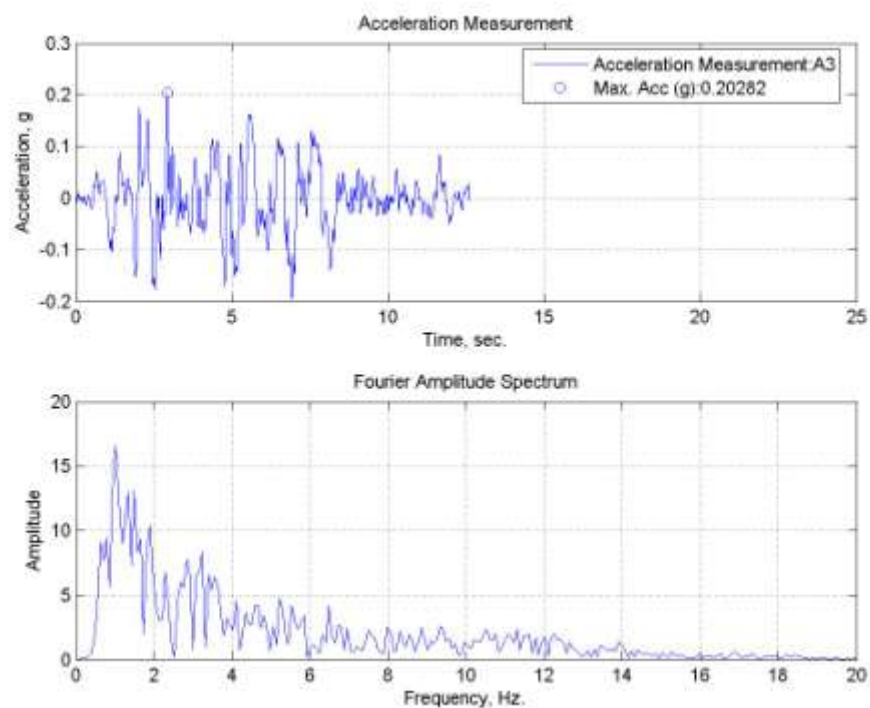


Figure A.108. A3, acceleration time history of TB20 specimen tested at 50°C.

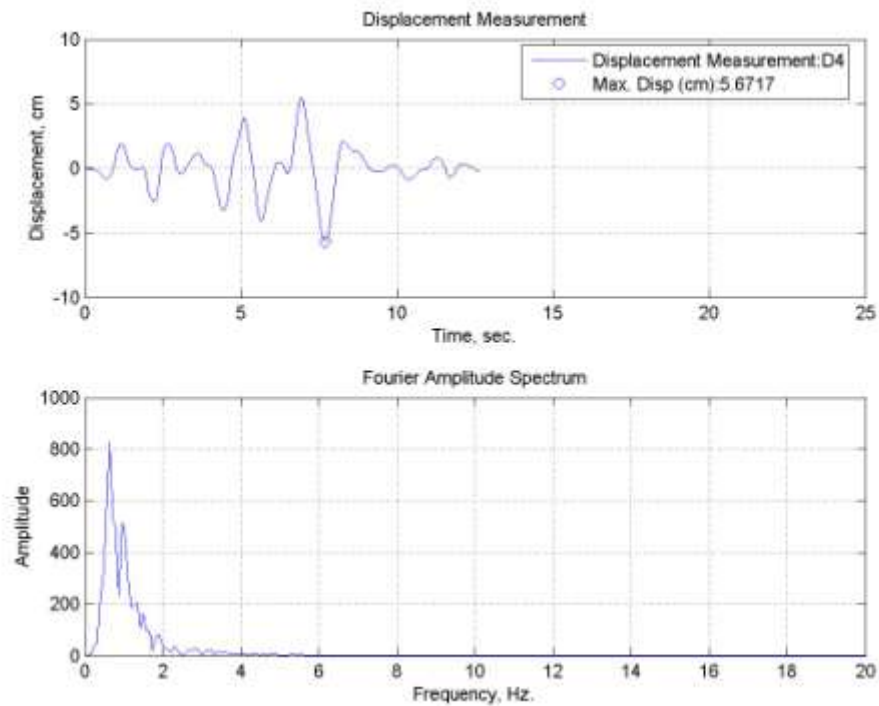


Figure A.109. Lateral displacement time history for TB20 specimen tested at 50°C.

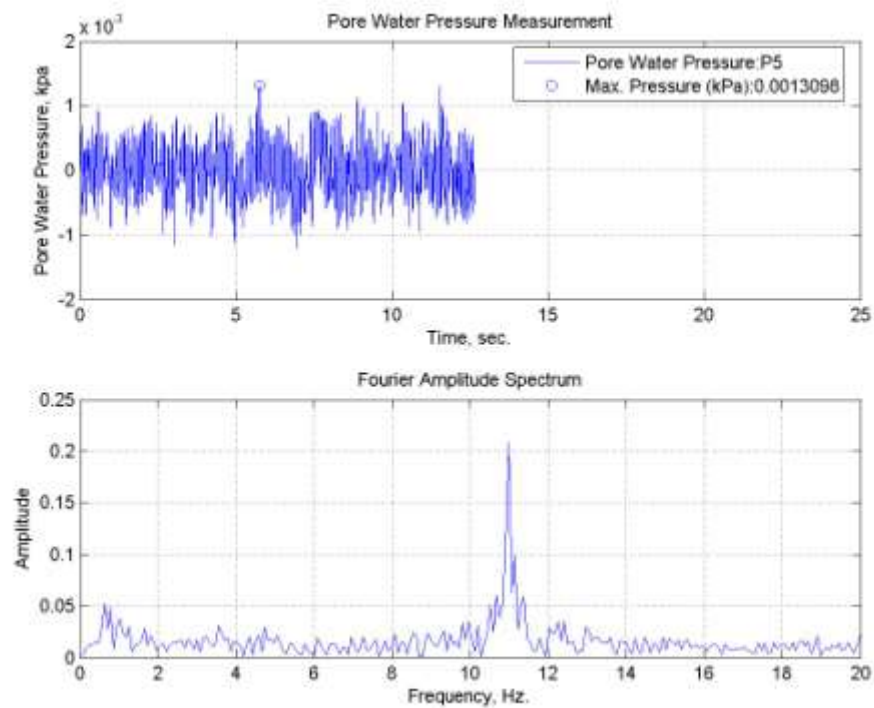


Figure A.110. Pore water pressure change of TB20 specimen tested at 50°C.

A.23. TB30 Specimen subjected to Sakarya (N-S) Earthquake Motion at 50°C

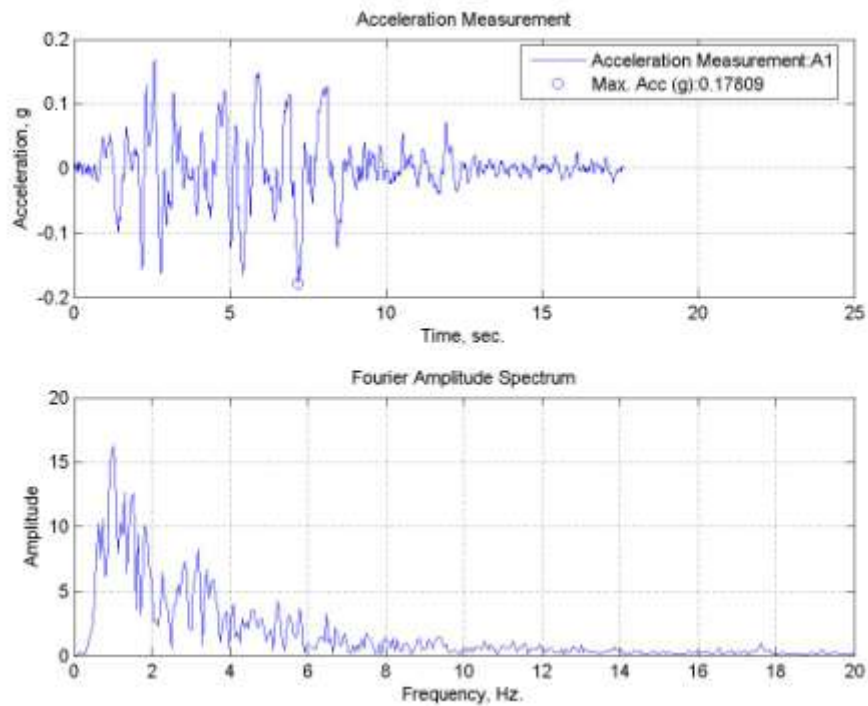


Figure A.111. A1, acceleration time history of TB30 specimen tested at 50°C.

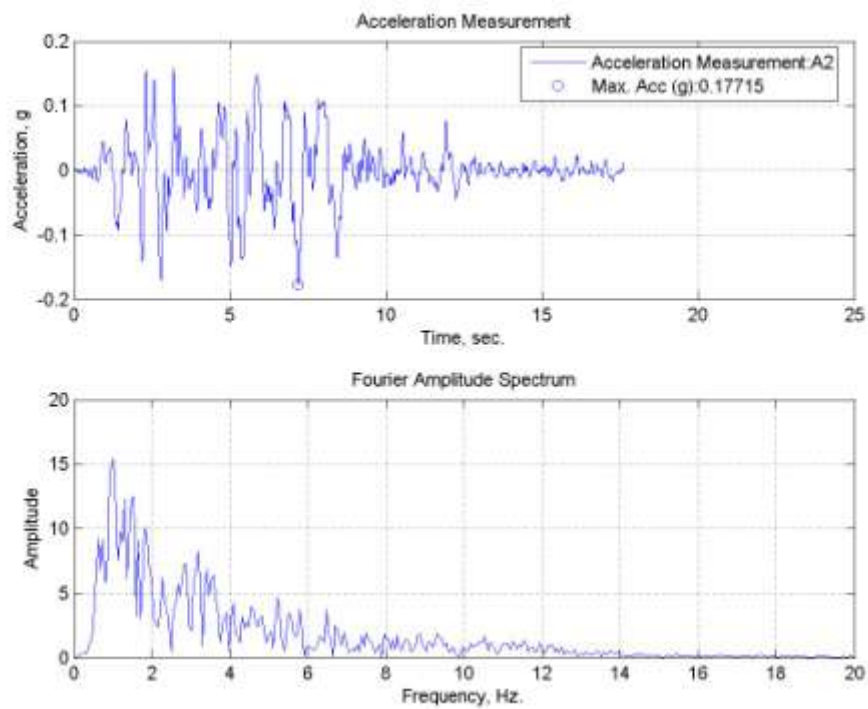


Figure A.112. A2, acceleration time history of TB30 specimen tested at 50°C.

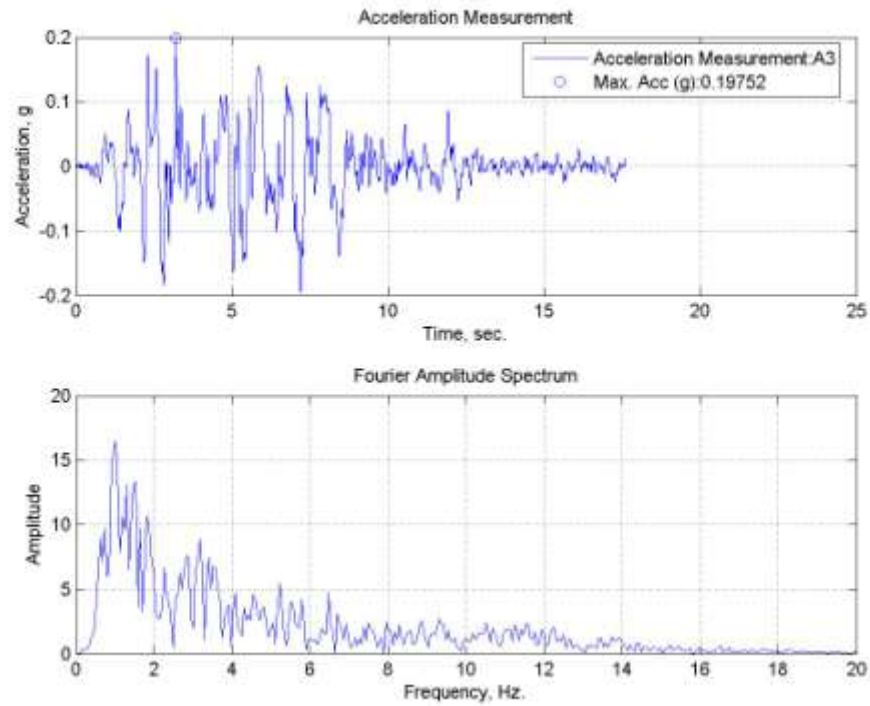


Figure A.113. A3, acceleration time history of TB30 specimen tested at 50°C.

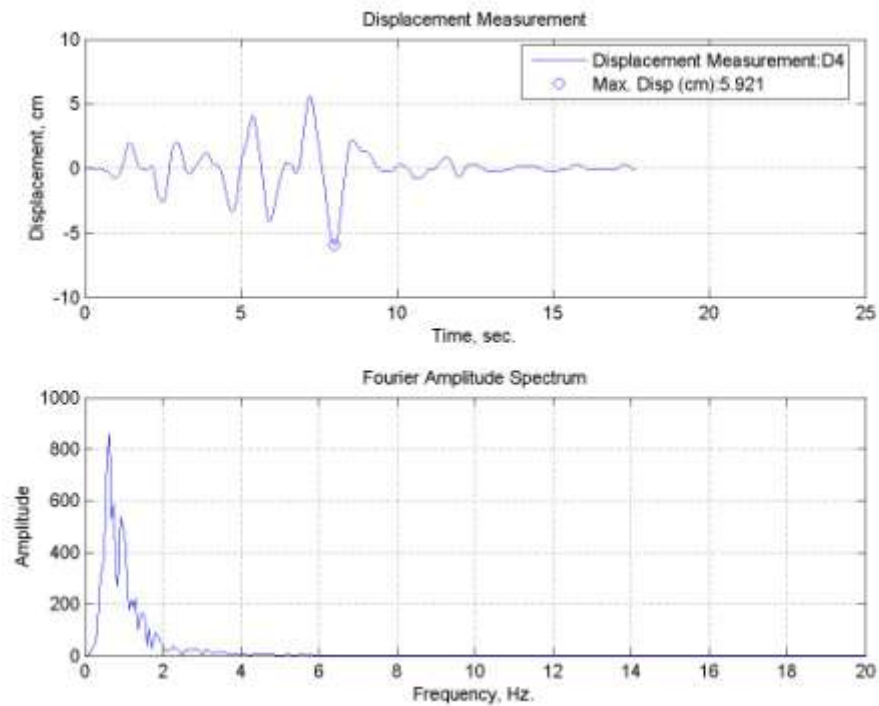


Figure A.114. Lateral displacement time history for TB30 specimen tested at 50°C.

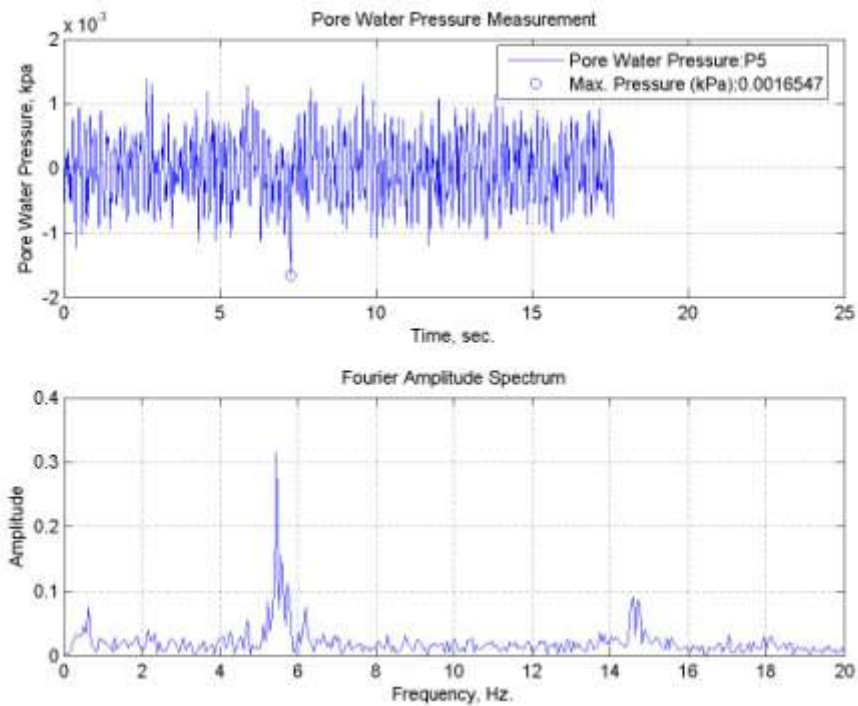


Figure A.115. Pore water pressure change of TB30 specimen tested at 50°C.

A.24. TC10 Specimen subjected to Sakarya (N-S) Earthquake Motion at 50°C

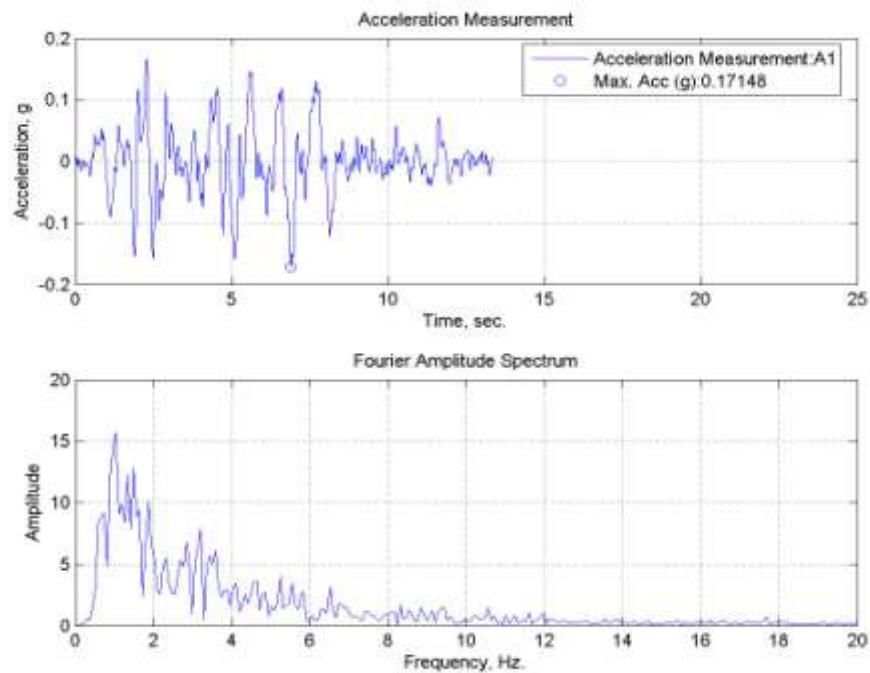


Figure A.116. A1, acceleration time history of TC10 specimen tested at 50°C.

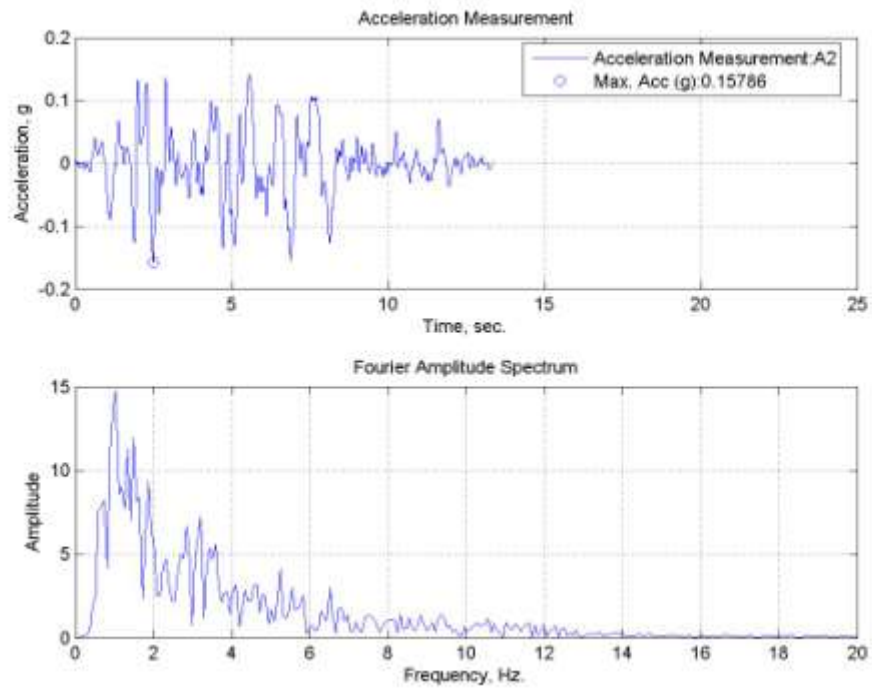


Figure A.117. A2, acceleration time history of TC10 specimen tested at 50°C.

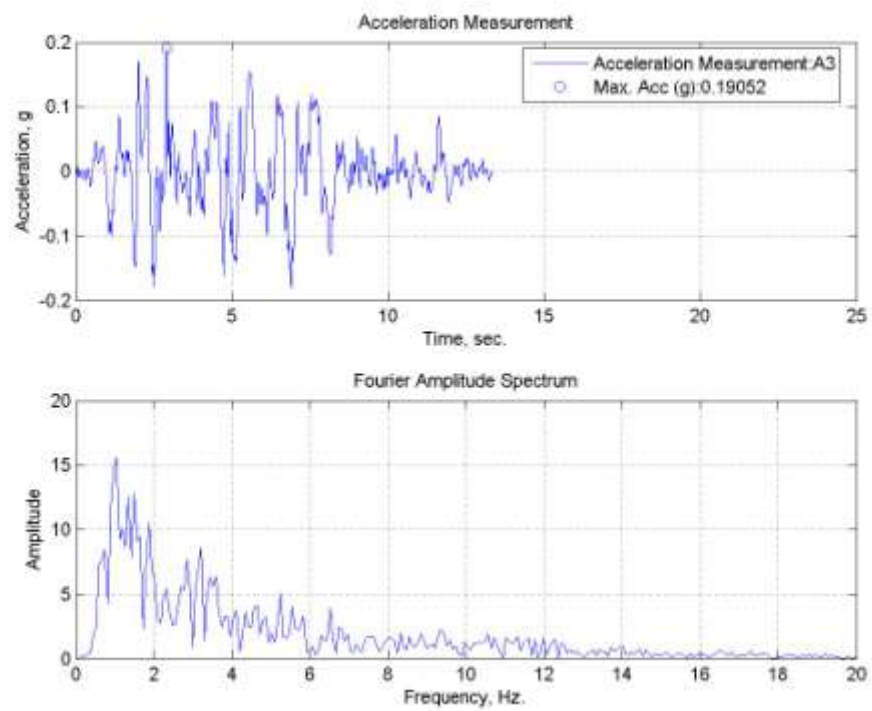


Figure A.118. A3, acceleration time history of TC10 specimen tested at 50°C.

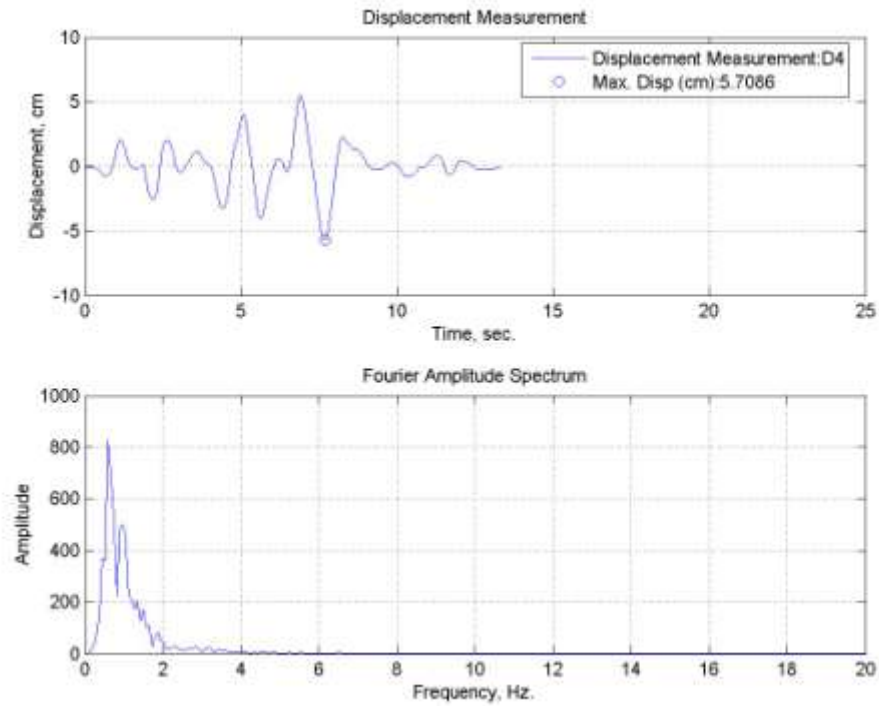


Figure A.119. Lateral displacement time history for TC10 specimen tested at 50°C.

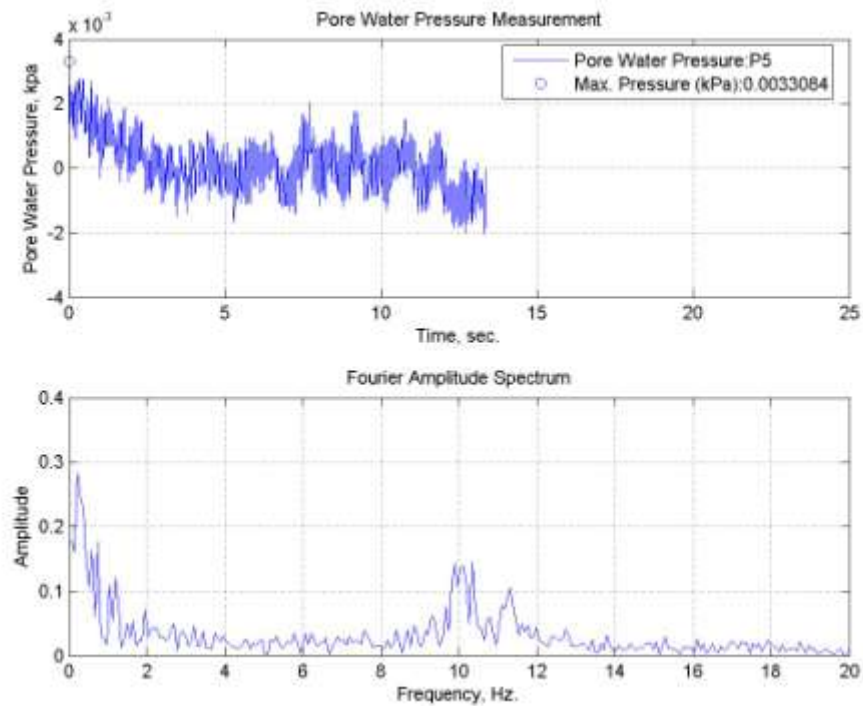


Figure A.120. Pore water pressure change of TC10 specimen tested at 50°C.

A.25. TC15 Specimen subjected to Sakarya (N-S) Earthquake Motion at 50°C

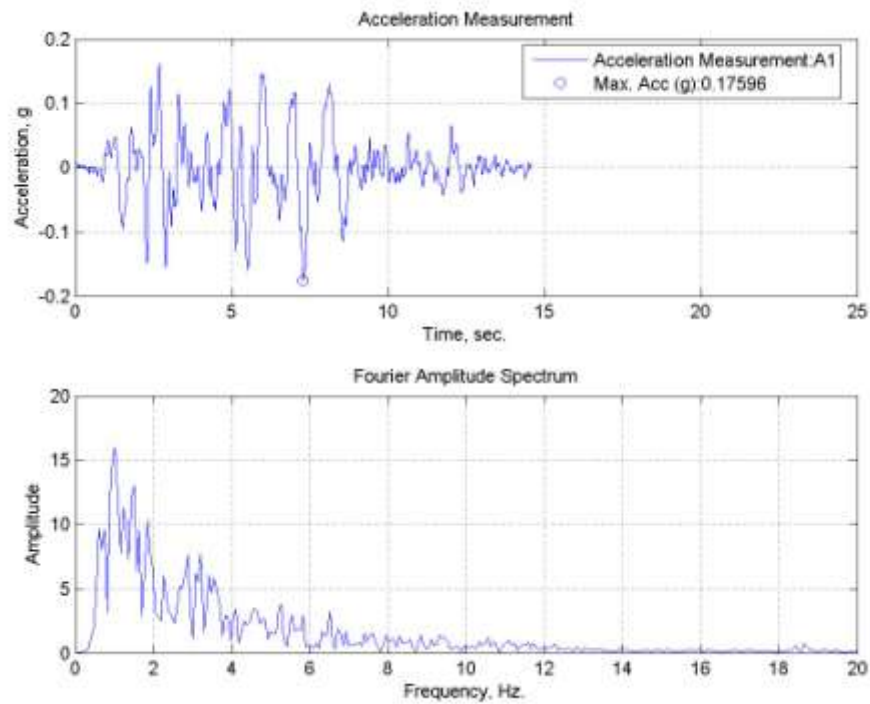


Figure A.121. A1, acceleration time history of TC15 specimen tested at 50°C.

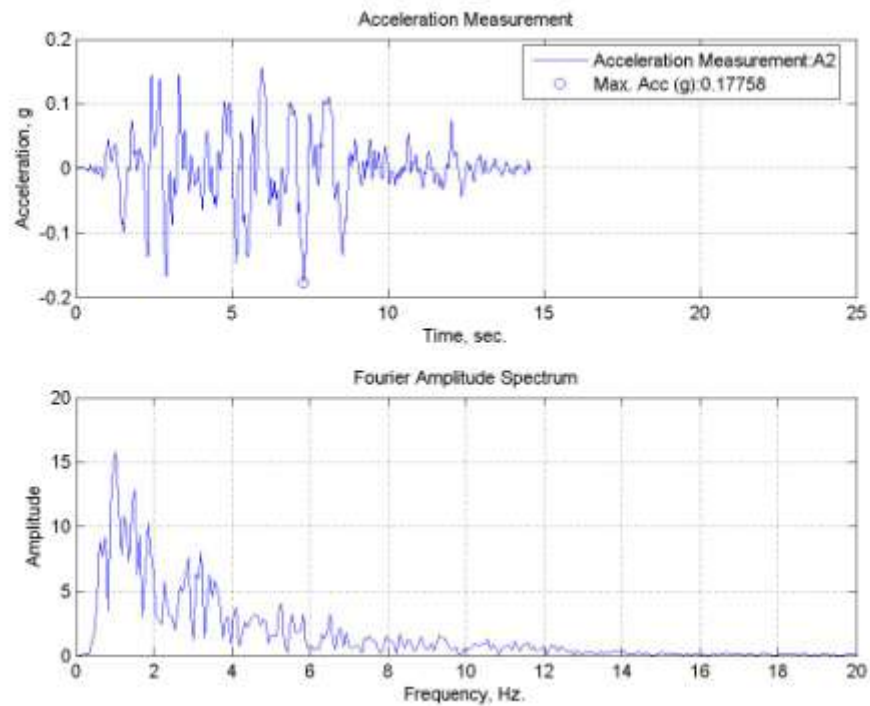


Figure A.122. A2, acceleration time history of TC15 specimen tested at 50°C.

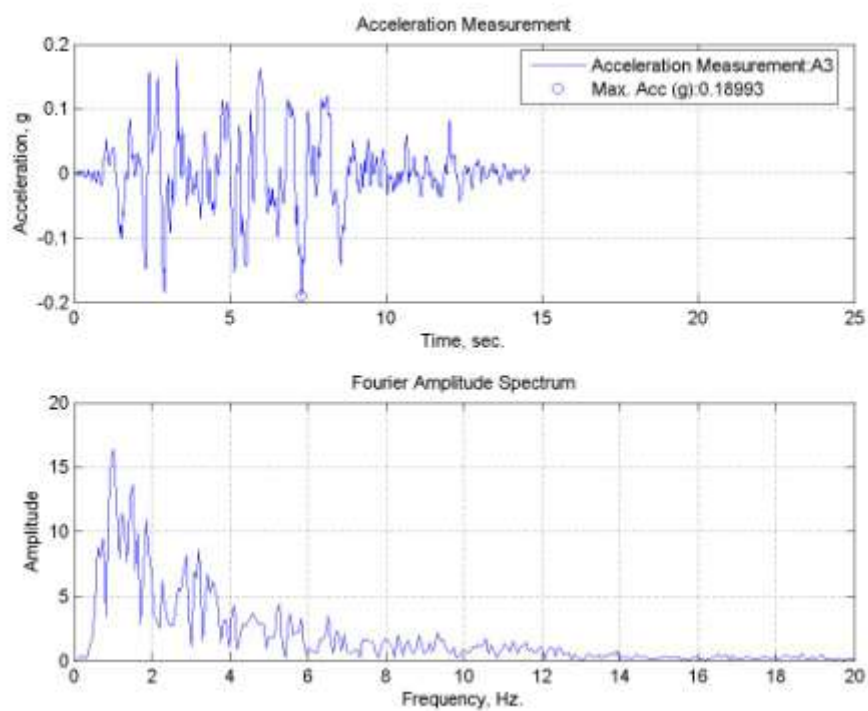


Figure A.123. A3, acceleration time history of TC15 specimen tested at 50°C.

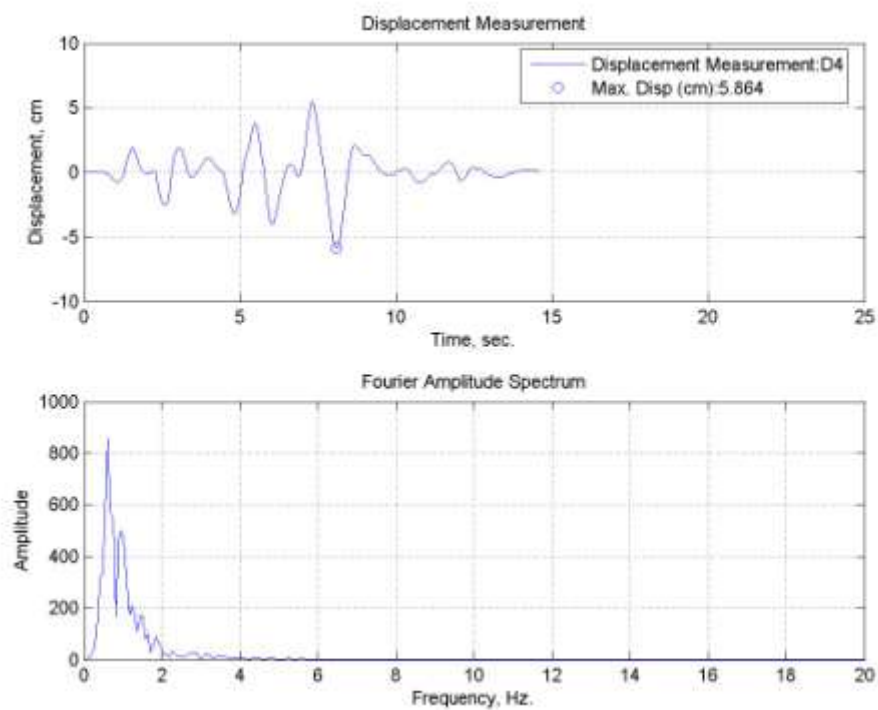


Figure A.124. Lateral displacement time history for TC15 specimen tested at 50°C.

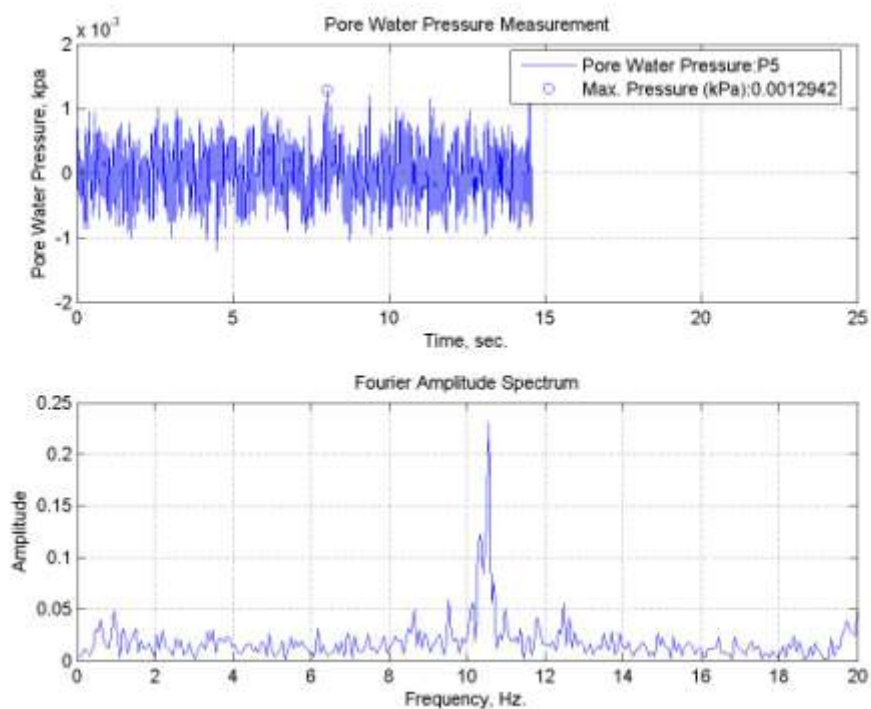


Figure A.125. Pore water pressure change of TC15 specimen tested at 50°C.

A.26. TC20 Specimen subjected to Sakarya (N-S) Earthquake Motion at 50°C

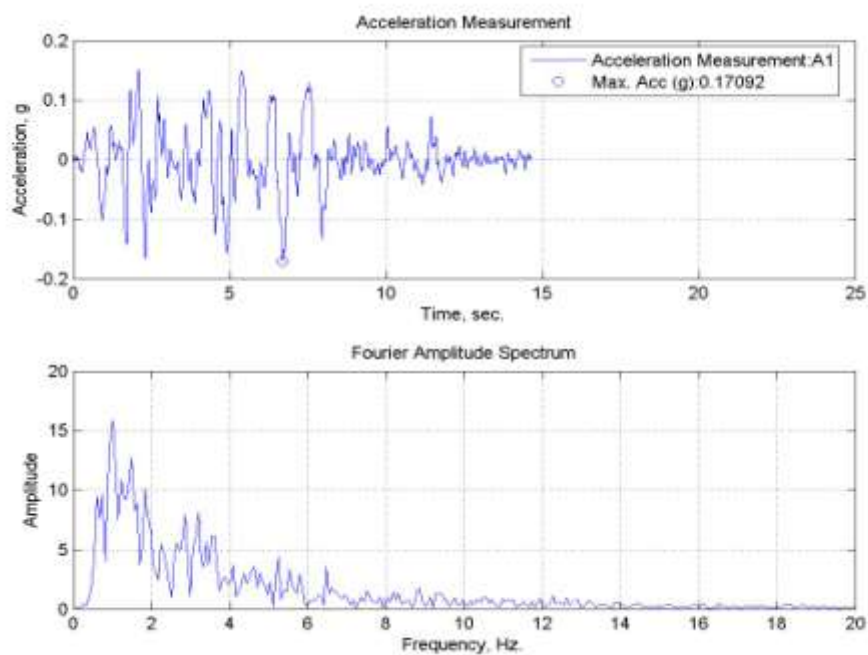


Figure A.126. A1, acceleration time history of TC20 specimen tested at 50°C.

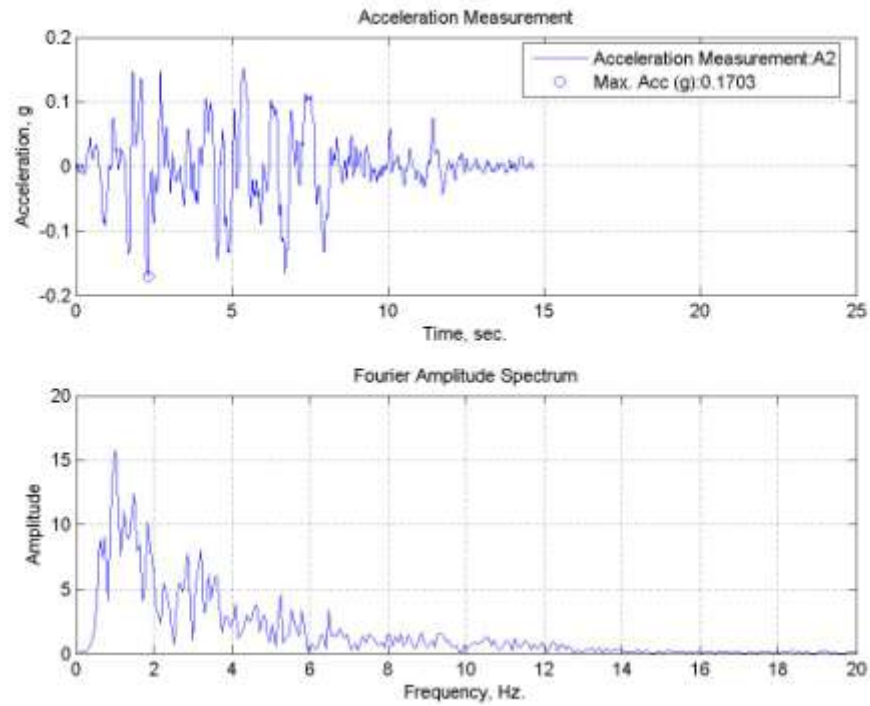


Figure A.127. A2, acceleration time history of TC20 specimen tested at 50°C.

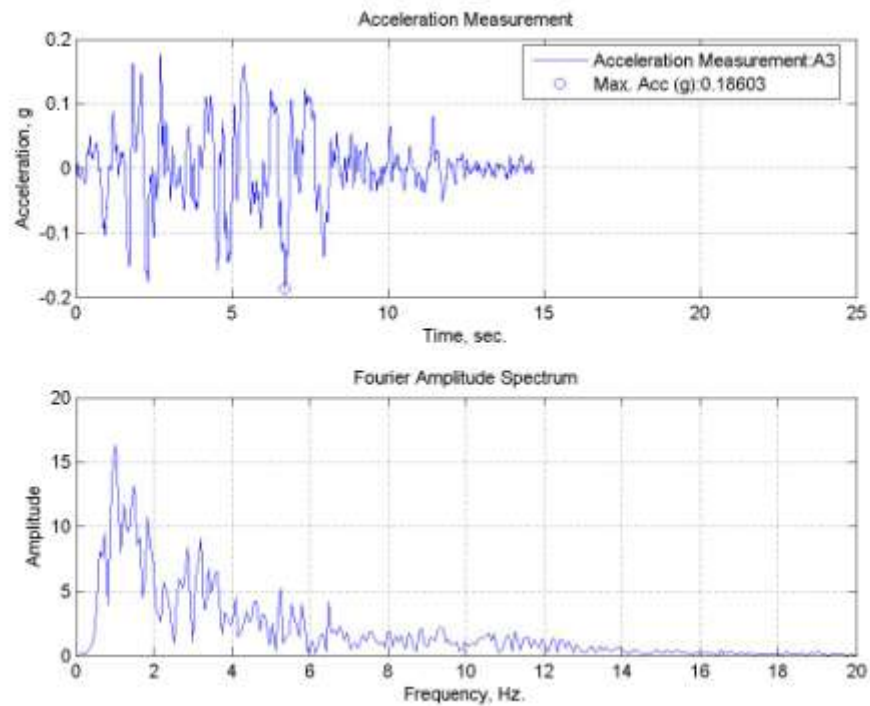


Figure A.128. A3, acceleration time history of TC20 specimen tested at 50°C.

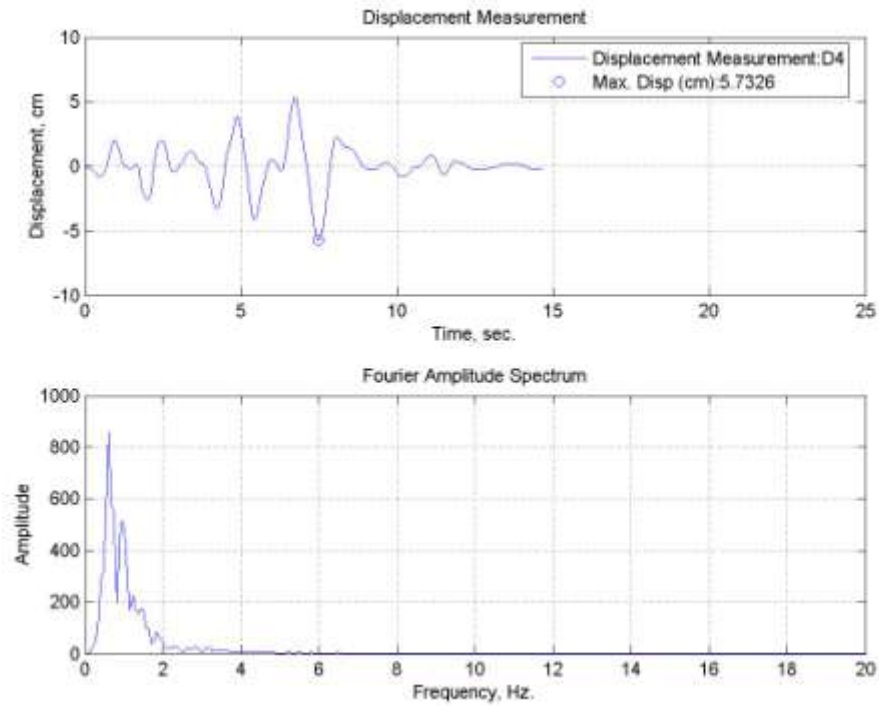


Figure A.129. Lateral displacement time history for TC20 specimen tested at 50°C.

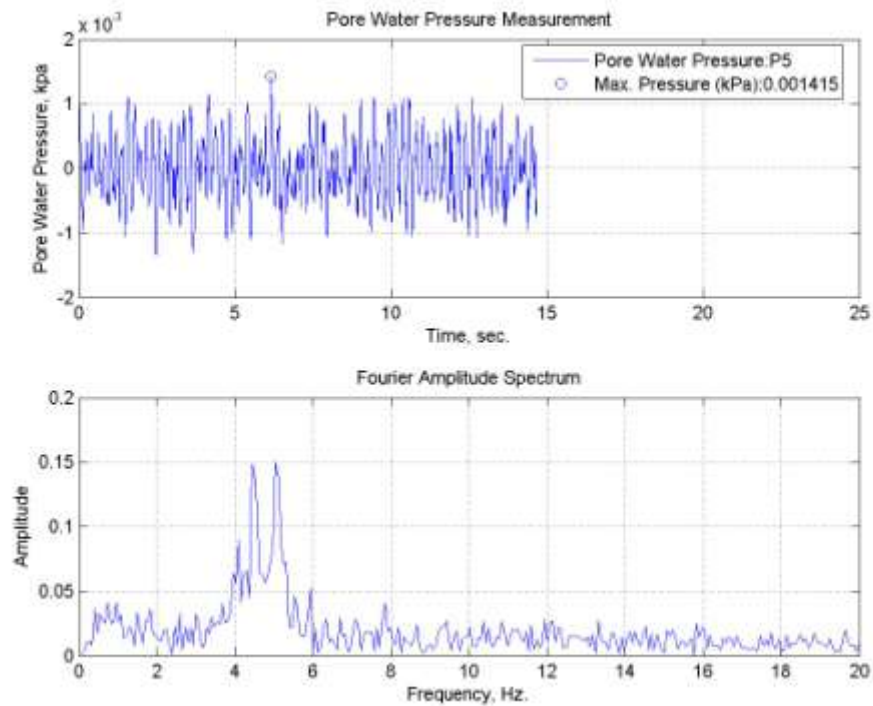


Figure A.130. Pore water pressure change of TC20 specimen tested at 50°C.

A.27. TC30 Specimen subjected to Sakarya (N-S) Earthquake Motion at 50°C

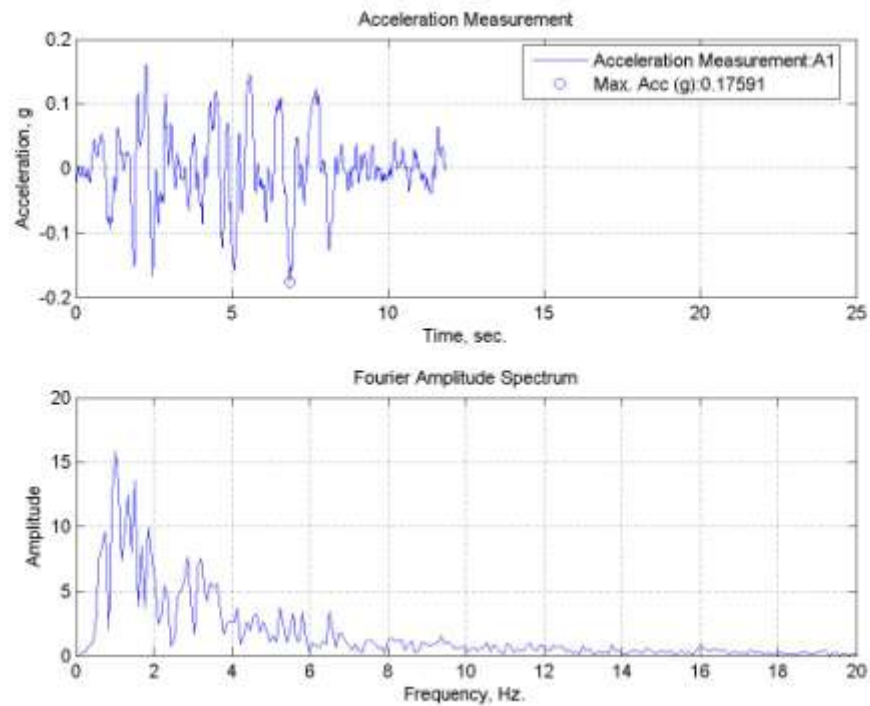


Figure A.131. A1, acceleration time history of TC30 specimen tested at 50°C.

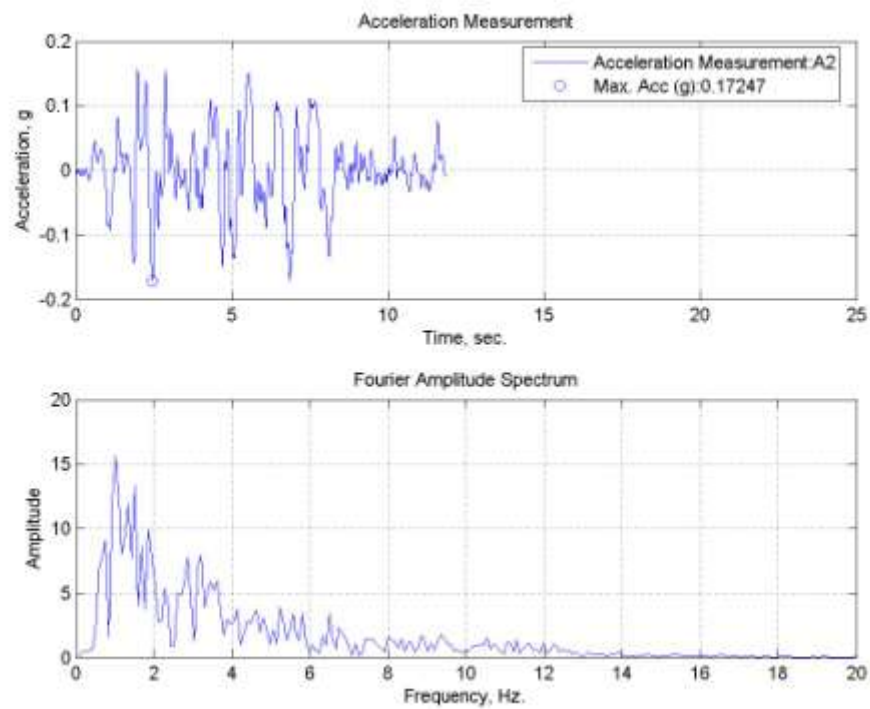


Figure A.132. A2, acceleration time history of TC30 specimen tested at 50°C.

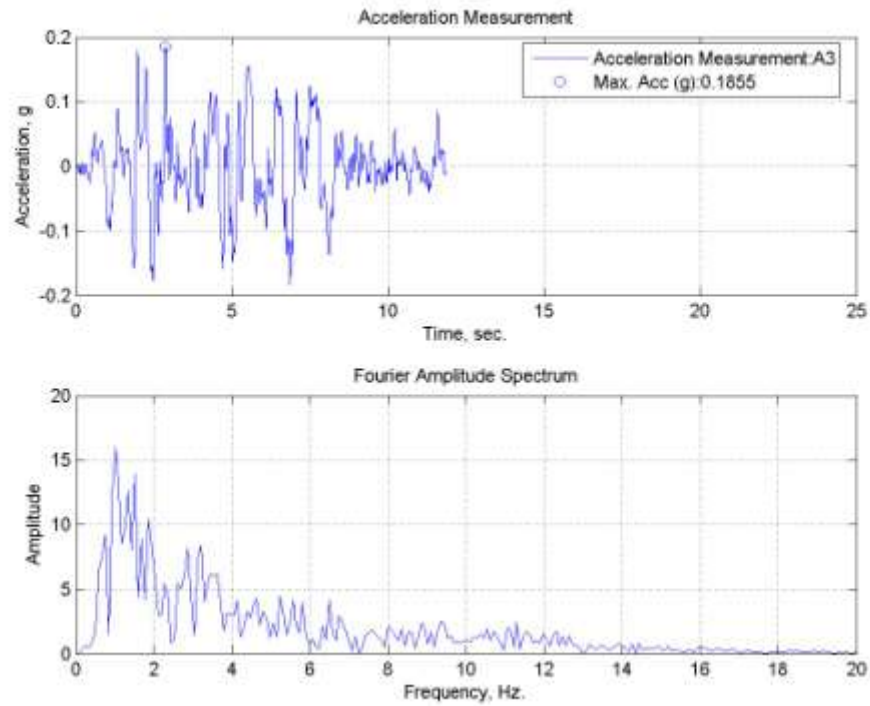


Figure A.133. A3, acceleration time history of TC30 specimen tested at 50°C.

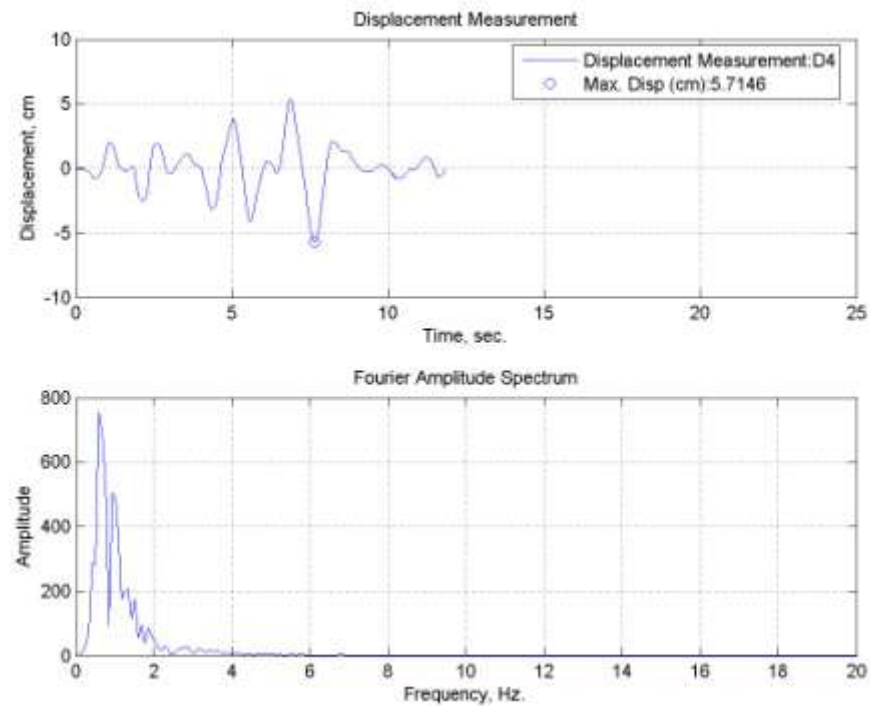


Figure A.134. Lateral displacement time history for TC30 specimen tested at 50°C.

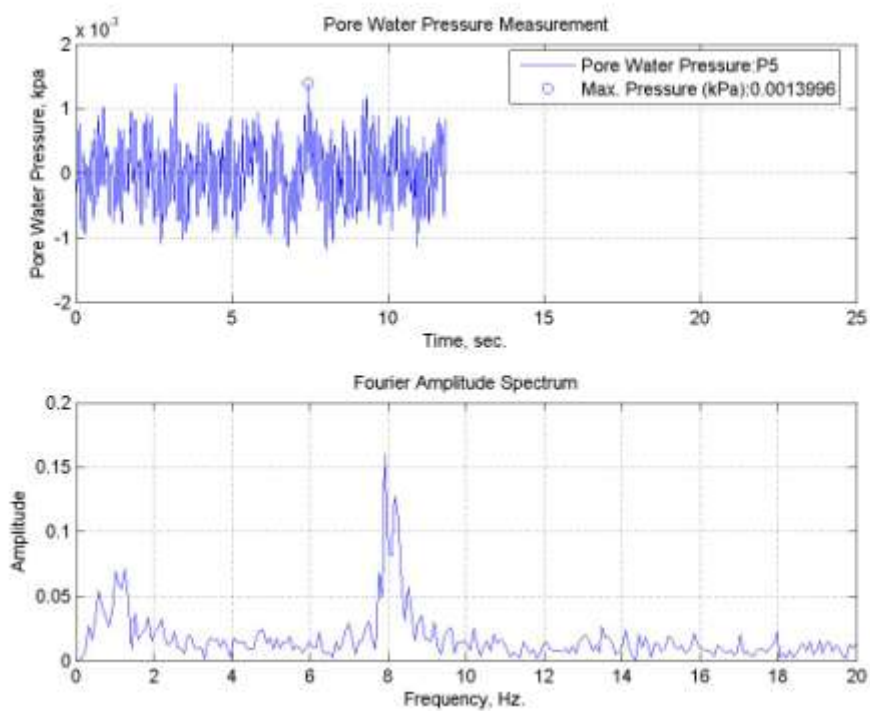


Figure A.135. Pore water pressure change of TC30 specimen tested at 50°C.

APPENDIX B: SHAKING TABLE TEST RESULTS OF TABAS (E-W) GROUND MOTIONS

B.1. Sand Specimen subjected to Tabas (E-W) Earthquake Motion at 0°C.

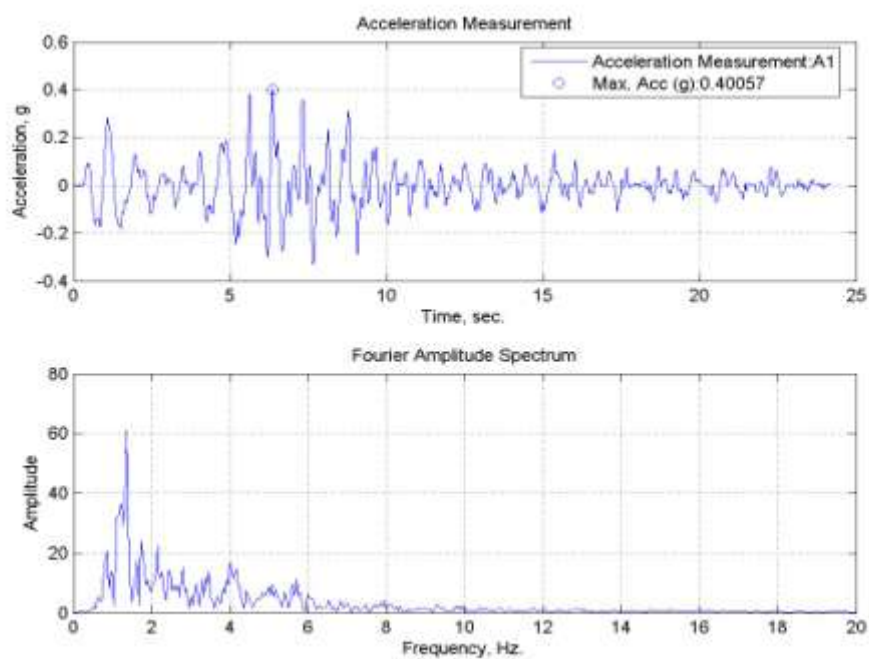


Figure B.1. A1, acceleration time history of sand specimen tested at 0°C.

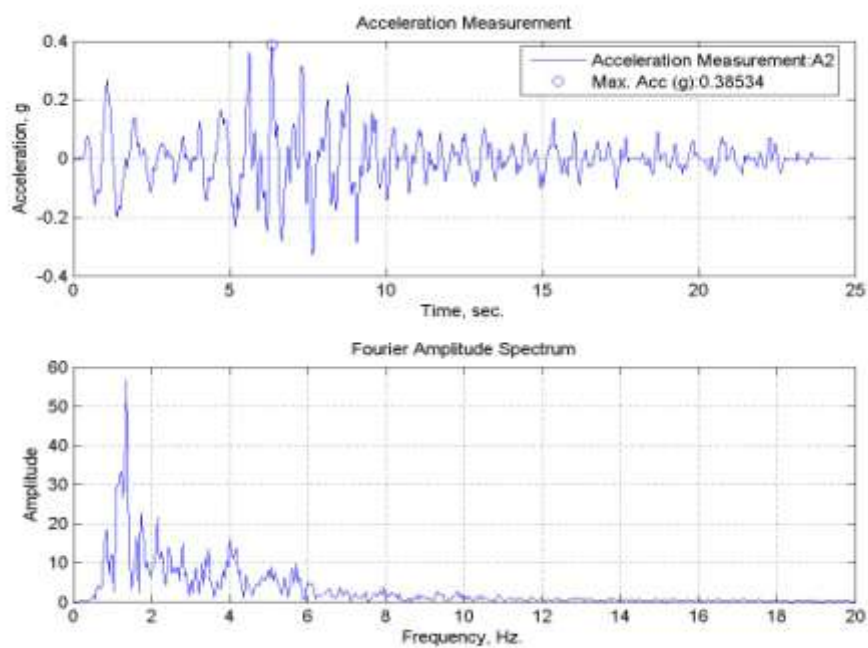


Figure B.2. A2, acceleration time history of sand specimen tested at 0°C.

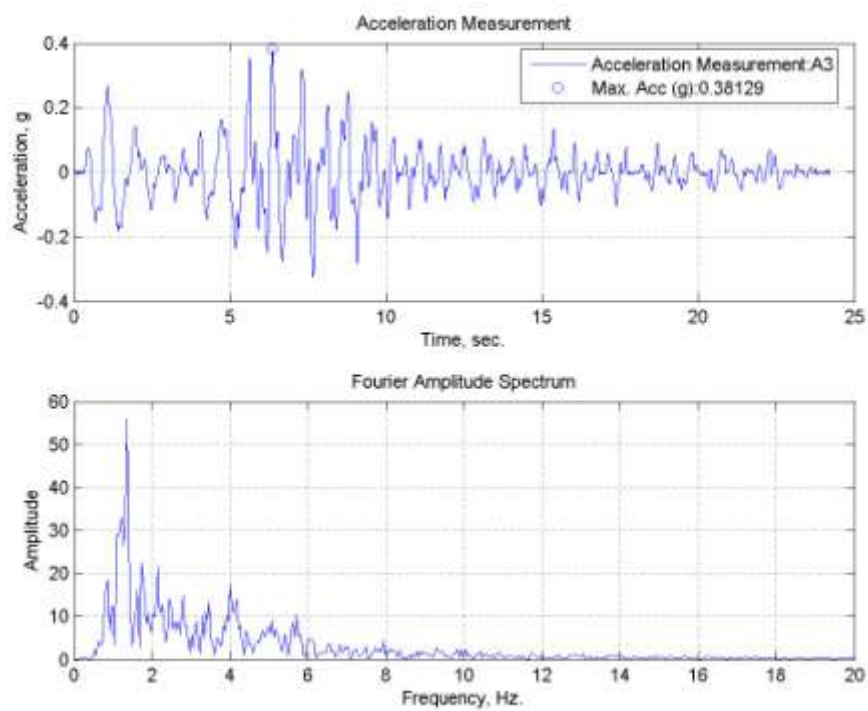


Figure B.3. A3, acceleration time history of sand specimen tested at 0°C.

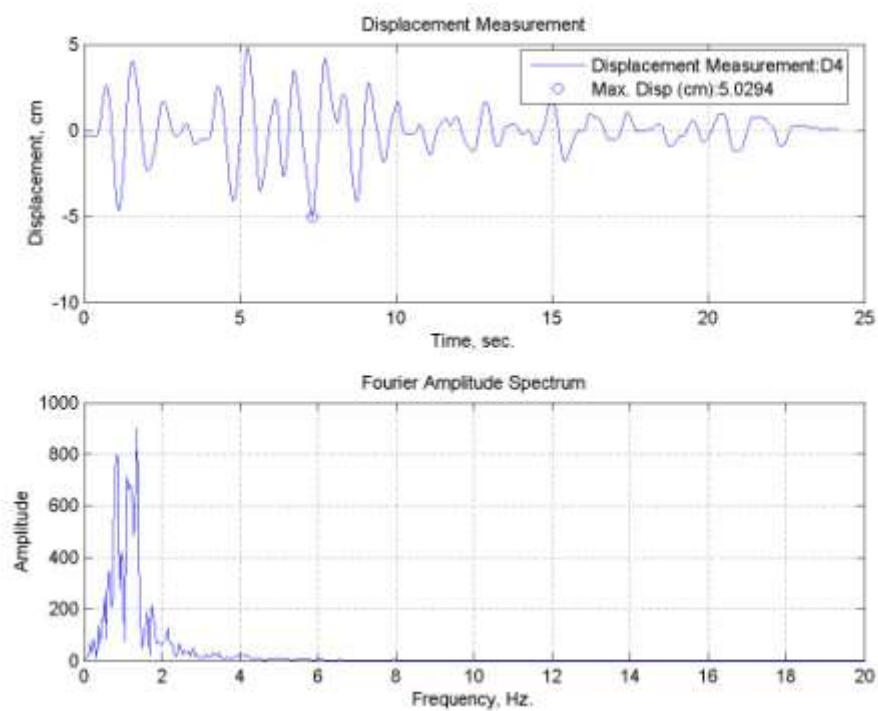


Figure B.4. Lateral displacement time history for sand specimen tested at 0°C.

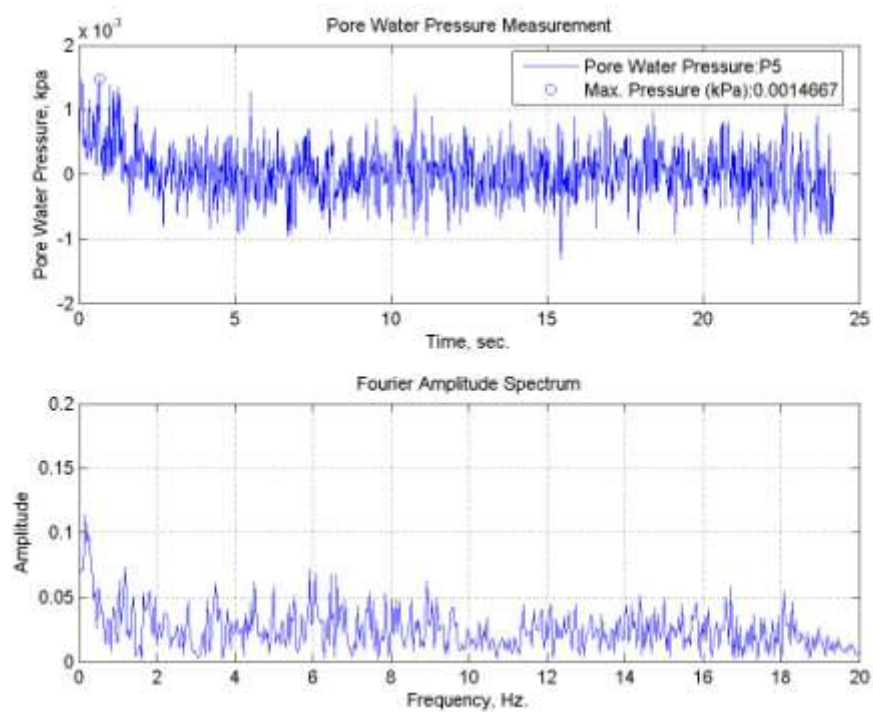


Figure B.5. Pore water pressure change of sand specimen tested at 0°C.

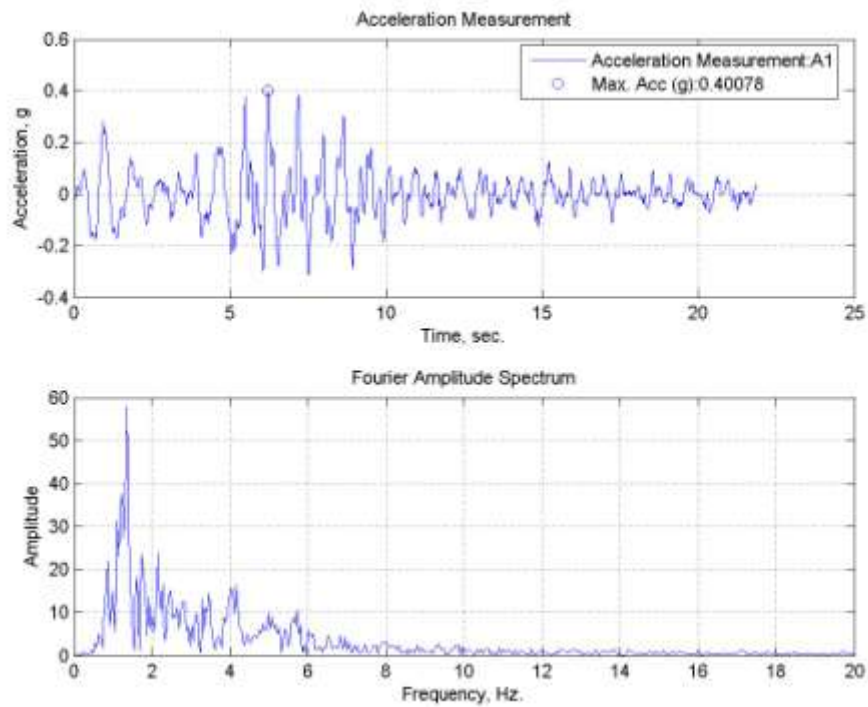
B.2. TB10 Specimen subjected to Tabas (E-W) Earthquake Motion at 0°C

Figure B.6. A1, acceleration time history of TB10 specimen tested at 0°C.

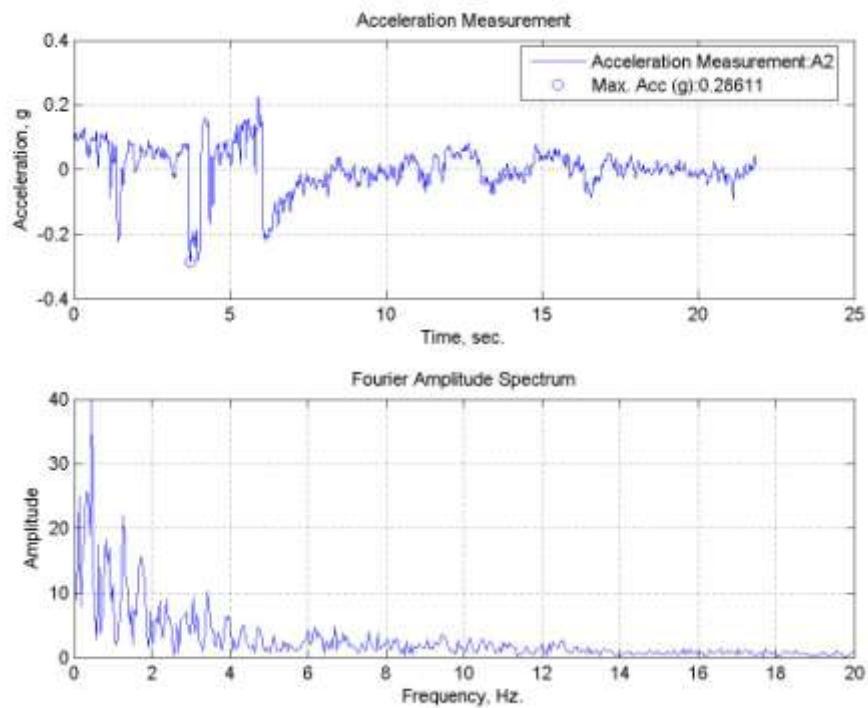


Figure B.7. A2, acceleration time history of TB10 specimen tested at 0°C.

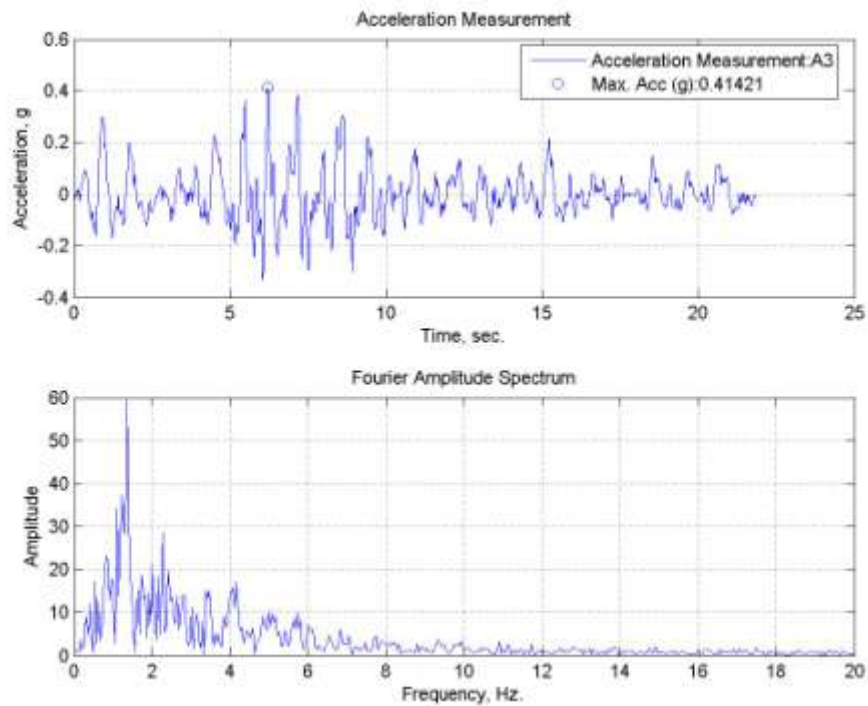


Figure B.8. A3, acceleration time history of TB10 specimen tested at 0°C.

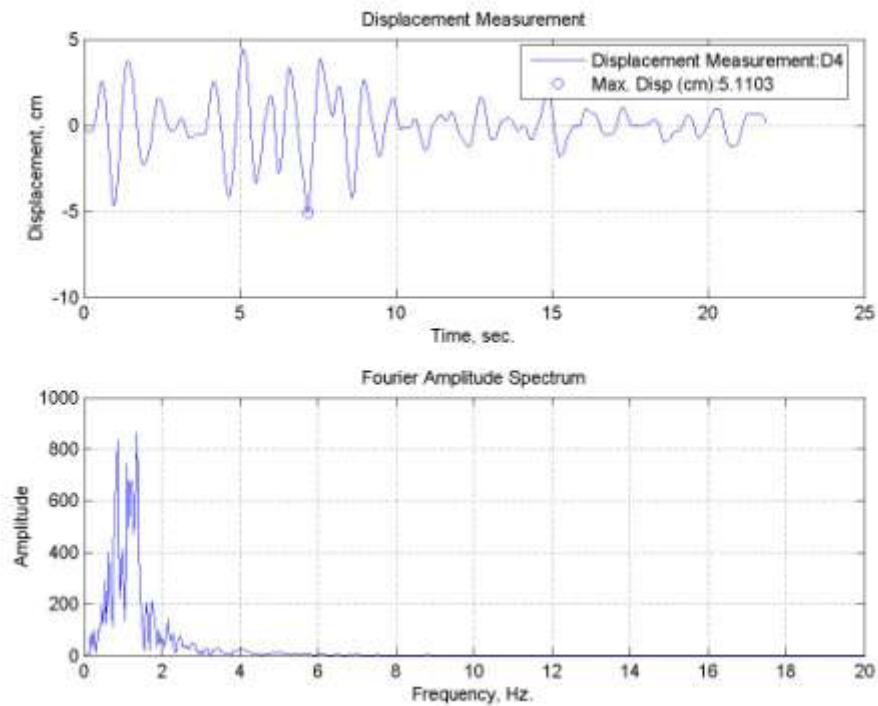


Figure B.9. Lateral displacement time history for TB10 specimen tested at 0°C.

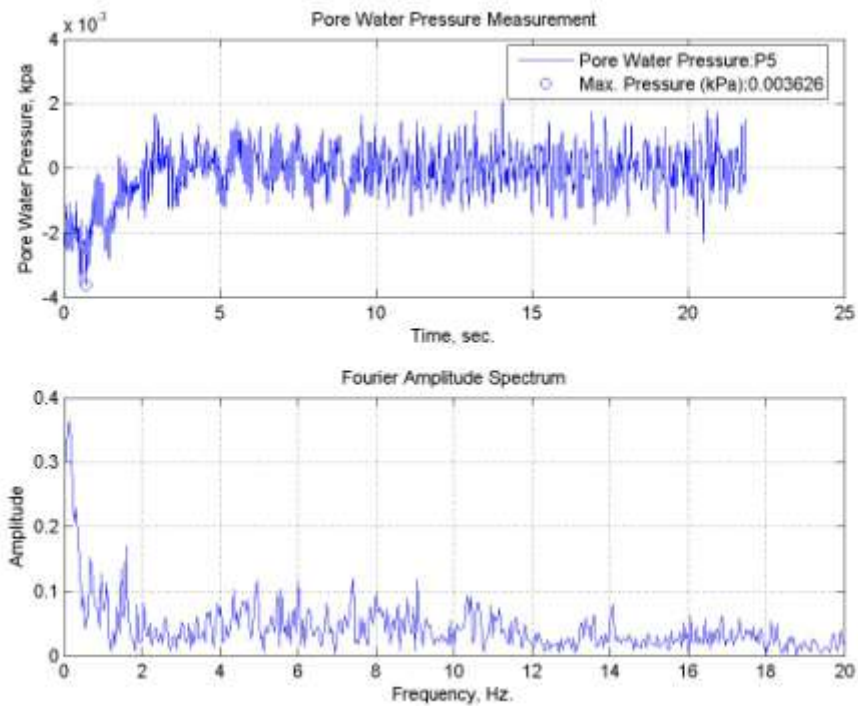


Figure B.10. Pore water pressure change of TB10 specimen tested at 0°C.

B.3. TB15 Specimen subjected to Tabas (E-W) Earthquake Motion at 0°C

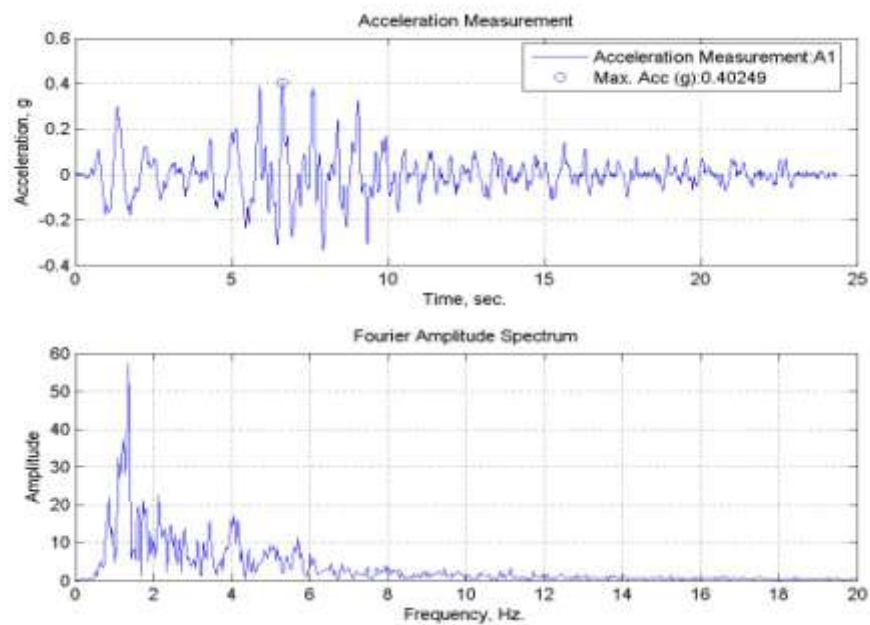


Figure B.11. A1, acceleration time history of TB15 specimen tested at 0°C.

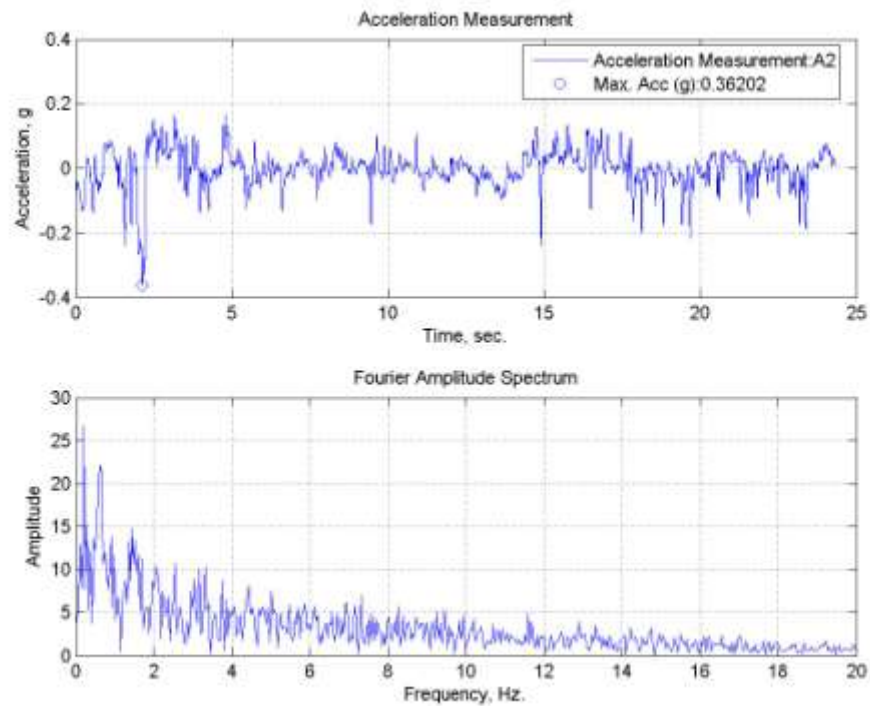


Figure B.12. A2, acceleration time history of TB15 specimen tested at 0°C.

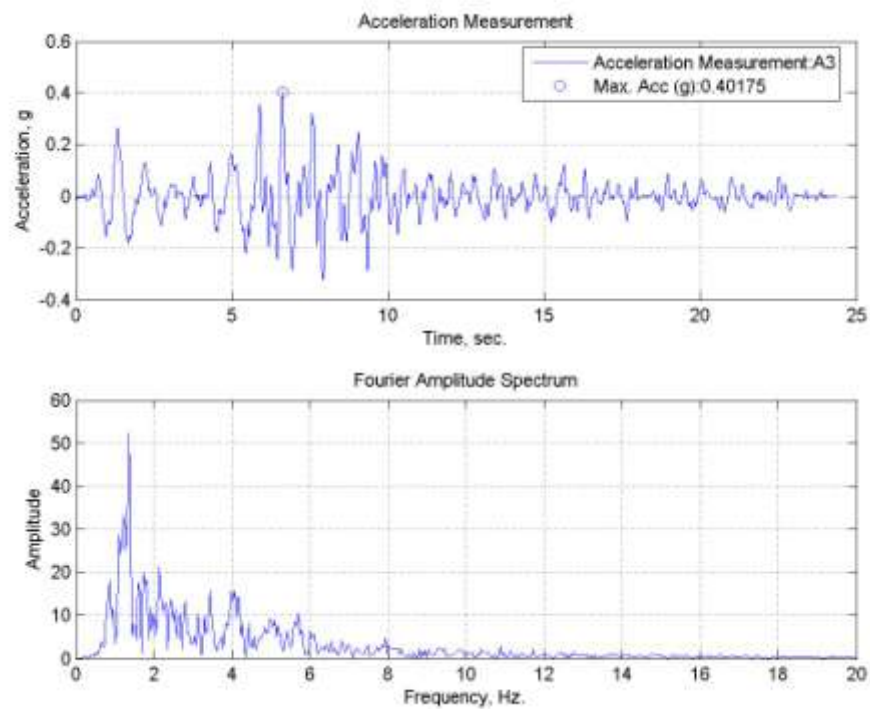


Figure B.13. A3, acceleration time history of TB15 specimen tested at 0°C.

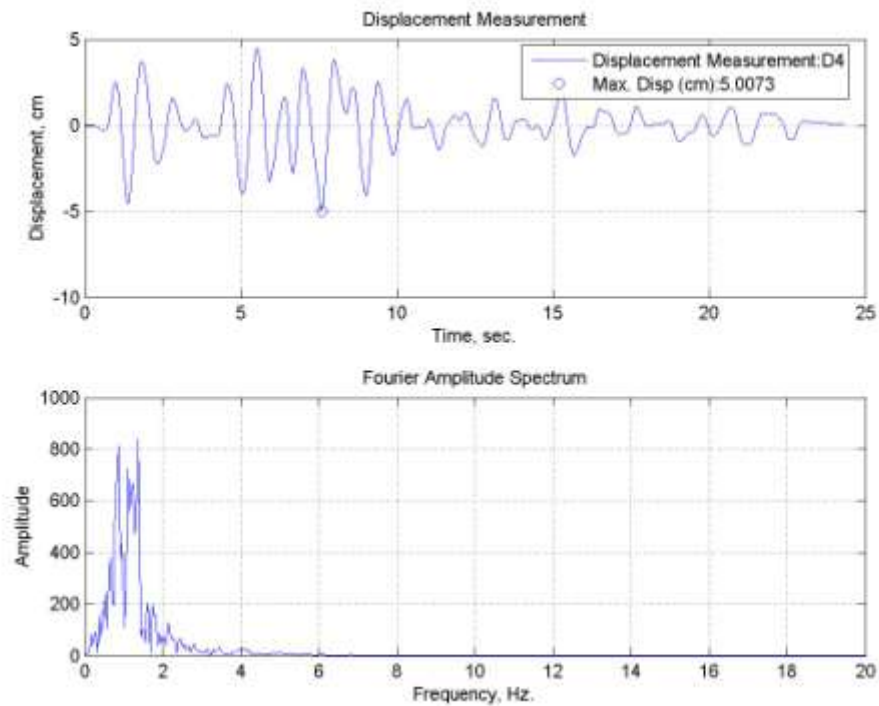


Figure B.14. Lateral displacement time history for TB15 specimen tested at 0°C.

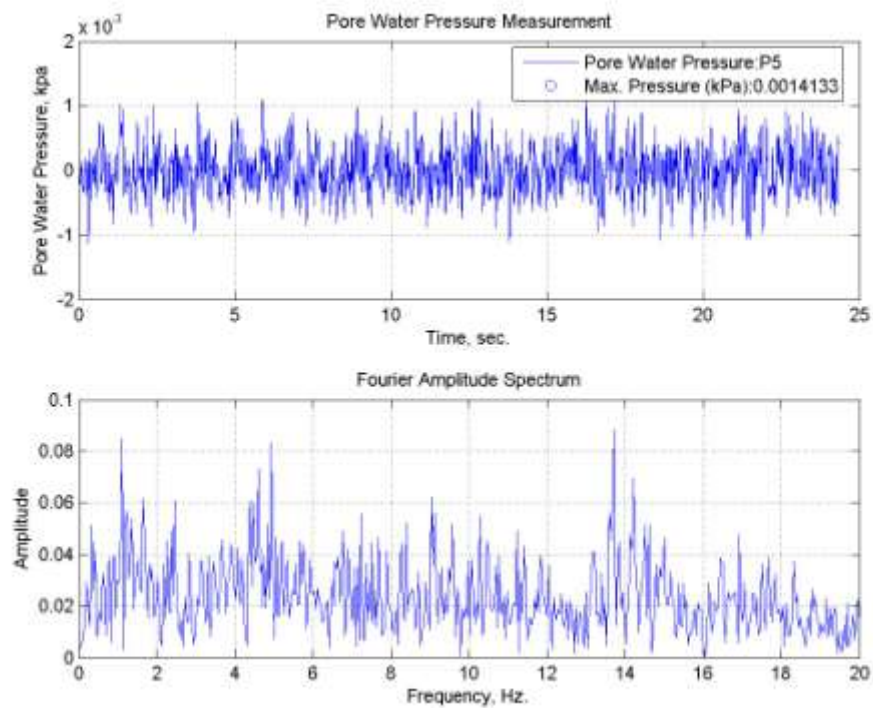


Figure B.15. Pore water pressure change of TB15 specimen tested at 0°C.

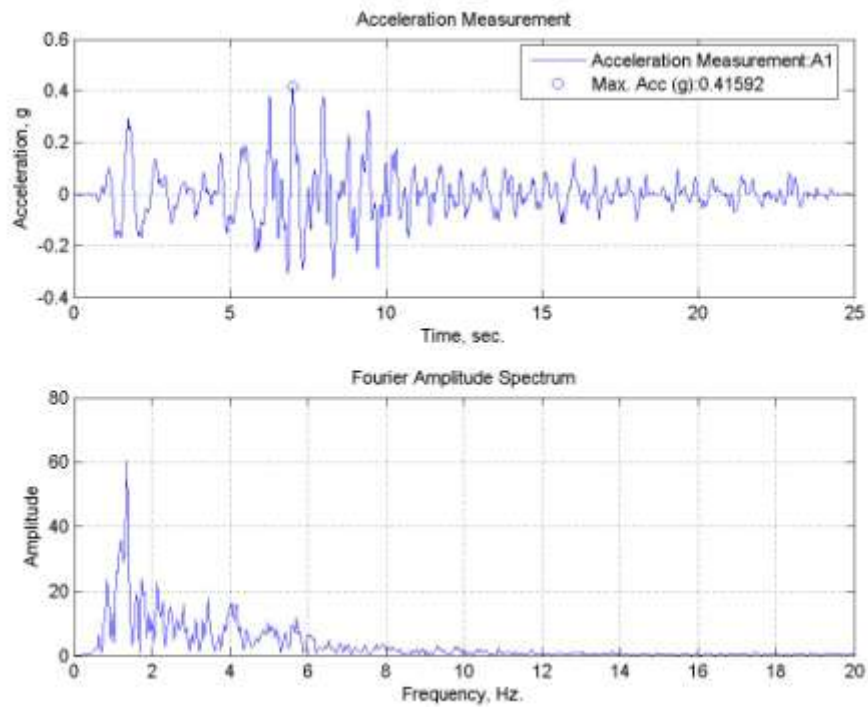
B.4. TB20 Specimen subjected to Tabas (E-W) Earthquake Motion at 0°C

Figure B.16. A1, acceleration time history of TB20 specimen tested at 0°C.

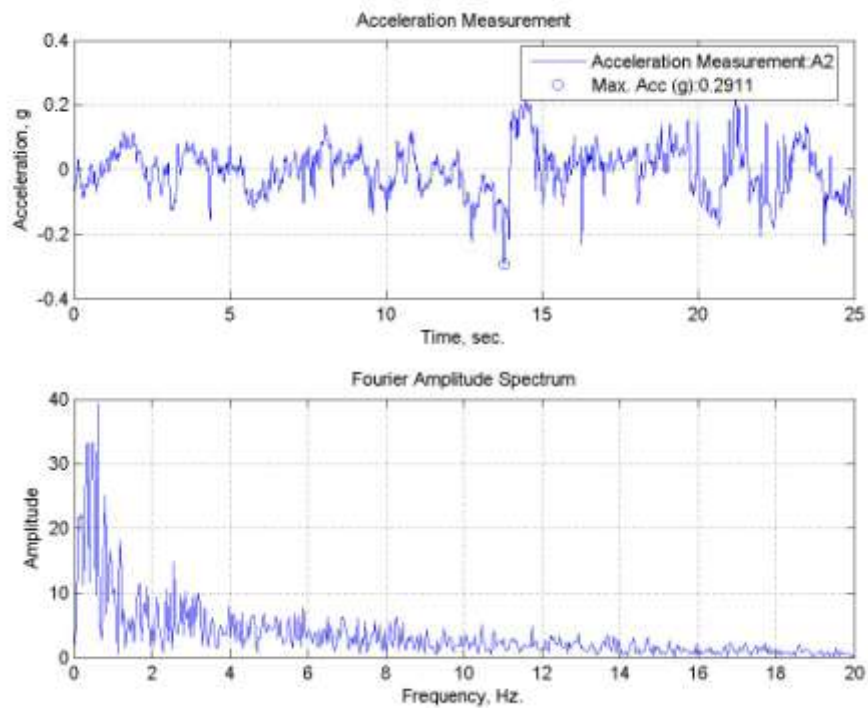


Figure B.17. A2, acceleration time history of TB20 specimen tested at 0°C.

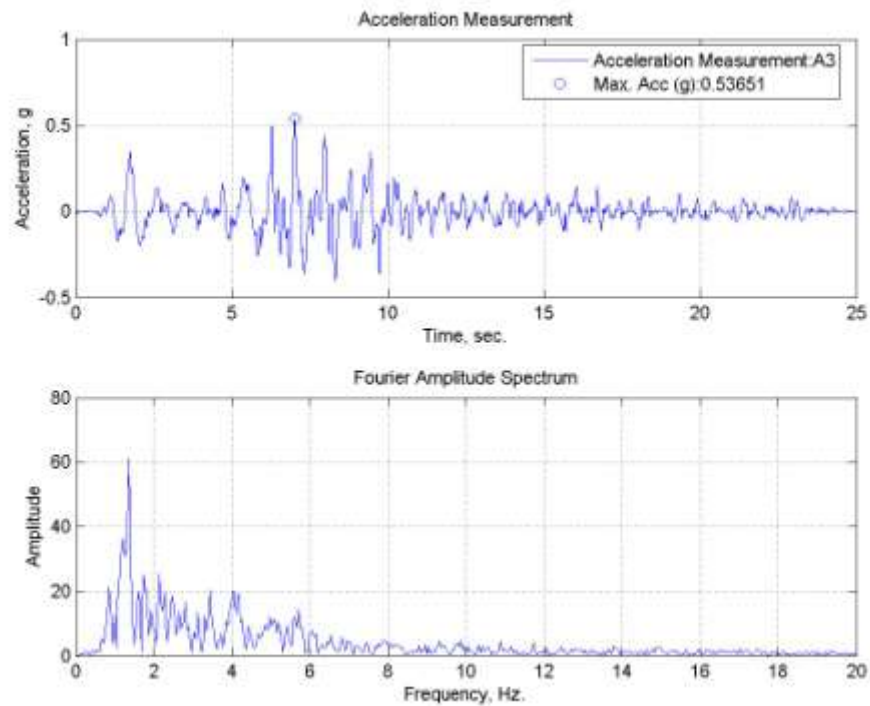


Figure B.18. A3, acceleration time history of TB20 specimen tested at 0°C.

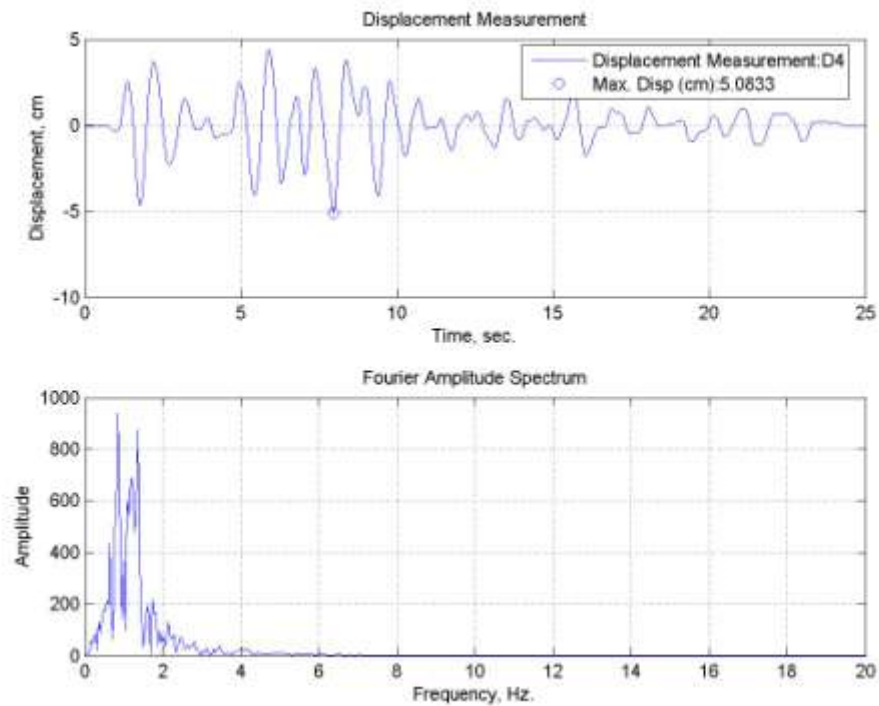


Figure B.19. Lateral displacement time history for TB20 specimen tested at 0°C.

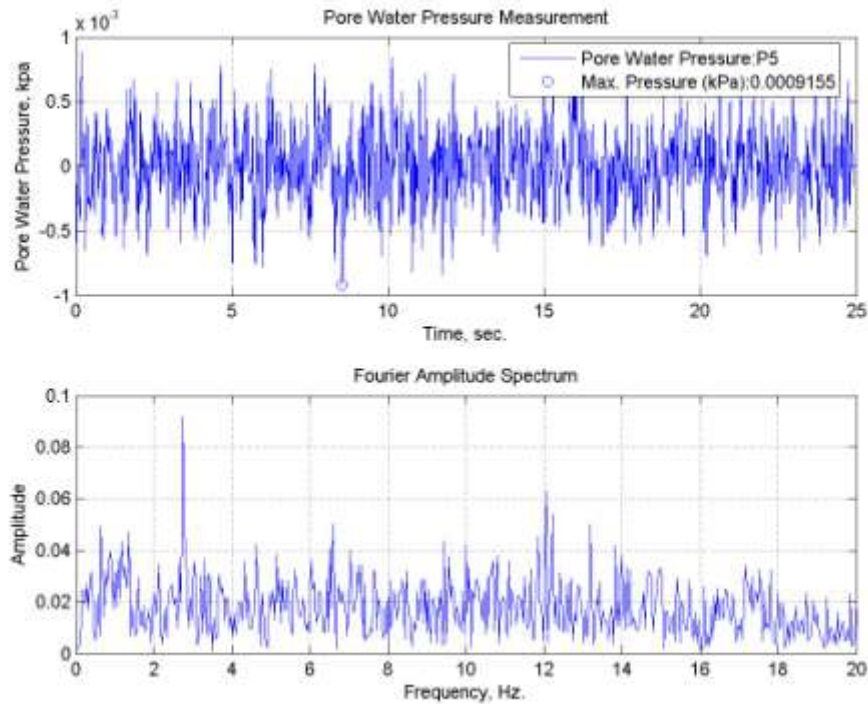


Figure B.20. Pore water pressure change of TB20 specimen tested at 0°C.

B.5. TB30 Specimen subjected to Tabas (E-W) Earthquake Motion at 0°C

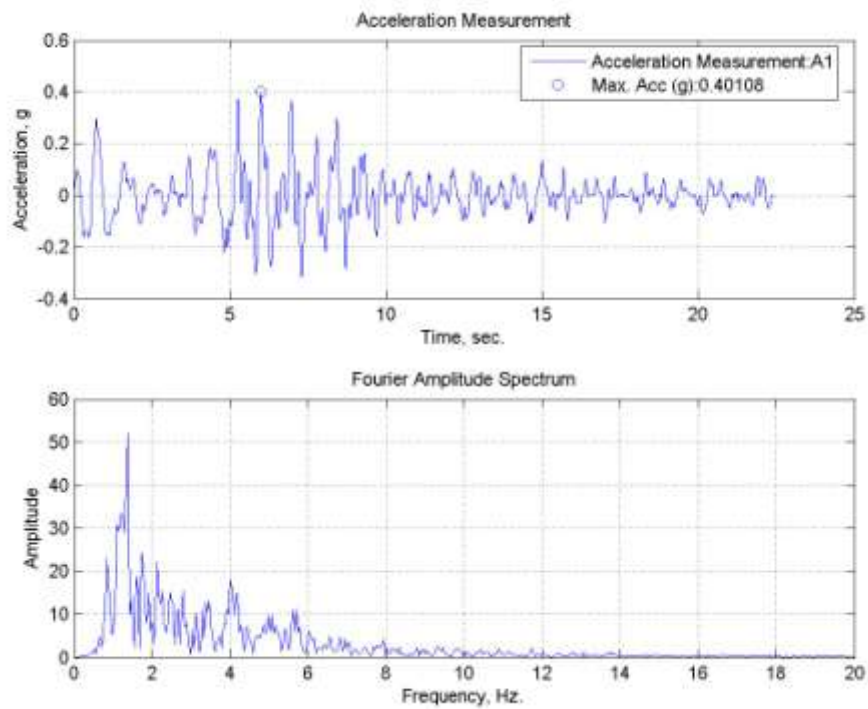


Figure B.21. A1, acceleration time history of TB30 specimen tested at 0°C.

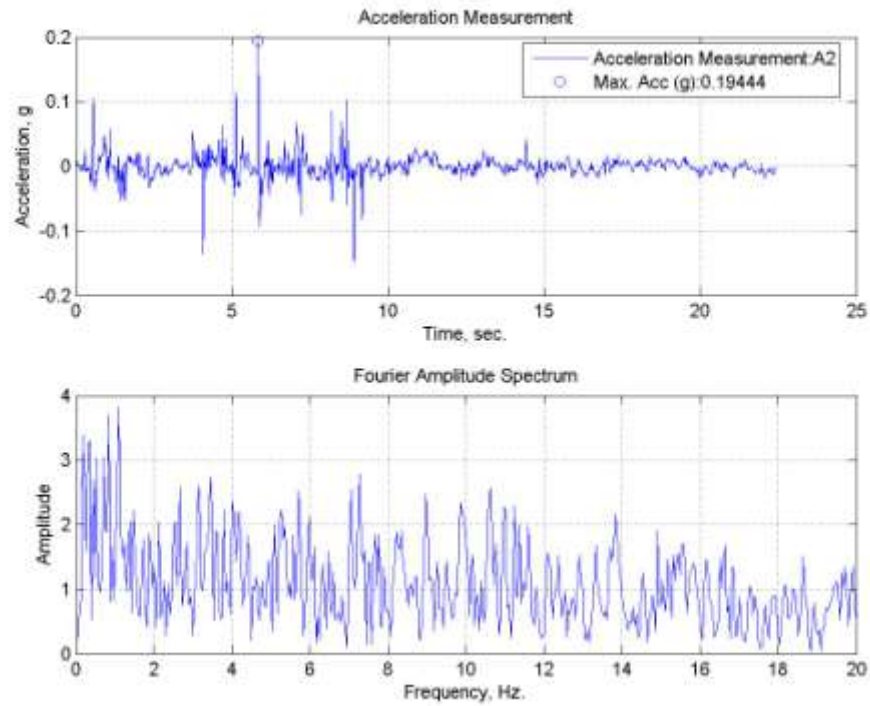


Figure B.22. A2, acceleration time history of TB30 specimen tested at 0°C.

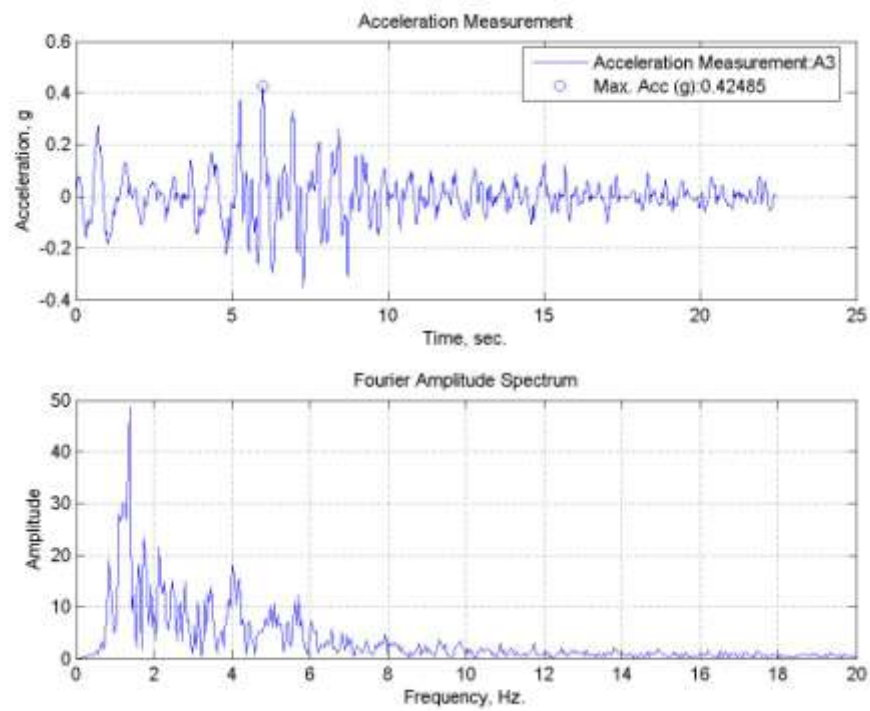


Figure B.23. A3, acceleration time history of TB30 specimen tested at 0°C.

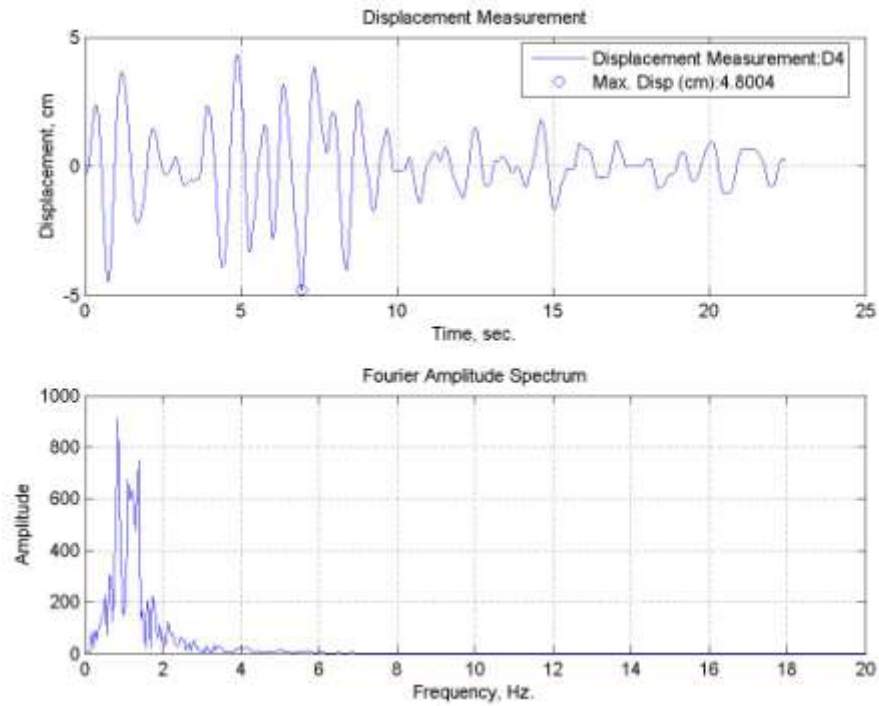


Figure B.24. Lateral displacement time history for TB30 specimen tested at 0°C.

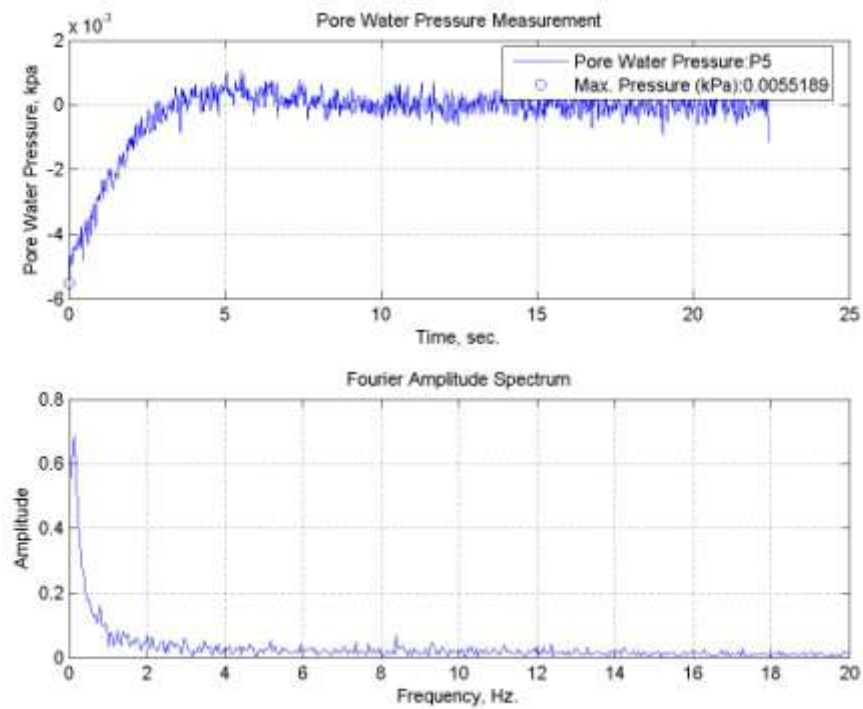


Figure B.25. Pore water pressure change of TB30 specimen tested at 0°C.

B.6. TC10 Specimen subjected to Tabas (E-W) Earthquake Motion at 0°C

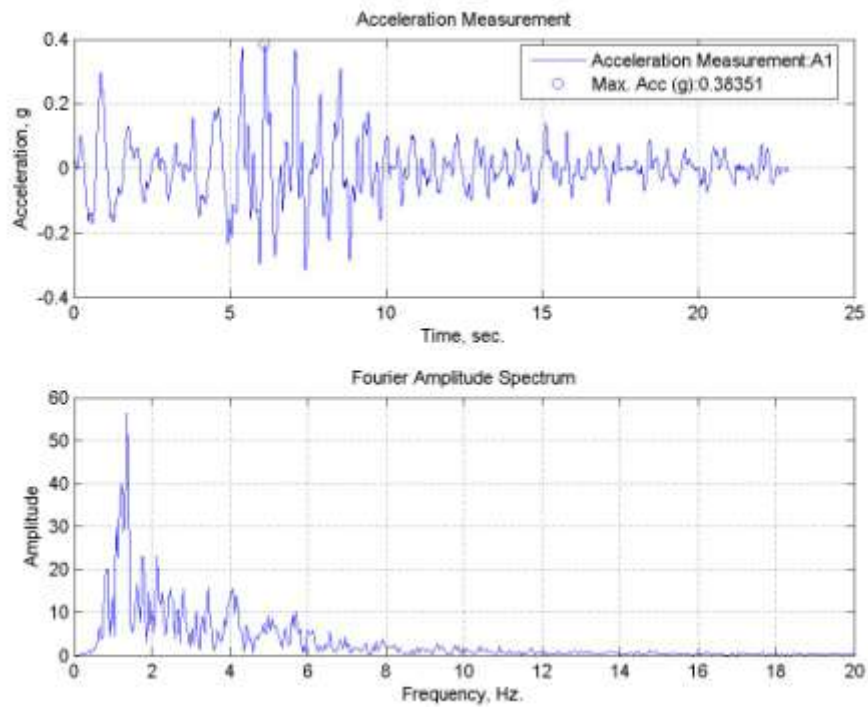


Figure B.26. A1, acceleration time history of TC10 specimen tested at 0°C.

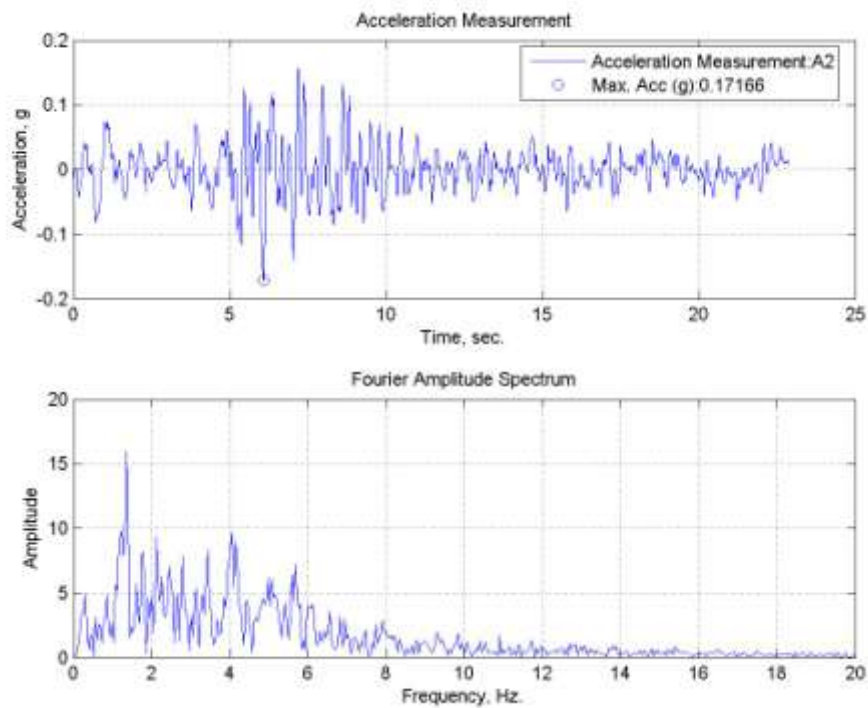


Figure B.27. A2, acceleration time history of TC10 specimen tested at 0°C.

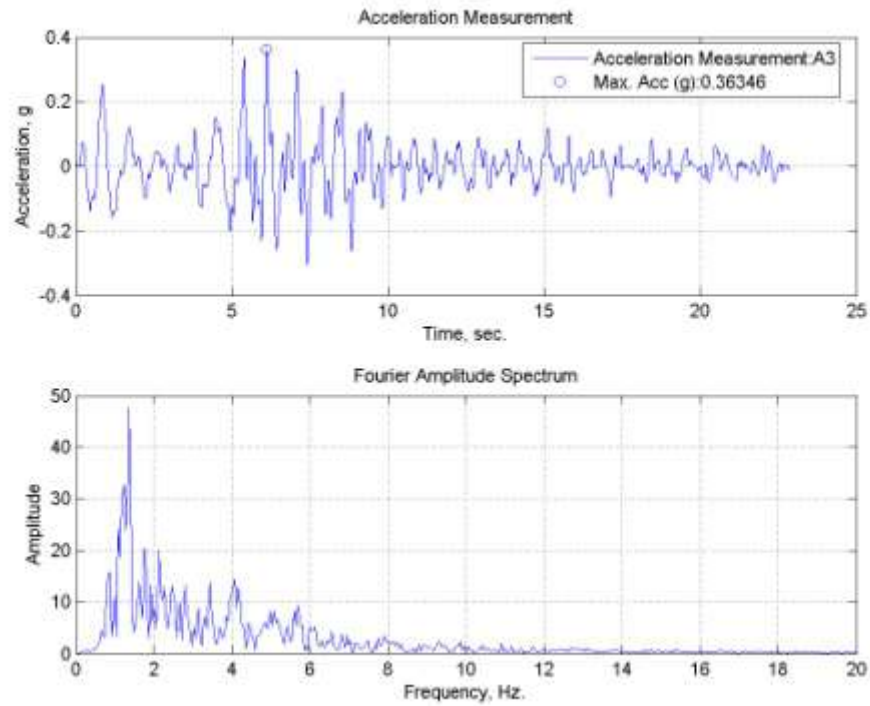


Figure B.28. A3, acceleration time history of TC10 specimen tested at 0°C.

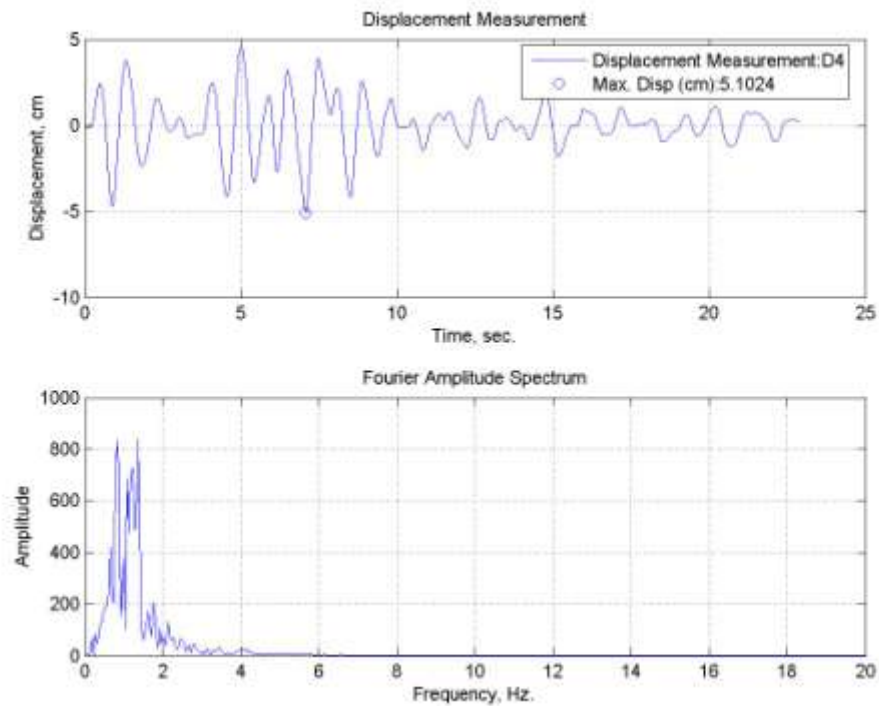


Figure B.29. Lateral displacement time history for TC10 specimen tested at 0°C.

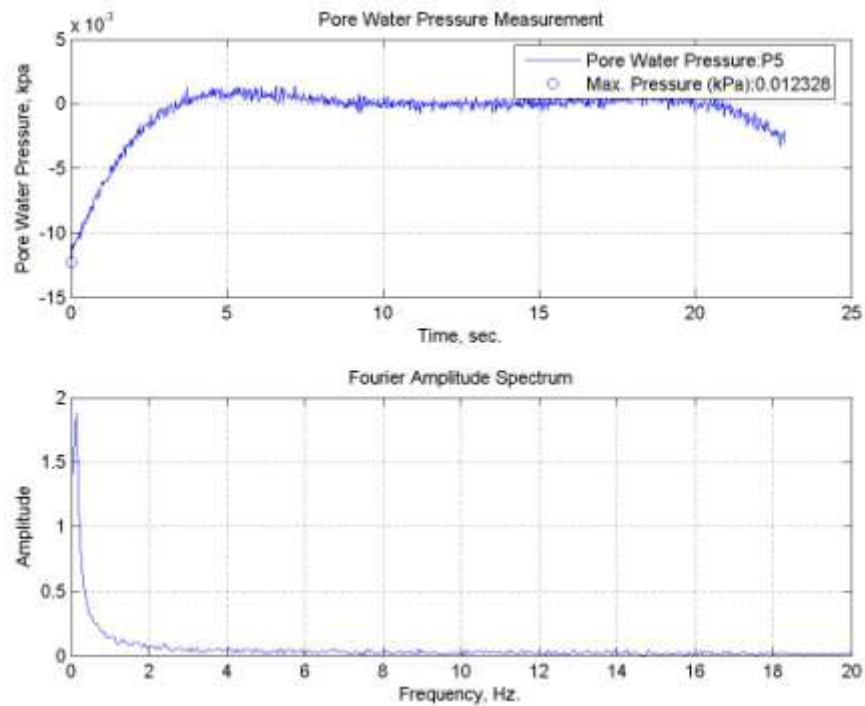


Figure B.30. Pore water pressure change of TC10 specimen tested at 0°C.

B.7. TC15 Specimen subjected to Tabas (E-W) Earthquake Motion at 0°C

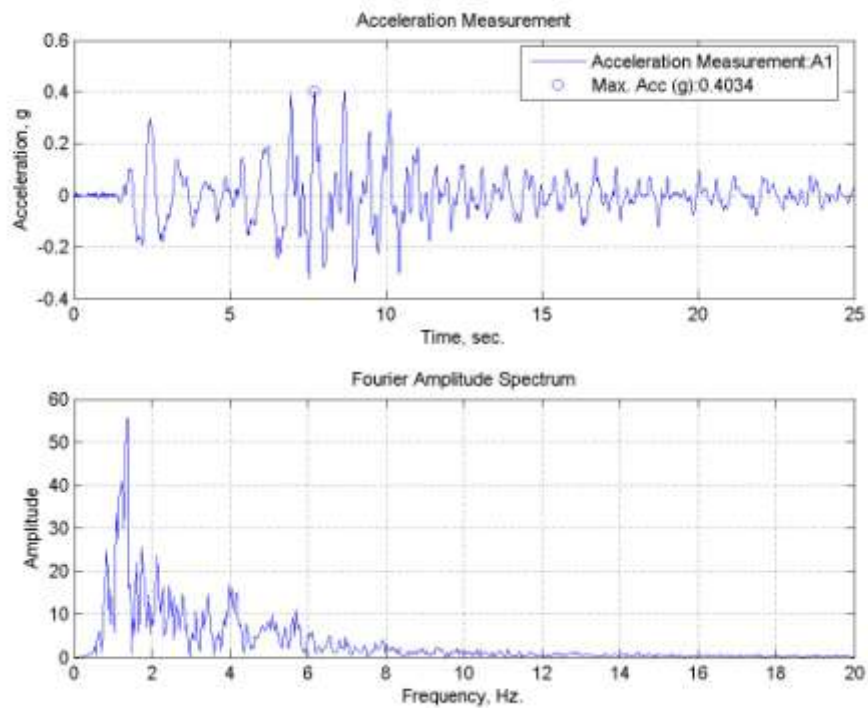


Figure B.31. A1, acceleration time history of TC15 specimen tested at 0°C.

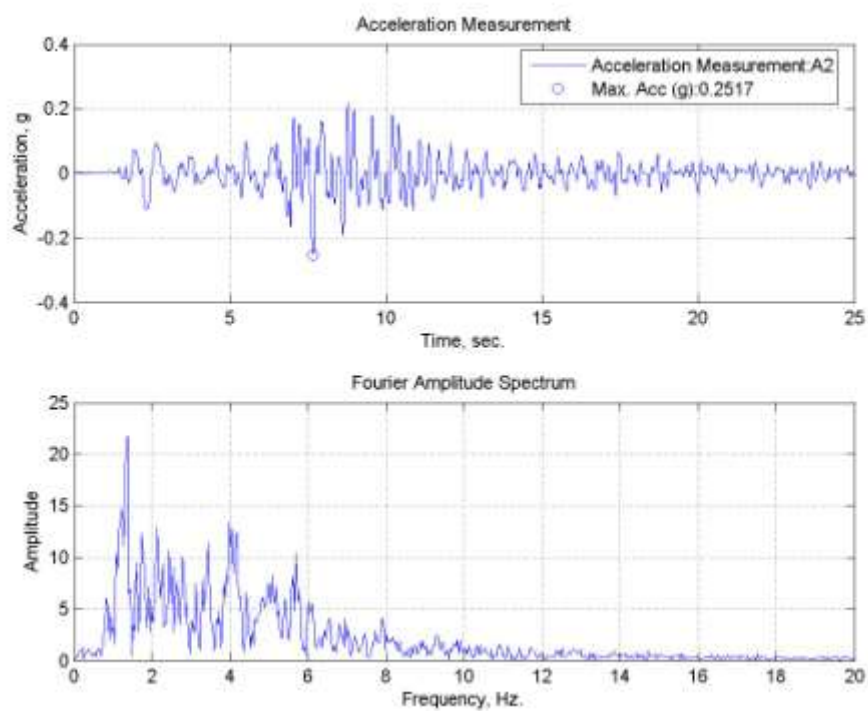


Figure B.32. A2, acceleration time history of TC15 specimen tested at 0°C.

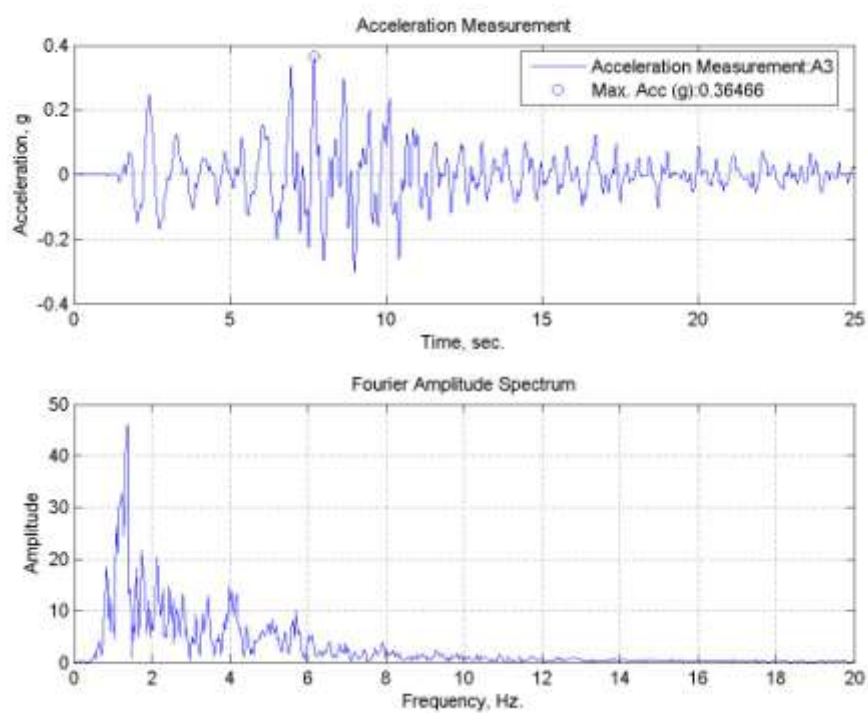


Figure B.33. A3, acceleration time history of TC15 specimen tested at 0°C.

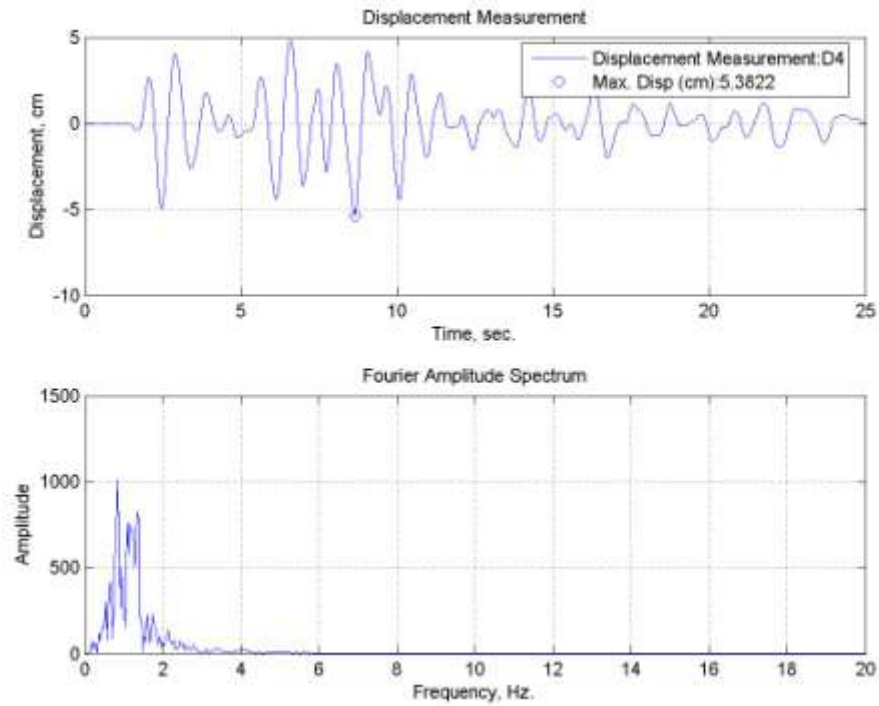


Figure B.34. Lateral displacement time history for TC15 specimen tested at 0°C.

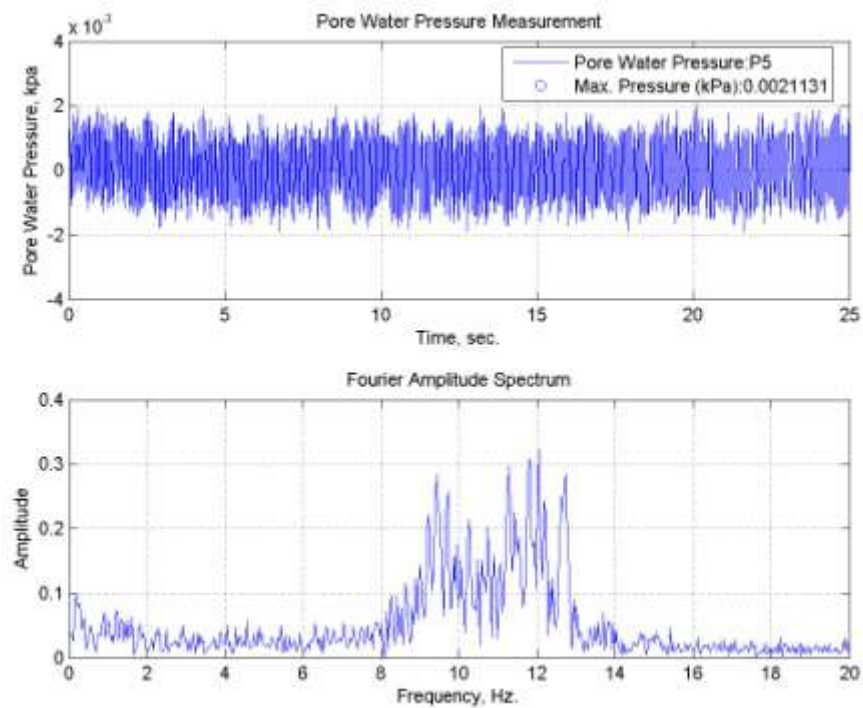


Figure B.35. Pore water pressure change of TC15 specimen tested at 0°C.

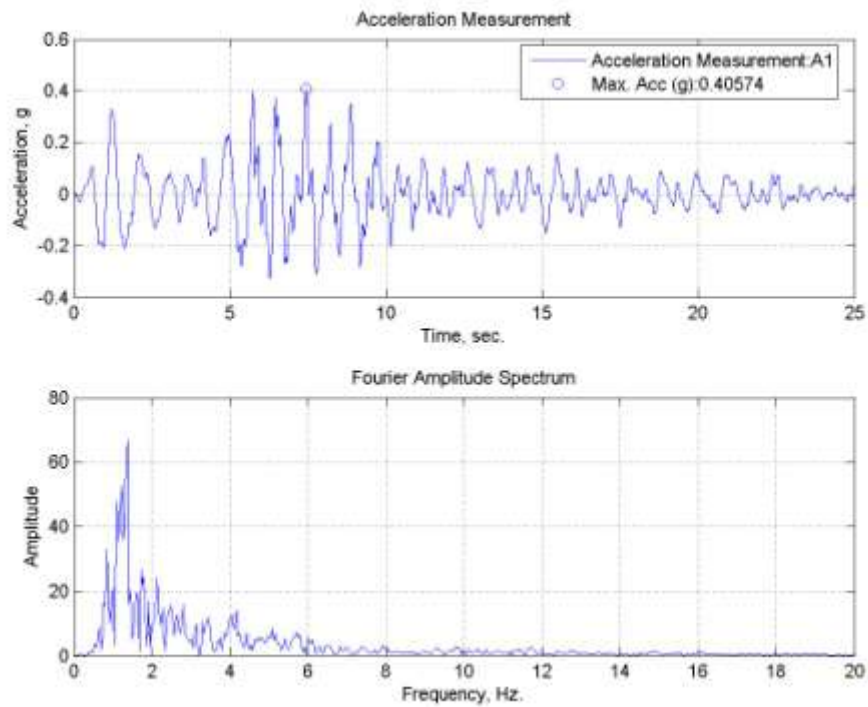
B.8. TC20 Specimen subjected to Tabas (E-W) Earthquake Motion at 0°C

Figure B.36. A1, acceleration time history of TC20 specimen tested at 0°C.

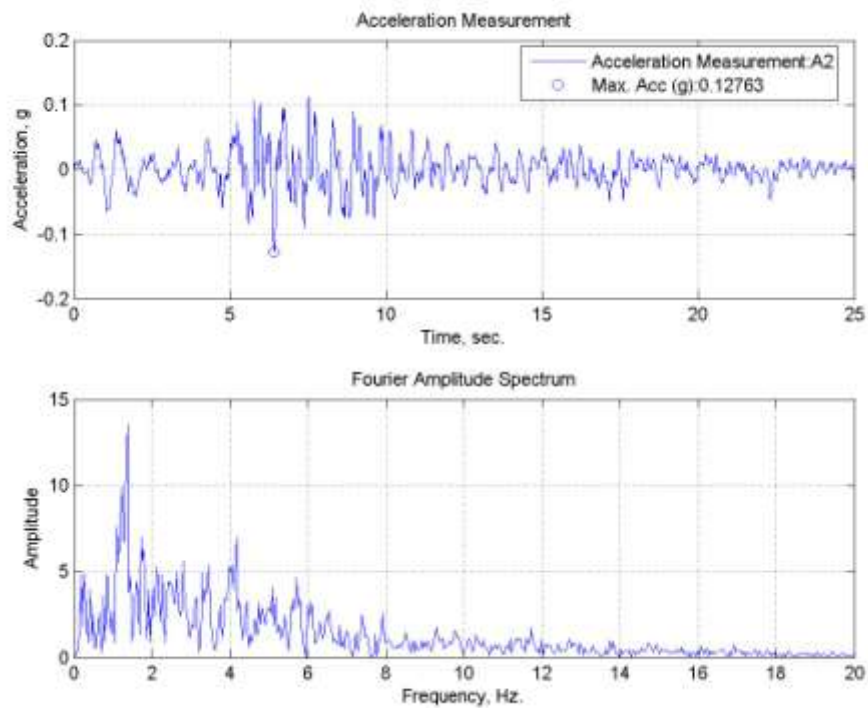


Figure B.37. A2, acceleration time history of TC20 specimen tested at 0°C.

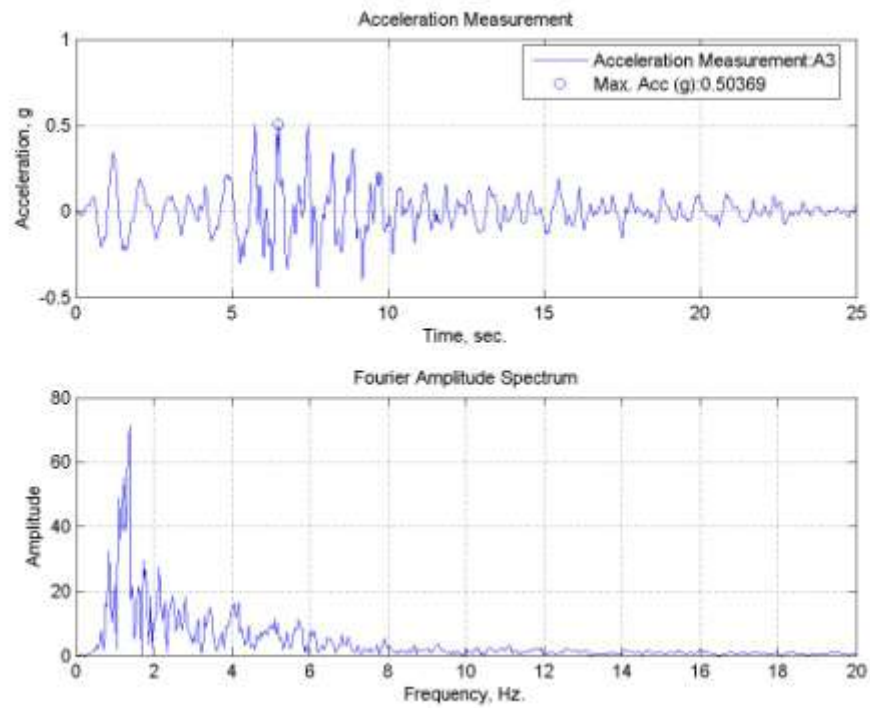


Figure B.38. A3, acceleration time history of TC20 specimen tested at 0°C.

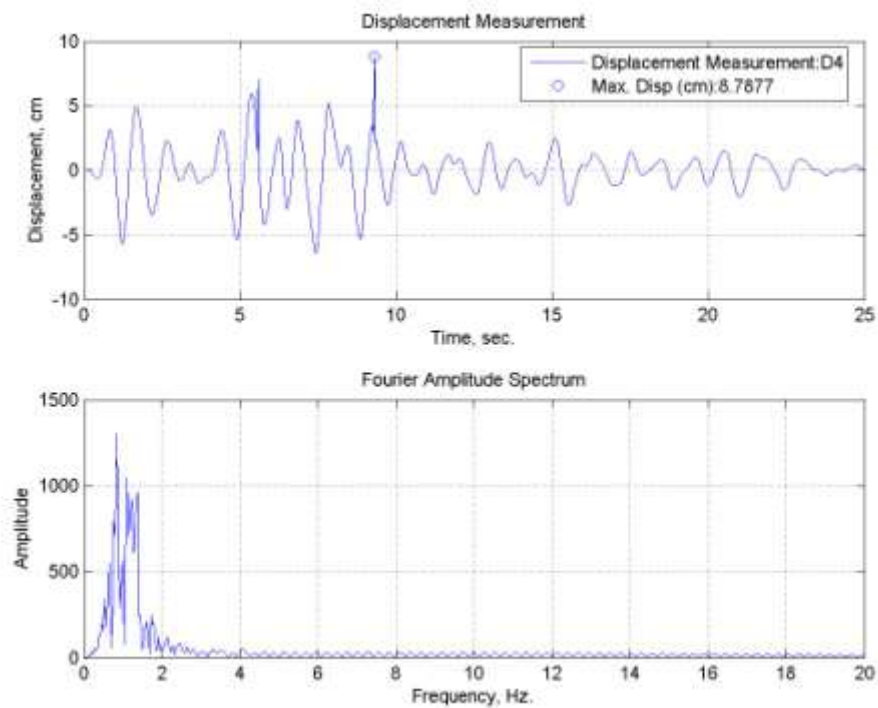


Figure B.39. Lateral displacement time history for TC20 specimen tested at 0°C.

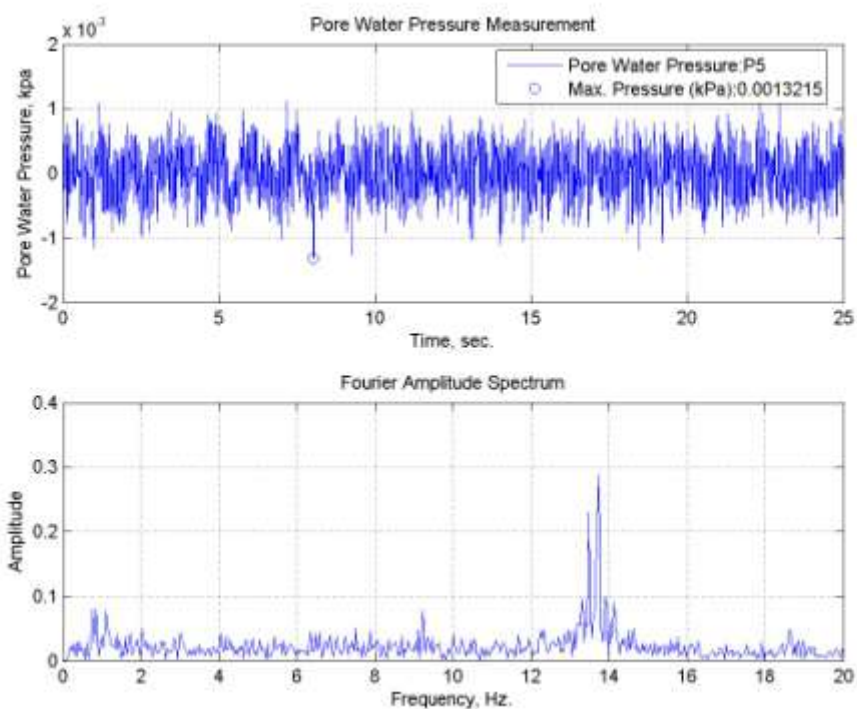


Figure B.40. Pore water pressure change of TC20 specimen tested at 0°C.

B.9. TC30 Specimen subjected to Tabas (E-W) Earthquake Motion at 0°C

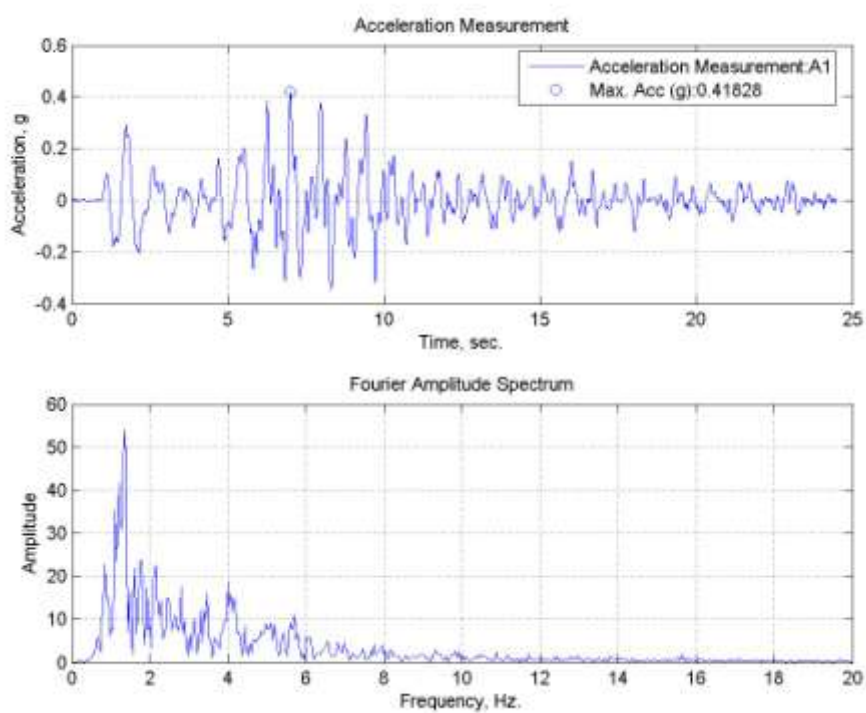


Figure B.41. A1, acceleration time history of TC30 specimen tested at 0°C.

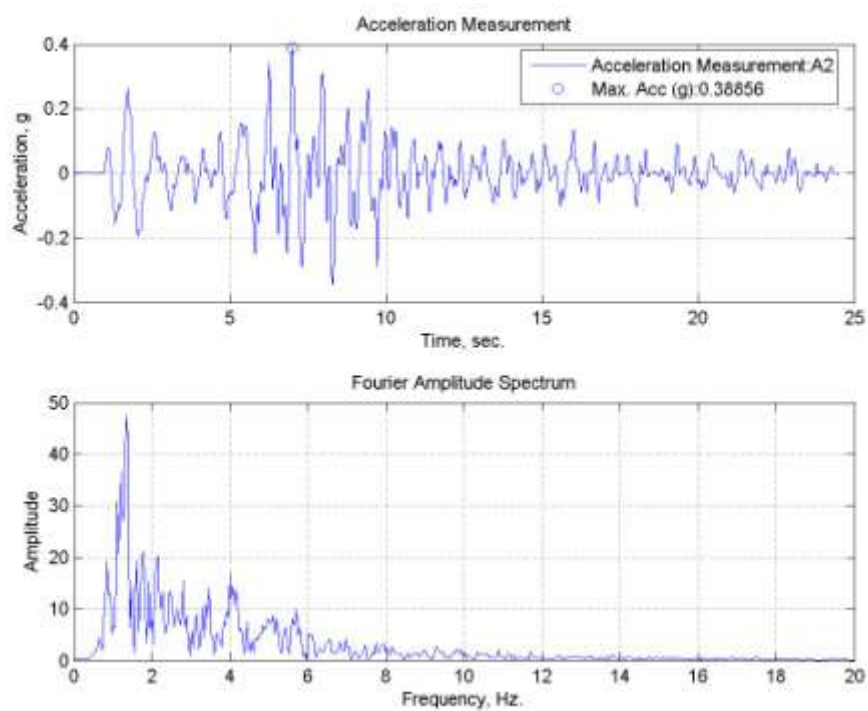


Figure B.42. A2, acceleration time history of TC30 specimen tested at 0°C.

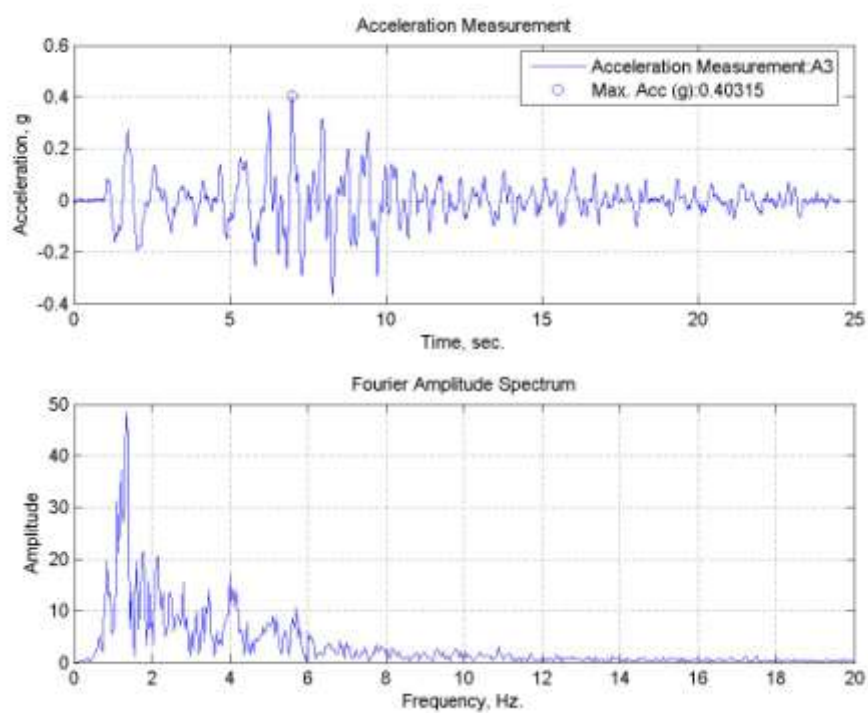


Figure B.43. A3, acceleration time history of TC30 specimen tested at 0°C.

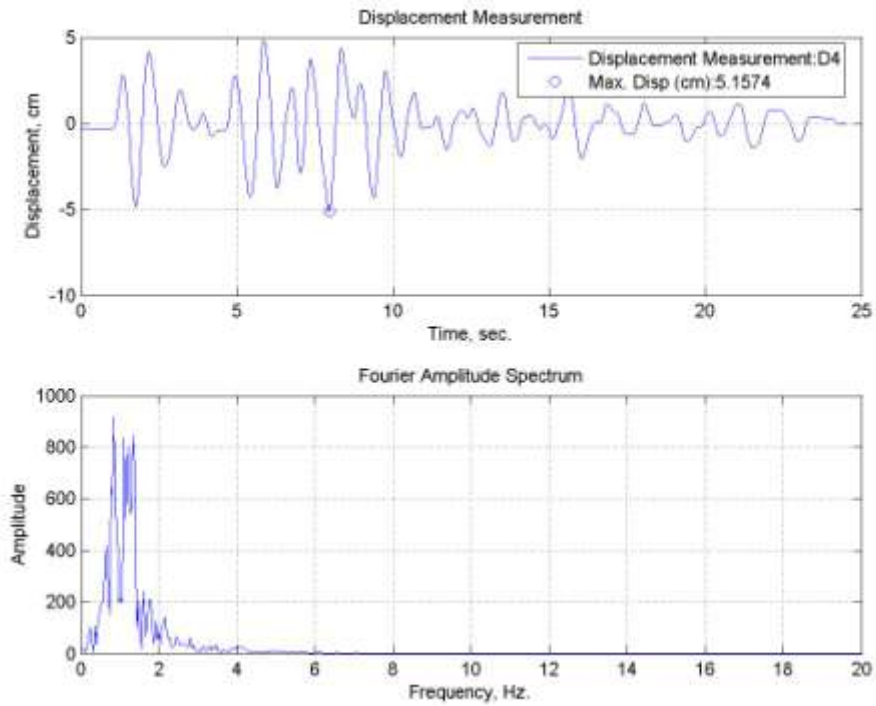


Figure B.44. Lateral displacement time history for TC30 specimen tested at 0°C.

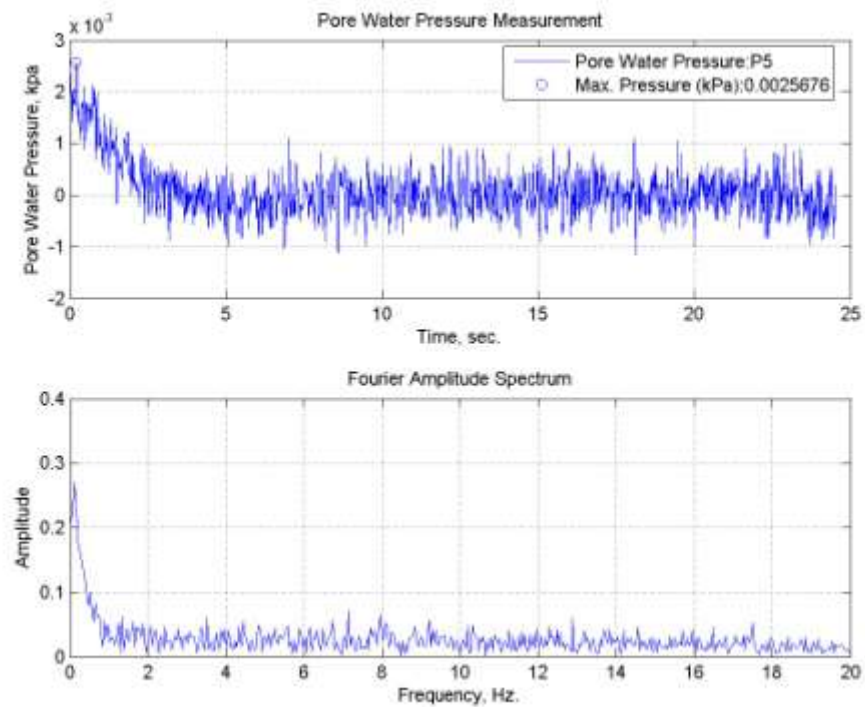


Figure B.45. Pore water pressure change of TC30 specimen tested at 0°C.

B.10. Sand Specimen subjected to Tabas (E-W) Earthquake Motion at Room Temperature

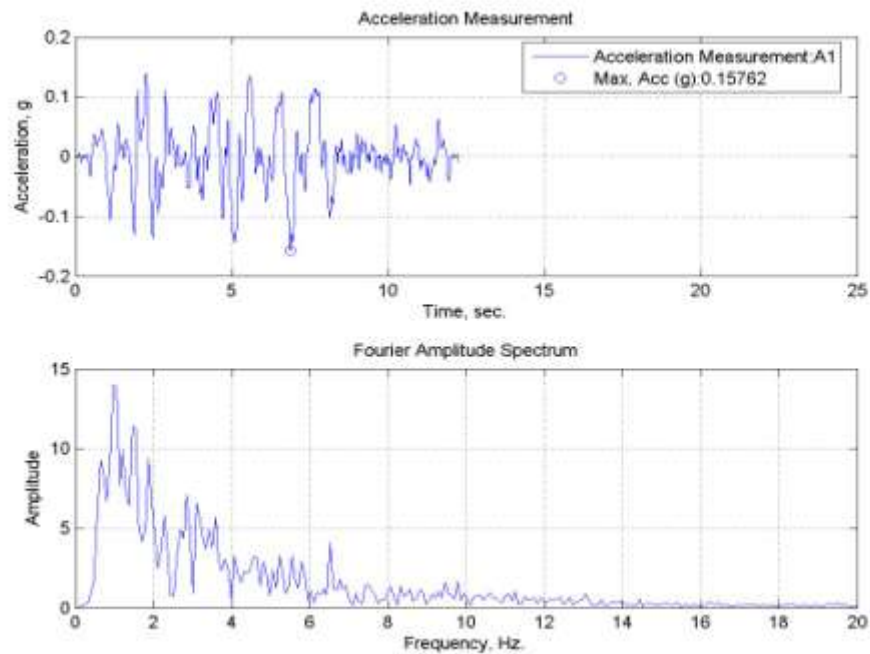


Figure B.46. A1, acceleration time history of sand specimen tested at room temperature.

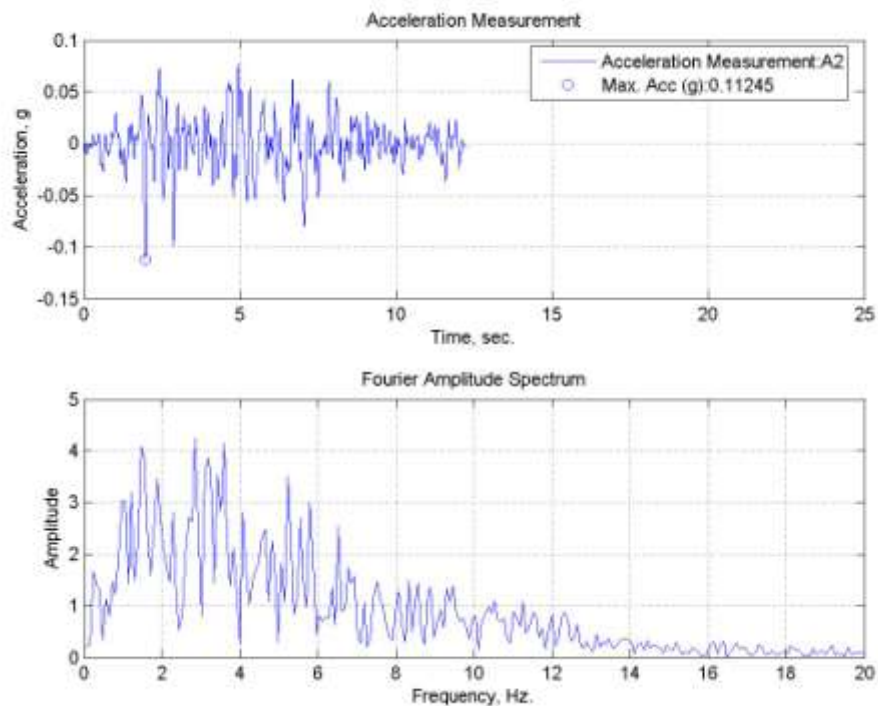


Figure B.47. A2, acceleration time history of sand specimen tested at room temperature.

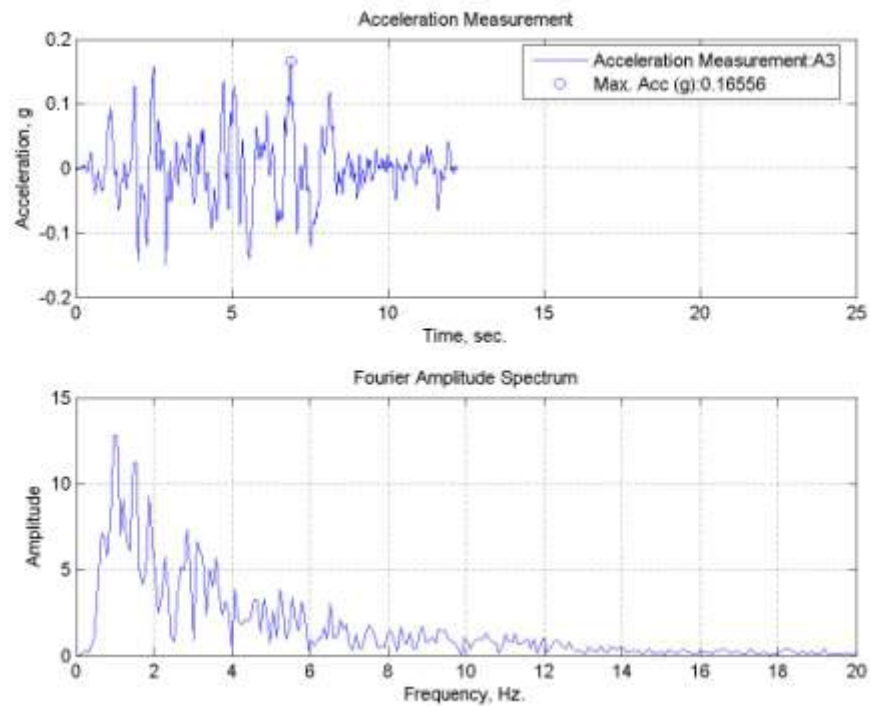


Figure B.48. A3, acceleration time history of sand specimen tested at room temperature.

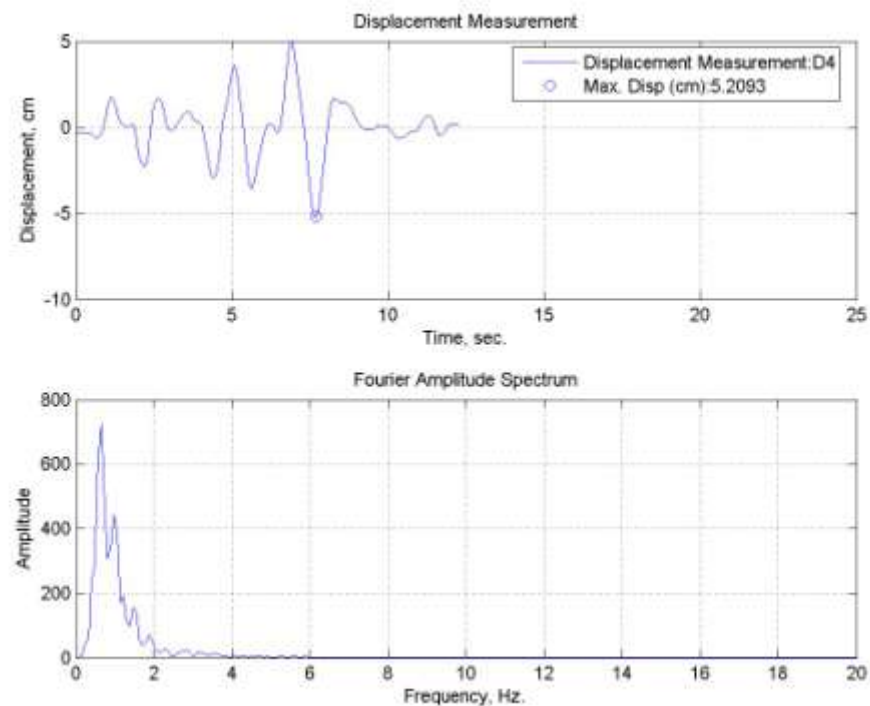


Figure B.49. Lateral displacement time history for sand specimen tested at room temperature.

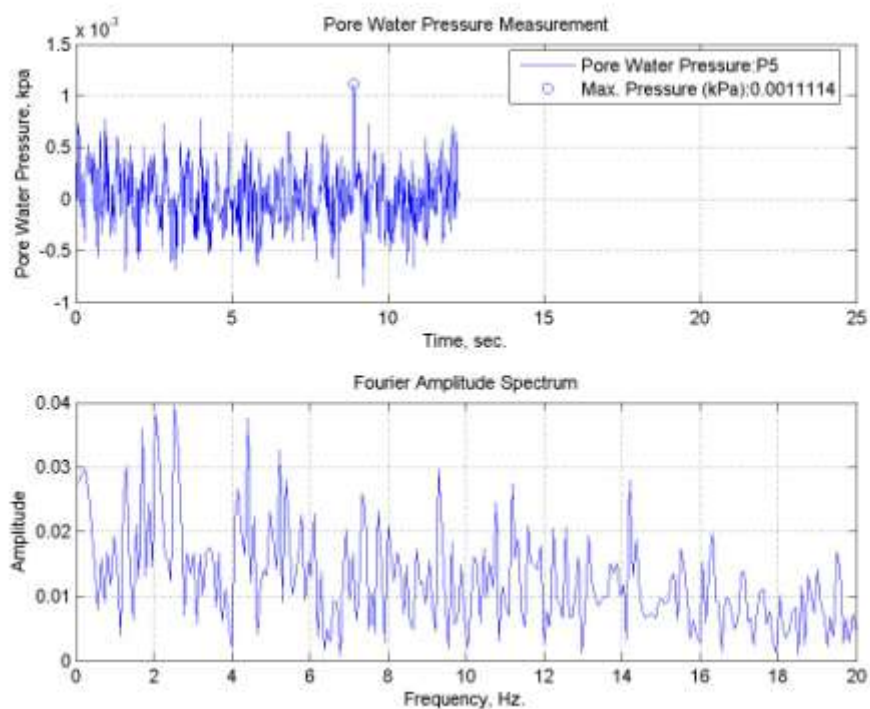


Figure B.50. Pore water pressure change of sand specimen tested at room temperature.

B.11. TB10 Specimen subjected to Tabas (E-W) Earthquake Motion at Room Temperature

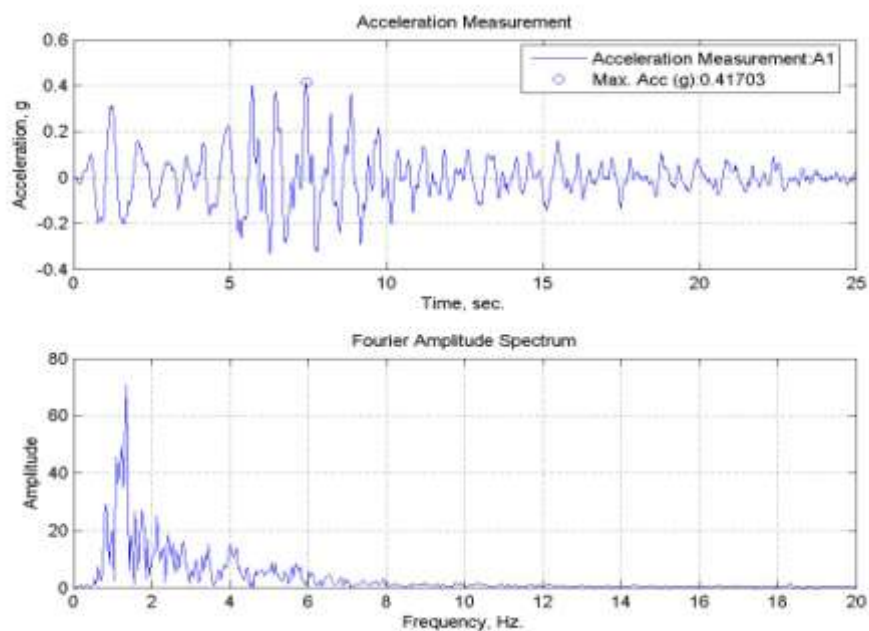


Figure B.51. A1, acceleration time history of TB10 specimen tested at room temperature.

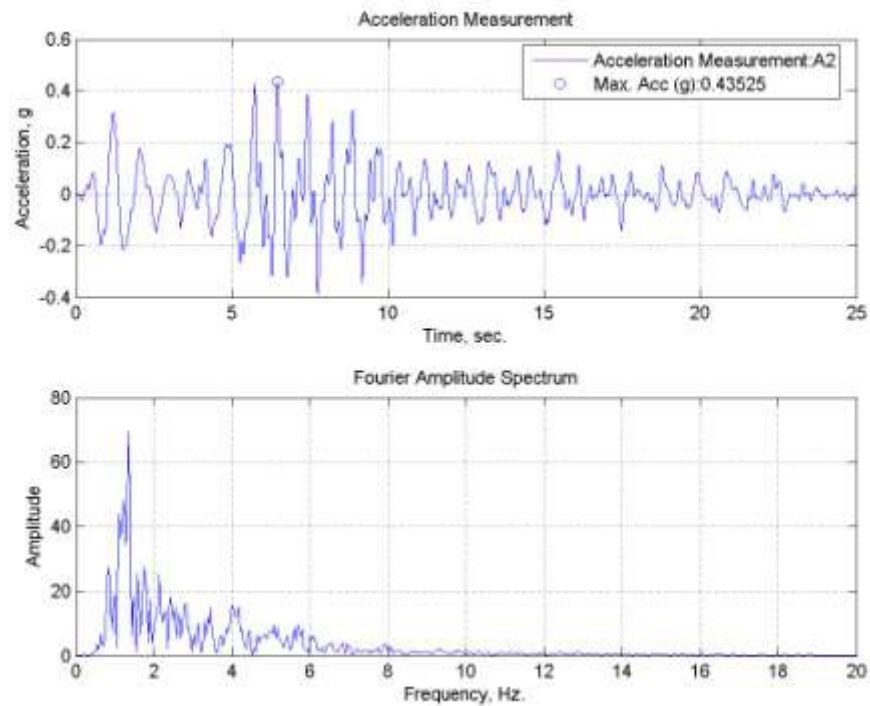


Figure B.52. A2, acceleration time history of TB10 specimen tested at room temperature.

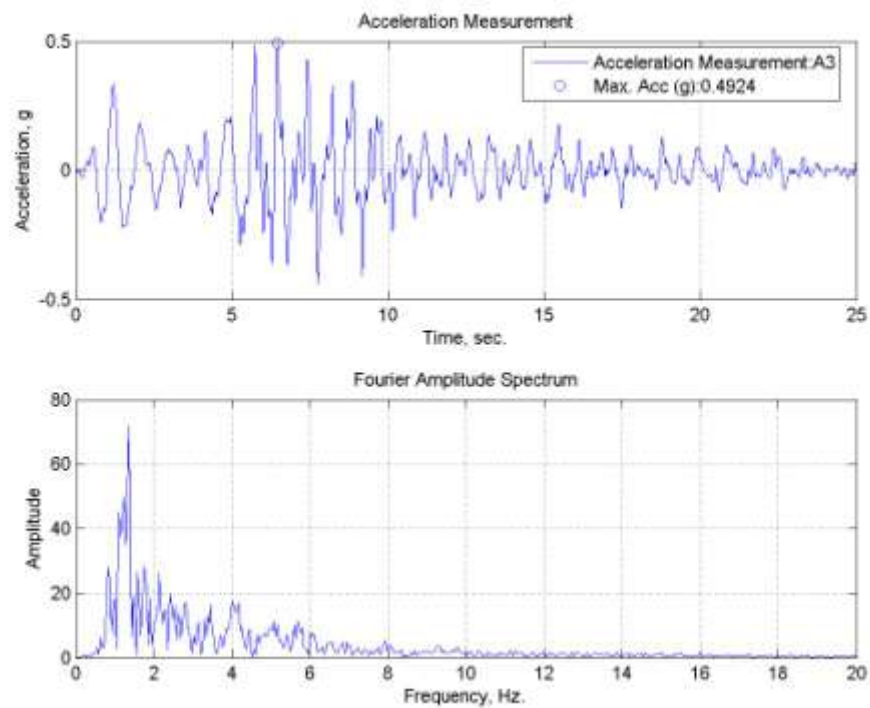


Figure B.53. A3, acceleration time history of TB10 specimen tested at room temperature.

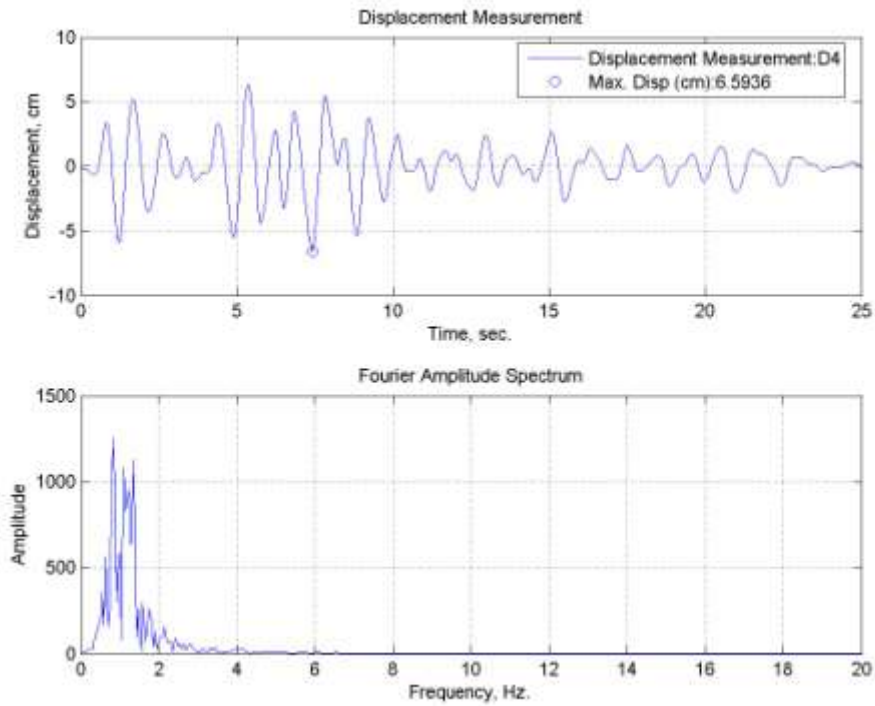


Figure B.54. Lateral displacement time history for TB10 specimen tested at room temperature.

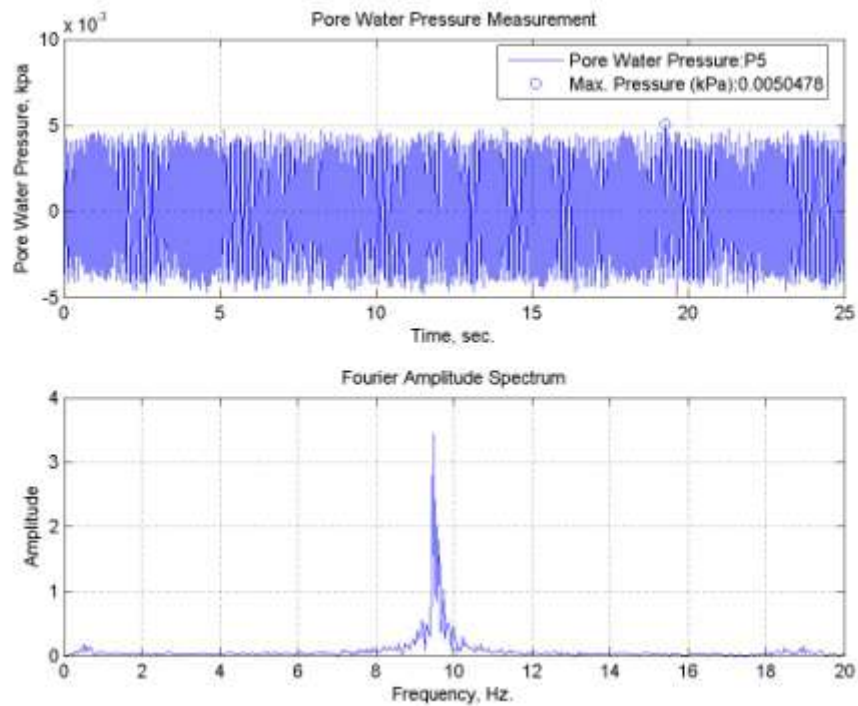


Figure B.55. Pore water pressure change of TB10 specimen tested at room temperature.

B.12. TB15 Specimen subjected to Tabas (E-W) Earthquake Motion at Room Temperature

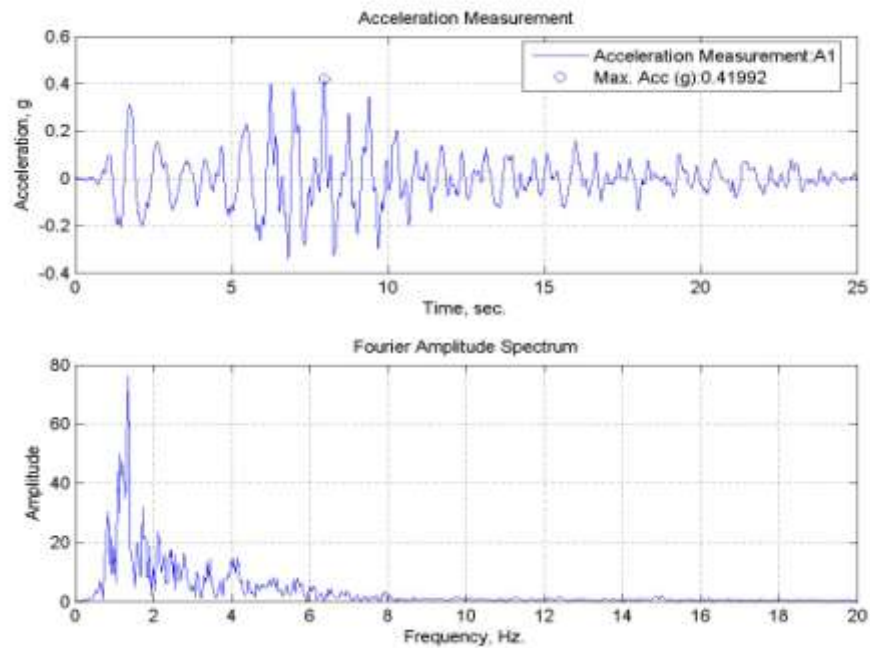


Figure B.56. A1, acceleration time history of TB15 specimen tested at room temperature.

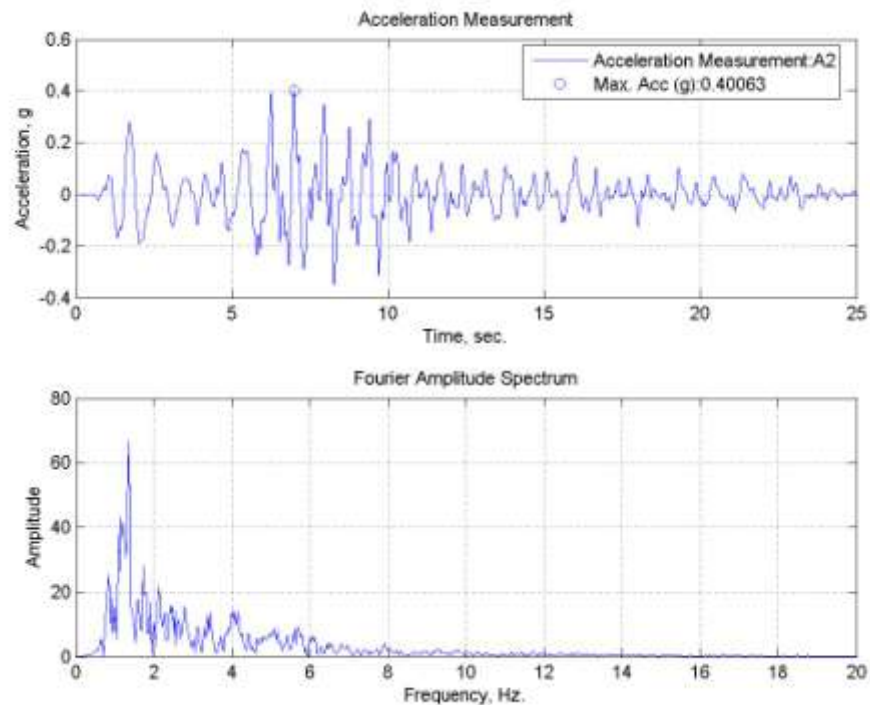


Figure B.57. A2, acceleration time history of TB15 specimen tested at room temperature.

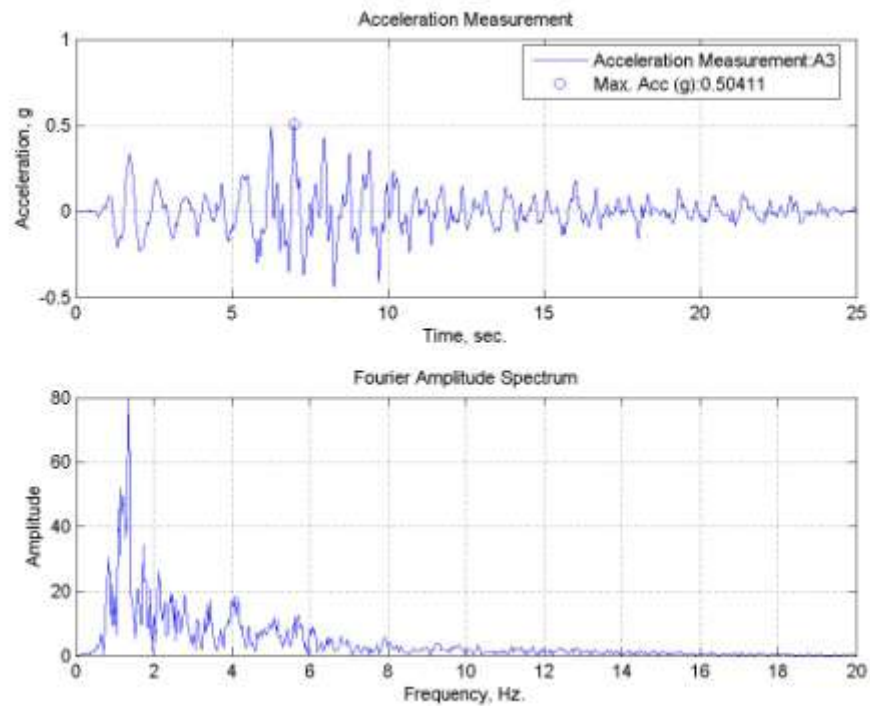


Figure B.58. A3, acceleration time history of TB15 specimen tested at room temperature.

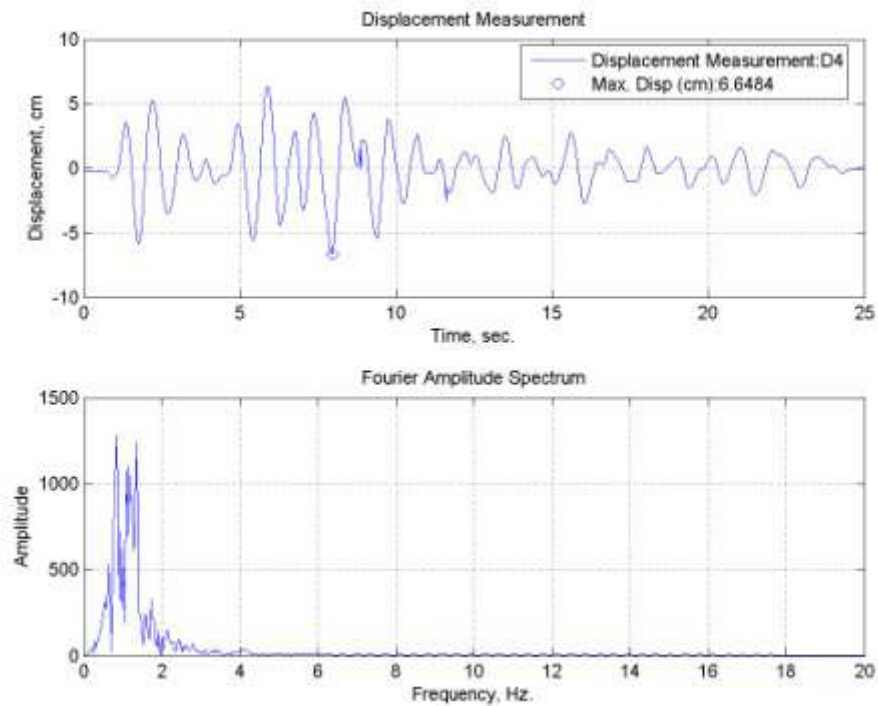


Figure B.59. Lateral displacement time history for TB15 specimen tested at room temperature.

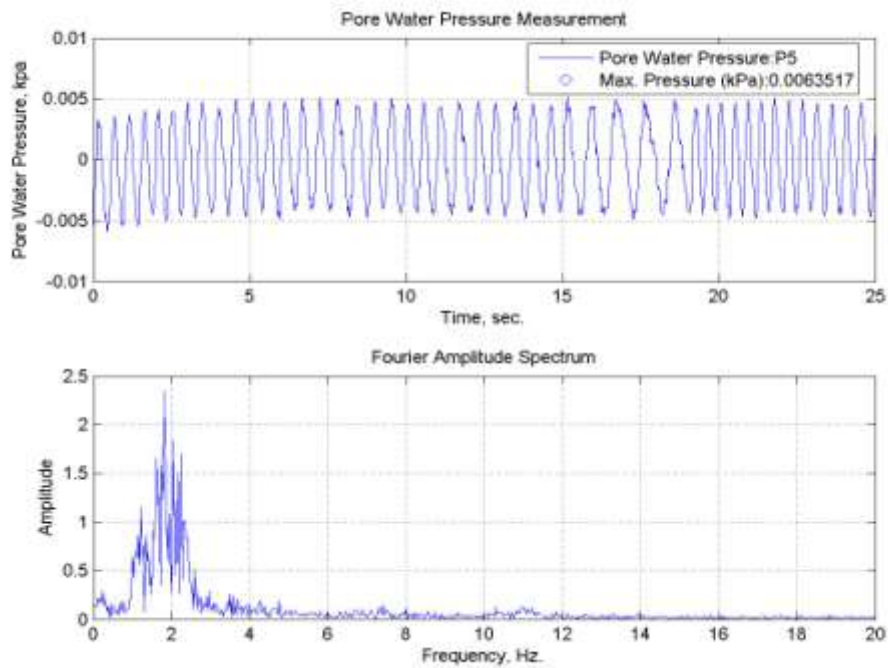


Figure B.60. Pore water pressure change of TB15 specimen tested at room temperature.

B.13. TB20 Specimen subjected to Tabas (E-W) Earthquake Motion at Room Temperature

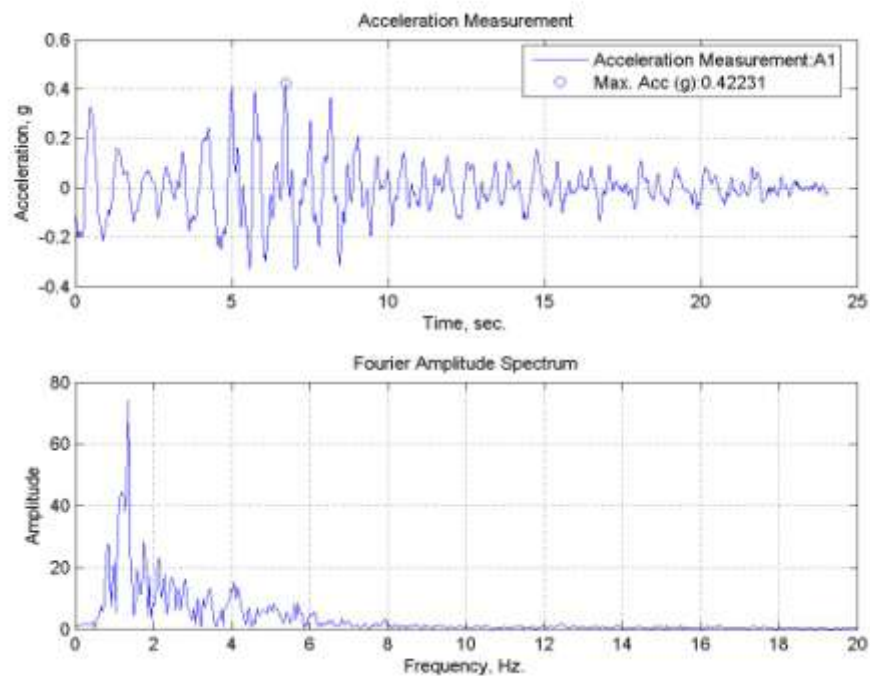


Figure B.61. A1, acceleration time history of TB20 specimen tested at room temperature.

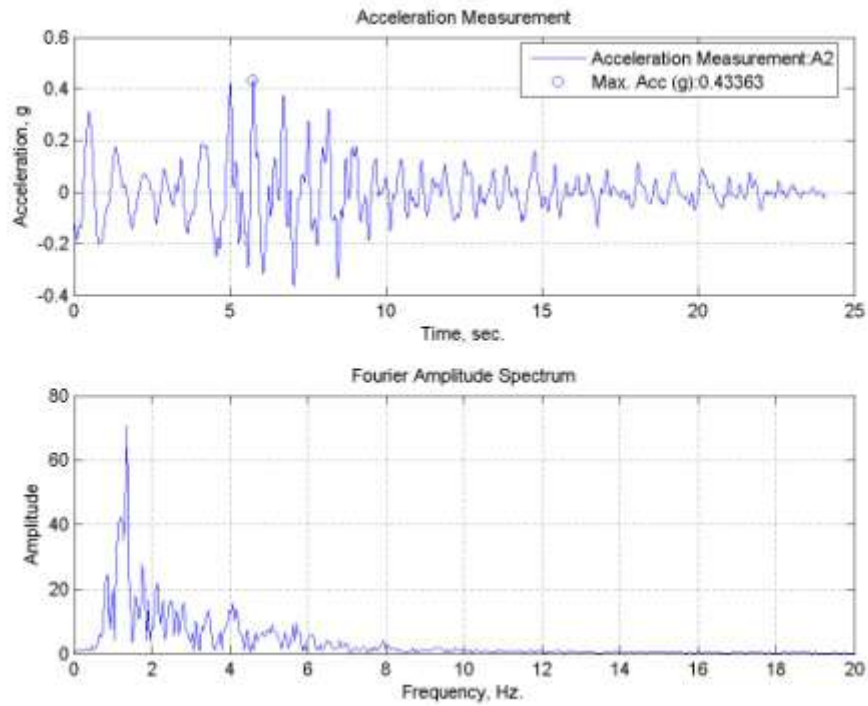


Figure B.62. A2, acceleration time history of TB20 specimen tested at room temperature.

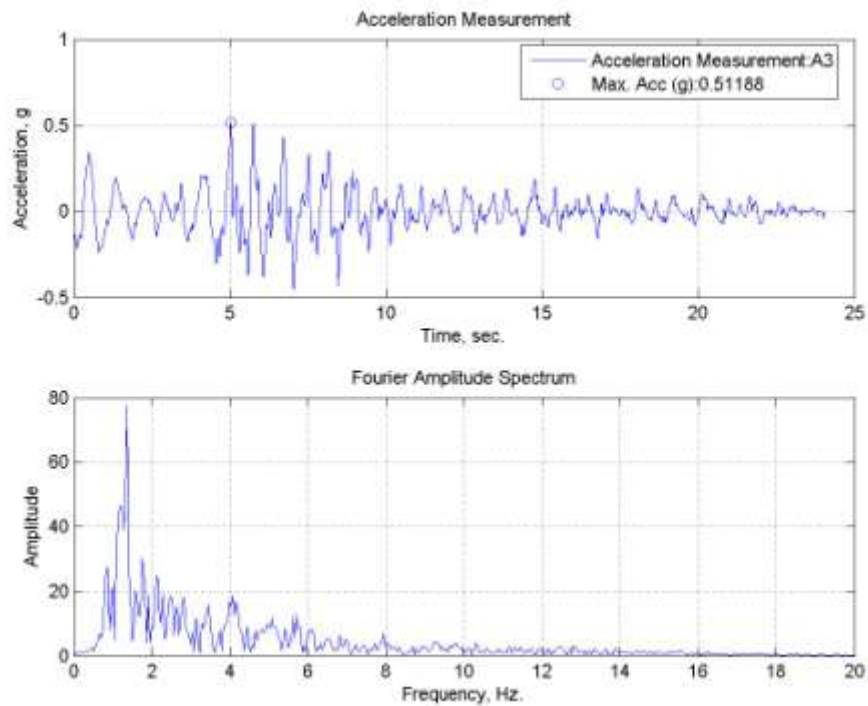


Figure B.63. A3, acceleration time history of TB20 specimen tested at room temperature.

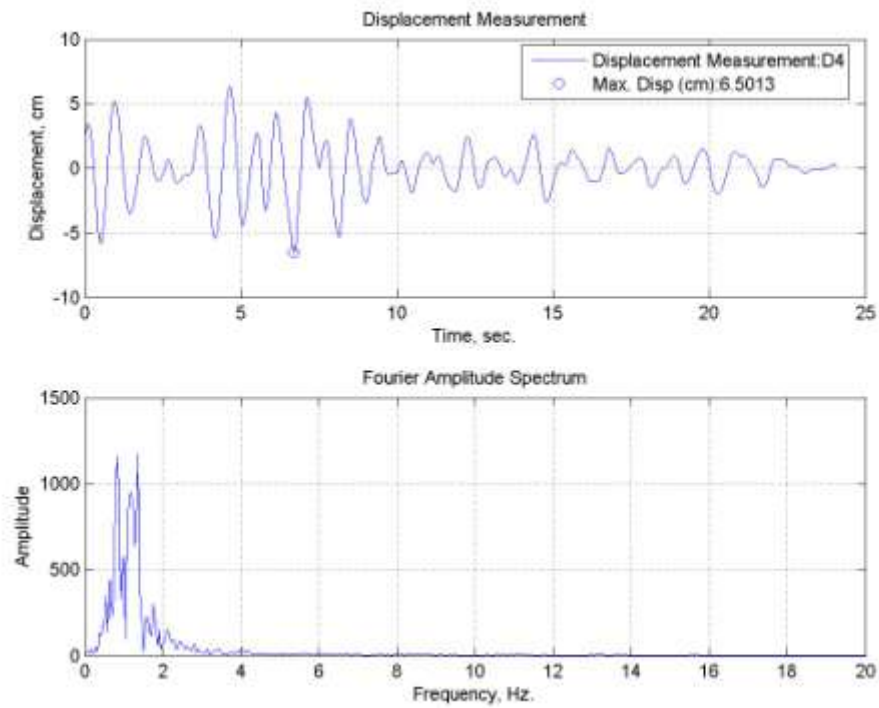


Figure B.64. Lateral displacement time history for TB20 specimen tested at room temperature.

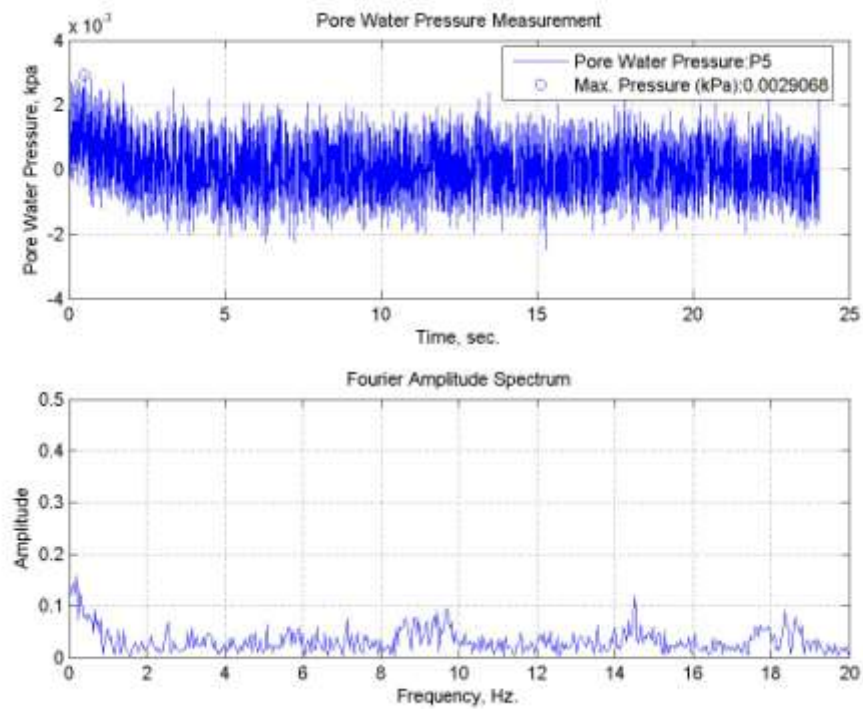


Figure B.65. Pore water pressure change of TB20 specimen tested at room temperature.

B.14. TB30 Specimen subjected to Tabas (E-W) Earthquake Motion at Room Temperature

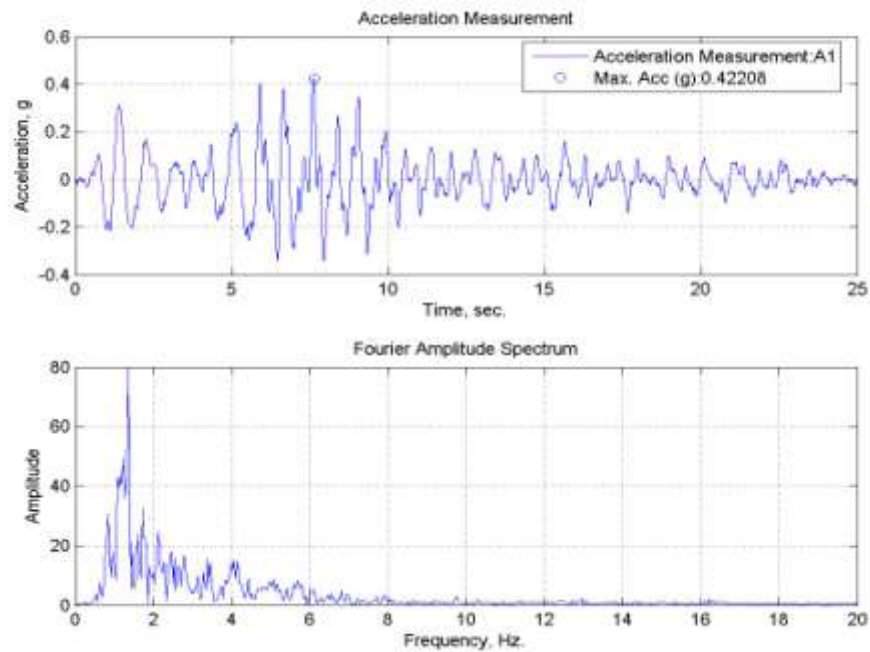


Figure B.66. A1, acceleration time history of TB30 specimen tested at room temperature.

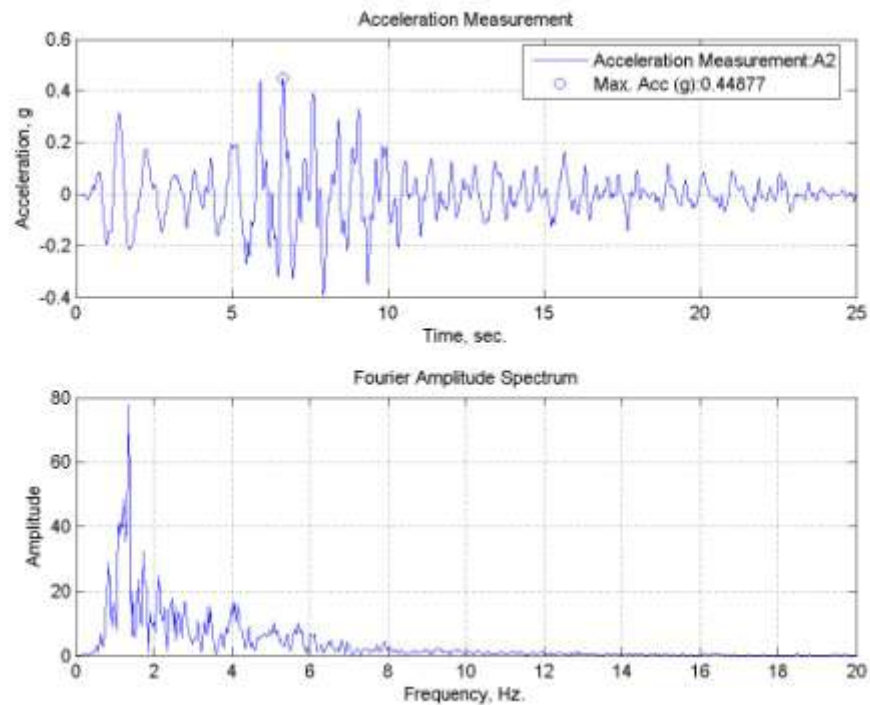


Figure B.67. A2, acceleration time history of TB30 specimen tested at room temperature.

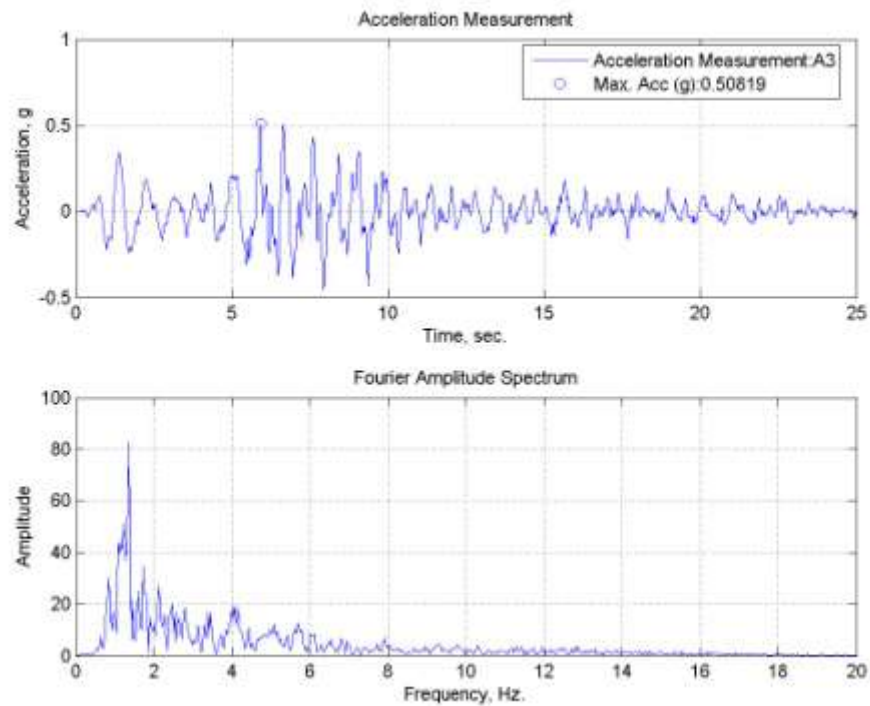


Figure B.68. A3, acceleration time history of TB30 specimen tested at room temperature.

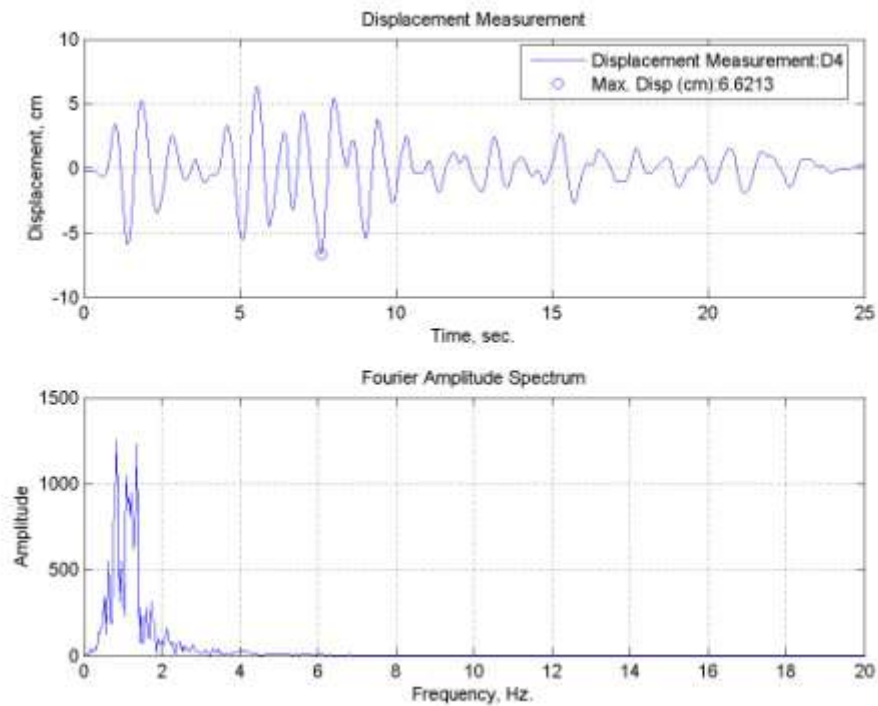


Figure B.69. Lateral displacement time history for TB30 specimen tested at room temperature.

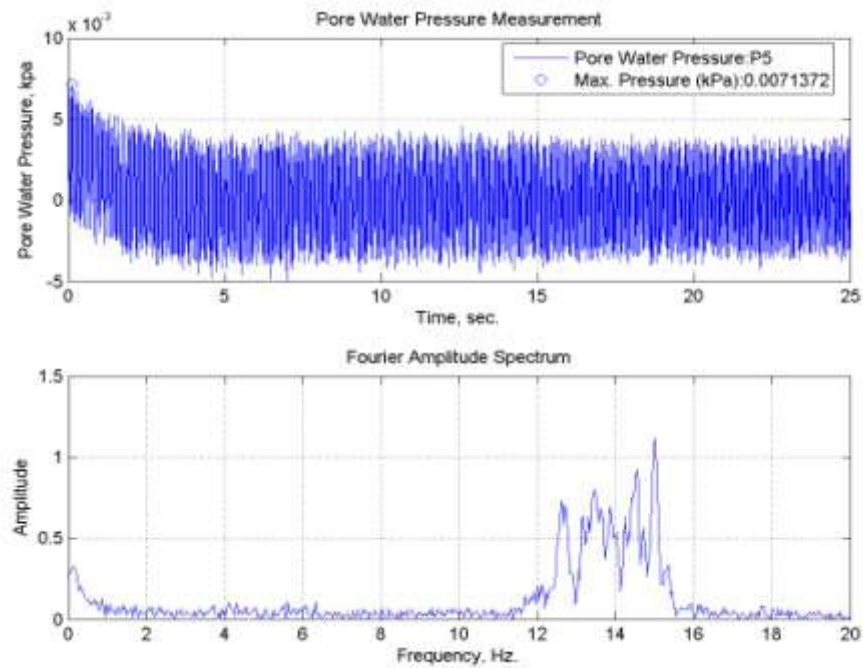


Figure B.70. Pore water pressure change of TB30 specimen tested at room temperature.

B.15. TC10 Specimen subjected to Tabas (E-W) Earthquake Motion at Room Temperature

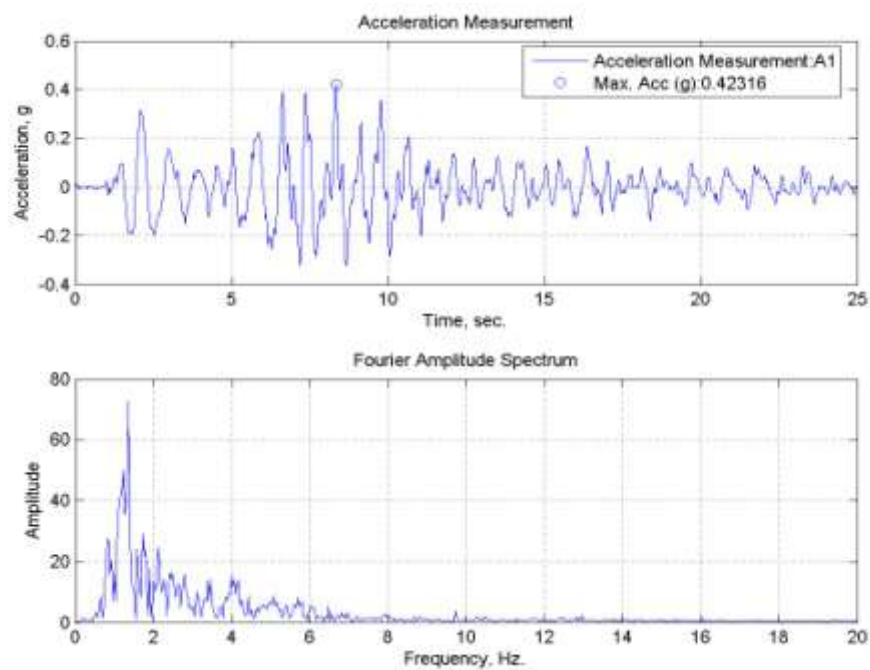


Figure B.71. A1, acceleration time history of TC10 specimen tested at room temperature.

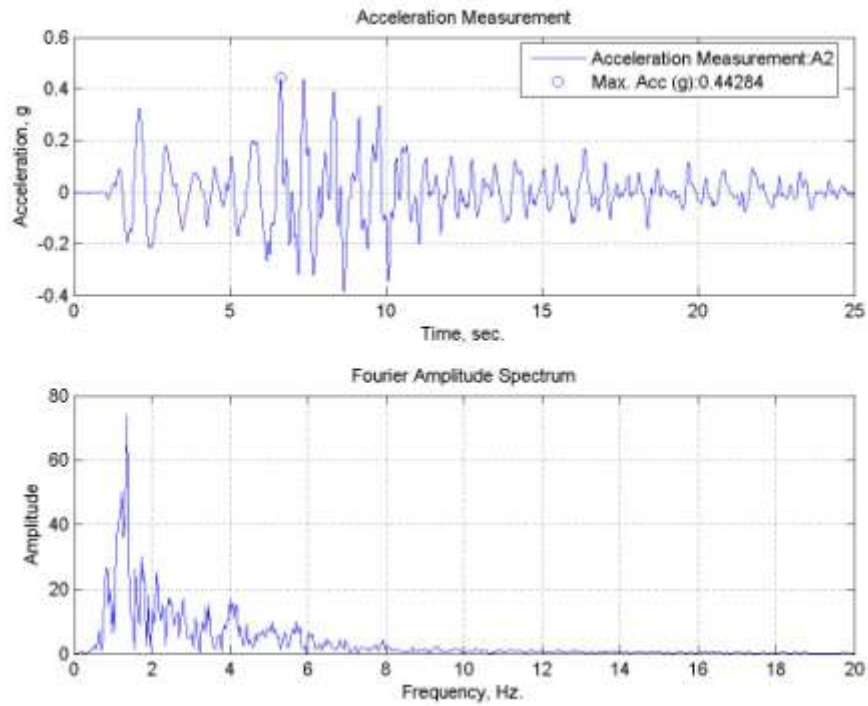


Figure B.72. A2, acceleration time history of TC10 specimen tested at room temperature.

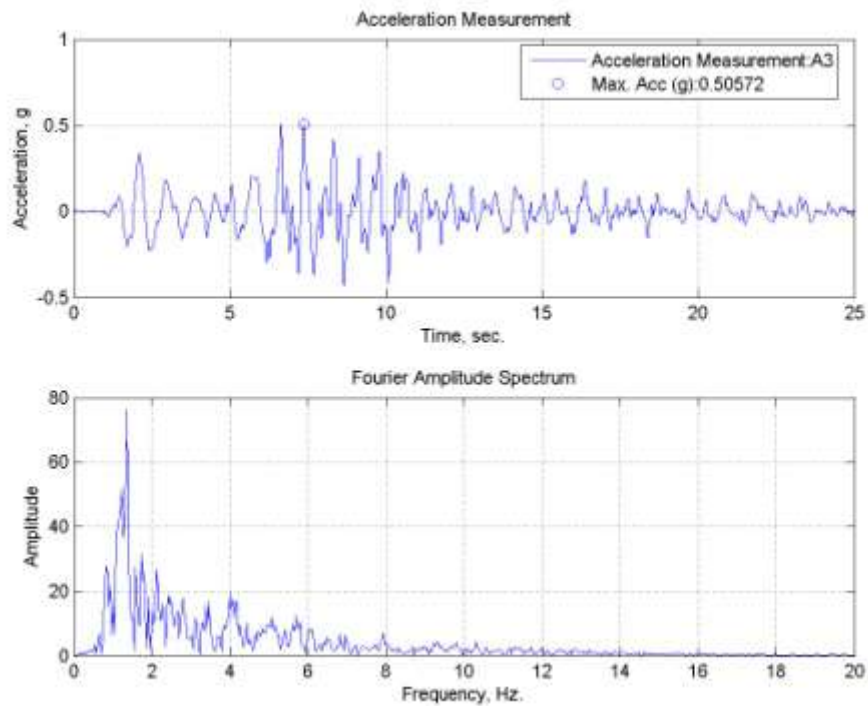


Figure B.73. A3, acceleration time history of TC10 specimen tested at room temperature.

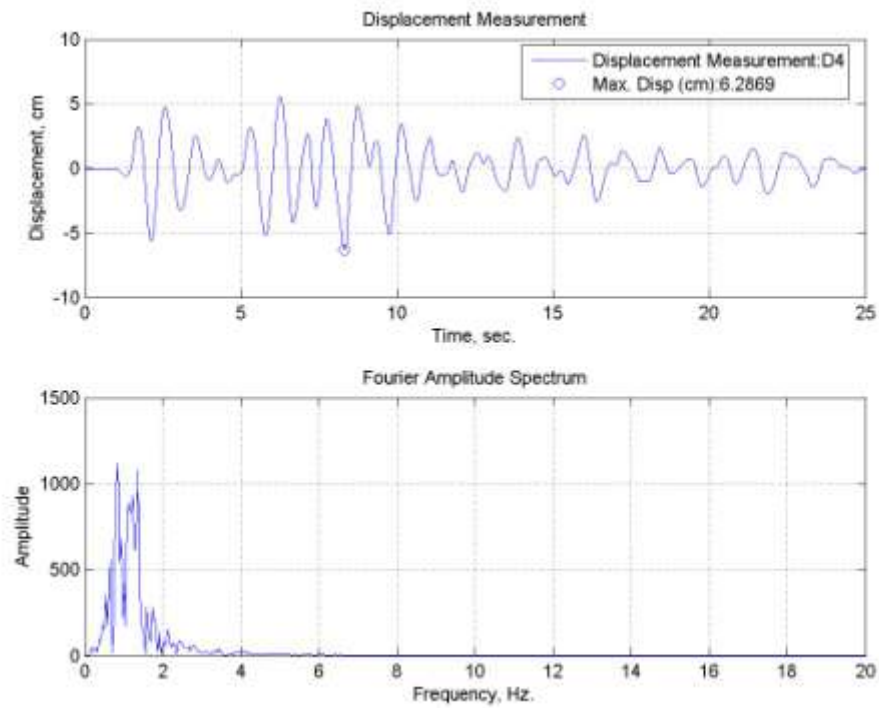


Figure B.74. Lateral displacement time history for TC10 specimen tested at room temperature.

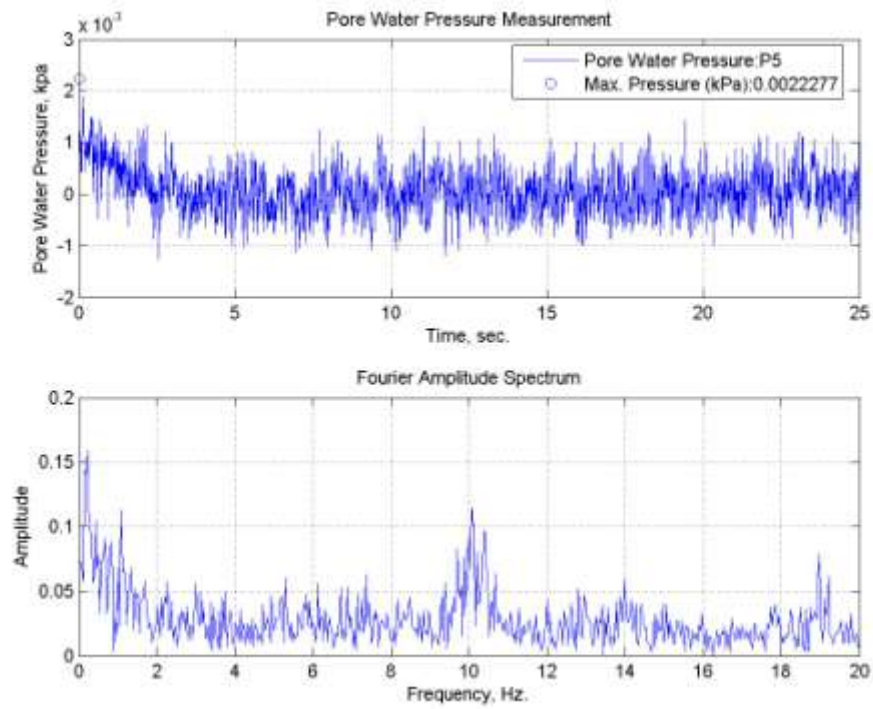


Figure B.75. Pore water pressure change of TC10 specimen tested at room temperature.

B.16. TC15 Specimen subjected to Tabas (E-W) Earthquake Motion at Room Temperature

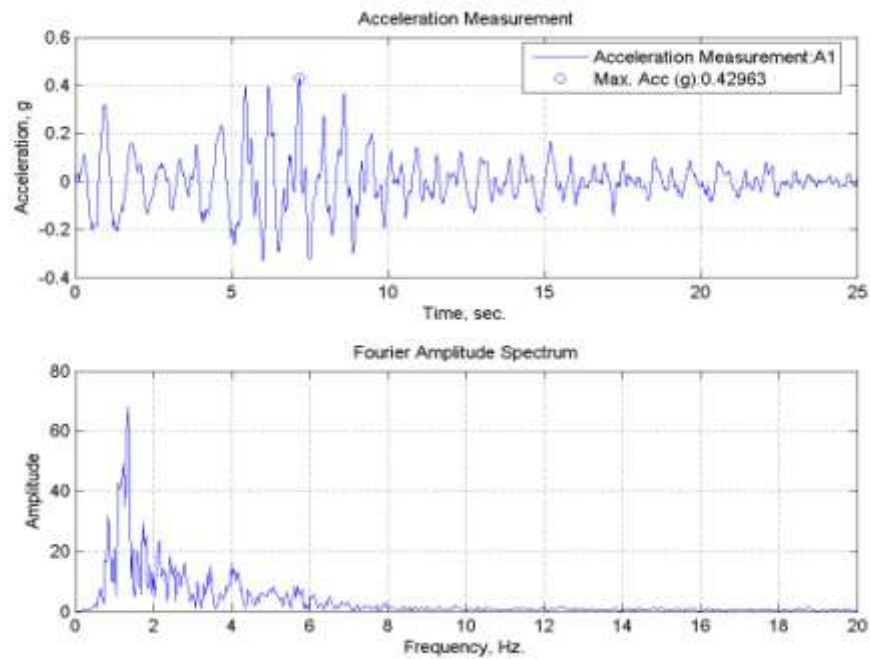


Figure B.76. A1, acceleration time history of TC15 specimen tested at room temperature.

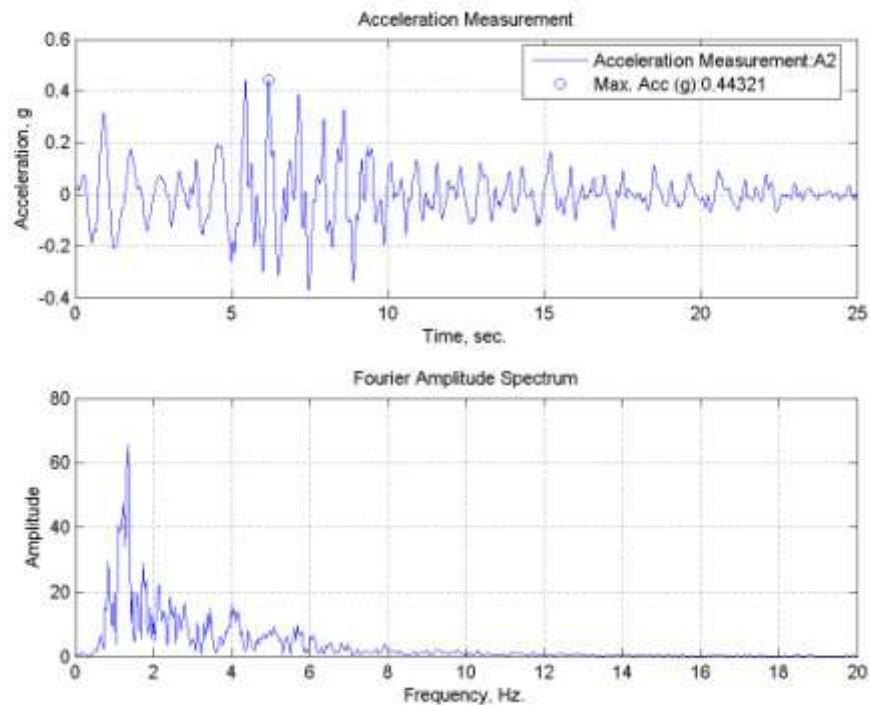


Figure B.77. A2, acceleration time history of TC15 specimen tested at room temperature.

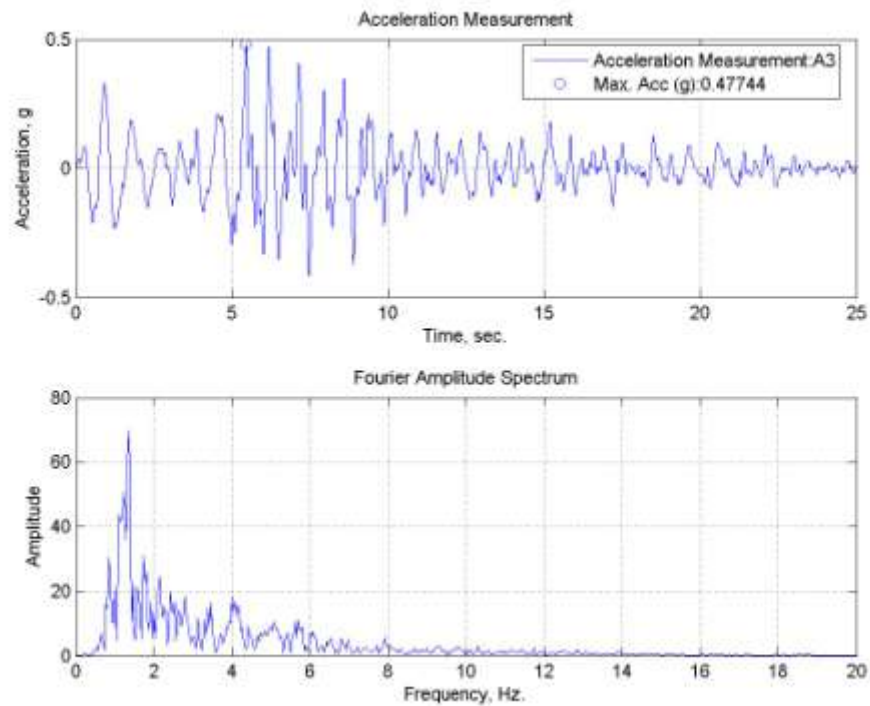


Figure B.78. A3, acceleration time history of TC15 specimen tested at room temperature.

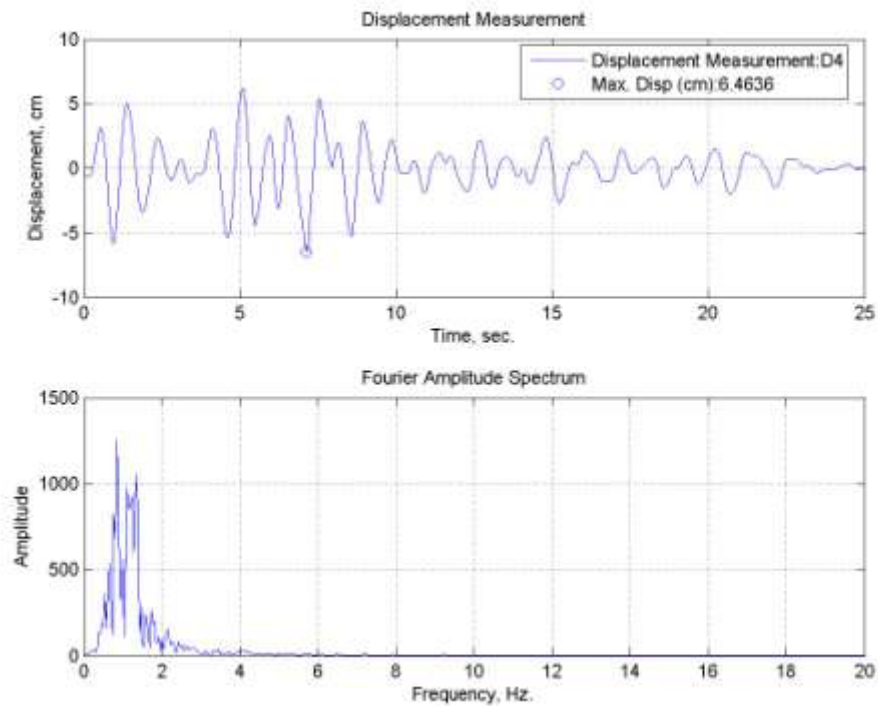


Figure B.79. Lateral displacement time history for TC15 specimen tested at room temperature.

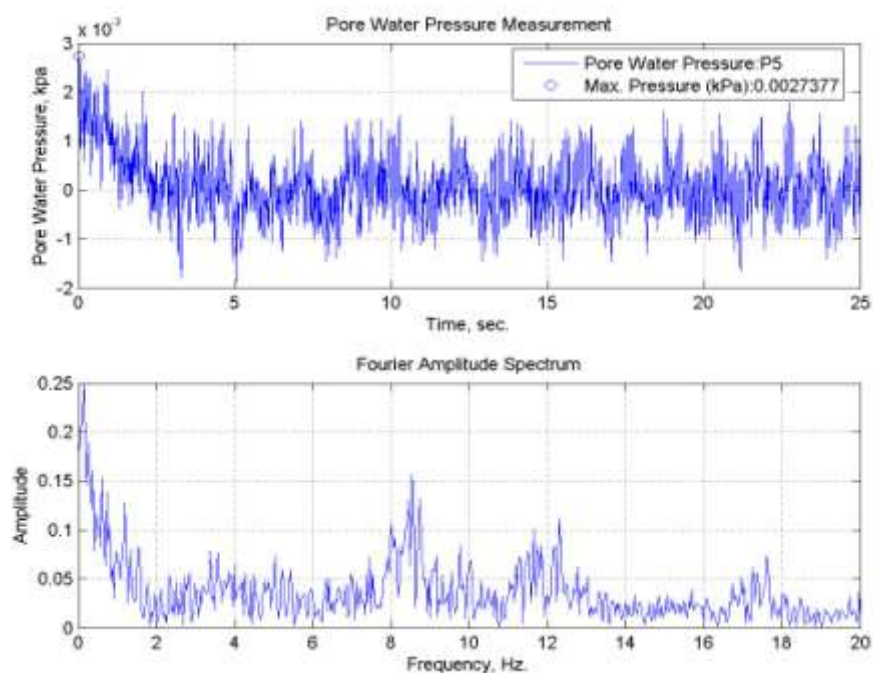


Figure B.80. Pore water pressure change of TC15 specimen tested at room temperature.

B.17. TC20 Specimen subjected to Tabas (E-W) Earthquake Motion at Room Temperature

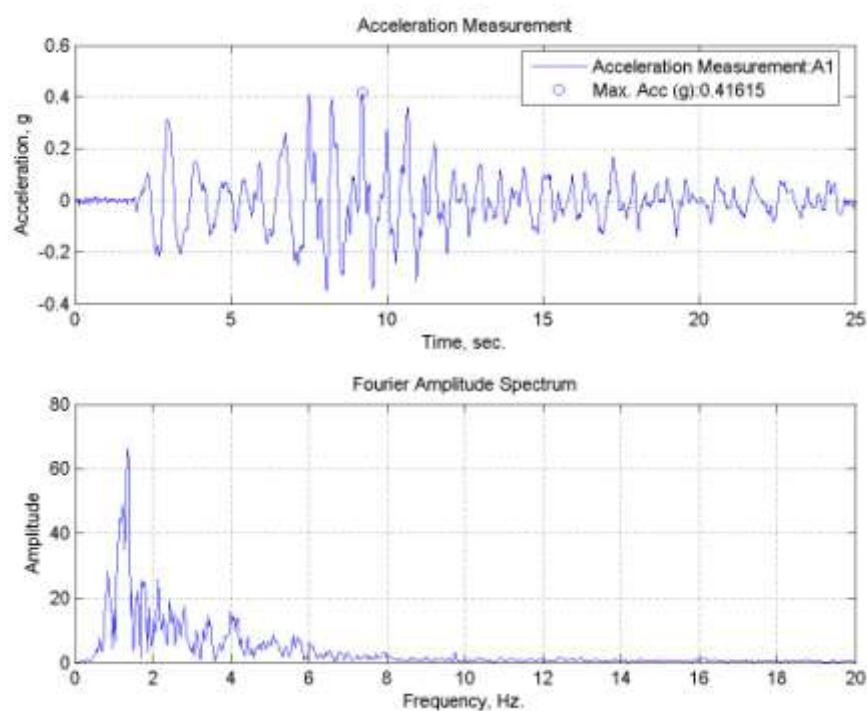


Figure B.81. A1, acceleration time history of TC20 specimen tested at room temperature.

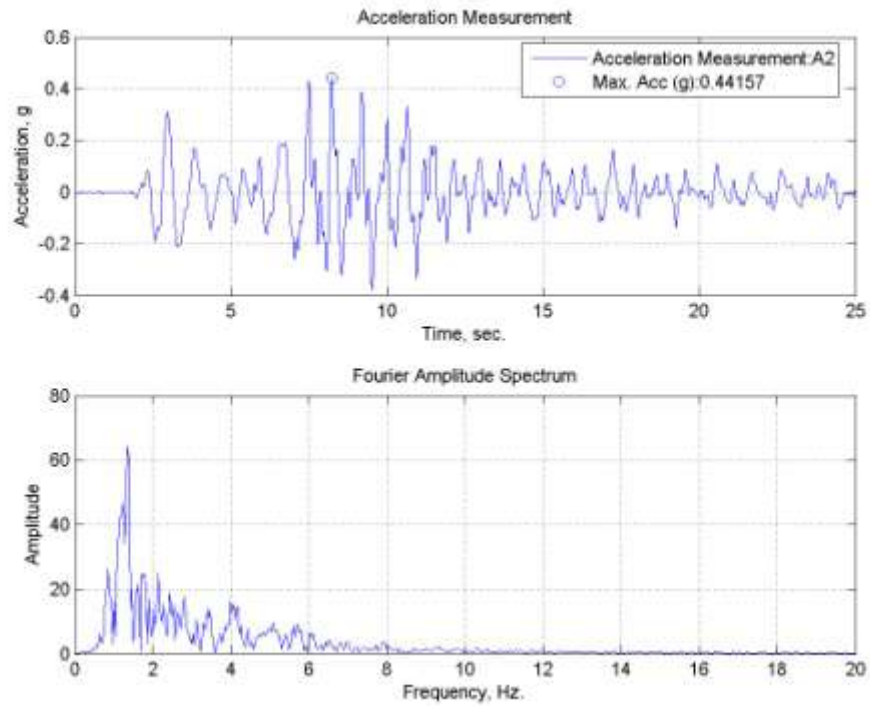


Figure B.82. A2, acceleration time history of TC20 specimen tested at room temperature.

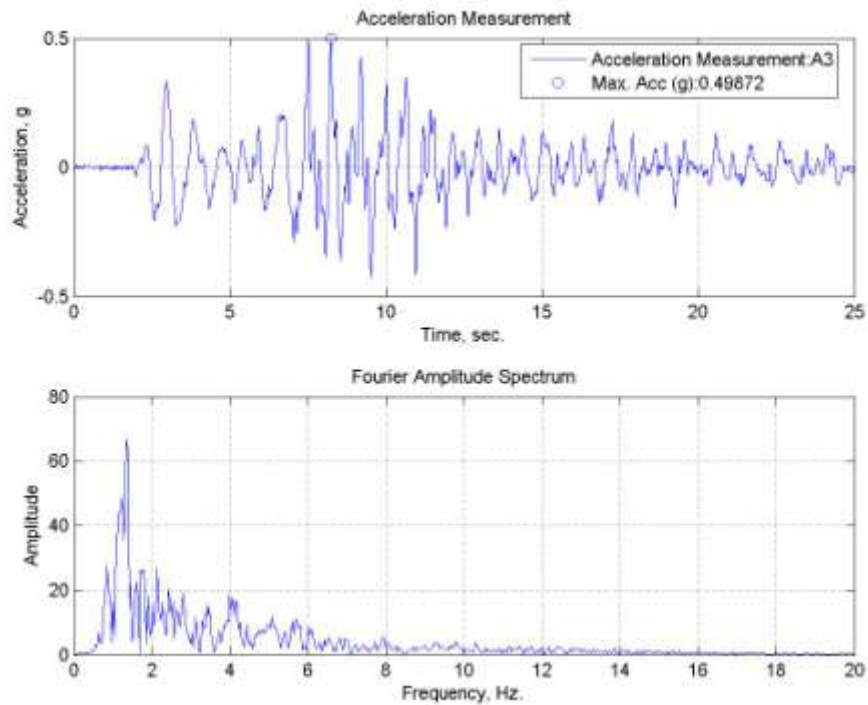


Figure B.83. A3, acceleration time history of TC20 specimen tested at room temperature.

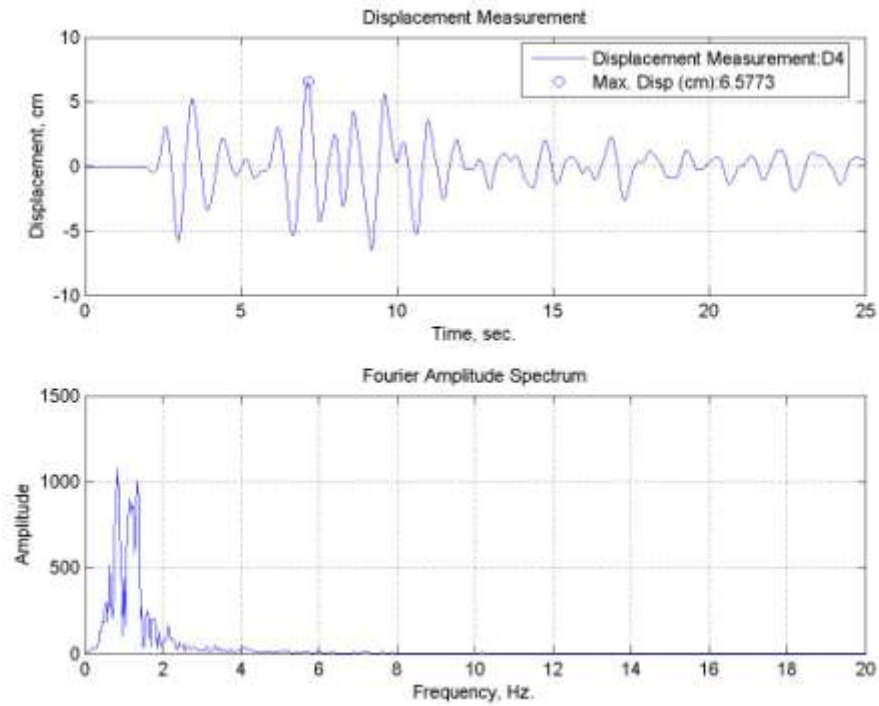


Figure B.84. Lateral displacement time history for TC20 specimen tested at room temperature.

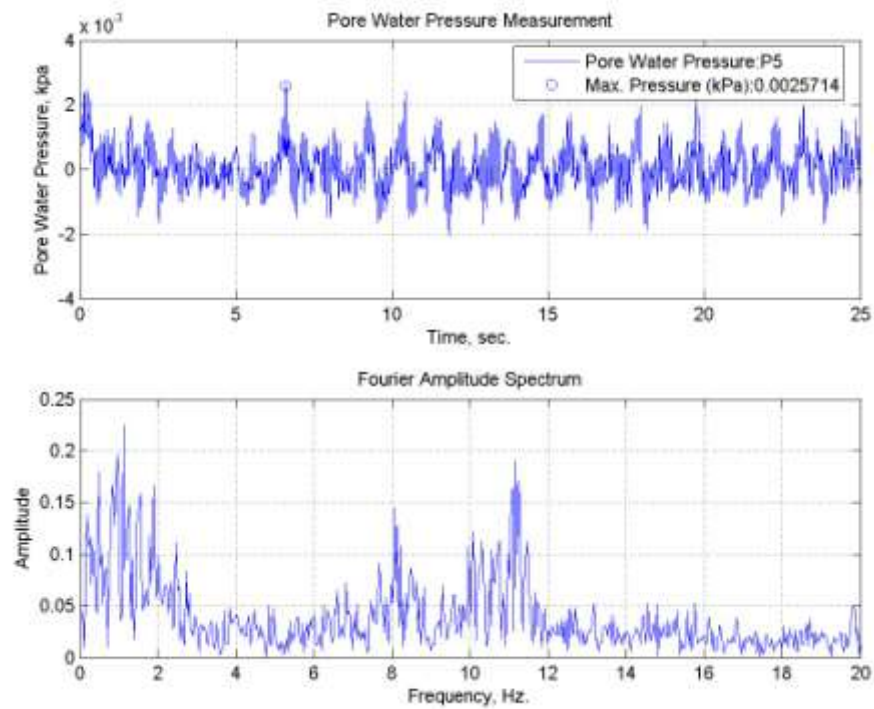


Figure B.85. Pore water pressure change of TC20 specimen tested at room temperature.

B.18. TC30 Specimen subjected to Tabas (E-W) Earthquake Motion at Room Temperature

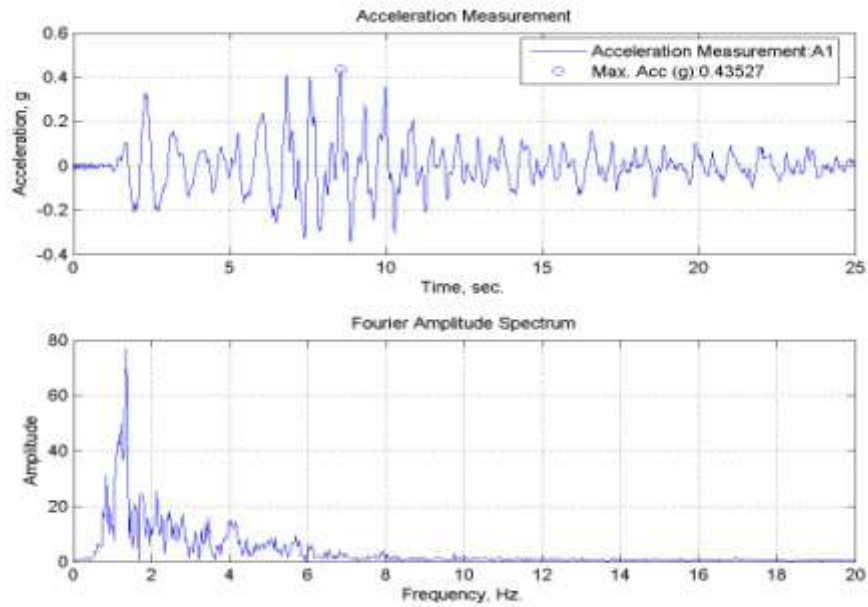


Figure B.86. A1, acceleration time history of TC30 specimen tested at room temperature.

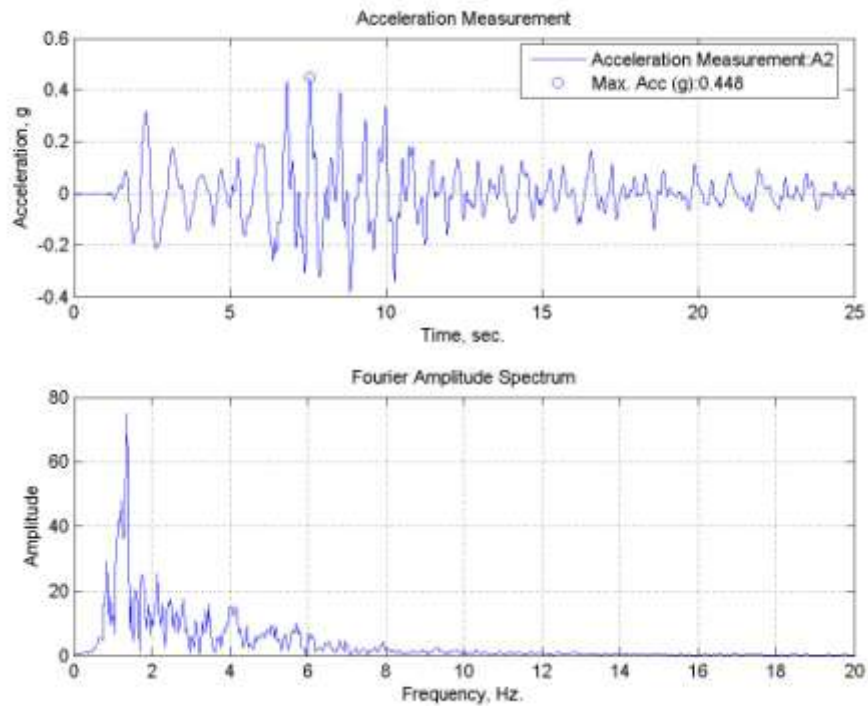


Figure B.87. A2, acceleration time history of TC30 specimen tested at room temperature.

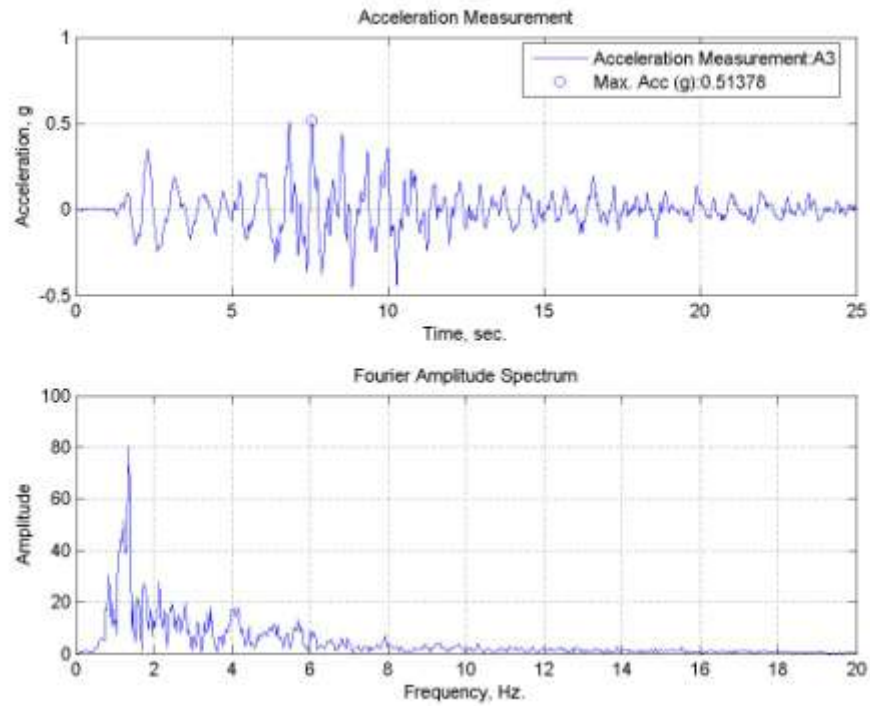


Figure B.88. A3, acceleration time history of TC30 specimen tested at room temperature.

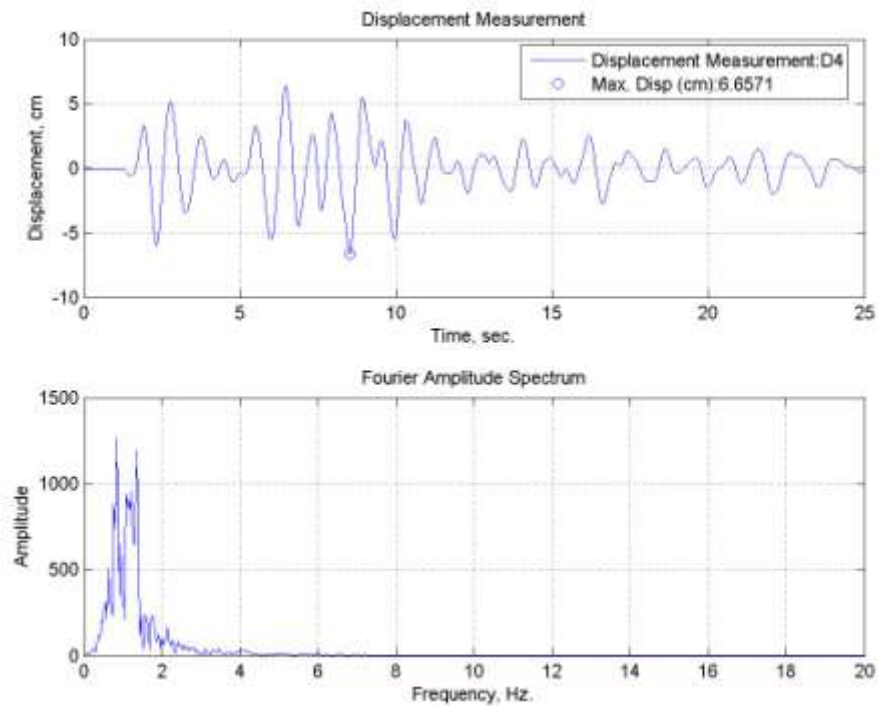


Figure B.89. Lateral displacement time history for TC30 specimen tested at room temperature.

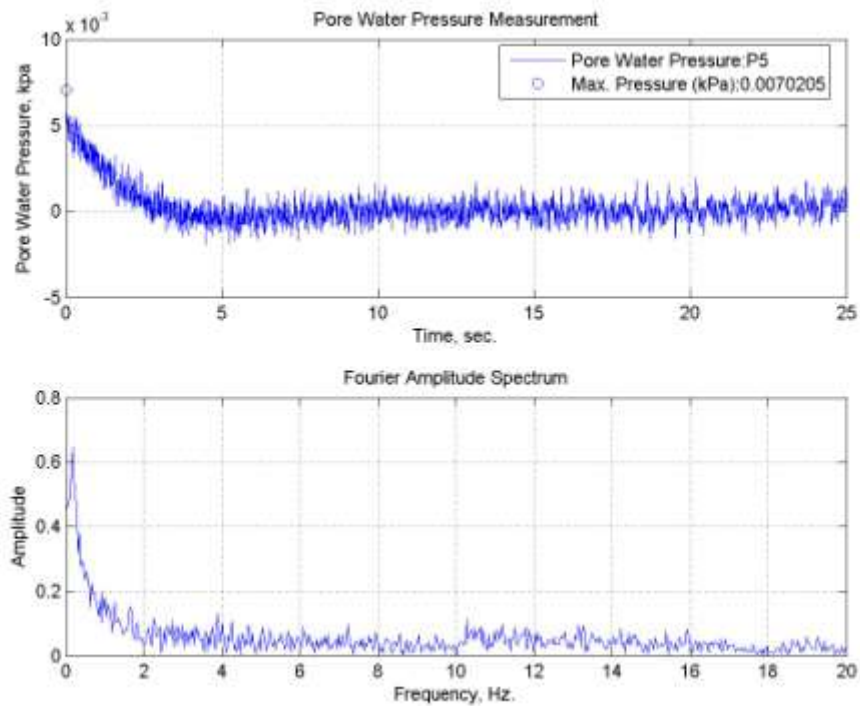


Figure B.90. Pore water pressure change of TC30 specimen tested at room temperature.

B.19. Sand Specimen subjected to Tabas (E-W) Earthquake Motion at 50°C

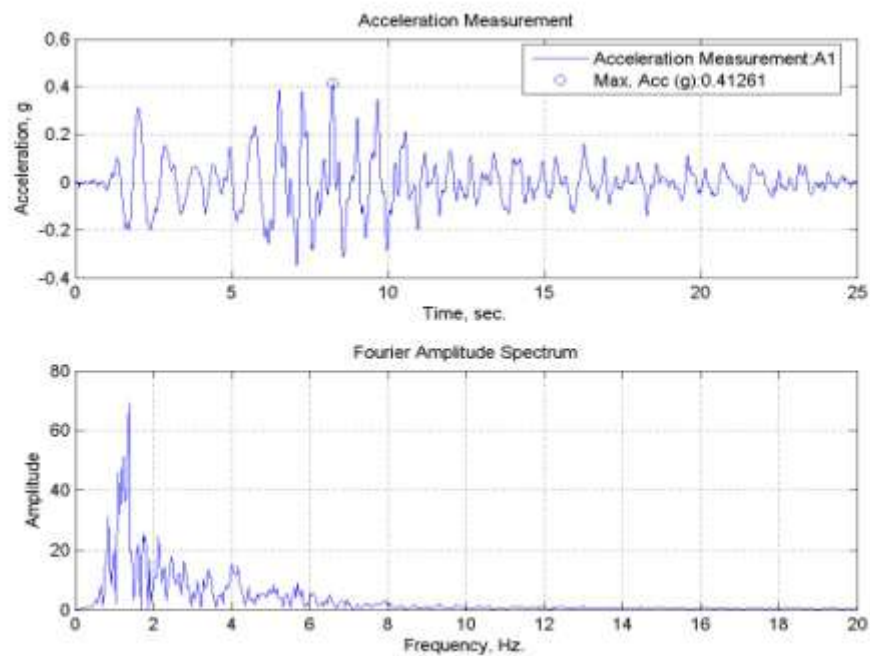


Figure B.91. A1, acceleration time history of sand specimen tested at 50°C.

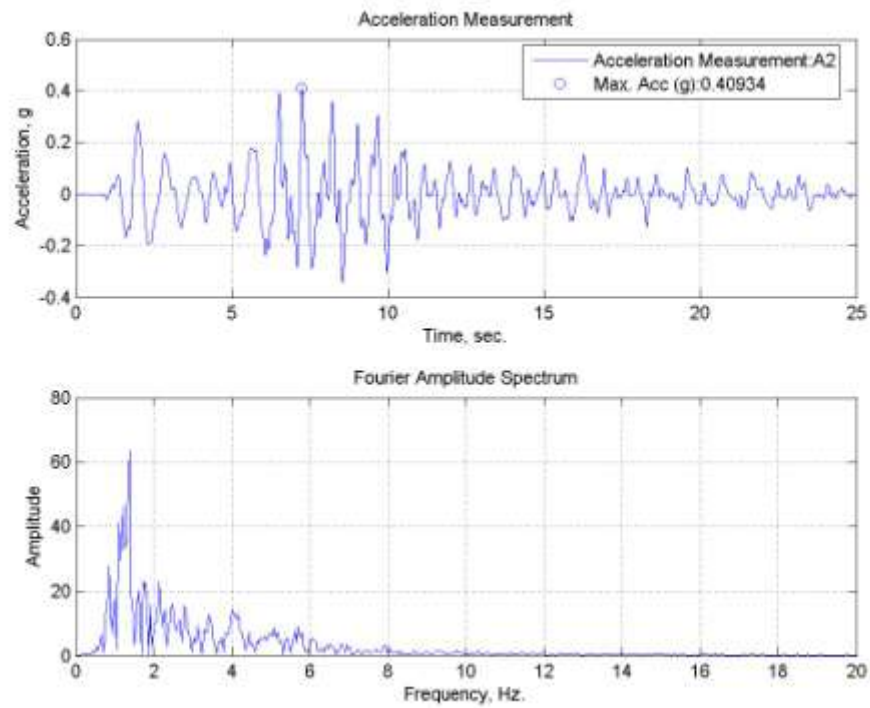


Figure B.92. A2, acceleration time history of sand specimen tested at 50°C.

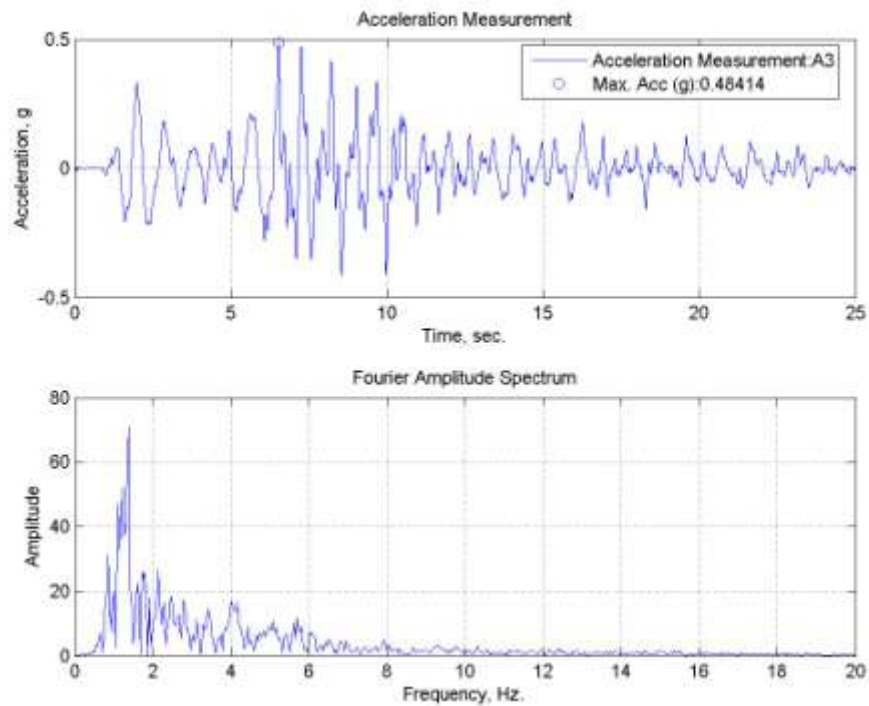


Figure B.93. A3, acceleration time history of sand specimen tested at 50°C.

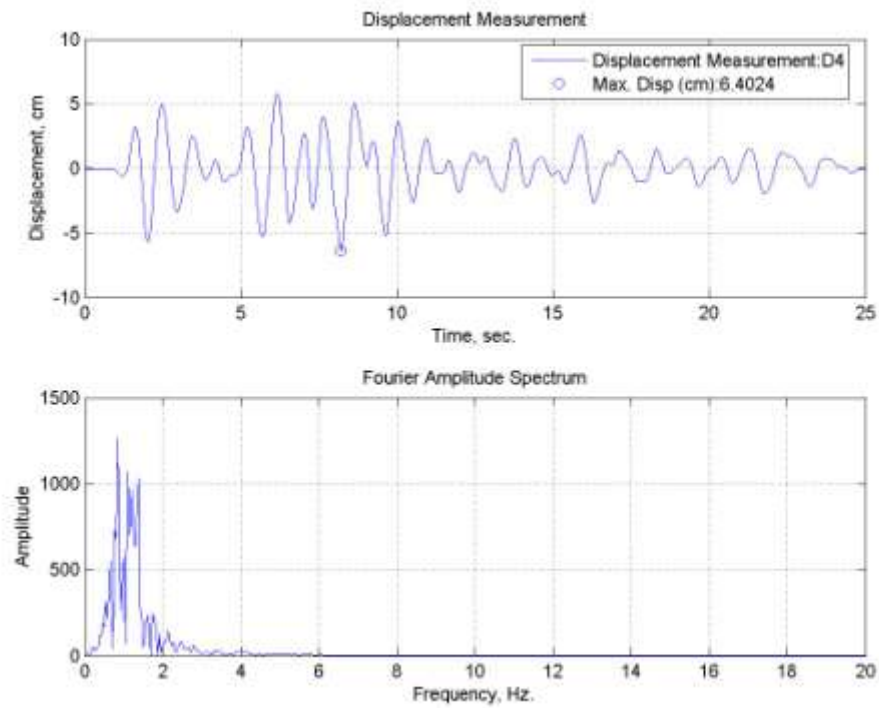


Figure B.94. Lateral displacement time history for sand specimen tested at 50°C.

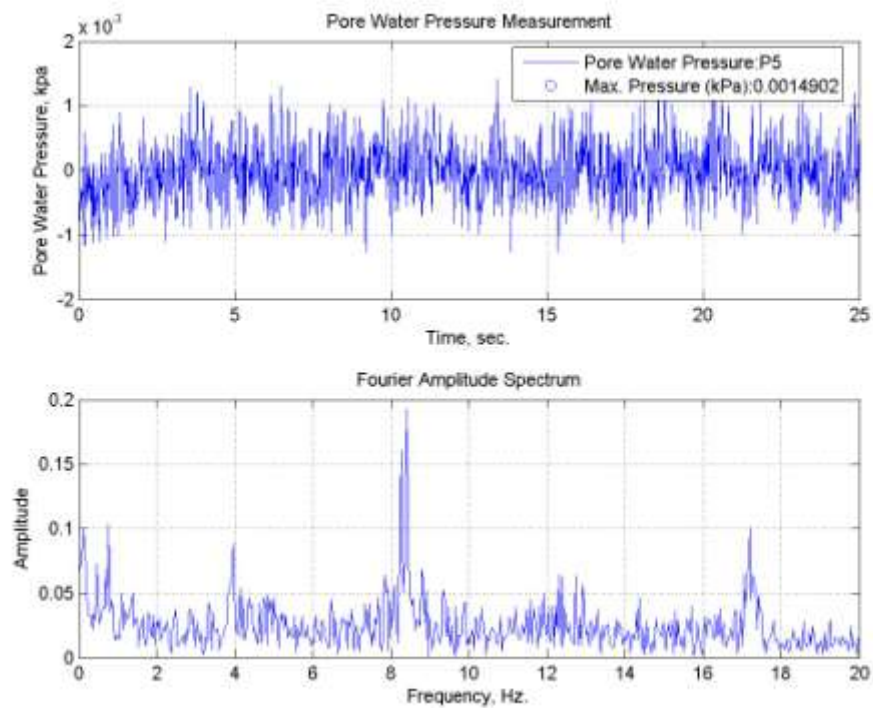


Figure B.95. Pore water pressure change of sand specimen tested at 50°C.

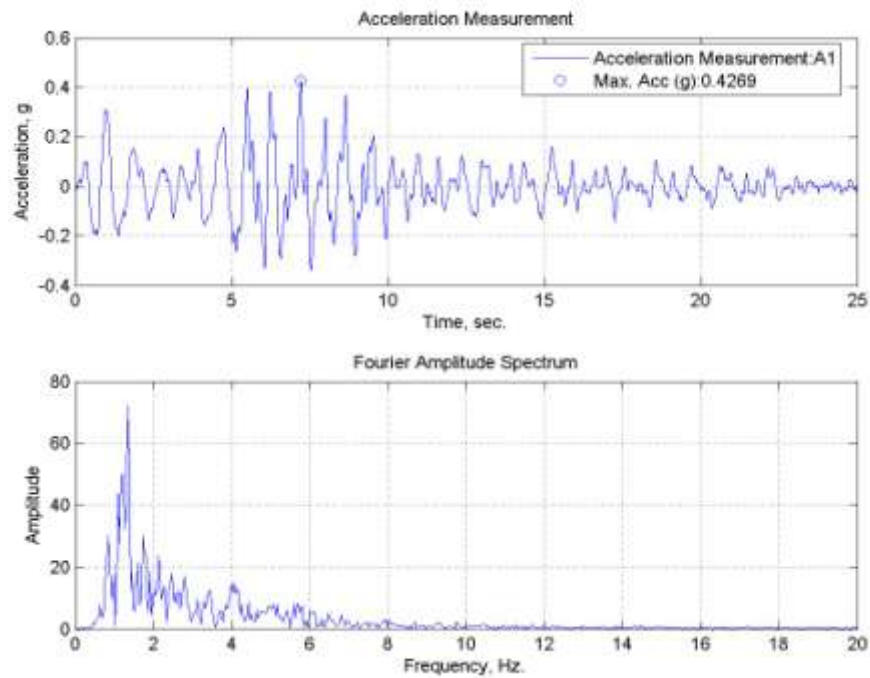
B.20. TB10 Specimen subjected to Tabas (E-W) Earthquake Motion at 50°C

Figure B.96. A1, acceleration time history of TB10 specimen tested at 50°C.

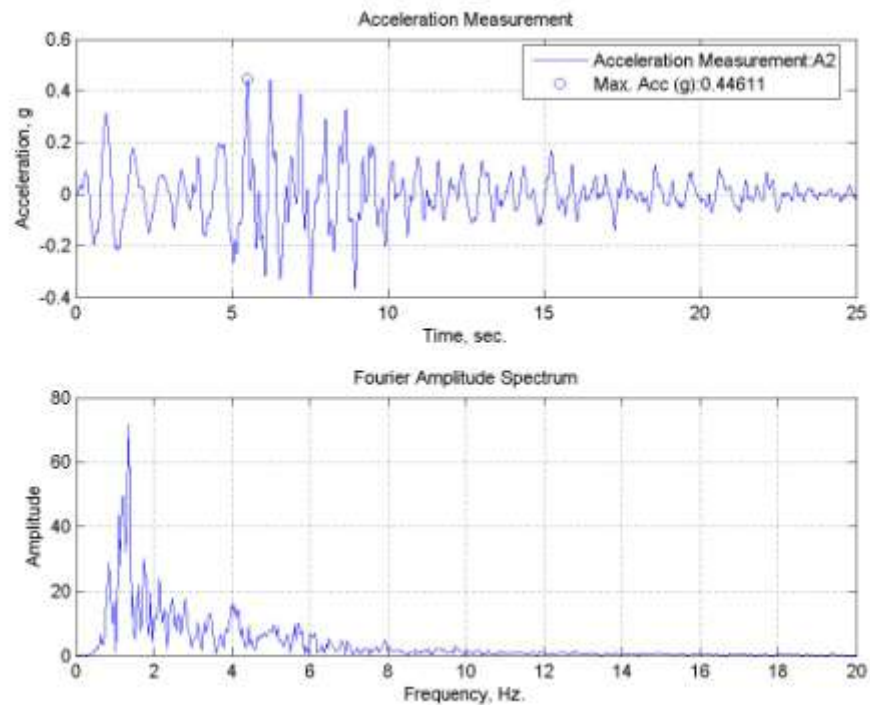


Figure B.97. A2, acceleration time history of TB10 specimen tested at 50°C.

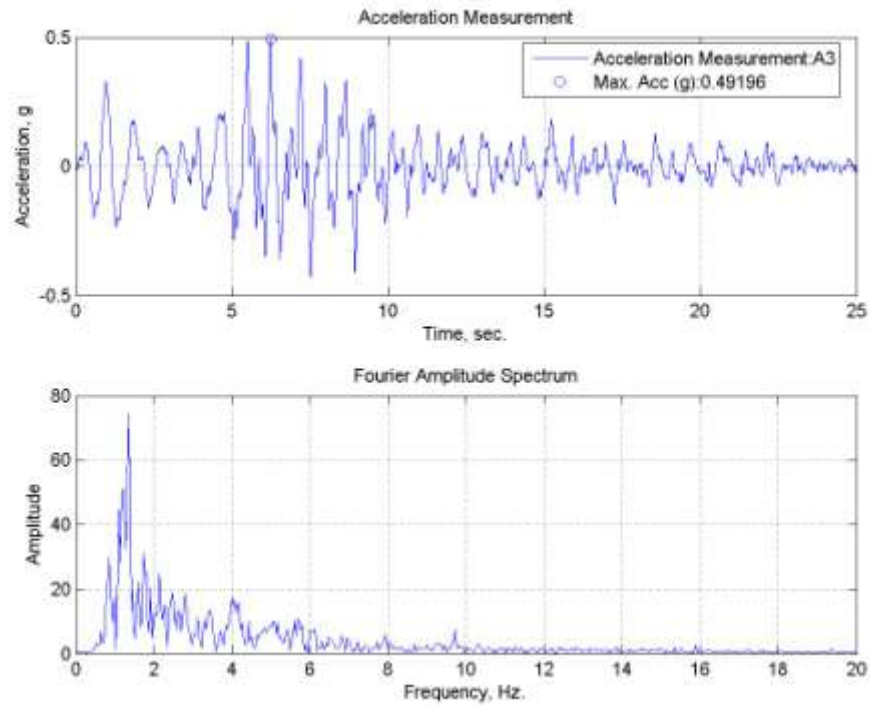


Figure B.98. A3, acceleration time history of TB10 specimen tested at 50°C.

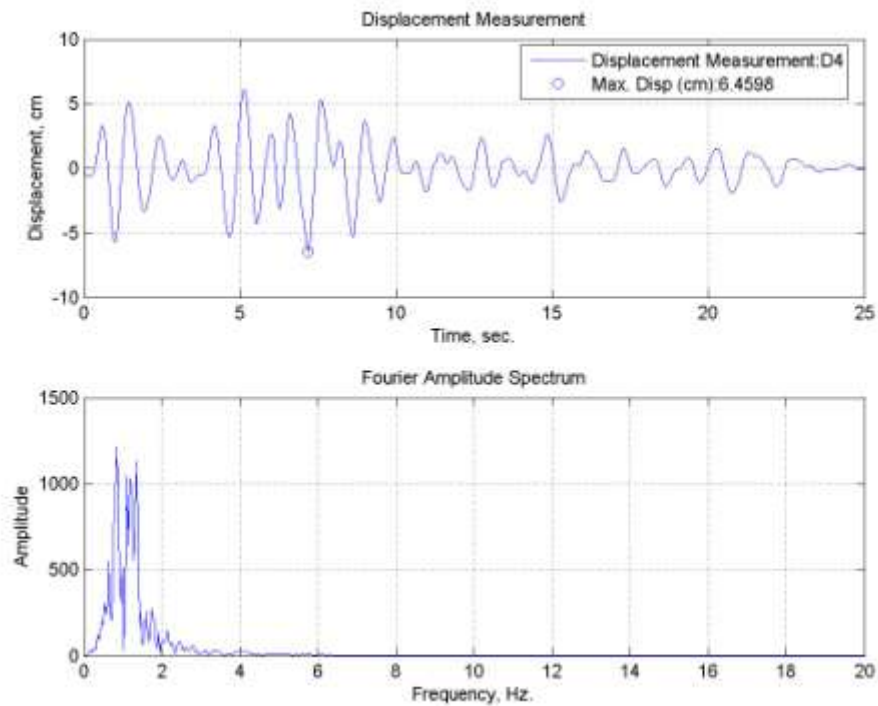


Figure B.99. Lateral displacement time history for TB10 specimen tested at 50°C.

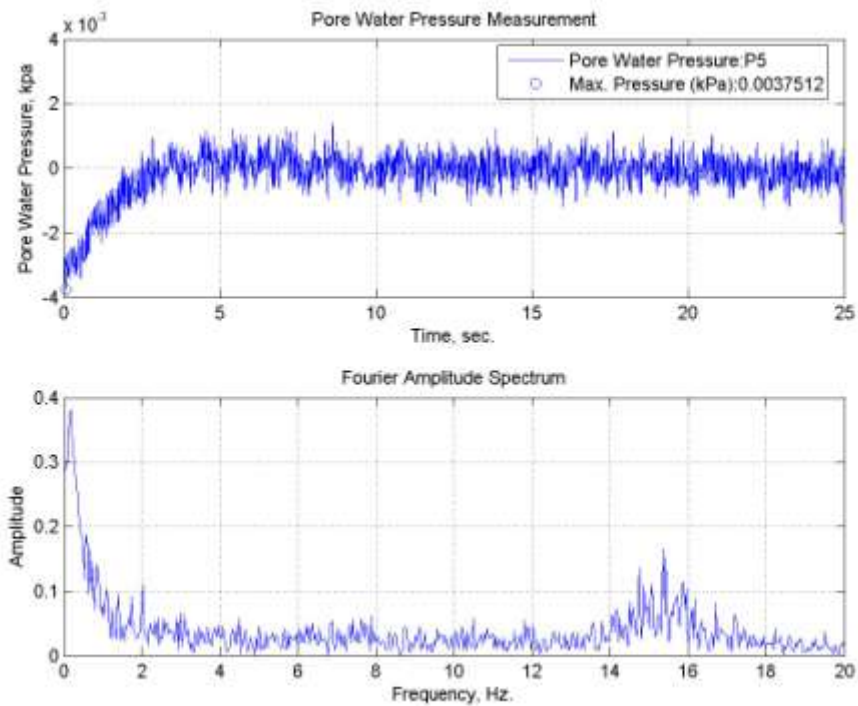


Figure B.100. Pore water pressure change of TB10 specimen tested at 50°C.

B.21. TB15 Specimen subjected to Tabas (E-W) Earthquake Motion at 50°C

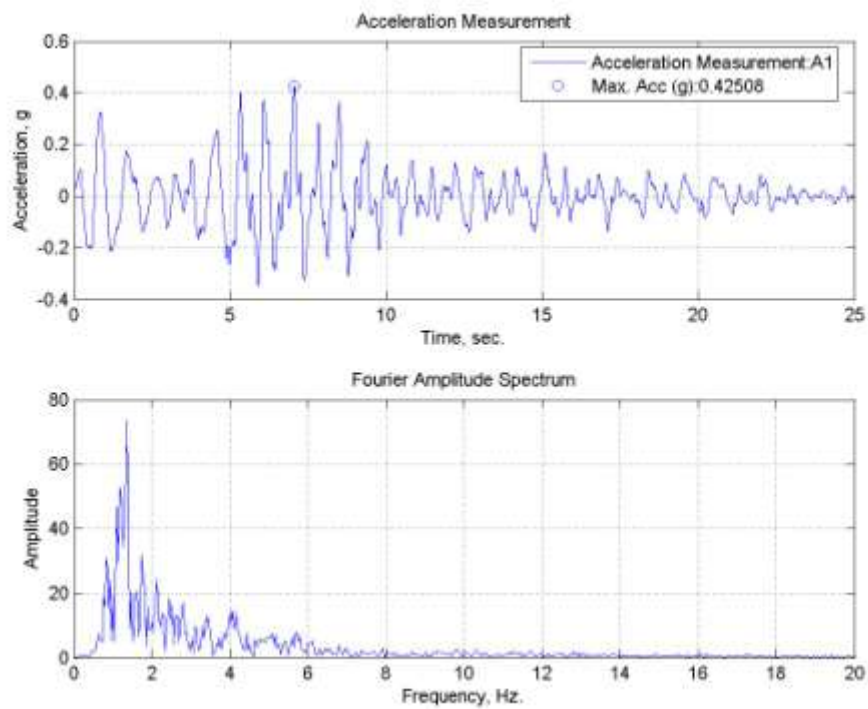


Figure B.101. A1, acceleration time history of TB15 specimen tested at 50°C.

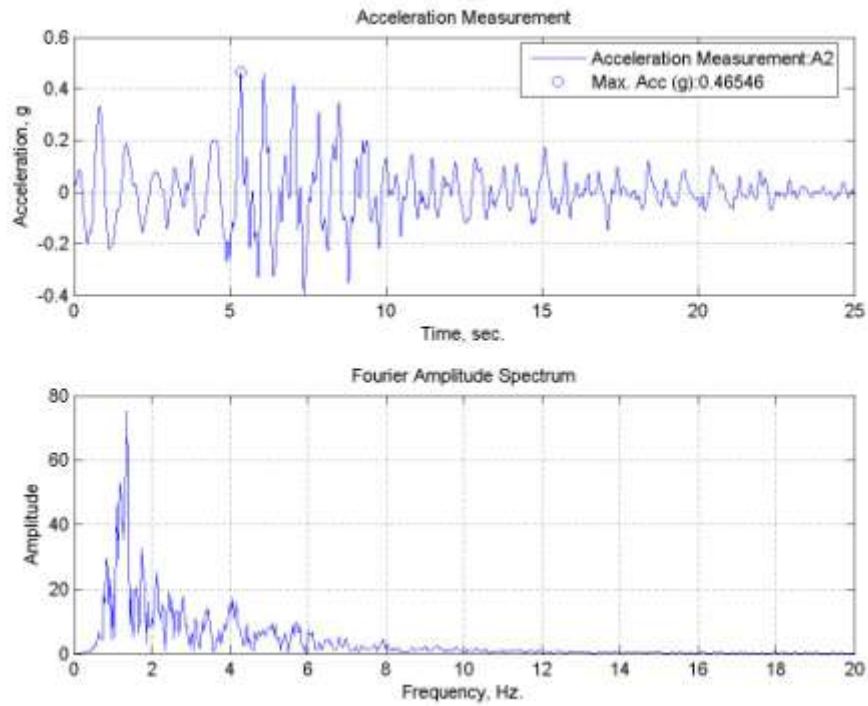


Figure B.102. A2, acceleration time history of TB15 specimen tested at 50°C.

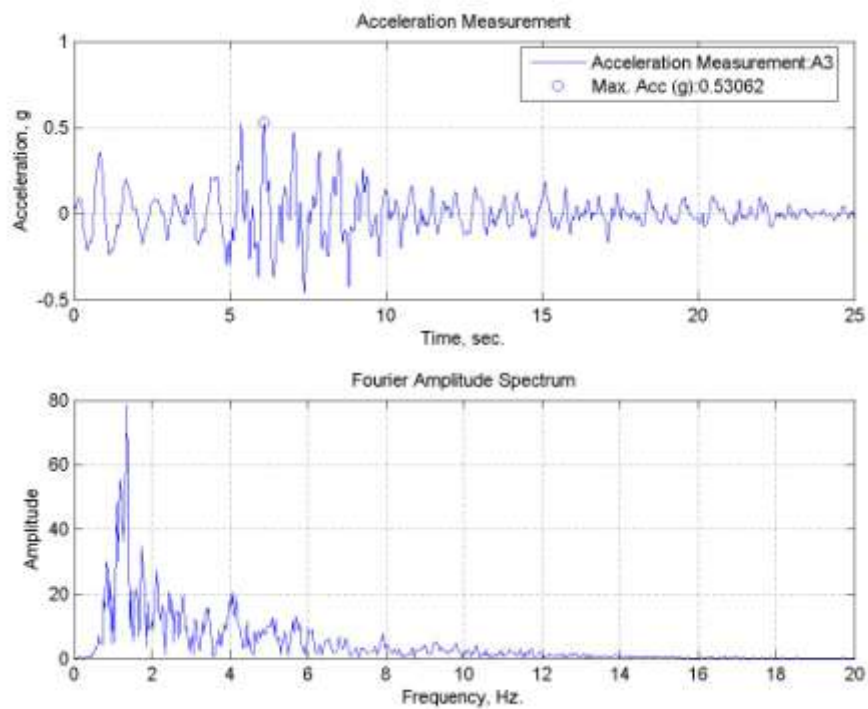


Figure B.103. A3, acceleration time history of TB15 specimen tested at 50°C.

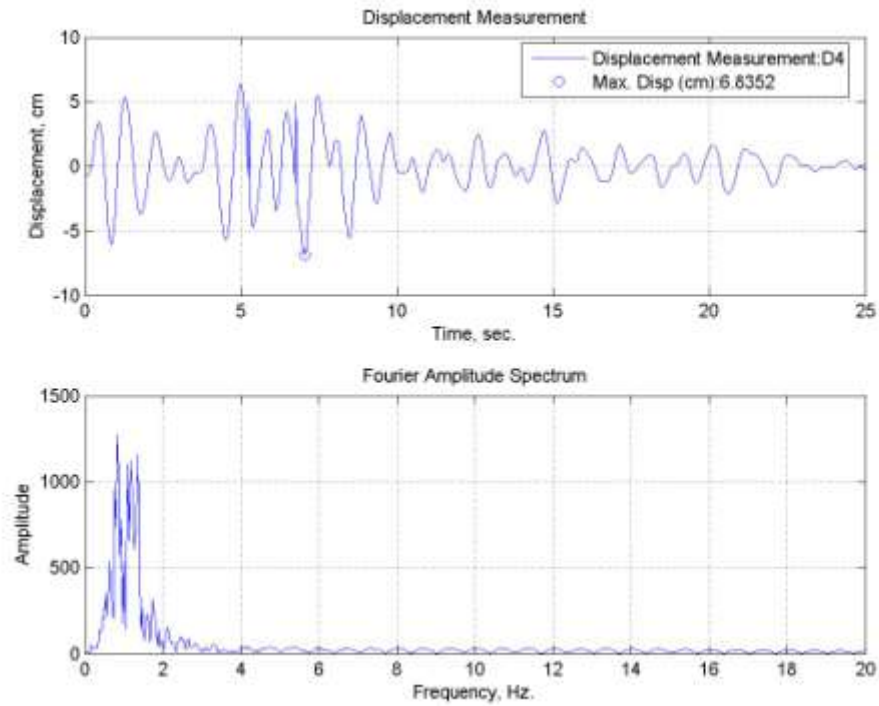


Figure B.104. Lateral displacement time history for TB15 specimen tested at 50°C.

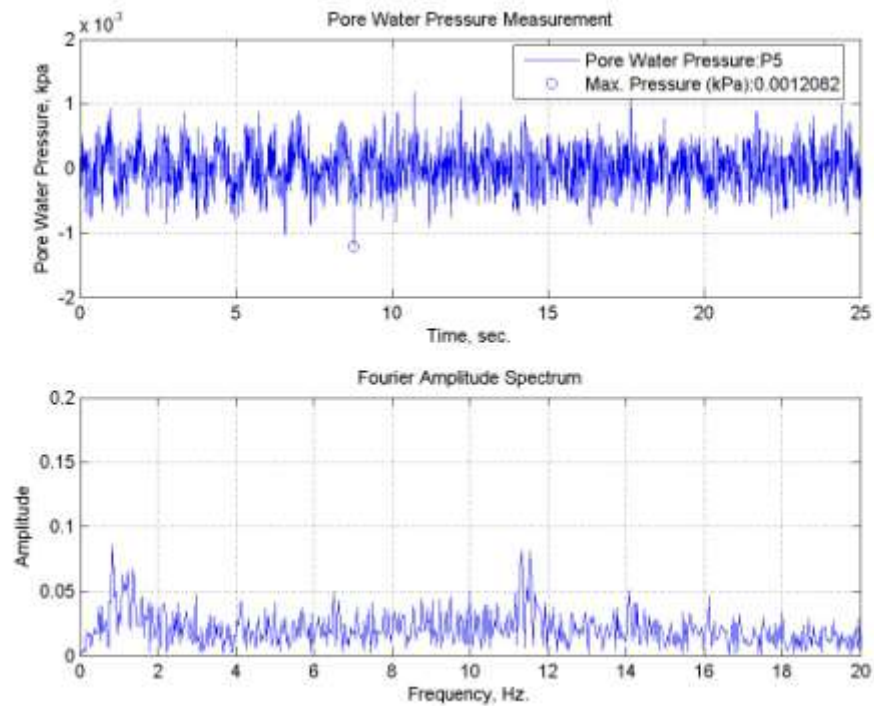


Figure B.105. Pore water pressure change of TB15 specimen tested at 50°C.

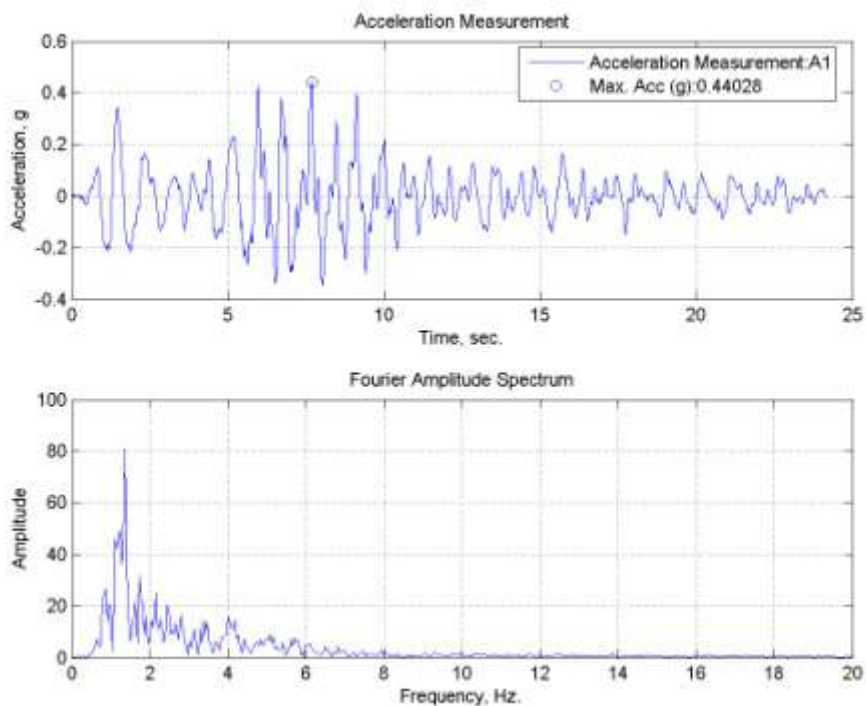
B.22. TB20 Specimen subjected to Tabas (E-W) Earthquake Motion at 50°C

Figure B.106. A1, acceleration time history of TB20 specimen tested at 50°C.

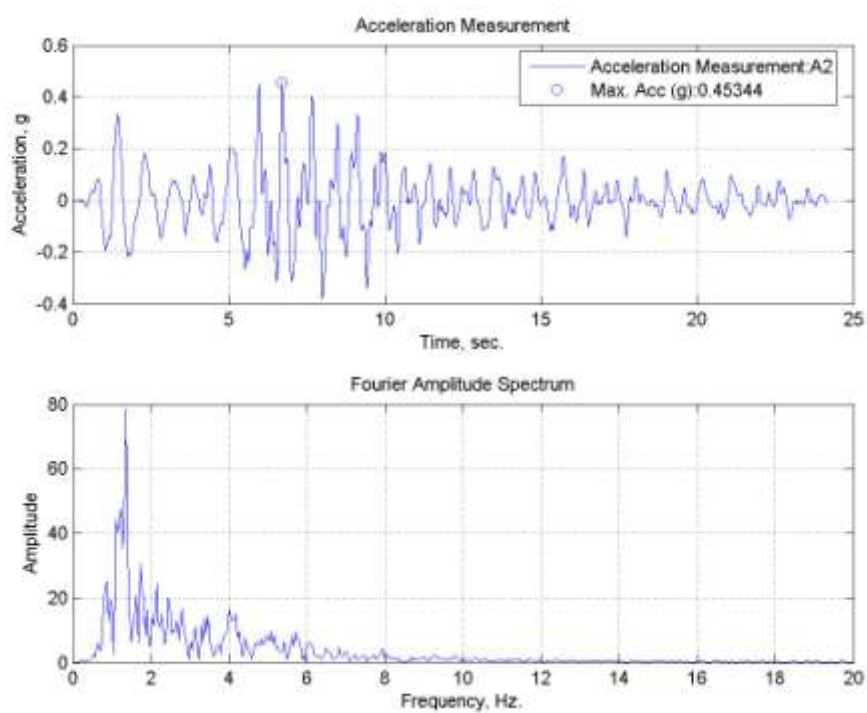


Figure B.107. A2, acceleration time history of TB20 specimen tested at 50°C.

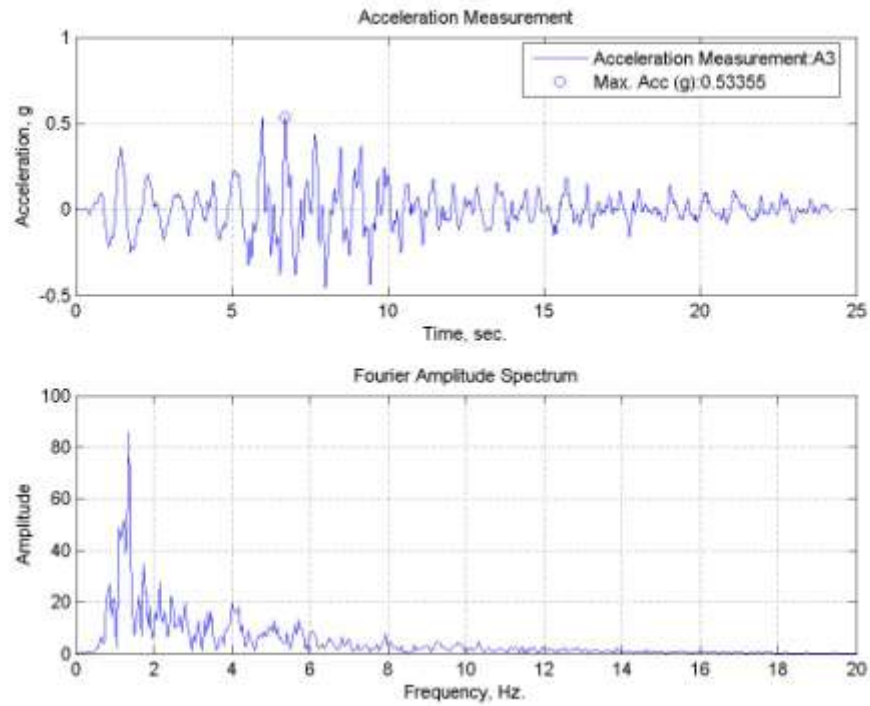


Figure B.108. A3, acceleration time history of TB20 specimen tested at 50°C.

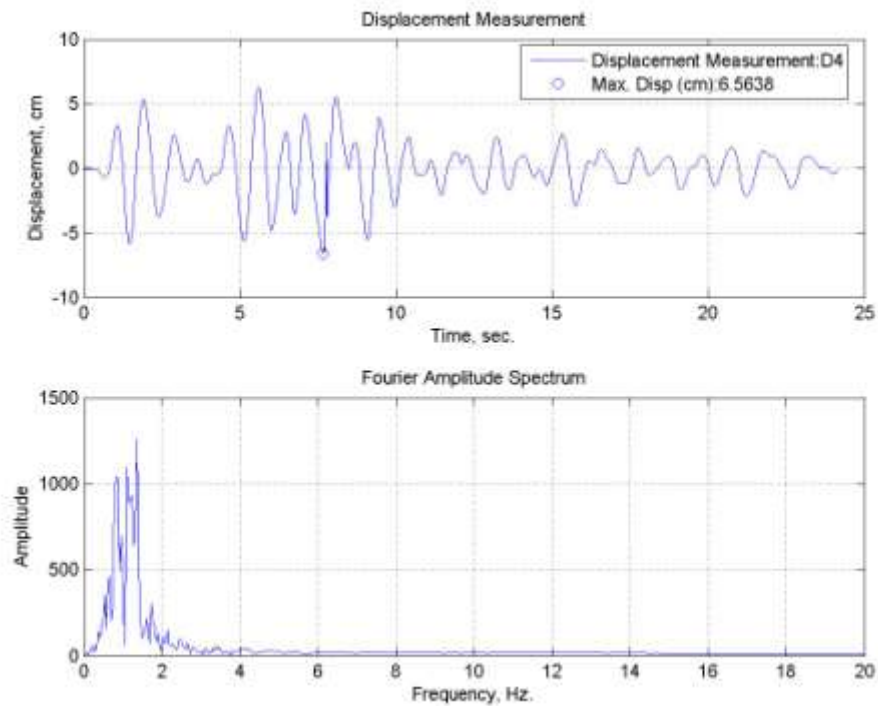


Figure B.109. Lateral displacement time history for TB20 specimen tested at 50°C.

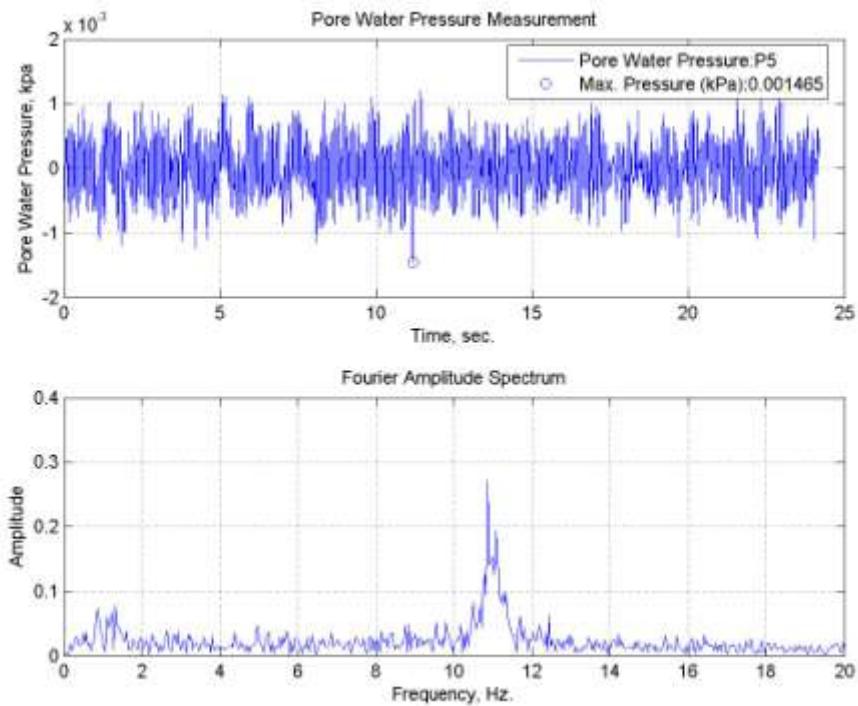


Figure B.110. Pore water pressure change of TB20 specimen tested at 50°C.

B.23. TB30 Specimen subjected to Tabas (E-W) Earthquake Motion at 50°C

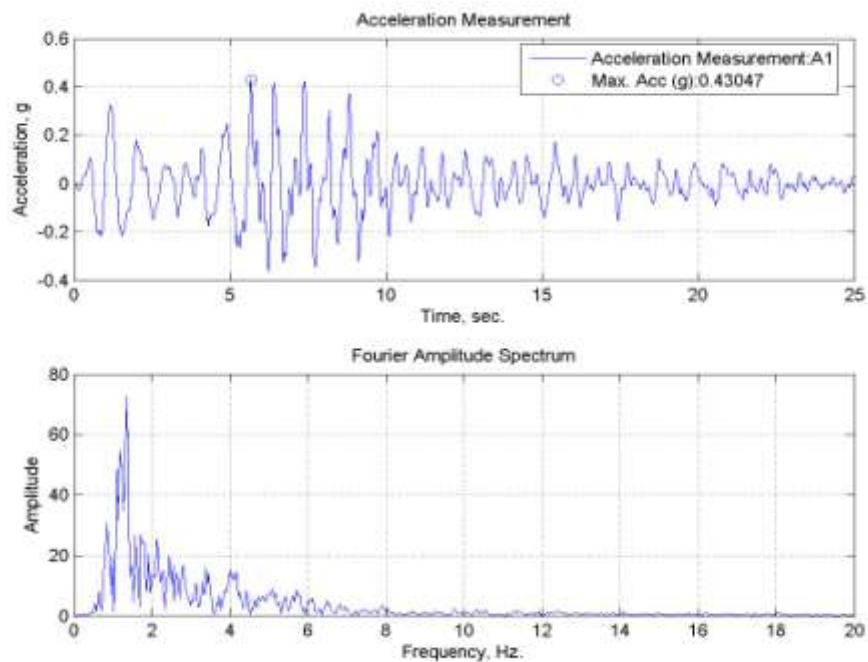


Figure B.111. A1, acceleration time history of TB30 specimen tested at 50°C.

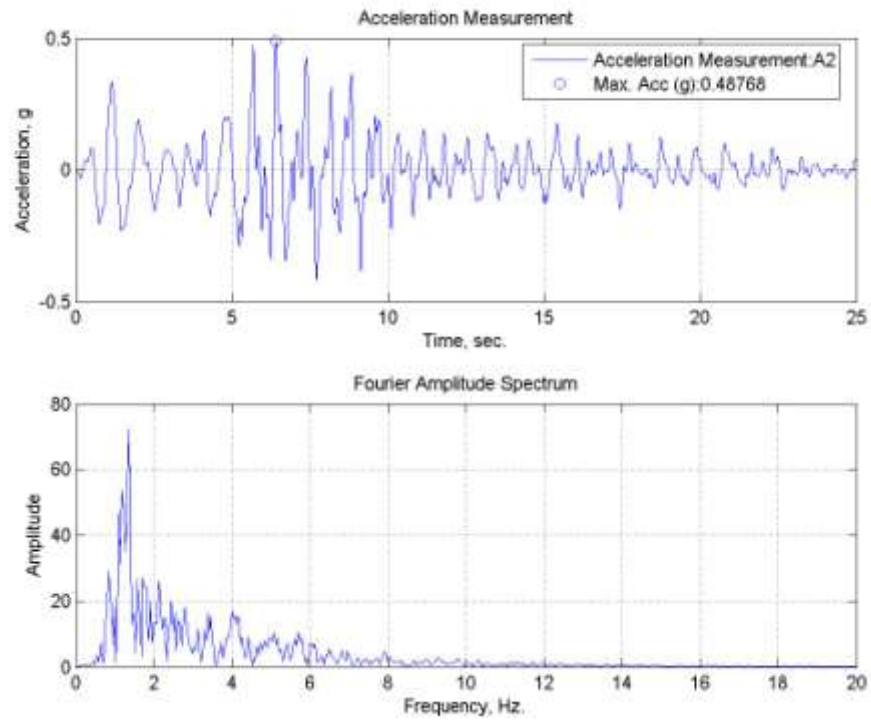


Figure B.112. A2, acceleration time history of TB30 specimen tested at 50°C.

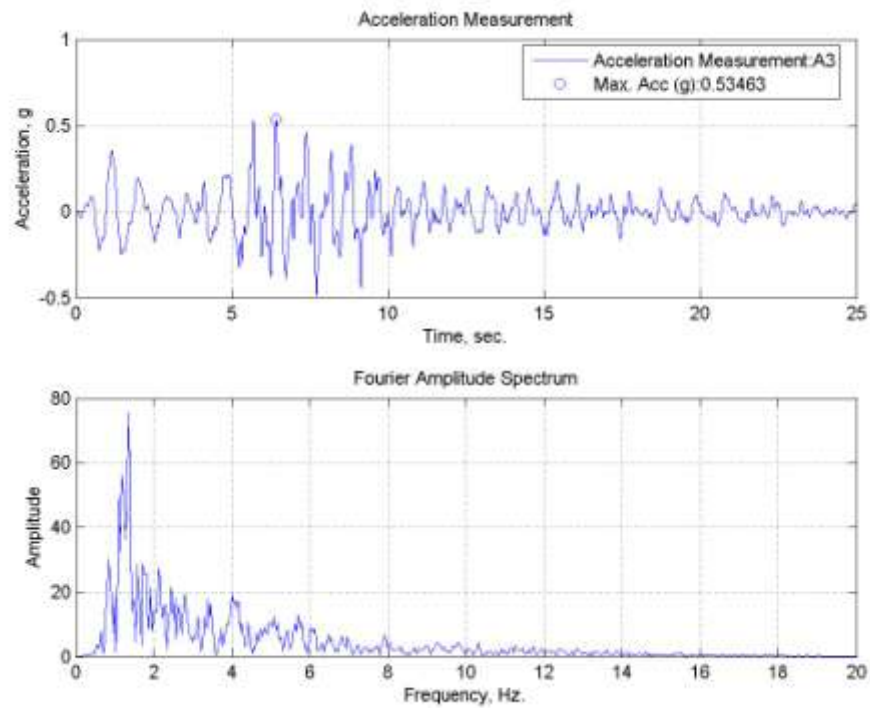


Figure B.113. A3, acceleration time history of TB30 specimen tested at 50°C.

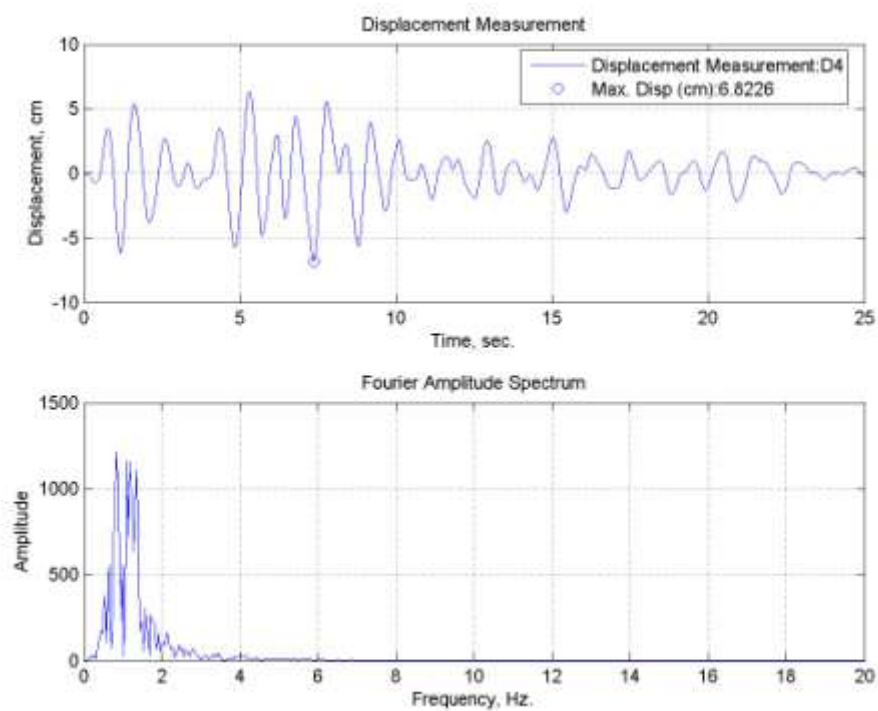


Figure B.114. Lateral displacement time history for TB30 specimen tested at 50°C.

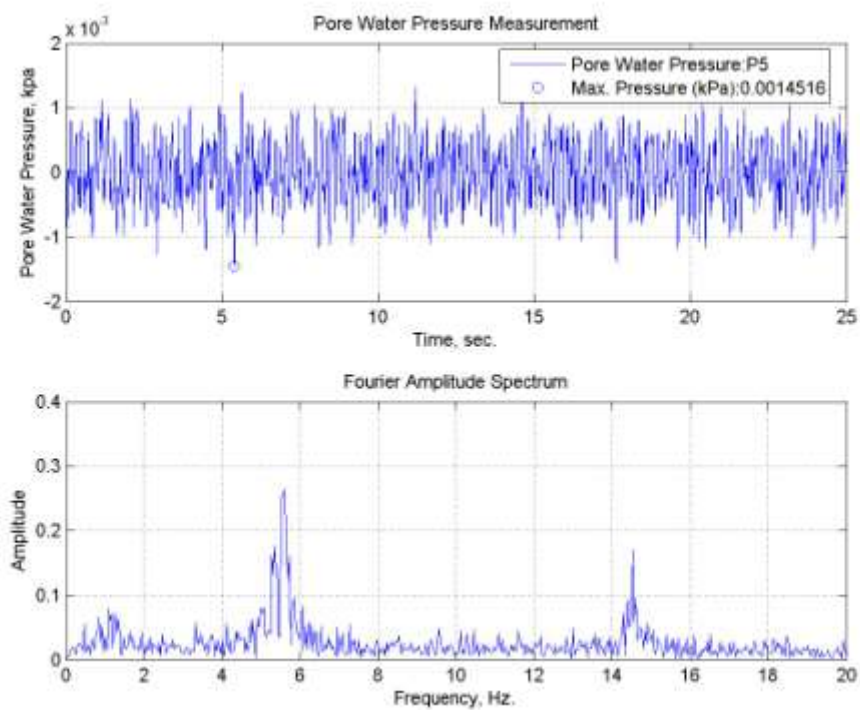


Figure B.115. Pore water pressure change of TB30 specimen tested at 50°C.

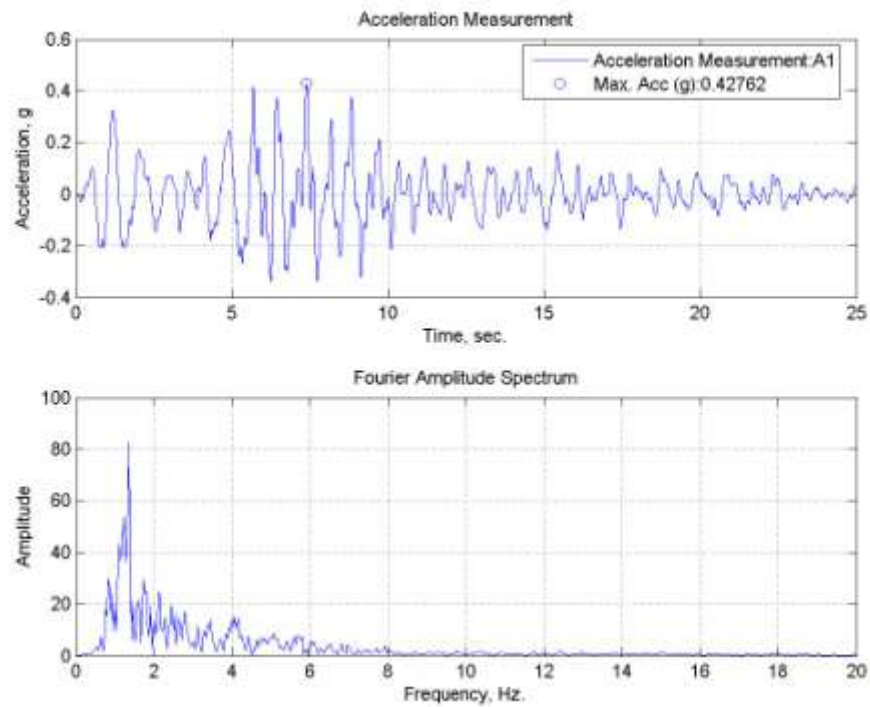
B.24. TC10 Specimen subjected to Tabas (E-W) Earthquake Motion at 50°C

Figure B.116. A1, acceleration time history of TC10 specimen tested at 50°C.

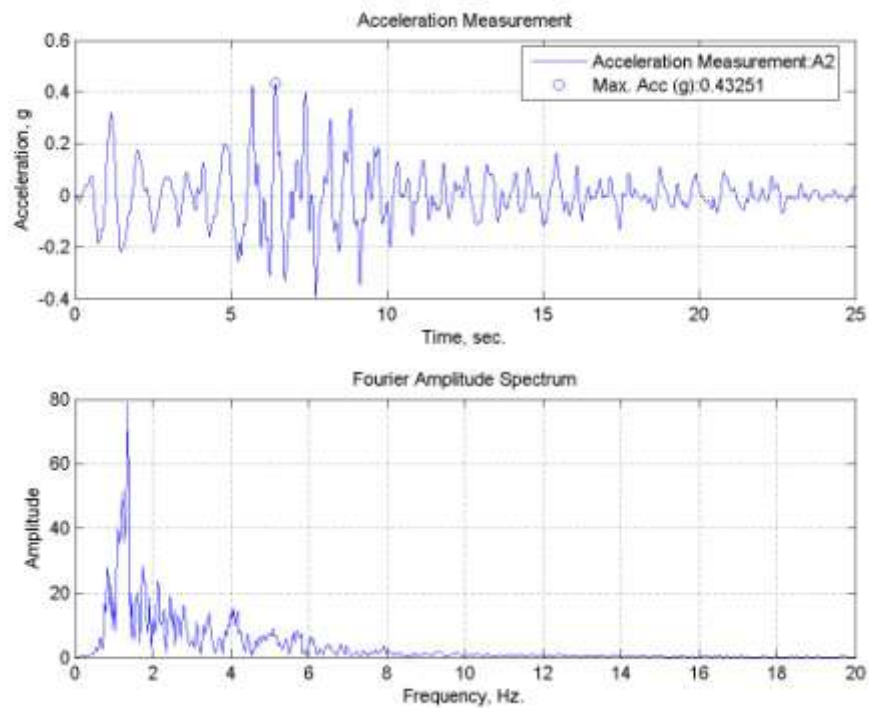


Figure B.117. A2, acceleration time history of TC10 specimen tested at 50°C.

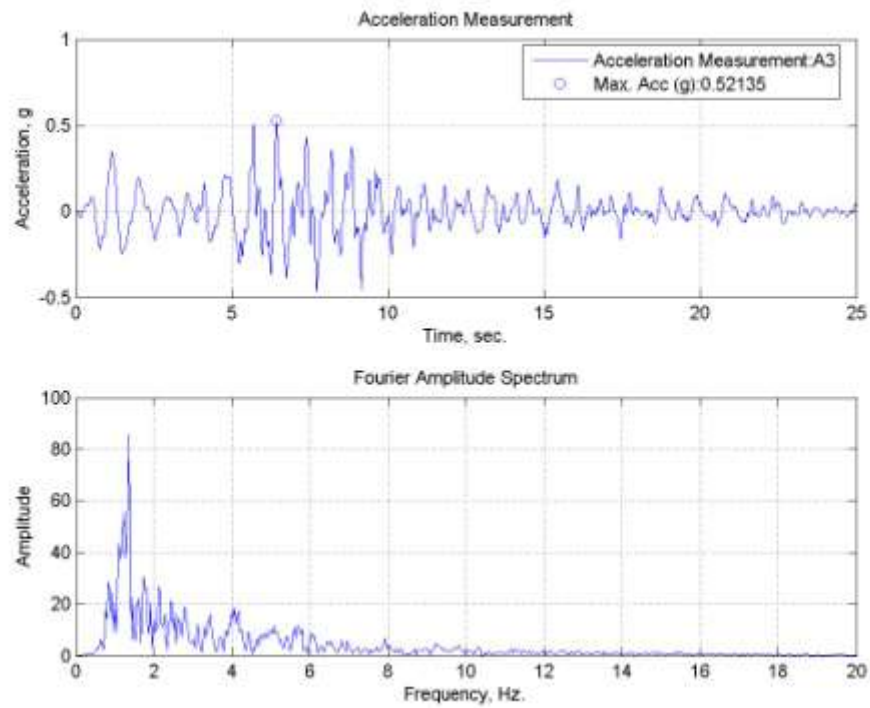


Figure B.118. A3, acceleration time history of TC10 specimen tested at 50°C.

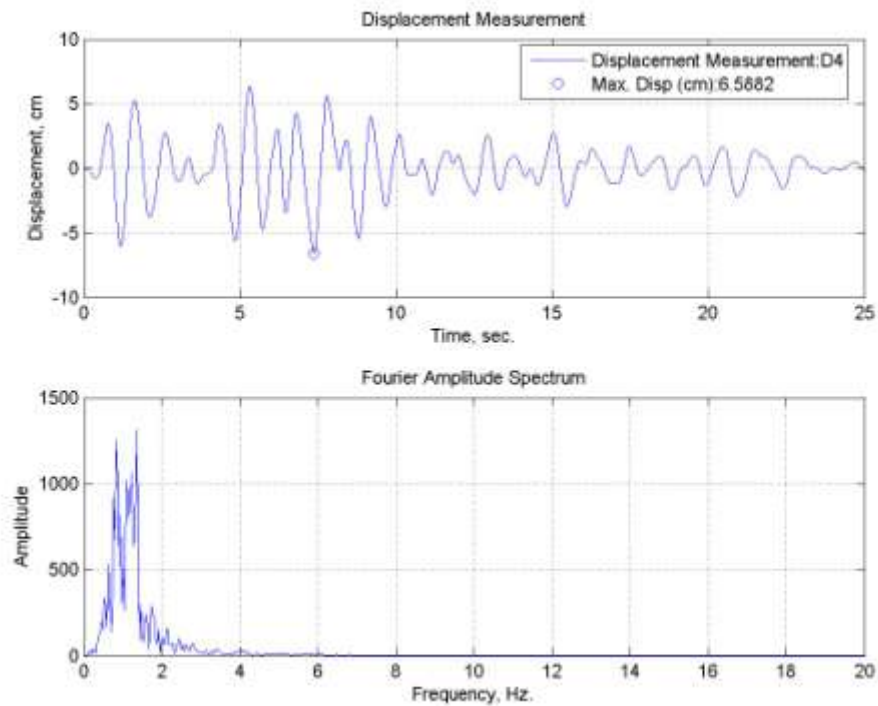


Figure B.119. Lateral displacement time history for TC10 specimen tested at 50°C.

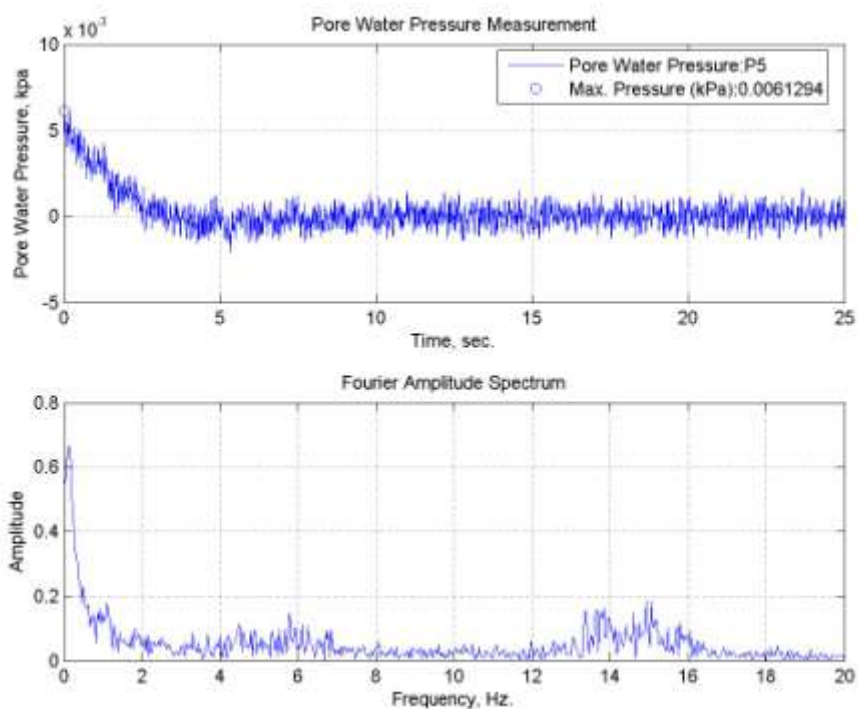


Figure B.120. Pore water pressure change of TC10 specimen tested at 50°C.

B.25. TC15 Specimen subjected to Tabas (E-W) Earthquake Motion at 50°C

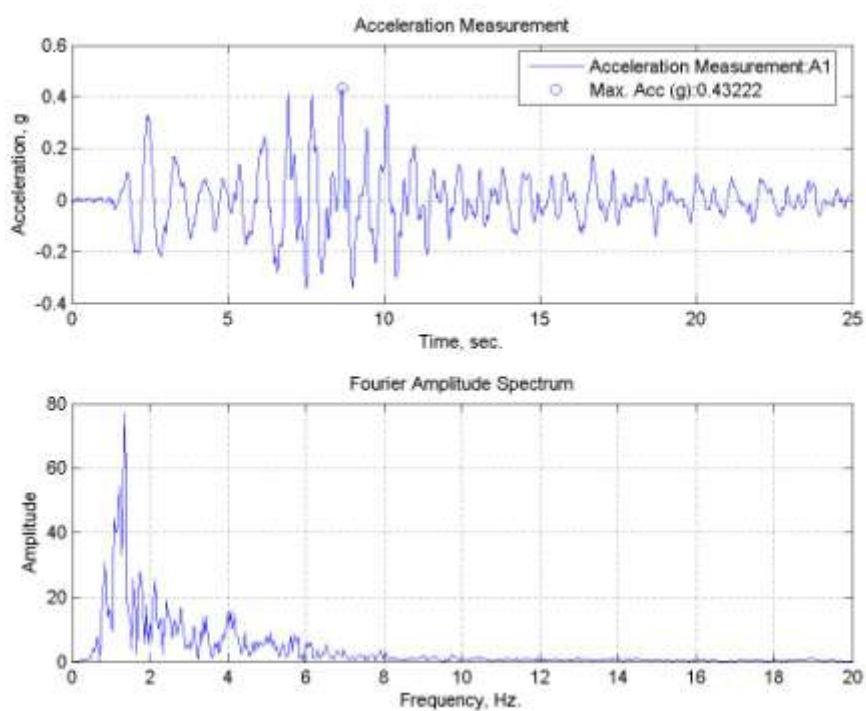


Figure B.121. A1, acceleration time history of TC15 specimen tested at 50°C.

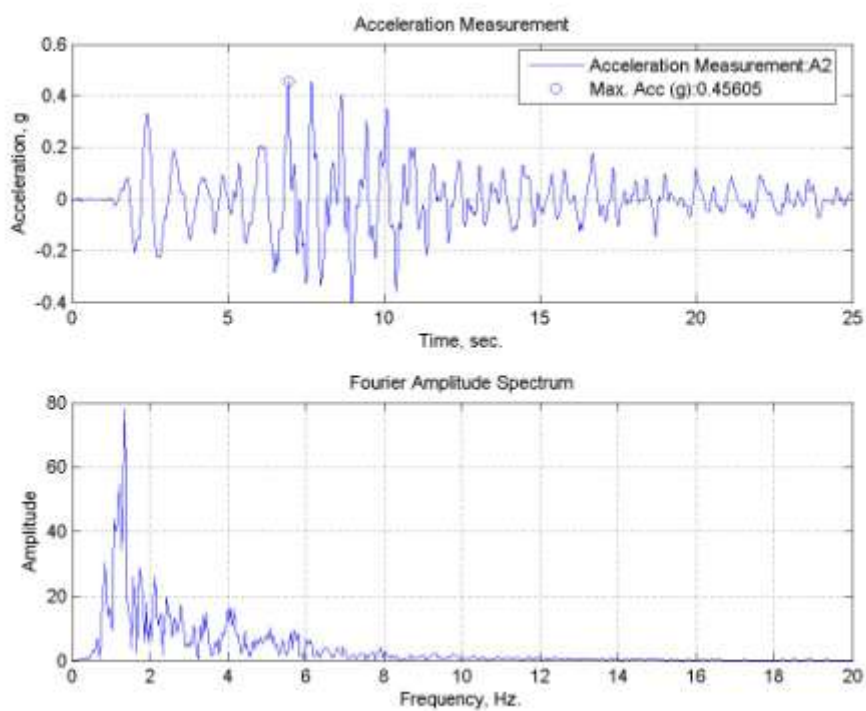


Figure B.122. A2, acceleration time history of TC15 specimen tested at 50°C.

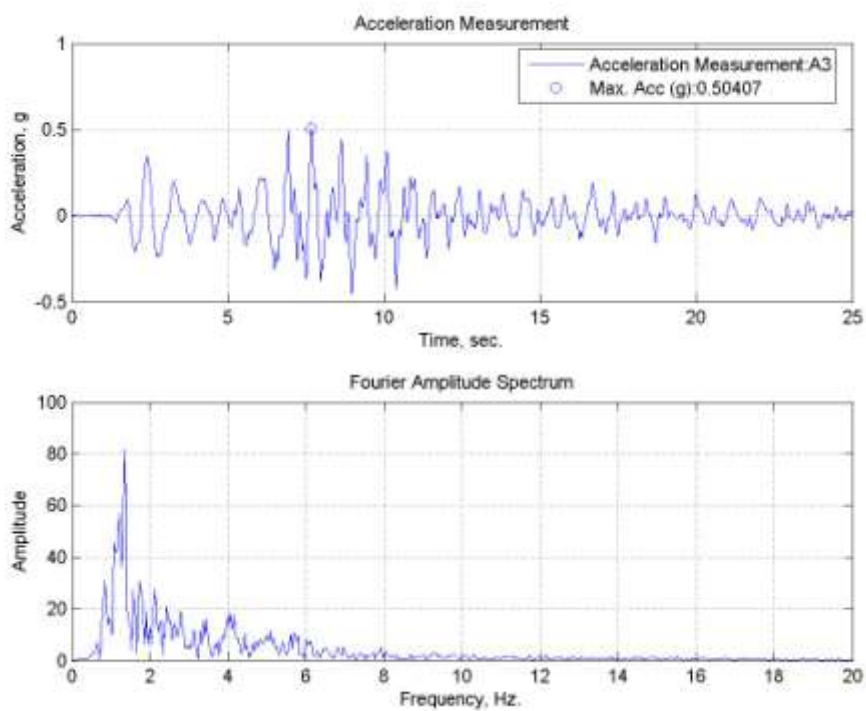


Figure B.123. A3, acceleration time history of TC15 specimen tested at 50°C.

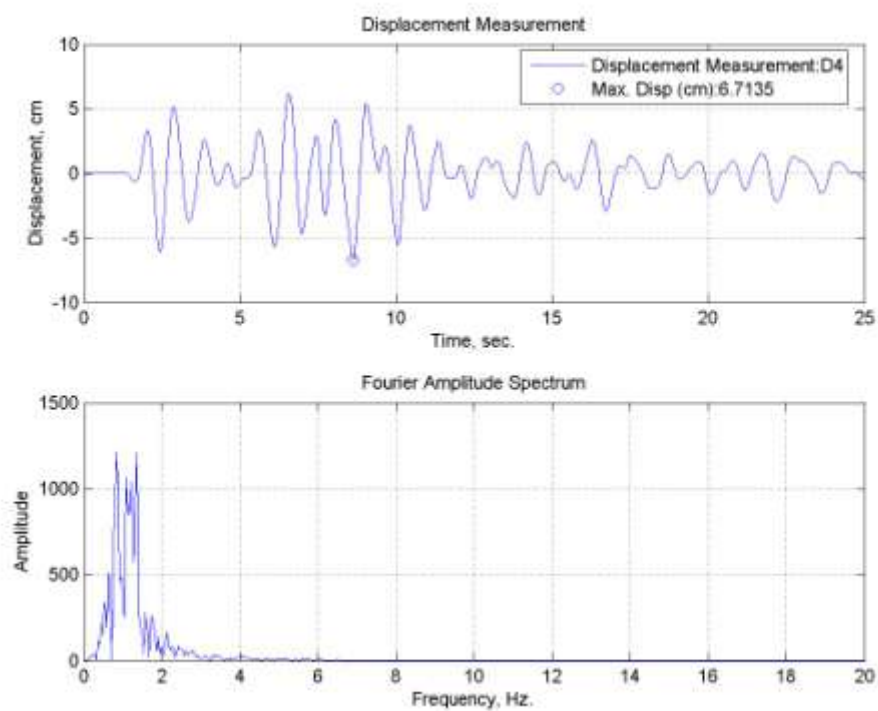


Figure B.124. Lateral displacement time history for TC15 specimen tested at 50°C.

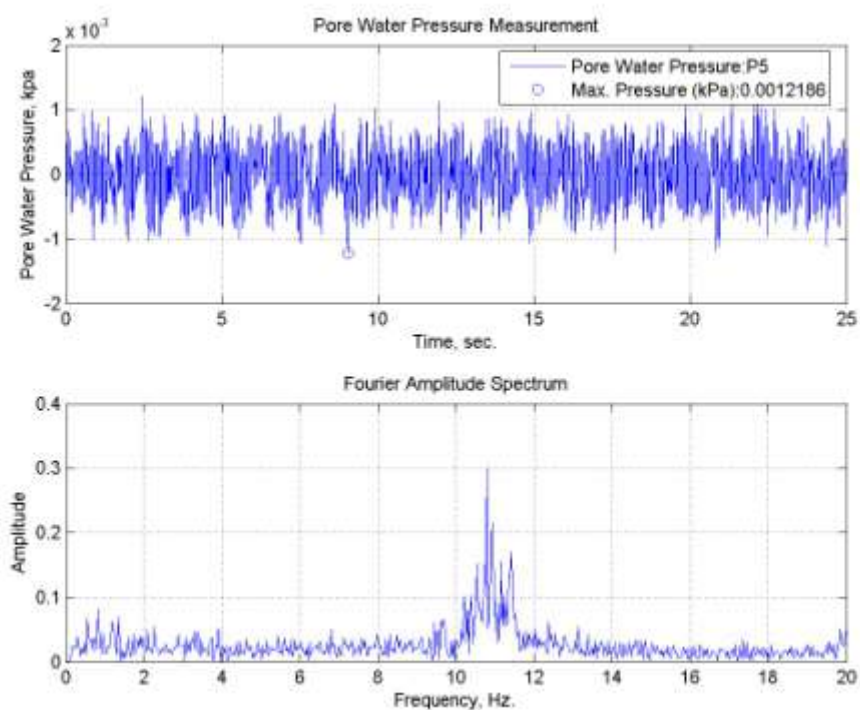


Figure B.125. Pore water pressure change of TC15 specimen tested at 50°C.

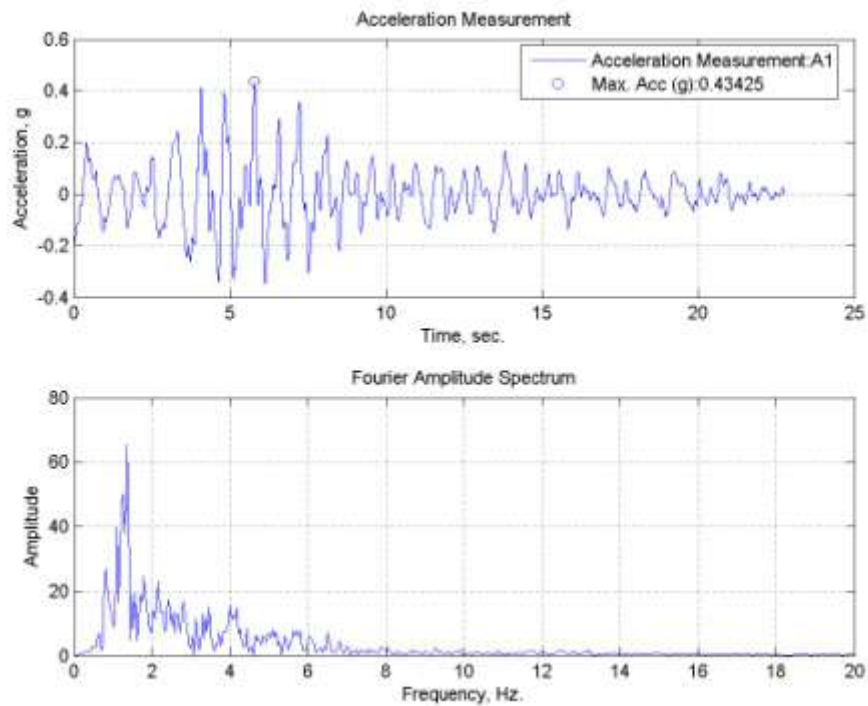
B.26. TC20 Specimen subjected to Tabas (E-W) Earthquake Motion at 50°C

Figure B.126. A1, acceleration time history of TC20 specimen tested at 50°C.

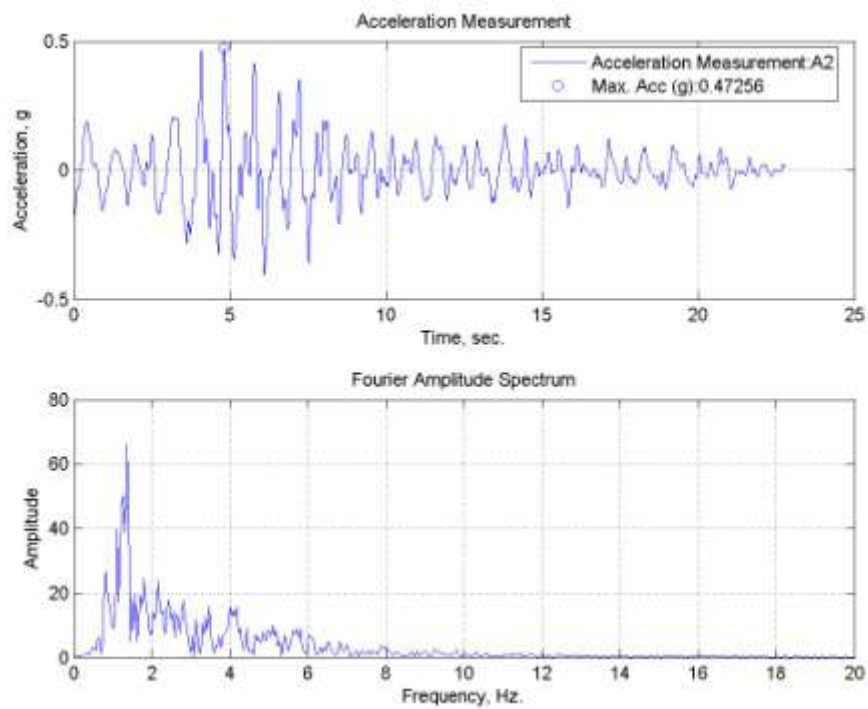


Figure B.127. A2, acceleration time history of TC20 specimen tested at 50°C.

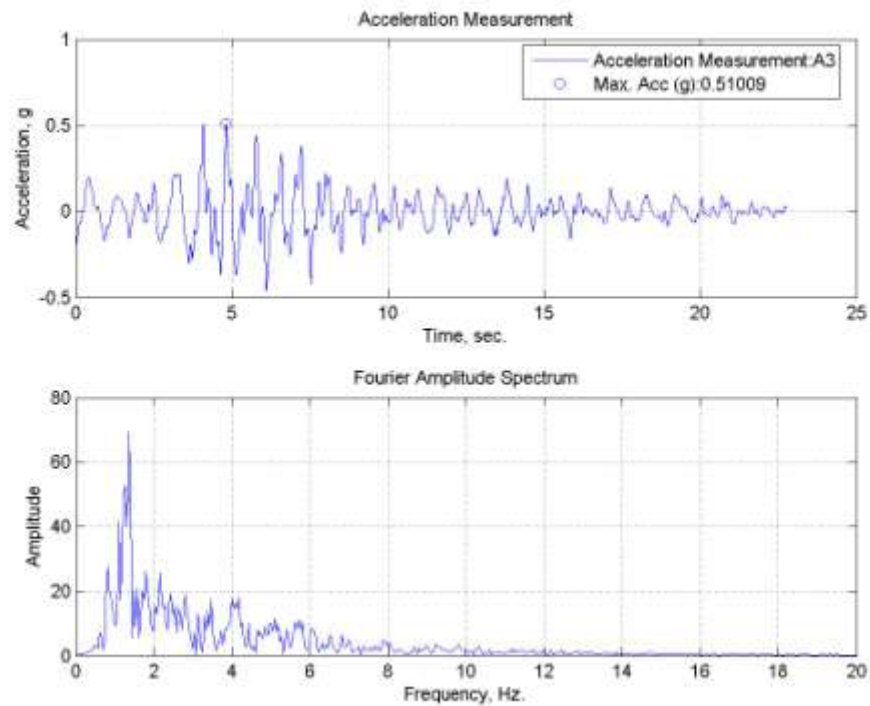


Figure B.128. A3, acceleration time history of TC20 specimen tested at 50°C.

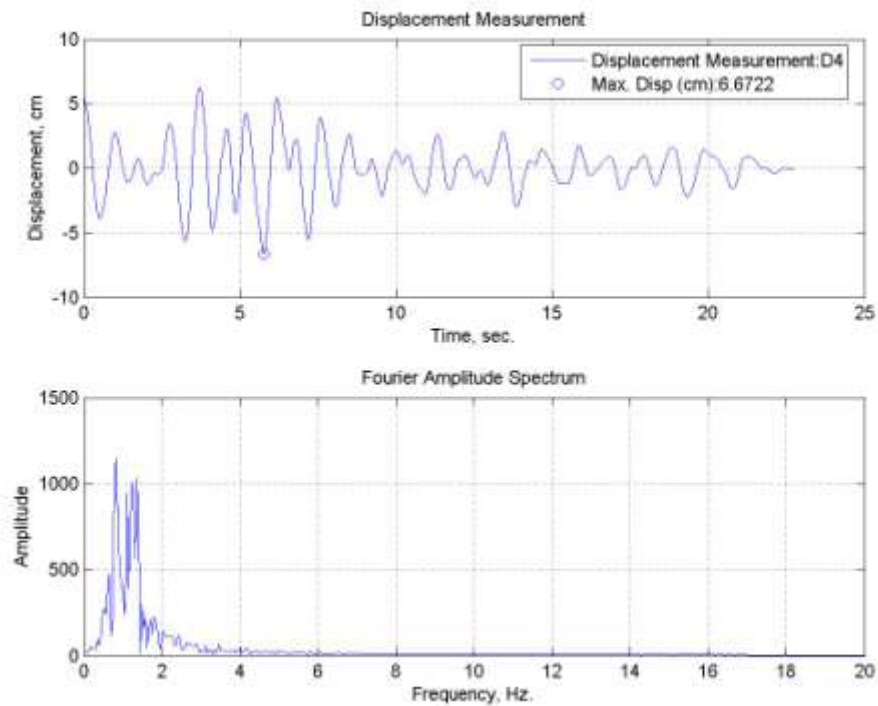


Figure B.129. Lateral displacement time history for TC20 specimen tested at 50°C.

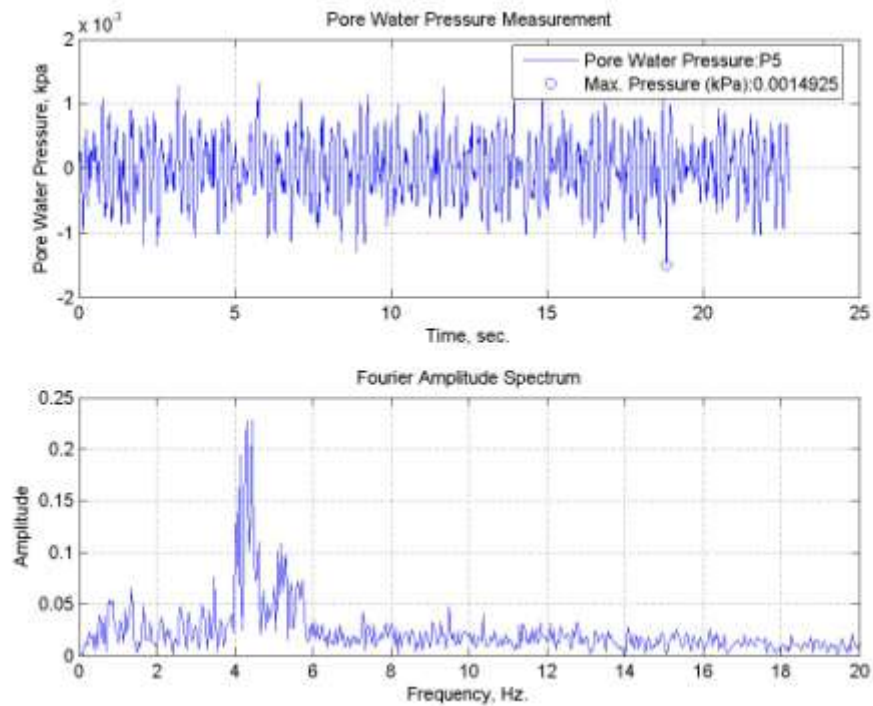


Figure B.130. Pore water pressure change of TC20 specimen tested at 50°C.

B.27. TC30 Specimen subjected to Tabas (E-W) Earthquake Motion at 50°C

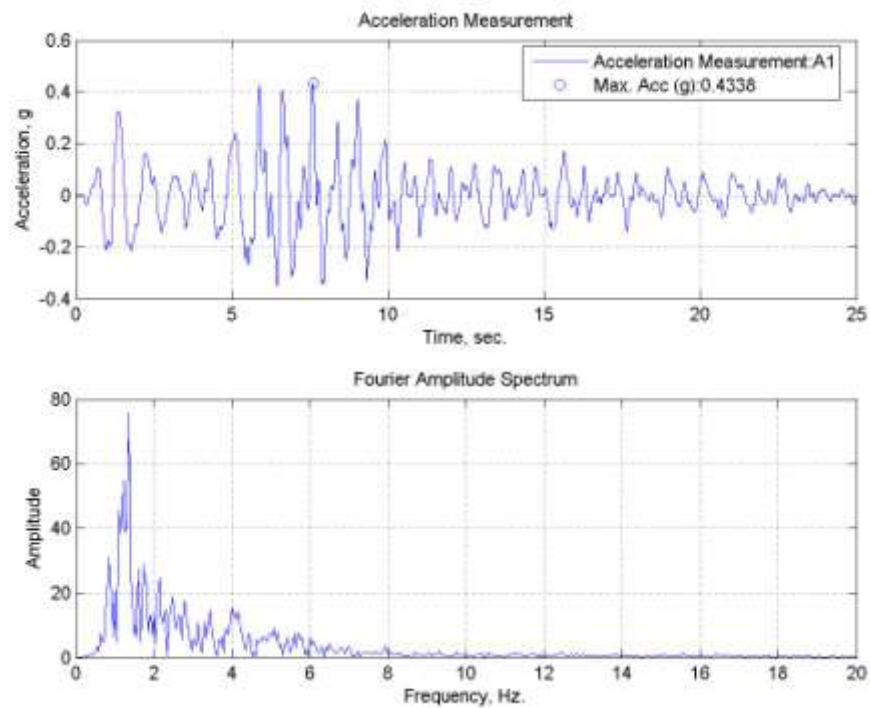


Figure B.131. A1, acceleration time history of TC30 specimen tested at 50°C.

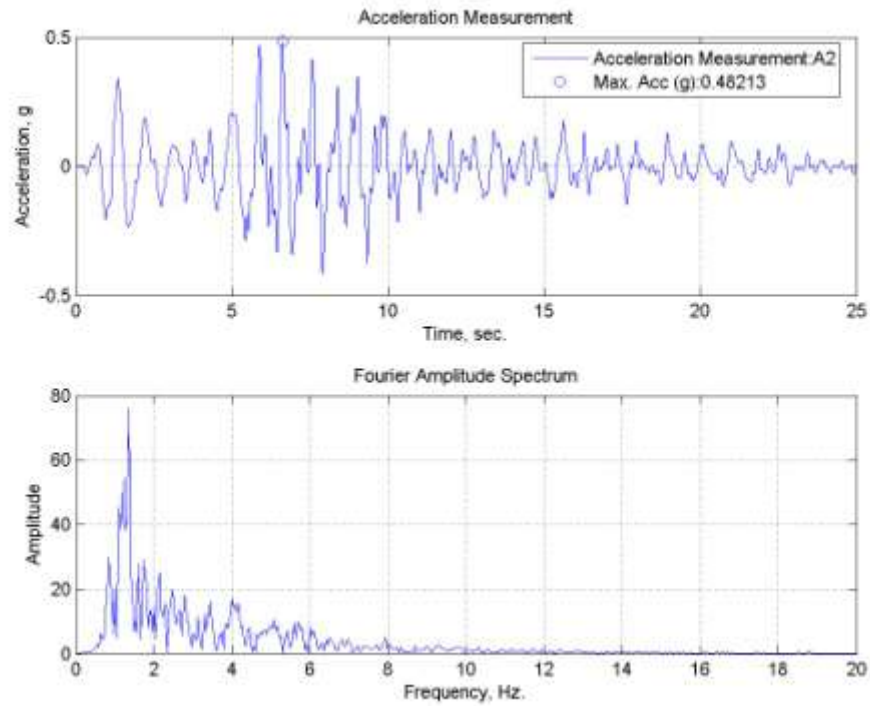


Figure B.132. A2, acceleration time history of TC30 specimen tested at 50°C.

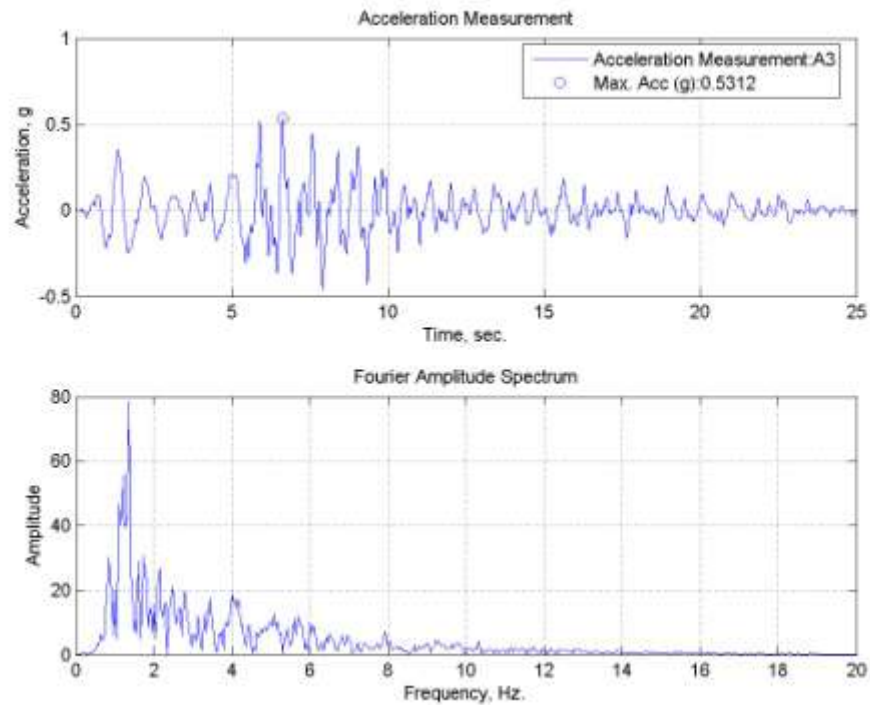


Figure B.133. A3, acceleration time history of TC30 specimen tested at 50°C.

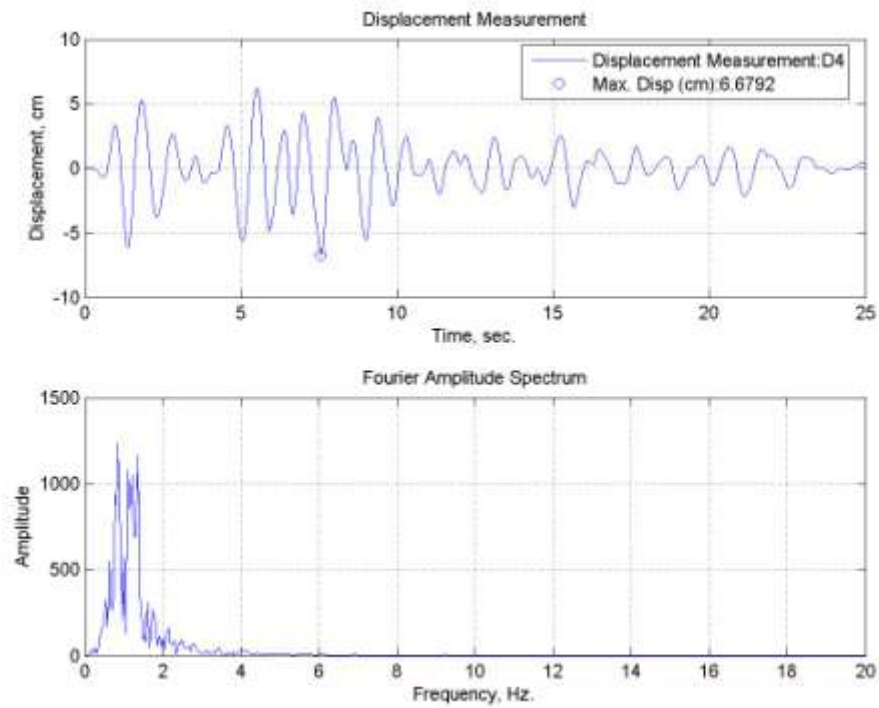


Figure B.134. Lateral displacement time history for TC30 specimen tested at 50°C.

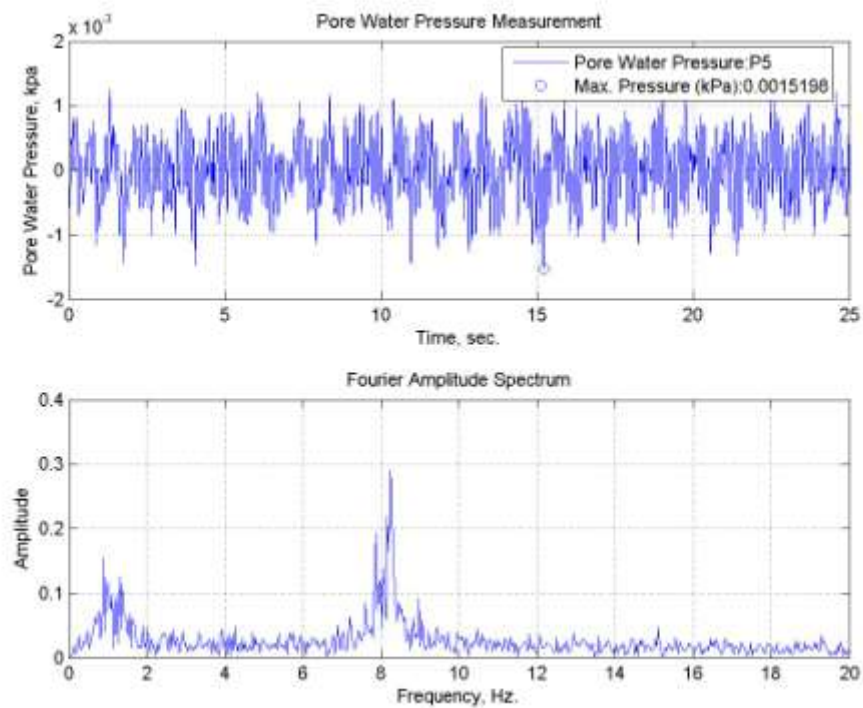


Figure B.135. Pore water pressure change of TC30 specimen tested at 50°C.

REFERENCES

- Ahmed, I. and C. W. Lovell, 1992, "Rubber Soils as Lightweight Geomaterial", *Transportation Research Record*, Vol. 1422, pp. 61-70.
- Anastasiadis A., K. Pitilakis and K. Senetakis, 2009, "Dynamic shear modulus and damping ratio curves of sand rubber mixtures", *Earthquake Geotechnical Engineering Satellite Conference, XVIIth International Conference on Soil Mechanics & Geotechnical Engineering*, Alexandria, Egypt.
- Arabani, M, S. M. Mirabdolazimi, A. R. Sasani, 2009, "The Effect of Tire waste Thread Mesh on the Dynamic of Asphalt Mixtures", *Construction and Building Materials*.
- ASTM D 854-02, 2002 ASTM D 854-02, *Standard test method for specific gravity of soil solids by water pycnometer, Annual Book of ASTM Standards*, American Society for Testing and Materials, West Conshohocken, pp. 1-7.
- ASTM D 1883-07, 2007, *Standard Test Method for CBR (California Bearing Ratio) of Laboratory-Compacted Soils*, American Society for Testing and Materials.
- ASTM D 3080., *Standard Test Method for Direct Shear Test of Soils under Consolidated Drained Conditions. ASTM International*, West Conshohocken, PA, USA.
- ASTM D3999, 2007, *Standard Test Method for Unconsolidated-Undrained Triaxial Compression Test on Cohesive Soils*, American Society for Testing and Materials.
- ASTM D 4253-00, 2002, *Standard test method for maximum index density and unit weight of soils using a vibratory table*, American Society for Testing and Materials.

ASTM D 4767-04, 2004, *Standard Test Method for Consolidated Undrained Triaxial Compression Test for Cohesive Soils*, American Society for Testing and Materials.

ASTM International Standarts, *Standard Test Method for Load Controlled Cyclic Triaxial Strength of Soil*, <http://www.astm.org/Standards/D5311.htm>, 2010.

ASTM D 6270-98, 1998, *Standard Practice for Use of Scrap Tires in Civil Engineering Applications*, American Society for Testing and Materials.

Attom, M.F., 2005, "The Use of Shredded Tire wastes to Improve the Geotechnical Engineering Properties of Sands", *Environmental Geology*, Vol. 49, pp.497-503.

Ayhan, V., 2007, *Determination and Assessment of Shear Strength Parameters of Sand with Tire Waste Inclusions*, M.S. Thesis, Bogazici University.

Bathurst, R. J., S. Zarnani and A.Gaskin, 2006, "Shaking Table Testing of Geofoam Seismic Buffers", *Soil Dynamics and Earthquake Engineering*, Vol. 27, pp. 324-332.

Bathurst, R. J., A. Keshavarz, S. Zarnani and W. A. Take, 2007, "A Simple Displacement Model for Reponse Analysis of EPS Geofoam Seismic Buffers ", *Soil Dynamics and Earthquake Engineering*, Vol. 27, pp. 344-353.

Bathurst, R. J. and S. Zarnani, 2008, "Numerical Modelling of EPS Seismic Buffers", *The 12th International Conference of International Association for Computer Methods and Advances in Geomechanics (IACMAG)*, pp. 425-432.

- Benson, C. and M. V. Khire, 1994, "Reinforcing Sand with Strips of Reclaimed High-Density Polyethylene", *Journal of Geotechnical and Geoenvironmental Engineering*, Vol. 120, No. 5, pp. 838-855.
- Benson, C. H., 1995, "Using Shredded Scrap Tires in Civil and Environmental Construction", *Resource Recycling*, Vol. 95, No. 2, pp. 1-4.
- Blockley, D., 1999, "Process modelling from reflective practice for engineering quality", *Civil Engineering and Environmental Systems*, Vol. 16, No. 4.
- Blumenthal, M., 2001, "What Works and What Doesn't Work in the Scrap Tire Industry", *Resource and Recycling*, Vol. 64, No. 4, pp. 200-207.
- Bolton, M. D., "Geotechnical Design of Retaining Walls", *The Structural Engineer*, Vol. 74, No. 21/5, pp. 365-369, 1996.
- Bolton, M. D. and J. M. R. Wilson, "Soil Stiffness and Damping", *Structural Dynamics*, Vol. 90, No. 1, pp. 209-216, 1990
- Bosscher, P. J., T. B. Edil, and S. Kuraoka, "Design of highway embankments using tire chips", *Geotechnical and Geoenvironmental Engineering*, Vol. 123, No. 4, pp. 295-304, 1997.
- Castro, G., "On the Behaviour of Soils During Earthquake", Elsevier Co., Winchester MA., 1987.
- Cerato, A. B and A. J. Lutenegeger, "Specimen Size and Scale Effects of Direct Shear Box Tests of Sands", *Geotechnical Testing Journal*, Vol. 29, No. 6, pp. 1-10, 2006.

- Cheung, T., D. C. Jansen, A. M. Asce and J. L. Hanson, “*Engineering Controlled Low Strength Materials Using Scrap Tire Rubber*”, California Poly State University, 2008.
- Crewe, A. J., M. L. Lings, C. A. Taylor, A. K. Yeung and R. Andrighetto, “Development of a Large Flexible Shear Stack for Testing Dry Sand and Simple Direct Foundations on a Shaking Table”, *European Seismic Design Practice*, pp. 163-168, 1995.
- Çağatay, A., 2008, *Investigation of The Effect of Tire Waste Inclusions on the Shear Strength Parameters of Sand*, M.S. Thesis, Bogazici University.
- Deng, An. and Y. Xiao, “ Measuring and Modelling Proportion-Dependent Stress-Strain Behaviour of EPS-Sand Mixture ”, *International Journal of Geomechanics*, Vol. 10, No. 6, pp. 214-222, 2010.
- Edil, T.B., “Mechanical Properties and Mass Behavior of Shredded Tire Soil Mixtures”, *Proceeding of the International Workshop on Lightweight Geomaterial*, Tokyo, 2002.
- Edil, T. B. and P. J. Bosscher, Development of Engineering Criteria for Shredded or Whole Tires in Highway Applications. Report No. WI 14-92, Department of Civil and Environmental Engineering, University of Wisconsin, Madison, 1992.
- Edil, T. B. and P. J. Bosscher, “Engineering Properties of Tire Chips and Soil Mixtures”, *Geotechnical Testing Journal*, Vol. 17, No. 4, pp. 453-464, 1994.
- Edinçliler, A., G. Baykal and K. Dengili, “Determination of Static and Dynamic Behaviour of Recycled Materials for Highways”, *Resources, Conservation and Recycling*, Vol. 42, pp. 223-237, 2004.

- Edinçliler, A. and V. Ayhan, “*Influence of Tire Fiber Inclusions on Shear Strength*”, Zemin Mekaniği ve Temel Mühendisliği Onüçüncü Ulusal Kongresi”, İstanbul Kültür Üniversitesi, İstanbul, 2010.
- Eseller-Bayat, E., "Seismic Response and Liquefaction Prevention of Sands Partially Saturated through Introduction of Gas Bubbles", Ph.D. Thesis, Northeastern University, Boston, 2009.
- ETRMA, End of Life tyres – “A Valuable Resource with a Wealth of Potential”, *Report of European Tyre & Rubber Manufacturers Association*, Brussel, 2006.
- Feng, Z.Y. and K. G. Sutter, “ Dynamic Properties of Granulated Rubber/Sand Mixtures”, *Geotechnical Testing Journal*, Vol. 23, No. 3, pp. 338-344, 2000.
- Foose, G. J., C.H.Benson and P.J. Bosscher, “Sand Reinforced with Rhredded Tire Wastes”, *Journal of Geotechnical Engineering*, Vol. 122, No. 9, pp. 760-767, 1996
- Finn, W. D. L., Bransby, P. L. and Pickering, D. J., “Effect of strain history on liquefaction of sand”, *Journal of the Soil Mechanics and Foundations Division*, Vol. 96, pp. 1917–1934, 1970.
- Gajo, A. and D. M . Wood, “Numerical Analysis of Shear Stack Under Dynamic Loading”, *11th European Conference on Earthquake Engineering*, 1998.
- Garga, V.K. & O’Shaughnessy, V., “Tire Reinforced Earthfill, Construction of a Test Fill, Performance, and Retaining Wall Design”, *Canadian Geotechnical Journal*, Vol. 37, pp. 75-96, 2000.

- Gazetas, G., "Vibrational Characteristics of soil deposits with variable velocity", *International Journal of Numerical and Analytical Methods*, Vol. 6, pp. 1-20, 1982.
- Ghazavi, M., "Shear Strength Characteristics of Sand-Mixed with Granular Rubber", *Geotechnical and Geological Engineering*, Vol. 22, pp. 401-416, 2004.
- Ghazavi, M. and M. A. Sakhi, "Influence of Optimized Tire shreds on Shear Strength Parameters of Sand", *International Journal of Geomechanics*, Vol. 5, No. 1, pp. 214-222, 2005.
- Ghazavi, M. and M. A. Sakhi, "Optimization of Aspect Ratio of Tire waste Shreds in Sand-Shred Mixtures Using CBR Tests", *Geotechnical Testing Journal*, Vol. 5, No. 1, pp. 58-6, 2005.
- Ghiassian, H., G. Poorebrahim and D. H. Gray, "Soil Reinforcement with Recycled Carpet Wastes", *Waste Management Research*, Vol. 22, pp. 108-114, 2004.
- Gotteland, P., S. Lambert and L. Balachowski, "Strength Characteristics of Tyre Chips-Sand Mixtures", *Studia Geotechnica et Mechanica*, Vol. 17, No. 1-2, 2005.
- Gray, D. H. and H. Ohashi, "Mechanics of fiber reinforcement in sand", *Journal of Geotechnical Engineering*, Vol. 109, No. 3, pp. 335-353, 1983.
- Gray, D. H. and T. Al-Refeai, "Behaviour of fabric versus fiber-reinforced sand.", *Journal Geotechnical Engineering*, Vol. 112, No. 8, pp. 804-820, 1986.
- Hazarika, H., "Mitigation of seismic Hazard on Retaining Structures", *Proceeding of the 11th International Offshore and Polar Engineering Conference*, pp. 459-464, 2001.

Hack, R., Z.Sicai, K.Turner, M.Hale, “How far will uncertainty of the subsurface limit the sustainability planning of the subsurface?”, <http://hack.home.xs4all.nl/WORKHack/research/uncerlik/index.html>., 2006.

Hoffmann, U., “Joint workshop of the Secretariat of the United Nations Conference on Trade and Development and the International Rubber Study Group on Rubber and the Environment”, 1998.

Humphrey, D. N., L. H. Chen, and R. Eaton, “Laboratory and field measurements of tire chips for use as subgrade insulation”, *Transportation Research Board 76th Annual Meeting*, Washington, 1997

Humphrey, D. N., T. Cosgrove, N. L. Whetten, and R. Hebert, “ Tire chips reduce lateral earth pressure against the walls of a rigid frame bridge”, *Seminar on Rehabilitation And Upgrades in Civil And Environmental Engineering*, 1997.

Humphrey, D. N. and W. L. Nickels, “Effect of tire chips as lightweight fill on pavement performance”, *Proceeding of XIV international Conference on Soil Mechanics and Foundation Engineering*, Balkema-Rotterdam, 1997.

Humphrey, D.N. and Tweedie, J.J., “Tire Shreds as Lightweight Fill for Retaining Walls- Results of Full Scale Field Trials”, *Proceeding of the International Workshop on Lightweight Geomaterial*, Tokyo, 2002.

Humphrey, D. N. and R. A. Eaton, “Tire chips as insulation beneath gravel surfaced roads”, *Proceeding of Frost in Geotechnical Engineering*, Balkema, Rotterdam, 1993.

- Ishihara K., “Stability of natural deposits during earthquakes”, *Proceedings of 11th International Conference on Soil Mechanics and Foundation Engineering*, Vol. 1, pp. 321-376, 1985.
- Ishihara, K. and M. Yoshimine, “Evaluation of settlements in sand deposits following liquefaction during earthquakes”, *Soils and Foundations*, Vol. 32 No. 1, pp. 173–188, 1992.
- Ishihara, K., “Liquefaction and flow failure during earthquakes”, *Geotechnique*, Vol. 43, No. 3, pp. 351-415, 1994.
- Ishihara, K., *Soil Behavior in Earthquake Geotechnics*, Oxford University Press Inc., New York, pp. 208–246, 1996.
- Koga, Y. and Matsuo, O., “Shaking table tests of embankments resting on liquefiable sandy ground”, *Soils and Foundations*, Vol. 30, No. 4, pp. 162-174, 1990.
- Kokusho, T., “Current state of research on flow failure considering void redistribution in liquefied deposits”, *Soil Dynamics and Earthquake Engineering*, Vol. 23, pp. 585-603, 2003.
- Lee, J. H., R. Salgado, A. Bernal and C. W. Lovell, “Shredded Tires and Rubber-Sand as Lightweight Backfill”, *Journal of Geotechnical and Geoenvironmental Engineering*, Vol. 125, No. 2, pp. 132–141, 1999.
- Masad, E., R. Taha, C. Ho and T. Papagiannakis, “Engineering Properties of Tire/Soil Mixtures as a Lightweight Fill Material”, *Geotechnical Testing Journal*, Vol. 19, No. 3, pp. 297-304, 1996.

- Maugeri, M., G. Musumeci, D. Novita and C. A. Taylor, "Shaking Table Test of Failure of a Shallow Foundation Subjected to an Eccentric Load", *Soil Dynamics and Earthquake Engineering*, Vol. 20, pp. 435-444, 2000.
- Michalowski, R. L. and A. Zhao, "Failure of Fiber-Reinforced Granular Soils", *Journal of Geotechnical and Geoenvironmental Engineering*, Vol. 122, No. 3, pp. 226-234, 1996.
- Michalowski, R. L. and J. Cernak, "Triaxial Compression of Sand Reinforced with Fibers", *Journal of Geotechnical and Geoenvironmental Engineering*, Vol. 129, No. 2, pp. 125-136, 2003.
- Moo-Young, H., K. Sellasie, D. Zeroka and G. Sabnis, "Physical and Chemical Properties of Recycled Tire Shreds for Use in Construction", *Journal of Geotechnical and Geoenvironmental Engineering*, Vol. 129, No. 10, pp. 921-929, 2003.
- Mortara, G., D. Ferrara and G. Fotia, "Simple Model for the Cyclic Behaviour of smooth Sand-Steel Interfaces", *Journal of Geotechnical and Geoenvironmental Engineering*, pp. 501-510, 2010.
- Orense, P. O., "*Geotechnical Hazards: Nature, Assessment, and Mitigation*", University of the Philippines Press, Michigan, 2003.
- Ozener, P.T., M.M. Berilgen and K. Özeydin, 2009, "Investigation of Liquefaction and Pore Water Pressure Development in Layered Sands", *Bulletin of Earthquake Engineering*, Vol.7, No.1, pp. 199-219.

- Pamukcu, S. and S.Akbulut, “Thermoelastic Enhancement of Damping of Sand Using Synthetic Ground Rubber”, *Journal of Geotechnical and Geoenvironmental Engineering*, Vol. 132, No. 4, pp. 501-510, 2006.
- Pitilakis D, M. Dietz, D. M. Wood , D. Clouteau and A. Modaressi, “Numerical simulation of dynamic soil-structure interaction in shaking table testing”, *Soil Dynamics and Earthquake Engineering*, Vol. 28, No. 6, pp. 453–467, 2008.
- Poulos, S. J., G. Castro, and W. France, “Liquefaction evaluation procedure” *Journal of Geotechnical Engineering*, Vol. 111, No. 6, pp. 772–792, 1985.
- Prasad S. K., I. Towhata, G. P. Chandradhara and P. Nanjundaswamy, “Shaking Table Tests in Earthquake Geotechnical Engineering”, *Current Science*, Vol. 87, No. 10, pp. 1398-1404, 2004.
- Rauch, A.F., “Soil Liquefaction in Earthquakes”, *Computer Simulation of Earthquake Effects*, Vol. 2, pp. 7-18, 2000.
- Ribay, E. D., I. D. Maigre, R. Cabrillac and D. Gouvenot, “Shear modulus and Damping Ratio of Grouted Sand”, *Soil Dynamics and Earthquake Engineering*, Vol. 24, pp. 461-471, 2004.
- Richards R, Elms D.G., and Budhu M., “Dynamic fluidization of soils”, *Journal of Geotechnical Engineering Division*, Vol. 116, No. 5, pp. 740-759, 1991.
- RMA, Scrap Tire Markets in the United States, Rubber Manufacturers Association Report, 2000.

RMA, Scrap Tire Markets in the United States, Rubber Manufacturers Association Report, 2006.

Robertson, P.K. and Fear, C.E., "Liquefaction of Sands and its Evaluation", *1st International Conference on Earthquake Geotechnical Engineering*, A.A. Balkema/Rotterdam/Brookfield, Arizona 1999.

Sadek, S., S. S. Najjar, A.M. Asce, and F. Freiha, "Shear strength of Fiber Reinforced Sands", *Journal of Geotechnical and Geoenvironmental Engineering*, Vol. 136, No. 3, pp. 490-499, 2010.

Scrap Tire Management Council, "Used Tire Facts and Information - What To Do With All These Tires?", <http://www.epa.state.il.us/land/tires/used-tires-facts-and-information.html>, 2010.

Seed, H.B., Idriss I.M., "Ground Motions and Soil Liquefaction During Earthquakes" Earthquake Research Institute, Berkeley, California, 1982.

Seed, H.B., Idriss, I.M, I.Arrango, "Evaluation of Liquefaction Potential Using filled Performance Data", *Journal of Geotechnical&Geoenvironmental Engineering*, Vol. 109, No. 3, pp. 458-482, 1983.

Sitharam, T. G., L.G. Raju and A. Sridharan, "Dynamic Properties and Liquefaction Potential of Soils", *Current Science*, Vol. 87, No. 10, pp. 1370-1378, 2004.

Stark, D.T. and M. Hussain, "Shear Strength in Preexisting Landslides", *Journal of Geotechnical and Geoenvironmental Engineering*, Vol. 137, No. 8, pp. 957-962, 2009.

- Tatlısoz, N., C. H. Benson and T. B. Edil., "Effect of Fines on Mechanical Properties of Soil-Tire Chip Mixtures", *Testing Soil Mixed with Waste or Recycled Materials*, 1997.
- Tatlısoz, N., T. B. Edil and C. H. Benson, "Interaction Between Reinforcing Geosynthetics and Soil-tire Chip Mixtures", *Geotechnical and Geoenvironmental Engineering*, Vol. 124, No. 11, pp. 1109-1119, 1998.
- Taylor, C. A., A. R. Dar and A. J. Crewe, "Shaking Table Modelling of Seismic Geotechnical Problems", pp. 441-446, 1995.
- Tsang, H.H., F.H. Fong, X.Xu and S.H.Lo, "Utilization of Scrap Tires for Earthquake Hazard Mitigation", pp. 171-182, 2010.
- Tsuchida H., "Prediction and Countermeasure Against the Liquefaction in Sand Deposits", *Abstract of the Seminar in the Port and Harbor Research Institute*, pp. 3.1-3.33, 1970.
- Turan, A., S. D. Hinchberger and H. E. Naggar, "Design and Commissioning of a Laminar Soil container for Use on small Shaking Tables", *Soil Dynamics and Earthquake Engineering*, Vol. 29, pp. 404-414, 2008.
- Turgut, P. and B.Yeşilata, "Physico-mechanical and Thermal Performances of Newly Developed Rubber-added Bricks", *Energy and Buildings*, Vol. 40, pp. 679-688, 2008.
- Tweedie, J. J., D. N. Humphrey and T. C. Sandford, "Tire shreds as lightweight retaining wall backfill: Active conditions" *Journal of Geotechnical and Geoenvironmental Engineering*, Vol. 124, No. 1, pp. 1061-1070, 1998.

Ueng., T, M. Wang, M. Chen, C. Chen and L.Pseng, “A Large Biaxial Shear Box for Shaking Table Test on Saturated Sand”, *Geotechnical Testing Journal*, Vol. 29, No. 1, pp. 1-8, 2006.

University Of British Columbia, “Static and Cyclic Triaxial Shear Device(s)”, http://www.rctlma.org/trans/road_main_slurry_seal.html, 2010.

USEPA, Management of Scrap Tires. The U.S. Environmental Protection Agency Report, 2006.

U.S. Department of Transportation Federal highway Administration, “User Guidelines for Waste and Byproduct Materials in Pavement Construction”, <http://www.tfhr.gov/hnr20/recycle/waste/st1.htm>, 2010.

Warith, M. A., E: Evgin, and P. A Benson, “Suitability of shredded tires for use in leachate collection systems.”, *Waste Management*, Vol. 24, No. 1, pp. 967-979, 2004.

Ueng. T., C. W. Wu, H. W. Cheng and C. H. Chen, “Settlements on Saturated Clean Sand Deposits in shaking Table Tests”, *Soil Dynamics and Earthquake Engineering*, Vol. 30, No. 1, pp. 50-60, 2010.

Wood, M. D., A. Crewe and C. Taylor, “Shaking Table Testing of Geotechnical Models”, *International Journal of Physical Modelling in Geotechnics*, Vol. 2, No.1, pp. 1-13, 2002.

Wu, W. Y., C. C. Benda and R. F. Cauley, “Triaxial Determination of Shear Strength of Tire Chips,” *Journal of Geotechnical and Geoenvironmental Engineering*, Vol. 123, No. 5, pp. 479-482, 1997.

- Xu, X., S. H. Lo and H. H. Tsang, "Earthquake Protection by Tire-Soil Mixtures: Numerical Study", *2009 NZSEE Conference*, New Zealand, 2009.
- Yang, S., R. A. Lohnes, B. H. Kjartanson, "Mechanical Properties of Shredded Tires" *Geotechnical Testing Journal*, Vol. 25, No. 1, pp. 44-52, 2002.
- Yang, H. S., D.J. Kim, Y. K. Lee, H. J. Kim, J. Y. Jeon and C. W. Kang, " Possibility of Using Tire waste Composites Reinforced with Rice Straw as Construction Materials", *Bioresource Technology*, Vol. 95, pp. 61-65, 2004.
- Yegian, M., E. Eseller and A. Alshawabkeh, "Preparation and Cyclic Testing of Partially Saturated Sands", *Proceedings of the Fourth International Conference on Unsaturated Soils*, Arizona, 2006.
- Yegian, M. K., E. Eseller-Bayat and A. Alshawabkeh, "Induced Partial Saturation for Liquefaction Mitigation: Experimental Investigation.", *Journal of Geotechnical and Geoenvironmental Engineering*, Vol. 133, No. 1, 2007.
- Venkatappa, R. and R. K. Dutta, "Compressibility and Strength Behaviour of Sand-Tyre Chip Mixtures", *Geotechnical and Geological Engineering*, Vol.24, No. 3, pp. 711- 724, 2006.
- Yesilata, B.and P.Turgut, "A Simple Dynamic Measurement Technique for Comparing Thermal Insulation Performances of Anisotropic Building Materials", *Energy and Building*, Vol. 39, pp. 1027-1034, 2007.
- Yesilata, B., Y.Isiker and P.Turgut, " Thermal Insulation Enhancement in Concretes by Adding Waste PET and Rubber Pieces ", *Construction and building Materials*, Vol. 23, pp. 1878-182, 2009.

- Yetimoglu, T. and O. Salbas, "A Study on Shear Strength of Sands Reinforced with Randomly Distributed Discrete Fibers", *Geotextiles and Geomembranes*, Vol. 21, pp. 103-110, 2003.
- Yetimoglu, T., M. İnanır and O. E. İnanır, "A Study on Bearing Capacity of Randomly Distributed Fiber-Reinforced Sand Fills Overlying Soft Clay", *Geotextiles and Geomembranes*, Vol. 23, pp. 174-183, 2005.
- Yoon, Y. W., S. B. Heo and K. S. Kim, "Geotechnical Performance of Tire wastes for Soil Reinforcement from Chamber Tests", *Geotextiles and Geomembranes*, Vol.26, pp. 100-107, 2008.
- Yoon, S., M. Prezzi, N. Z. Siddiki and B. Kim, "Construction of a Test Embankment Using a Sand-Tire Shred Mixture as Fill Material", *Waste Management*, Vol.26, No. 3, pp. 1033- 1044, 2003.
- Youd, T. L. and S. G. Gilstrap, "Liquefaction and deformation of silty and fine-grained soils", *Proceedings of 2nd International Conference on Earthquake Geotechnical Engineering*, Vol. 3, pp. 1013–1020, Lisbon, 1999.
- Youd, T.L., and D.M. Perkins, "Mapping liquefaction-induced ground failure potential", *Journal of the Geotechnical Engineering Division*, p. 443-446, 1978.
- Young, H.M., K. Sellasie, Zeroka and G. Sabris, "Physical and chemical properties of recycled tire shreds for use in construction", *Journal of Environmental Engineering*, Vol. 129, No. 10, pp. 921-929, 2003.
- Zarnani, S., and R. J. Bathurst, "Numerical investigation of geofoam seismic buffers using FLAC", *In Proceedings of the North American Geosynthetics Society (NAGS)/GRI19 Conference*, Las Vegas, 2005.

Zarnani, S., and R. J. Bathurst, "Numerical modeling of EPS seismic buffer shaking table tests", *Geotextiles and Geomembranes*, Vol. 26, No. 5, pp. 371-383, 2008.

Zarnani, S., and R. J. Bathurst, "Numerical Modelling of EPS Seismic Buffer Shaking Table Test", *The 12th International Conference of International Association for Computer Methods and Advances in Geomechanics (IACMAG)*, India, 2008.

Zhi, W. H., X. He and X. X. Jian, "Review of Tire waste Reuse&Recycling in China", *Advances in Natural Science*, Vol. 2, No. 1, pp. 31-39, 2009.

Zhong, X. G., X. Zeng and J. G. Rose, "Shear Modulus and Damping Ratio of Rubber-modified Asphalt Mixes and Unsaturated Subgrade Soils", *Journal of Materials in Civil Engineering*, Vol. 14, No. 6, pp. 496-501, 2002.

Zornberg, J. G., "Discrete Framework for Limit Equilibrium Analysis of Fiber-Reinforced Soil", *Geotechnique*, Vol. 52, No. 8, pp. 593-604, 2002.

Zornberg, J. G., A. R. Cabral and C. Viratjandr, "Behaviour of Tire Shred-Sand Mixtures", *Canadian Geotechnical Journal*, Vol. 41, pp. 227-241, 2004.